



Cyprus  
University of  
Technology

Faculty of Engineering  
and Technology

**Doctoral Dissertation**

**MONITORING AND ASSESSMENT OF THE IMPACT OF  
NATURAL HAZARDS ON INFRASTRUCTURE  
RESILIENCE USING EARTH OBSERVATION  
TECHNIQUES**

**Marios Tzouvaras**

**Limassol, April 2020**



CYPRUS UNIVERSITY OF TECHNOLOGY  
FACULTY OF ENGINEERING AND TECHNOLOGY  
DEPARTMENT OF CIVIL ENGINEERING AND GEOMATICS

Doctoral Dissertation

MONITORING AND ASSESSMENT OF THE IMPACT OF  
NATURAL HAZARDS ON INFRASTRUCTURE RESILIENCE  
USING EARTH OBSERVATION TECHNIQUES

Marios Tzouvaras

Limassol, April 2020

# Approval Form

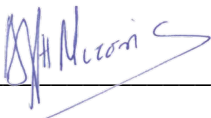
Doctoral Dissertation

## **MONITORING AND ASSESSMENT OF THE IMPACT OF NATURAL HAZARDS ON INFRASTRUCTURE RESILIENCE USING EARTH OBSERVATION TECHNIQUES**

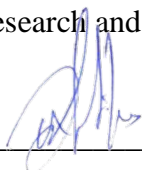
Presented by

Marios Tzouvaras

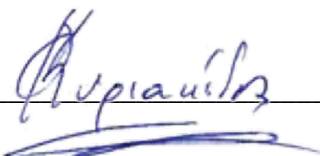
Supervisor: Diofantos G. Hadjimitsis, Professor, Cyprus University of Technology

Signature  \_\_\_\_\_

Member of the Examination Committee: Nektarios Chrysoulakis, Director of Research,  
Foundation for Research and Technology – Hellas (FORTH)

Signature  \_\_\_\_\_

Member of the Examination Committee: Phaedon Kyriakidis, Professor, Cyprus  
University of Technology

Signature  \_\_\_\_\_

Cyprus University of Technology

Limassol, April 2020

Doctoral Dissertation

**MONITORING AND ASSESSMENT OF THE IMPACT OF  
NATURAL HAZARDS ON INFRASTRUCTURE RESILIENCE  
USING EARTH OBSERVATION TECHNIQUES**

Presented by

Marios Tzouvaras

Supervising Committee:

Supervisor: Diofantos G. Hadjimitsis, Professor

Member of the committee: Evangelos Akylas, Associate Professor

Member of the committee: Andreas Andreou, Professor

Cyprus University of Technology

Limassol, April 2020

## **Copyrights**

Copyright © 2020 Marios Tzouvaras

All rights reserved.

The approval of the dissertation by the Department of Civil Engineering and Geomatics does not imply necessarily the approval by the Department of the views of the writer.

*Αφιερώνω την παρούσα διατριβή στη σύζυγο μου Έλενα, στην κόρη μου Μελίνα, στους γονείς μου Κωνσταντίνο και Ελένη και στον αδερφό μου Δημήτρη. Όλοι τους, με την αγάπη τους, τη συνεχή τους συμπαράσταση και την υπομονή τους, μου έδωσαν τη δύναμη να συνεχίσω να εργάζομαι στην Διδακτορική μου διατριβή έως και την ολοκλήρωσή της.*

## ACKNOWLEDGEMENTS

The present study was carried out under the PhD course of studies of the Department of Civil Engineering and Geomatics at the Cyprus University of Technology (CUT), within the activities of the ERATOSTHENES Research Centre (ERC) (Remote Sensing and Geo-environment Research Lab), and under the auspices of the ‘EXCELSIOR’ – ERATOSTHENES: Excellence Research Centre for Earth Surveillance and Space-Based Monitoring of the Environment Horizon 2020 Widespread Teaming project (<https://excelsior2020.eu/>). ‘EXCELSIOR’ has received funding from the European Union’s Horizon 2020 research and innovation programme (Grant Agreement No 857510) and from the Government of the Republic of Cyprus through the Directorate General for the European Programmes, Coordination and Development.

Moreover, part of the research presented in this PhD thesis was conducted in the framework of CLIMA – “Cultural Landscape risk Identification, Management and Assessment” project (<http://www.clima-project.eu/>), funded through the Joint Programming Initiative for Cultural Heritage (KOINA/IJKII-Heritage Plus/0314/07). Last but not least, the present research was carried out partially within the CyCLOPS project (<https://cyclops-rpf.eu/>), which stands for Cyprus Continuously Operating Natural Hazards Monitoring and Prevention System (RPF/INFRASTRUCTURES/1216/0050). CyCLOPS is co-financed by the European Union Regional Fund and the Republic of Cyprus through the Research Promotion Foundation.

First of all, I would like to express my sincere gratitude and appreciation to my PhD supervisor Professor Diofantos G. Hadjimitsis who supported this study during this period. His guidance and contributions were precious, enlightening and encouraging. I would also like to thank my advisory committee, Associate Professor Evangelos Akylas, Chair of the Department of Civil Engineering and Geomatics and Professor Andreas Andreou at the Department of Electrical Engineering, Computer Engineering and Informatics, for their continuous support and advice throughout my PhD studies. Moreover, I would like to thank the members of my thesis examination committee, Dr. Nektarios Chrysoulakis, Director of Research at the Foundation for Research and Technology – Hellas (FORTH) in Heraklion, Greece and Professor Phaedon Kyriakidis



at the Department of Civil Engineering and Geomatics and Dean of Faculty of Engineering and Technology at CUT, for their advice and constructive feedback.

I am especially indebted to Assistant Professor Chris Danezis at the Department of Civil Engineering and Geomatics, and Postdoctoral Researcher Dr. Athos Agapiou, for their valuable scientific inputs and the constructive exchange of ideas during my PhD studies, as well as their contributions and remarks in the various journal and conference publications. Furthermore, I would like to thank all my colleagues at the ERATOSTHENES Research Centre for the cooperation that we had all these years in the context of our research activities and for their continuous support and assistance during my research.

Last, but certainly not least, I would like to express my appreciation for the continuous encouragement and support of my family and friends.

The author would like to thank the support of the Remote Sensing and Geo-Environment Lab (ERC group) at the Department of Civil Engineering and Geomatics of the Cyprus University of Technology and the 'EXCELSIOR' H2020 Teaming Project. The Remote Sensing and Geo-Environment Lab (ERC group) at the Department of Civil Engineering and Geomatics is on the way to be upgraded to ERATOSTHENES Centre of Excellence (ECoE) through 'EXCELSIOR' H2020 Widespread Teaming project ([www.excelsior2020.eu](http://www.excelsior2020.eu)). Indeed, this thesis is under the auspices of all the activities of the 'ERATOSTHENES: Excellence Research Centre for Earth Surveillance and Space-Based Monitoring of the Environment'- 'EXCELSIOR' project that has received funding from the European Union's Horizon 2020 research and innovation programme under Grant Agreement No 857510 and from the Government of the Republic of Cyprus through the Directorate General for the European Programmes, Coordination and Development.



This project has received funding from the European Union's Horizon 2020 research and innovation programme under grant agreement No 857510.



This project has received funding from the Government of the Republic of Cyprus through the Directorate General of the European's Programmes, Coordination and Development.

## RELEVANT PUBLICATIONS

### Journals and Conference papers

**Tzouvaras, M.**, Danezis, C. and Hadjimitsis, D. G. (2020). Small scale landslide detection using Sentinel-1 interferometric SAR coherence. **Remote Sensing 2020**. **(Submitted – Pending decision)**

**Tzouvaras, M.**, Danezis, C. and Hadjimitsis, D. G. (2020). Differential SAR Interferometry using Sentinel-1 imagery – Limitations in monitoring fast moving land displacements. **Geosciences 2020**. **(Accepted with major corrections / New revised paper submitted)**

**Tzouvaras, M.**, Kouhartsiouk, D., Agapiou, A., Danezis, C. and Hadjimitsis, D. G. (2019). The Use of Sentinel-1 Synthetic Aperture Radar (SAR) Images and Open-Source Software for Cultural Heritage: An Example from Paphos Area in Cyprus for Mapping Landscape Changes after a 5.6 Magnitude Earthquake. **Remote Sensing 2019**, 11(15), 1766. <https://doi.org/10.3390/rs11151766>

Danezis, C., Hadjimitsis, D., Eineder, M., Brcic, R., Agapiou, A., Themistocleous, K., Mendonidis, E., Christofe, A. and **Tzouvaras, M.** (2019). CyCLOPS: A Novel Strategic Research Infrastructure Unit for Continuous Integrated Spaced-based Monitoring of Geohazards. 4<sup>th</sup> Joint International Symposium on Deformation Monitoring (**JISDM**), 15-17 May 2019, Athens, Greece

Themistocleous, K., Cuca, B., Agapiou, A., Lysandrou, V., **Tzouvaras, M.**, Hadjimitsis, D. G., Kyriakides, F., Kouhartsiouk, D., Margottini, C., Spizzichino, D., Cigna, F., Crosta G., Frattini P. and Merodo, J. A. F. (2016). The protection of cultural heritage sites from geo-hazards: The PROTHEGO project. **EUROMED 2016**, 10059 Lecture Notes in Computer Science, 91–98. [https://doi.org/10.1007/978-3-319-48974-2\\_11](https://doi.org/10.1007/978-3-319-48974-2_11)

Cuca, B., **Tzouvaras, M.**, Agapiou, A., Lysandrou, V., Themistocleous, K., Nisantzi, A. and Hadjimitsis, D. G. (2016). Earth observation technologies in service to the cultural landscape of Cyprus: risk identification and assessment. Fourth International Conference on Remote Sensing and Geoinformation of the Environment (**RSCy2016**), 96880Y. <https://doi.org/10.1117/12.2241669>

Alexakis, D., Agapiou, A., **Tzouvaras, M.**, Themistocleous, K., Neocleous, K., Michaelides, S., and Hadjimitsis, D. G. (2014). Integrated use of GIS and remote sensing for monitoring landslides in transportation pavements: the case study of Paphos area in Cyprus. **Natural Hazards**, 72(1), 119–141. <https://doi.org/10.1007/s11069-013-0770-3>

### **Conference posters and presentations**

**Tzouvaras, M.**, Agapiou, A., Nisantzi, A., Themistocleous, K. and Hadjimitsis, D.G., CLIMA" – Cultural Landscape risk Identification, Management and Assessment: An integrated approach in the Eastern Mediterranean Region by the ERATOSTHENES Research Centre. In: Proceedings of the **European Geosciences Union General Assembly**, 8-13 April 2018, Vienna, Austria.

**Tzouvaras, M.**, Hadjimitsis, D.G., Agapiou, A., Themistocleous, K., Nisantzi, A., and Christofi, A., Monitoring of land movements through InSAR processing in Cyprus in the framework of CLIMA project - Cultural Landscape risk Identification, Management and Assessment (in Greek), **EuroMed 2017**, 1-3 December 2017, Volos, Greece.

**Tzouvaras, M.**, Lysandrou, V., Nisantzi, A., Kouhartsiouk, D., Themistocleous, K., Papoutsas, C., Neocleous, K., Christofe, A., Mettas, C., Evagorou, E., Kyriakidis, P., Hadjimitsis, D.G., "CLIMA", Cultural Landscape risk Identification, Management and Assessment - A JPI project at ERATOSTHENES Research Centre in Cyprus. **RSPSoc 2017**. 5-8 September 2017, London, UK.

Di Iorio, A., Salvi, M.C., De Angeli, S., Cuca, B., **Tzouvaras, M.**, Kouhartsiouk, D., Hadjimitsis, D.G., Wilson, C., and Jepsen, M.R., CLIMA: An interactive WebGIS platform for risk assessment in Cultural Heritage, Fifth International Conference on Remote Sensing and Geoinformation of the Environment (**RSCy2017**), 20-23 March, 2017, Cyprus.

Themistocleous, K., Cuca, B., Agapiou, A., Lysandrou, V., **Tzouvaras, M.**, Michaelides, S., Hadjimitsis, D.G., Margottini, C., Cigna, F., Crosta, G., Merodo, F.J.A., The protection of cultural heritage sites from geo-hazards. In: Proceedings of the **European Geosciences Union General Assembly**, 17-22 April 2016, Vienna, Austria.

Cuca, B., Agapiou, A., Lysandrou, V., Themistocleous, K., **Tzouvaras, M.**, Nisantzi, A., Michaelides, S. and Hadjimitsis, D.G., Impact of the Climate Change on Cultural Heritage Sites in Cyprus. In: Proceedings of the **European Geosciences Union General Assembly**, 17-22 April 2016, Vienna, Austria.

Cuca B., **Tzouvaras M.**, Agapiou A., Lysandrou V., Themistocleous K., Nisantzi A., and Hadjimitsis D.G., The contribution of innovative technologies for protection and management of Cultural Landscapes in Cyprus: Nea Paphos case study, The 5<sup>th</sup> LE NOTRE Landscape Forum Landscape: From Natural to Cultural, 16-20 March 2016, Paphos, Cyprus.

## **ABSTRACT**

Infrastructure is designed to be operational under normal circumstances and to cope with common natural disruptions such as rainfall, snow and excessive heat. However, extreme natural hazards can lead to severe problems not only at the areas where such events occur, but also at neighbouring regions or even the entire country.

The main aim of this PhD thesis is the development of a novel methodology for the identification of areas susceptible to land movements and the systematic monitoring of land displacement at areas of interest in Cyprus, such as areas with critical infrastructure, areas of Cultural Heritage (UNESCO sites) and other urban areas, through Earth Observation (EO) techniques. Freely available Copernicus data such as those from the Sentinel missions and datasets from other Copernicus contributing missions (Landsat TM), as well as open-source European Space Agency (ESA) SNAP software were used in the entire process. Three case study areas were selected based on the site geology and the risk that land movements can cause to the general public, critical infrastructure and to Cultural Heritage monuments.

The development of landslide hazard maps was carried out, in one case study area, via the Analytic Hierarchy Process (AHP) methodology, using Landsat TM imagery. Coherent Change Detection (CCD) and Differential Interferometric SAR (DInSAR) methods, exploiting a series of Sentinel-1 SAR images, were used for monitoring land displacement caused by earthquakes and landslides, affecting different areas in Cyprus. For the calibration of the proposed EO based methodology, and the validation of the results obtained through the DInSAR processing of Sentinel-1 acquisitions, coordinates from the permanent Global Navigation Satellite System (GNSS) stations of the Cyprus Positioning System (CYPOS) network, operated by the Department of Lands and Surveys were used.

The main outcome of this PhD thesis is the development of a novel Earth Observation based methodology integrating the CCD and DInSAR techniques for the systematic identification of areas susceptible to natural hazards, such as earthquakes and landslides, and the continuous monitoring of such land displacement phenomena based on the analysis of optical and Synthetic Aperture Radar (SAR) satellite data, leading to a systematic way of monitoring land movements on a larger scale. Rapid detection and

more detailed multi-pass products were developed using the proposed DInSAR and CCD methodologies, for the detection and monitoring of natural hazards and their impact on critical infrastructure resilience.

The proposed methodology might lay the foundations for the development of an automated Early Warning System that will facilitate the operation of the country's emergency mechanism and warn public authorities and the general public in a timely manner for an upcoming danger. Moreover, it can also serve as a guidance/consultation tool for public authorities and decision-makers regarding the identification of high-risk areas in terms of land displacement on time and the adoption of preventive protection measures on Cultural Heritage landscapes and critical infrastructure.

**Keywords:** Coherence, Infrastructure resilience, Land displacement, Natural hazards, SAR interferometry

## ΠΕΡΙΛΗΨΗ

Οι υποδομές σχεδιάζονται και κατασκευάζονται για να λειτουργούν υπό κανονικές συνθήκες και να είναι ανθεκτικές σε κοινές φυσικές διαταραχές όπως βροχοπτώσεις, χιόνι και υπερβολική θερμότητα. Ωστόσο, οι ακραίοι φυσικοί κίνδυνοι μπορούν να οδηγήσουν σε σοβαρά προβλήματα όχι μόνο στις περιοχές όπου συμβαίνουν τέτοια γεγονότα, αλλά και σε γειτονικές περιοχές ή ακόμη και σε ολόκληρη τη χώρα.

Ο κύριος στόχος αυτής της διδακτορικής διατριβής είναι η ανάπτυξη μιας νέας καινοτόμου μεθοδολογίας για τον προσδιορισμό των περιοχών που είναι ευάλωτες σε μετατοπίσεις εδάφους και η συστηματική παρακολούθηση των εκτοπίσεων γης σε περιοχές ενδιαφέροντος στην Κύπρο, όπως περιοχές με κρίσιμες υποδομές, περιοχές πολιτιστικής κληρονομιάς (μνημεία UNESCO) και άλλες αστικές περιοχές, μέσω τεχνικών Παρατήρησης της Γης. Διαθέσιμα δωρεάν δορυφορικά δεδομένα Copernicus, όπως αυτά από τις αποστολές Sentinel και δεδομένα από άλλες αποστολές συνεισφοράς στο Copernicus (Landsat TM), καθώς και το λογισμικό ανοιχτού κώδικα SNAP του Ευρωπαϊκού Οργανισμού Διαστήματος (ESA) χρησιμοποιήθηκαν σε ολόκληρη τη διαδικασία. Επιλέχθηκαν τρεις περιοχές μελέτης με βάση τη γεωλογία τους και τον κίνδυνο που μπορεί να προκαλέσουν μετακινήσεις εδάφους στο ευρύ κοινό, σε κρίσιμες υποδομές και σε μνημεία πολιτιστικής κληρονομιάς.

Η ανάπτυξη χαρτών κινδύνου κατολισθήσεων πραγματοποιήθηκε, σε μία περιοχή μελέτης, μέσω της μεθοδολογίας της Αναλυτικής Ιεραρχικής Διαδικασίας (AHP), χρησιμοποιώντας εικόνες Landsat TM. Οι μέθοδοι Εντοπισμού Συνεκτικών Μεταβολών (CCD) και Διαφορικής Συμβολομετρίας ραντάρ (DInSAR), αξιοποιώντας μια σειρά εικόνων ραντάρ Sentinel-1, χρησιμοποιήθηκαν για την παρακολούθηση μετακινήσεων εδάφους που προκλήθηκαν από σεισμούς και κατολισθήσεις, επηρεάζοντας διάφορες περιοχές στην Κύπρο. Για τη βαθμονόμηση της προτεινόμενης μεθοδολογίας, που βασίζεται σε τεχνικές Παρατήρησης της Γης, και τον έλεγχο αξιοπιστίας των αποτελεσμάτων που υπολογίστηκαν μέσω της ανάλυσης και επεξεργασίας εικόνων Sentinel-1 με τη μέθοδο DInSAR, χρησιμοποιήθηκαν συντεταγμένες από τους μόνιμους σταθμούς GNSS (Παγκόσμιο Δορυφορικό Σύστημα Πλοήγησης) του Κυπριακού Δικτύου Μόνιμων Σταθμών Αναφοράς CYPOS, που λειτουργεί και διαχειρίζεται από το Τμήμα Κτηματολογίου και Χωρομετρίας της Κύπρου.



Το κύριο αποτέλεσμα της παρούσας διδακτορικής διατριβής είναι η ανάπτυξη μιας καινοτόμου μεθοδολογίας, βασισμένη σε τεχνικές Παρατήρησης της Γης, που ενσωματώνει τις μεθόδους CCD και DInSAR για τη συστηματική αναγνώριση περιοχών ευπαθών σε φυσικούς κινδύνους, όπως σεισμούς και κατολισθήσεις, και η συνεχής παρακολούθηση τέτοιων φαινομένων μετακινήσεων εδάφους, μέσω της ανάλυσης δορυφορικών οπτικών εικόνων και εικόνων συνθετικού διαφράγματος ραντάρ (SAR), οδηγώντας στο συστηματικό τρόπο παρακολούθησης των κινήσεων εδάφους σε μεγαλύτερη κλίμακα. Προϊόντα ταχέως εντοπισμού και πιο λεπτομερή προϊόντα πολλαπλής διέλευσης (multi-pass) αναπτύχθηκαν χρησιμοποιώντας τις προτεινόμενες μεθοδολογίες DInSAR και CCD, για τον εντοπισμό και την παρακολούθηση φυσικών κινδύνων και τον αντίκτυπό τους στην ανθεκτικότητα των κρίσιμων υποδομών.

Η προτεινόμενη μεθοδολογία μπορεί να θέσει τα θεμέλια για την ανάπτυξη ενός αυτοματοποιημένου συστήματος έγκαιρης προειδοποίησης (Early Warning System), που θα διευκολύνει τη λειτουργία του μηχανισμού έκτακτης ανάγκης της χώρας και θα προειδοποιεί τις δημόσιες αρχές και το ευρύ κοινό εγκαίρως για έναν επικείμενο κίνδυνο. Επιπρόσθετα, μπορεί να χρησιμοποιηθεί ως εργαλείο καθοδήγησης / διαβούλευσης για τις δημόσιες αρχές και τους υπευθύνους λήψης αποφάσεων σχετικά με τον έγκαιρο προσδιορισμό των περιοχών υψηλού κινδύνου όσον αφορά την μετατόπιση εδάφους και την υιοθέτηση προληπτικών μέτρων προστασίας σε περιοχές πολιτιστικής κληρονομιάς και κρίσιμων υποδομών.

# TABLE OF CONTENTS

ACKNOWLEDGEMENTS .....	vii
RELEVANT PUBLICATIONS .....	x
ABSTRACT.....	xiii
ΠΕΡΙΛΗΨΗ.....	xv
TABLE OF CONTENTS.....	xvii
LIST OF TABLES.....	xxi
LIST OF FIGURES .....	xxiii
LIST OF ABBREVIATIONS.....	xxxii
1 Introduction.....	1
1.1 Factors triggering land movements.....	3
1.1.1 Geology.....	4
1.1.2 Seismicity.....	5
1.1.3 Climate and precipitation.....	8
1.2 The importance of using Earth Observation for monitoring land movements.	10
1.3 Structure of thesis.....	13
2 Literature review.....	14
2.1 Natural hazards.....	14
2.2 Monitoring natural hazards through conventional methods.....	19
2.2.1 Geodetic techniques .....	19
2.2.2 Photogrammetric techniques.....	20
2.2.3 Geophysical techniques .....	21
2.2.4 Geotechnical techniques .....	23
2.2.5 The case of Cyprus .....	23
2.3 Monitoring natural hazards through Earth Observation.....	30

3	Methodology .....	45
3.1	Areas of study .....	45
3.1.1	Statos – Agios Photios .....	46
3.1.2	Nea Paphos – Tombs of the Kings.....	49
3.1.3	Pissouri – Petra tou Romiou .....	54
3.2	Data and software.....	59
3.2.1	Data.....	59
3.2.1.1	Optical data.....	59
3.2.1.2	SAR data.....	62
3.2.1.3	Other data .....	66
3.2.2	Software .....	67
3.2.2.1	SNAP .....	67
3.2.2.2	SNAPHU .....	68
3.2.2.3	Other software .....	69
3.3	Methods.....	70
3.3.1	Development of land displacement susceptibility maps.....	70
3.3.1.1	Slope .....	74
3.3.1.2	Land use.....	75
3.3.1.3	Aspect .....	76
3.3.1.4	Faults .....	76
3.3.1.5	Drainage network .....	77
3.3.1.6	Road network.....	79
3.3.1.7	Relief .....	79
3.3.1.8	Lithology .....	80
3.3.1.9	Precipitation.....	81
3.3.2	Development of coherence and land displacement maps .....	84

3.3.2.1	Data acquisition .....	86
3.3.2.2	Data input .....	90
3.3.2.3	Coregistration .....	90
3.3.2.4	Development of interferogram .....	93
3.3.2.5	Topographic phase removal .....	93
3.3.2.6	Phase filtering .....	94
3.3.2.7	Phase unwrapping.....	94
3.3.2.8	Conversion of phase to displacement .....	95
3.3.2.9	Geometric correction .....	96
3.3.2.10	Coherence masking .....	96
3.3.2.11	Displacement map .....	96
3.3.3	Calibration and validation methodology of DInSAR results.....	97
4	Results.....	100
4.1	Implementation of AHP methodology .....	100
4.1.1	Calibration and validation of results .....	102
4.2	Implementation of DInSAR methodology .....	104
4.2.1	Nea Paphos – Tombs of the Kings.....	105
4.2.1.1	Calibration and validation of results.....	111
4.2.2	Pissouri – Petra tou Romiou .....	114
4.3	Implementation of CCD methodology.....	144
4.3.1	Statistical analysis .....	151
4.3.2	Coherent Change Detection analysis .....	178
4.3.2.1	Identification of natural hazards .....	187
4.3.2.2	Validation of methodology .....	201
5	Discussion.....	210
	CONCLUSIONS .....	218

REFERENCES .....	223
APPENDIX I – Statistical tests .....	253
APPENDIX II – ROC analysis .....	268

## LIST OF TABLES

Table 1: Cyprus meteorological data 1991-2014.....	10
Table 2: Landsat 5 TM bands and their spatial resolutions .....	60
Table 3: Acquired Landsat 5 TM image characteristics .....	60
Table 4: Sentinel-2 bands and their spatial resolutions .....	61
Table 5: Sentinel-1 SAR image characteristics – Nea Paphos-Tombs of the Kings .....	64
Table 6: Sentinel-1 SAR image characteristics – Pissouri-Petra tou Romiou.....	65
Table 7: Slope classification and rating.....	74
Table 8: Land use classification and rating .....	75
Table 9: Parameters, classes and rating values – Statos-Agios Photios .....	82
Table 10: Sentinel-1 SAR images – Nea Paphos – Tombs of the Kings.....	87
Table 11: Sentinel-1 SAR image characteristics – Pissouri – Petra tou Romiou .....	88
Table 12: Estimated positions (values in m) and horizontal and vertical velocities of the CYPOS GNSS stations (values in mm/year).....	98
Table 13: AHP matrix – Statos-Agios Photios .....	100
Table 14: SAR image interferometric pairs – Pissouri-Petra tou Romiou .....	115
Table 15: Displacement results AOI – Pissouri.....	135
Table 16: Displacement results AOI – Petra tou Romiou .....	136
Table 17: Coherence results AOI – Pissouri.....	141
Table 18: Coherence results AOI – Petra tou Romiou .....	142
Table 19: SAR image interferometric pairs – Pissouri-Petra tou Romiou .....	145
Table 20: Coherence values – Sentinel-1A ascending.....	152
Table 21: Coherence values – Sentinel-1A ascending – AOI .....	153
Table 22: Coherence values – Sentinel-1A descending.....	155
Table 23: Coherence values – Sentinel-1A descending – AOI .....	156

Table 24: Coherence values – Sentinel-1B ascending.....	159
Table 25: Coherence values – Sentinel-1B ascending – AOI.....	160
Table 26: Coherence values – Sentinel-1B descending.....	162
Table 27: Coherence values – Sentinel-1B descending – AOI.....	163
Table 28: Co-event SAR pairs .....	195
Table 29: ROC analysis – Summary statistics.....	200

## LIST OF FIGURES

Figure 1: Land movements in the form of landslide (left) and rock fall (right) events in Cyprus (source: Cyprus Geological Survey Department) .....	2
Figure 2: The geological zones of Cyprus (source: Cyprus Geological Survey Department) .....	4
Figure 3: The Cyprus Arc and the adjacent tectonic plates (Geological Survey Department, 2012) .....	6
Figure 4: Seismicity of Cyprus 1896-2019 (Geological Survey Department, 2019) .....	7
Figure 5: Köppen-Geiger climate classification map – Cyprus belongs to Csa and BSh types .....	8
Figure 6: (a) Present (1980-2016) and (b) future (2071-2100) Köppen-Geiger climate classification map of Cyprus (Beck <i>et al.</i> , 2018).....	9
Figure 7: The seismic zoning map of Cyprus (Cyprus Organisation for Standardisation, 2004) .....	15
Figure 8: The seismic hazard distribution map of Cyprus (World Health Organization, 2010).....	16
Figure 9: Geological suitability zone map of Cyprus (source: Geological Survey Department) .....	24
Figure 10: Landslide susceptibility map (Hart and Hearn, 2010; Hearn and Hart, 2019) .....	25
Figure 11: Landslide inventory map of Cyprus (source: Geological Survey Department) .....	26
Figure 12: The Cyprus Seismological Network (source: Geological Survey Department) .....	27
Figure 13: The primary seismological centre (left) and the prototype seismological station GSD in Nicosia (right) (source: Geological Survey Department) .....	28
Figure 14: The earthquake and other geological hazards risk map (source: Geological Survey Department).....	29



Figure 15: Interferometric Synthetic Aperture Radar principle (Geoscience Australia, 2014) .....	34
Figure 16: The three case study areas of (a) Statos – Agios Photios, (b) Nea Paphos – Tombs of the Kings and (c) Pissouri – Petra tou Romiou .....	45
Figure 17: The Statos – Agios Photios study area .....	46
Figure 18: Geological map of the study area – Statos – Agios Photios.....	47
Figure 19: The evacuated village of Statos (left). Rockslide in chalk across a roadcut (right) .....	48
Figure 20: The case study of Nea Paphos – Tombs of the Kings .....	49
Figure 21: The archaeological site of Nea Paphos (left) and the “Tombs of the Kings” (right) (source: Department of Antiquities) .....	50
Figure 22: Nea Paphos and Tombs of the Kings archaeological structure .....	51
Figure 23: Geological map of the study area – Nea Paphos – Tombs of the Kings .....	52
Figure 24: Examples of degradation of the structures present in the area of Nea Paphos, mainly caused by the seismic activities and erosion (source: Dr K. Themistocleous, CUT team). .....	53
Figure 25: Map of Paphos and the epicentre of the 15 April 2015 earthquake .....	53
Figure 26: The case study area by the A6 motorway near Pissouri.....	54
Figure 27: The case study area next to the old Limassol-Paphos road near Petra tou Romiou.....	55
Figure 28: Geological map of the study area – Pissouri – Petra tou Romiou. Case study (a) by the A6 motorway near Pissouri and (b) next to the old Limassol-Paphos road near Petra tou Romiou .....	56
Figure 29: Landslide on the Paphos-Limassol motorway near Pissouri (source: Geological Survey Department) .....	57
Figure 30: Landslide near Paphos-Limassol old road next to Petra tou Romiou (source: Geological Survey Department) .....	58

Figure 31: Landslides (a) next to the Paphos-Limassol motorway and (b) next to Paphos-Limassol old road near Petra tou Romiou (source: Geological Survey Department) .....	58
Figure 32: The Copernicus Open Access Hub.....	62
Figure 33: Sentinel-1 acquisition modes (ESA, no date b).....	63
Figure 34: Selection of area of interest – Copernicus Open Access Hub.....	64
Figure 35: The interface of SNAP software .....	67
Figure 36: The interface of SNAPHU software.....	68
Figure 37: Flow chart of the proposed AHP methodology.....	71
Figure 38: Slope classes – Statos-Agios Photios .....	74
Figure 39: Land use map – Statos-Agios Photios.....	75
Figure 40: Aspect classes – Statos-Agios Photios .....	76
Figure 41: Faults and buffer zones – Statos-Agios Photios.....	77
Figure 42: Drainage network numbered according to Strahler order .....	78
Figure 43: Streams and buffer zones – Statos-Agios Photios.....	78
Figure 44: Roads and buffer zones – Statos-Agios Photios.....	79
Figure 45: Relief map – Statos-Agios Photios.....	80
Figure 46: Lithology map – Statos-Agios Photios.....	81
Figure 47: Precipitation map – Statos-Agios Photios.....	82
Figure 48: Outline of the coherence and displacement map processing chain .....	84
Figure 49. SRTM coverage (USGS, no date b) .....	92
Figure 50. RGB representation of SAR pair coregistration 04.02.2019-16.02.2019 .....	92
Figure 51: Phase unwrapping principle (Braun and Veci, 2020) .....	94
Figure 52: The CYPOS permanent GNSS network.....	97
Figure 53: Final landslide hazard map – Statos-Agios Photios .....	102
Figure 54: Areas affected by recorded landslide events – Statos-Agios Photios .....	103

Figure 55: Landslide hazard zonation map – Statos-Agios Photios broader area .....	104
Figure 56: InSAR Stack Overview – Nea Paphos-Tombs of the Kings.....	105
Figure 57. Geometric distortions – (a) Foreshortening and (b) shadowing effects (ESA, 2014).....	106
Figure 58: Geometry of ascending (left) and descending (right) satellite orbits.....	106
Figure 59: Coregistered images – Intensity IW2 band (master & slave) – Nea Paphos-Tombs of the Kings.....	107
Figure 60: Interferogram Result – Nea Paphos-Tombs of the Kings .....	108
Figure 61: Deburst Result – Nea Paphos-Tombs of the Kings.....	108
Figure 62: Interferogram Result after Topographic Phase Removal – Nea Paphos-Tombs of the Kings.....	109
Figure 63: Differential interferogram after the application of phase filtering at (a) western Cyprus; (b) “Nea Paphos”; and (c) “Tombs of the Kings”. .....	109
Figure 64: The SAR acquisition geometry .....	110
Figure 65: Relative displacement map – Nea Paphos-Tombs of the Kings .....	111
Figure 66: Displacement Map Result – Geo-referenced – Nea Paphos-Tombs of the Kings.....	112
Figure 67: Final displacement map at (a) western Cyprus; (b) “Nea Paphos”; and (c) “Tombs of the Kings” .....	113
Figure 68: Final displacement map at (a) historic centre of Paphos; (b) Nea Paphos and (c) Tombs of the Kings .....	114
Figure 69. RGB representation of SAR image pair coregistration – Pissouri-Petra tou Romiou.....	116
Figure 70. Interferograms of SAR image pairs – Pissouri-Petra tou Romiou .....	116
Figure 71. Coherence maps of SAR image pairs – Pissouri-Petra tou Romiou .....	117
Figure 72: Landslide areas indicated in red near Pissouri by the motorway A6 (left) and near Petra tou Romiou next to the old Paphos-Limassol road (right) .....	117

Figure 73: Interferograms at the area of the landslide near Pissouri by the motorway A6 .....	118
Figure 74: Interferograms at the area of the landslide near Petra tou Romiou.....	119
Figure 75: Interferograms of S1A and S1B descending pairs at the area near Pissouri	120
Figure 76. Unwrapped interferograms of SAR image pairs – Pissouri-Petra tou Romiou .....	121
Figure 77: Development of a stack of displacement maps .....	121
Figure 78: Absolute LoS displacement maps and histograms – Pissouri-Petra tou Romiou.....	122
Figure 79: Displacement maps at the landslide area near Pissouri.....	124
Figure 80: Displacement maps at the landslide area near Petra tou Romiou .....	126
Figure 81: Development of average displacement maps – Band Maths.....	126
Figure 82: Average LoS displacement maps and histograms – Pissouri-Petra tou Romiou.....	127
Figure 83: Average LoS displacement map – Pissouri.....	127
Figure 84: Average LoS displacement map – Petra tou Romiou .....	128
Figure 85: Landslide near Pissouri by the A6 motorway (Geological Survey Department) .....	128
Figure 86: Landslide near Petra tou Romiou (Geological Survey Department).....	129
Figure 87: Decomposition of LoS displacement into vertical and east-west components .....	129
Figure 88: Incident angle as seen in image metadata .....	130
Figure 89: Average vertical displacement maps – Pissouri-Petra tou Romiou .....	130
Figure 90: Average E-W displacement maps – Pissouri-Petra tou Romiou.....	131
Figure 91: Final displacement maps – Pissouri .....	132
Figure 92: Final displacement maps – Petra tou Romiou.....	134
Figure 93: Average coherence map – Pissouri .....	138

Figure 94: Average coherence map – Petra tou Romiou .....	138
Figure 95: RGB (left) and NDVI (right) from Sentinel-2 image.....	140
Figure 96: Average coherence map (NDVI mask) – Pissouri .....	140
Figure 97: Average coherence map (NDVI mask) – Petra tou Romiou.....	142
Figure 98: The extents of the February 15, 2019 landslide near Pissouri .....	144
Figure 99: Timeline of SAR acquisitions and events .....	146
Figure 100: Coherence maps development methodology.....	146
Figure 101: Coherence maps – Sentinel-1A ascending .....	147
Figure 102: Coherence maps – Sentinel-1A descending .....	148
Figure 103: Coherence maps – Sentinel-1B ascending .....	149
Figure 104: Coherence maps – Sentinel-1B descending .....	150
Figure 105: Coherence maps – Point grid .....	151
Figure 106: Coherence changes – Sentinel-1A ascending.....	154
Figure 107: Coherence changes – Sentinel-1A ascending – AOI .....	154
Figure 108: Coherence changes – Sentinel-1A descending.....	157
Figure 109: Coherence changes – Sentinel-1A descending – AOI .....	157
Figure 110: Coherence changes – Sentinel-1A average .....	158
Figure 111: Coherence changes – Sentinel-1A average – AOI.....	158
Figure 112: Coherence changes – Sentinel-1B ascending.....	161
Figure 113: Coherence changes – Sentinel-1B ascending – AOI.....	161
Figure 114: Coherence changes – Sentinel-1B descending.....	164
Figure 115: Coherence changes – Sentinel-1B descending – AOI.....	164
Figure 116: Coherence changes – Sentinel-1B average .....	165
Figure 117: Coherence changes – Sentinel-1B average – AOI .....	166
Figure 118: Coherence changes – S1A and S1B ascending .....	167
Figure 119: Coherence changes – S1A and S1B ascending – AOI.....	168

Figure 120: Coherence changes – S1A and S1B descending .....	168
Figure 121: Coherence changes – S1A and S1B descending – AOI .....	169
Figure 122: Coherence changes – S1A and S1B average.....	170
Figure 123: Coherence changes – S1A and S1B average – AOI.....	170
Figure 124: Rehabilitation works at the landslide area – Pissouri (Geological Survey Department) .....	171
Figure 125: Timeline of SAR acquisitions and events .....	172
Figure 126: Coherence changes in the 3 periods for the entire area (left) and the AOI (right) .....	173
Figure 127: Coherence changes – Average .....	174
Figure 128: Coherence changes – Average – AOI .....	176
Figure 129: Raster calculator – Coherence averaging .....	178
Figure 130: Pre-event coherence map – Sentinel-1A ascending .....	179
Figure 131: Co-event coherence map – Sentinel-1A ascending.....	179
Figure 132: Post-event coherence map – Sentinel-1A ascending.....	180
Figure 133: Pre-event coherence map – Sentinel-1A descending .....	180
Figure 134: Co-event coherence map – Sentinel-1A descending.....	181
Figure 135: Post-event coherence map – Sentinel-1A descending.....	181
Figure 136: Pre-event coherence map – Sentinel-1B ascending .....	182
Figure 137: Co-event coherence map – Sentinel-1B ascending.....	182
Figure 138: Post-event coherence map – Sentinel-1B ascending.....	183
Figure 139: Pre-event coherence map – Sentinel-1B descending .....	183
Figure 140: Co-event coherence map – Sentinel-1B descending.....	184
Figure 141: Post-event coherence map – Sentinel-1B descending.....	184
Figure 142: Pre-event coherence map – Average.....	185
Figure 143: Co-event coherence map – Average.....	185

Figure 144: Post-event coherence map – Average .....	186
Figure 145: Raster calculator – Coherence difference (left) and normalised difference (right) .....	187
Figure 146: Average natural coherence loss .....	188
Figure 147: Coherence difference map – Sentinel-1A ascending .....	190
Figure 148: Normalised coherence difference map – Sentinel-1A ascending.....	190
Figure 149: Coherence difference map – Sentinel-1A descending .....	191
Figure 150: Normalised coherence difference map – Sentinel-1A descending.....	191
Figure 151: Coherence difference map – Sentinel-1B ascending.....	192
Figure 152: Normalised coherence difference map – Sentinel-1B ascending.....	192
Figure 153: Coherence difference map – Sentinel-1B descending.....	193
Figure 154: Normalised coherence difference map – Sentinel-1B descending.....	193
Figure 155: Coherence difference map – Average .....	196
Figure 156: Normalised coherence difference map – Average .....	196
Figure 157: Coherence difference map – Sentinel-1B average .....	197
Figure 158: Normalised coherence difference map – Sentinel-1B average .....	198
Figure 159: ROC curves for coherence difference (left) and normalised coherence difference (right) – Sentinel-1B average .....	199
Figure 160: Coherence difference map – Sentinel-1A ascending .....	201
Figure 161: Normalised coherence difference map – Sentinel-1A ascending.....	202
Figure 162: Coherence difference map – Sentinel-1A descending .....	202
Figure 163: Normalised coherence difference map – Sentinel-1A descending.....	203
Figure 164: Coherence difference map – Sentinel-1B ascending.....	203
Figure 165: Normalised coherence difference map – Sentinel-1B ascending.....	204
Figure 166: Coherence difference map – Sentinel-1B descending.....	204
Figure 167: Normalised coherence difference map – Sentinel-1B descending.....	205

Figure 168: Coherence difference map – Average .....	206
Figure 169: Normalised coherence difference map – Average .....	207
Figure 170: Coherence difference map – Sentinel-1A and Sentinel-1B ascending .....	208
Figure 171: Normalised coherence difference map – Sentinel-1A and Sentinel-1B ascending .....	208
Figure 172: The proposed CCD methodology.....	212
Figure 173: The contribution of Copernicus, ESA, and Stanford University on natural hazards monitoring via DInSAR and CCD methodologies .....	213
Figure 174: The AHP methodology for the continuous monitoring of land displacement susceptibility .....	213
Figure 175: The integrated CCD – DInSAR methodology for the continuous monitoring of land movements.....	214
Figure 176: The integration of DInSAR processing results and GNSS measurements	216



## LIST OF ABBREVIATIONS

AGOS:	Australian Geophysical Observing System
AHP:	Analytical Hierarchy Process
ARIA:	Advanced Rapid Imaging and Analysis
AOI:	Area Of Interest
ASTER:	Advanced Spaceborne Thermal Emission and Reflection
ATI:	Along Track Interferometry
CCD:	Coherent Change Detection
CI:	Consistency Index
CLC:	CORINE Land Cover
CORS:	Continuously Operating Reference Station
COSMO:	Constellation of Small Satellites for Mediterranean basin Observation
CR:	Consistency Ratio
CORS:	Continuously Operating Reference Stations
CYPOS:	Cyprus Positioning System
DAS:	Data Acquisition Station
DInSAR:	Differential Interferometric Synthetic Aperture Radar
DLR:	Deutschen Zentrum für Luft- und Raumfahrt (German: German Aerospace Centre)
DLS:	Department of Lands and Surveys
DP:	Darkest Pixel
DEM:	Digital Elevation Model
ECOE:	Eratosthenes Centre of Excellence

EMMENA:	Easter Mediterranean, Middle East and North Africa
ESD:	Enhanced Spectral Diversity
EO:	Earth Observation
ERT:	Electrical Resistivity Test
ESA:	European Space Agency
ETEK:	Technical Chamber of Cyprus
EW:	Extra-Wide
EWS:	Early Warning Systems
GCP:	Ground Control Point
GDEM:	Global Digital Elevation Model
GEONET:	GPS Earth Observation Network
GIS:	Geographic Information System
GNSS:	Global Navigation Satellite System
GPR:	Ground Penetrating Radar
GPS:	Global Positioning System
GRD:	Ground Range Detected
GSD:	Geological Survey Department
HH:	Horizontal – Horizontal
HV:	Horizontal – Vertical
IGS:	International GNSS Service
InSAR:	Interferometric Synthetic Aperture Radar
IW:	Interferometric Wide
IPTA:	Interferometric Point Target Analysis
KML:	Keyhole Markup Language
KMZ:	Keyhole Markup language Zipped

LHZM:	Landslide Hazard Zonation Map
LoS:	Line-of-Sight
LULC:	Land Use/ Land Cover
NIR:	Near Infra-Red
NRT:	Near Real Time
OCN:	Ocean
PAN:	Panchromatic
PANGA:	Pacific Northwest Geodetic Array
PS:	Persistent/Permanent Scatterer
PSI:	Persistent Scatterer Interferometry
PSInSAR:	Permanent Scatterer SAR Interferometry
PCA:	Principal Component Analysis
RGB:	Red Green Blue
RI:	Random consistency Index
ROC:	Receiver Operating Characteristic
S1:	Sentinel-1
S1A:	Sentinel-1A
S1B:	Sentinel-1B
S1TBX:	Sentinel-1 Toolbox
SAR:	Synthetic Aperture Radar
SBAS:	Small Baseline Subsets
SCIGN:	Southern California Integrated GPS Network
SLC:	Single Look Complex
SM:	Stripmap
SNAP:	Sentinel Applications Platform

SP:	Self-Potential
SqueeSAR:	“Squeezed” SAR
SRTM:	Shuttle Radar Topography Mission
SWIR:	Short Wave Infra-Red
TIR:	Thermal Infra-Red
TM:	Thematic Mapper
TOPS:	Terrain Observation with Progressive Scans
TOPSAR:	Terrain Observation with Progressive Scans SAR
UAV:	Unmanned Aerial Vehicle
USA:	United States of America
USGS:	United States Geological Survey
VH:	Vertical – Horizontal
VIS:	Visible
VNIR:	Visible Near Infra-Red
VV:	Vertical – Vertical
WGS 84:	World Geodetic System 1984
WV:	Wave

# 1 Introduction

Infrastructure is designed to be operational under normal circumstances and to cope with common natural disruptions such as rainfall, snow and excessive heat. However, extreme natural hazards can lead to severe problems not only at the areas where such events occur, but also at neighbouring regions or even the entire country as they can make parts of a road network virtually impassable (Rodrigue, Comtois and Slack, 2006). Disruptions in the operation of a single road can cause significant economic and social strains. Given the value of a functional road transportation system, it is of great importance to be able to predict the impacts of disruptions to the system, the most likely location they might occur, and where the impacts would be the most severe (Jenelius and Mattsson, 2012).

The reliability of critical civil infrastructure, such as transportation systems, public buildings, i.e. hospitals, schools, etc., is of key interest during all the stages of planning and construction, from the conception of the idea until its realisation. Many different actors are involved during this process, like infrastructure users, planners and designers at all levels, both in the public and private sectors (Jenelius, Petersen and Mattsson, 2006). Moreover, the safety of citizens and infrastructure users is of the greatest importance, thus built-up areas must be properly specified, after careful and considerate planning by the relevant responsible authorities, in geologically suitable areas with low risk for various natural hazards.

Cultural landscapes of Europe, often characterised and enhanced by the presence of exposed and buried archaeological remains, are endangered by environmental processes and anthropogenic pressures and, more specifically, by intensive agriculture activities, climate change and natural hazards (Cuca *et al.*, 2016). The international community is very sensitive regarding the protection of the religious and cultural heritage worldwide, as it is evident from the number of Conventions and Protocols adopted for the protection of cultural heritage, as well as for the return of such cultural heritage artefacts to their rightful owners (Ministry of Foreign Affairs, no date). In 2005, the World Heritage Centre of UNESCO performed a survey among the Member States to assess the major threats of climate change and their possible impact to natural and cultural heritage (World Heritage Centre UNESCO, 2007). The climate threats raised for cultural World Heritage sites involved Hurricane storms (11 sites), Sea-level rise (9 sites), Erosion (both wind and

water driven) (8 sites), Flooding (7 sites), Rainfall increase (4 sites), Drought (3 sites), Desertification (2 sites) and Rise in temperature (1 site).

The history and culture of Cyprus is among the oldest in the world. This rich cultural landscape involves hundreds of archaeological sites scattered throughout the island, representing various historical periods in the island's evolution, with three of them, “Paphos”, “Choirokoitia” and “Painted churches in the Troodos region” being in the list of UNESCO World Heritage Sites<sup>1</sup>.

In Cyprus, extreme weather conditions such as drought and heavy rainfall can lead to amplification of the soil erosion processes. Furthermore, Cyprus is in an area of high susceptibility to seismic activities and landslides. The main geotechnical problems that take place are landslides, rock falls and ground subsidence, posing a constant threat not only for built-up areas and civil infrastructure, such as roads, bridges, tunnels, etc., but also to the cultural heritage monuments and landscapes (Figure 1).



**Figure 1:** Land movements in the form of landslide (left) and rock fall (right) events in Cyprus (source: Cyprus Geological Survey Department)

In the western part of Cyprus, especially in the Paphos District, relatively large landslides take place, due to the presence of geological formations prone to landslides, like the Mamonía mélangé and the Kannaviou bentonitic clays (Alexandris, Griva and Abarioti, 2016). In Limassol District, located in the southwestern part of the island, landslide phenomena take place less frequently, relating mainly to the Lower Marls of the Lefkara Formation as well as the Moni Formation. Rockfalls are observed mainly in the mountainous areas of Cyprus and in natural and manmade slopes. Last but not least, due

---

<sup>1</sup> UNESCO World Heritage List: <https://whc.unesco.org/en/list/>

to nature of the main soil types in Cyprus ground, i.e. marls, clays and gypsum, ground subsidence is a frequent phenomenon, as it is highly related to the geological conditions and the mechanical properties of the ground itself (Research & Development Center-Intercollege, 2004a). Under adverse morphological and hydrogeological conditions, hazardous landslides can occur in areas, even when landslide prone formations are not present (Alexandris, Griva and Abarioti, 2016).

Extensive research has been conducted studying several slope failures in Cyprus (Pantazis, 1969; Charalambous and Petrides, 1997; Hart *et al.*, 2010; Hart and Hearn, 2013) and emphasised on the effect and the importance of landside hazards, especially in the western part of Cyprus.

A detailed analysis of the geological, climate conditions and seismicity of Cyprus, factors that can lead to land displacement phenomena is carried out in *section 1.1* of the present thesis. Following, the importance of using Earth Observation for monitoring natural hazards, especially landslides and land subsidence, is highlighted in *section 1.2* of the thesis. At the end of this chapter, the structure of the present dissertation is presented.

## **1.1 Factors triggering land movements**

Land movements can be caused by geological factors (soil stability, lithology, faults, etc.); geomorphological factors, such as soil erosion in the case of Cyprus, vegetation removal due to fire or draught and volcanic or tectonic uplift; physical factors, such as topography, tectonic activity, intense rainfall and snow melt; and factors associated with human activity, such as excavations, agricultural activities, mining and deforestation (Cruden and Varnes, 1996).

In this section, the factors of geology, seismicity, and climate and precipitation are presented and analysed, to provide a detailed overview of the current conditions in Cyprus that enhance the susceptibility of specific areas to land movements.

### 1.1.1 Geology

The geological genesis of Cyprus took place through a series of complex tectonic episodes in the broader context of the subduction of the African plate under the Eurasian plate. Geologically, Cyprus is divided into four geological terranes, as shown in Figure 2: the Keryneia Terrane; the Troodos Terrane (or Troodos Ophiolite complex); the Mamonia Terrane; and the Circum Troodos Sedimentary Succession (Geological Survey Department, 2016).

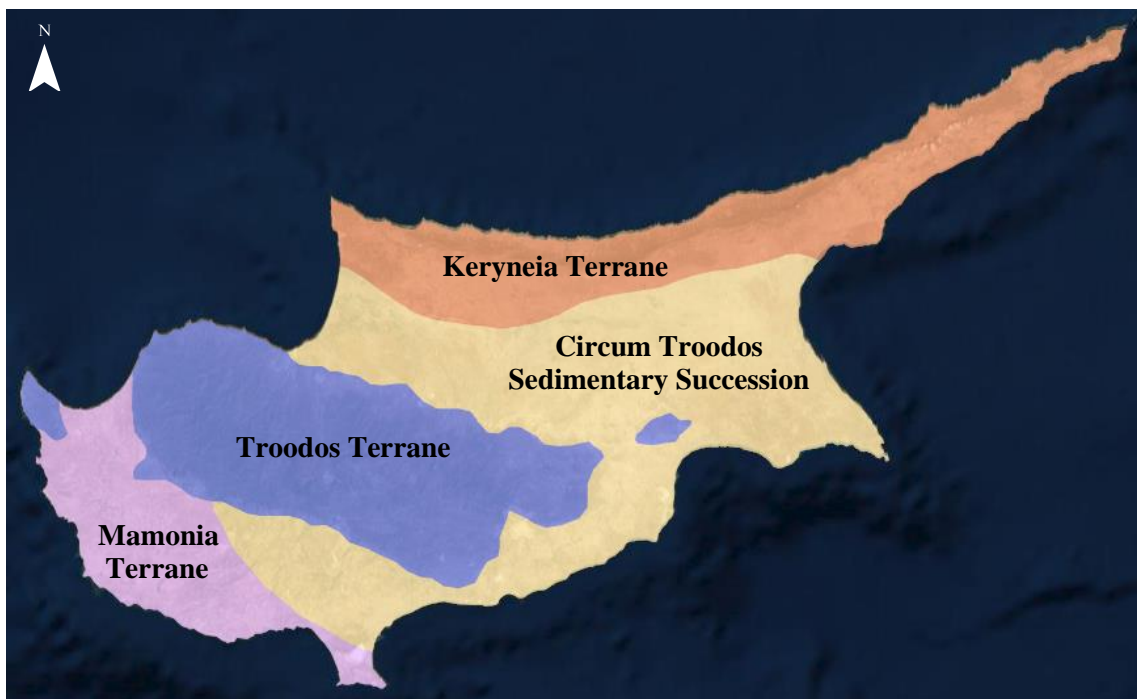


**Figure 2:** The geological zones of Cyprus (source: Cyprus Geological Survey Department)

The Keryneia Terrane is the geological zone located at the northern part of Cyprus and is the southern-most portion of the Tauro-Diranide Alpine Zone. The base of the Zone is mostly composed of a series of allochthonous massive and recrystallised limestones, dolomites and marbles of Permian-Carboniferous to Lower Cretaceous age (350-135 Ma). These are stratigraphically followed by younger autochthonous sedimentary rocks of Upper Cretaceous to Middle Miocene age (67-15 Ma), on which the older allochthonous formations have been thrust southward (Research & Development Center-Intercollege, 2004b; Geological Survey Department, 2016).

The Troodos Terrane dominates the central part of the island. It was formed in the Upper Cretaceous (90 Ma) on the Neotethys sea floor, which then extended from the Pyrenees



through the Alps to the Himalayas (Geological Survey Department, 2016). It is a fragment of a fully developed oceanic crust, consisting of plutonic, intrusive and volcanic rocks and chemical sediments (Research & Development Center-Intercollege, 2004b). The stratigraphy of the ophiolite shows a topographic inversion, with the lower suites of rocks outcropping on the highest points of the range, while the stratigraphically higher rocks appear on the flanks of the Troodos massif. The diapiric uplift of its core took place in many episodes with more intense uplift taking place in the Pleistocene (2.6 Ma) (Geological Survey Department, 2016).

The Mamonia Terrane is in the district of Paphos in the southwestern part of Cyprus. It constitutes a series of igneous, sedimentary and metamorphic rocks, ranging in age from Middle Triassic to Upper Cretaceous (230-75 Ma). These rocks, which are regarded as allochthonous in relation to the overlying autochthonous carbonate successions and the Troodos ophiolite rocks, were placed over and adjacent to the Troodos ophiolite during the Maastrichtian (Research & Development Center-Intercollege, 2004b; Geological Survey Department, 2016).

The Circum Troodos Sedimentary Succession, ranging in age from the Upper Cretaceous through the Pleistocene (67 Ma to recent years), covers the area between the Keryneia and Troodos Terranes as well as the southern part of the island. It consists of bentonitic clays, volcanoclastics, marls, chalks, cherts, limestones, calcarenites, evaporites and clastic sediments (Research & Development Center-Intercollege, 2004b).

The area geology plays an important role on the behaviour of land during a seismic event or a landslide. This tendency, especially in Cyprus, is intensified by the long history of powerful seismic activity in the region.

### **1.1.2 Seismicity**

Cyprus is in the earthquake zone of the Alps-Himalayas, where 15% of earthquakes occur worldwide. The seismicity of Cyprus is mainly attributed to the "Cyprus Arc", which is the tectonic boundary between the African and Eurasian lithospheric plate in the Eastern Mediterranean region (Figure 3). The African plate moves north to the plate of Eurasia resulting in the collision of the two plates and the dive of the African plate under the

microplate of Anatolia (part of the Eurasian plate) (Geological Survey Department, 2012, 2014).

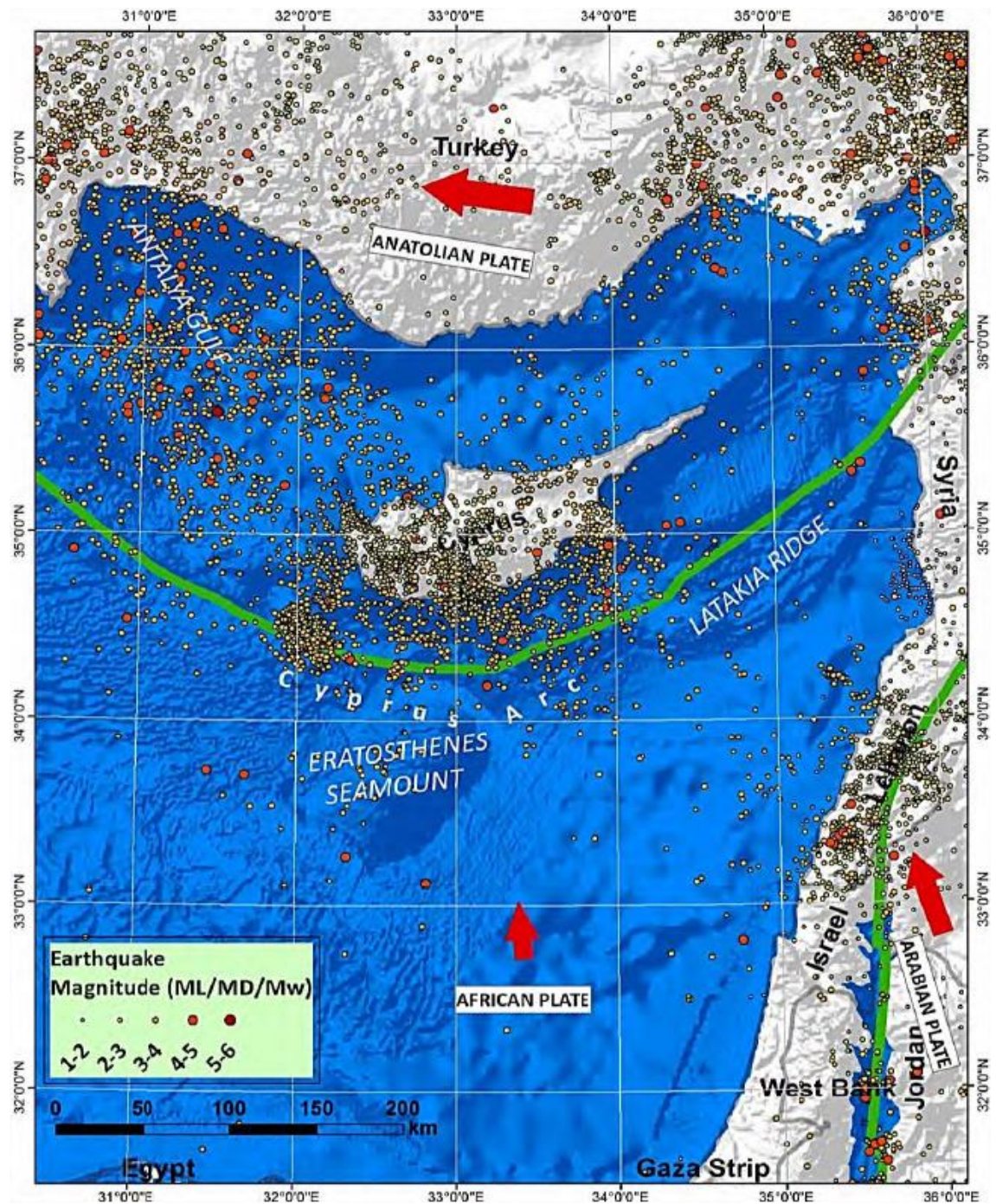


**Figure 3:** The Cyprus Arc and the adjacent tectonic plates (Geological Survey Department, 2012)

The western part of the Cyprus Arc exhibits intense seismic activity with intermediate depth earthquakes (up to 130km) near Antalya Bay, where subduction is active. The central part, which is located between the south coast of Cyprus and Eratosthenes

Seamount and extends to the Latakia Ridge, also exhibits strong seismicity, mainly with surface earthquakes. This is where the strongest earthquake of the last 50 years occurred on the 9<sup>th</sup> of October 1996 (magnitude 6.5) with the epicentre about 50km south-west of Paphos. The eastern part has low seismicity in the absence of intermediate depth earthquakes, possibly due to inactive subduction. The strongest seismicity of Cyprus is observed in the central-western part of the Cyprus Arc and in terrestrial faults in Paphos, Limassol and Larnaca. The seismicity of Cyprus 1896-2019 is presented in Figure 4.

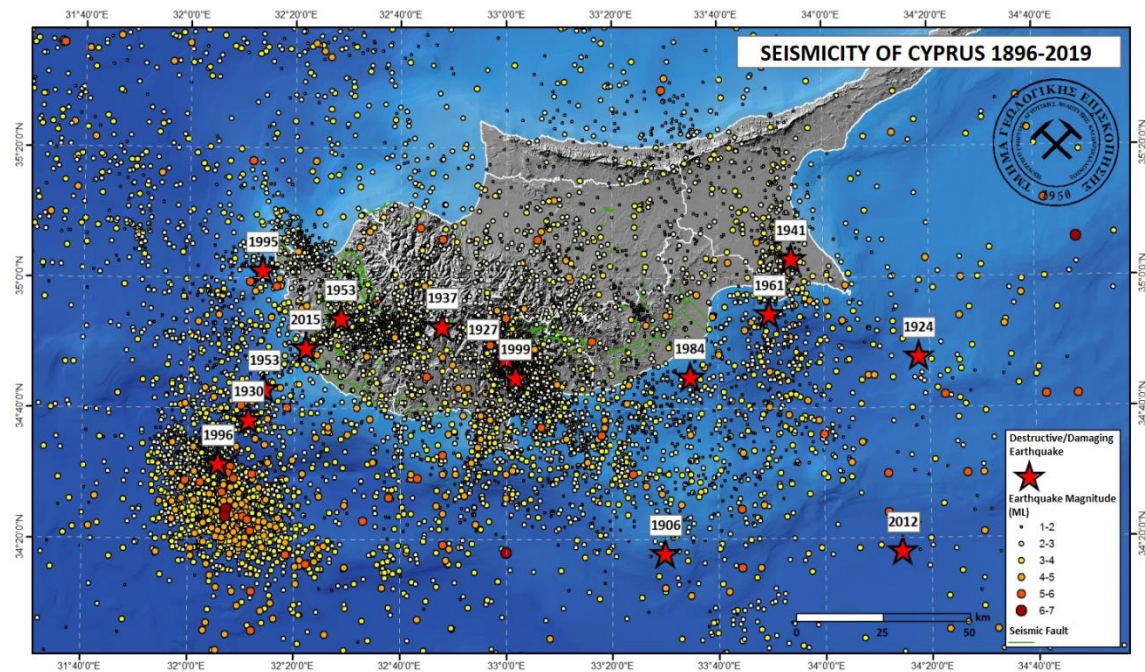


**Figure 4:** Seismicity of Cyprus 1896-2019 (Geological Survey Department, 2019)

With Cyprus often being affected by catastrophic earthquakes, it is very important to monitor the seismicity of our region not because lives can be saved directly by forecasting the phenomenon, but because lives can be saved indirectly with constant improvement of the earthquake protection measures applied in the country.

Earthquakes are natural phenomena that humans cannot prevent. However, the effects of earthquakes on structures and the environment in general can be significantly reduced or even eliminated, providing protection to people. Therefore, our initial focus should be on the study and better understanding of the seismicity of Cyprus, and on the study of land behaviour during an earthquake.

Today, the seismic activity of Cyprus and the Eastern Mediterranean is being monitored by the Cyprus Geological Survey Department, of the Ministry of Agriculture, Natural

Resources and Environment, through a comprehensive Seismological Network (12 stations), a network of accelerometers and other relevant facilities. Seismological data are received, recorded and processed and after evaluation of the seismological parameters, the general public is informed through its website and mass media.

### 1.1.3 Climate and precipitation

Cyprus has a semi-arid climate type (BSh), in the north-eastern part of island, and a hot Mediterranean climate type (Csa), in the rest of the island according to Köppen-Geiger climate classification, with very mild winters and warm to hot summers as shown in Figure 5. Snowfall appears only in the Troodos mountains in the central part of the Cyprus island. Summers are generally dry with rain occurring mostly between November and March (Aschmann, 1973; Peel, Finlayson and McMahon, 2007).



**Figure 5:** Köppen-Geiger climate classification map – Cyprus belongs to Csa and BSh types

Csa climate type is characterised by hot dry weather with limited rainfall especially during winter. Term “C” means that the average temperature for the coldest month fluctuates between 18°C and 0°C (or –3°C) and the average temperature of the warmest month is above 10°C, term “s” explains that the rainfall of the driest month is under 30mm and amounts for 1/3 of the rainfall of the wettest month and finally term “a” indicates that the average temperature for the warmest month is above 22°C.

BSh climate type is defined by very little precipitation. These climates tend to have hot, sometimes extremely hot, summers and warm to cool winters, with some to minimal precipitation. Hot semi-arid climates are found mostly around the fringes of subtropical deserts. Term “BS” means that there is little precipitation, in the range of 50%-100% of a specific threshold (combination of temperature and precipitation), and the climate is defined as semi-arid: steppe (Peel, Finlayson and McMahon, 2007; Beck *et al.*, 2018). The term “h” indicates that the average annual temperature is above 18°C and the average temperature of the coldest month is above 0°C (or -3°C) (Cereceda *et al.*, 2008).

Based on a study for the development of future Köppen-Geiger climate classification maps, Cyprus coastal areas are expected to convert from Mediterranean hot summer climate (Csa) to hot semi-arid steppe climate (BSh) areas in the future (Beck *et al.*, 2018), as presented in Figure 6.

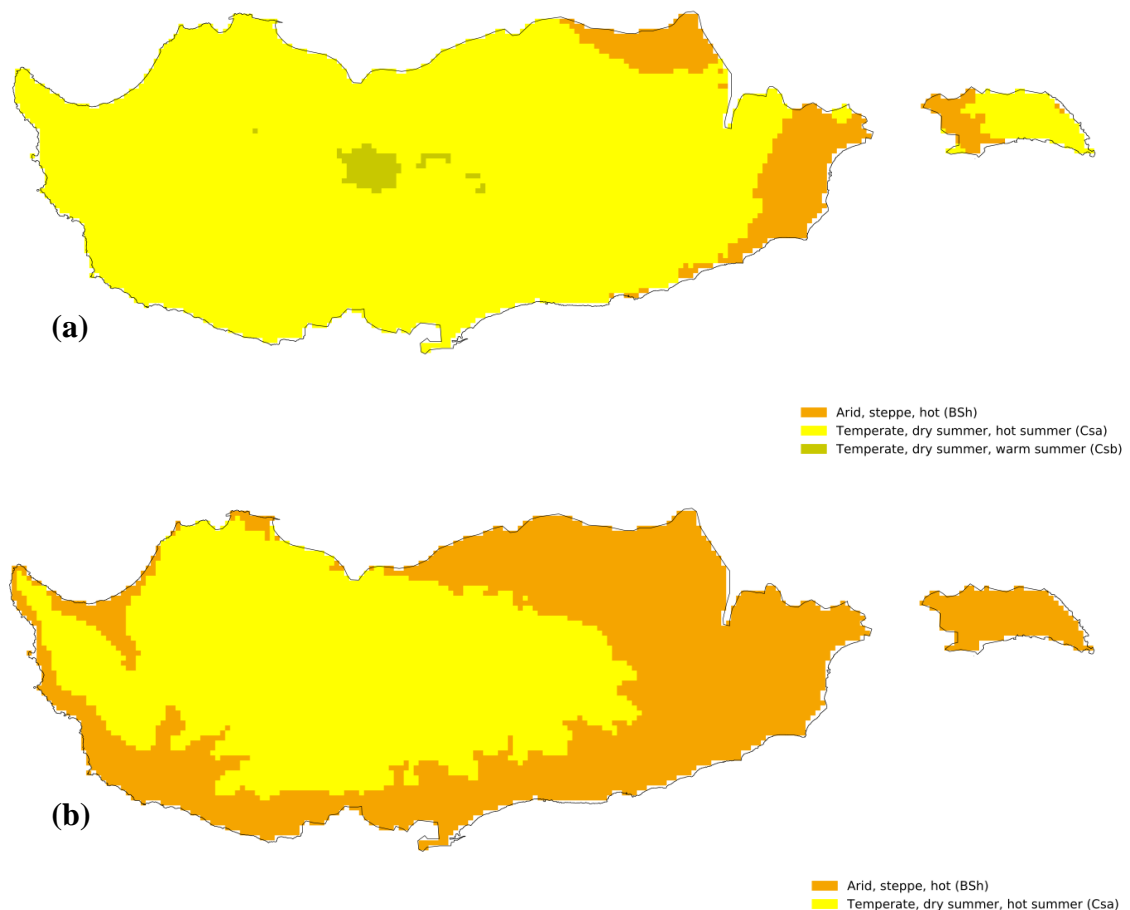


**Figure 6:** (a) Present (1980-2016) and (b) future (2071-2100) Köppen-Geiger climate classification map of Cyprus (Beck *et al.*, 2018)

Therefore, Cyprus has an ideal Mediterranean climate with mild wet winters and dry hot summers which are stretched between middle of May to middle of October. The winters are quite short and not too cold, and most of the precipitation occurs between December and February. Along the coast, the sea breeze affects the temperature especially during summer.

Finally, the average temperature and precipitation statistics for Cyprus for the period 1991-2014, which are presented in Table 1, clearly show the dry summer climate.

**Table 1:** Cyprus meteorological data 1991-2014

	<b>Average</b>
<b>Temperature (°C)</b>	17.7
<b>Max Temperature (°C)</b>	24.2
<b>Min Temperature (°C)</b>	13.1
<b>Precipitation (mm/year)</b>	470.2

*Source:* Department of Meteorology, Cyprus

Extreme meteorological phenomena occur rarely in Cyprus, like severe rainfalls, floods and severe thunderstorms. These extraordinary events combined with the geological properties in some areas and the seismically stressed ground, can lead to land movements, in terms of land subsidence/uplift or landslides, causing severe damages to critical infrastructure and urban areas.

## **1.2 The importance of using Earth Observation for monitoring land movements**

The collection of data and parameters for the detection of land movements via conventional means, such as the establishment of ground-based monitoring infrastructure and the conduction of extensive geotechnical studies, is time and money consuming. Additionally, the data collected are mostly point-based and rather limited spatially, which is insufficient, especially in the case that large areas are affected.

Remote Sensing has evolved as a powerful and non-invasive tool of investigation that allows to identify, observe, interpret and measure objects, surfaces or phenomena and to identify, map and evaluate the risks treating such features, without getting in direct contact with them (Wiseman and El-Baz, 2007; Parcak, 2009; Lasaponara and Masini, 2012). When using EO methods, the first and most important step for mapping and detection of any event taking place in a region, is the systematic collection and analysis of all available remote sensing data, obtained from either airborne or satellite platforms.

Optical satellite images offer a fast and economical alternative to monitor changes on the earth's surface over large and difficult to access areas. The availability of cloud-free images is very important and depends on the geographical position and the prevailing weather conditions of the area under study. Mediterranean countries seem ideal for the use of optical remote sensing data since they are characterised by clear weather conditions, and thus abundance in cloud-free images. This is very important when using satellite remote sensing in multitemporal studies for monitoring large areas. In Cyprus, the availability of cloud-free images increases the potential of using satellite remote sensing techniques successfully (Hadjimitsis, 2010). The use of remote sensing imagery can assist in more efficient monitoring, time savings as well as cost-efficient updating of existing land displacement inventories for the areas of interest.

Aerial images from historical and more recent archives, as well as photos obtained through Unmanned Aerial Vehicle (UAV) campaigns over areas of interest, can also be collected and used for interpretation and monitoring purposes. In fact, UAVs is becoming lately a common remote sensing method due to the ease of use and the quality of the processed images (Colomina and Molina, 2014; Yao, Qin and Chen, 2019). UAVs benefit from the fact that they fly at low altitude, in comparison to airplanes and satellites, thus producing images that are not affected greatly by atmospheric effects. They can also be deployed on demand easily to collect valuable information for monitoring and assessment purposes. Field spectroradiometers, multispectral cameras, infrared cameras and thermal cameras can be attached to UAVs to be used in different remote sensing applications, such as agriculture, land use changes, infrastructure monitoring, etc.

However, the weather conditions and the presence of sun light are the main limiting factors in passive remote sensing techniques. For visible wavelengths, the sun's energy is reflected, whereas for thermal infrared wavelengths, the sun's energy is absorbed and

then re-emitted. Quickbird, WorldView, MODIS, SPOT and Landsat are all passive sensors that can only measure radiation emitted by the sun and either reflected and/or emitted by the Earth. In general, passive sensors that are sensitive only to visible and near-infrared wavelengths are useless for remote sensing applications at areas with cloud-covered skies.

Active sensors, on the other hand, do not depend on solar energy and generate their own energy source for illumination. The produced radiation is directed towards the object under study and returns to the sensor after being reflected from the object. This characteristic allows active sensors, such as the Synthetic Aperture Radar (SAR), to acquire images and obtain measurements anytime, day or night and regardless of the weather conditions, as radar signals can penetrate clouds. The characteristics of the active satellite sensors allow for the systematic monitoring of natural hazards and their impact on infrastructure throughout the year over large areas and irrespective of weather conditions, day and night.

Nowadays, there is a wide range of optical and SAR satellite images that can be used for the monitoring of civil infrastructure and cultural landscapes. However, these images vary in resolution depending on the satellite/sensor characteristics. Despite that many of these satellite systems are currently inactive, their archived data can still be exploited for research. Their different spatial, spectral and temporal resolution characteristics can be useful for the detection and monitoring of changes in landscape. The processing of both archive images (Landsat, Worldview, QuickBird, etc.) and novel data, such as Sentinel-1 and Sentinel-2, can strongly contribute towards the identification, monitoring and assessment of risks to which built environment and cultural landscapes are currently subjected to worldwide (Agapiou *et al.*, 2014).

Numerous research activities focus on the use of Earth Observation and Remote Sensing technologies, as presented in detail in *section 2.3*, combined with Geographic Information Systems (GIS) in an effort to improve systematic monitoring of cultural heritage monuments and sites (Hadjimitsis *et al.*, 2013) and infrastructure resilience (Alexakis *et al.*, 2014).

Added value to monitoring the effects of land displacement phenomena to areas of interest can be given with the exploitation of freely available optical and radar satellite data that are currently provided by the Copernicus Sentinel missions. Obtaining information



regarding land movements/displacement over time in a specific area of interest has become easier lately, as free satellite data can be obtained on a regular basis, such as Sentinel-1 and Sentinel-2, that can be processed and used in the benefit of the greater good. A detailed description of the satellite data is provided in *section 3.2.1* of the present dissertation.

The spatial and temporal characteristics of the passive and active sensors used in remote sensing, with their very short revisit times and high coverage, can overcome all obstacles that can hinder the monitoring of natural hazards via conventional means, such as area inaccessibility, bad weather conditions and high infrastructure cost. Earth Observation can show the way for a systematic monitoring of land movements and assessment of their impact on infrastructure resilience over large areas in a timely manner, regardless of weather conditions, time of day, and at a very limited cost for data processing.

### **1.3 Structure of thesis**

The present thesis is organised as follows: In *Chapter 2*, a literature review is conducted on the use of earth observation techniques for the detection of natural hazards, and more specifically land movements/displacement. Then in *Chapter 3*, the case study areas, the data and software used, and the methodology applied for the identification of the areas susceptible to land movements, and for monitoring land displacement are presented in detail. In *Chapter 4*, the results that were obtained from the application of the proposed methodology are presented and analysed. In *Chapter 5*, the findings from the application of the proposed methodology are discussed further. Finally, the concluding remarks along with a summary of the findings, innovation of the suggested methodology and future work are showcased at the end of the present thesis.

## 2 Literature review

Cyprus, being located on the Mediterranean fault zone (Cyprus Arc), as presented in *section 1.1.2*, exhibits a unique geodynamic regime since its tectonic evolution is driven by the interaction of the Eurasian and the African plate. Besides its seismological interest, many active landslides and slope instabilities, in areas of steep topography occur in Cyprus, having substantial impact to the built environment, by posing an imminent threat for entire settlements, critical infrastructure and cultural heritage landmarks.

To date, the combined result of landslides and earthquakes in Cyprus has led to the abandonment and relocation of many villages, especially in Paphos District, endangered vulnerable archaeological sites, and caused the destruction of properties, infrastructure and road networks. Current research infrastructure for monitoring and better understanding of these natural hazards is limited to conventional equipment, such as seismographs, geophones and inclinometers, and, thus, no systematic research has been conducted to monitor ground deformation events with high accuracy and dense spatial resolution, in a timely manner.

In this section, a literature review is carried out regarding the natural hazards that occur most often in Cyprus, based on the characteristics that were presented in *section 1.1*, the conventional methods that are currently being used for monitoring natural hazards worldwide, and finally, how Earth Observation techniques can be applied to monitor natural hazards and their impacts on infrastructure resilience.

### 2.1 Natural hazards

Seismic events are episodes of release of accumulated stress in the earth's crust and can result in surface deformation, which may be observed in the form of ground surface rupture, subsidence and/or uplift (Mathew, Majumdar and Kumar, 2015).

In fact, earthquakes are one of the major triggers of landslides in hilly areas besides rainfall and anthropogenic factors. The seismic induced ground acceleration enhances the shear stress along slopes and results in the factor of safety of the slope forming material to fall below unity, triggering slope failures and hence the magnitude of the earthquakes and the mechanism of movement along the source fault positively influence the number

of landslides that are triggered or reactivated during a seismic event, in addition to the terrain and geological factors (Mathew, Majumdar and Kumar, 2015).

Cyprus is frequently affected by catastrophic earthquakes, due to its position at the tectonic boundary between the African and Eurasian lithospheric plate in the Eastern Mediterranean region. Earthquakes are natural phenomena that humans cannot prevent. However, the effects of earthquakes on structures and the environment in general can be significantly reduced or even eliminated, providing at the same time protection to people. Therefore, our initial focus should be on the study and better understanding of the seismicity of Cyprus, and on the study of land behaviour during an earthquake.

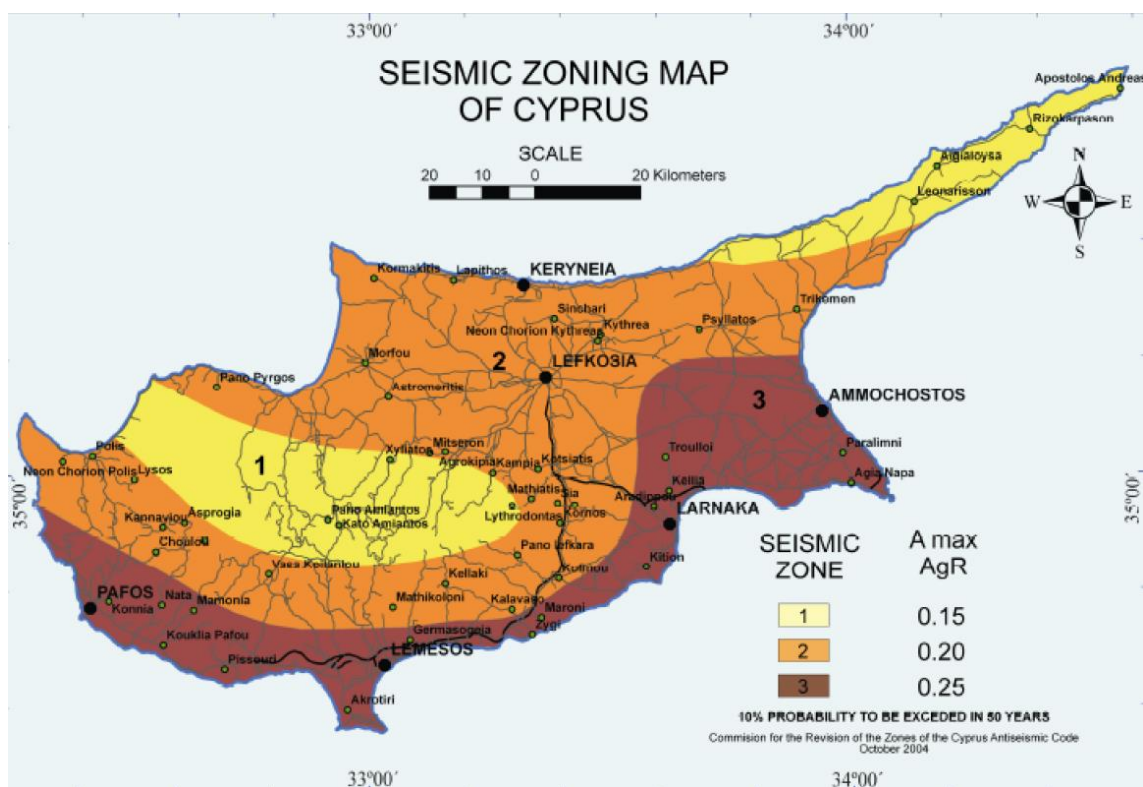


**Figure 7:** The seismic zoning map of Cyprus (Cyprus Organisation for Standardisation, 2004)

Since 2004, the seismic zoning map of Cyprus, as presented in Figure 7, is used as part of the National Annex to CYS EN 1998-1:2004 (Cyprus Organisation for Standardisation, 2004). However, the World Health Organization in 2010, published a seismic hazard distribution world map (Figure 8) with similar results for Cyprus. More specifically, Paphos and Limassol Districts at the south-southwest, and Larnaca, Famagusta and Nicosia Districts at the east-southeast of the island show the greatest risk in earthquake occurrence. The rest of the island is at medium risk related to seismic activity.

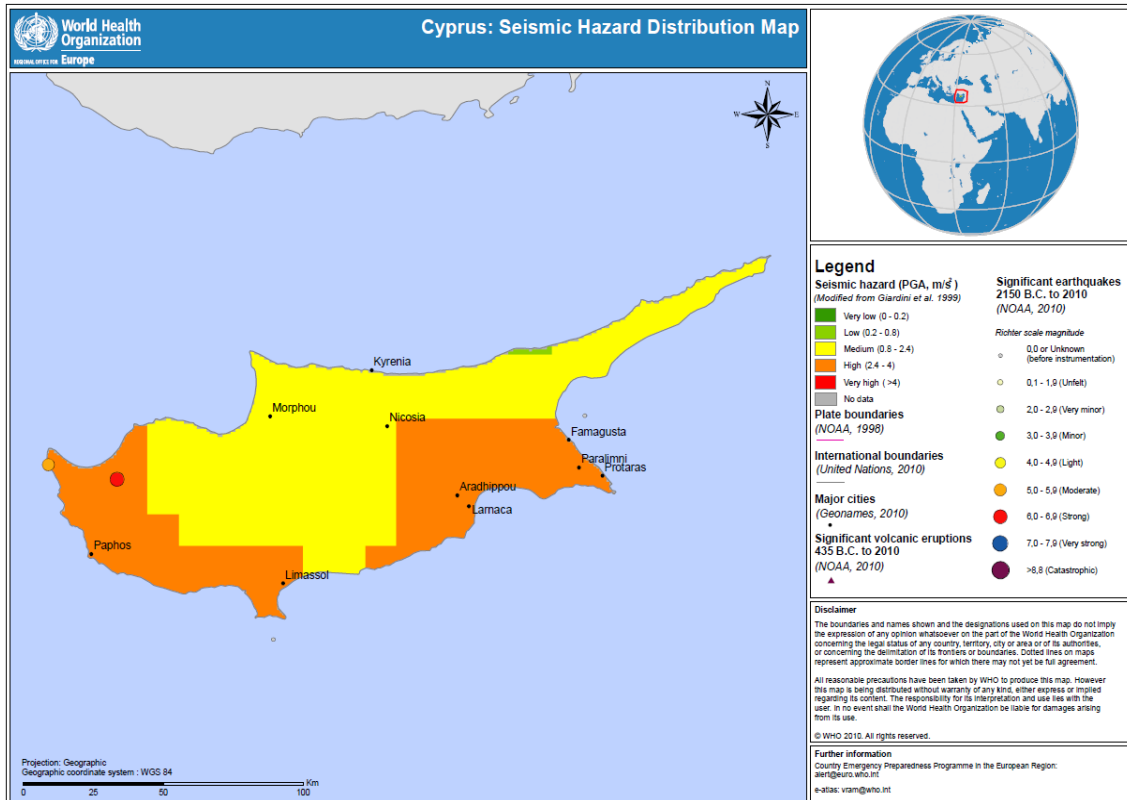


**Figure 8:** The seismic hazard distribution map of Cyprus (World Health Organization, 2010)

It is of great importance to monitor the seismicity of a region not only because lives can be saved directly by forecasting the phenomenon, but also because lives can be saved indirectly with constant improvement of the earthquake protection measures applied in the country. The area's geology plays a major role on the land behaviour during a seismic event or a landslide. This tendency, especially in Cyprus, is intensified by the long history of powerful seismic activity in the region.

Landslides and other slope instability events occur in Cyprus mainly in hilly and mountainous areas, due to the presence of weak and vulnerable geological conditions and the steep topography. Anthropogenic factors, such as excavation, agricultural activities, removal of vegetation can be landslide triggering factors. Additionally, despite the relatively warm and dry climate of Cyprus, extreme meteorological phenomena, such as heavy rainfalls, floods and severe thunderstorms, occur rarely. These extraordinary events combined with geological properties in some areas can lead to land movements, in terms of land subsidence or landslides, causing severe damages to critical infrastructures and urban areas (Geological Survey Department, 2013).

In Cyprus, the most severe landslides for the built environment have taken place in the mountainous and hilly areas of Paphos and Limassol district, causing damages to residences, civil infrastructure networks, such as roads and road networks, utility services pipelines, etc. Considering the impact of these phenomena combined with damages due to seismic events, villages such as Statos, Agios Photios, Kivides and Korfi have been abandoned and relocated at safer areas after the recommendations provided by the Geological Survey Department (Geological Survey Department, 2013).

During the last decades, there has been a continuous demand for residential development in the island, leading at the same time to the construction of utility services and road networks connecting the newly built areas. Housing projects and other infrastructure are potentially being built in areas with geotechnical problems. In order to avoid construction damages, a detailed geotechnical survey should be carried out prior to the construction of a new project. This can assist in the adoption of preventive measures so as to cope with the geological and geotechnical conditions of the area, or even suggest that the area is unstable and should be completely avoided.

Several geotechnical field investigations have been conducted by the GSD in collaboration with the British Geological Survey between 1985 and 1986 in Paphos District, and especially in the villages of Agios Photios, Kannaviou, Pentalia and Simou, areas prone to landslides (Northmore *et al.*, 1986, 1988).

Following that, a comprehensive study was carried out in Paphos District by the GSD in collaboration with Scott Wilson Co. in the framework of a research project in 2008-2010, in order to identify and map the various types of landslides through extensive geological and geotechnical investigations, and interpretation of aerial photographs and QuickBird high-resolution satellite imagery for observation and verification of the results (Hart and Hearn, 2010, 2013; Hearn *et al.*, 2018).

In all cases, extensive geological and geotechnical field investigations were conducted to develop landslide susceptibility maps. Features such as back scarps, failed material, intermediate scarps, etc., that assisted in the assessment of landslide triggering factors, failure mechanisms and events, were identified. The landslide susceptibility maps that were developed from these studies, along with the development of relevant ground suitability maps, are currently being used as tools by the infrastructure management authorities and other local authorities responsible to issue planning and building permits.

However, the provision of information in a timely manner is of great importance in cases of the occurrence of potentially hazardous events, when human lives are in danger. Nowadays, there is an emerging need for real-time and/or near real-time monitoring systems, the so-called Early Warning Systems (EWS), in order to be able to inform the general public on time for an upcoming danger (Intrieri *et al.*, 2013; Guzzetti *et al.*, 2020). EWS are defined as “The set of capacities needed to generate and disseminate timely and meaningful warning information to enable individuals, communities and organizations threatened by a hazard to prepare and to act appropriately and in sufficient time to reduce the possibility of harm or loss.” (United Nations, 2009).

To achieve real-time and/or near real-time monitoring, measurements must be acquired continuously to detect ground movements, and sent remotely to servers without the interference of personnel. Moreover, data processing must be performed automatically in a very short time (Yin *et al.*, 2010). The selection of the appropriate monitoring method and equipment are vital, as the entire process from data acquisition to the release of the warning must be fully automated for a real-time hazard assessment (Sorensen, 2000).

There are many techniques for monitoring land movements due to landslides or earthquakes. These techniques can be classified as ground-based or satellite-based geodetic, geotechnical or physical, photogrammetric, and Earth Observation (EO) techniques (Savvaidis, 2003). For each one of these categories, different instrumentation and equipment needs to be installed or used for periodic monitoring or for continuous data collection either remotely or in-situ (Liu and Wang, 2008).

In-situ monitoring methods can provide near-real-time high-resolution data regarding land displacement at individual points, from the first few minutes until one hour from the first signs of a geo-hazard (Manconi and Giordan, 2016; Guzzetti *et al.*, 2020). These methods together with the available technologically advanced monitoring equipment, can assist in the immediate detection of land movements, to enable the authorities responsible and the general public to make timely decisions about safety in the occurrence of potentially hazardous events (Reid *et al.*, 2012; Allasia *et al.*, 2013; Guzzetti *et al.*, 2020). Nowadays, with the availability of data from Copernicus and other contributing missions, the integration of conventional techniques (geotechnical investigations), with Earth Observation techniques allows for the implementation of near real-time EWS.

An analysis of the existing in-situ and remote (EO) monitoring methods is carried out in *sections 2.2 and 2.3* of the present thesis. The various methods used for monitoring land movements and assessing the impact of such phenomena, like seismic events and landslides on infrastructure resilience are presented, categorised into conventional and Earth Observation techniques.

## **2.2 Monitoring natural hazards through conventional methods**

There is great variety of conventional methods that are currently being applied for monitoring natural hazards, and more specifically the ground deformation they generate. The selection of the appropriate techniques is case and event-specific and depends on various criteria.

More specifically, the type of risk, the accessibility to the area, the susceptibility of the area to damage, the expected impact, the availability of resources and the availability of field work time play a very important role in the selection process. In this section, the various conventional techniques that are used in landslide and vertical ground displacement studies are presented.

### **2.2.1 Geodetic techniques**

Conventional ground-based geodetic methods have been used widely in deformation surveys. They can provide absolute position, in the form of coordinates, of a specific point on the ground. Additionally, they can be used to evaluate the accuracy of their measurements globally and they are suitable to use in any environment (Dzurisin, 2007a). Horizontal and/or vertical displacement vectors of targets can be calculated, after appropriate processing, for ground deformation monitoring and landslides (Savvaïdis, 2003; Dzurisin, 2007a; Liu and Wang, 2008), via two basic methodologies:

- Establishment of horizontal triangulation or vertical/elevation control networks at the study area with appropriate control points at the area of deformation.
- Angle and distance measurements to prisms located on the area under study by total stations.

However, ground-based geodetic surveys are time consuming as they usually last for several days and require the work of many operators, depending on the complexity of work. Therefore, they can hardly be used for continuous ground displacement monitoring, due to the high cost of the equipment and the number of personnel that needs to be involved. Due to the introduction of Global Navigation Satellite Systems (GNSS), they are not usually used for land displacement monitoring (Dzurisin, 2007a).

GNSS have many advantages over conventional ground-based geodetic techniques and they have proved to achieve reliable results of high accuracy through different application methodologies (Savvaïdis, 2003; Liu and Wang, 2008; Gu and Wang, 2013). Station selection is easier as there is no need for visibility between the stations, and measurements can be carried out throughout the day and night, under all weather conditions (Savvaïdis, 2003; Dzurisin, 2007b). GNSS techniques can assist in ground displacement investigations, by measuring time series of coordinates at specific points within the deformation area. There are numerous applications of episodic GNSS techniques in small-scale projects and continuous monitoring ones in larger scale projects (Dzurisin, 2007b; Murray-Moraleda, 2011; Gualandi *et al.*, 2017; Barzaghi *et al.*, 2018).

Moreover, extensive GNSS/GPS networks have been established worldwide for monitoring crustal deformation, such as the GEONET in Japan consisting of over 1000 GPS stations, the CORS, SCIGN and PANGA networks operated by different organisations in the USA (Dzurisin, 2007b). They are case specific, as they differ in the overall application cost (equipment installation and maintenance), and the type and accuracy of data they provide.

### **2.2.2 Photogrammetric techniques**

In photogrammetric techniques, the XYZ position of a target is obtained from photographs taken from two or more survey points with known coordinates and a known relative orientation of the cameras. Aerial and terrestrial photogrammetry techniques, due to their advantageous characteristics, have been used widely in ground subsidence studies (Liu and Wang, 2008). They can provide three-dimensional coordinates for an infinite number of points in minimal fieldwork time (Thompson and Schilling, 2007).



Ground-based photography has been used for monitoring landslides at local scale level, whereas aerial photography for the identification and analysis of landslides at a large scale (Savvaïdis, 2003; Liu and Wang, 2008). However, aerial photography disadvantages in terms of temporal resolution due to the very high cost for programming flights to obtain aerial photos. On the other hand, terrestrial photogrammetry, where special cameras are employed to take photos at ground locations, can effectively be used at inaccessible sites, providing highly accurate positioning information over a period of time recording landscape changes (Thompson and Schilling, 2007).

Photogrammetric techniques are generally preferable than conventional ground-based surveying methods, especially in cases of inaccessible areas, or limited field survey time.

### **2.2.3 Geophysical techniques**

Geophysical techniques are used in landslide investigation and provide sub-surface information and more specifically the physical characteristics of rocks and soils. Borehole investigation and the close collaboration with expert geologists, hydrogeologists, geotechnical engineers and geomorphologists are necessary for data calibration (Jongmans and Garambois, 2007; Pazzi, Morelli and Fanti, 2019). The various methods, the related instrumentation and some of their limitations are described in brief below:

- Seismic methods generally make use of geophones as receivers of elastic waves that are generated by various sources (explosives, earthquakes, rock-falls, etc.). Based on the measurement methodology, they are categorised as follows:
  - Seismic reflection: Capable for imaging the geometry of the landslide structure through the installation of arrays of geophones. However, it needs greater effort than other techniques, making it time consuming and costly. It is rarely used in landslide investigations (Kearey, Brooks and Hill, 2002; Bichler *et al.*, 2004; Grit and Kanli, 2016).
  - Seismic refraction: Measures the travel time of compressional waves through sub-surface layers. It can be applied in landslide investigation for determining the depth to bedrock (Kearey, Brooks and Hill, 2002). It has a limitation in the penetration depth as it can only detect waves at a depth up to 30 meters (Jongmans and Garambois, 2007).

- Seismic tomography: It has been used for landslide investigation in rock conditions (Meric *et al.*, 2005) through geophones and boreholes. In comparison with the seismic refraction method, tomography needs more field effort (Jongmans and Garambois, 2007).
- Seismic noise measurements: They are used quite often, since 2000, in earthquake engineering. It is a cost effective technique and requires easy to deploy instruments (Méric *et al.*, 2007; Pilz *et al.*, 2014).
- Surface waves: This method has provided reliable results in monitoring landslides. However, as the method is based only on one-dimension approximation, it fails in the investigation of two or three-dimensional structures (Foti, 2005).
- Electrical methods: They are mainly applied to investigate the electrical resistivity at the ground surface via electrodes and a measuring device (Jongmans and Garambois, 2007; Pazzi, Morelli and Fanti, 2019). The various techniques are:
  - Electrical resistivity: Measures the current potential differences between the current and the measuring electrodes. In landslide investigations, Electrical Resistivity Test (ERT) is used to identify the location of the sliding plan and can assist in the identification of changes due to ground movement (Godio and Bottino, 2001; Bell *et al.*, 2006; Pasierb, Grodecki and Gwózdź, 2019). A disadvantage of this method is the difficulty to specify the resolution of the survey.
  - Spontaneous potential: Measures the natural electrical potential difference between pairs of electrodes connected to a voltmeter (Reynolds, 2011). Only few hydro-geophysical methods were applied on landslides, except those conducted with the Self-Potential method (SP), which is the easier to deploy and monitor for moisture-induced landslides (Baroň and Supper, 2013; Akinlabi, Akinrimisi and Fabunmi, 2018; Whiteley *et al.*, 2019). There is no quantitative interpretation on the fluid source limiting the application of SP in landslide investigations.
- Electromagnetic methods: They are used often for landslide investigations for the definition of the unstable mass boundaries (Meric *et al.*, 2005; Bell *et al.*, 2006). They are conducted with two horizontal loops and a ground conductivity meter, providing a single electrical resistivity value used in the mapping of the

underlying geology (Jongmans and Garambois, 2007; Reynolds, 2011). However, to achieve proper interpretation in landslide investigations, these results need to be combined with other geophysical techniques (Meric *et al.*, 2005).

- Ground Penetrating Radar (GPR): A very popular technique that is used in geosciences due to its high resolution, its sensitivity to electromagnetic contrasts and the penetration depth when operating in low frequency (Reynolds, 2011). The equipment is very easy to use and transfer. However, their inability to identify water saturated soil layers; and their significantly reduced penetration depth when soil discontinuities are present, have minimised its use potential for landslide investigations (Jongmans and Garambois, 2007; Pazzi, Morelli and Fanti, 2019).
- Gravimetry methods: They are used to study landslide geometry by lightweight instrumentation (gravimeters). Gravimetric studies can provide useful information for slope stability analysis (Jongmans and Garambois, 2007), although they are not commonly used, as they require time consuming and rather difficult data processing (Reynolds, 2011).

#### **2.2.4 Geotechnical techniques**

Geotechnical techniques are used to monitor the relative ground displacement through the installation of sensors in the area under study. The main sensors used for ground deformation monitoring are extensometers and inclinometers; whereas piezometers provide data about the groundwater pressure; strain meters and pressure cells measure total stress in soil (Dunncliff, 1994; Hill and Sippel, 2002). These sensors can either store the measured data internally or transfer the measurements automatically to a database and/or computer. Meteorological sensors are also used for deformation monitoring, as they provide important measurements, i.e. precipitation, or measurements that are used to calibrate other geotechnical sensors.

#### **2.2.5 The case of Cyprus**

In Cyprus, the Cyprus Geological Survey Department (GSD), of the Ministry of Agriculture, Natural Resources and Environment undertakes the planning, execution and

evaluation of the required geological and geotechnical investigations prior to the technical construction works of the public development projects. GSD is also responsible for conducting studies related to natural geological hazards such as landslides and land subsidence (Geological Survey Department, no date a).

Furthermore, GSD is responsible to determine the geological suitability zones. This includes the preparation of specialised geological and geotechnical surveys to obtain the required information for the planning and safe urban development of an area. These studies include geotechnical drilling investigations, geological mapping activities and geophysical excavations (boreholes).

To date, the geological suitability map, as shown in Figure 9, covers approximately 9.65% of Cyprus, and more specifically (a) the mountainous and semi-mountainous Paphos District; and small parts of (b) Limassol; (c) Larnaca; and (d) Famagusta (Geological Survey Department, no date a). This information is rather limited and there is a great need to cover more areas and continuous update the relevant information.



**Figure 9:** Geological suitability zone map of Cyprus (source: Geological Survey Department<sup>2</sup>)

<sup>2</sup> Digitised map based on data obtained from the Geological Survey Department

Additionally, GSD carries out land displacement monitoring and assessment studies, in various areas in Cyprus, known for their geological problems, especially in Paphos and Limassol Districts. Between 1985 and 1986, geotechnical landslide investigations have been conducted by the GSD in collaboration with the British Geological Survey in Paphos District, and especially in areas susceptible to landslides (Northmore *et al.*, 1986, 1988). Moreover, a comprehensive landslide study was carried out in Paphos District by the GSD in collaboration with Scott Wilson Co. in 2008-2010, to identify and map the various types of landslides, resulting in the “Paphos Landslide Study” (Hart and Hearn, 2010, 2013; Hearn *et al.*, 2018). In the framework of this study, a landslide inventory was developed, and aerial photograph interpretation, extensive field mapping and ground investigations were carried out to record the landslide distribution, and assess the landslide susceptibility, hazard and risk across the area of interest (Hart and Hearn, 2010). These studies showed how the identification of the geomorphological features in an area can assist in the identification of landslides and the assessment of their impact on infrastructure and residential areas (Hearn *et al.*, 2018). In all cases, extensive field investigations were conducted to develop landslide susceptibility maps (Figure 10).

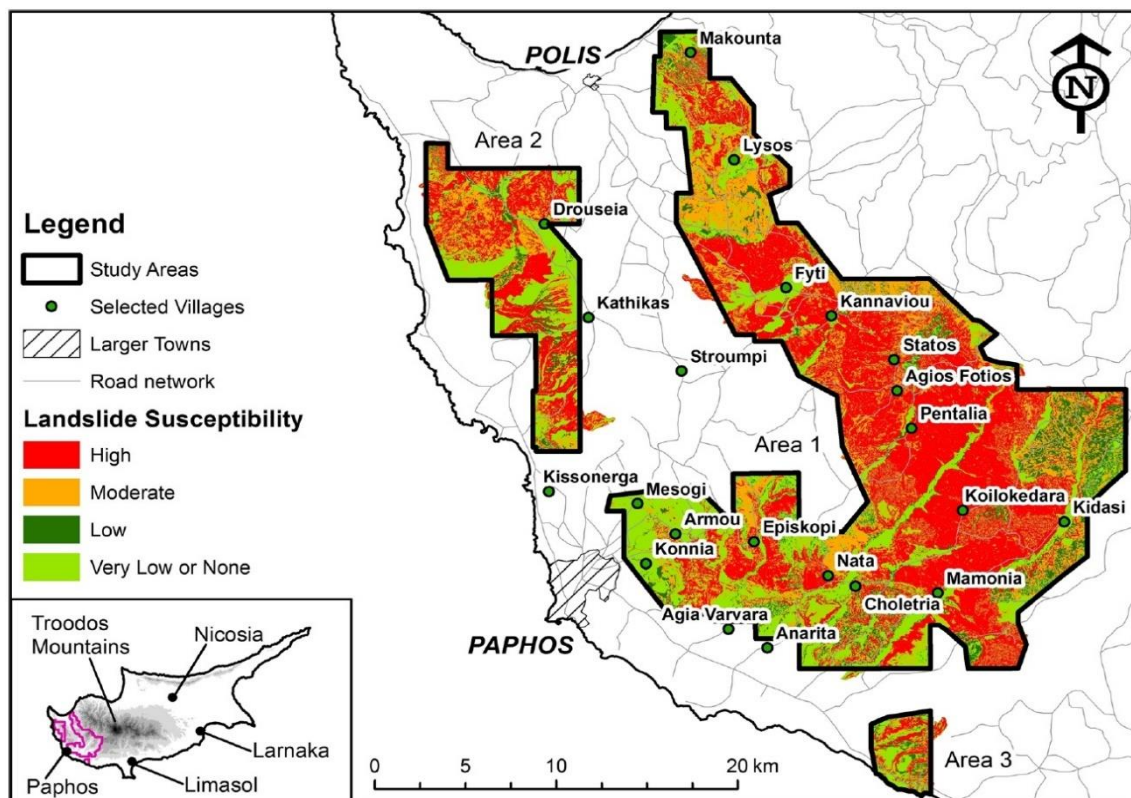


**Figure 10:** Landslide susceptibility map (Hart and Hearn, 2010; Hearn and Hart, 2019)

Furthermore, an inventory of all landslide events that occurred in Cyprus was developed by the GSD based on these studies, as presented in Figure 11, and is continuously updated based on new ground deformation events that take place. It is clear, that the vast majority of the landslides that occurred in Cyprus, took place in Paphos District.

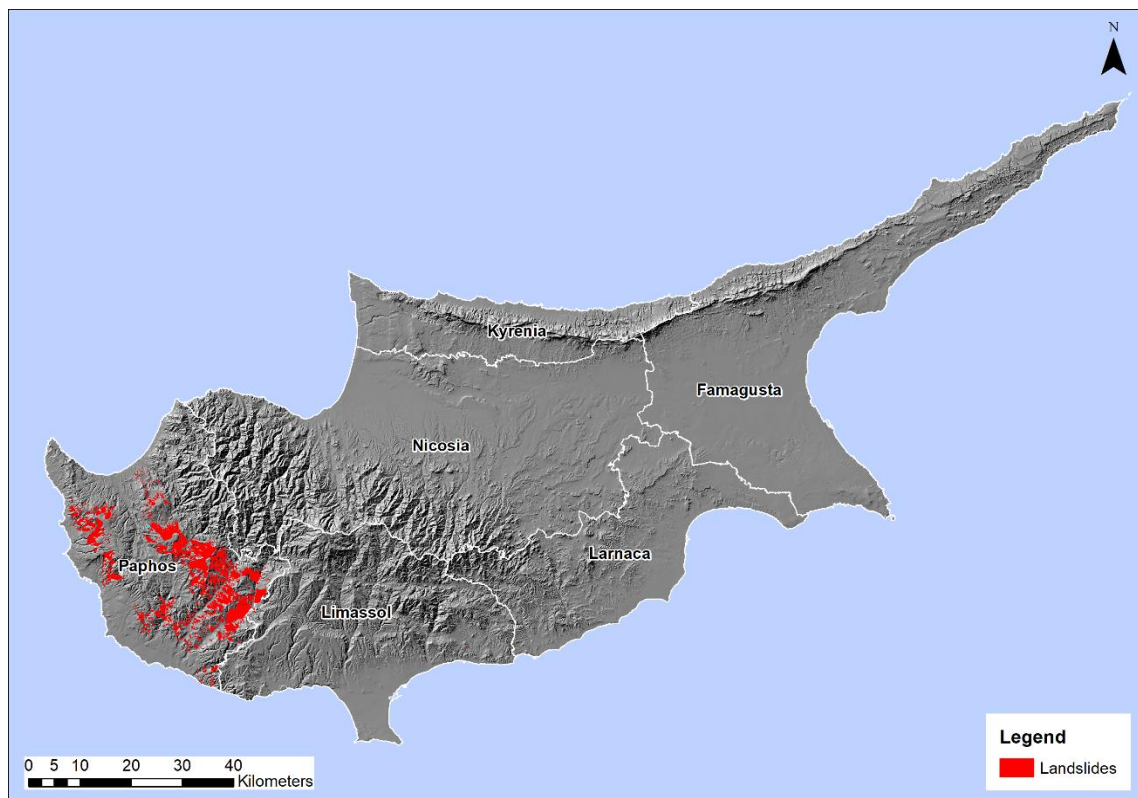


**Figure 11:** Landslide inventory map of Cyprus (source: Geological Survey Department<sup>3</sup>)

The landslide susceptibility map, that was developed from these studies, and the landslide inventory map are still being updated by the Geological Survey Department, and they are used as decision-making tools by infrastructure management authorities to issue planning and building permits.

Today, the systematic monitoring of ground movements is carried out using electronic equipment (inclinometers), which are essential tools for monitoring active landslides and, under certain circumstances, facilitates early warning of landslide activation. These studies are targeted in areas, where specific settlements were abandoned due to serious ground stability issues, as in the case of Statos and Agios Photios villages that is presented in detail in *section 3.1.1*.

---

<sup>3</sup> Digitised map based on data obtained from the Geological Survey Department

Currently, 26 exploration boreholes and wells, with a total depth of 561 meters, are being monitored by GSD in Pissouri, Armou, Letimbou, Nata, Pentalia, Choletria, Panagia, Asbestos, Petra tou Romiou and Pano Deftera – Panagia Chrysopiliotissa. New areas are added every year to the existing monitoring network, based on the arising geological problems (Geological Survey Department, no date a).

Seismic events are also being monitored by the GSD, through a permanent comprehensive Seismological Network, consisting of 12 stations and 2 seismological centres, a network of accelerometers and other relevant facilities (Figure 12 and Figure 13).

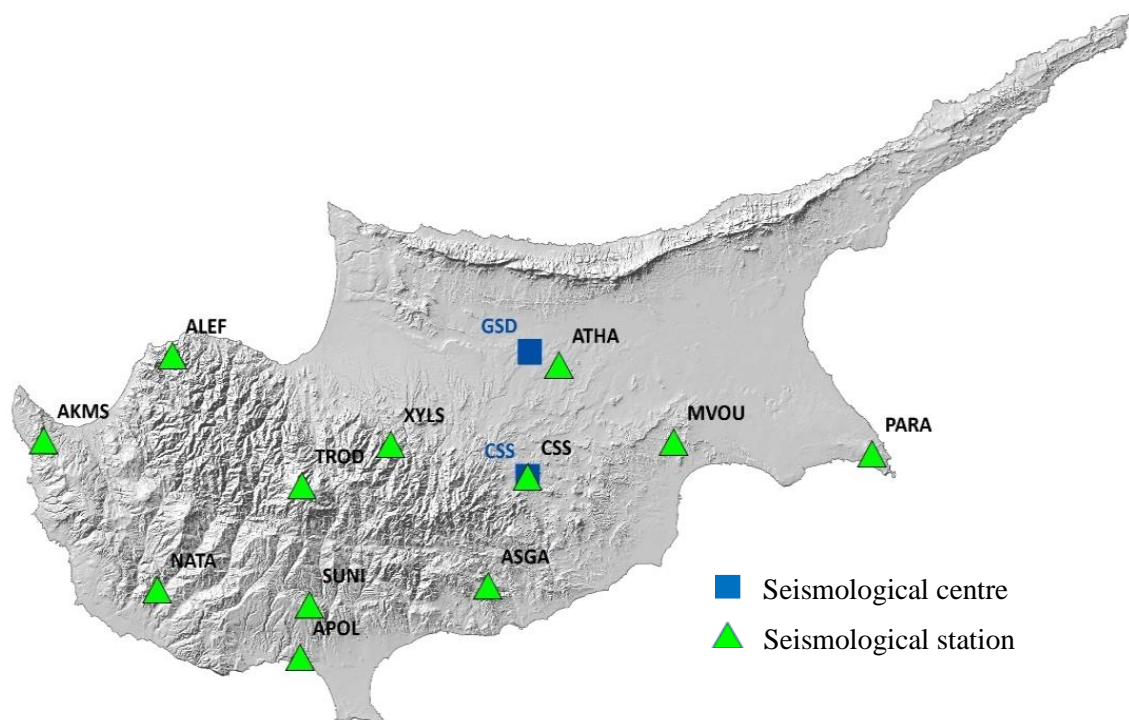


**Figure 12:** The Cyprus Seismological Network (source: Geological Survey Department)

Each one of these 12 seismological stations is equipped with the following instruments (Geological Survey Department, 2018):

- State-of-the-art three-component, broadband and high-resolution seismometer.
- Digital seismograph (digitiser) that converts ground vibrations recorded by the seismometer into a digital signal.
- Satellite modem for data transmission and two-way connection of the station with the seismological centres.
- Satellite antenna (VSAT) for data transmission and two-way telecommunication of the station with the seismological centres.

- GPRS modem for transmitting data (backup) over terrestrial internet.
- External GPS receiver for accurate time setting, to allow accurate seismic vibration recording time from the seismometer, accurate coordinates and altitude of each station.
- Standalone power system including batteries and photovoltaics for autonomous and seamless power supply throughout the year.

The new seismic network is also equipped with a private satellite network with real-time earthquake detection and processing, including data management software with 24/7 high availability network monitoring (Nanometrics, 2015). Seismological data are received, recorded and processed and after evaluation of the seismological parameters, the general public is informed through its website and mass media.



**Figure 13:** The primary seismological centre (left) and the prototype seismological station GSD in Nicosia (right) (source: Geological Survey Department)

The primary seismological centre GSD, located in Nicosia, and the back-up centre CSS, in Mathiatis, record about 2000 earthquakes yearly, 1300 of which have their epicentre in the wider area of Cyprus. However, only a small portion of these, approximately 0.5%, are perceived by Cyprus citizens (Geological Survey Department, no date c).

The Geological Survey Department, based on the studies presented above, the extensive network of inclinometers and exploration boreholes that it possesses, has developed a risk map for earthquakes and other hydro-geological hazards. This map, which is a continuation of the map developed in the “Paphos Landslide Study”, is mostly focused in



Paphos District, as shown in Figure 14. It is being continuously updated by the GSD and is free to access via the national open data portal<sup>4</sup>, according to the INSPIRE Directive<sup>5</sup>.

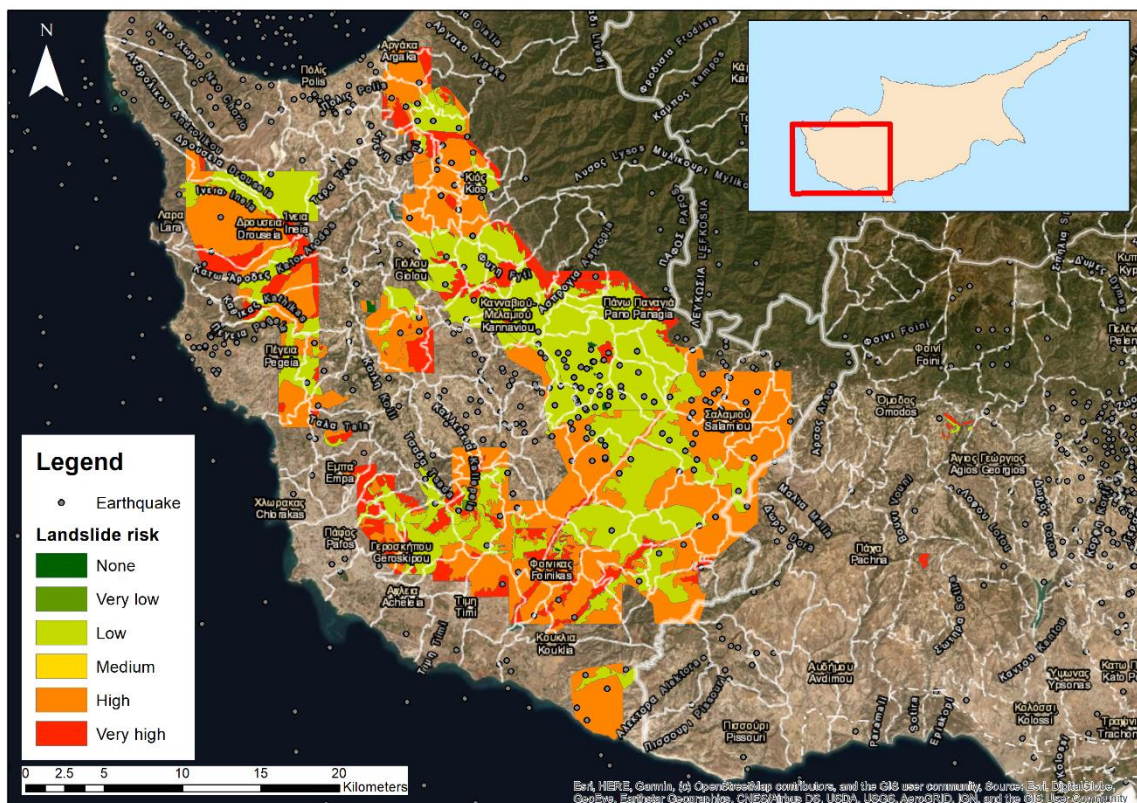


**Figure 14:** The earthquake and other geological hazards risk map (source: Geological Survey Department<sup>6</sup>)

The mapping of geologically suitable areas (Figure 9) and landslide susceptible areas can assist in the prevention of catastrophic events and mitigate their impact on infrastructure, by prohibiting any new development in high-risk areas and by instructing appropriate geotechnical investigations and the application of case-specific stabilisation measures.

The identification and monitoring of seismic and landslide events through traditional means can be achieved, as described earlier, through the establishment of expensive ground-based monitoring infrastructure and extensive field inspection studies. These conventional methods can provide detailed information on surface and sub-surface

<sup>4</sup> National open data portal: <https://www.data.gov.cy/node/1925?language=en>

<sup>5</sup> The INSPIRE Directive: <https://inspire.ec.europa.eu/legislation-details/directive-20072ec-article-17>

<sup>6</sup> Digitised map based on data obtained by the Geological Survey Department

process characteristics contributing to the principle understanding of the nature of the phenomenon (Teshebaeva *et al.*, 2015).

Currently, the monitoring of natural hazards is achieved by conventional equipment, such as seismographs and inclinometers, which are sometimes outdated. Additionally, borehole investigations are carried out by the GSD, as described before. Unfortunately, this has led to the insufficient recording of events for monitoring geo-hazards as the data collecting techniques are rather time consuming.

These data are not always available and the process for producing a dataset that can be used with confidence, is quite long, which is not always compatible with the short time scales of engineering investigations (Hearn *et al.*, 2018; Hearn and Hart, 2019). Moreover, these time and money consuming methods are mostly point-based and are rather limited in the spatial extent of the monitored area, which is especially insufficient if large areas are affected (Teshebaeva *et al.*, 2015).

### **2.3 Monitoring natural hazards through Earth Observation**

Physical constraints tend to restrict the topology of transportation networks and make them nearly planar, making them sensitive to failures (Patuelli *et al.*, 2007). Therefore, the road network vulnerability analysis is very important for road network planning, construction and management (Yang and Qian, 2012). Lately, investments have been made in infrastructure for planning, designing and operating more resilient transportation systems to cope with emerging risks (Transportation Research Board, 2009).

Qualitative landslide risk analysis and geotechnical engineering have proved to be very useful in route selection, road design and road construction in order to construct roads with significantly less risk to landslides. This is very important, because landslides and slope instabilities often lead to economic losses, property damages and high maintenance costs, as well as injuries or fatalities (Das *et al.*, 2010).

Land movements occur due to complex interactions among many partially inter-related factors. The observation of the Earth from space has many uses in the natural sciences, but it is only in the last decades that technological advances have also extended to land movements (Tofani *et al.*, 2013). During this period, numerous studies have extensively

used geo-information techniques such as remote sensing, GIS, spectroradiometry and Lidar in applications related to the natural disasters and landslide risk assessment (Ardizzone *et al.*, 2007; Biswajeet and Saro, 2007; Tsai *et al.*, 2010; Rossi and Reichenbach, 2016). Although the prediction of a land displacement event is difficult in space and time, a study area can be ranked according to its susceptibility to land movements in order to possibly minimise future infrastructure damage (Saha *et al.*, 2005). Land displacement susceptibility is the likelihood for a land displacement event, like landslide or subsidence/uplift, to take place in an area. It depends on the area stability and the presence of a set factors triggering land movements, such as the geology, the seismicity and the climate/precipitation of the area as described in *section 1.1* of the present thesis (Crozier and Glade, 2012).

Landslide hazard assessment and risk management can be accomplished by providing the risk managers with easily accessible and continuous landslide susceptibility information of the study area (Galli *et al.*, 2008; Kouli *et al.*, 2013; Alexakis *et al.*, 2014). A landslide hazard susceptibility map depicts areas in which landslides are likely to occur in the future by correlating some of the main factors that contribute to landslides with the past distribution of slope failures (Fall, Azzam and Noubactep, 2006). In addition, satellite remote sensing techniques have been widely used in landslide susceptibility assessment in terms of development of landslide inventory maps (Saha, Gupta and Arora, 2002; Lee and Lee, 2006; Fourniadis, Liu and Mason, 2007; Park and Chi, 2008; Pradhan, 2010). Satellite imagery offers a fast and economical alternative to monitor land movements over large and inaccessible areas. The availability of cloud-free images for such projects is crucial and depends greatly on the geographical position and the prevailing weather conditions of the area of interest.

Numerous statistically based landslide investigation methods have been used for landslide susceptibility modelling and area zoning (Reichenbach *et al.*, 2018). Land displacement susceptibility mapping can be either qualitative or quantitative. Qualitative methods are subjective, as they represent the susceptible levels in descriptive expressions and depend on expert opinions. On the other hand, quantitative methods are based on numerical expressions of the relationship between triggering factors and landslides (Guzzetti *et al.*, 1999). In literature, many different methods for landslide susceptibility mapping have

been suggested, such as the Analytical Hierarchy Process (AHP), bivariate, multivariate, logistic regression, fuzzy logic and artificial neural network analysis (Yalcin *et al.*, 2011). AHP, has proved to be a very useful tool for decision makers and has been used widely in many research fields, such as cultural heritage conservation (Yau, 2009; Nicu, 2016), land subsidence susceptibility (Zhu *et al.*, 2013; Bhattarai and Kondoh, 2017; Andriani *et al.*, 2018; Ghorbanzadeh, Feizizadeh and Blaschke, 2018; Lyu *et al.*, 2019), landslide susceptibility (Yoshimatsu and Abe, 2006; Yalcin, 2008; Pourghasemi, Pradhan and Gokceoglu, 2012; Kayastha, Dhital and De Smedt, 2013; Althuwaynee *et al.*, 2014; Chen *et al.*, 2016; Mandal and Mandal, 2018; Yan *et al.*, 2019), land suitability analysis (Quinn, Schiel and Caruso, 2015; Bozdağ, Yavuz and Günay, 2016; Dedeoğlu and Dengiz, 2019), groundwater potential assessment (Oikonomidis *et al.*, 2015; Kaur *et al.*, 2020) and soil erosion (Ni, Li and Borthwick, 2008; Haidara *et al.*, 2019; Saha *et al.*, 2019).

AHP is a knowledge driven qualitative method, in which experts' opinion plays a crucial role. It can be applied in GIS, combining a number of landslides triggering factors in the form of layers/maps. Then, based on the recorded past landslide events, and the experts' knowledge of the residing factors within the area of interest, weights are assigned to certain combinations of factors. The summation of all factors and their weights leads to the development of the susceptibility map (Saaty, 1980). Although, AHP is a subjective method due to its dependency on the opinion of experts, the weights assigned to the factors are clear and can be discussed among experts and decision makers.

Nevertheless, apart from the passive remote sensing techniques that were described above, active remote sensing techniques are currently being used in various applications and can provide complimentary information to optical systems. The key advantages of active remote sensing, as presented in *section 1.2* of the present thesis, are the capability to acquire images 24 hours a day, i.e. day and night, and in all weather conditions as microwaves are unobstructed by clouds.

Satellite-borne radar remote sensing can be used to measure surface backscattering, surface topography and rainfall distribution. Synthetic Aperture Radar (SAR) measures backscattered emitted radar signals, which consist of amplitude (strength of radar response) and phase (fraction of one complete sin wave cycle / single SAR wavelength). Amplitude depends on the incidence angle, the ground roughness and the soil moisture, whereas phase mainly depends on the distance between the antenna and the target, such

as the land and sea (Le Mouélic *et al.*, 2005; Ferretti *et al.*, 2007). SAR performs particularly well in change detection applications, as SAR sensors produce well-calibrated imagery of high quality and good geo-location accuracy (Closson and Milisavljevic, 2017). SAR acquisitions can be used for the development of Digital Elevation Models (DEMs), the detection of oil spills, ship detection, earthquake deformation, land subsidence, land use/land change applications in terms of forest and agriculture monitoring, ice monitoring and urban mapping, as well as climate change monitoring (Engram *et al.*, 2018; Khati *et al.*, 2018; Liu *et al.*, 2019).

Interferometric Synthetic Aperture Radar (InSAR) is a space-based technique that can determine the Earth's surface topography and its temporal changes over large areas (e.g., 100 x 100 km), with line-of-sight (LoS) accuracy of millimetres (Le Mouélic *et al.*, 2005; Ferretti *et al.*, 2007; Veci, 2016; Braun and Veci, 2020). InSAR is based on the principle of combining the phase information of two SAR observations of the same area taken from different positions. These observations may be made by different sensors but with nearly identical radar system parameters. Since phase is highly correlated to topographic characteristics this forms the foundation for the derivation of distance information about the Earth's terrain and subsequently uplifting or subsidence (Ferretti *et al.*, 2007; Veci, 2016; Braun and Veci, 2020). A pair of SAR acquisitions can generate three interferometric products (Closson and Milisavljevic, 2017):

1. An amplitude image (intensity) often used to locate points of interest.
2. A phase difference image or interferogram, used to show either the topographic contribution or ground displacements.
3. A coherence image showing the confidence level of each pixel in the interferogram.

InSAR technique can be used to assess the impact of natural hazards to critical infrastructure, as it can detect areas and rates of land movements, caused by earthquakes and landslides. Indeed, InSAR techniques have been used in monitoring landslide phenomena since the mid 90's (Fruneau, Achache and Delacourt, 1996).

InSAR is a powerful tool to assess the slope deformation related to the activation landslides, as well as vertical land movements, i.e. land subsidence and uplift. With the increasing availability of suitable radar data, advanced time-series analysis techniques have been developed, which allow for the quantitative derivation of spatially variable

deformation rates with increasing improvements in the temporal resolution. The resulting satellite InSAR techniques have been successfully applied for the quantitative analysis of land movements in a variety of environments (Wasowski and Bovenga, 2014; Teshebaeva *et al.*, 2015).

InSAR can assist in the derivation of topographic information of very high spatial resolution about the landscape from radar images, via which, landscape changes can be detected and mapped with very high precision. To detect changes in topography between two observations, Along Track Interferometry (ATI) can be used. In general, platforms in repeat pass ATI do not follow identical paths resulting at the same time to some cross-track separation too (Richards, 2009). Thus, repeat pass ATI can be used both for the detection of topography as well as terrain changes (Figure 15).

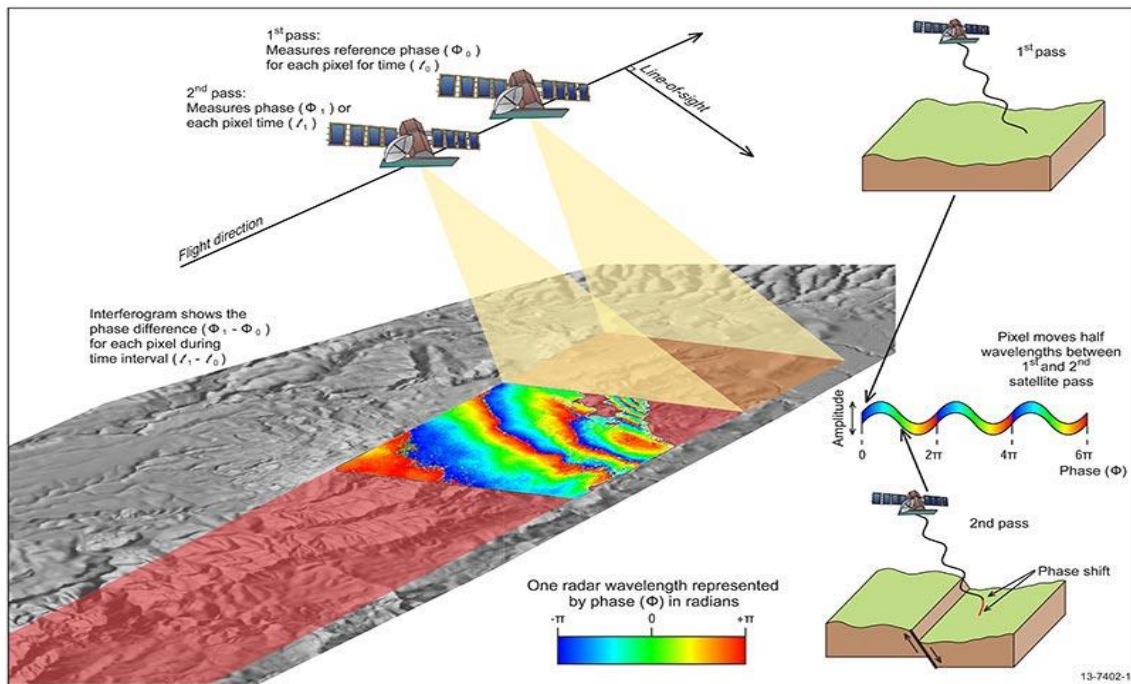


**Figure 15:** Interferometric Synthetic Aperture Radar principle (Geoscience Australia, 2014)

For acquisitions with small perpendicular baseline and short temporal baseline, the amplitude and phase of the object responses may be considered identical (Ferro-Famil and Pottier, 2014). In this case, when a feature on the landscape shifts during two SAR acquisitions, an interferometric phase difference will be measured for the relevant pixels as follows:

$$\Delta\phi_{\text{change}} = \frac{4\pi}{\lambda} \Delta r_r \quad (\text{Eq. 1})$$

where:

$\Delta r_r$ : the relative displacement projected on the slant range direction.

$\lambda$ : the transmitted wavelength

In the case that there is also an across track baseline, apart from the phase shift related to the time variation described by *Equation 1*, a phase change will occur associated with the topography. As a result, the total interferometric phase difference would be a function of both the topography and its change. To monitor land movements, the change in interferometric phase with land displacement between radar image acquisitions needs to be calculated, thus the contribution of the topography must be subtracted from the overall result. The above can be achieved via the application of Differential SAR Interferometry (DInSAR) (Ferretti *et al.*, 2007). If a suitable Digital Elevation Model (DEM) is available, the effect of the topography can be subtracted pixel by pixel from the interferometric phase, providing a differential interferogram, and therefore, land movements can be measured and monitored between two or more SAR acquisitions.

DInSAR technique is based on the theory that, due to the very high stability of the satellite orbits, the exploitation of the information carried by the phase difference between two or more SAR images is possible, looking at the same scene from different geometries (Ferretti *et al.*, 2007; Polcari *et al.*, 2014; Veci, 2016; Braun and Veci, 2020). The availability of large datasets and the multi-pass DInSAR methodology, can lead to more accurate estimations of the atmospheric contribution and topographic phase components, allowing at the same time the reduction of error sources (Zebker, Rosen and Hensley, 1997; Polcari *et al.*, 2014; Yu, Li and Penna, 2018). Moreover, the temporal density of SAR imagery facilitates the study of the temporal evolution of a natural hazard, through the development of a time series and the calculation of the rate of deformation (Polcari *et al.*, 2014).

The quality of DInSAR findings can be also measured by a variable called coherence, which depends on the nature of the surface being studied. Changes in the surface reflectivity over time due to vegetation or other natural phenomena decorrelate the measurements significantly (Zebker and Villasenor, 1992). As a result, most conventional InSAR studies tend to focus on dry and sparsely vegetated regions, which fits perfectly in our case studies in Cyprus.

Unfortunately, interferometric phase is also influenced by other factors, as presented in *Equation 2*, such as the atmosphere, pixel reflectivity, radar system phase noise and the uncertainty in knowing the platform position and baseline.

$$\Delta\varphi = \Delta\varphi_{\text{topo}} + \Delta\varphi_{\text{disp}} + \Delta\varphi_{\text{atm}} + \Delta\varphi_{\text{pixel}} + \Delta\varphi_{\text{noise}} + \Delta\varphi_{\text{error}} \quad (\text{Eq. 2})$$

The error associated with atmospheric effect be corrected by stacking or averaging many interferograms, since the atmospheric effect has short spatial correlation length with virtually no temporal correlation between data acquisition times (Zebker, Rosen and Hensley, 1997; Ouchi, 2013; Yu, Li and Penna, 2018).

Several studies have been carried out on investigating the effectiveness of Differential SAR Interferometry (DInSAR) on the detection of land movements. DInSAR has been used successfully for monitoring land subsidence and uplift (Bhattacharya *et al.*, 2014; Mullissa *et al.*, 2017; Da Lio and Tosi, 2018; Liosis *et al.*, 2018; Tzouvaras *et al.*, 2019; Morishita *et al.*, 2020), with particular applications such as landslides (Di Martire *et al.*, 2016; Bovenga *et al.*, 2017; Strozzi *et al.*, 2018) and other ground displacements caused by natural occurring phenomena such as earthquakes (Pieraccini *et al.*, 2002; Lin-lin *et al.*, 2003; Dong *et al.*, 2011), volcano eruptions (Pritchard and Simons, 2002; Pavez *et al.*, 2006; Meyer *et al.*, 2015; Schaefer *et al.*, 2019), and also human activities (Bitelli *et al.*, 2010; Hsieh *et al.*, 2011). Last but not least, DInSAR has proved to be effective in identifying damages in large civil infrastructure like roads, road networks (D'Aranno *et al.*, 2019) and dams (Corsetti *et al.*, 2018), assisting in that way in planning infrastructure maintenance works.

DInSAR can be used to detect and monitor, under certain conditions, ground deformations on a centimetric scale, with a good spatial resolution (a few meters), offering an effective method for assessing land movements over large areas (Raucoules *et al.*, 2009). These characteristics are making DInSAR one of the most promising space-geodetic techniques for monitoring Earth's surface deformations (Klees and Massonnet, 1998). Therefore, DInSAR techniques can be used for various engineering applications, such as land use and urban planning, as they contribute to the better understanding of an area's geomorphology and assist in the impact assessment of natural hazards, such as earthquakes and landslides (Hearn and Duncumb, 2018; Hearn *et al.*, 2018).



In the last couple decades, advanced DInSAR techniques have been developed, such as the Persistent Scatterers (PS), Interferometric Point Target Analysis (IPTA) and Small Baseline Subsets (SBAS), exploiting extensively the satellite capabilities. This is achieved through the use of large SAR image datasets of the same area, acquired at different times and with different perpendicular baselines, i.e. a multi-pass DInSAR approach (Polcari *et al.*, 2014). This allows the development of the displacement time series and the more precise calculation of surface deformation rates with millimetric accuracy (Le Mouélic *et al.*, 2005; Polcari *et al.*, 2014).

Applications of Earth Observation for cultural heritage have rapidly increased in the last years. A review of the available literature indicates a growing interest in the exploitation of active satellite sensors with particular emphasis on the use of SAR data (Agapiou and Lysandrou, 2015; Chen, Lasaponara and Masini, 2017; Tapete and Cigna, 2017a).

In recent years, there has been a growing interest in the use of remote sensing techniques, such as the application of DInSAR for deformation monitoring, for risk monitoring and assessment of cultural heritage (Zhou, Chen and Guo, 2015; Cuca *et al.*, 2016). This interest was further enhanced by free provision and access to SAR data of various spatial resolutions and temporal coverage. Research interests have often focused on identifying the perspectives of SAR remote sensing for cultural heritage applications (Lasaponara and Masini, 2011; Tapete and Cigna, 2017b). In other cases, the aim has been to monitor cultural heritage sites and assess the risk of geo-hazards (Chen, Lasaponara and Masini, 2017; Tapete and Cigna, 2017a; Tzouvaras *et al.*, 2019).

Polarimetric C- and L-band SAR sensitivity has been analysed with buried archaeological structures (Stewart, Lasaponara and Schiavon, 2014), and integration of radar and laser-based remote sensing techniques for monitoring structural deformation of archaeological monuments has also been studied (Tapete *et al.*, 2013).

Additionally, Persistent Scatterer Interferometry (PSI) techniques such as Permanent Scatterer SAR Interferometry (PSInSAR) and “Squeezed” SAR (SqueeSAR) have proven to be suitable for deformation analyses in cultural heritage sites (Tapete *et al.*, 2012). The latter, however, require continuous information on the precise position of a number of scatterers, which can be features such as roof tops, bridges, antennas, corner reflectors etc., to provide accurate results on ground deformation. This information is provided in terms of coordinates measured via geodetic surveys, or via the installation of permanent

GNSS antennas and/or other expensive infrastructure at the desired locations, leading in turn to additional costs.

Based on these studies, the selection of the type of SAR data should be case-specific and should always be based on the properties and characteristics of the area of interest and its surroundings to achieve optimum results. Therefore, SAR acquisitions with a long wavelength (L-band, P-band, etc.), having enhanced capabilities for penetration, are recommended for areas covered with vegetation, whereas in the cases of DInSAR and MT-InSAR, SAR data with a short wavelength (C-band) are preferred, as there is a need to improve the accuracy of the calculated deformations. In the case of early warning systems and detailed monitoring, high-resolution SAR data are required (Chen, Lasaponara and Masini, 2017). Integration of different SAR interferometry techniques can overcome any obstacles by combining their respective advantages (Zhou, Chen and Guo, 2015).

DInSAR is a very promising methodology for monitoring ground displacement over large areas at Line-of-Sight, providing important information for monitoring natural hazards. However, several criteria have to be met, as described before, the most important being the maintenance of coherence, at some extent, during the period of study (Rocca *et al.*, 2000). Nevertheless, the low spatial resolution characteristics of some satellite imagery impose some limitations. Additionally, in some cases the temporal resolution is also very limited.

The increase in spatial resolution, as in the case of TerraSAR-X and COSMO-SkyMed, and in temporal resolution, as in the case of the Sentinel-1 constellation, are two main developments in this domain. The free, full, and open data policy adopted by the Copernicus program, which foresees free access to the Sentinel datasets, can be considered as a milestone for the scientific progress of radar space technology (ESA, no date e). The launch of Sentinel-1A in 2014 and Sentinel-1B two years later, has made possible the systematic supply of data for multitemporal analyses.

Indeed the characteristics of the Copernicus missions, such as the 12-day repeat cycle of the Sentinel-1 sensors in a single pass, ascending or descending, or the 6-day repeat cycle that the two-satellite constellation offers at the equator, can be used for mapping rapid changes in the landscape such as those in the case of an earthquake. Additionally, the spatial resolution of Interferometric Wide (IW) swath images for Level-1 Single Look

Complex (SLC) products varies from 2.7 x 22m to 3.5 x 22m provides additional advantages compared to their predecessors. Considering the fact, that these Copernicus Sentinel-1 data are freely distributed datasets, provided by the European Space Agency (ESA), along with the availability of open-source software for processing these images, provide us the opportunity to systematically monitor and assess the impact of natural hazards to cultural heritage and built environment worldwide, overcoming area inaccessibility issues and weather conditions, even in regions and countries with limited budgets (Cuca *et al.*, 2016; Themistocleous *et al.*, 2016; Tzouvaras *et al.*, 2019).

Nevertheless, DInSAR is not an absolute measurement methodology. This is not due to the resolution of the processed SAR images, but because the displacement values that are calculated at the end of DInSAR processing show the relative change in position between the acquisition time of the first image to the acquisition time of the second image. This matter, in fact, does not allow the identification and monitoring of the impact that the natural hazard has to the area of interest, in its full extent and on a global scale.

Therefore, the final DInSAR products need to be ultimately tied with some stable points, or points of known subsidence or uplift, to convert relative values to absolute ones. Geodetic surveys are the most common way to supply absolute global information, in terms of changes in coordinates, on the behaviour of an object under investigation. The integration of DInSAR analysis with GNSS techniques is vital, as GNSS measurements can calibrate and validate the results obtained from DInSAR processing and thus minimise errors. Hence, the combination of the characteristics of an integrated DInSAR-GNSS technique provides us the opportunity to measure vertical ground deformations with sub-centimetric precision and unparalleled spatial coverage.

Several attempts have been made to integrate space-based techniques (SAR) and ground-based ones for the measurement and monitoring of ground deformation. Validation of the results from DInSAR processing have been conducted by theodolite and Electronic Distance Meter (EDM) measurements of selected benchmarks (Tarchi *et al.*, 2003). In other cases, results from DInSAR processing are compared with findings from GPS campaigns, through different methodologies (Lu, 2005; Biggs *et al.*, 2007; Calamia *et al.*, 2008; Wei, Sandwell and Smith-Konter, 2010; Béjar-Pizarro *et al.*, 2016; Tzouvaras *et al.*, 2019). Since 2013, the Australian Geophysical Observing System (AGOS), an innovative network that combines an array of 40 radar corner reflectors, co-located GNSS

instrumentation, and a repository of X-band and C-band SAR data, operates for the measurement of crustal deformation (Garthwaite *et al.*, 2013). However, the optimum combination of DInSAR and GNSS technologies is still under research worldwide.

Despite their capability to monitor efficiently vertical land movements, i.e. subsidence or uplift, certain transformations need to be applied in order to fully integrate the two measurement techniques, as they differ significantly in the type of data they collect, their geometries, and their coverage. Thus, the 3-dimensional coordinates obtained from GNSS should be transformed into 1-dimension DInSAR Line-of-Sight ones, or the LoS displacement values from DInSAR processing should be converted to vertical ground displacement (Parker *et al.*, 2017).

Additionally, although the moderate spatial resolution of the IW swath images for Level-1 SLC products (2.7 x 22m to 3.5 x 22m), that are available for Cyprus, has proven to be satisfactory for the detection of land subsidence and/or uplift (Liosis *et al.*, 2018; Tzouvaras *et al.*, 2019; Morishita *et al.*, 2020), the detailed study and monitoring of more complex ground displacement phenomena, especially of fast-moving landslides and slope deformations cannot be achieved using Sentinel-1 images due to the limitations of the C-band wavelength and the images' medium spatial resolution (Kyriou and Nikolakopoulos, 2018; Kovács *et al.*, 2019).

This is due to a limitation called temporal phase aliasing, which mainly affects the phase unwrapping step of the DInSAR methodology (Rabus and Pichierri, 2018; Manconi, 2019), when the displacement of a pixel or an area under investigation exceeds the value of  $\lambda/4$  between two consecutive satellite acquisitions that form an interferometric SAR pair (Moretto *et al.*, 2017; Manconi *et al.*, 2018).  $\lambda$  is the wavelength of the SAR sensor, which in the case of Sentinel-1 satellite's C-band is approximately 5.55cm. Temporal phase aliasing thresholds for the currently available SAR satellites have been calculated based on their nominal wavelengths and revisit times (Wasowski and Bovenga, 2014; Moretto *et al.*, 2017; Manconi *et al.*, 2018; Manconi, 2019). In fact, this limitation can lead to confusing results as any ground deformation, that is observed between two consecutive SAR acquisitions, exceeds this threshold of 1.39cm, in the case of Sentinel-1, and can be two, three or n times greater than this value, can be underestimated as all these deformations produce the same observed phase.

The exploitation of higher resolution images from TerraSAR-X and COSMO-SkyMed missions has provided more reliable outputs applying DInSAR methodology for monitoring landslide phenomena (Wasowski and Bovenga, 2014; Di Martire *et al.*, 2016; Bovenga *et al.*, 2017, 2018).

In the case of fast-moving land displacement events, interferometric SAR coherence can be used instead, serving as an additional diagnostic source of information regarding changes in topography. Coherence is one of the products of the InSAR methodology, as described before, and a measure of the quality of the produced interferogram. It describes the similarity of the reflected radar signal between two images (Rocca *et al.*, 2000). SAR coherence  $\gamma$  is calculated, as shown, in *Equation 3*, where  $n$  is the number of pixels,  $A_i$  and  $B_i$  are the complex SAR images A (master) and B (slave) respectively and the \* denotes the complex conjugate.

$$\gamma = \frac{\frac{1}{n} \left| \sum_{i=1}^n A_i \cdot B_i^* \right|}{\sqrt{\frac{1}{n} \left( \sum_{i=1}^n A_i \cdot A_i^* \sum_{i=1}^n B_i \cdot B_i^* \right)}} \quad (\text{Eq. 3})$$

It ranges from 0, i.e. complete phase decorrelation (interferometric phase is pure noise) to 1, i.e. complete phase correlation (Rocca *et al.*, 2000; Rosen *et al.*, 2000). The overall coherence of a single pixel is determined by a number of factors and is usually expressed by *Equation 4*, as follows:

$$\gamma_{\text{overall}} = \gamma_{\text{thermal}} \cdot \gamma_{\text{spatial}} \cdot \gamma_{\text{temporal}} \quad (\text{Eq. 4})$$

where  $\gamma_{\text{temporal}}$  is the temporal component of coherence,  $\gamma_{\text{spatial}}$  is the spatial component of coherence, and  $\gamma_{\text{thermal}}$  is the thermal component of coherence (Zebker and Villasenor, 1992). If one or more of the three components of coherence decorrelates, the entire radar signal will also decorrelate. Thermal coherence is related to radar signal noise, and its decorrelation is rather trivial (Zebker and Villasenor, 1992). Spatial coherence depends on the area's topography, and the characteristics of the satellite, such as the geometry of image acquisition and the radar wavelength (Zebker and Villasenor, 1992; Burrows *et al.*, 2019).

On the other hand, the temporal component of coherence depends on changes on the ground surface, that appears as variations in the scattering properties of the target pixels

in the area of interest between the two SAR images of the interferometric pair (Zebker and Villasenor, 1992; Lu *et al.*, 2018; Burrows *et al.*, 2019). To detect these changes, the two images of the same scene must be acquired with a same incident angle, but at different times. Any changes in the surface reflectivity are considered as a phase decorrelation of the pixels between the two images (Rocca *et al.*, 2000; Closson and Milisavljevic, 2017). Thus, even the smallest changes in an area of interest, between two images, can be detected, by means of a reduction in the temporal component of coherence and consequently in the overall coherence. In general, a random change of the position and physical properties of a specific point on the surface of the Earth can be detected as low coherence of a pair of images (Rocca *et al.*, 2000).

The Coherent Change Detection (CCD) technique is useful for detecting changes of a centimetre scale but, being a statistical value, it cannot provide quantitative information about ground displacement (Closson and Milisavljevic, 2017). CCD has been used in several applications, such as monitoring land use / land cover changes (Abdelfattah and Nicolas, 2006; Parihar *et al.*, 2014; Zahid Khalil and Saad-ul-Haque, 2018; Pan, Hu and Wang, 2019; Yun *et al.*, 2019), as well as agricultural studies (Erten *et al.*, 2016; Tamm *et al.*, 2016; Liu *et al.*, 2019) and forestry applications (Suga and Takeuchi, 2000; Canisius *et al.*, 2019; Durieux *et al.*, 2019; Ban *et al.*, 2020; Hirschmugl *et al.*, 2020), and lately in earthquake impact assessment (Lu *et al.*, 2018; Monti-Guarnieri *et al.*, 2018; Burrows *et al.*, 2019; Uemoto *et al.*, 2019; Jung and Yun, 2020).

CCD techniques present limitations related to the radar interferometric methods that were analysed earlier. Steep slopes, forests, and areas with high moisture can lead to decorrelated phase signal in very limited time (less than a day). Vegetated or water surfaces, due to their continuous variations appear to have low coherence values (Bouaraba *et al.*, 2014; Closson and Milisavljevic, 2017). Moreover, coherence values decrease with larger image temporal baselines and larger perpendicular baseline lengths between the two images (preferable to be in the range of 0-400m). Coregistration must be performed accurately, as it significantly affects the coherence map, as it also happens in the case of the developed interferogram (Rocca *et al.*, 2000; Bouaraba *et al.*, 2014; Veci, 2016; Braun and Veci, 2020). Last but not least, the poor resampling can lead to low coherence during InSAR processing (Zebker and Villasenor, 1992; Rosen *et al.*, 2000; Bouaraba, Acheroy and Closson, 2013; Closson and Milisavljevic, 2017).

CCD technique is less efficient in areas with high human activity, or where the underlying geological formations are too hard to record detectable surface modifications. Seasonal variations, such as varying weather conditions, can also affect the estimated coherence (Rocca *et al.*, 2000; Bouaraba, Acheroy and Closson, 2013; Lu *et al.*, 2018). However, the identification of changes in coherence through Interferometric SAR processing can provide useful information for the rapid detection of natural hazards (Plank, Twele and Martinis, 2016; Watanabe *et al.*, 2016; Jung and Yun, 2020). Indeed, NASA's Advanced Rapid Imaging and Analysis (ARIA) project uses SAR coherence to develop damage proxy maps following earthquakes, hurricanes and wildfires in urban areas to inform and improve the awareness of emergency response mechanisms following natural hazards (NASA, no date; Burrows *et al.*, 2019).

Lately, the latter has been also accomplished using Sentinel-1 data in the cases of earthquake induced natural disasters (Lu *et al.*, 2018; Washaya, Balz and Mohamadi, 2018; Burrows *et al.*, 2019). However, there are no attempts, in literature, regarding the application of the Coherent Change Detection (CCD) methodology, for the identification and monitoring of fast-moving landslides induced by heavy rainfall in rural/sub-urban areas, as in the case study of Pissouri-Petra tou Romiou, exploiting Sentinel-1 SAR data.

The main goal of the present study is to systematically monitor and assess the resilience of infrastructure, such as cultural heritage and built environment with regards to natural hazards and more specifically, land movements, either caused by seismic events or landslides, at three case studies in Paphos and Limassol District using Earth Observation techniques, through the exploitation of free datasets and open software, aiming to demonstrate the capabilities that can be offered by such solutions. Due to the fact that the three case study areas have different geomorphological characteristics and attributes, an overall methodological approach was developed for the identification of areas vulnerable to land movements and the monitoring and detection of these phenomena and their impact to infrastructure resilience.

Freely available archive optical remote sensing data, such as Landsat imagery, and Geographic Information Systems (GIS) were used for the identification of areas/zones vulnerable to landslides and other land displacement phenomena. Moreover, freely available satellite data that are currently provided by the Copernicus Sentinel missions, such as Sentinel-1 SAR images and Sentinel-2 optical images, were exploited along with

suitable DEMs in order to detect land movements through the application of DInSAR and CCD techniques.

Based on the characteristics of the Sentinel-1 satellites, mentioned before, such as the short revisit time, the medium resolution images, and the fact that Cyprus, almost in its entirety, is included in a single SAR image, a novel methodology for the calibration and validation of the absolute land displacement values, through GNSS 3D coordinates, is proposed to overcome the limitations of DInSAR, as found in literature.

Indeed, this is a first attempt to develop a methodology for systematically monitoring natural hazards and their impact to infrastructure resilience, that its application, from the acquisition of images, to the monitoring of ground deformation, its calculation in absolute values and the calibration/validation of the results, is completely free.

Moreover, it is the first time that CCD methodology is applied for the identification of landslides triggered by rainfall, a fact that is quite common in many geological and geomorphological settings in Cyprus and worldwide.

The methodological approach is described in detail and analysed thoroughly in the next section of the thesis.



### 3 Methodology

In this section, the areas of study, their characteristics and the hazards that they are susceptible to are presented in *section 3.1*. Then, the data and software used for the application of the proposed methodology are described in *section 3.2*. Finally, in *section 3.3*, the overall methodology and the steps of the two processing chains that are applied for case study areas, is analysed thoroughly.

#### 3.1 Areas of study

Three case studies are selected for the application of the methodology proposed for identifying susceptibility to ground deformation events and for monitoring land movements as a result of earthquakes and landslides. These are: a) Statos – Agios Photios, b) Nea Paphos – Tombs of the Kings and c) Pissouri – Petra tou Romiou.



**Figure 16:** The three case study areas of (a) Statos – Agios Photios, (b) Nea Paphos – Tombs of the Kings and (c) Pissouri – Petra tou Romiou

The selection of the case study areas are based on the area susceptibility to natural hazards and the importance of the area, in terms of the proximity to residential areas, as in the case of Statos – Agios Photios, critical infrastructure (Pissouri – Petra tou Romiou), or the presence of cultural heritage monuments, as in the case study area of Nea Paphos – Tombs of the Kings.

### 3.1.1 Statos – Agios Photios

The village of Statos - Agios Photios is located in the western part of Cyprus and more specifically in the north-eastern part of Paphos District (Figure 17). Its main part is rather hilly and mountainous, covered by bare soil or coniferous forest.

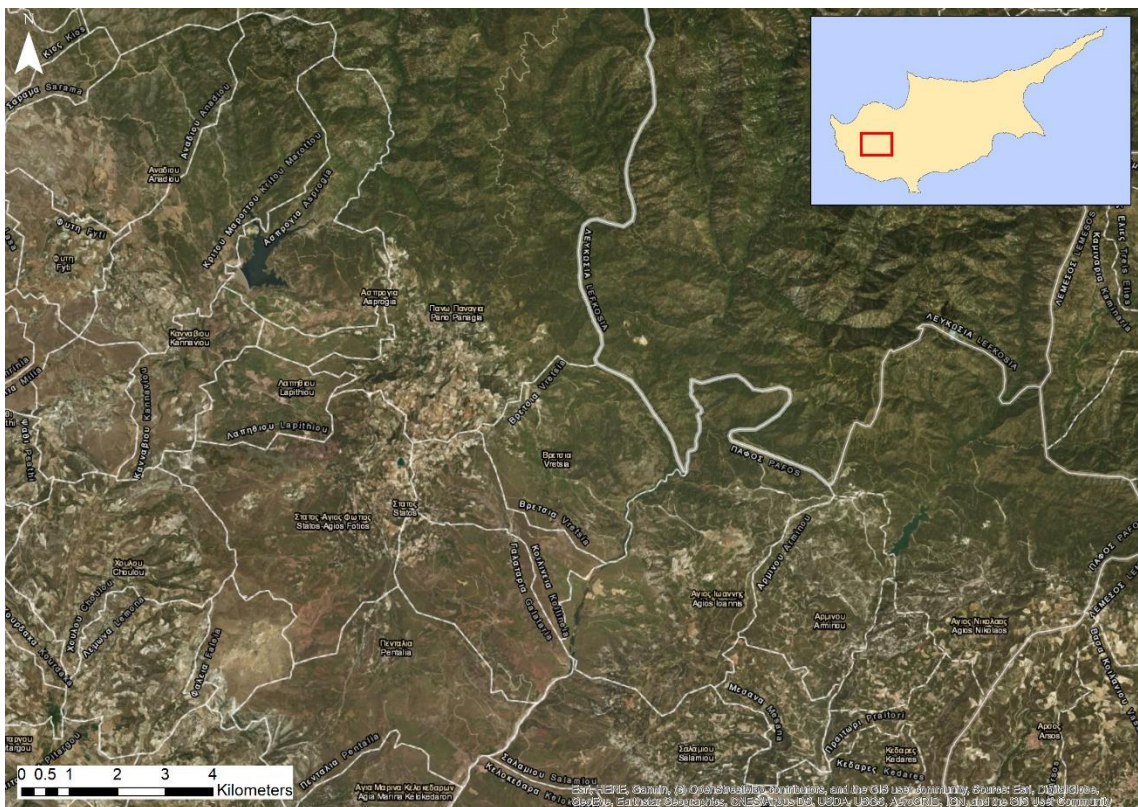


**Figure 17:** The Statos – Agios Photios study area

In Paphos District, between the Troodos Mountains and the sea, deposits of massive breccias (melange formation) are widely exposed. The area’s geology consists mainly of these deposits, which are rich in clay minerals. These deposits are susceptible to

landslides, with this susceptibility being enhanced due to the area's steep anaglyph and the long history of seismicity in the area (Pantazis, 1969; Northmore *et al.*, 1986, 1988). According to the geological map (Figure 18), the study area is occupied by alluvium-colluvium deposits on its northern part and lavas, marls/chalks (Lefkara formation-Mamonia Complex) and marl, clay, sandstone and limestone melange (Kannaviou formation) in the central and southern part. The marls act as reservoirs releasing water into the clay and sandstones (Alexakis *et al.*, 2014).

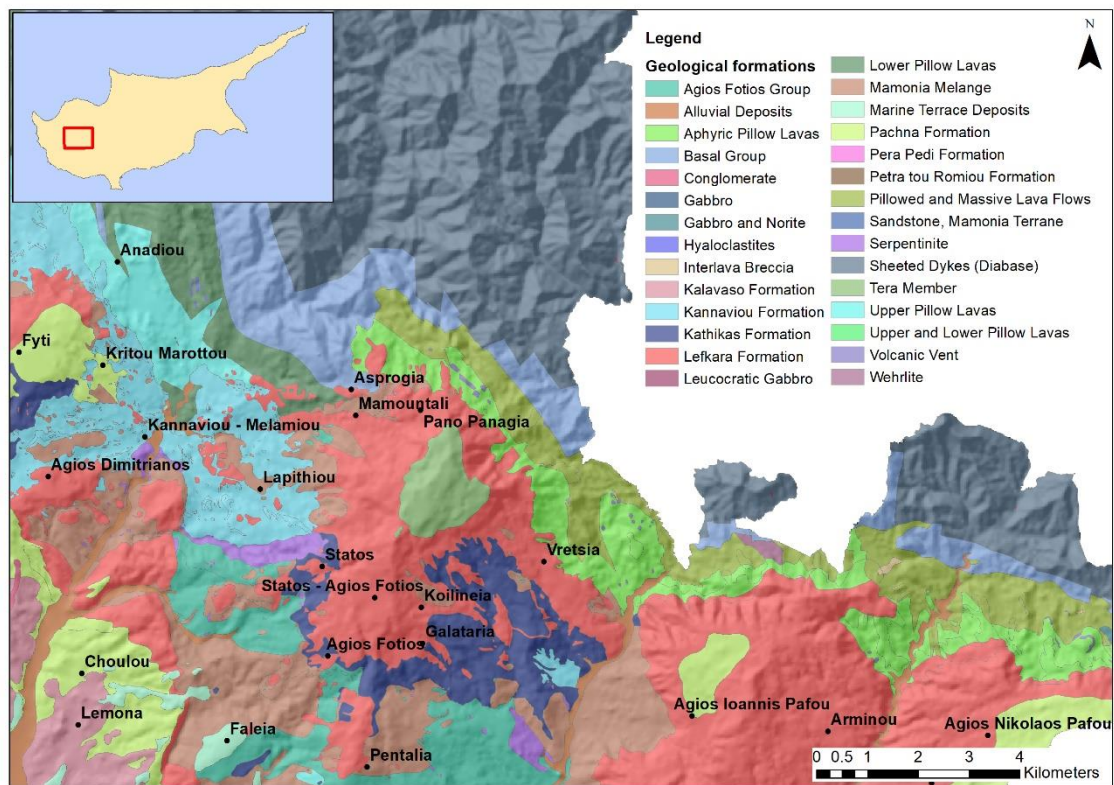


**Figure 18:** Geological map of the study area – Statos – Agios Photios

According to historical data from the Cyprus Geological Survey Department, the area was affected by a destructive double earthquake measuring 6.5 that occurred in Paphos District on the 10<sup>th</sup> of September 1953 (Mercier, Vergely and Delibassis, 1973; Geological Survey Department, 2014).

All 158 villages of Paphos District suffered from damages mainly caused by landslides and ground cracking, but the villages of Stroumpi, Axylou, Kithasi, Lapithiou and Fasoula were destroyed. The shocks were strongly felt in Lebanon, Israel, Egypt, Greece and Turkey (Paphos Life, no date).

The catastrophic earthquake triggered landslide events that occurred later in 1965, following heavy rainfall, in the broader area of Statos and Agios Photios villages. The landslides caused severe damages to residences and the broader road network. Due to the hazardous state of the area, both villages were relocated some kilometres eastern of the original location and their residents decided to unite into the present Statos – Agios Photios village (Community Council of Statos-Agios Photios, no date).

On the 9<sup>th</sup> of October 1996, a 6.8 earthquake occurred southwest of Cyprus and affected Pentalia village, which is located within the study area, causing creep movements. The area is covered by sandstones, clay and marls melange, formations prone to landslides (Kalogeras, Stavrakakis and Solomi, 1999). The village was abandoned and re-established southern, in the present location of New Pentalia village.



**Figure 19:** The evacuated village of Statos (left). Rockslide in chalk across a roadcut (right)

Moreover, until recently, numerous landslide events have been recorded within the study area and especially across the road-cuts, causing damages to critical infrastructure, such as roads and road networks, leading to mobility issues for citizens and tourists.

Due to the long history of Statos – Agios Photios area in landslides and other land displacement events, this area was used for the development of the land displacement susceptibility map described in *section 3.3.1 Development of land displacement susceptibility maps*.

### 3.1.2 Nea Paphos – Tombs of the Kings

The second area of study is the wider region of the city of Paphos, located in the western part of Cyprus (Figure 20). In this region, important archaeological sites and monuments attract thousands of tourists every year. The sites are scattered around the wider area of the city, while the main attractions are “Nea Paphos” and the “Tombs of the Kings” sites, which were inscribed on the World Heritage List of UNESCO in 1980. These sites, placed in the most western part of Paphos, preserve a unique heritage identity of the island, revealing the rich cultural heritage of the area (Department of Antiquities, no date c).

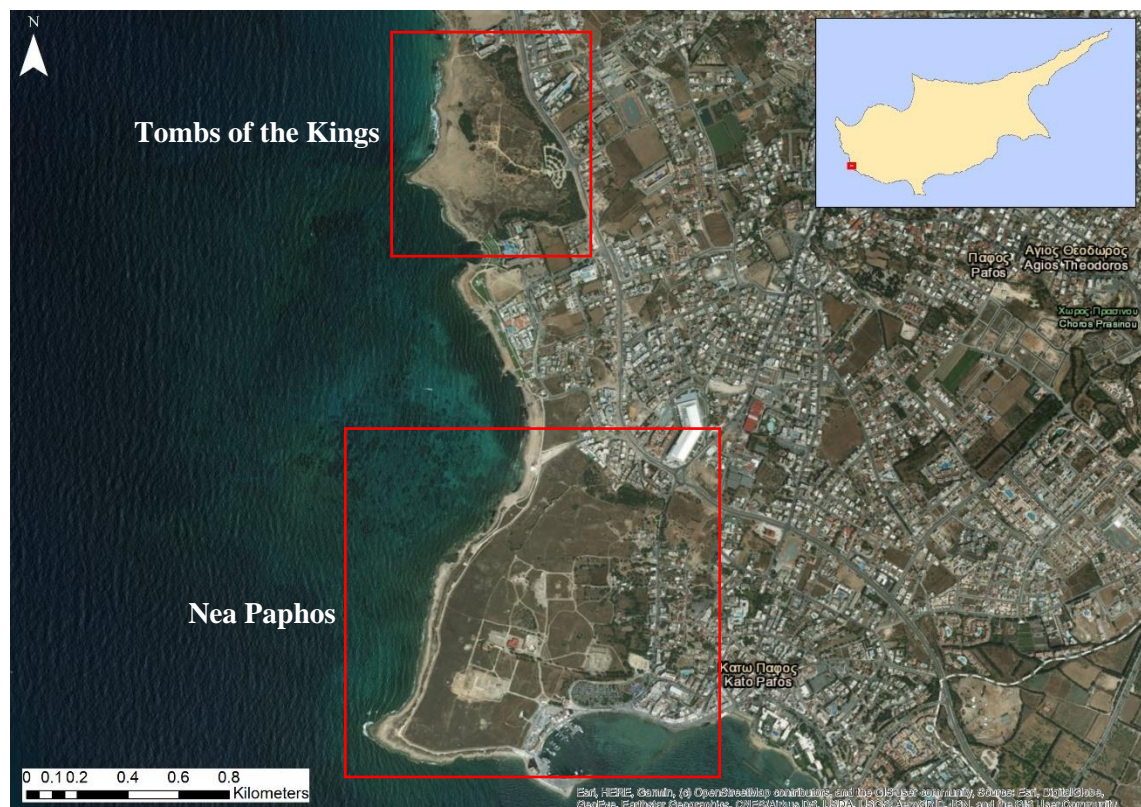


**Figure 20:** The case study of Nea Paphos – Tombs of the Kings

“Nea Paphos” is considered one of the most important sites of the island. It was founded at the end of the 4<sup>th</sup> century and in the beginning of the 3<sup>rd</sup> century B.C., when Cyprus became part of the Ptolemaic kingdom. Nea Paphos became the centre of Ptolemaic administration on the island. Until the end of the 2<sup>nd</sup> century B.C., Nea Paphos was the capital of the whole island and remained as such until the 4<sup>th</sup> century A.D (Department of Antiquities, no date a). The remains that can be visited today are mainly dated to the Hellenistic and Roman periods. Nea Paphos was a harbour town and a planned city. The

city seems to have already been fortified by Nicocles, and the city walls formed a considerable work of defence. Most of their superstructure has disappeared or quarried, but the course of the city wall can be traced over most of its length by the rock-cut foundations (Department of Antiquities, no date a).

Systematic excavations at Nea Paphos started in 1962 by the Department of Antiquities, and many of the ancient town's administrative buildings as well as private houses and ecclesiastical buildings came to light. Important monuments of the site are considered the Roman villas with impressive floor mosaics, such as the "House of Dionysos", the "House of Aion", and the "House of Orpheus". Moreover, the civic centre of Nea Paphos was situated in the north-western part of the city and included the important public buildings of the town, such as the Agora, the theatre, and the Asklepieion, parts of which can be visited today (Department of Antiquities, no date a).



**Figure 21:** The archaeological site of Nea Paphos (left) and the "Tombs of the Kings" (right) (source: Department of Antiquities)

The "Tombs of the Kings" archaeological site is an impressive necropolis that is located to the north along the coast from the harbour of Kato Paphos. It is part of the Archaeological Park of Kato Paphos and is in the UNESCO World Heritage Sites list since 1980. It was built during the Hellenistic period (3<sup>rd</sup> century B.C.) to satisfy the needs of the newly founded Nea Paphos (Department of Antiquities, no date b).

They are thought to have been the burial sites of aristocrats and high officials and its name relates to the impressive character of its burial monuments. In 1977, systematic excavations were carried out by the Department of Antiquities, which revealed eight large tomb complexes. Most of the underground tombs are carved out of solid rock and date back to the Hellenistic and Roman periods. They are similar to tombs found in

Alexandria, demonstrating the close relations between the two cities during the Hellenistic period (Department of Antiquities, no date b).

The ancient sites lay about 12km northwest of the ancient capital of the island called Palaepaphos (Figure 22). The average terrain elevation of the case study is approximately 13m above sea level. The landscape in Paphos varies from the coastal plain, the hilly area extending from the coastal plain up to the igneous rocks of Paphos forest and finally to the mountainous region of Troodos Mountain to the north.

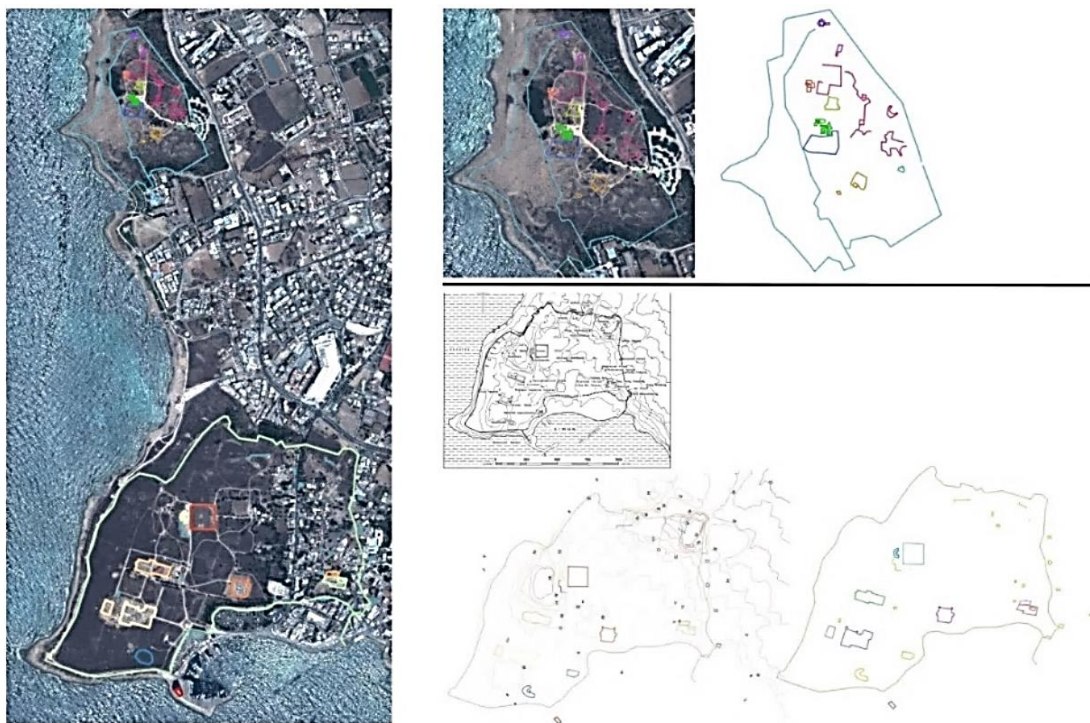


**Figure 22:** Nea Paphos and Tombs of the Kings archaeological structure

The geology of Paphos city and the location of the two cultural heritage sites that constitute the study area are presented in Figure 23. The case study of “Nea Paphos – Tombs of the Kings” lies in the Mamonia Terrane. The Mamonia Terrane, as described in detail in *Chapter 1 Introduction* of this report, constitutes a diverse and structurally complex assemblage of igneous, sedimentary and metamorphic rocks, ranging in age from Middle Triassic to Upper Cretaceous (230-75 Ma) (Research & Development Center-Intercollege, 2004b; Geological Survey Department, 2016).

They occur only on the southern part of Cyprus with extensive outcrops in the Paphos region. The stratigraphic classification of the Mamonia Terrane poses problems; however, three main groups can be identified (Geological Survey Department, 2016):

- Volcanic (lavas) and sedimentary rocks (recrystallised limestones) of the Diarizos Group.
- Pelagic sedimentary rocks (limestones, mudstones and quartzitic sandstones) of the Agios Fotios Group.
- Metamorphic rocks (schists and marbles) of the Agia Varvara formation. These rocks were derived from the metamorphism of the Diarizos Group.

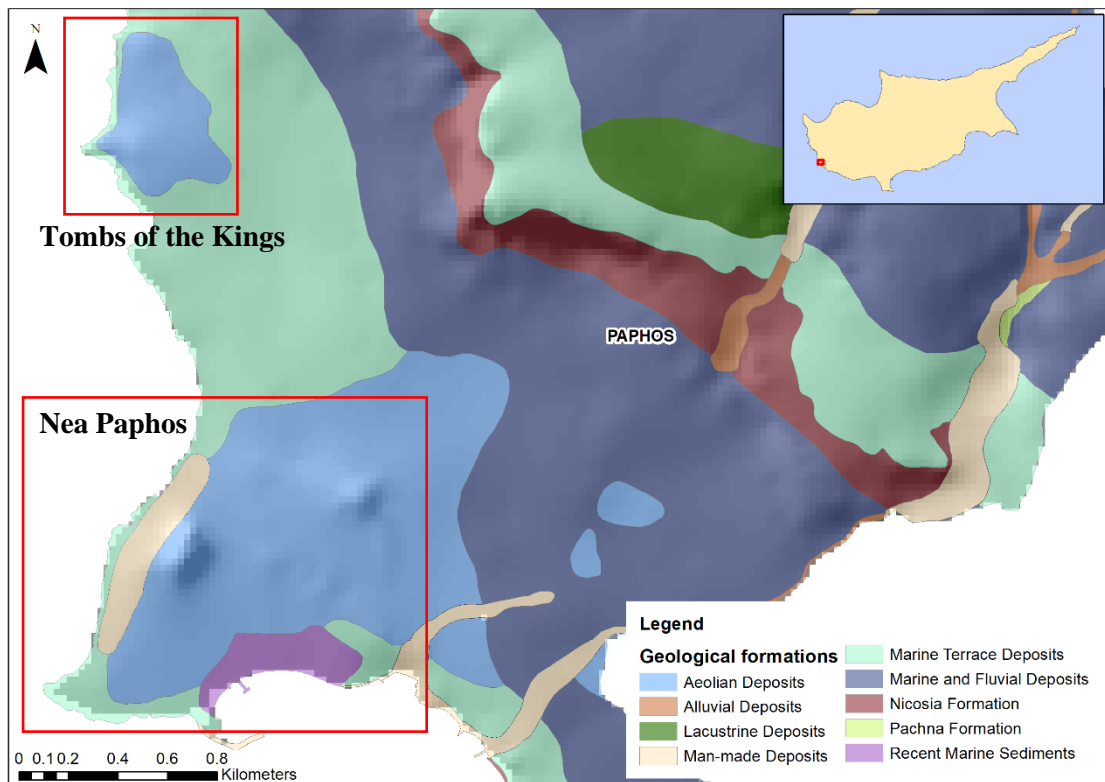


**Figure 23:** Geological map of the study area – Nea Paphos – Tombs of the Kings

Both archaeological sites, as seen in Figure 23, lie on aeolian deposits, consisting of loess, which are made up of windblown grains of sand or dust. There are also marine terrace deposits adjacent to the sea, whereas in the case of Nea Paphos site, there are man-made deposits to the west near the ancient walls. The high degree of soil erosion in combination with the clays and steep topography are considered some of the factors for ground instability in the Paphos District. This tendency is intensified by the powerful seismic activity in the region. Issues with ground stability and consequently structural stability of the ancient residues can be considered as a result of land movement mainly caused by the seismic activity of the area. Some examples of degradation are shown in Figure 24.





**Figure 24:** Examples of degradation of the structures present in the area of Nea Paphos, mainly caused by the seismic activities and erosion (source: Dr K. Themistocleous, CUT team).

It is possible that these monuments were built over unstable underlying ground conditions, thus increasing the risk for severe damages or even their collapse. Cyprus is located within a seismically active zone, a fact that further enhances the importance of monitoring cultural heritage sites. Paphos is situated in the most tectonic region of Cyprus, and several earthquakes have been reported in the past. One of the most devastating earthquakes in the area was the 6.5 Richter earthquake in 1953, which had a result of 40 people killed, 100 people injured, and 4000 people becoming homeless.

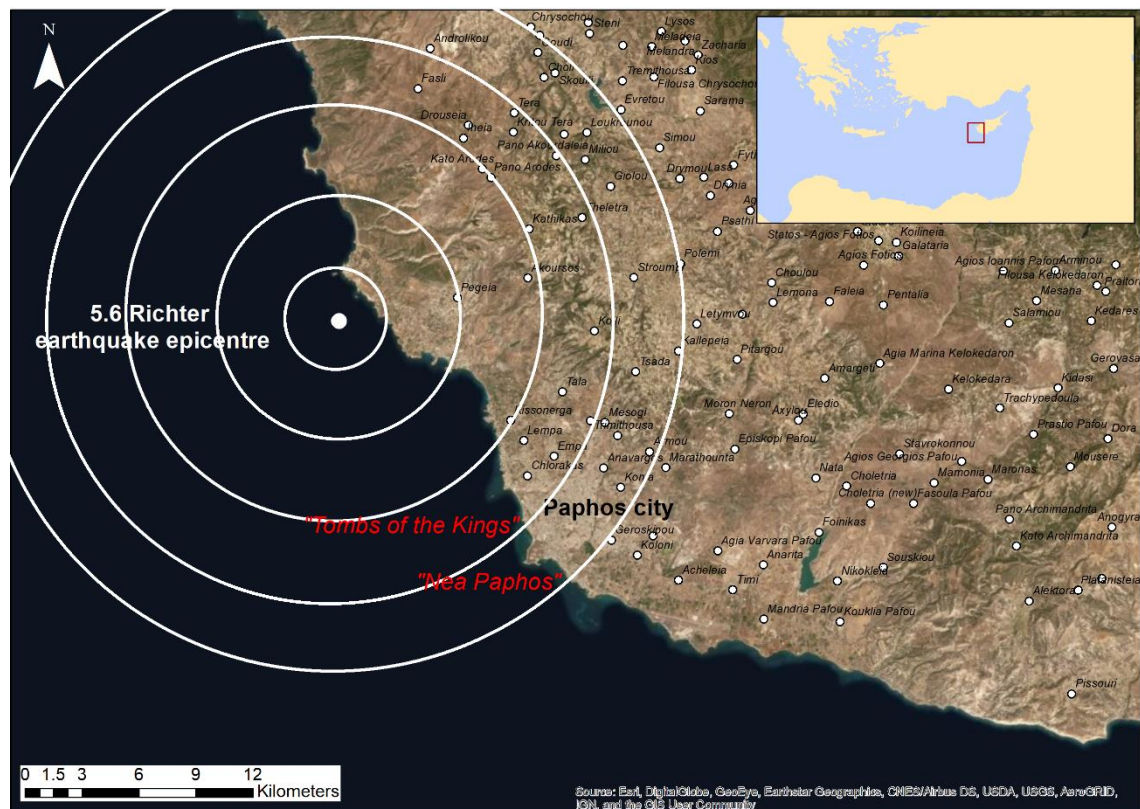


**Figure 25:** Map of Paphos and the epicentre of the 15 April 2015 earthquake

On 15 April 2015, at 8:25 AM UTC, Cyprus was hit by a new earthquake, as shown in Figure 25. The earthquake had a magnitude 5.6 on the Richter scale with an epicentre

3km offshore, west of Kissonerga, and 8km northwest of Paphos (Geological Survey Department, no date b). The earthquake was strongly felt throughout Cyprus. Many minor earthquakes occurred in the vicinity during the day raising concern to citizens and local authorities. In total, the post-seismic sequence consisted of around 60 smaller scale earthquakes in the same epicentral area.

### 3.1.3 Pissouri – Petra tou Romiou

Two areas, at the south-west part of the island, near Pissouri and the tourist site of “Petra tou Romiou” are studied. They are located in Limassol and Paphos District respectively, between the villages of Pissouri and Koukليا and lies in an area between the A6 motorway and the coastal road (old Limassol-Paphos road) connecting the cities of Limassol and Paphos, with thousands of people commuting every day using the specific part of the road network. The extents of the two case study areas and the specific parts of the roads that were closed due to individual landslide events are shown in Figure 26 and Figure 27.



**Figure 26:** The case study area by the A6 motorway near Pissouri



**Figure 27:** The case study area next to the old Limassol-Paphos road near Petra tou Romiou

The geology of the area consists of rocks with various mechanical properties, relating to resistance to erosion and weathering, such as bentonite, lava, limestone, quartz sandstone, argillaceous shale and hornstone, serpentinite, pyroxenite, gabbro, chalks and marls (Cyprus Tourism Organisation, no date). The most resistant rocks lie over the very soft and fragmented masses. The overall geology of the case study area is shown in Figure 28.

The wider area of Petra tou Romiou, near the village of Kouklia, lies on a complex geology with the formations of the Mamonia Complex, the Troodos Ophiolite Complex, the Kannaviou Formation, the Lefkara Formation, the Pachna Formation, as well as the Plio-Pleistocene deep-sea and alluvial depositions. The limestone of Petra tou Romiou is exposed in detached blocks of various sizes, as the Fasoulla lavas of the Fasoulla formation (Cyprus Tourism Organisation, no date; Geological Survey Department, 2016).

Pissouri, located at the south-east part of the case study area, is covered by sediments of Pliocene-Pleistocene age, most notably calcarenites, carbonate marls and sandstones of the Nicosia formation, as in the case of the case study area near A6 motorway (Alexandris, Griva and Abarioti, 2016). Underneath lies the Pissouri marl, which is characterised by

sandy interlayers. The marlstone is susceptible to fast weathering and in most sites the fresh marl is covered by a layer of weathered marl (Stow, Braakenburg and Xenophonos, 1995). The case study area located near “Petra tou Romiou” and the surrounding area between the villages of Kouklia and Pissouri lies mainly on the Pachna Formation, i.e. which consists of yellowish marls and chalks (Geological Survey Department, 2016).

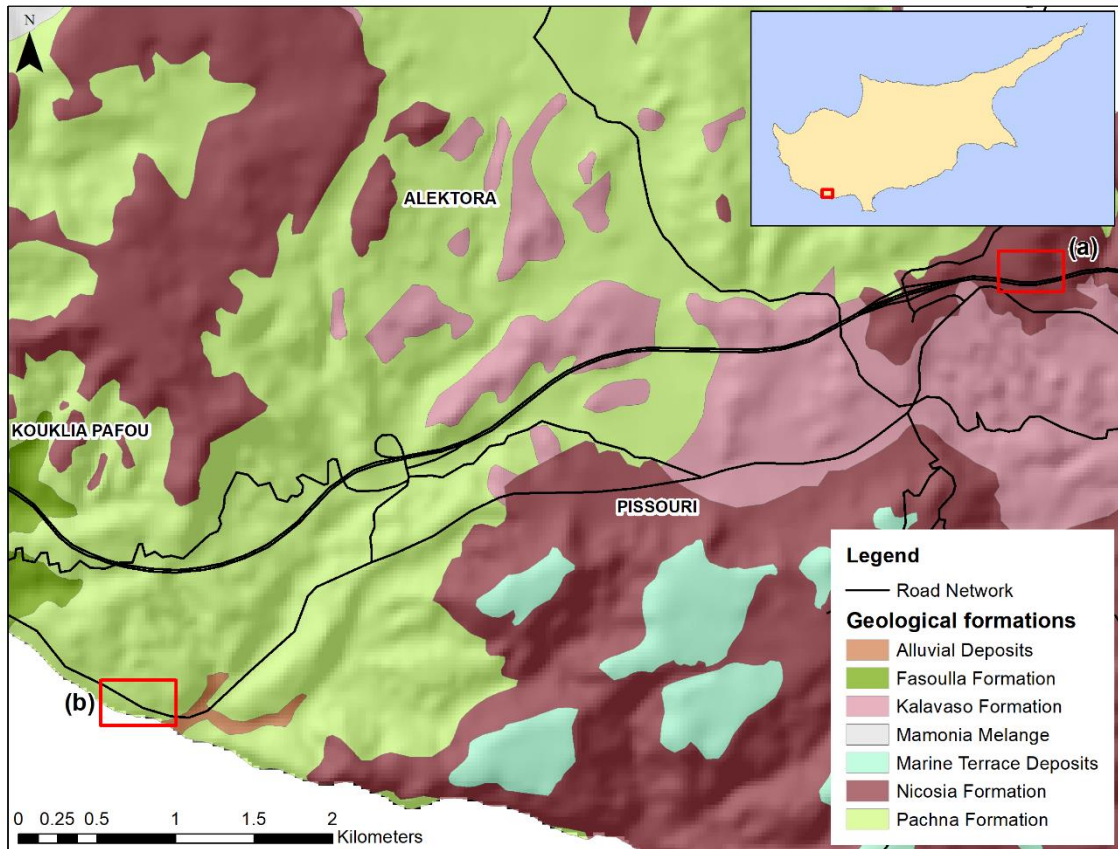


**Figure 28:** Geological map of the study area – Pissouri – Petra tou Romiou. Case study (a) by the A6 motorway near Pissouri and (b) next to the old Limassol-Paphos road near Petra tou Romiou

In this area, the soils are particularly problematic and prone to landslides, rockslides and other geotechnical failures. Numerous landslide and rockslide events have occurred following mainly extreme rainfall during the last decade having a significant impact to citizens as they led to road closures due to the proximity of the “problematic” soils to the road network (new and old motorway) connecting the cities of Limassol and Paphos.

More specifically, in January 2014, landslides and rockslides occurred in the areas adjacent to “Petra tou Romiou” leading to the closure of approximately 1.5km stretch of road in the direction from Paphos to Limassol for numerous days, diverting the traffic to other parts of the adjacent road network. Works for soil removal, slope normalisation and

lining of stairs were carried out. During the winter of 2014-2015, landslides and rockslides took place in the same area, where the landslide of January 2014 occurred, and also in adjacent areas. Several parts of the old Limassol-Paphos road as well as of the new motorway connecting the two cities, remained closed because of mud and rocks on the road caused by a landslide. Traffic was diverted to alternative routes, causing significant disruption to everyday commute.

In the present thesis, two individual landslide events were studied. The first one took place on 15 February 2019, following substantial rainfall, next to the Paphos – Limassol motorway A6, in the direction from Paphos to Limassol between exits of Avdimou and Pissouri (Figure 29). Extensive earthworks were carried out to remove the disturbed soil and the Paphos-Limassol motorway was given back to traffic on the 23<sup>rd</sup> of March 2019.



**Figure 29:** Landslide on the Paphos-Limassol motorway near Pissouri (source: Geological Survey Department)

Moreover, a landslide that took place on the 20<sup>th</sup> of February 2019, following heavy rainfall, was studied (Figure 30). A 3km long part of the old road from Paphos to Limassol was closed, approximately 200m away from “Petra to Romiou”. Structural issues were found in that part of the road, which remains closed until today for security reasons. The Department of Public Works<sup>7</sup>, of the Ministry of Transport, Communications and Works, is in charge of the rehabilitation works, which are currently at the stage of planning and design. The access from Paphos to Limassol, is still carried out only through the Paphos – Limassol motorway A6. The extensive precipitation and residing soil erosion issues were found to be the main reasons for this phenomenon.

---

<sup>7</sup> Department of Public Works:

[http://www.mcw.gov.cy/mcw/pwd/pwd.nsf/index\\_gr/index\\_gr?opendocument](http://www.mcw.gov.cy/mcw/pwd/pwd.nsf/index_gr/index_gr?opendocument)



**Figure 30:** Landslide near Paphos-Limassol old road next to Petra tou Romiou (source: Geological Survey Department)

Based on the landslide inventory provided by the Geological Survey Department, landslides were never recorded before in both areas, as shown in Figure 31.

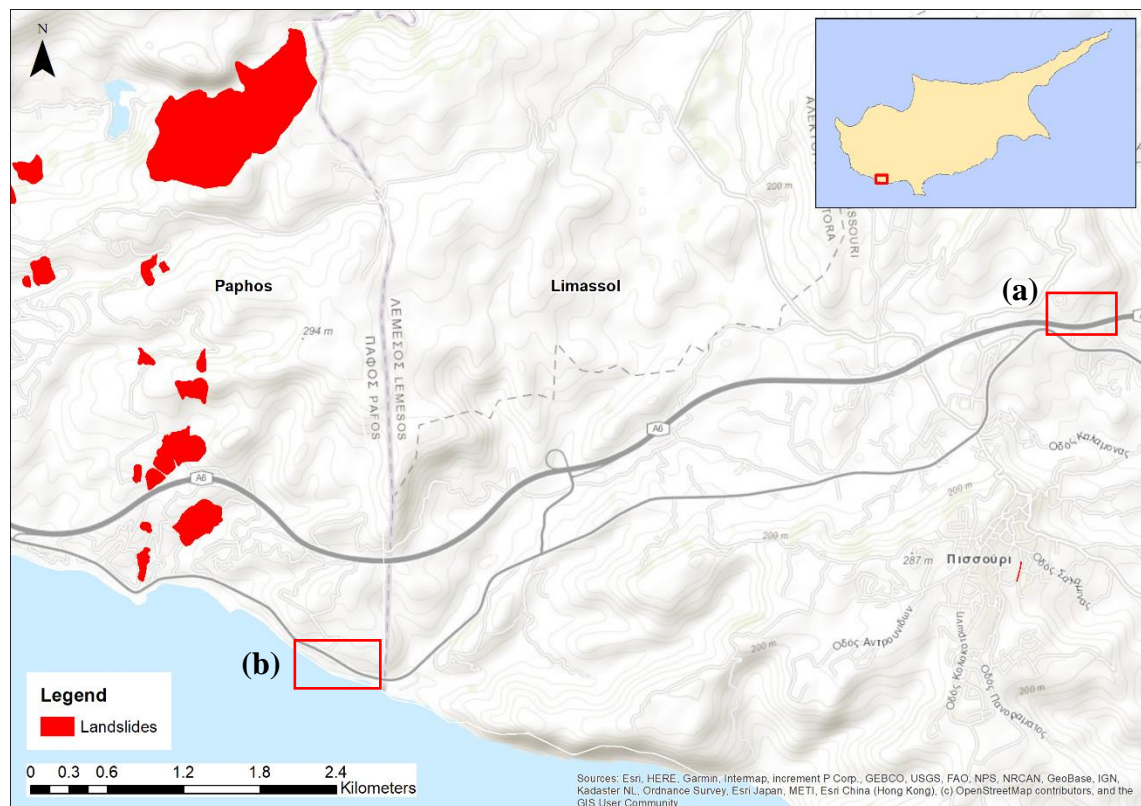


**Figure 31:** Landslides (a) next to the Paphos-Limassol motorway and (b) next to Paphos-Limassol old road near Petra tou Romiou (source: Geological Survey Department<sup>8</sup>)

<sup>8</sup> Digitised map based on data obtained from the Geological Survey Department

## 3.2 Data and software

The data and software that were used in the present thesis for the application of the proposed methodology are described in this section. Satellite data, optical and SAR, and other information are presented in *section 3.2.1*, and the software used for the analysis and processing of the datasets are presented in *section 3.2.2*.

### 3.2.1 Data

#### 3.2.1.1 Optical data

The development of the landslide hazard map for the case study of Statos – Agios Photios was performed in the framework of research published in 2014 and prior to the launch of the two Sentinel-2 satellites. More specifically, Sentinel-2A was launched on the 23<sup>rd</sup> of June 2015 and Sentinel-2B was launched on the 7<sup>th</sup> of March 2017.

Therefore, for the needs of the study, one Landsat 5-TM satellite image was downloaded from the USGS Earth Explorer<sup>9</sup>. A pansharpened multispectral QuickBird image (0.6m resolution – VIS, NIR) was also downloaded for year 2010 to assist in the mapping of various parameters that could not be observed via the medium-resolution Landsat images and improve the accuracy of the developed maps. These images were analysed in order to identify all the factors required to perform the Analytic Hierarchy Process (AHP) methodology for the development of the landslide hazard map for the case study of Statos – Agios Photios, as presented in *section 3.3.1*.

The Landsat Thematic Mapper (TM) sensor was carried on Landsat 4 and Landsat 5, and created images of six spectral bands with a spatial resolution of 30m for Bands 1-5 and 7, and one thermal band at 120m resolution (Table 2). The approximate scene size is 170km north-south and 183 km east-west (Earth Observing System, no date).

Due to their low spatial resolution, Landsat TM images could not be used to distinguish individual houses or trees, but for monitoring urban sprawl or deforestation over large areas (USGS, no date a).

---

<sup>9</sup> USGS Earth Explorer: <https://earthexplorer.usgs.gov/>


**Table 2:** Landsat 5 TM bands and their spatial resolutions

Landsat 5 TM bands	Wavelength (nm)	Resolution (m)
Band 1 – Visible	450-520	30
Band 2 – Visible	520-600	30
Band 3 – Visible	630-690	30
Band 4 – Near-Infrared	760-900	30
Band 5 – Near-Infrared	1550-1750	30
Band 6 – Thermal	10400-12500	120
Band 7 – Mid-Infrared	2080-2350	30

Source: United States Geological Survey, Landsat 5

The Landsat 5 TM image (30m resolution – VIS, NIR) that was downloaded, and its characteristics are presented in Table 3. The acquisition date was solely governed by the availability of a cloud-free image on the specific date.

**Table 3:** Acquired Landsat 5 TM image characteristics

<b>Landsat Product Identifier</b>	LT05_L1TP_176036_20100827_20161013_01_T1	
<b>Acquisition Date</b>	27/08/2010	
<b>Spacecraft Id.</b>	LANDSAT_5	
<b>WRS Path / Row</b>	176 / 036	
<b>Scene Cloud Cover</b>	2	
<b>Image Quality</b>	9	
<b>Data Type Level-1</b>	TM_L1TP	
<b>UTM Zone</b>	36	
<b>Datum</b>	WGS84	
<b>Centre Latitude</b>	34°37'28.20"N	
<b>Centre Longitude</b>	33°05'15.72"E	

During the application of the DInSAR and CCD methodologies, Sentinel-2 images were used for the calculation of the NDVI, that was used for the removal of the effect of vegetation from the displacement and coherence map products.

In fact, a Sentinel-2 image was downloaded from the Copernicus open access hub (S2A\_MSIL2A\_20190203T083141\_N0211\_R021\_T36SVD\_20190203T111709), dated



3 February 2019. This was the closest to the landslides cloud-free and atmospherically corrected image (Level-2A).

The Copernicus Sentinel-2 mission comprises a constellation of two polar-orbiting satellites, Sentinel-2A and Sentinel-2B, placed in the same sun-synchronous orbit, phased at 180° to each other. It is mainly used for the systematic monitoring of land surface changes, and its wide swath width (290km) and high revisit time (10 days at the equator with one satellite, and 5 days with 2 satellites under cloud-free conditions which results in 2-3 days at mid-latitudes) support monitoring of Earth's surface changes. The coverage limits are from between latitudes 56° south and 84° north (ESA, no date c).

The 13 spectral bands of Sentinel-2 range from the Visible Near (VNIR) and Near Infra-Red (NIR) to the Short Wave Infra-Red (SWIR) at different spatial resolutions ranging from 10 to 60 meters on the ground, as shown in Table 4. The four bands at 10m resolution ensure continuity with older missions, like SPOT-5 and Landsat-8 and support user requirements for basic land-cover classification. The six bands at 20m resolution address requirements for enhanced land-cover classification and for the retrieval of geophysical parameters. Finally, three bands at 60m resolution are mainly dedicated to atmospheric corrections and cirrus-cloud screening (ESA, no date c).

**Table 4:** Sentinel-2 bands and their spatial resolutions

Sentinel-2 bands	Wavelength (nm)	Resolution (m)
Band 1 – Coastal aerosol	443	60
Band 2 – Blue	490	10
Band 3 – Green	560	10
Band 4 – Red	665	10
Band 5 – Vegetation Red Edge	705	20
Band 6 – Vegetation Red Edge	740	20
Band 7 – Vegetation Red Edge	783	20
Band 8 – NIR	842	10
Band 8A – Vegetation Red Edge	865	20
Band 9 – Water vapour	940	60
Band 10 – SWIR – Cirrus	1375	60
Band 11 – SWIR	1610	20
Band 12 – SWIR	2190	20

Source: European Space Agency, Sentinel-2 mission

### 3.2.1.2 SAR data

Sentinel-1 SAR acquisitions were downloaded from the European Space Agency (ESA) Copernicus Open Access Hub<sup>10</sup> to study the impact of earthquakes and landslides to infrastructure in the case studies of Nea Paphos – Tombs of the Kings and Pissouri – Petra tou Romiou. Specific events were chosen, a seismic event and two landslide events, as presented in *sections 3.1.2* and *3.1.3* respectively.

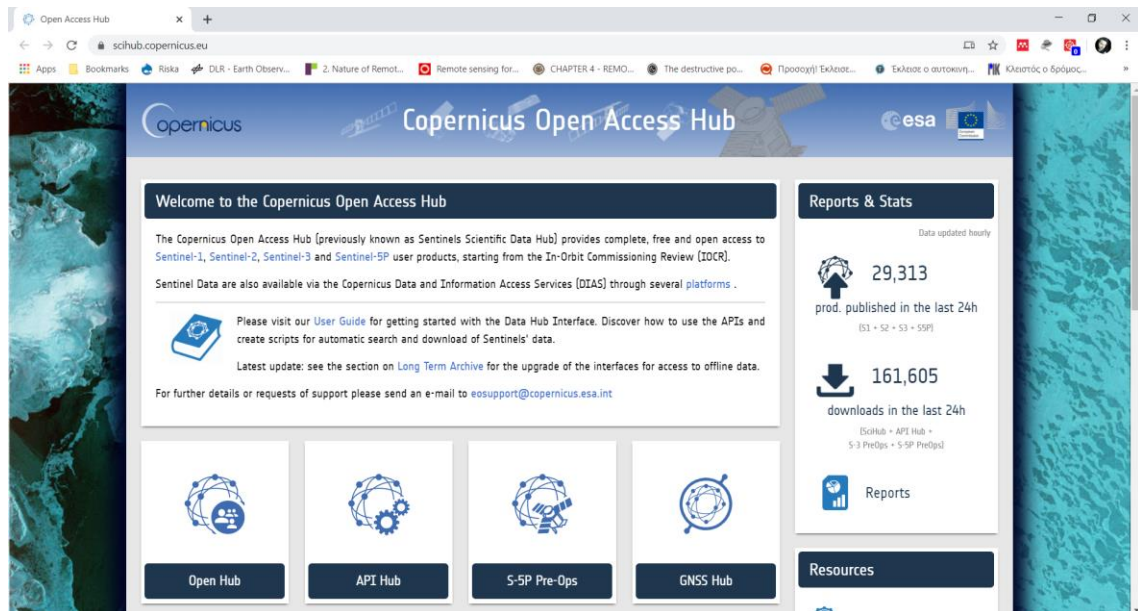


**Figure 32:** The Copernicus Open Access Hub

The Sentinel-1 mission consists of a constellation of two polar-orbiting satellites, Sentinel-1A and Sentinel-1B, sharing the same orbital plane. It performs C-band (central frequency of 5.404 GHz or  $\sim 5.547\text{cm}$ ) Synthetic Aperture Radar (SAR) imaging, operating at wavelengths unobstructed by cloud cover or a lack of illumination, acquiring imagery during day and night and under all weather conditions (ESA, no date b).

The Sentinel-1 satellites provide free of charge imagery in four exclusive acquisition modes, Stripmap (SM), Interferometric Wide (IW) swath, Extra-Wide (EW) swath and Wave (WV), with different resolution (down to 5m) and coverage characteristics (up to 400km). Each mode can potentially produce products at SAR Level-0, Level-1 SLC, Level-1 GRD, and Level-2 OCN, that can be used in different thematic areas and

<sup>10</sup> Copernicus Open Access Hub: <https://scihub.copernicus.eu/>

applications. Data products are available in single polarisation (VV or HH) for WV mode and dual polarisation (VV+VH or HH+HV) or single polarisation (HH or VV) for SM, IW and EW modes (ESA, no date b). Each Sentinel-1 satellite offers a 12-day revisit cycle in IW swath mode in a single pass, whereas the constellation of the two Sentinels have a 6-day revisit cycle at the equator (ESA, no date b).

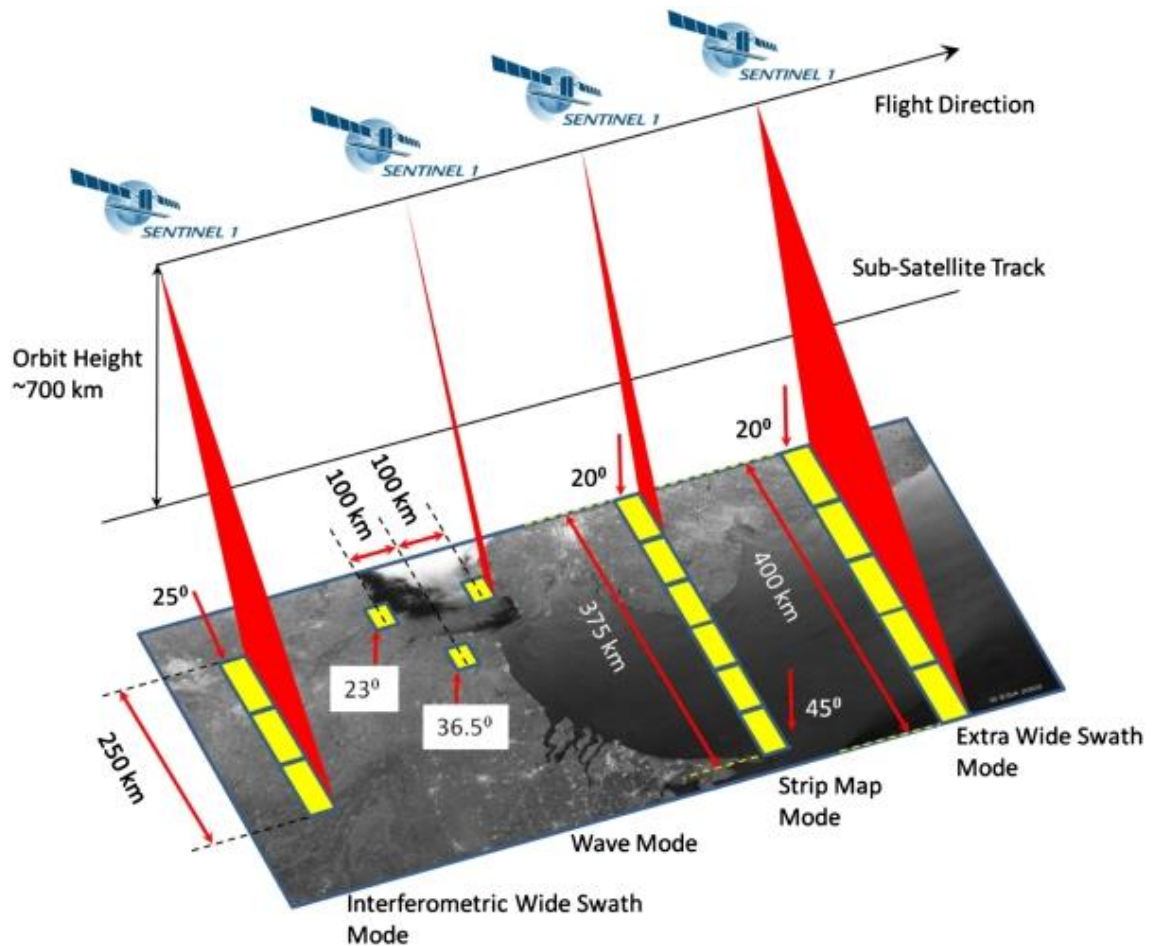


**Figure 33:** Sentinel-1 acquisition modes (ESA, no date b)

The very short revisit times of the Sentinel-1 satellites, the fast product delivery ranging from 1 to 24 hours, and the availability of precise measurements of spacecraft position and attitude for each observation, offer reliable and systematic monitoring over large areas. As suggested by ESA, the primary conflict-free mode for observations over land is the Interferometric Wide (IW) swath mode, with VV+VH polarisation. The resolution of IW swath images for Level-1 SLC products varies from 2.7 x 22m to 3.5 x 22m.

For the case study of Nea Paphos – Tombs of the Kings, two pairs of IW swath mode SLC products with VV+VH polarisation were downloaded before and after the

earthquake event. For the case study of Pissouri – Petra tou Romiou, due to the nature and complexity of the natural hazard phenomenon under investigation, 32 Sentinel-1 (16 S1A and 16 S1B) images were downloaded for the period starting from 11 January 2019 until 12 April 2019, to carry out a comprehensive study on the evolution of the landslide. A pre-selection of the downloaded images was carried out prior to interferometric processing. The acquisition of the SAR images was performed through the Copernicus Open Access Hub by specifying the area of interest for each case, as shown in Figure 34.

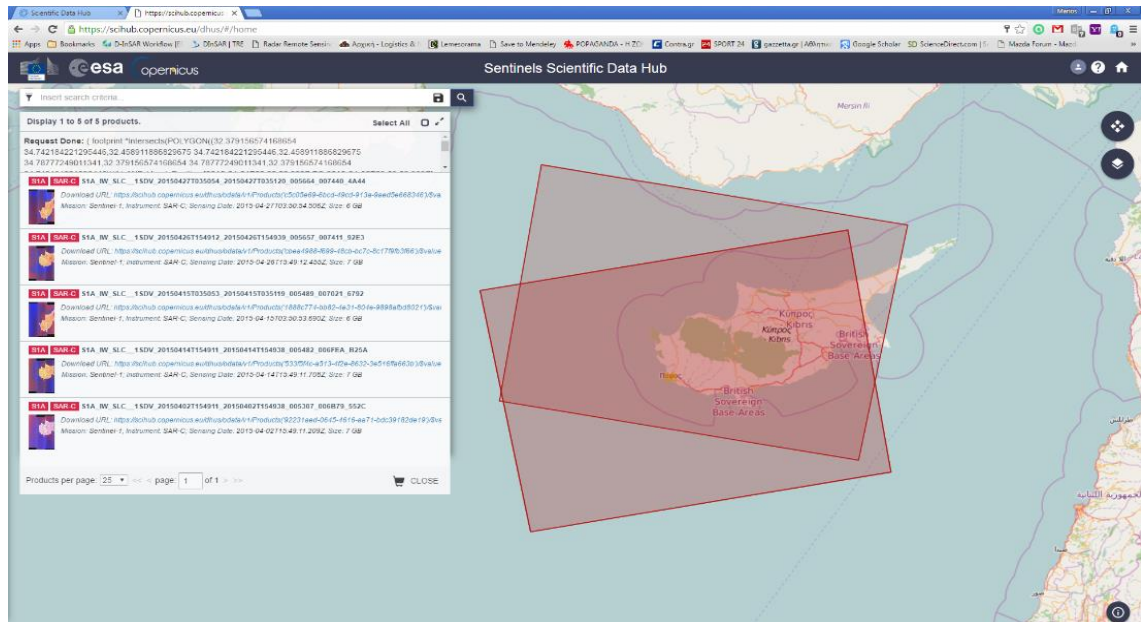


**Figure 34:** Selection of area of interest – Copernicus Open Access Hub

A detailed list of the characteristics of the acquired images for the two case study site is presented in Table 5 and Table 6.

**Table 5:** Sentinel-1 SAR image characteristics – Nea Paphos-Tombs of the Kings

Platform	Date	Time	Pass direction	Polarisation	Mode / type	Relative orbit
Sentinel-1A	14/04/2015	15:49:38	Ascending	VV VH	IW/SLC	160
Sentinel-1A	15/04/2015	03:51:19	Descending	VV VH	IW/SLC	167
Sentinel-1A	26/04/2015	15:49:39	Ascending	VV VH	IW/SLC	160
Sentinel-1A	27/04/2015	03:51:20	Descending	VV VH	IW/SLC	167

**Table 6:** Sentinel-1 SAR image characteristics – Pissouri-Petra tou Romiou

<b>Platform</b>	<b>Date</b>	<b>Time</b>	<b>Pass direction</b>	<b>Polarisation</b>	<b>Mode / type</b>	<b>Relative orbit</b>
Sentinel-1A	11/01/2019	15:49:53	Ascending	VV VH	IW/SLC	160
Sentinel-1A	12/01/2019	03:51:43	Descending	VV VH	IW/SLC	167
Sentinel-1B	17/01/2019	15:49:27	Ascending	VV VH	IW/SLC	160
Sentinel-1B	18/01/2019	03:51:07	Descending	VV VH	IW/SLC	167
Sentinel-1A	23/01/2019	15:49:53	Ascending	VV VH	IW/SLC	160
Sentinel-1A	24/01/2019	03:51:43	Descending	VV VH	IW/SLC	167
Sentinel-1B	29/01/2019	15:49:26	Ascending	VV VH	IW/SLC	160
Sentinel-1B	30/01/2019	03:51:07	Descending	VV VH	IW/SLC	167
Sentinel-1A	04/02/2019	15:49:52	Ascending	VV VH	IW/SLC	160
Sentinel-1A	05/02/2019	03:51:42	Descending	VV VH	IW/SLC	167
Sentinel-1B	10/02/2019	15:49:26	Ascending	VV VH	IW/SLC	160
Sentinel-1B	11/02/2019	03:51:06	Descending	VV VH	IW/SLC	167
Sentinel-1A	16/02/2019	15:49:52	Ascending	VV VH	IW/SLC	160
Sentinel-1A	17/02/2019	03:51:42	Descending	VV VH	IW/SLC	167
Sentinel-1B	22/02/2019	15:49:26	Ascending	VV VH	IW/SLC	160
Sentinel-1B	23/02/2019	03:51:06	Descending	VV VH	IW/SLC	167
Sentinel-1A	28/02/2019	15:49:52	Ascending	VV VH	IW/SLC	160
Sentinel-1A	01/03/2019	03:51:42	Descending	VV VH	IW/SLC	167
Sentinel-1B	06/03/2019	15:49:26	Ascending	VV VH	IW/SLC	160
Sentinel-1B	07/03/2019	03:51:06	Descending	VV VH	IW/SLC	167
Sentinel-1A	12/03/2019	15:49:52	Ascending	VV VH	IW/SLC	160
Sentinel-1A	13/03/2019	03:51:42	Descending	VV VH	IW/SLC	167
Sentinel-1B	18/03/2019	15:49:26	Ascending	VV VH	IW/SLC	160
Sentinel-1B	19/03/2019	03:51:06	Descending	VV VH	IW/SLC	167
Sentinel-1A	24/03/2019	15:49:52	Ascending	VV VH	IW/SLC	160
Sentinel-1A	25/03/2019	03:51:42	Descending	VV VH	IW/SLC	167
Sentinel-1B	30/03/2019	15:49:26	Ascending	VV VH	IW/SLC	160
Sentinel-1B	31/03/2019	03:51:06	Descending	VV VH	IW/SLC	167
Sentinel-1A	05/04/2019	15:49:52	Ascending	VV VH	IW/SLC	160
Sentinel-1A	06/04/2019	03:51:43	Descending	VV VH	IW/SLC	167
Sentinel-1B	11/04/2019	15:49:26	Ascending	VV VH	IW/SLC	160
Sentinel-1B	12/04/2019	03:51:07	Descending	VV VH	IW/SLC	167

### **3.2.1.3 Other data**

A Digital Elevation Model (DEM) was used to generate geomorphologic parameters, such as aspect, slope and drainage network, factors that were used in the application of the AHP methodology for the development of land displacement susceptibility maps. The DEM of 25m pixel size was provided by the Department of Lands and Surveys of Cyprus and created with the use of orthorectified stereo pairs of aerial photos covering the study area (scale 1:5,000).

At the step of pre-processing of the optical images, geometric corrections were carried out using several Ground Control Points (GCPs). Topographical maps (scale 1:5000 and 1:2000) were used to locate the position of GCPs in conjunction with the island's shoreline.

Geological maps of the areas under study were used to locate the areas' main tectonic faults and for the digitisation of the zones of geological formations in GIS environment. This information was used to identify areas susceptible to land movements.

Moreover, annual precipitation data were collected from the Cyprus Meteorological Service stations to incorporate them in the AHP methodology.

For DInSAR processing, SRTM 3sec and SRTM 1sec HGT Digital Elevation Models were automatically downloaded through SNAP software, and were used at the steps of coregistration, development of interferogram, the removal of topographic phase and the geometric correction of the displacement and coherence maps.

Sentinel-1 precise orbits, that were downloaded automatically through SNAP software, were used during the application of DInSAR and CCD methodologies, at the step of coregistration.

Finally, coordinates of the CYPOS network permanent GNSS stations were used on the SAR images acquisition dates to perform the calibration and validation of the land displacement results obtained at the end of the DInSAR processing chain.

## 3.2.2 Software

### 3.2.2.1 SNAP

The processing of Sentinel-1 SAR acquisitions was carried out using the open-source software Sentinel Applications Platform (SNAP) (version 5.0, as of 5<sup>th</sup> of December 2016 and version 7.0 of 22<sup>nd</sup> of July 2019) (ESA, no date f). The open source policy and the great number of capabilities make it an ideal candidate software for SAR as well as optical imagery processing. Within SNAP, the Sentinel-1 Toolbox (S1TBX) was used for the application of the proposed DInSAR and CCD processing chains, presented in *section 3.3.2*.

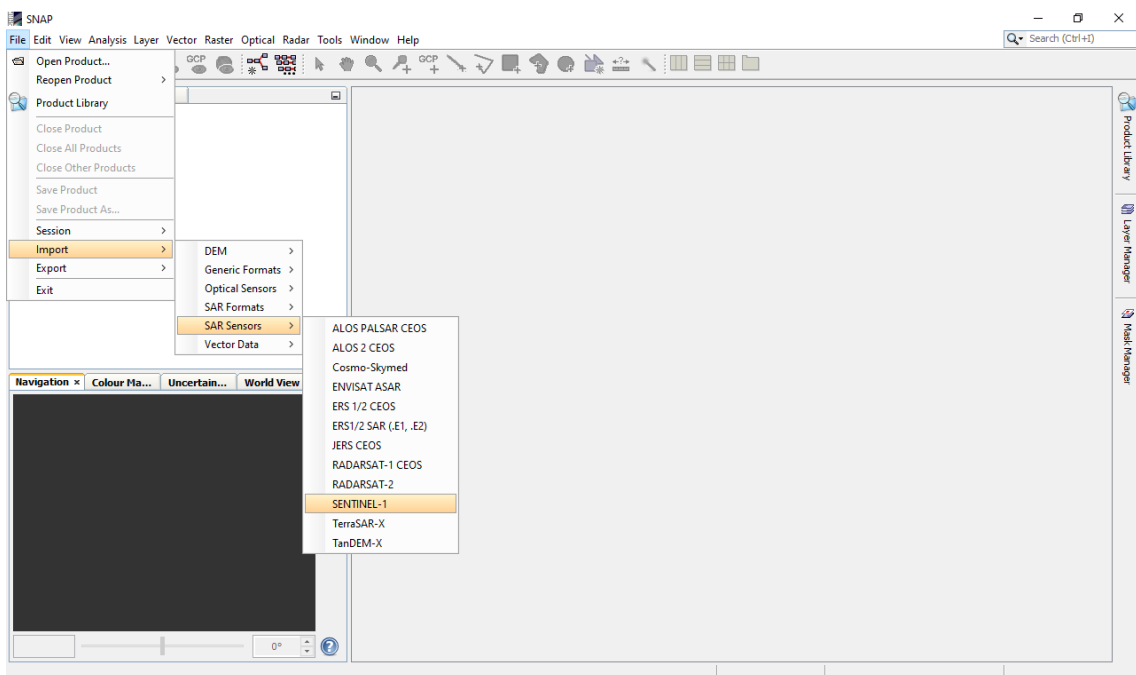


**Figure 35:** The interface of SNAP software

S1TBX consists of a collection of processing tools, data product readers and writers and a display and analysis application to support the large archive of data from ESA SAR missions including SENTINEL-1, ERS-1 & 2 and ENVISAT, as well as third party SAR data from ALOS PALSAR, TerraSAR-X, COSMO-SkyMed and RADARSAT-2 (ESA, no date d). The Toolbox includes tools for calibration, speckle filtering, coregistration, orthorectification, mosaicking, data conversion, polarimetry and interferometry. S1TBX is developed for ESA by Array Systems Computing in partnership with DLR, Brockmann Consult and OceanDataLab (ESA, no date d).

Moreover, the NDVI processor module of SNAP was used for the processing of Sentinel-2 imagery that was then used as a mask to remove the effect of vegetation from the coherence maps and displacement maps that were developed from the application of the DInSAR and CCD methodologies.

### 3.2.2.2 SNAPHU

SNAPHU v1.4.2 software (Stanford Radar Interferometry Research Group, 1995), a statistical-cost network-flow algorithm for phase unwrapping developed at Stanford University, was used for the phase unwrapping process of the DInSAR methodology.

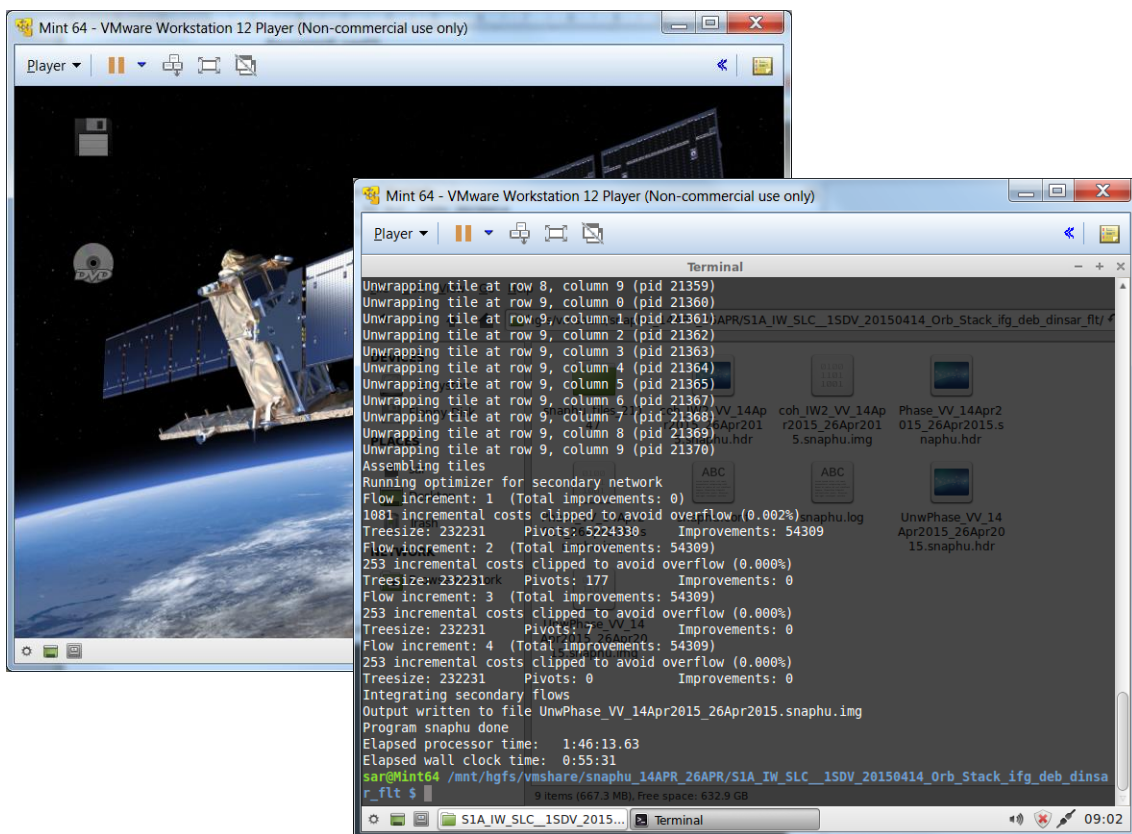


**Figure 36:** The interface of SNAPHU software

SNAPHU is an implementation of the Statistical-cost, Network-flow Algorithm for Phase Unwrapping (Chen and Zebker, 2001a, 2001b, 2002). This algorithm solves phase unwrapping as a maximum a posteriori probability estimation problem, aiming to compute the most likely unwrapped solution based on the observable input data. Because the statistics relating the input data to the solution depend on the measured quantity,



SNAPHU uses three built-in statistical models, for topography data, deformation data, and smooth generic data. The optimisation problem is solved approximately using network-flow techniques (Stanford Radar Interferometry Research Group, 1995). SNAPHU always produces complete unwrapped solutions, and its accuracy is comparable to or better than that of other available algorithms. The execution time of SNAPHU depends on the interferogram complexity. In single-tile mode the memory required is on the order of 100 MB per 1,000,000 pixels in the input interferogram. The software is written in C and can be operated on most Unix/Linux platforms (Stanford Radar Interferometry Research Group, 1995).

In 2019, a SNAPHU plugin was introduced within the SNAP environment (Braun and Veci, 2020). Therefore, the phase unwrapping step of the Interferometric processing of the time series of SAR images, for the case study area of Pissouri – Petra tou Romiou, was carried out within the environment of SNAP software.

### **3.2.2.3 Other software**

ArcGIS Desktop 10.6.1 from Esri was used for the application of AHP methodology and for the visualisation of the processing results from DInSAR and CCD methodologies. ArcGIS was also used for the extraction of displacement and coherence values from the displacement and coherence maps produced. Additionally, the Raster Calculator tool was used for the development of the NDVI mask, and for the calculation of coherence difference and normalised coherence difference values.

Microsoft EXCEL software was used for the mathematical calculations, simple and more complex ones, in the present study. More specifically, it was used in the calculation of weight factors in the AHP methodology and for the analysis of the findings from the application of DInSAR and CCD methodologies as described in *section 4* of this thesis.

Last but not least, the ROC Analysis web-based calculator for ROC curves was used for the ROC analysis of the coherence difference and normalised coherence difference indicators during the CCD methodology (Eng, no date).

### 3.3 Methods

An integration of auxiliary and satellite data was conducted in the case study of Statos – Agios Photios. More specifically, topographic maps, Digital Elevation Models (DEM), meteorological data (precipitation), as well as Landsat TM data were used, for the development of landslide susceptibility maps via remote sensing and GIS techniques.

Furthermore, SAR images from the recently launched ESA's satellite Sentinel-1 were used together with appropriate DEMs to produce coherence and land displacement maps through the application of Differential Interferometric SAR (DInSAR) and Coherent Change Detection (CCD) processing.

Finally, in *section 3.3.3*, a calibration and validation methodology for the results of the DInSAR methodology is presented.

#### 3.3.1 Development of land displacement susceptibility maps

The methodology for the development of land displacement susceptibility map is based on a Qualitative knowledge-driven approach, the Analytical Hierarchy Process (AHP), which is shown diagrammatically in Figure 37. The general methodology was included in a publication, I co-authored, titled "*Integrated use of GIS and remote sensing for monitoring landslides in transportation pavements: the case study of Paphos area in Cyprus*" (Alexakis *et al.*, 2014).

In general, it is applied in GIS environment by combining a number of factors (layers) that are considered to be important for the generation of landslide events. As analysed below, specific weights are assigned to these factors by experts, resulting, after processing, in a final landslide susceptibility map for the area of interest. The various steps of the proposed methodology are the following:

1. Mapping of known landslide events
2. Definition of the case study area
3. Acquisition of medium and high-resolution satellite imagery
4. Pre-processing (geometric corrections) of satellite imagery
5. Application of radiometric corrections to satellite imagery

6. Application of atmospheric correction to satellite imagery
7. Post-processing
8. Development of land use/land cover, faults and road network layers
9. Extraction of topographical characteristics / GIS data (slope, aspect, etc.)
10. Identification of parameters related to landslide probability
11. Implementation of parameters in GIS and their reclassification with weights
12. Application of AHP method – landslide susceptibility map
13. Evaluation of results

In-situ field visits were carried out in Paphos District to map known landslide events and record the landslide occurrence in the area. Following this step and based on its findings, the case study area was clearly defined. Appropriate medium and high spatial resolution optical images, such as Landsat TM and QuickBird were acquired in order to monitor land use changes, faults and the road network in the area of interest. At the step of pre-processing, geometric corrections were carried out using several Ground Control Points (GCPs) and a second-order polynomial fit.

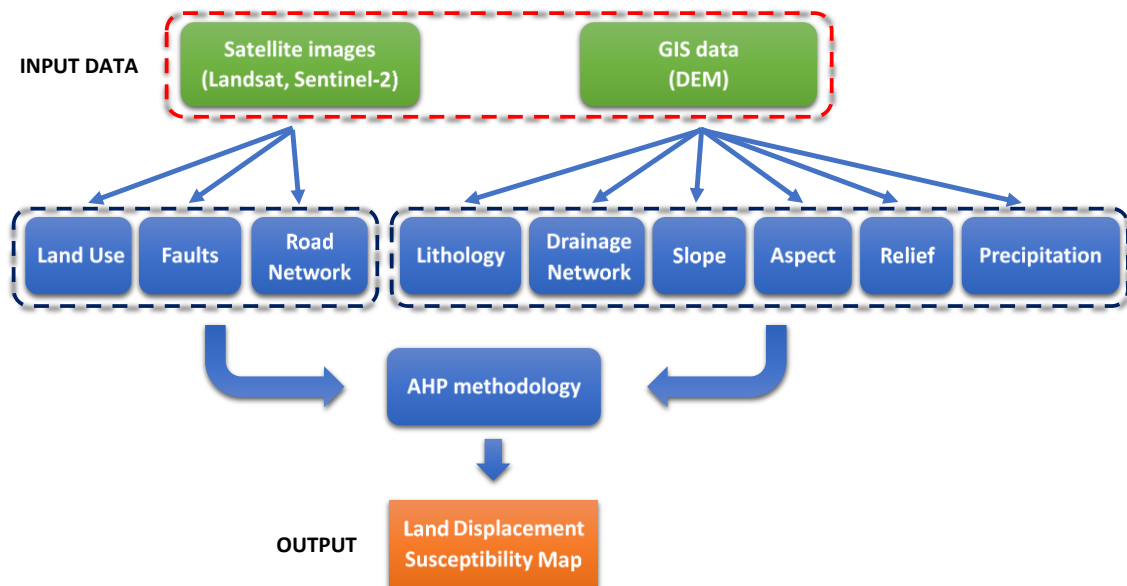


**Figure 37:** Flow chart of the proposed AHP methodology

For this purpose, detailed topographical maps (scale 1:5000 and 1:2000) were used to locate the position of GCPs in conjunction with the island’s shoreline. Moreover, radiometric corrections were applied to the acquired images. These are crucial for optical

imagery, as variations in illumination, i.e. earth to sun distance correction, and viewing geometry, i.e. sun elevation correction should be minimised in multitemporal analysis.

Atmospheric correction, which is considered to be one of the most difficult tasks in the pre-processing of image data, was then applied. This is due to the fact that the distributions and intensities of these effects are often inadequately known. From literature, it is generally accepted that Darkest Pixel (DP) atmospheric correction technique can be applied through the use of dark targets that are included in the satellite images (Hadjimitsis, Clayton and Hope, 2004; Hadjimitsis, 2010; Agapiou *et al.*, 2011). In the present case study, the Asprokremmos Dam, a deep inland water body, was used as a dark object. An assumption is made in principle in such cases, that the signal reaching a satellite sensor, originating from a dark object, and its dark pixels, is contributed to by the atmosphere at visible wavelengths. Moreover, near infrared and middle infrared images are assumed to be free of atmospheric scattering effects (Lu *et al.*, 2002). Therefore, the surface reflectance of the dark target, is approximated to have zero surface reflectance. The atmospheric path radiance adds to the surface radiance of the dark target, giving the target radiance at the sensor.

Following the pre-processing steps, several digital layers were developed during the image post-processing analysis, such as the Land Use/ Land Cover (LULC), the position of faults and road network in the area of study. These layers were used for the creation of the landslide hazard map. Moreover, topographic characteristics, such as slope, surface hydrological information and aspect were obtained from the area's DEM.

The following nine parameters were considered for the calculation of landslide probability, and they were implemented in GIS environment in the form of layers:

1. Slope
2. Land use
3. Aspect
4. Faults
5. Drainage Network
6. Road network
7. Relief
8. Lithology
9. Precipitation

A team of experts in the field were contacted, such as geologists, geotechnical and civil engineers, from the Department of Public Works<sup>11</sup> of the Ministry of Transport, Communications and Works; and the Technical Chamber of Cyprus (ETEK)<sup>12</sup>. They have extensive field knowledge of the land displacement mechanisms and the importance of the aforementioned factors in the initiation of ground movements. Therefore, they assisted in the re-classification of these parameters with certain weights, according to their contribution to landslides.

As a next step, the Analytical Hierarchy Process (AHP) methodology was applied to compare the different parameters and their importance in relation to landslide risk, leading to the assignment a final weight factor. The AHP methodology (Saaty, 1980), as described in *section 2 Literature review* and more specifically in *section 2.3*, has been used widely in remote sensing applications and is considered a powerful tool that can be used to analyse multiple and conflicting criteria and objectives, and make decisions resulting in a ranking of preferences derived from a set of alternatives (Yalcin *et al.*, 2011).

In more detail, during the application of the AHP, a set of evaluation criteria is set that will be used in the decision-making process. Then, a weight of importance is assigned to each evaluation criterion according to the decision maker's pairwise comparisons of the criteria. As a next step, for each criterion, a score from 1 to 9 is assigned to each factor, based on the effectiveness of the factors in relation to the criterion under study. Finally, the criteria weights and parameters scores are combined to derive a final score of significance and subsequently an overall ranking for each parameter with respect to all the set criteria (Saaty, 1987, 2008).

The resulting landslide susceptibility map was then validated against the inventory of known landslides in the study area (Figure 11) and the earthquake and other geological hazards risk map developed by the Geological Survey Department (Figure 14). In this section, the nine parameters that are associated with landslide susceptibility are presented and analysed below along with their calculations via remote sensing and GIS techniques.

---

<sup>11</sup> Department of Public Works:

[http://www.mcw.gov.cy/mcw/pwd/pwd.nsf/index\\_gr/index\\_gr?opendocument](http://www.mcw.gov.cy/mcw/pwd/pwd.nsf/index_gr/index_gr?opendocument)

<sup>12</sup> Technical Chamber of Cyprus: <https://www.etek.org.cy/site-menu-82-en.php>

### 3.3.1.1 Slope

Slope and slope stability play a crucial role in landslide vulnerability. In general, shear stress in soil increases when there is also an increase in slope angle. Subsequently, landslides occur at a low frequency at gentle slopes, due to the lower shear stresses associated with small slopes (Duncan, 1996).

The slope map of the study area was developed from a DEM that was provided by the Department of Lands and Surveys. Its values extent from 0° to 51° with the steep slopes distributed primarily in the northern part of the case study area. The slope values derived from the DEM were classified in GIS environment in seven categories (0°–5°, 5°–10°, 10°–20°, 20°–30°, 30°–40°, 40°–50°, >50°) as presented in Figure 38. Based on experts' opinion, a rating was assigned to each slope category as shown in Table 7.

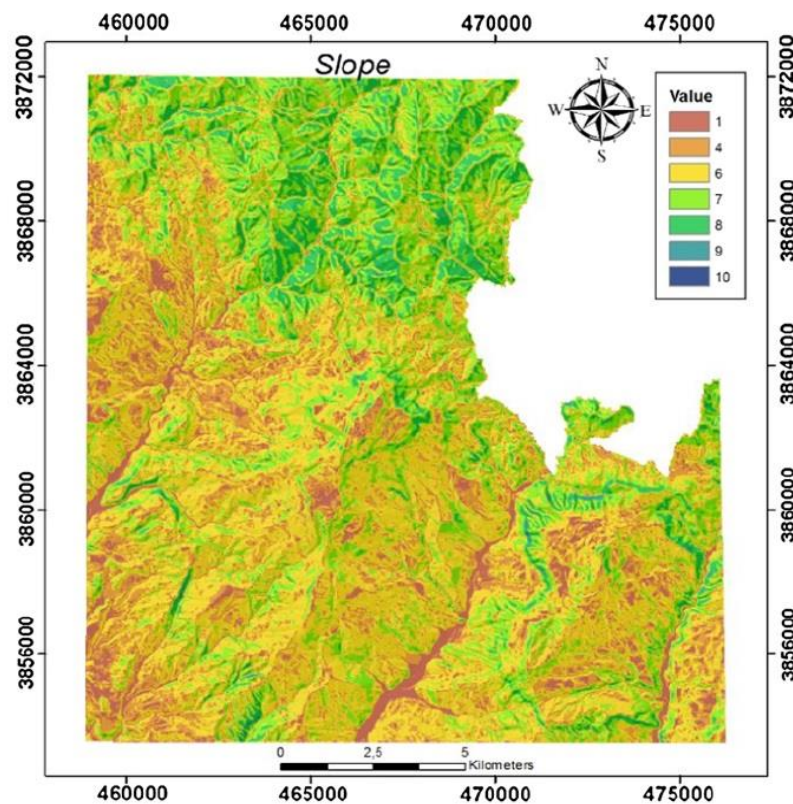


**Figure 38:** Slope classes – Statos-Agios Photios

**Table 7:** Slope classification and rating

Slope	0°–5°	5°–10°	10°–20°	20°–30°	30°–40°	40°–50°	>50°
Rating	1	4	6	7	8	9	10

### 3.3.1.2 Land use

In general, vegetation through their roots provide stabilising mechanical properties to slopes. Landslides occur mainly in non-vegetated areas where there is no or minimum root strength (Montgomery *et al.*, 2000). A Land Use map, using a QuickBird high resolution image to improve its accuracy, was developed for year 2010 as presented in Figure 39. Urban, water, vegetation and bare soil were the four land use types used in the AHP methodology. Based on experts' opinion, a rating was assigned to each land use type as shown in Table 8.

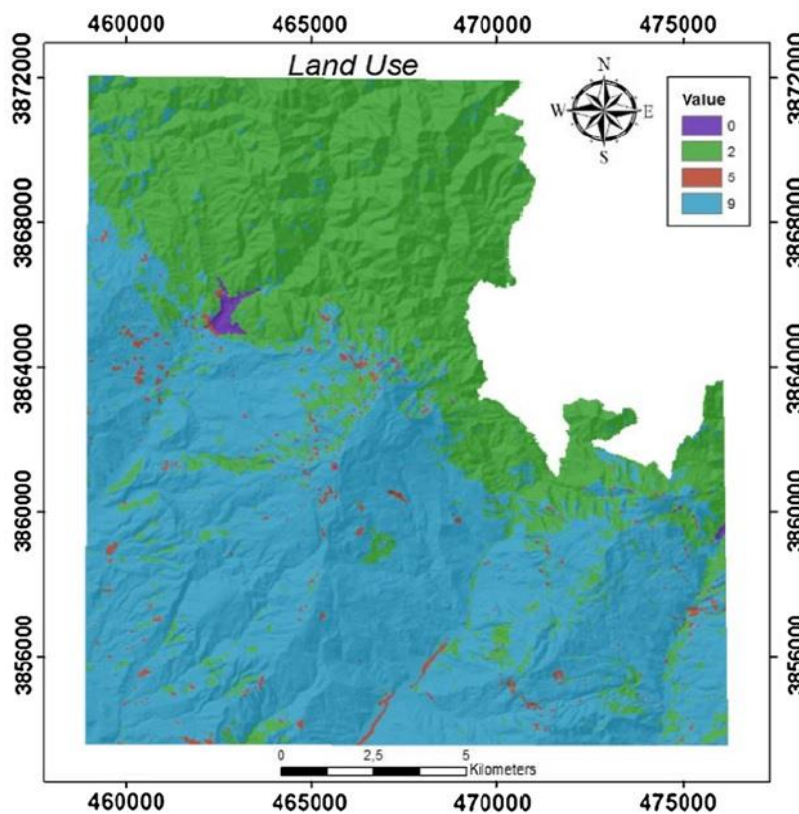


**Figure 39:** Land use map – Statos-Agios Photios

**Table 8:** Land use classification and rating

Land use	Water	Vegetation	Urban	Bare soil
Rating	0	2	5	9

### 3.3.1.3 Aspect

From literature, landslide susceptibility is affected greatly by aspect (Lee, 2005; Galli *et al.*, 2008). For the case study, the aspect map was derived from the initial DEM of the study area following a classification, that was carried out in GIS environment, in nine categories (flat, north, northeast, east, southeast, south, southwest, west, northwest). These 9 categories were then grouped into 4 new categories that are mainly affected by the area's precipitation phenomena. Based on the meteorological data that were analysed for the area of study, the southeast-south and northeast-east facing hill slopes are mainly affected by rainfall. Therefore, higher values were assigned in these two categories, while lower values were assigned in the rest (Figure 40).

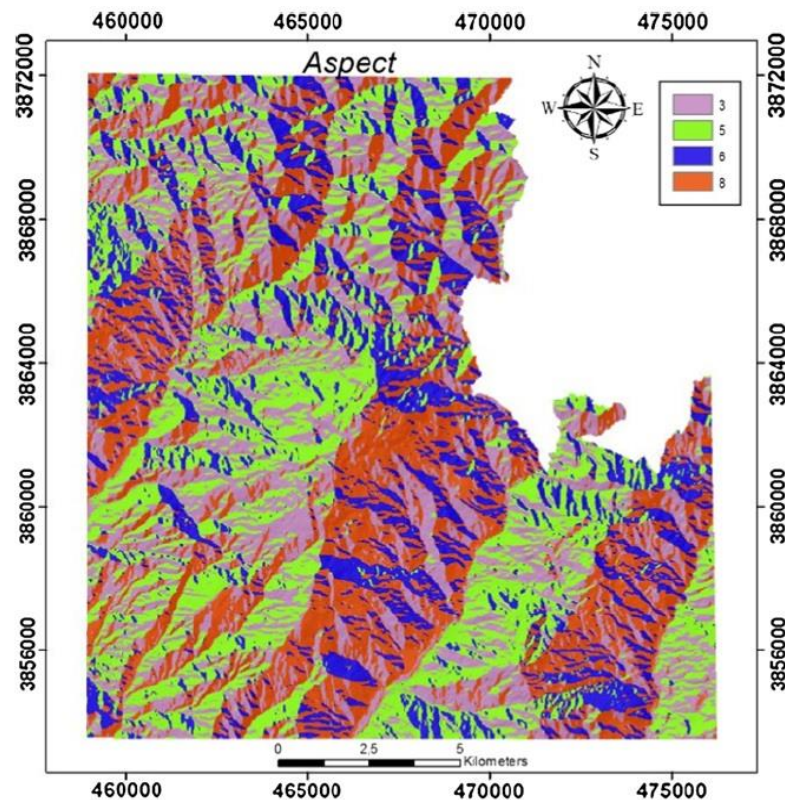


**Figure 40:** Aspect classes – Statos-Agios Photios

### 3.3.1.4 Faults

The proximity of an area to faults increases the probability of landslide generation (Lee, 2005). Geological maps and a Landsat 5 TM image were used to detect the area's main tectonic discontinuities, and the results were inserted as a layer in GIS environment. The



results were classified based on the area's current geological map in two classes: definite and undefined. Finally, a buffer zone of 500m was created around definite faults and a buffer zone of 250m around undefined faults to depict the areas that potentially face greater danger due to their proximity to faults (Figure 41).

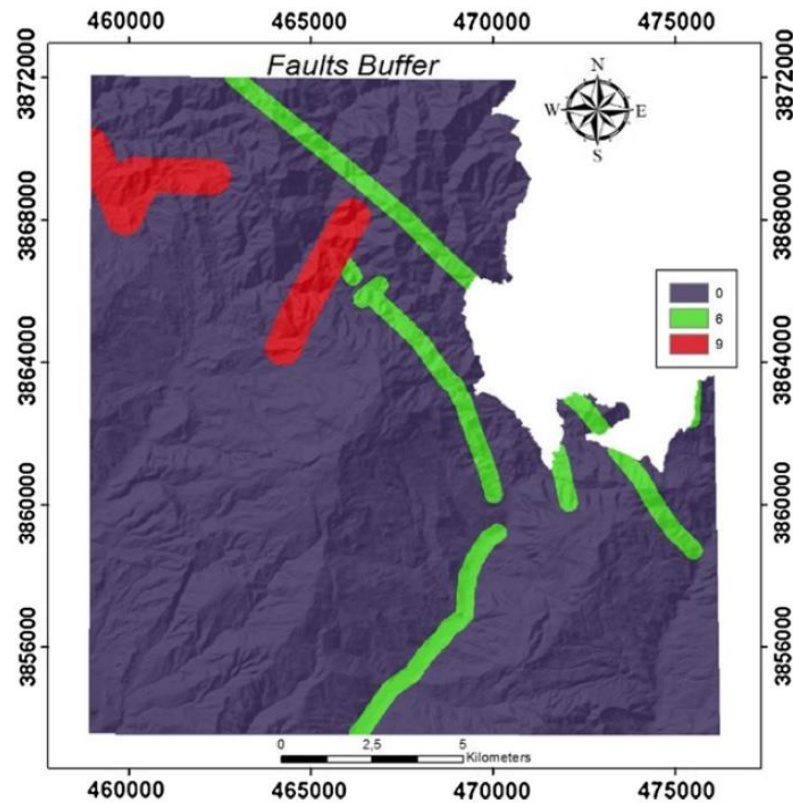


**Figure 41:** Faults and buffer zones – Statos-Agios Photios

### 3.3.1.5 Drainage network

The proximity of areas to drainage networks has proved to be critical in the susceptibility of these areas to landslides. Water courses tend to erode the slopes by saturating their lower parts (Saha, Gupta and Arora, 2002; Yalcin *et al.*, 2011). In our case study, the drainage network was extracted from the DEM. In some cases, certain areas with missing information, due to resolution limitations, were filled in through the use of a QuickBird image. The streams of the drainage network were then numbered according to Strahler's order (1<sup>st</sup> – 6<sup>th</sup> order) and they were grouped into three categories, i.e. 1<sup>st</sup>–2<sup>nd</sup>, 3<sup>rd</sup>–4<sup>th</sup> and 5<sup>th</sup>–6<sup>th</sup> (Figure 42). Then, buffer zones of 50m, 100m and 250–500m were created around the three developed groups, respectively as shown in Figure 43.

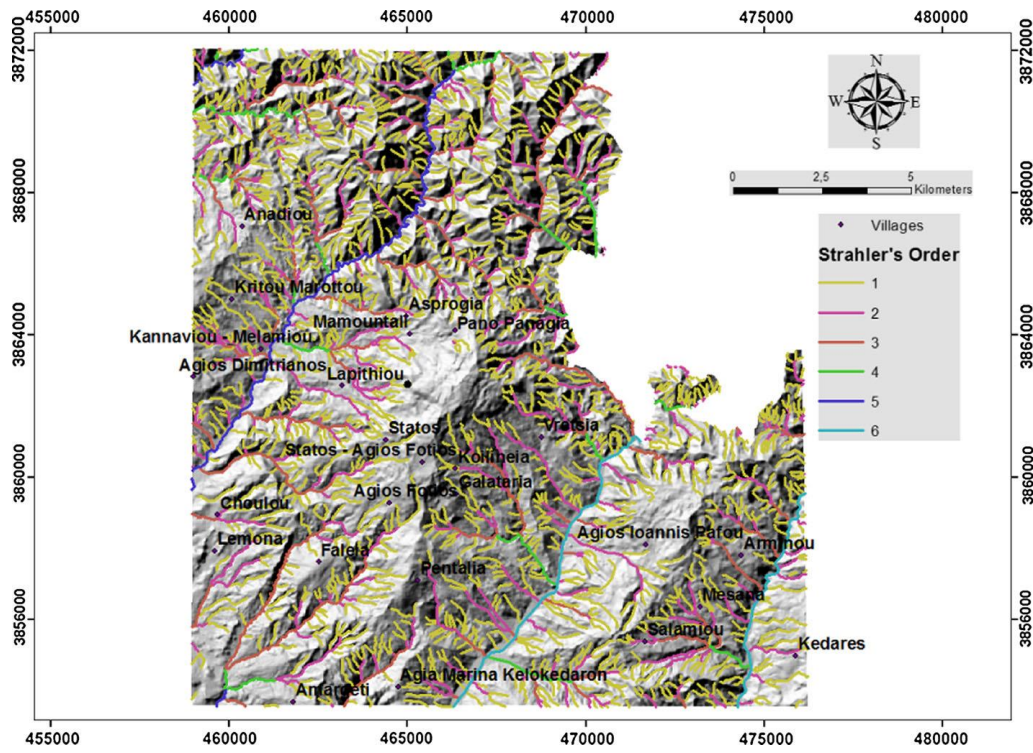


**Figure 42:** Drainage network numbered according to Strahler order

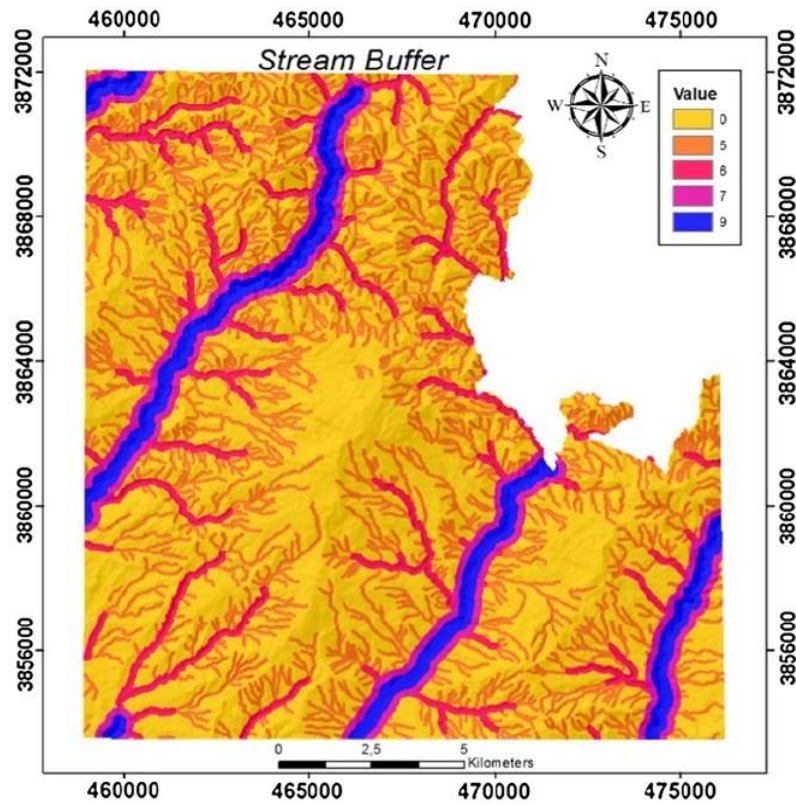


**Figure 43:** Streams and buffer zones – Statos-Agios Photios

### 3.3.1.6 Road network

The expansion of the road network is considered to be a key factor for landslide hazard zonation. The road network of the study area was extracted from two sources, the topographic map of the area, from which the road network was digitised in GIS environment, and the QuickBird high-resolution image to update the digitised road network. Three buffer zones of 50m each, i.e. 50m, 100m and 150m, were created around the main paved road network and a buffer zone of 50m was created around the loose unpaved roads (Figure 44).

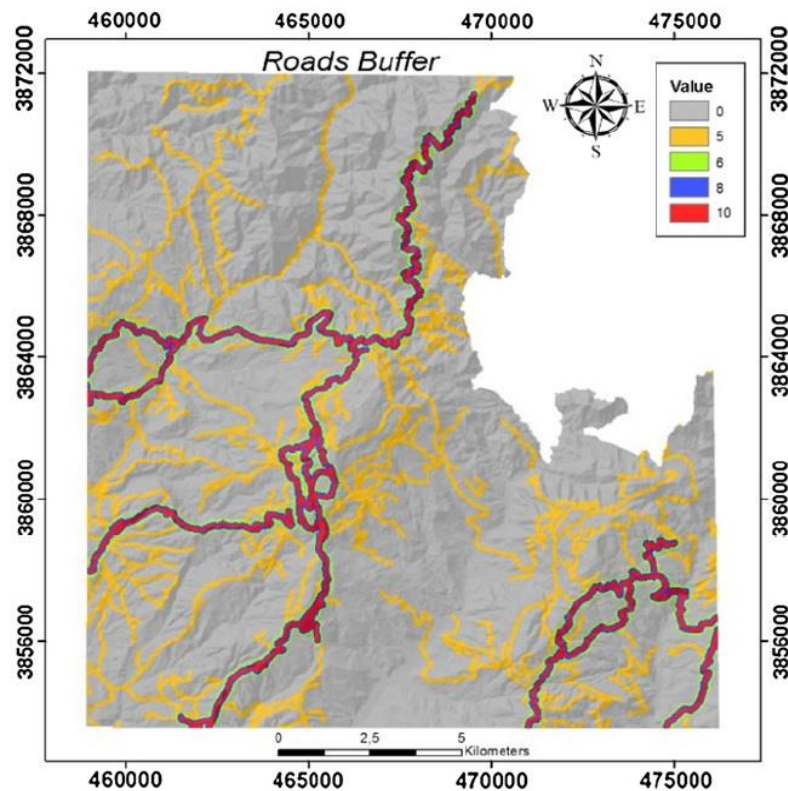


**Figure 44:** Roads and buffer zones – Statos-Agios Photios

### 3.3.1.7 Relief

In the area of study, the elevation ranges approximately from 200m to 1,200m with the vast majority of the steep slopes located in higher elevations. Therefore, the DEM was reclassified and greater values were assigned to areas with higher elevation. The relief map was classified into ten classes of 100m each as shown in Figure 45. More specifically, the classes created were 180m, 280m, 380m, 480m...1180m.

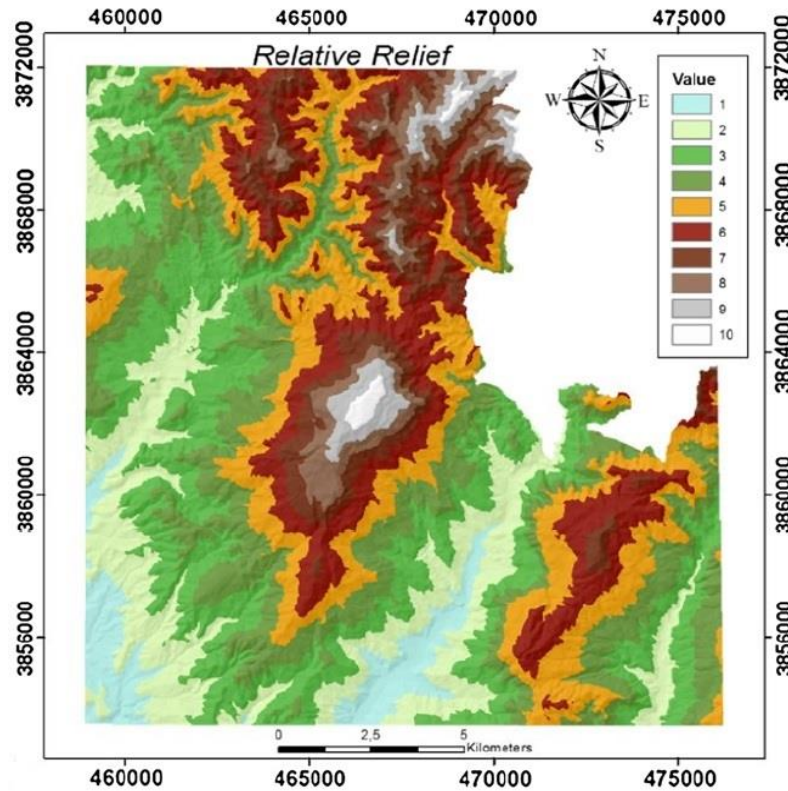


**Figure 45:** Relief map – Stalos-Agios Photios

### 3.3.1.8 Lithology

As it was mentioned in *section 3.1*, the geological formations of marls, chalks, alluvium and sandstones, limestone melanges at the Stalos-Agios Photios area, make it extremely susceptible to landslides. These rocks form the geological formations of Lefkara, Kathikas, Kannaviou, Apalos and Athalassas together with the lava origin formations of Mamonía complex.

After the digitisation and the classification of the geological formations in five categories in GIS environment, values were assigned in each one of them, with greater values assigned to marl formations (Figure 46).

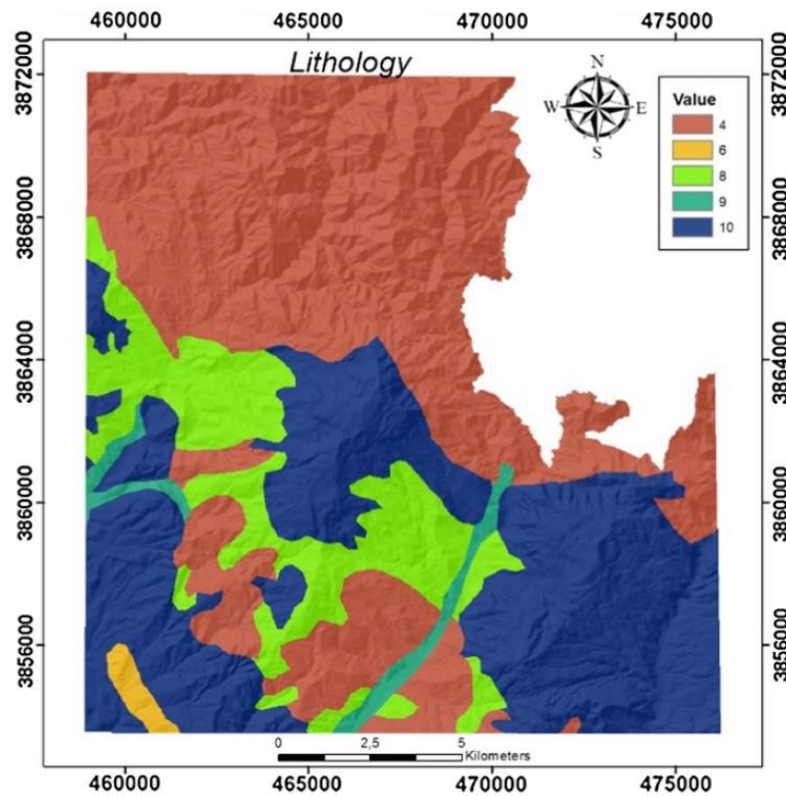


**Figure 46:** Lithology map – Statos-Agios Photios

### 3.3.1.9 Precipitation

Precipitation, as presented in *section 1.1.3* of the present thesis, is considered as one of the most triggering factors of landslides (Kouli *et al.*, 2010). Therefore, annual precipitation data were collected from the Cyprus Meteorological Service stations and interpolated, to create a continuous layer of data.

In the area of study, the precipitation ranges from 750mm to 1,150mm in the mountainous areas. Five classes of precipitation were created, starting from 750mm until the maximum of 1,150mm with a 100mm step. Greater values were assigned to the areas with high precipitation (Figure 47).

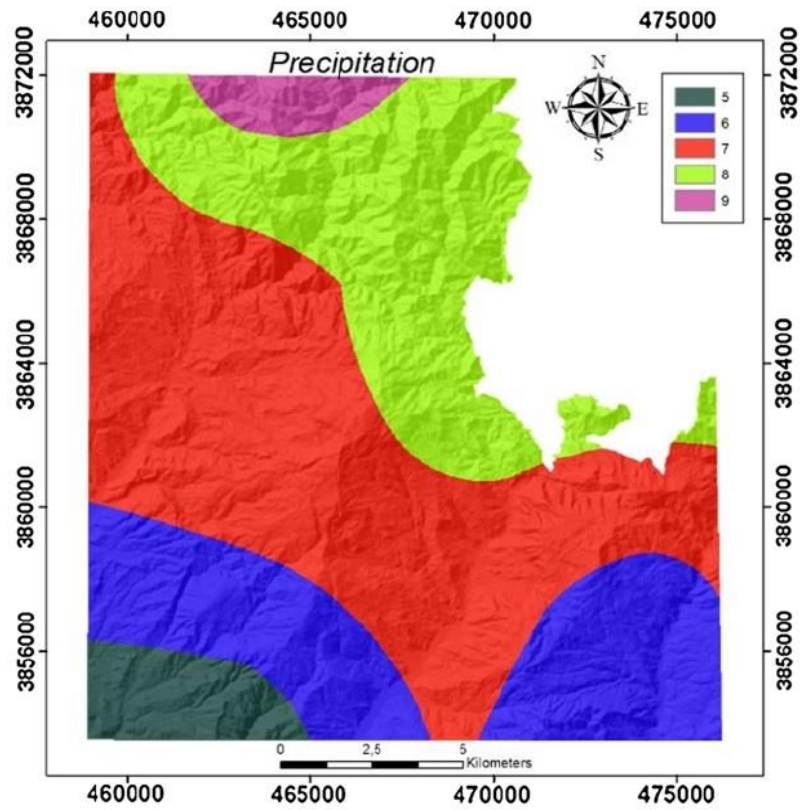


**Figure 47:** Precipitation map – Stalos-Agios Photios

The parameters, the classes and the values that were assigned to the classes of all 9 parameters are presented in Table 9.

**Table 9:** Parameters, classes and rating values – Stalos-Agios Photios

Parameter	Classes	Buffer	Value
Slope	>50°		10
	40°–50°		9
	30°–40°		8
	20°–30°		7
	10°–20		6
	5°–10°		4
	0°–5°		1
Land use	Bare soil		9
	Urban		5
	Vegetation		2
	Water		0
Aspect	SE, S		8

	NE, E		6
	NW, N		5
	SW, W		3
<b>Faults</b>	Definite	500	9
	Undefined	250	6
<b>Drainage network</b>	5 <sup>th</sup> -6 <sup>th</sup> order	250	9
	5 <sup>th</sup> -6 <sup>th</sup> order	250-500	7
	3 <sup>rd</sup> -4 <sup>th</sup> order	100	6
	1 <sup>st</sup> -2 <sup>nd</sup> order	50	5
	No stream		0
<b>Road network</b>	Paved	50	10
	Paved	100	8
	Paved	150	6
	Unpaved	50	5
<b>Relief</b>	1,180		10
	980		9
	880		8
	780		7
	680		6
	580		5
	480		4
	380		3
	280		2
	180		1
<b>Lithology</b>	Marl		10
	Alluvium		9
	Melange		8
	Limestone, sandstone		6
	Lavas		4
<b>Precipitation</b>	1,150		9
	1,050		8
	950		7
	850		6
	750		5

### 3.3.2 Development of coherence and land displacement maps

An overview of the methodology steps that were carried out for the detection and calculation of land movements in the areas of study is presented in Figure 48. This methodology has been published with title “*The Use of Sentinel-1 Synthetic Aperture Radar (SAR) Images and Open-Source Software for Cultural Heritage: An Example from Paphos Area in Cyprus for Mapping Landscape Changes after a 5.6 Magnitude Earthquake*” (Tzouvaras *et al.*, 2019). For the purposes of the current study, Sentinel-1 images were used. However, this methodology can be applied for various SAR sensors, such as COSMO-SkyMed, TerraSAR-X, RADARSAT, ALOS PALSAR, etc., which are also supported by SNAP software as described in *section 3.2.2*.

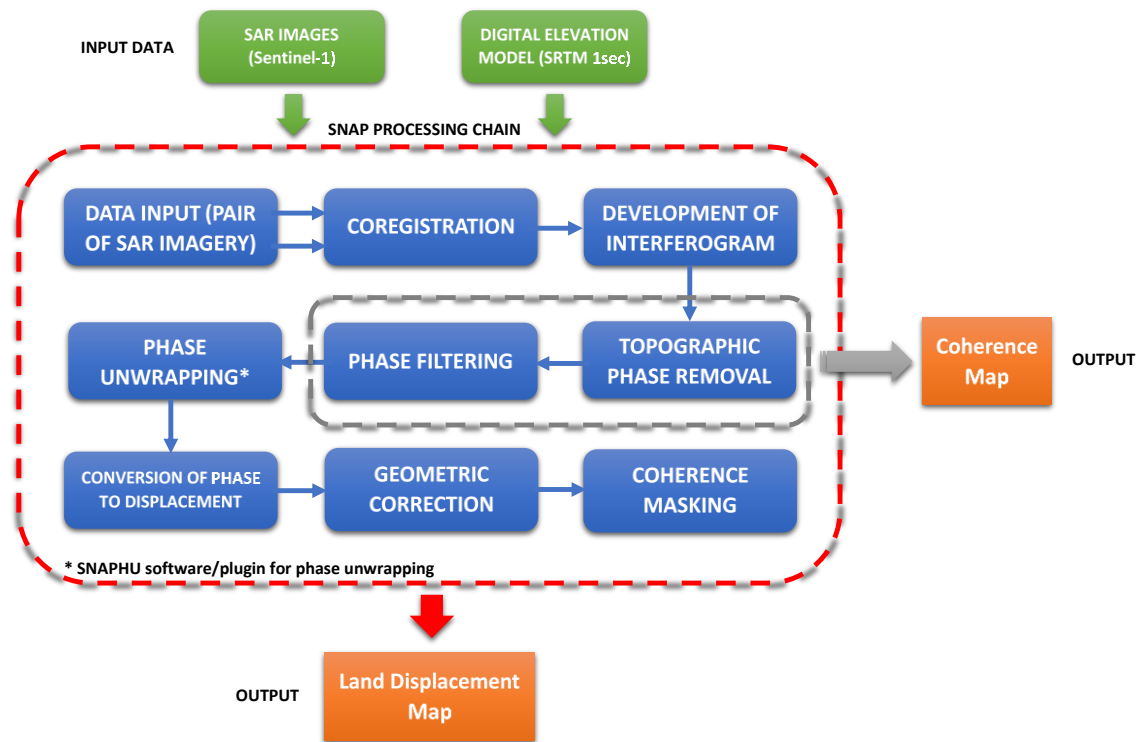


**Figure 48:** Outline of the coherence and displacement map processing chain

For interferometric analysis, high coherence between the two image acquisitions is very important. Coherence is used as a quantitative indicator of the quality of the associated interferogram and is an indication of any significant radar signal changes between acquisitions. Surface cover changes, such as vegetation growth, often exhibit and introduce sudden changes in coherence in SAR imagery. Thus, for higher accuracy of results, it is suggested that the final displacement maps are masked according to high



coherence for land cover such as urban areas. However, coherence changes (see *section 2.3*) can provide valuable information regarding sudden changes on the earth's surface.

Therefore, it is recommended that the acquisition times for the pair of SAR images are temporally close in order to minimise the loss of coherence. Small perpendicular baseline interferograms are preferable, as these do not suffer from geometric decorrelation, show good fringes, and are usually easy to unwrap (Ferretti *et al.*, 2007). For DInSAR, the limit of their perpendicular baselines was set to 200m (Le Mouélic *et al.*, 2005). In general, DInSAR favours short baselines (less than 200m) for C-band systems. Due to the high revisit frequency and the excellent orbital accuracy of Sentinel-1, the perpendicular baseline is usually not a limiting factor, facilitating the application of InSAR in many countries (Kovács *et al.*, 2019). The perpendicular baseline aspect, though, can be used to select the optimal pair of images (Höser, 2018).

Two pairs of SAR acquisitions, one ascending and one descending, were downloaded from the European Space Agency (ESA) Copernicus Open Access Hub<sup>13</sup> to study the earthquake's effects in the case study of Nea Paphos – Tombs of the Kings (*section 3.1.2*). From these two pairs, the optimal pair was selected, based on the image pair characteristics and more importantly the image acquisition geometry, to be used in the proposed DInSAR methodology. In the case study of Pissouri – Petra tou Romiou, a total of 32 SAR images were downloaded to study the evolution and impact of the two landslide events, that took place in February 2019, as described in detail in *section 3.1.3*.

After downloading the pairs of Sentinel-1 images, these were inserted into the SNAP software v5.0 (see *section 3.2.2*). The open-source policy and the great number of capabilities make it an ideal candidate software for SAR processing. SNAPHU v1.4.2 software (see *section 3.2.2*), a statistical-cost network-flow algorithm for phase unwrapping developed at Stanford University, was used for the phase unwrapping step of the methodology, as shown in Figure 48.

The coregistration step followed, and then the interferograms were developed. Images were aligned and matched, in each case, using coarse followed by DEM-assisted fine coregistration of subpixel accuracy. The derived original interferograms were used to

---

<sup>13</sup> Copernicus Open Access Hub: <https://scihub.copernicus.eu/>

remove the topographic phase using the DEM that was automatically acquired by the SNAP software in order to produce the differential interferograms. After the completion of this step, the differential interferograms and the coherence maps were produced. Coherence maps were used for the rapid identification of areas that were affected by the natural hazards, as it will be analysed further in *section 4 Results*.

The Goldstein phase filter was then applied to enhance the developed interferograms and make the interferometric fringes visually clearer. Then, phase unwrapping was carried out using the SNAPHU software for each case. After importing the results back in SNAP, the phase values were converted to displacement values. In order to obtain accurate results, geometric correction and coherence masking were applied to lead to the final output, which was the displacement map.

The calibration and validation of DInSAR results was carried out based on the known absolute three-dimensional positions of the permanent GNSS stations, of the Cyprus Positioning System (CYPOS) network, on the SAR images acquisition dates. Moreover, results from a study carried out on the linear and non-linear deformation effects in the permanent GNSS network of Cyprus can also be used (Danezis, Chatzinikos and Kotsakis, 2019). The proposed methodology is further explained in detail in *section 3.3.3*.

### **3.3.2.1 Data acquisition**

In order to study the deformation caused by the earthquake and its effects to the wider area of Paphos, four SAR images, i.e. two images before and two images after the earthquake occurred were obtained to be used in the proposed DInSAR methodology. Two ascending and two descending Sentinel-1 IW SLC SAR images were acquired, forming two co-seismic pairs, one ascending pair between 14 April 2015, i.e. one day before the earthquake, and 26 April 2015 and one descending pair with images on 15 April 2015 (day that the earthquake occurred) and 27 April 2015. Sentinel-1B satellite was not launched until April 25, 2016, so all images acquired were from Sentinel-1A satellite, with a temporal baseline of 12 days.

For the case study of Pissouri – Petra tou Romiou, initially ten SAR images were downloaded, six Sentinel-1A images (3 ascending and 3 descending) and four Sentinel-1B images (2 ascending and 2 descending). These images were used to form 6 co-event

pairs to study the two landslide events that took place near Pissouri and Petra tou Romiou on 15 February 2019 and 20 February 2019 respectively. After the application of DInSAR methodology, it was necessary to download another 22 SAR images, i.e. 32 images in total, to study the two landslide events further, forming a total of 28 interferometric SAR pairs, with all images in the respective SAR pairs being acquired 12 days apart.

Sentinel-1 SAR images were downloaded freely from the Copernicus Open Access Hub after registration. After completing registration and logging in with a username and password, the area of interest was selected for both case studies by creating each time a rectangle containing the area under study.

For the case study of Nea Paphos – Tombs of the Kings, the following criteria were used:

- Sensing period: 1/4/2015 – 30/4/2015
- Product type: SLC (Single Look Complex)
- Polarisation: VV+VH
- Sensor mode: IW (Interferometric Wide swath)

The four images that were downloaded for DInSAR processing are presented below in Table 10. The image on 15 of April 2015 was downloaded, as it was acquired before the time that the earthquake occurred (08:25 AM UTC).

**Table 10:** Sentinel-1 SAR images – Nea Paphos – Tombs of the Kings

Platform	Date	Time	Name	Pass direction
Sentinel-1A	14/04/2015	15:49:38	S1A_IW_SLC_1SDV_20150414T154938_005482_006FEA_FA5F	Ascending
Sentinel-1A	15/04/2015	03:51:19	S1A_IW_SLC_1SDV_20150415T035119_005489_007021_6792	Descending
Sentinel-1A	26/04/2015	15:49:39	S1A_IW_SLC_1SDV_20150426T154939_005657_007411_92E3	Ascending
Sentinel-1A	27/04/2015	03:51:20	S1A_IW_SLC_1SDV_20150427T035120_005664_007440_4A44	Descending

For the case study of Pissouri – Petra tou Romiou, the following criteria were filled in:

- Sensing period: 10/1/2019 – 15/4/2019
- Product type: SLC (Single Look Complex)
- Polarisation: VV+VH
- Sensor mode: IW (Interferometric Wide swath)

The 32 images that were downloaded for processing are presented below in Table 11.

**Table 11:** Sentinel-1 SAR image characteristics – Pissouri – Petra tou Romiou

<b>Platform</b>	<b>Date</b>	<b>Time</b>	<b>Name</b>	<b>Pass direction</b>
Sentinel-1A	11/01/2019	15:49:53	S1A_IW_SLC__1SDV_20190111T154925_20190111T154953_025432_02D14A_9784	Ascending
Sentinel-1A	12/01/2019	03:51:43	S1A_IW_SLC__1SDV_20190112T035116_20190112T035143_025439_02D183_B26B	Descending
Sentinel-1B	17/01/2019	15:49:27	S1B_IW_SLC__1SDV_20190117T154900_20190117T154927_014536_01B131_A3CA	Ascending
Sentinel-1B	18/01/2019	03:51:07	S1B_IW_SLC__1SDV_20190118T035040_20190118T035107_014543_01B170_7D79	Descending
Sentinel-1A	23/01/2019	15:49:53	S1A_IW_SLC__1SDV_20190123T154925_20190123T154953_025607_02D7AD_62A1	Ascending
Sentinel-1A	24/01/2019	03:51:43	S1A_IW_SLC__1SDV_20190124T035116_20190124T035143_025614_02D7E5_0D38	Descending
Sentinel-1B	29/01/2019	15:49:26	S1B_IW_SLC__1SDV_20190129T154859_20190129T154926_014711_01B6D1_AADD	Ascending
Sentinel-1B	30/01/2019	03:51:07	S1B_IW_SLC__1SDV_20190130T035040_20190130T035107_014718_01B710_5334	Descending
Sentinel-1A	04/02/2019	15:49:52	S1A_IW_SLC__1SDV_20190204T154924_20190204T154952_025782_02DE08_3142	Ascending
Sentinel-1A	05/02/2019	03:51:42	S1A_IW_SLC__1SDV_20190205T035115_20190205T035142_025789_02DE41_F5E2	Descending
Sentinel-1B	10/02/2019	15:49:26	S1B_IW_SLC__1SDV_20190210T154859_20190210T154926_014886_01BC91_396F	Ascending

Sentinel-1B	11/02/2019	03:51:06	S1B_IW_SLC__1SDV_2019021 1T035039_20190211T035106_01 4893_01BCCD_D8D0	Descending
Sentinel-1A	16/02/2019	15:49:52	S1A_IW_SLC__1SDV_2019021 6T154924_20190216T154952_02 5957_02E43B_F0A1	Ascending
Sentinel-1A	17/02/2019	03:51:42	S1A_IW_SLC__1SDV_2019021 7T035115_20190217T035142_02 5964_02E473_35E0	Descending
Sentinel-1B	22/02/2019	15:49:26	S1B_IW_SLC__1SDV_2019022 2T154859_20190222T154926_01 5061_01C24C_DF08	Ascending
Sentinel-1B	23/02/2019	03:51:06	S1B_IW_SLC__1SDV_2019022 3T035039_20190223T035106_01 5068_01C287_F087	Descending
Sentinel-1A	28/02/2019	15:49:52	S1A_IW_SLC__1SDV_2019022 8T154924_20190228T154952_02 6132_02EA77_D663	Ascending
Sentinel-1A	01/03/2019	03:51:42	S1A_IW_SLC__1SDV_2019030 1T035115_20190301T035142_02 6139_02EAB6_082C	Descending
Sentinel-1B	06/03/2019	15:49:26	S1B_IW_SLC__1SDV_2019030 6T154859_20190306T154926_01 5236_01C814_1E64	Ascending
Sentinel-1B	07/03/2019	03:51:06	S1B_IW_SLC__1SDV_2019030 7T035039_20190307T035106_01 5243_01C850_0684	Descending
Sentinel-1A	12/03/2019	15:49:52	S1A_IW_SLC__1SDV_2019031 2T154924_20190312T154952_02 6307_02F0D5_B33B	Ascending
Sentinel-1A	13/03/2019	03:51:42	S1A_IW_SLC__1SDV_2019031 3T035115_20190313T035142_02 6314_02F112_228D	Descending
Sentinel-1B	18/03/2019	15:49:26	S1B_IW_SLC__1SDV_2019031 8T154859_20190318T154926_01 5411_01CDBD_37E7	Ascending
Sentinel-1B	19/03/2019	03:51:06	S1B_IW_SLC__1SDV_2019031 9T035039_20190319T035106_01 5418_01CDFB_15DF	Descending
Sentinel-1A	24/03/2019	15:49:52	S1A_IW_SLC__1SDV_2019032 4T154924_20190324T154952_02 6482_02F74C_F05A	Ascending
Sentinel-1A	25/03/2019	03:51:42	S1A_IW_SLC__1SDV_2019032 5T035115_20190325T035142_02 6489_02F78B_4E80	Descending
Sentinel-1B	30/03/2019	15:49:26	S1B_IW_SLC__1SDV_2019033 0T154859_20190330T154926_01 5586_01D376_DF9A	Ascending

Sentinel-1B	31/03/2019	03:51:06	S1B_IW_SLC__1SDV_20190331T035039_20190331T035106_015593_01D3B2_8DAE	Descending
Sentinel-1A	05/04/2019	15:49:52	S1A_IW_SLC__1SDV_20190405T154924_20190405T154952_026657_02FDC3_8FE0	Ascending
Sentinel-1A	06/04/2019	03:51:43	S1A_IW_SLC__1SDV_20190406T035116_20190406T035143_026664_02FE02_B80D	Descending
Sentinel-1B	11/04/2019	15:49:26	S1B_IW_SLC__1SDV_20190411T154926_20190411T154926_015761_01D947_90DD	Ascending
Sentinel-1B	12/04/2019	03:51:07	S1B_IW_SLC__1SDV_20190412T035040_20190412T035107_015768_01D985_4FA0	Descending

### 3.3.2.2 Data input

As it was mentioned earlier, the processing of radar images was carried out in SNAP software. The downloaded images were imported one by one in .zip format, as they were downloaded from the Copernicus Open Access Hub, by selecting the “Import Product” command. The two products can then be seen in the “Product Explorer” section of the screen. By selecting the options under the product names, information regarding the SAR images can be found, such as metadata, bands, vector data, etc. Additionally, by selecting the “Worldview” tab, the location of the two acquired images can be viewed.

In order to check the suitability of the pair of downloaded SAR images, the perpendicular baseline, modelled coherence and height ambiguity of the image pair need to be overviewed. This is achieved through “InSAR Stack Overview” command.

Moreover, the geometry of the image acquisition, based on the pass direction of the satellite, i.e. ascending or descending, in relation to the orientation of the area under study, needs to be carefully considered, as errors can be introduced in the processing steps due to foreshortening and shadow effects.

### 3.3.2.3 Coregistration

The two (or more) images must be coregistered into a stack. One image was selected as the master (the older acquisition) and the other as the slave (the most recent acquisition).

During this process, the pixels in the slave image were aligned with the master image to sub-pixel accuracy. Coregistration ensures that each ground target contributes to the same (range, azimuth) pixel in both the master and the slave images (Veci, 2016; Braun and Veci, 2020).

Terrain Observation with Progressive Scans (TOPS) Coregistration with Enhanced Spectral Diversity (ESD) was applied to achieve fine azimuth coregistration accuracy (Yague-Martinez *et al.*, 2016). Coregistration with ESD consists of a graph that reads two products, selects a single sub-swath with TOPSAR-Split, applies a precise orbit correction with Apply-Orbit-File and performs a DEM assisted Back-Geocoding coregistration, before applying Enhanced Spectral Diversity (Liosis *et al.*, 2018).

ESD is a co-registration method that exploits the overlapping area between two consecutive bursts to estimate the mis-registration with the required sensitivity (Yague-Martinez *et al.*, 2016). However, a prior fine co-registration step is a prerequisite for the ESD, such as back-geocoding. After selecting S1 TOPS Coregistration with ESD, a new window opens with several tabs guiding the user through the coregistration process.

The first acquisition, in chronological order, was set as the master image whereas the second as the slave image. Additionally, the bursts that include the area under study were selected to reduce the processing time. It is compulsory to select the same sub-swath, given that they have the same orbit, but different bursts can be selected in the two images.

Sentinel Precise Orbits, downloaded automatically by SNAP, were used to complete the task, which contain information about the position of the satellite during the acquisition of SAR data. If precise orbits are not available, the option “Restituted orbits” from the drop-down menu can be selected, which may not be as accurate as the Precise orbits but will be better than the predicted orbits available within the product.

Additionally, the SRTM (Shuttle Radar Topography Mission) 1sec HGT DEM was used, and the bilinear interpolation resampling method was chosen to achieve more accurate results of the subpixel coregistration. SRTM 1sec HGT DEM is available between 60° North and 54° South (Figure 49), and has a resolution of 30m (USGS, no date b).

When available, DEMs of higher resolution, such as ASTER GDEM (Global Digital Elevation Model), and so on, can be used instead to improve the results even further. The coregistration result was manually assessed by vertically displaying both images at the

same time. Coherence is also a good indicator for the successful completion of the coregistration step, as a higher coherence area indicates a better coregistration location (Li and Bethel, 2008).

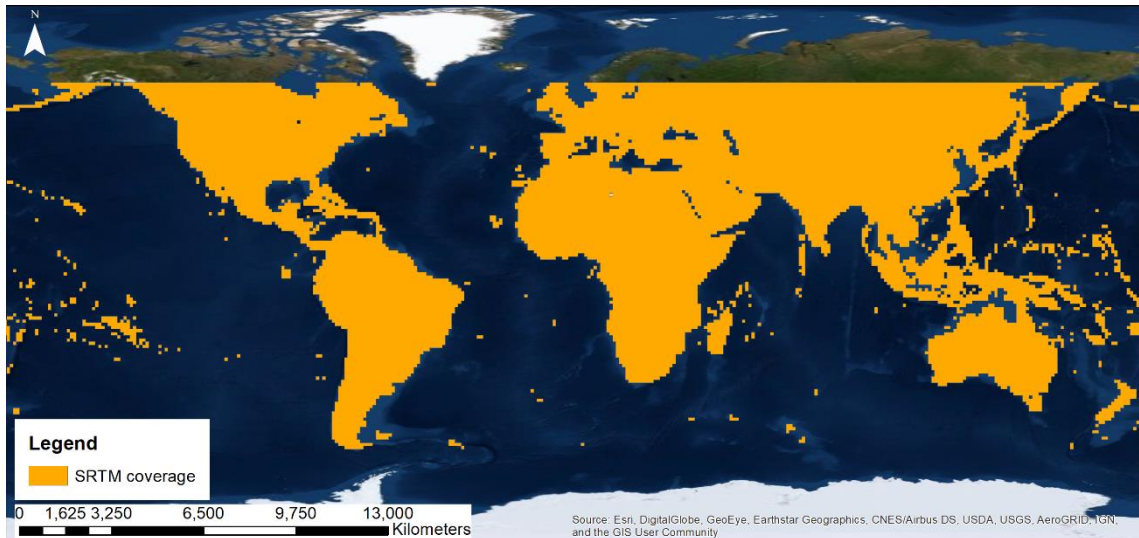


**Figure 49.** SRTM coverage (USGS, no date b)<sup>14</sup>

The resulting coregistered stack product appears in the Product Explorer. The coregistration result can be manually assessed by vertically displaying at the same time both images. The corresponding points between the two images can be selected using the synchronisation cursor position option.

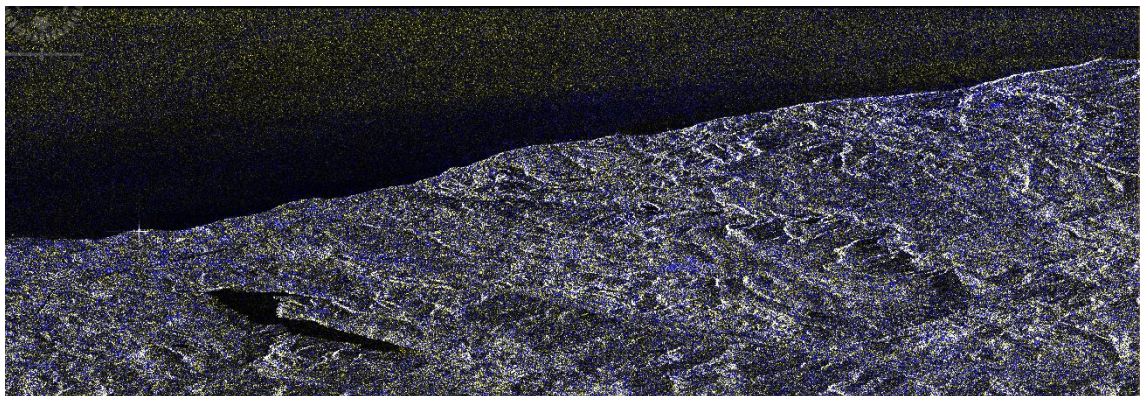


**Figure 50.** RGB representation of SAR pair coregistration 04.02.2019-16.02.2019

Additionally, the coregistration result can be checked by creating an RGB representation (Figure 50) of the master and slave images to see if the images are correctly aligned. The

---

<sup>14</sup> Digitised map based on data obtained from the United States Geological Survey (USGS)



master image was selected for red and green channels and the slave image for blue channel (Braun and Veci, 2020).

The quality of the results from the interferometric processing step, i.e. the interferogram and coherence maps, is greatly affected by the quality of the coregistration.

#### ***3.3.2.4 Development of interferogram***

This step leads both to the development of the Interferogram and the Coherence images. Additionally, the synthesized interferogram from the Reference DEM Step is combined with the interferogram from the Input interferometric pair to create the Differential Interferogram. The resulting interferogram will appear in the Product Explorer. Opening the drop-down menu for bands and double-clicking on phase will show the result.

The fringes represent the changes in phase between the two images in terms of radians of a full  $2\pi$  cycle. Each cycle of colours represents half the sensor's wavelength. In the case of Sentinel-1, each cycle represents a line-of-sight phase displacement of approximately 2.7cm. In general, the closer the distance between the fringes, the greater is the shift in position of the surface. Where no clear colours are visible, this is the result of phase noise, which in turn is due to temporal change of the scatterers. This is also an indicator of low coherence points. The black line in the displayed Interferogram between the two bursts can be removed by the S1 TOPS Deburst tool.

#### ***3.3.2.5 Topographic phase removal***

The produced interferogram, essentially being the difference between the phases of two SAR images, is influenced by the topography, as it is highly correlated to elevation. To derive a SAR Interferogram without the influence of the surface elevation, a DEM was used to simulate the topographic fringes (topographic phase) which were then removed from the produced Interferogram. During this step, the option of including an external DEM as user input or the automatic download of a DEM is offered. The products after the completion of this step are the differential interferogram and the coherence maps, the latter of which will be used in the application of CCD methodology. The coherence maps produced need to be geo-located, as in the case of displacement maps presented in *section*

3.3.2.9 *Geometric correction*. The CCD methodology process will be analysed further in chapter *Results*.

### 3.3.2.6 *Phase filtering*

Goldstein phase filtering was then carried out prior to unwrapping, as a preparatory step for increasing the signal-to-noise ratio. The differential interferogram produced in the previous step contains information regarding elevation displacement. The resulting interferogram after the application of Goldstein Phase Filtering is the result of this step. The other product of the previous step, the coherence map remains the same.

### 3.3.2.7 *Phase unwrapping*

The Differential Interferogram calculated in the previous step contains information regarding the elevation displacement. The process of converting the interferogram from a cyclical to a linear format is called interferogram phase "unwrapping" (Figure 51). This step was carried out in order to calculate the absolute phase, which can then be transformed into height or displacement.

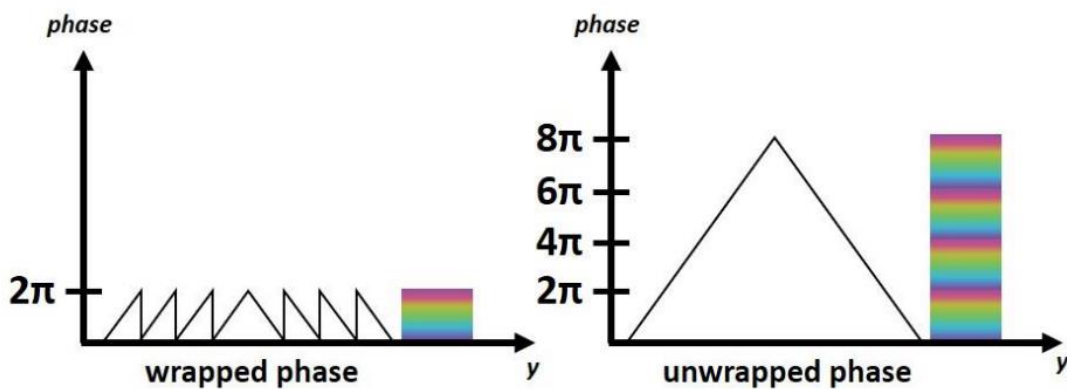


**Figure 51:** Phase unwrapping principle (Braun and Veci, 2020)

The quality of unwrapped results depends greatly on the input coherence. Thus, only areas with high coherence can provide reliable results. This "unwrapping" can be difficult, or even disrupted, in areas with geometric distortions (steep terrain) or low coherence (due to under-sampling or noise). However, interferogram filtering can be used during this process to minimize the number of errors.

Phase unwrapping was carried out in SNAPHU software plugin. SNAPHU is a statistical-cost network-flow algorithm for phase unwrapping developed at Stanford University by Curtis Chen and Howard Zebker. More details can be seen at *section 3.2.2* of the present thesis. SNAPHU uses an iterative optimization procedure. The execution time of this process depends largely on the complexity of the interferogram. In case the unwrapping process fails due to lack of memory, a subset of the area can be created to reduce processing time. The results of this step were then used as an input to SNAP software.

This process produces the final unwrapped interferogram that was then used to convert phase to displacement.

### ***3.3.2.8 Conversion of phase to displacement***

One of the final steps of the process in the conversion of phase to displacement, leading to the calculation of either LoS displacement and/or vertical and horizontal land movements/ displacement. These findings assist in the assessment of the impact of the natural hazards under study on critical infrastructure of interest, such as sites of Cultural Heritage in the case study of Nea Paphos – Tombs of the Kings, or road network in the case study of Pissouri – Petra tou Romiou.

Firstly, the location of a stable pixel or a pixel of a known displacement between the two acquisitions must be identified. Such information can be acquired from Global Navigation Satellite System (GNSS) receivers. The value of the pixel of known displacement was then used to convert relative displacement values to absolute ones. This was achieved by subtracting the value of the specific pixel from all the pixels in the areas of interest. If more than one pixel with such information was available, it could be used to validate the final output of the displacement map.

At this stage, the displacement values are relative. Further processing is required to calculate the absolute displacement values. As aforementioned, in order to achieve this, a point of known displacement between the two SAR image acquisitions was incorporated into the procedure. In order to define the exact position of the point, the produced displacement image above needed to be geometrically corrected. The result of this step was the development of geo-referenced displacement maps.

### ***3.3.2.9 Geometric correction***

Range-Doppler Terrain Correction was applied in order to geocode the displacement map product. In this step, the resampling method of bilinear interpolation and the Map projection of WGS 84 were selected. Areas without elevation were masked out, based on the DEM used, from the geo-referenced displacement map. The geo-referenced displacement map is the product of this step.

### ***3.3.2.10 Coherence masking***

Following completion of the aforementioned steps, the resulting displacement map for our area of interest was produced. For a higher accuracy of results, it is suggested that the final displacement map is masked to remove regions of low coherence. This can allow us to exclude all vegetated land cover from the displacement map, which often introduces errors to results because of temporal variations, and enabled us to concentrate on coherent areas such as urban cover.

### ***3.3.2.11 Displacement map***

This is the final step of the proposed methodology as the final LoS, vertical and/or horizontal displacement maps were produced. Values of positive or negative LoS displacement, maximum uplift and subsidence, as well as land movements in the east-west direction were calculated depending on the natural hazard under study, to show the impact of earthquakes and landslides on each area of interest.

More specifically, in the case study of Nea Paphos – Tombs of the Kings, a vertical displacement map was developed, showing uplift and subsidence (vertical land displacement) as the aftermath of the seismic event that took place on the 15<sup>th</sup> of April 2015. For the impact assessment study of the landslide events that took place in Pissouri and Petra tou Romiou by the A6 motorway and the old Limassol – Paphos road respectively, LoS, vertical and east-west horizontal displacement maps were developed to study the more complex nature of the landslide phenomena.

### 3.3.3 Calibration and validation methodology of DInSAR results

In this section, a first attempt is made for the integration of GNSS measurements and results from DInSAR processing, by combining the characteristics of both measurement techniques, the absolute positioning information of individual points provided from GNSS and the relative displacement information provided by DInSAR processing and the spatial and temporal characteristics of SAR datasets.

The calibration and validation of all DInSAR results will be carried out based on the known three-dimensional absolute positions of the seven permanent GNSS stations<sup>15</sup>, that comprise the Cyprus Positioning System (CYPOS) network.

CYPOS, operates in Cyprus under the auspices of the Department of Lands and Surveys (DLS) at its current form since 2010. CYPOS covers the free areas of the Republic of Cyprus with inter-station distances of about 60km (Department of Lands and Surveys, 2016). The permanent GNSS stations, as shown in Figure 52, are located in Nicosia (LEFK), Limassol (LEME), Larnaca (LARN), Paphos (PAFO), Paralimni (PARA), Polis (POLI) and Evrychou (EVRY).



**Figure 52:** The CYPOS permanent GNSS network

---

<sup>15</sup> The data used for the calibration and validation of this thesis were kindly provided by the Cyprus Department of Lands and Surveys.

The network is in continuous operation all year round (24/7/365) and transmits data in support of the requirements for various surveying and geodetic engineering applications. These data are available for free, through the DLS INSPIRE GeoPortal of Cyprus<sup>16</sup>, to all citizens in Cyprus after registration and proof of identity. The positioning data that are collected by this network offer useful information for the study of the behaviour of the crustal deformation field in Cyprus. The nature of the data, as they can be downloaded daily and analysed, can assist in the task of calibration and validation of the results obtained from DInSAR processing.

Based on these data, a multi-year study of daily GNSS data, was conducted from November 2011 until January 2017, on the position of the seven permanent CYPOS GNSS stations (Danezis, Chatzinikos and Kotsakis, 2019). The results of the study for the estimated positions and the horizontal and vertical velocities at the seven CYPOS GNSS stations are summarised in Table 12.

**Table 12:** Estimated positions (values in m) and horizontal and vertical velocities of the CYPOS GNSS stations (values in mm/year)

<b>Station</b>	<b>Validity period</b>	<b>X (t<sub>0</sub>)</b>	<b>Y (t<sub>0</sub>)</b>	<b>Z (t<sub>0</sub>)</b>	<b>V north</b>	<b>V east</b>	<b>V up</b>
<b>EVRY</b>	<i>A</i>	4389846.035	2839909.319	3641645.008	14.7	19.5	0.2
<b>LARN</b>	<i>A</i>	4358623.310	2899369.048	3631599.949	13.6	20.2	-4.9
<b>LEFK</b>	<i>B</i>	4360035.737	2870860.968	3652605.816	16.3	19.3	0.1
	<i>C</i>	4360035.736	2870860.987	3652605.816	16.4	19.3	0.2
<b>LEME</b>	<i>A</i>	4403058.471	2862122.638	3607630.266	15.6	20.3	0.3
<b>NICO</b>	<i>A</i>	4359415.715	2874117.069	3650777.829	15.7	18.9	-0.3
	<i>D</i>	4427028.128	2812497.092	3617359.846	16.1	19.6	1.7
<b>PAFO</b>	<i>E</i>	4427028.124	2812497.091	3617359.841	15.9	19.7	1.6
	<i>A</i>	4335378.631	2922300.281	3641064.127	17.2	18.9	0.6
<b>POLI</b>	<i>A</i>	4413130.062	2803627.159	3640911.041	14.2	19.1	-0.4

(\*) The following time periods apply to the above results:

A: 30/11/2011 – 28/1/2017; B: 30/11/2011 – 21/3/2013; C: 22/3/2013 – 28/1/2017; D: 30/11/2011 – 9/3/2016; E: 10/3/2016 – 28/1/2017

<sup>16</sup> The DLS INSPIRE GeoPortal: <https://eservices.dls.moi.gov.cy/#/national/inspiregeoportalmapviewer>

More specifically, the 3D coordinates of the nearest CYPOS station to the case study areas were used, at both SAR acquisition dates, prior and after a seismic or landslide event. In the case that such information is not available, the estimated velocities of the CYPOS GNSS stations (Danezis, Chatzinikos and Kotsakis, 2019), can be used to calculate the expected position of the CYPOS station nearest to the area of interest at the required dates. The values of expected displacement were then calculated at the case study areas on the specific dates that the land displacement phenomena took place.

These results were used for the calibration of the results obtained from DInSAR processing. Finally, the calibrated absolute displacement results from the DInSAR processing can be compared against the known positions of the remaining 6 CYPOS network stations, for validation purposes.

In the case study of Nea Paphos – Tombs of the Kings the known position of the CYPOS station named PAFO was used for the conversion of relative displacement values to absolute ones and the calibration of the vertical displacement. Moreover, results from a field GNSS survey were also used for the validation of the DInSAR displacement results, as presented in *section 4.2.1.1*.

## 4 Results

The results from the application of the proposed methodologies for each case study area are presented in detail in this chapter. In section 4.1, the results from the application of the AHP methodology are presented for the case study of Statos – Agios Photios. Then, in sections 4.2 and 4.3, the results from DInSAR and CCD processing are presented respectively for Nea Paphos – Tombs of the Kings and Pissouri – Petra tou Romiou.

### 4.1 Implementation of AHP methodology

The application of the AHP methodology along with the final land displacement hazard map that was developed, are presented below for the case study area of Statos – Agios Photios.

According to the AHP methodology, a pair-wise comparison of the contribution of each factor to the event under study was established. Answers from experts were collected on the reciprocal matrix, and the appropriate eigenvector solution method was then employed to calculate the factor weights, as presented in Table 13.

**Table 13:** AHP matrix – Statos-Agios Photios

Factors	F1	F2	F3	F4	F5	F6	F7	F8	F9	Total sum	Normalised weights
<b>1. Slope</b>	1	3	7	3	5	5	7	1/3	7	38.33	0.200
<b>2. Land use</b>	1/3	1	7	1/3	3	3	5	1/5	3	22.86	0.119
<b>3. Aspect</b>	1/7	1/7	1	1/7	1/5	1/5	3	1/9	1/3	5.12	0.026
<b>4. Faults</b>	1/3	3	7	1	3	5	7	1/3	7	33.66	0.176
<b>5. Drainage network</b>	1/5	1/3	5	1/3	1	3	5	1/5	3	18.06	0.094
<b>6. Road network</b>	1/5	1/3	5	1/5	1/3	1	5	1/5	3	15.26	0.079
<b>7. Relief</b>	1/7	1/5	1/3	1/7	1/5	1/5	1	1/9	1/3	2.65	0.013
<b>8. Lithology</b>	3	5	9	3	5	5	9	1	7	47.00	0.245
<b>9. Precipitation</b>	1/7	1/3	3	1/7	1/3	1/3	3	1/7	1	8.41	0.043
										<b>191.35</b>	



The above results revealed the significance of the factors of lithology (24.5%) and slope (20%) in the development of the model compared with the relief factor, which was considered to be the least important (1.3%). After the calculation of the normalised weights, the Consistency Ratio (CR) was calculated to check the consistency of the responses. For that reason, the Consistency Index (CI) was calculated from *Equation 5*.

$$CI = \frac{\lambda_{\max} - n}{n - 1} = \frac{9.656 - 9}{9 - 1} = 0.082 \quad (\text{Eq. 5})$$

where:

$\lambda_{\max}$ : the largest eigenvector and n is the number of criteria used in the study.

n: the number of factors considered in the study.

The value of  $\lambda_{\max}$  was calculated with the use of Microsoft EXCEL software (*section 3.2.2*) following the calculation of the correlation matrix for the 9 aforementioned factors. The final CR was calculated through *Equation 6*.

$$CR = \frac{CI}{RI} = \frac{0.082}{1.45} = 0.057 \quad (\text{Eq. 6})$$

where RI is the Random consistency Index.

For the 9 factors that we study, RI is equal to 1.45. If CR exceeds 0.1, the set of judgments may be too inconsistent to be reliable (Saaty, 1980). However, in practice, CRs of little over 0.1 are accepted and the extracted weight values are considered as reliable. In fact, the result of  $CR = 0.057$  appears to be well below the 0.1 threshold, proving that the judgements that were made concerning the impact of each individual factor has on the landslide susceptibility of the area under study are rather reliable.

The final landslide hazard map (Figure 53) was developed in GIS environment by summing up, through Boolean operators, the product of each category, which has been rated accordingly for its subcategories, as presented in detail at the end of *section 3.3.1*. The landslide susceptibility with the corresponding weights of significance was calculated by *Equation 7* as:

$$\begin{aligned} \text{Landslide susceptibility} &= & (\text{Eq. 7}) \\ &= F1 \times 0.200 + F2 \times 0.119 + F3 \times 0.026 + F4 \times 0.176 + F5 \times 0.094 \\ &+ F6 \times 0.079 + F7 \times 0.013 + F8 \times 0.245 + F9 \times 0.043 \end{aligned}$$

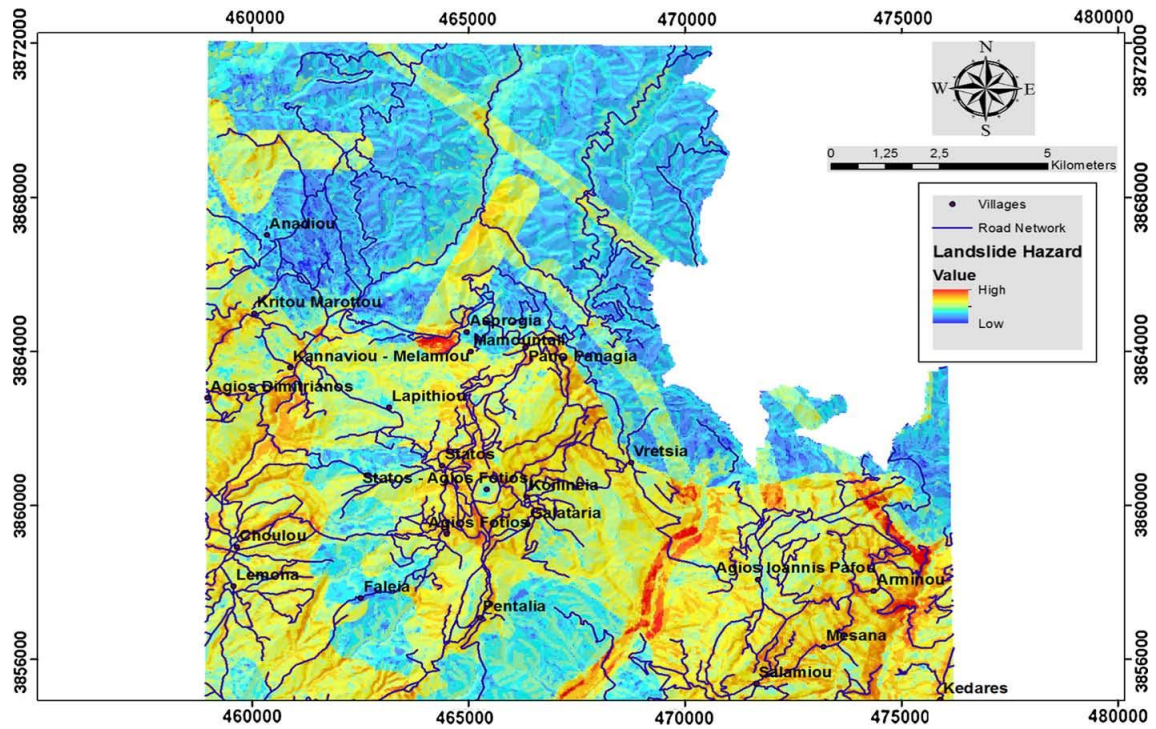


**Figure 53:** Final landslide hazard map – Statos-Agios Photios

#### 4.1.1 Calibration and validation of results

The produced landslide hazard map was then validated for its accuracy with recorded landslide events that occurred in the area with good results, as shown in Figure 54.

More specifically, Figure 54a, show the overall area that was affected by the 1965 landslide. Moreover, the place where the two villages, i.e. Agios Photios and Statos were relocated and the new village of Statos-Agios Photios was established (indicated with arrow) can be clearly seen to the east of the affected area. It can be clearly seen in the proposed map, that it is located at an area of low landslide hazard.

In Figure 54b, the location of a major landslide event that occurred on the main road between Statos-Agios Photios village and Panayia village, near Chrysorrogiatissa monastery, can be seen in the black circle.

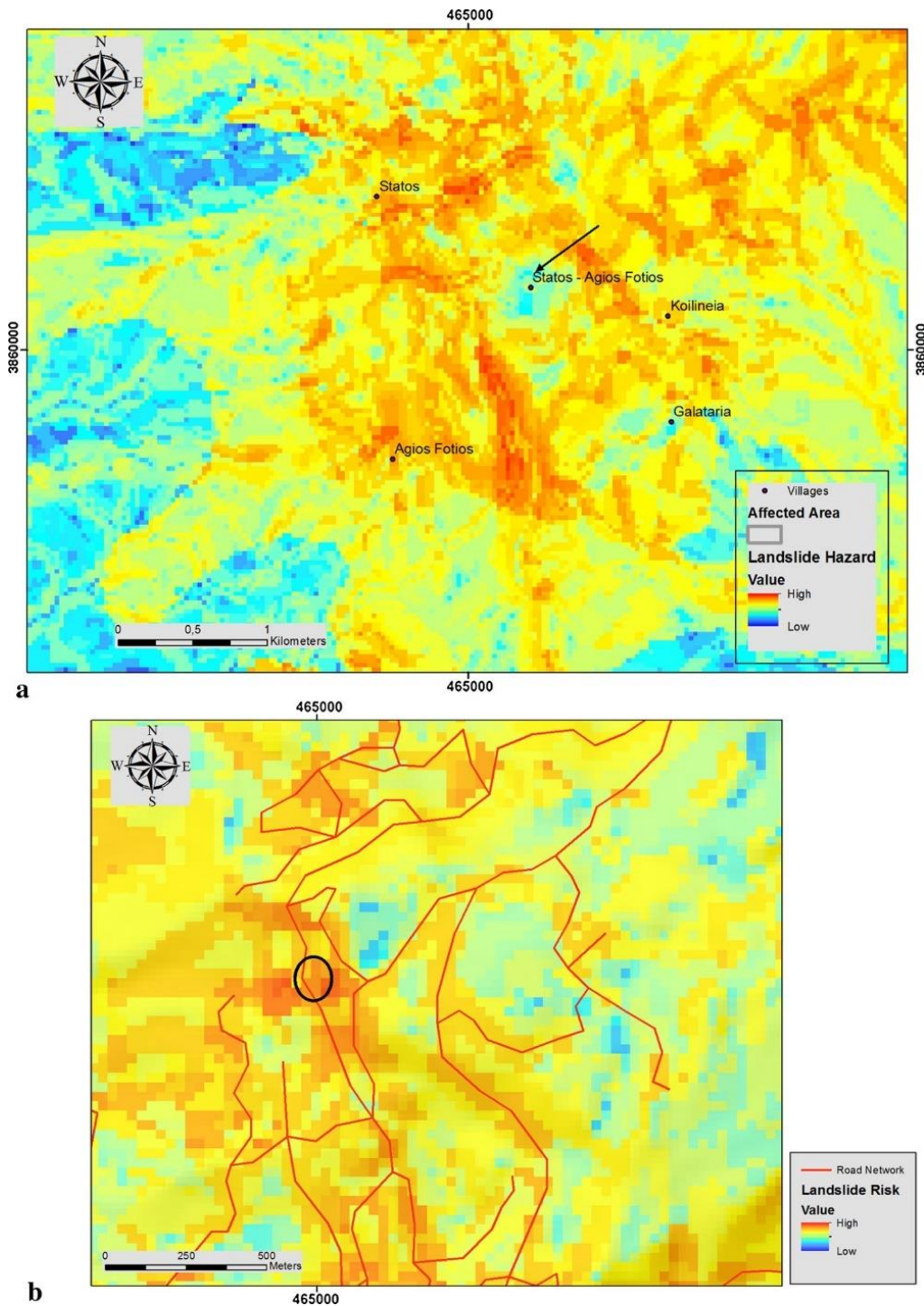


**Figure 54:** Areas affected by recorded landslide events – Statos-Agios Photios

Subsequently, the landslide hazard map was transformed to Landslide Hazard Zonation Map (LHZM), as shown in Figure 55. The GIS layer was reclassified, according to the Natural Breaks method (Jenks, 1967), into five major classes: very high hazard, high hazard, moderate hazard, low hazard and very low hazard. The road network was then superimposed over the final LHZM.

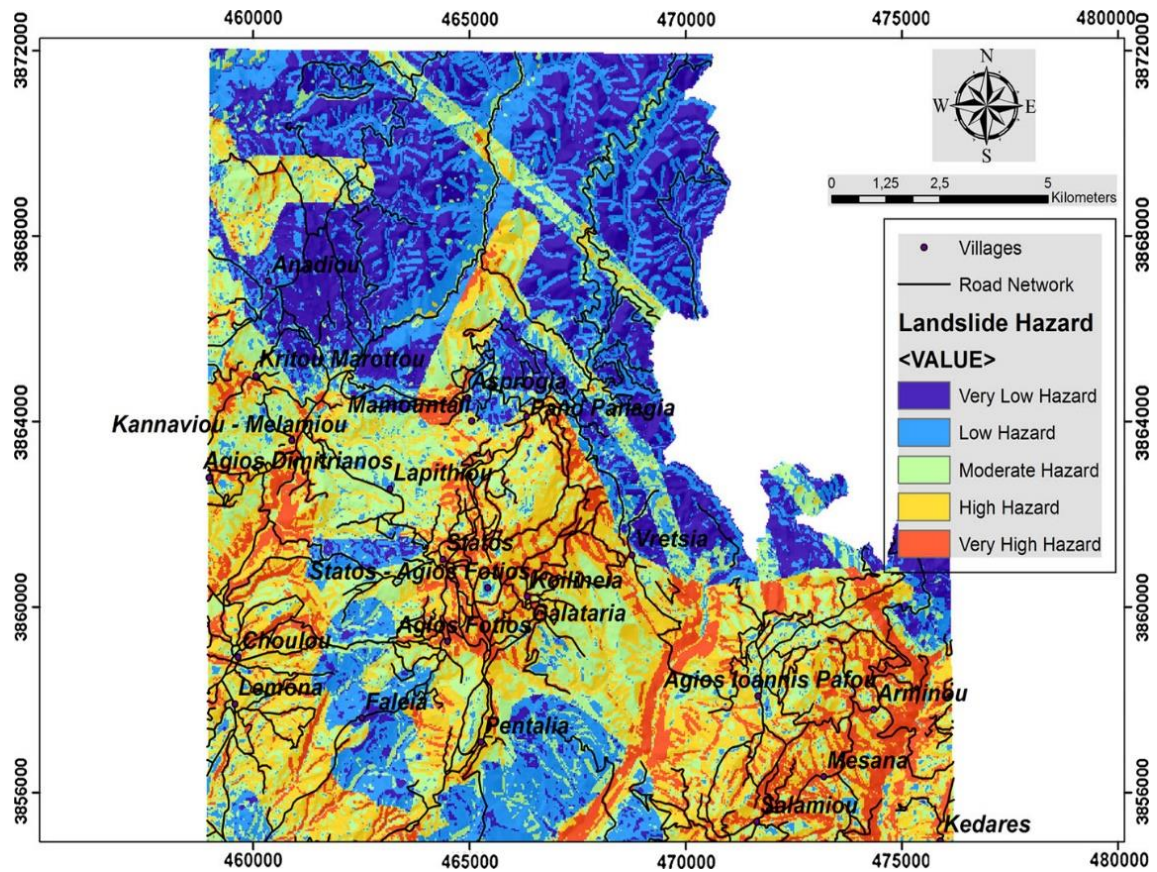


**Figure 55:** Landslide hazard zonation map – Statos-Agios Photios broader area

It is clear, that the vast majority of the road network in the broader area of Statos – Agios Photios is vulnerable to landslides. Additionally, the same situation exists at the south-eastern part of the study area in the broader area of Arminou, Mesana and Salamiou villages; at the road eastern of Asprogia village as well as in the western part of the broader area of Kannaviou, Choulou and Agios Dimitrianos villages.

## 4.2 Implementation of DInSAR methodology

In this section of the thesis, and more specifically, in *section 4.2.1*, the results from the application of the DInSAR methodology for the case study area of Nea Paphos – Tombs of the Kings are presented. In *section 4.2.2*, the impact of two individual landslides that occurred in the case study area of Pissouri – Petra tou Romiou is studied using the same methodology.

#### 4.2.1 Nea Paphos – Tombs of the Kings

For the case study of Nea Paphos – Tombs of the Kings, four SAR images were downloaded from the Copernicus Open Access Hub, as described in *section 3.3.2*. These acquisitions were then imported in SNAP software one by one in .zip format, by selecting the “Import Product” command.

The suitability of both SAR image pairs was checked, via an overview of the perpendicular baseline and other image pair characteristics, such as the temporal baseline, and the modelled coherence, that was carried out through “InSAR Stack Overview” command (Figure 56).

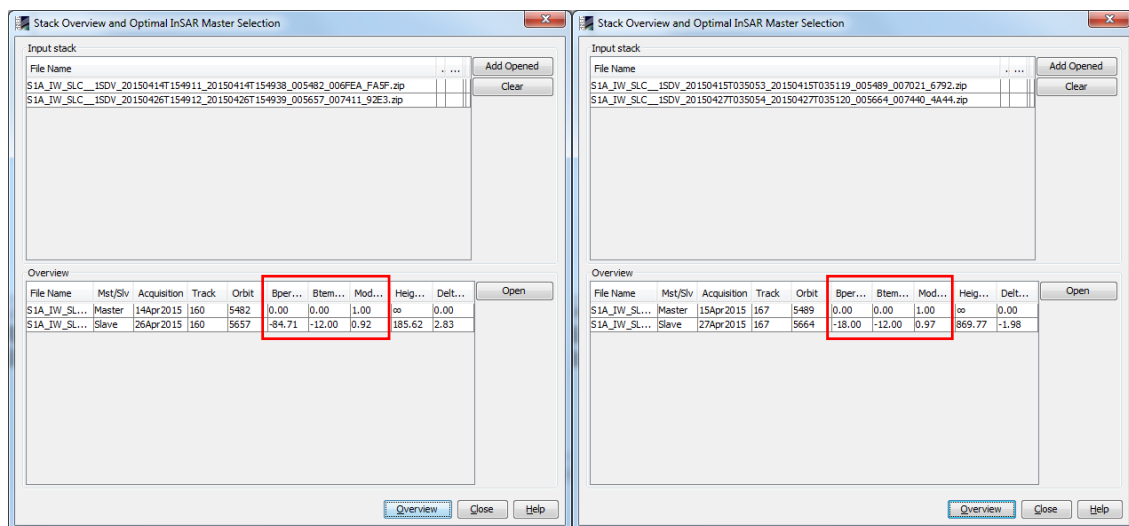


**Figure 56:** InSAR Stack Overview – Nea Paphos-Tombs of the Kings

In both pairs, the temporal baseline is 12 days, however, there appears to be a difference with regards to the perpendicular baseline and the height of ambiguity. The perpendicular baseline for the first image pair (14 April 2015 – 26 April 2015) is -84.71m, i.e. the slave image was acquired from a position of -84.71m in relation to the acquisition position of the master image whereas in the case of the second image pair (15 April 2015 – 27 April 2015), the perpendicular baseline is -18.00m. Despite this difference both perpendicular baselines are below the threshold of 200m that was originally set in *section 3.3.2* (Le Mouélic *et al.*, 2005). The modelled coherence values for both pairs appear to be high, 0.92 for the first pair and 0.97 for the second one.

Moreover, another important aspect that needs to be considered carefully is the image acquisition geometry in relation with the orientation of the area under study. In fact,

ascending and descending SAR images cannot always be used for the study of the same area, because the selection of the wrong SAR image pair might introduce errors in the processing steps due to foreshortening and shadow effects, as shown in Figure 57.

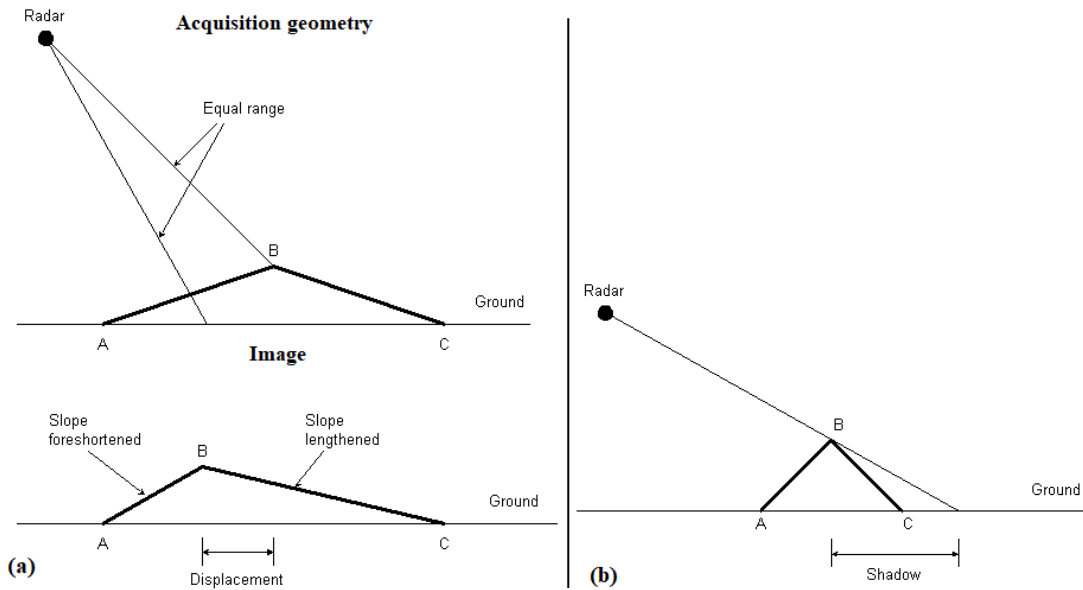


**Figure 57.** Geometric distortions – (a) Foreshortening and (b) shadowing effects (ESA, 2014)

In the case of Nea Paphos – Tombs of the Kings, both Cultural heritage sites are located on a level area next to the sea, facing towards the southwest – west direction with overlooking mountains and steep slopes to the north and northeast. Due to the geometry of the ascending and descending satellite orbits (Figure 58), the pair of ascending images was selected for DInSAR processing as it was expected to be affected the least by foreshortening and/or shadowing effects.

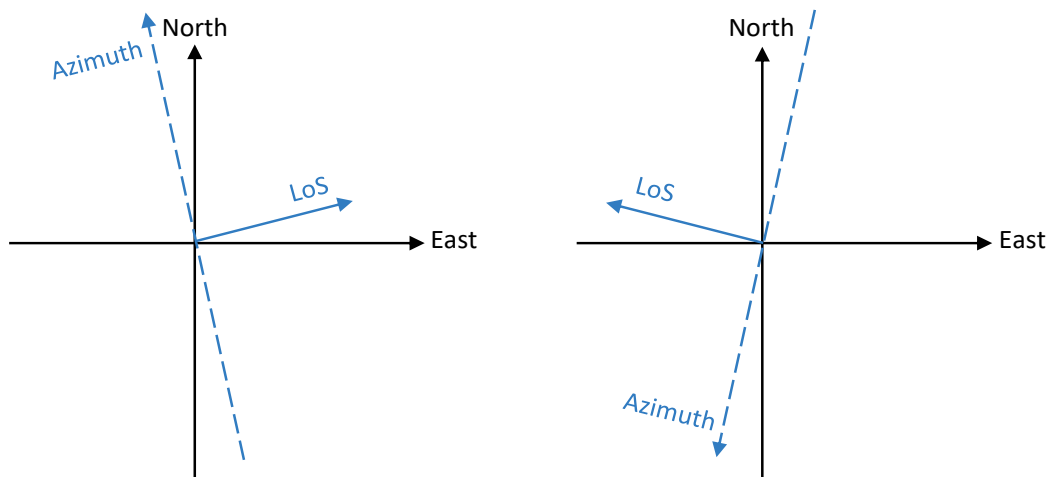


**Figure 58:** Geometry of ascending (left) and descending (right) satellite orbits

The two images that were selected, were then coregistered into a stack through the “TOPS Coregistration with ESD” tool. Within the coregistration process, the first acquisition, in chronological order (14/04/2015), was set as the master image whereas the second as the slave image (26/04/2015). Additionally, the specific bursts that include the area under study were selected to reduce the processing time. In our case, bursts 5 and 6 were selected.

Coherence was also very high in both images, being a good indicator for the successful completion of the coregistration step, as a higher coherence area indicates a better coregistration location (Li and Bethel, 2008).

The resulting coregistered stack product appears in the Product Explorer (Figure 59). The coregistration result was manually assessed by vertically displaying at the same time both images. The corresponding points between the two images was selected using the synchronisation cursor position option.

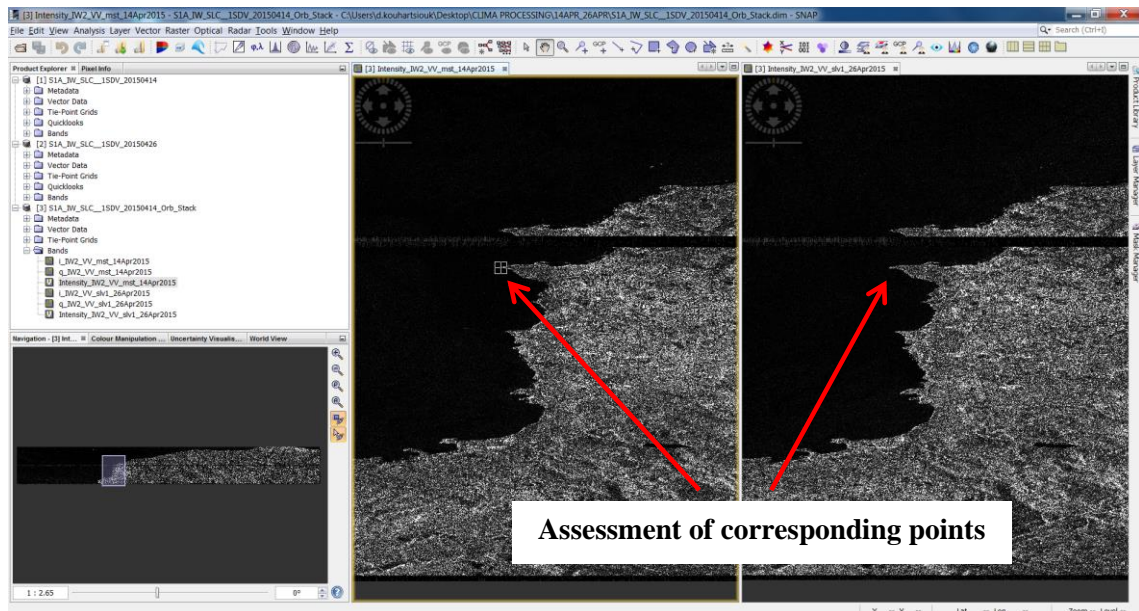


**Figure 59:** Coregistered images – Intensity IW2 band (master & slave) – Nea Paphos-Tombs of the Kings

The resulting interferogram can be seen in the Product Explorer by opening the drop-down menu for bands and double-clicking on phase to display the result (Figure 60).

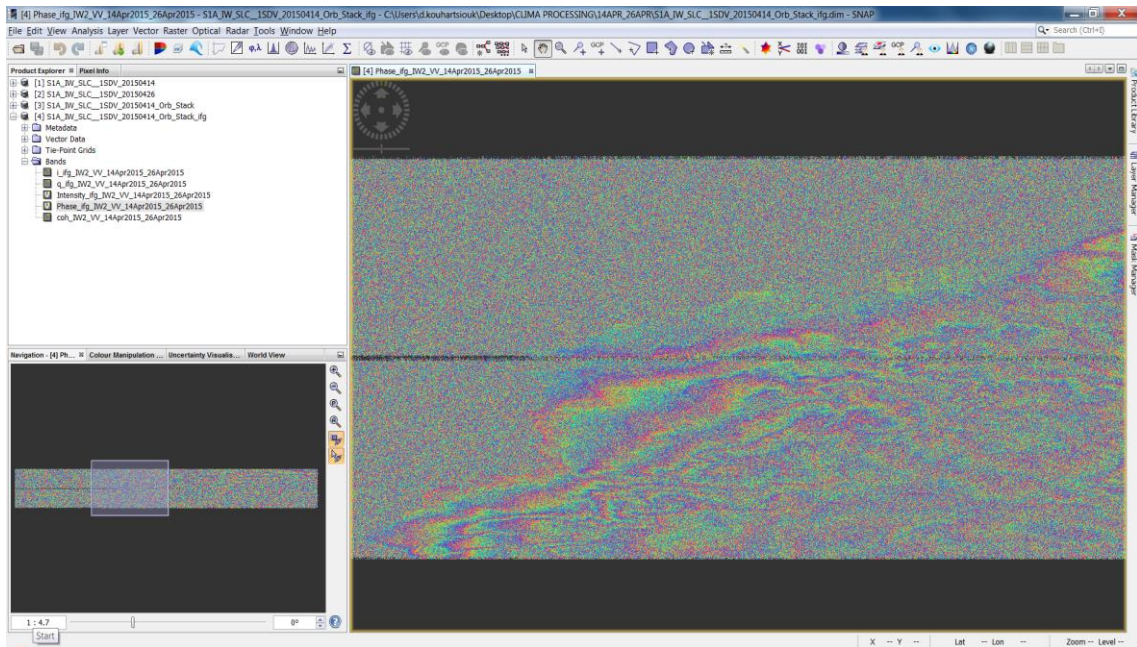


**Figure 60:** Interferogram Result – Nea Paphos-Tombs of the Kings

There was a clear black line in the resulting interferogram between the two bursts, which was then removed by using the S-1 TOPS Deburst tool.

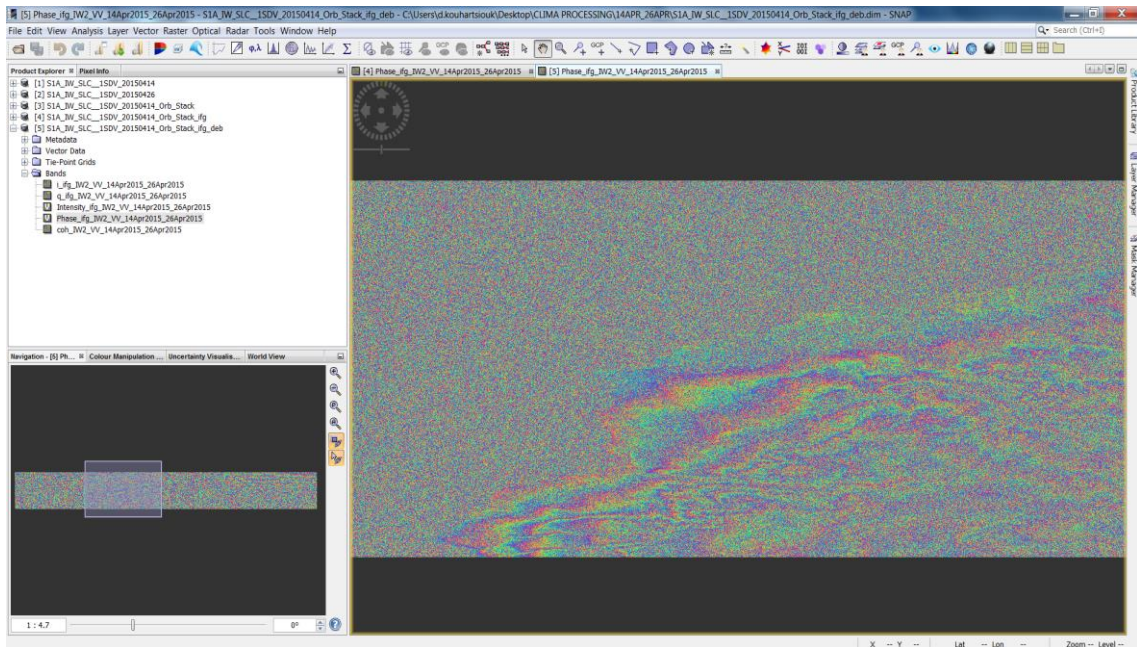


**Figure 61:** Deburst Result – Nea Paphos-Tombs of the Kings

During the step of topographic phase removal, a SRTM 1sec HGT DEM was used and was automatically downloaded from SNAP software to complete this step. The result after the removal of topographic phase by using the DEM is presented in Figure 62.



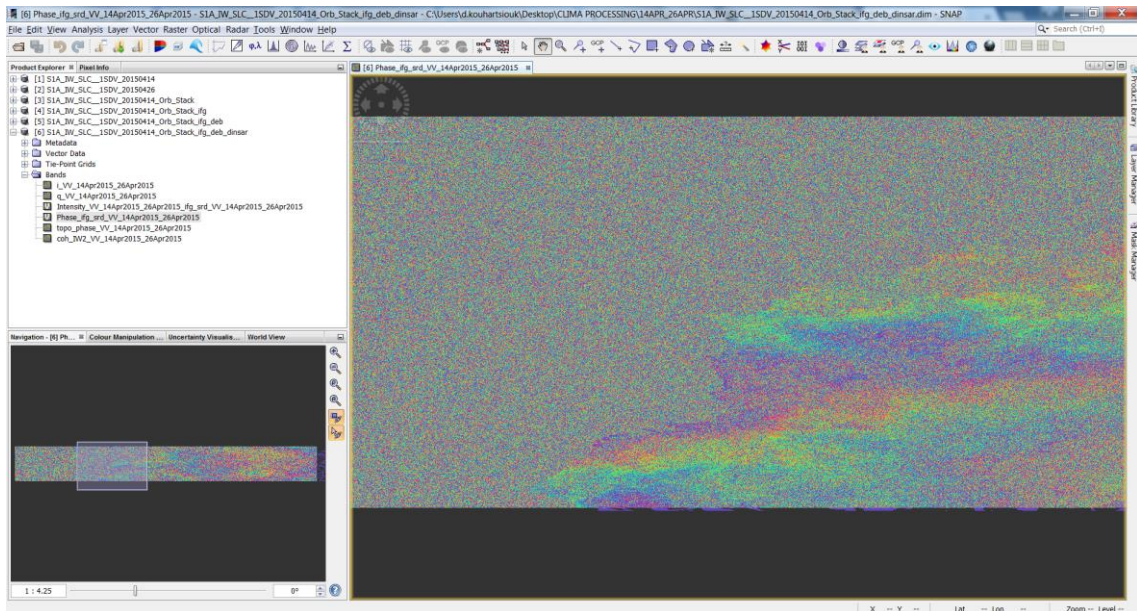


**Figure 62:** Interferogram Result after Topographic Phase Removal – Nea Paphos-Tombs of the Kings

The resulting interferogram after the application of Goldstein Phase Filtering is presented in Figure 63, after using ArcGIS software (see *section 3.2.2.3*) for visualisation purposes.

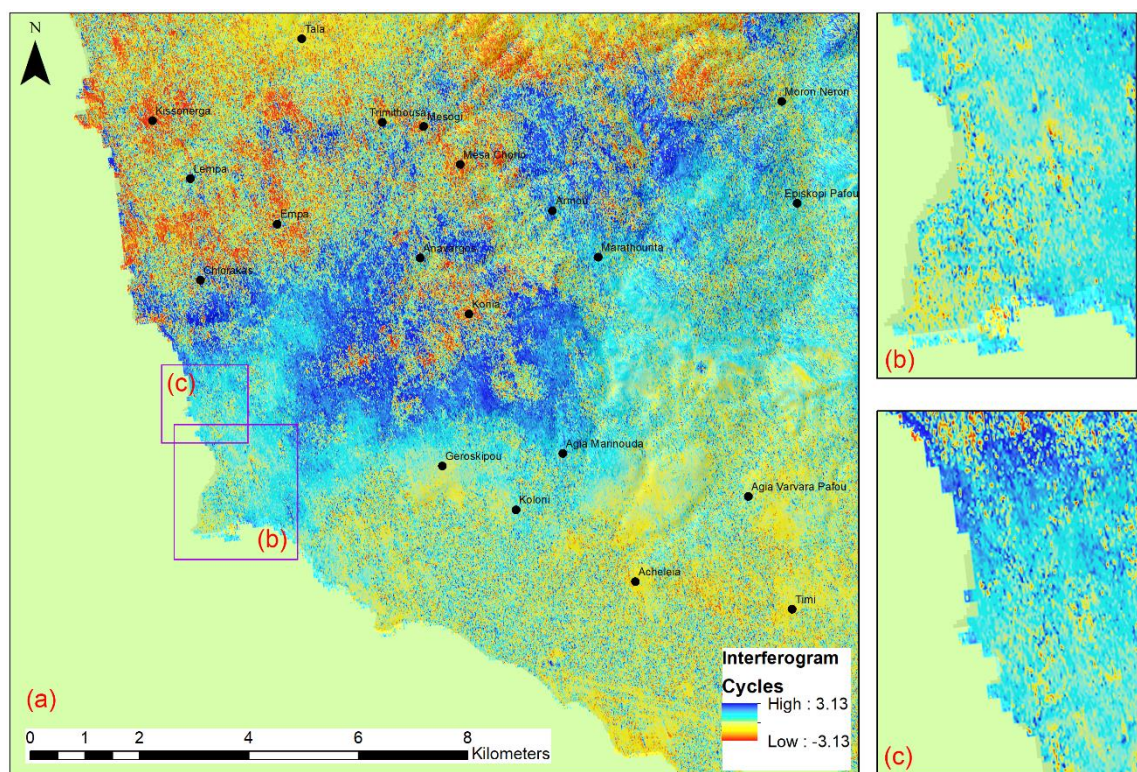


**Figure 63:** Differential interferogram after the application of phase filtering at (a) western Cyprus; (b) “Nea Paphos”; and (c) “Tombs of the Kings”.

SNAPHU software was then used to carry out the phase unwrapping step, after exporting the result from the previous step from SNAP. The result of the unwrapping step was then used as an input to SNAP software.

Moreover, phase was converted to displacement, leading to the calculation of vertical land movements/ displacement in mm. From the geometry of SAR acquisitions (Figure 64), to convert the unwrapped Line-of-Sight (LoS) phase  $\varphi$  to vertical displacement in millimetres, *Equation 8* was used:

$$\text{vertical displacement} = \frac{\varphi_{\text{unwrapped}} \cdot \lambda}{-4\pi \cdot \cos \theta_{\text{incident}}} \quad (\text{Eq. 8})$$

where:

$\varphi_{\text{unwrapped}}$ : the unwrapped LoS phase

$\lambda$ : the wavelength of SAR signal in mm

$\theta_{\text{incident}}$ : the incident angle of the scene

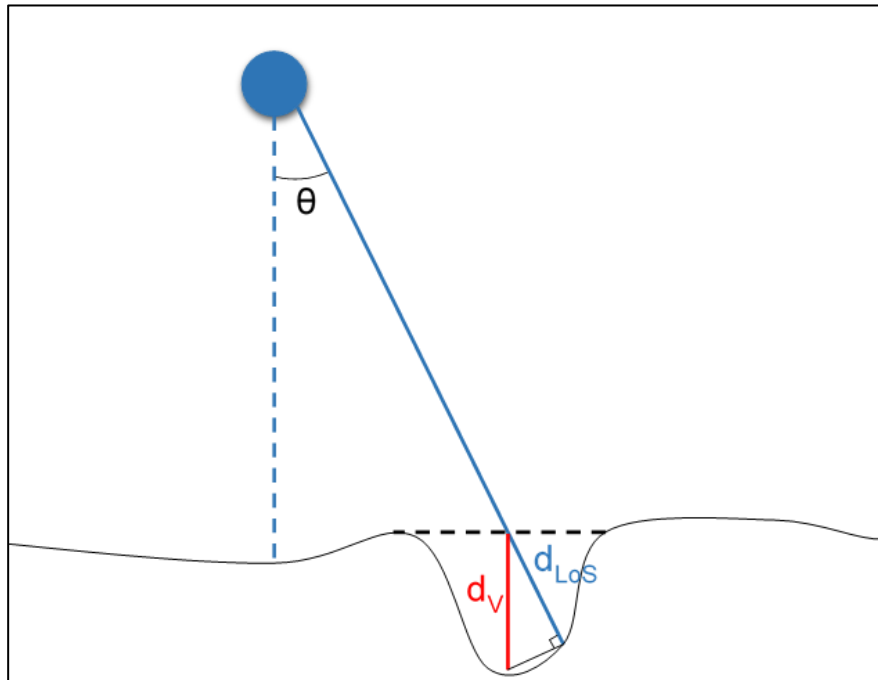


**Figure 64:** The SAR acquisition geometry

However, the calculated displacement values are relative (Figure 65) and further processing was required to calculate the absolute displacement values, incorporating a reference point of known displacement into the procedure.

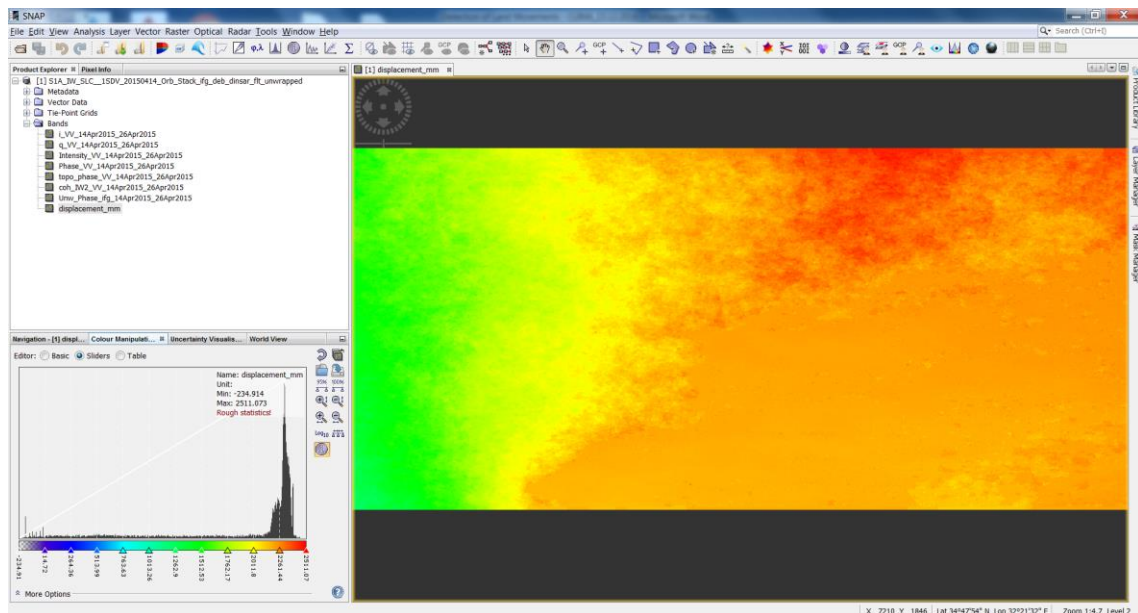


**Figure 65:** Relative displacement map – Nea Paphos-Tombs of the Kings

#### *4.2.1.1 Calibration and validation of results*

In Paphos, the department of Civil Engineering and Geomatics of the Cyprus University of Technology conducted an analysis on the deformation introduced at the Continuously Operating Reference Station (CORS) PAFO. PAFO is located within the area of interest and is one of the stations of the Cyprus Positioning System (CYPOS), the national reference station network operated by the Department of Lands and Surveys. Deformation analysis was conducted by processing daily GNSS observation files for the timespan 14–16 April 2015 (i.e., before and after the earthquake event).

GNSS processing was carried out using Leica Geo Office v.8.40. Specifically, an ionospheric-free linear combination was used using precise ephemeris and clock products and the Hopfield tropospheric model. An elevation cut-off angle of  $15^\circ$  was further imposed to exclude low-elevation satellites from the final solution. Reference data were obtained by the IGS (International GNSS Service) station NICO for the same period. Furthermore, the observations were inspected, both automatically and manually, for cycle slips to enhance the quality of the observations and the accuracy of the final solution.

The results indicated that the specific station did not show any statistically significant displacement (vertical displacement of 0.5mm was observed); thus, PAFO was

considered stable and was set as “Zero Point Reference.” It is noted that GNSS performance suffers in the vertical component because of the architecture of the system (only satellites above the horizon are used). However, with appropriate processing techniques, results at the millimetre level can be obtained.

Taking this into account, our result was further supported by the findings of a recent study, which examined daily solutions from PAFO station for a time span of 5 years using the Bernese GNSS v.5.2 software (Danezis, Chatzinikos and Kotsakis, 2019). The latter concluded that vertical velocities on the order of 1.6mm/year occurred at this location.

To determine the exact position of the point, the produced displacement map above needed to be geometrically corrected. The result of this step was the development of a geo-referenced displacement map. The geo-referenced displacement map produced (WGS84), after the application of Range-Doppler Terrain Correction, is shown in Figure 66.

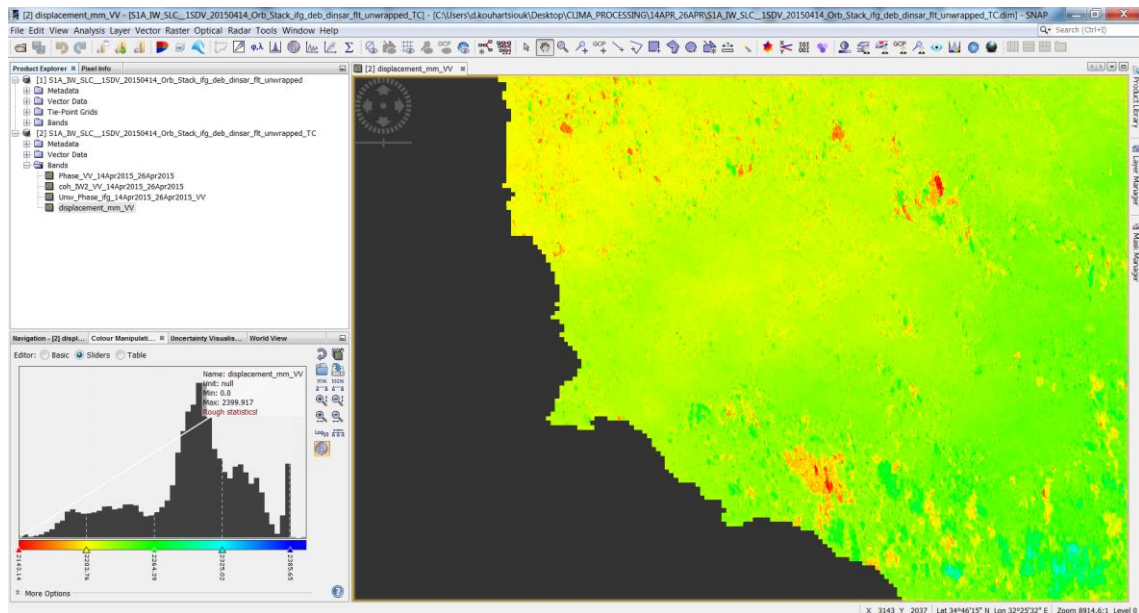


**Figure 66:** Displacement Map Result – Geo-referenced – Nea Paphos-Tombs of the Kings

Following the completion of the aforementioned steps, the resulting displacement map for our area of interest was produced, indicating vertical displacement ranging between – 79.43 and 102.92mm.

For a higher accuracy of results, a coherence mask was applied to remove regions of low coherence. For our case study, all areas with coherence less than 0.6 were chosen as the

mask. This allowed us to exclude all vegetated land cover from the displacement map, which often introduces errors to results because of temporal variations, and allowed us to concentrate on coherent areas, as in the case of urban areas.

The final vertical displacement map is shown in Figure 67. From the figure, it is clear that during the 12 days between the two SAR acquisitions there was a maximum uplift of 74mm and a maximum subsidence of 31mm.

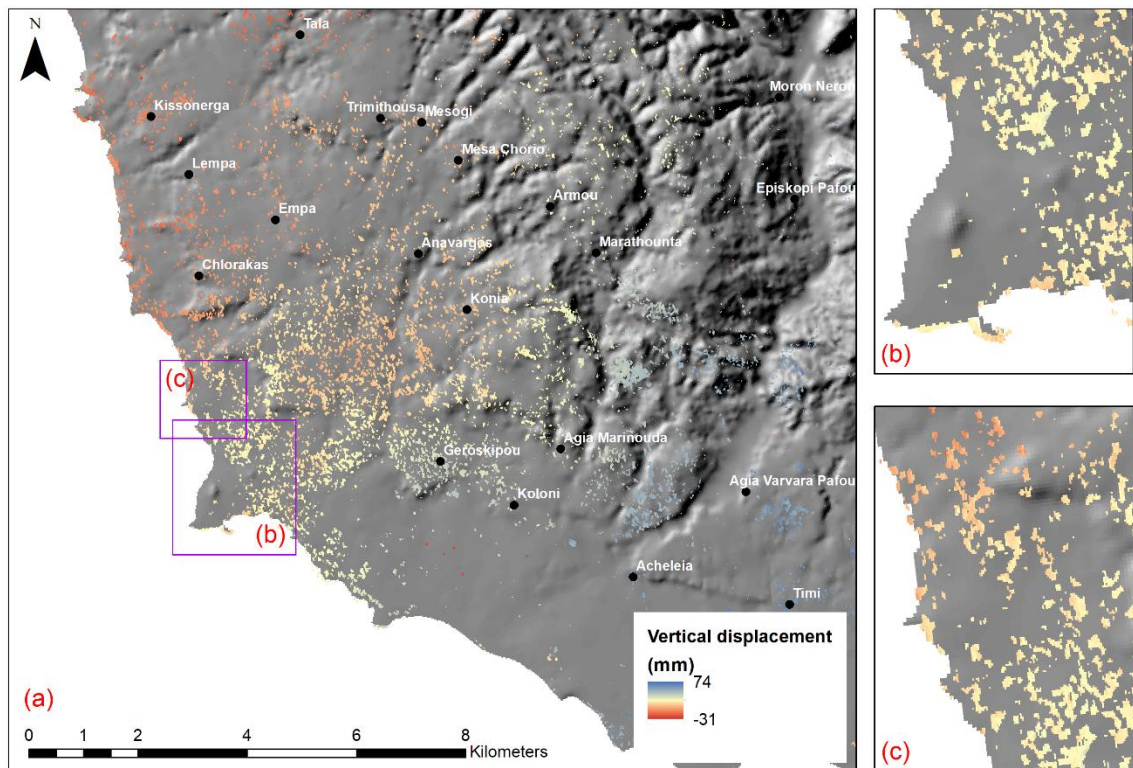


**Figure 67:** Final displacement map at (a) western Cyprus; (b) “Nea Paphos”; and (c) “Tombs of the Kings”

Based on the findings of DInSAR processing, a further investigation of the displacement characteristics, in sites of cultural heritage interest was performed. As shown in Figure 68, two important archaeological sites of Cyprus, namely the “Nea Paphos” (Figure 68b) and “Tombs of the Kings” (Figure 68c), as well as the broader area of the historic centre of Paphos (Figure 68a) were studied.

The analysis shows that displacement was close to 0mm in both UNESCO World Heritage sites. Some areas, mainly in the southern part of “Nea Paphos”, indicated minor vertical displacement (subsidence), which were, however, modern constructions.



**Figure 68:** Final displacement map at (a) historic centre of Paphos; (b) Nea Paphos and (c) Tombs of the Kings

A similar pattern was also observed in the “Tombs of the Kings” site, where hotels and buildings in the eastern part of the site showed some small subsidence in contrast to the archaeological site in the west. On the contrary, in the wider area of the historic centre of Paphos, a negative vertical displacement (subsidence) was recorded in the eastern and northern parts. The western part of that region seems to be unaffected from the event.

#### 4.2.2 Pissouri – Petra tou Romiou

For the case study of Pissouri – Petra tou Romiou, initially ten SAR images were downloaded, six Sentinel-1A images (3 ascending and 3 descending) and four Sentinel-1B images (2 ascending and 2 descending). These images were used to form six co-event pairs to study the two landslide events that took place near Pissouri and Petra tou Romiou on 15 February 2019 and 20 February 2019 respectively.

The suitability of all SAR image pairs was checked, via an overview of the perpendicular baseline and other image pair characteristics, such as the temporal baseline and the

modelled coherence, that was carried out through “InSAR Stack Overview” command. The characteristics of the co-event SAR pairs are presented in Table 14.

**Table 14:** SAR image interferometric pairs – Pissouri-Petra tou Romiou

No.	Platform	Date (master)	Date (slave)	Pass direction	Temp. baseline	Perp. baseline	Modelled coherence
1	Sentinel-1A	04/02/2019	16/02/2019	Ascending	12 days	102.44m	0.90
2	Sentinel-1A	05/02/2019	17/02/2019	Descending	12 days	12.46m	0.98
3	Sentinel-1B	10/02/2019	22/02/2019	Ascending	12 days	17.44m	0.97
4	Sentinel-1B	11/02/2019	23/02/2019	Descending	12 days	86.63m	0.92
5	Sentinel-1A	16/02/2019	28/02/2019	Ascending	12 days	84.72m	0.92
6	Sentinel-1A	17/02/2019	01/03/2019	Descending	12 days	14.88m	0.97

The perpendicular baselines for all six co-event SAR pairs are shorter than the threshold of 200m that was set. Moreover, all six pairs show high modelled coherence equal or greater than 0.90. However, the modelled coherence shown above is only an estimate. The coherence of the interferometric pair will be calculated after the completion of the step of the interferogram formation.

Landslides took place in both areas on slopes facing towards the south, and thus there is no preferred satellite pass direction, compared with the case study of Nea Paphos – Tombs of the Kings. Therefore, all six pairs were processed further using the proposed DInSAR processing chain. Interferometric pairs 1, 2, 3 and 4 were used to study the landslide that occurred on the 15<sup>th</sup> February 2019 near Pissouri, next to the A6 motorway, whereas the interferometric pairs 3, 4, 5 and 6 were used to investigate the impact of the landslide that took place near Petra tou Romiou by the old Paphos-Limassol road.

Following the same procedure, as in the case of Nea Paphos – Tombs of the Kings, the SAR images were coregistered in pairs, and the result of coregistration was checked by developing RGB representations of the master and slave images to see if the images were correctly aligned. The master image was selected for red and green channels and the slave image for blue channel (Braun and Veci, 2020). The results of coregistration for the six interferometric pairs are presented in Figure 69.

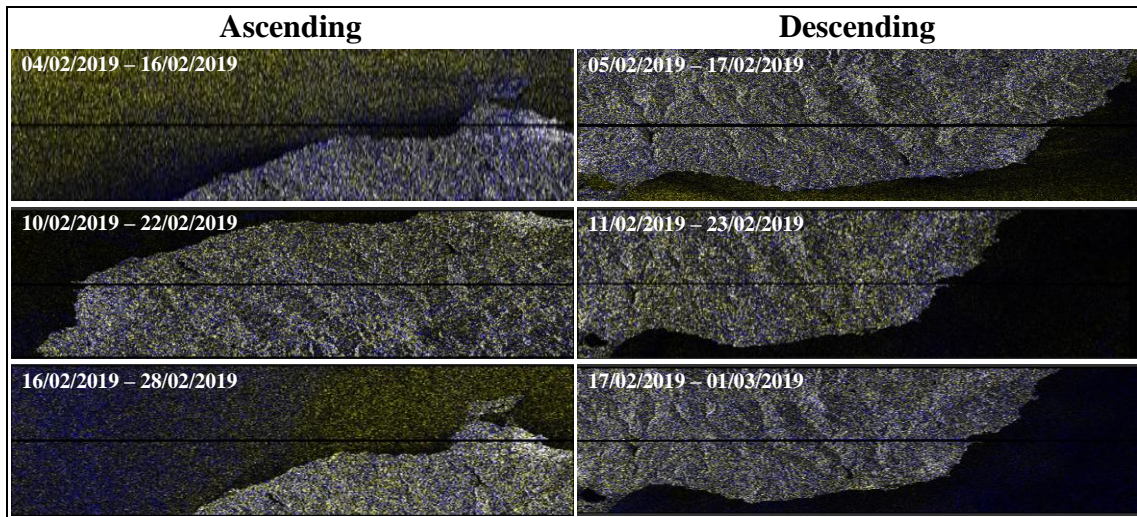


**Figure 69.** RGB representation of SAR image pair coregistration – Pissouri-Petra tou Romiou

Interferograms and coherence maps were then produced for the six interferometric pairs. To produce the final products, the topography component was removed by using the SRTM 1sec HGT DEM, and the black line between the bursts of the image was removed using the Deburst tool. Finally, Goldstein phase filter was then applied to enhance the developed interferograms and make the interferometric fringes visually clearer. The final interferograms and coherence maps, geo-located for easier visualisation, are presented in Figure 70 and Figure 71 respectively.

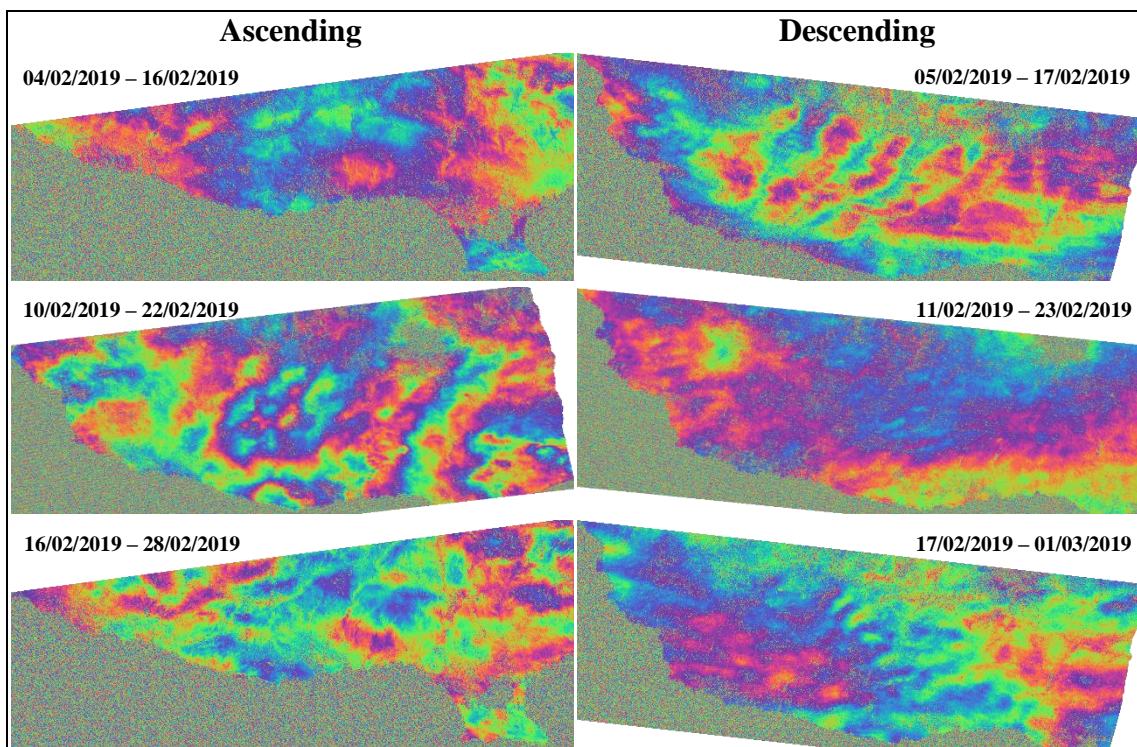


**Figure 70.** Interferograms of SAR image pairs – Pissouri-Petra tou Romiou



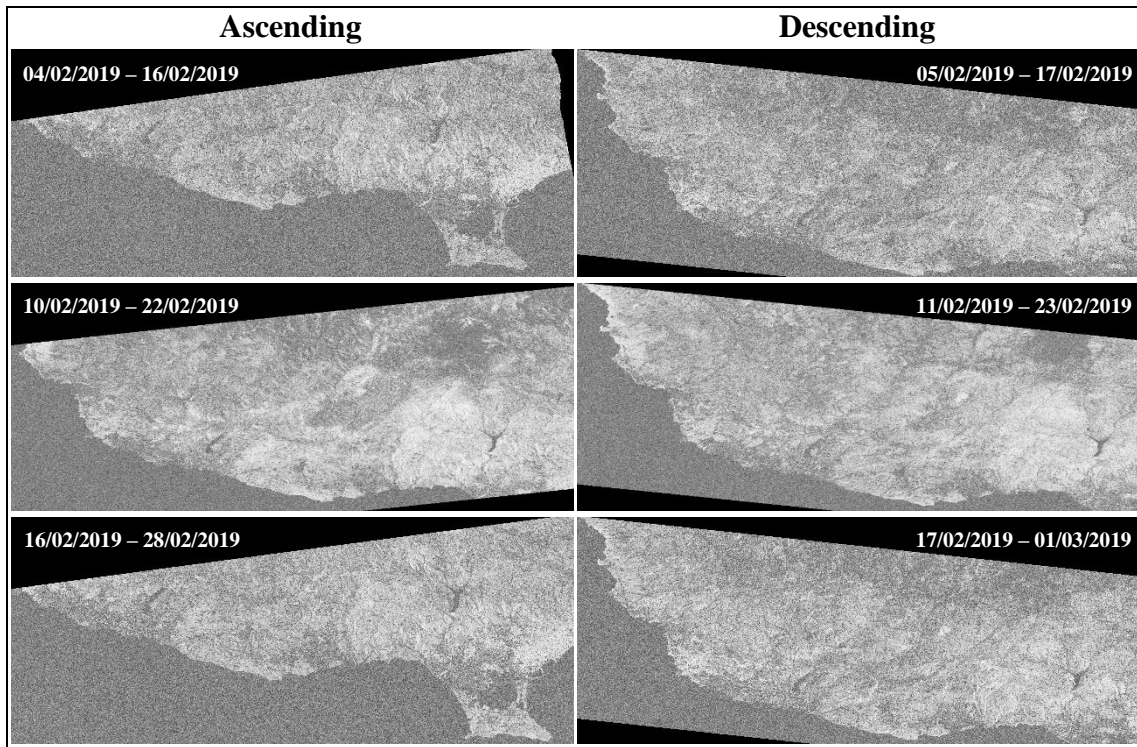


**Figure 71.** Coherence maps of SAR image pairs – Pissouri-Petra tou Romiou

The interferograms were then converted into KMZ files to be overlaid in Google Earth to check for any fringes that could potentially indicate the sudden change on the Earth's surface in the two areas of interest. The wider areas of the two landslide events were defined based on directions by the Geological Survey Department as shown in Figure 72.

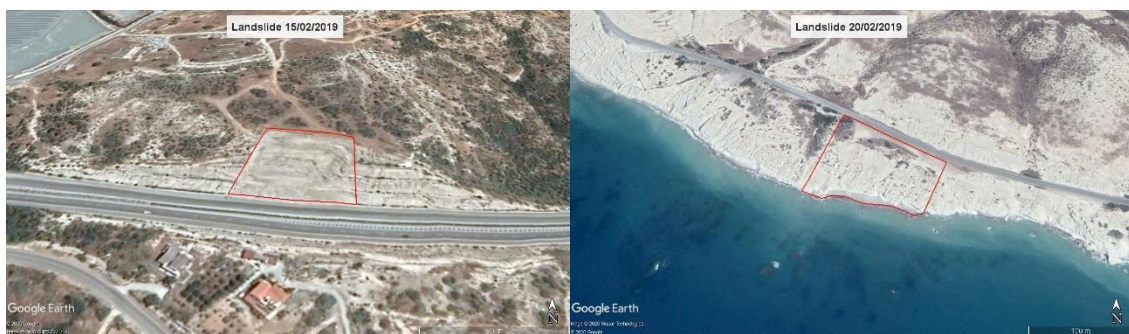


**Figure 72:** Landslide areas indicated in red near Pissouri by the motorway A6 (left) and near Petra tou Romiou next to the old Paphos-Limassol road (right)

The interferograms produced in SNAP were then inserted into Google Earth and the results are presented for the landslide near Pissouri in Figure 73 and for the landslide near Petra tou Romiou in Figure 74. The black lines in all interferograms in both figures, are the limits of motorway A6 and the coastline respectively.

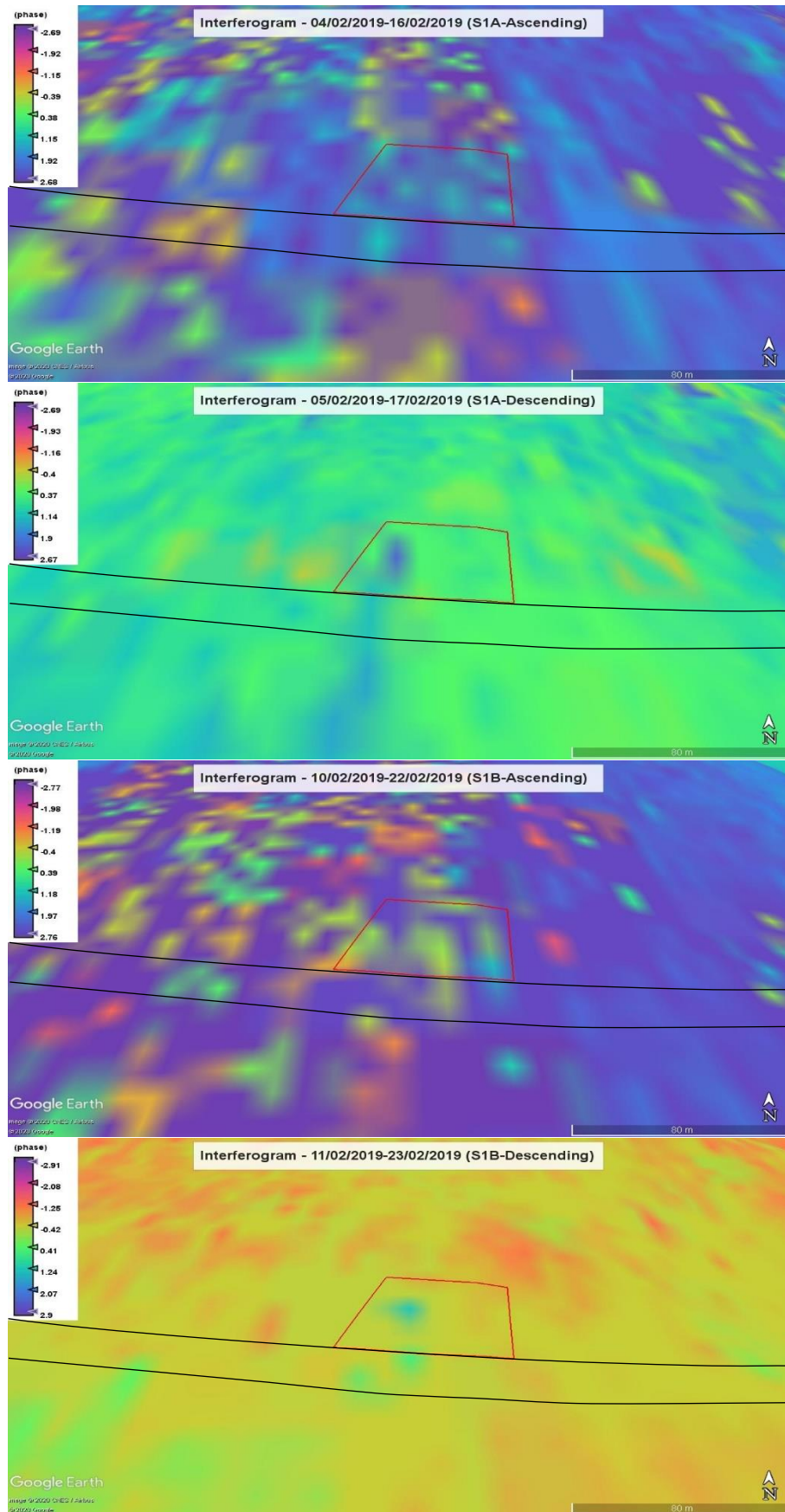


**Figure 73:** Interferograms at the area of the landslide near Pissouri by the motorway A6

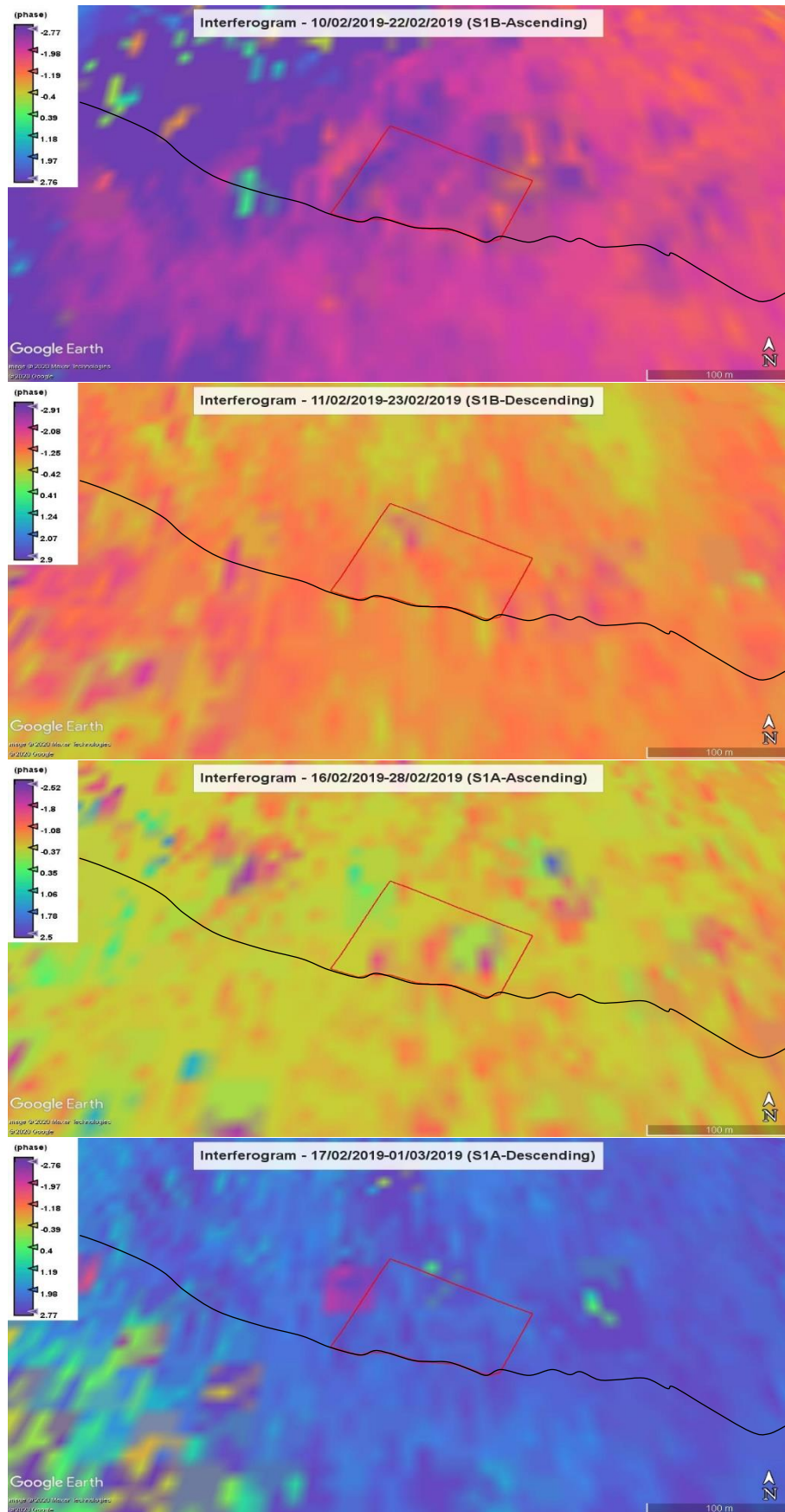


**Figure 74:** Interferograms at the area of the landslide near Petra tou Romiou

The fringes, or else the colour variations, represent phase changes between two images in terms of radians of a full  $2\pi$  cycle. Each cycle of colours represents half the sensor's wavelength, i.e. in the case of Sentinel-1, it represents a LoS displacement of  $\sim 2.7\text{cm}$ .

In Figure 73, i.e. the case of the 15<sup>th</sup> of February landslide near Pissouri, it can be seen that there is substantial phase noise in both ascending S1A and S1B SAR image pairs at the landslide area and the areas nearby. The noise at the north of the landslide outlined area could be due to the vegetation and at the south due to the presence of the motorway (Figure 72). Additionally, as analysed in literature (Zebker and Villasenor, 1992; Rocca *et al.*, 2000; Bouaraba *et al.*, 2014; Closson and Milisavljevic, 2017), heavy rainfall and changes in soil moisture can alter the radar signal significantly leading to loss of coherence. However, in both cases with pairs of descending S1A and S1B images dated 05/02/2019-17/02/2019 and 11/02/2019-23/02/2019 respectively, there appears to be a clear phase shift at the western part of the landslide area, as shown in the red circled areas in Figure 75.

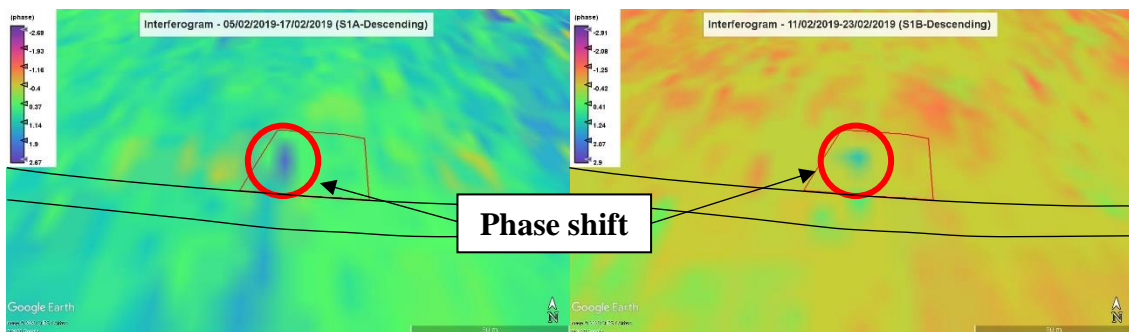


**Figure 75:** Interferograms of S1A and S1B descending pairs at the area near Pissouri

In Figure 74, i.e. the case of the 20<sup>th</sup> of February landslide near Petra tou Romiou, it can be seen that there is phase noise in all interferometric SAR image pairs to the west and northwest from the outlined landslide. It is clear from Figure 72, that this is mainly due to the existing vegetation, that leads to a reduction in the radar signal coherence. There is also significant phase noise to the south after the black line (coastline), as sea is characterised by very low, close to zero, coherence.

The 6 produced interferograms, were then unwrapped within SNAP, using the SNAPHU plugin, which was included in SNAP in 2019 (see *section 3.2.2.2 SNAPHU*). The unwrapping results are then re-imported to the DInSAR processing chain and appear in the Product explorer, as presented in Figure 76.

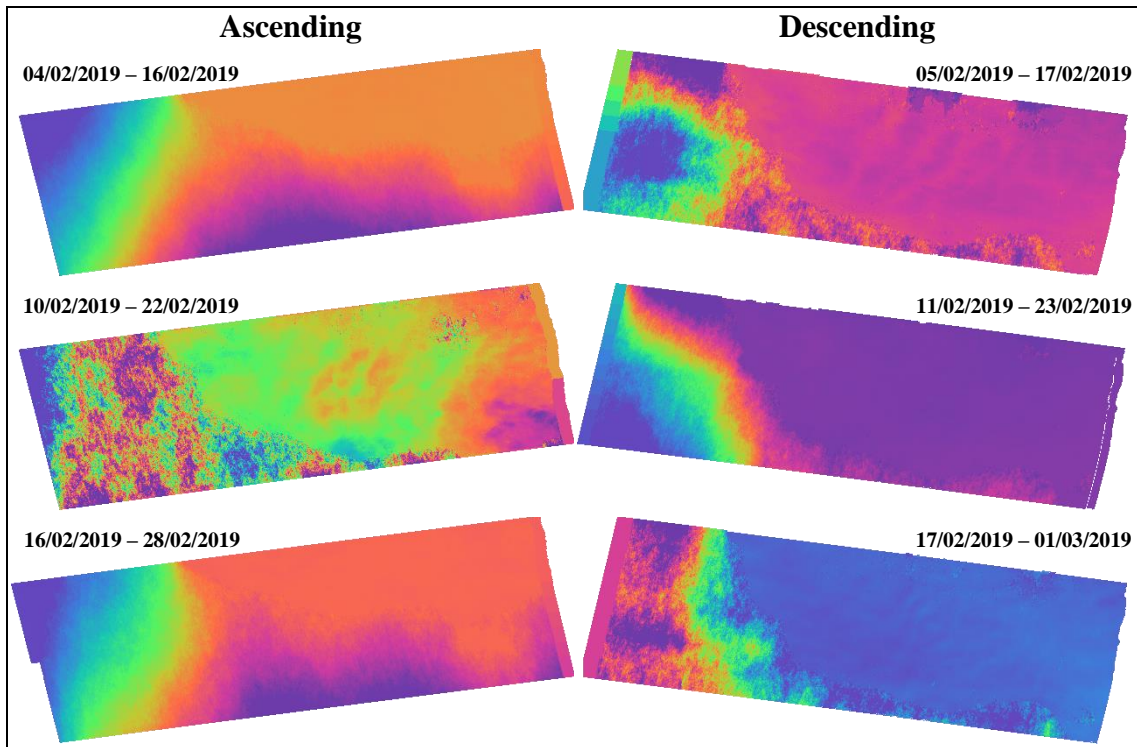


**Figure 76.** Unwrapped interferograms of SAR image pairs – Pissouri-Petra tou Romiou

Following, the unwrapped interferograms were used to convert phase to displacement. Due to the complexity of the land movements in the case of landslides, unwrapped phase was converted to LoS displacement, i.e. land movements along the slant range direction of the satellite. This step was carried out using the Phase to Displacement SNAP module.

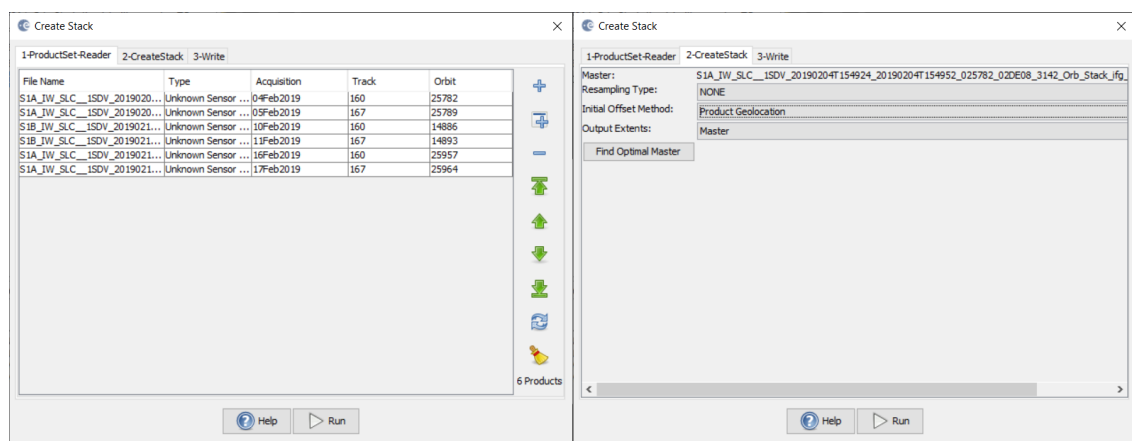


**Figure 77:** Development of a stack of displacement maps

All displacement products were then geo-located using the Range-Doppler Terrain Correction function. Finally, the individual displacement products were stacked in chronological order using Geolocation as initial offset method (Figure 77).

The final displacement maps and their histograms are presented below in Figure 78.

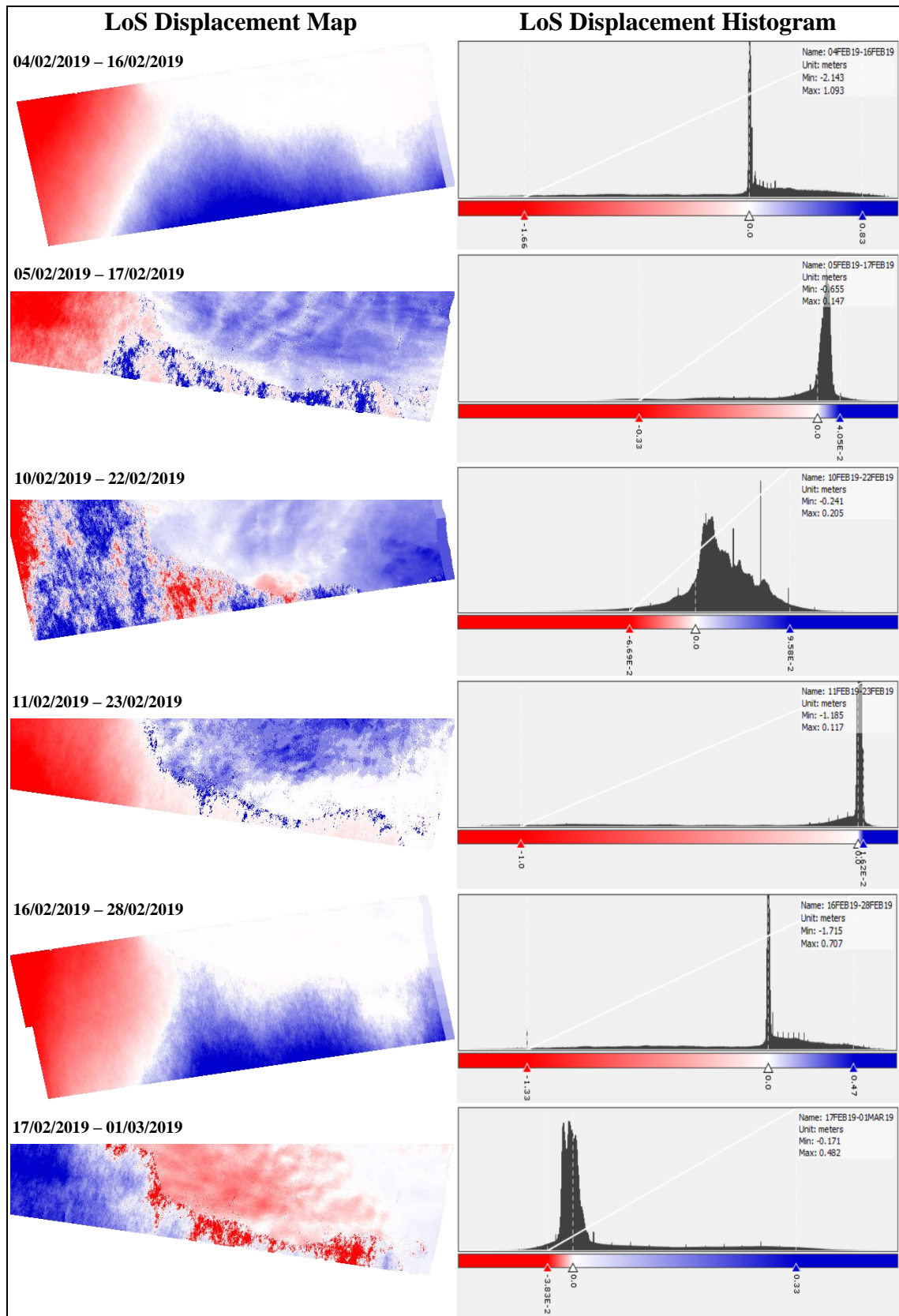


**Figure 78:** Absolute LoS displacement maps and histograms – Pissouri-Petra tou Romiou

Following the geo-location of all displacement maps, the relative LoS displacement values that were calculated at this stage, were converted to absolute values, by specifying a point of high coherence in the area, in our case a nearby building. The pixel value of displacement at the coordinates of the building were subtracted by all the displacement map values in all six cases individually.

In Figure 78, areas with zero or nearly zero displacement are marked white, areas where uplift occurred with blue and areas that subsidence took place with red colour. According to the histograms, at the right side of the figure, in the first product, i.e. 4/2/2019-16/2/2019, displacement varies from -2.143m to 1.093m; in the second map (5/2/2019-17/2/2019), displacement varies from -0.655 to 0.147m; in the third one, i.e. 10/2/2019-22/2/2019, displacement values vary from -0.241 to 0.205m; in the fourth map (11/2/2019-23/2/2019), displacement varies from -1.185m to 0.117m; in the fifth displacement map, i.e. 16/2/2019-28/2/2019, values vary from -1.715m to 0.707m and in the sixth map (17/2/2019-1/3/2019), displacement values vary from -0.171m to 0.482m.

In all cases, the extreme displacement values, in intense red and blue colour appear at the sea area around Cyprus, and the majority of the pixel values of displacement inland are around zero, with some small variations, seen in light red and blue, for subsidence and uplift respectively. In the cases where more intense red and blue colours can be seen inland in the displacement maps, this is since zero is close to the confidence intervals of the histogram for 95% level of confidence. The displacement maps produced in SNAP were then inserted into Google Earth and the results are presented for the landslide near Pissouri in Figure 79 and for the landslide near Petra tou Romiou in Figure 80.



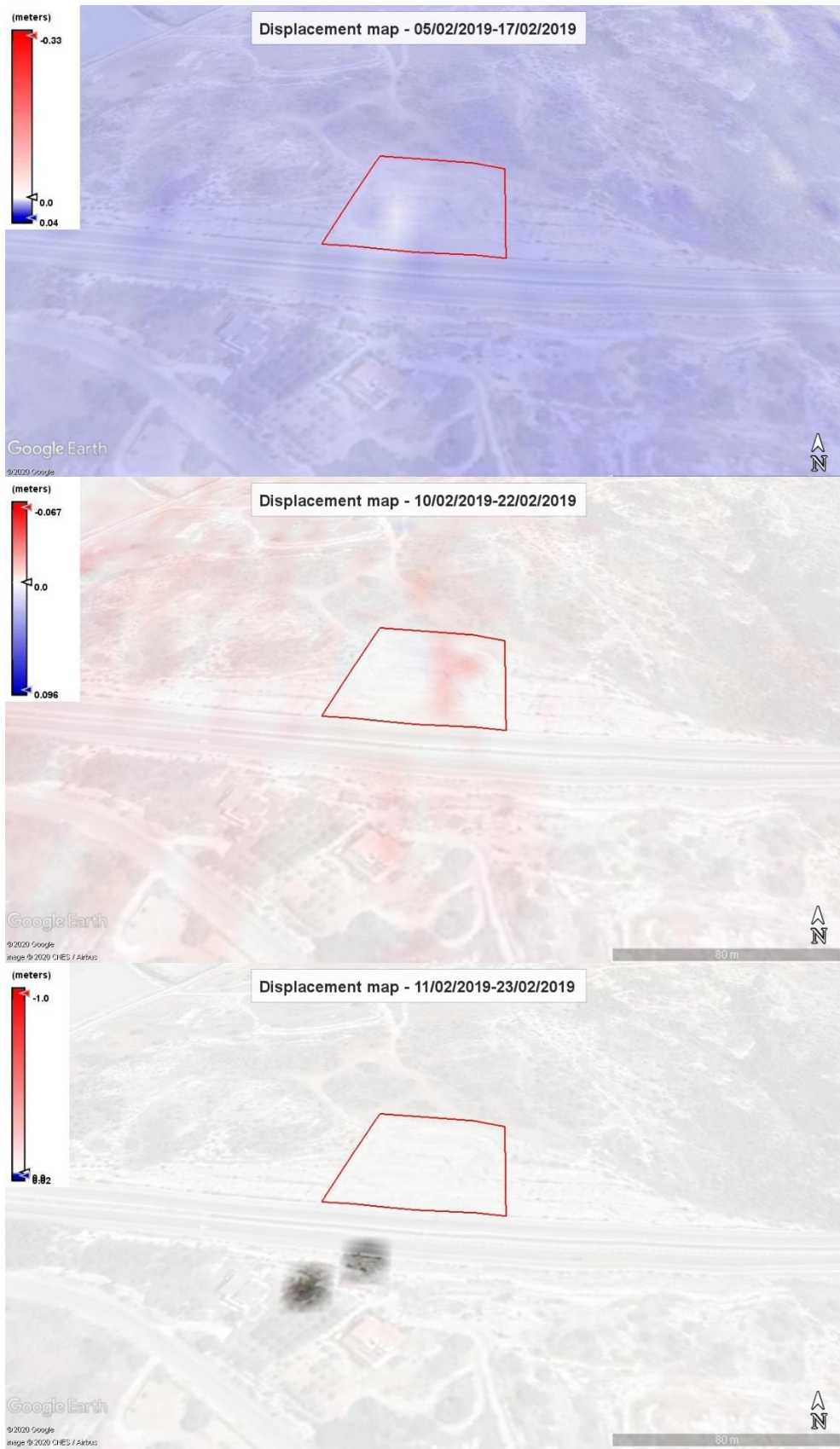


**Figure 79:** Displacement maps at the landslide area near Pissouri







**Figure 80:** Displacement maps at the landslide area near Petra tou Romiou

In both sites, zero and/or near to zero LoS displacements were calculated. As stated in the *Literature review*, the averaging or stacking of many interferometric products can assist in minimising or even correcting the error associated with the atmospheric effect, since the atmospheric effect has short spatial correlation length with virtually no temporal correlation between data acquisition times (Zebker, Rosen and Hensley, 1997; Ouchi, 2013; Yu, Li and Penna, 2018). The averaging of the geo-located displacement maps for each landslide event was performed via the Band Maths module, as shown in Figure 81.

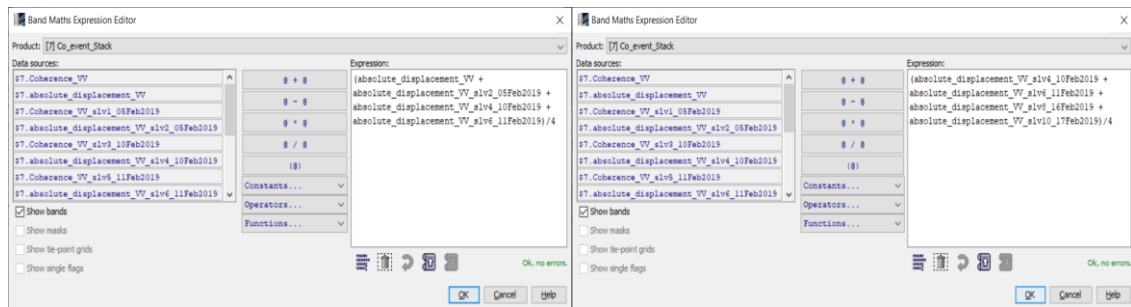


**Figure 81:** Development of average displacement maps – Band Maths

Thus, displacement maps dated 4/2/2019-16/2/2019, 5/2/2019-17/2/2019, 10/2/2019-22/2/2019 and 11/2/2019-23/2/2019 were used to develop the average displacement map for the landslide near Pissouri (15 February 2019); and displacement maps of 10/2/2019-22/2/2019, 11/2/2019-23/2/2019, 16/2/2019-28/2/2019 and 17/2/2019-1/3/2019 were combined for the average displacement map for the second landslide event (20 February 2019). The average displacement maps and their histograms are presented in Figure 82.

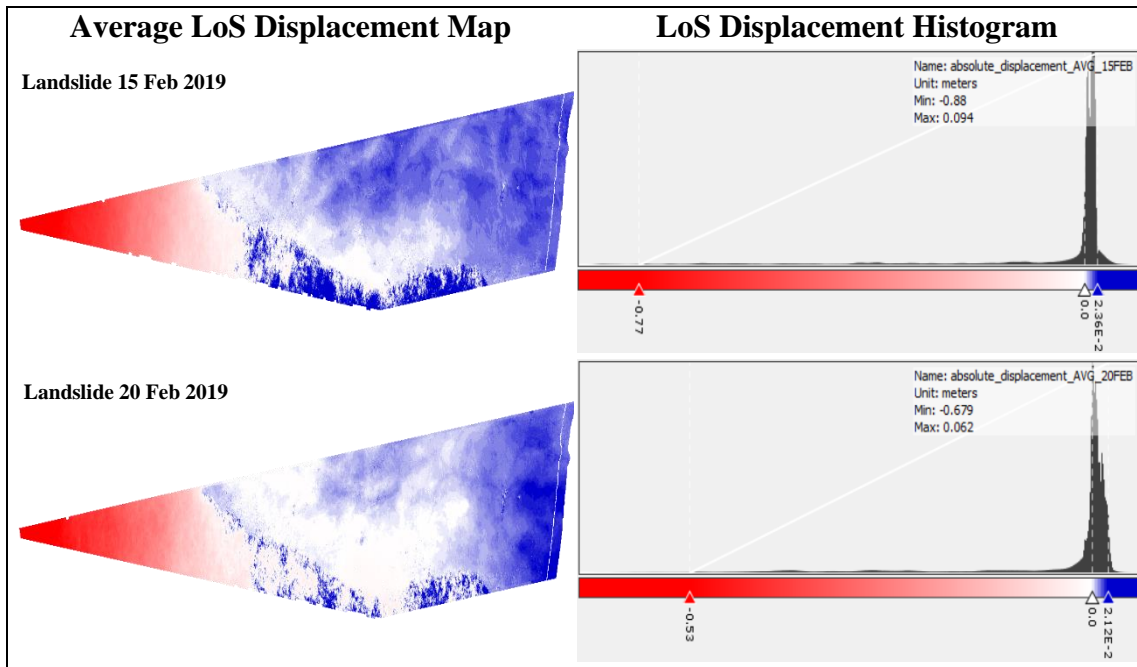


**Figure 82:** Average LoS displacement maps and histograms – Pissouri-Petra tou Romiou

In both cases, as it was also observed in the analysis of Figure 78, the extreme displacement values, in intense red and blue colour appear at the sea area around Cyprus, and the majority of the pixel values of displacement inland are around zero, with some small variations, seen in light blue, i.e. uplift. In cases where more intense blue colours can be seen inland, this is because zero is close to the maximum confidence interval of the histogram for 95% level of confidence. The results overlaid in Google Earth are presented in Figure 83 and Figure 84.



**Figure 83:** Average LoS displacement map – Pissouri

At the landslide area near Pissouri, LoS displacement values are nearly zero, with an exception at the north part of the area, where a small positive displacement, along the satellite track, in the range of 1cm is observed, seen in light blue. At the landslide area near Petra tou Romiou, as seen in Figure 84, LoS displacement values are nearly zero.

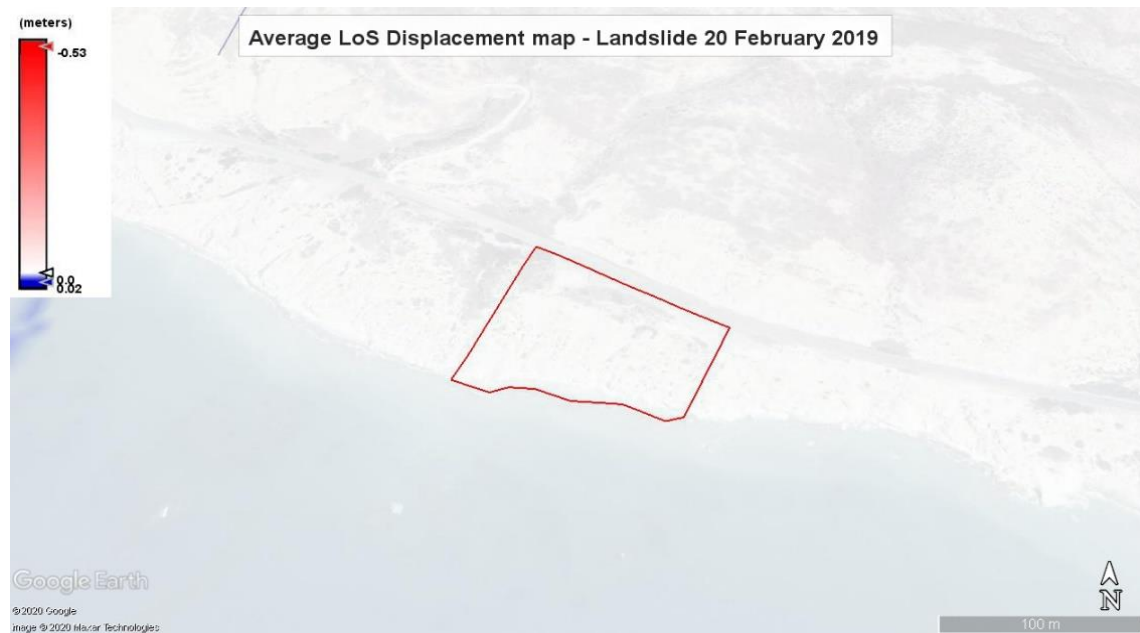


**Figure 84:** Average LoS displacement map – Petra tou Romiou

As seen in Figure 85 and Figure 86, none of the LoS displacement maps showed the real extent of the two landslide events. An attempt was made to decompose the LoS displacement into vertical, i.e. up/down and horizontal, East-West only, components, to investigate both events further. The North-South part of the horizontal displacement needs different processing with various combinations of ascending and descending SAR images (Dalla Via, Crosetto and Crippa, 2012; Jo, Jung and Yun, 2017; Fan *et al.*, 2019).



**Figure 85:** Landslide near Pissouri by the A6 motorway (Geological Survey Department)



**Figure 86:** Landslide near Petra tou Romiou (Geological Survey Department)

The calculation of the vertical (up-down) and east-west displacement components can be achieved using the already developed average LoS displacement products from the ascending and descending image pairs, together with the scene's incidence angle from *Equations 9* derived from the acquisition geometry as presented in Figure 87.

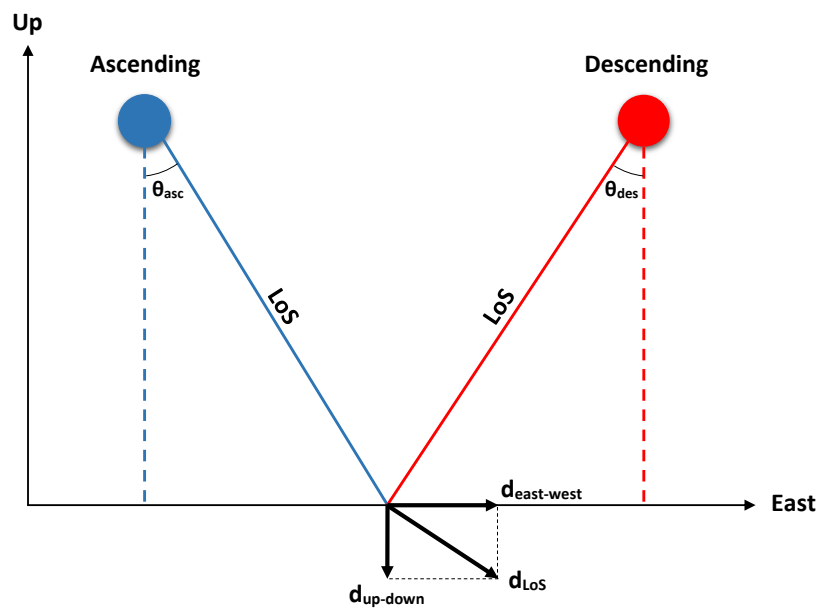


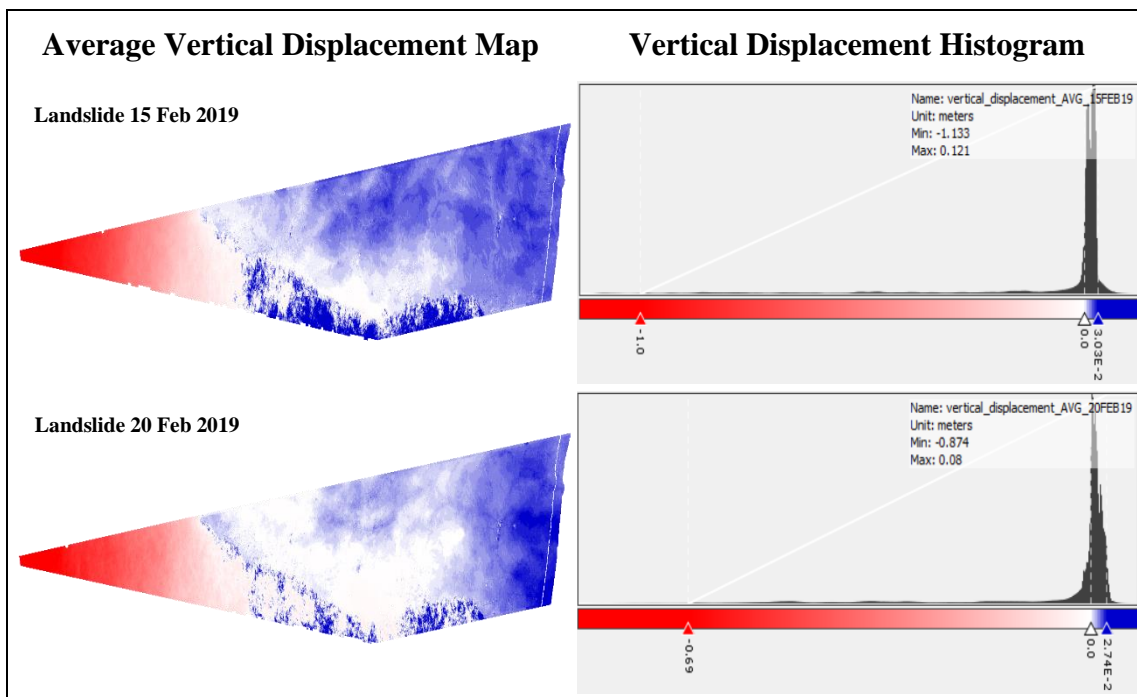
**Figure 87:** Decomposition of LoS displacement into vertical and east-west components

$$\text{Displacement}_{\text{up-down}} = \frac{\text{Displacement}_{\text{LoS}}}{\cos \theta_{\text{incident}}} , \text{Displacement}_{\text{E-W}} = \frac{\text{Displacement}_{\text{LoS}}}{\sin \theta_{\text{incident}}} \quad (\text{Eq. 9})$$

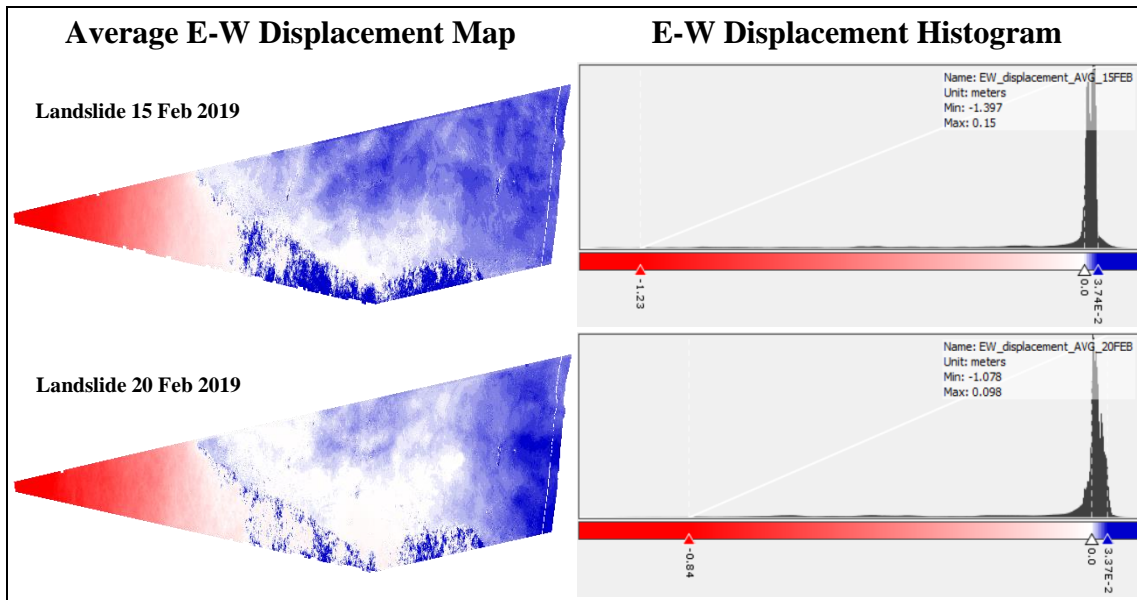
Name	Value	Type	Unit	Description
BurstBoundary				
Look_Direction_List				
PRODUCT	S1A_IW_SLC__1SDV_20190204T154924_20190204T154924	ascii		Product name
PRODUCT_TYPE	SLC	ascii		Product type
SPH_DESCRIPTOR	Sentinel-1 IW Level-1 SLC Product	ascii		Description
MISSION	SENTINEL-1A	ascii		Satellite mission
ACQUISITION_MODE	IW	ascii		Acquisition mode
antenna_pointing	right	ascii		Right or left facing
BEAMS	-	ascii		Beams used
SWATH	IW2	ascii		Swath name
PROC_TIME	04-FEB-2019 18:25:08.217863	uint32	utc	Processed time
Processing_system_identifier	ESA Sentinel-1 IPF 002.91	ascii		Processing system identifier
orbit_cycle	161	int32		Cycle
REL_ORBIT	160	int32		Track
ABS_ORBIT	25782	int32		Orbit
STATE_VECTOR_TIME	04-FEB-2019 15:48:18.689067	uint32	utc	Time of orbit state vector
VECTOR_SOURCE	-	ascii		State vector source
incidence_near	36.23292922973633	float64	deg	
incidence_far	41.859822992579986	float64	deg	
slice_num	7	int32		Slice number
data_take_id	187912	int32		Data take identifier
first_line_time	04-FEB-2019 15:49:43.774875	uint32	utc	First zero doppler azimuth time
last_line_time	04-FEB-2019 15:49:49.618821	uint32	utc	Last zero doppler azimuth time
first_near_lat	34.86002275275159	float64	deg	
first_near_long	32.06910238508459	float64	deg	
first_far_lat	34.86002275275159	float64	deg	
first_far_long	33.154428765389056	float64	deg	
last_near_lat	34.36062485213382	float64	deg	
last_near_long	32.06910238508459	float64	deg	

**Figure 88:** Incident angle as seen in image metadata

The incident angle, as obtained from the image metadata in SNAP (Figure 88), ranges from  $36.23^\circ$  to  $41.86^\circ$ . The mean incident angle, ( $39.05^\circ$ ) was used in the calculations of vertical and east-west displacements. The two maps that were produced for the landslide events for vertical and E-W displacement are presented in Figure 89 and Figure 90 respectively. Pixel size of all displacement products is 11.4m x 11.4m.

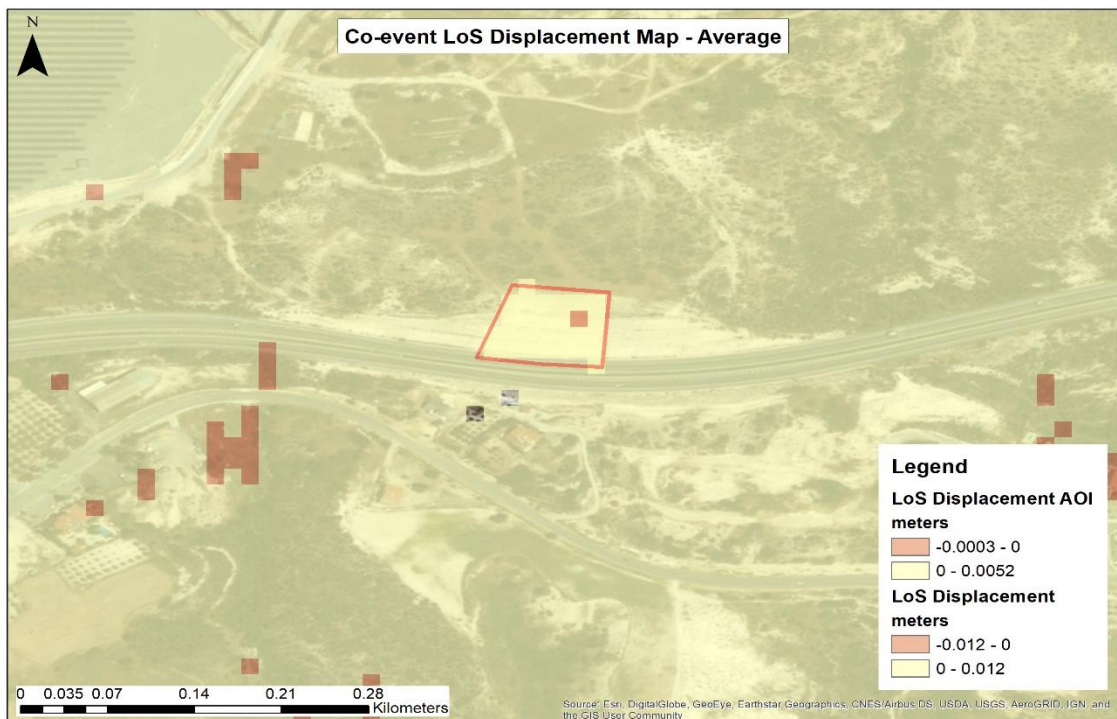


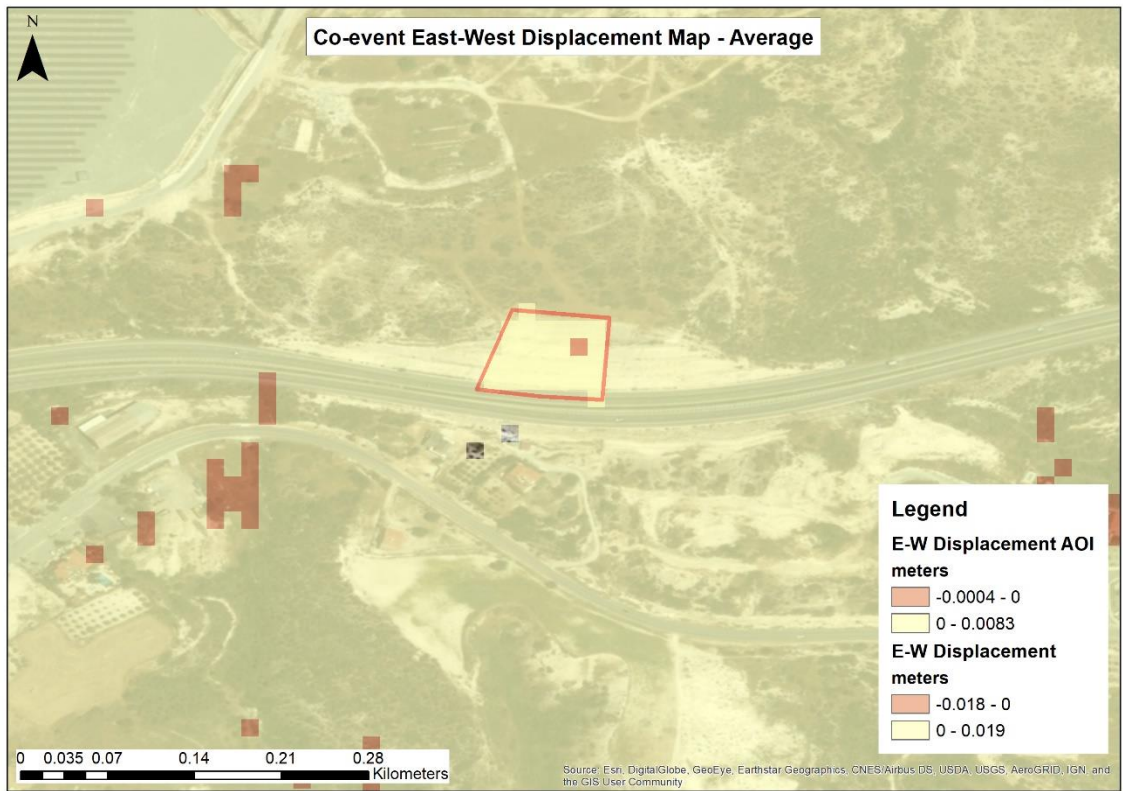
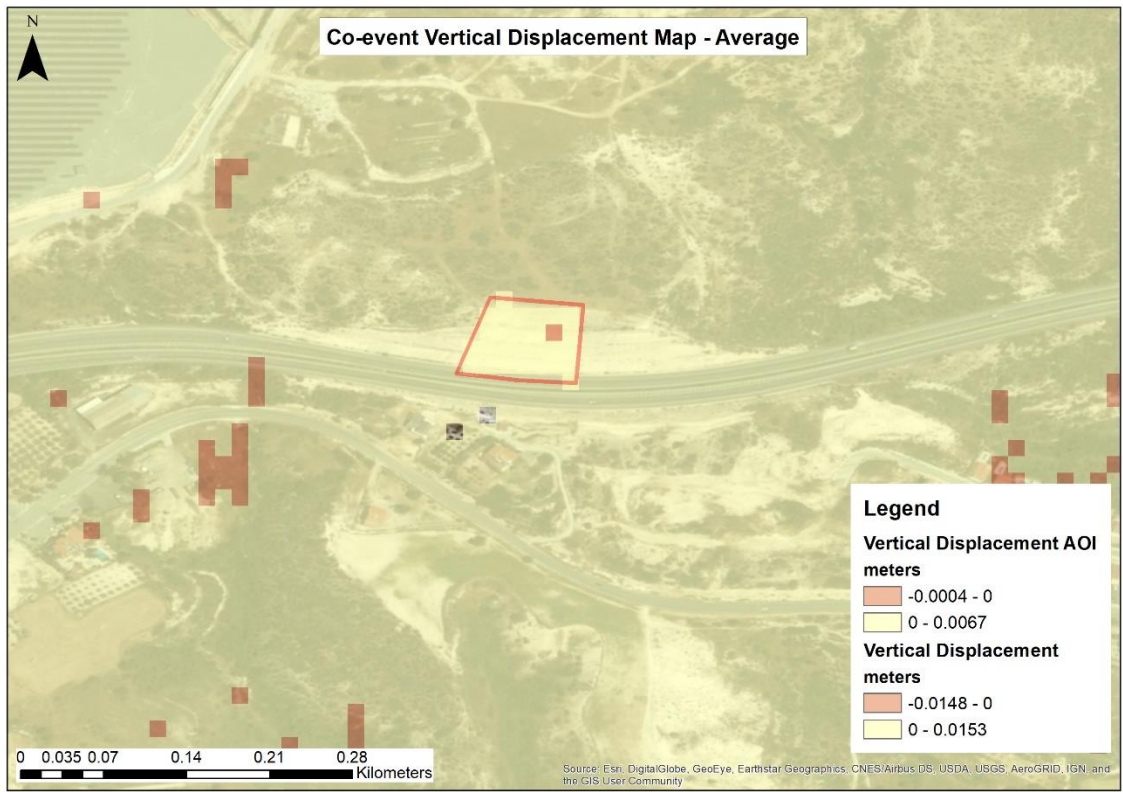
**Figure 89:** Average vertical displacement maps – Pissouri-Petra tou Romiou



**Figure 90:** Average E-W displacement maps – Pissouri-Petra tou Romiou

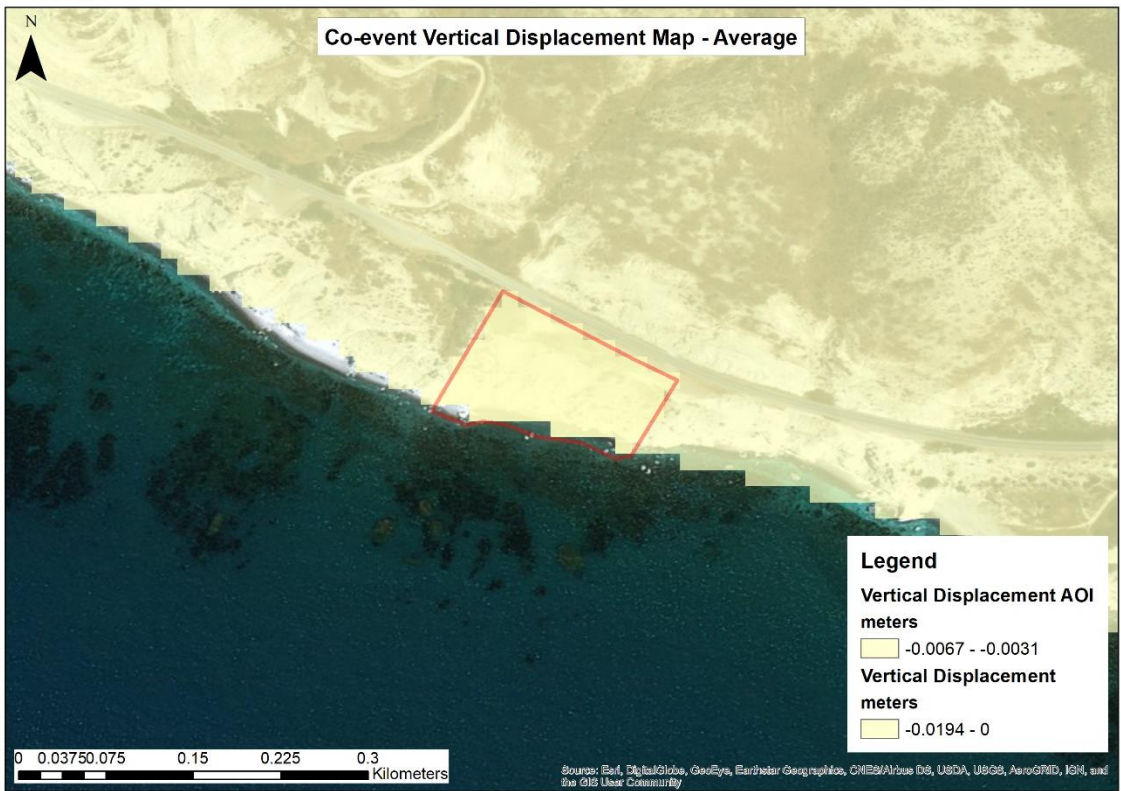
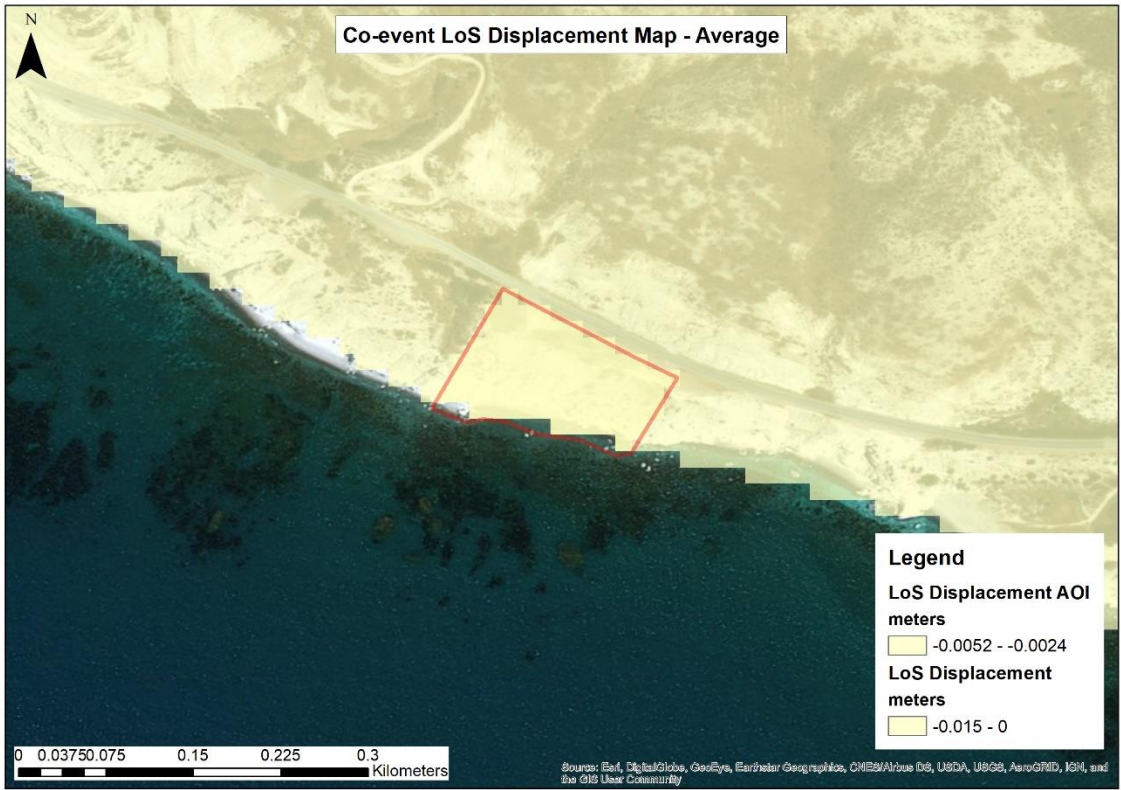
Due to the magnitude of the incident angle,  $\theta = 39.05^\circ$ , displacement values increased for the vertical and east-west components but not significantly, as expected, since the denominator in both equations was above 0.5, i.e. 0.777 for the vertical and 0.63 for the east-west displacement. The displacement maps from SNAP were then inserted in ArcGIS, where the sea was subtracted and displacement values were classified, for the development of the final displacement products, as presented in Figure 91 and Figure 92 for Pissouri and Petra tou Romiou respectively.





**Figure 91:** Final displacement maps – Missouri





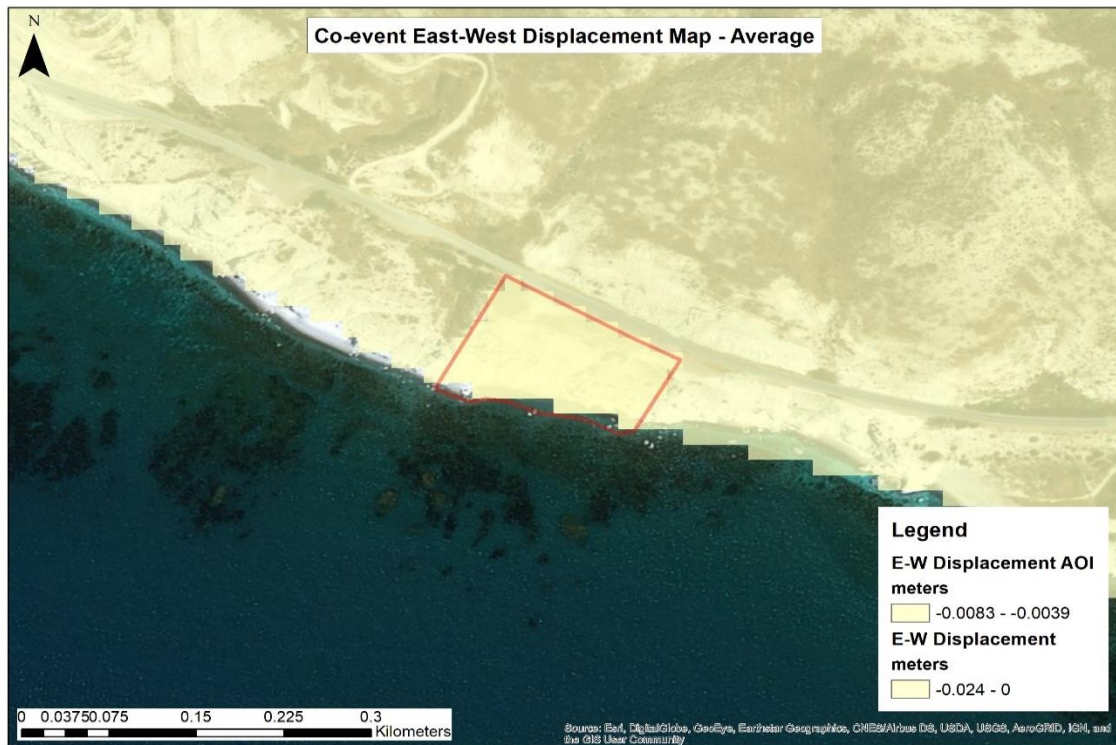


**Figure 92:** Final displacement maps – Petra tou Romiou

In Figure 91 and Figure 92 the legends at the bottom right, show the classes of displacement values within the Area of Interest (AOI) boundaries and these of the entire scene. The AOI is the area within the red polygon in each case.

The AOI near Pissouri shows a maximum uplift of 6.7mm with the average being 3.9mm (min +0.9mm and max +6.7mm). In the east-west direction the entire area seems to have moved to the east with the maximum shift being 8mm and the minimum 1.1mm (average eastwards +4.8mm). The only exception is a small area (a single pixel) at the northeast part of the AOI, which appears to have marginally subsided (-0.4mm) and moved to the west (-0.4mm). As the standard deviation for the 29 points that the AOI consists of, is  $\pm 1.8$ mm for the vertical displacement component and  $\pm 2.2$ mm for the East-West displacement, these subsiding and westbound movements are considered insignificant.

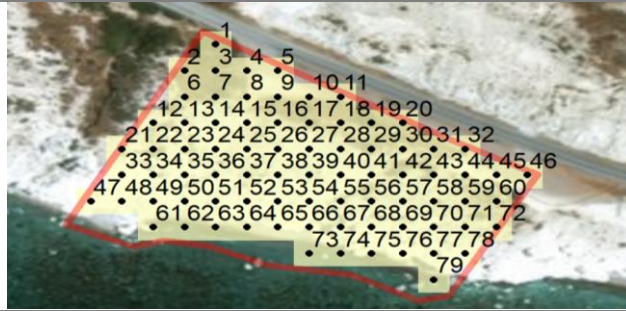
The AOI near Petra tou Romiou, which consists of 79 points, seems to have subsided by 5.3mm on average with the maximum subsidence (negative values) being 6.7mm and the minimum 3.1mm. Moreover, the AOI appears to have moved to the west by maximum 8.3mm and minimum 3.9mm (average 6.5mm). Standard deviations for the up-down and east-west displacements are  $\pm 0.8$ mm and  $\pm 0.9$ mm respectively. All displacement values are presented in Table 15 and Table 16.

**Table 15:** Displacement results AOI – Pissouri



Point	Displacement (m)		
	LOS (m)	Vertical (m)	East-West (m)
1	0.0033	0.0043	0.0053
2	0.0047	0.0061	0.0075
3	0.0027	0.0034	0.0042
4	0.0052	0.0067	0.0083
5	0.0010	0.0013	0.0016
6	0.0042	0.0054	0.0066
7	0.0041	0.0053	0.0065
8	0.0045	0.0058	0.0071
9	0.0020	0.0026	0.0032
10	0.0048	0.0061	0.0076
11	0.0007	0.0009	0.0011
12	-0.0003	-0.0004	-0.0004
13	0.0036	0.0047	0.0058
14	0.0028	0.0037	0.0045
15	0.0037	0.0048	0.0059
16	0.0019	0.0025	0.0031
17	0.0041	0.0052	0.0065
18	0.0013	0.0017	0.0021
19	0.0033	0.0042	0.0052
20	0.0035	0.0046	0.0056
21	0.0031	0.0039	0.0049
22	0.0023	0.0030	0.0037
23	0.0012	0.0015	0.0019
24	0.0033	0.0043	0.0053
25	0.0014	0.0018	0.0022
26	0.0034	0.0044	0.0054
27	0.0037	0.0048	0.0059
28	0.0042	0.0054	0.0067
<b>Average</b>	<b>0.0030</b>	<b>0.0039</b>	<b>0.0048</b>
<b>Min</b>	<b>-0.0003</b>	<b>-0.0004</b>	<b>-0.0004</b>
<b>Max</b>	<b>0.0052</b>	<b>0.0067</b>	<b>0.0083</b>
<b>St. Deviation</b>	<b>0.0014</b>	<b>0.0018</b>	<b>0.0022</b>

**Table 16:** Displacement results AOI – Petra tou Romiou



Point	Displacement			Point	Displacement		
	LOS (m)	Vertical (m)	East-West (m)		LOS (m)	Vertical (m)	East-West (m)
1	-0.0051	-0.0066	-0.0082	43	-0.0044	-0.0056	-0.0069
2	-0.0048	-0.0062	-0.0077	44	-0.0036	-0.0047	-0.0058
3	-0.0038	-0.0049	-0.0061	45	-0.0044	-0.0057	-0.0070
4	-0.0036	-0.0047	-0.0058	46	-0.0045	-0.0058	-0.0072
5	-0.0048	-0.0061	-0.0076	47	-0.0039	-0.0051	-0.0062
6	-0.0047	-0.0061	-0.0075	48	-0.0039	-0.0050	-0.0062
7	-0.0039	-0.0050	-0.0061	49	-0.0043	-0.0056	-0.0069
8	-0.0041	-0.0052	-0.0064	50	-0.0024	-0.0031	-0.0039
9	-0.0050	-0.0064	-0.0079	51	-0.0039	-0.0050	-0.0062
10	-0.0050	-0.0064	-0.0079	52	-0.0046	-0.0060	-0.0074
11	-0.0045	-0.0058	-0.0071	53	-0.0036	-0.0046	-0.0057
12	-0.0038	-0.0049	-0.0061	54	-0.0036	-0.0046	-0.0056
13	-0.0043	-0.0056	-0.0069	55	-0.0037	-0.0048	-0.0059
14	-0.0052	-0.0067	-0.0083	56	-0.0044	-0.0057	-0.0070
15	-0.0033	-0.0043	-0.0053	57	-0.0043	-0.0055	-0.0068
16	-0.0045	-0.0058	-0.0072	58	-0.0035	-0.0045	-0.0055
17	-0.0042	-0.0055	-0.0067	59	-0.0040	-0.0052	-0.0064
18	-0.0042	-0.0054	-0.0067	60	-0.0043	-0.0055	-0.0068
19	-0.0043	-0.0056	-0.0068	61	-0.0044	-0.0056	-0.0069
20	-0.0044	-0.0057	-0.0070	62	-0.0029	-0.0038	-0.0047
21	-0.0043	-0.0055	-0.0068	63	-0.0042	-0.0054	-0.0066
22	-0.0041	-0.0053	-0.0066	64	-0.0047	-0.0060	-0.0075
23	-0.0048	-0.0062	-0.0076	65	-0.0041	-0.0052	-0.0064
24	-0.0050	-0.0064	-0.0079	66	-0.0040	-0.0052	-0.0064
25	-0.0042	-0.0055	-0.0067	67	-0.0042	-0.0054	-0.0066
26	-0.0039	-0.0051	-0.0062	68	-0.0042	-0.0054	-0.0066
27	-0.0035	-0.0045	-0.0056	69	-0.0048	-0.0062	-0.0077
28	-0.0045	-0.0058	-0.0072	70	-0.0024	-0.0031	-0.0039
29	-0.0037	-0.0048	-0.0059	71	-0.0051	-0.0066	-0.0081
30	-0.0043	-0.0055	-0.0068	72	-0.0044	-0.0056	-0.0069
31	-0.0043	-0.0055	-0.0068	73	-0.0041	-0.0053	-0.0065
32	-0.0038	-0.0049	-0.0061	74	-0.0035	-0.0045	-0.0056
33	-0.0037	-0.0048	-0.0059	75	-0.0041	-0.0053	-0.0065
34	-0.0045	-0.0057	-0.0071	76	-0.0050	-0.0065	-0.0080
35	-0.0037	-0.0047	-0.0058	77	-0.0030	-0.0039	-0.0048
36	-0.0043	-0.0055	-0.0068	78	-0.0045	-0.0058	-0.0071
37	-0.0047	-0.0061	-0.0075	79	-0.0040	-0.0052	-0.0064
38	-0.0033	-0.0042	-0.0052	<b>Average</b>	<b>-0.0041</b>	<b>-0.0053</b>	<b>-0.0065</b>
39	-0.0026	-0.0033	-0.0041	<b>Min</b>	<b>-0.0052</b>	<b>-0.0067</b>	<b>-0.0083</b>
40	-0.0037	-0.0047	-0.0058	<b>Max</b>	<b>-0.0024</b>	<b>-0.0031</b>	<b>-0.0039</b>
41	-0.0044	-0.0056	-0.0069	<b>St.</b>	<b>0.0006</b>	<b>0.0008</b>	<b>0.0009</b>
42	-0.0040	-0.0051	-0.0063	<b>Deviation</b>			

Based on the information obtained through photos of the landslide that were kindly provided by the Geological Survey Department, as well as from site visits, the DInSAR displacement results are underestimated.

A proper selection of the suitable images for the case study was performed, with minimum temporal baselines and avoiding, at the same time, geometric distortion issues, that could arise from the area's topography. Moreover, a stack of interferograms was created with six individual co-event interferometric pairs in order to minimise the atmospheric effect on the displacement calculations and provide us with displacement in the vertical and east-west directions.

However, as found in literature, the moderate spatial resolution of the IW swath images for Level-1 SLC products (2.7 x 22m to 3.5 x 22m), that are available for Cyprus, has proven to be inadequate for the detailed study and monitoring of more complex ground displacement phenomena, such as fast-moving landslides and slope deformations (Kyriou and Nikolakopoulos, 2018; Kovács *et al.*, 2019).

This is mainly due to a limitation called temporal phase aliasing, which affects the accuracy of DInSAR results due to issues created during the phase unwrapping step of the DInSAR methodology (Rabus and Pichierri, 2018; Manconi, 2019), when the displacement of a pixel or an area under investigation exceeds the value of  $\lambda/4$  between two consecutive satellite acquisitions that form an interferometric SAR pair (Moretto *et al.*, 2017; Manconi *et al.*, 2018).  $\lambda$  is the wavelength of the SAR sensor, which in the case of Sentinel-1 satellite's C-band is approximately 5.55cm. In fact, this limitation can lead to confusing results as any ground deformation, that is observed between two consecutive SAR acquisitions, exceeds this threshold of 1.39cm, in the case of Sentinel-1, and can be two, three or n times greater than this value, can be underestimated as all these deformations produce the same observed phase.

Furthermore, the coherence values were studied in both areas of interest to investigate the reason behind the small displacement values calculated through the proposed DInSAR methodology. The coherence products were geo-located and stacked and the average maps were produced via the Band Maths module. The results for Pissouri and Petra tou Romiou are presented in Figure 93 and Figure 94 respectively.

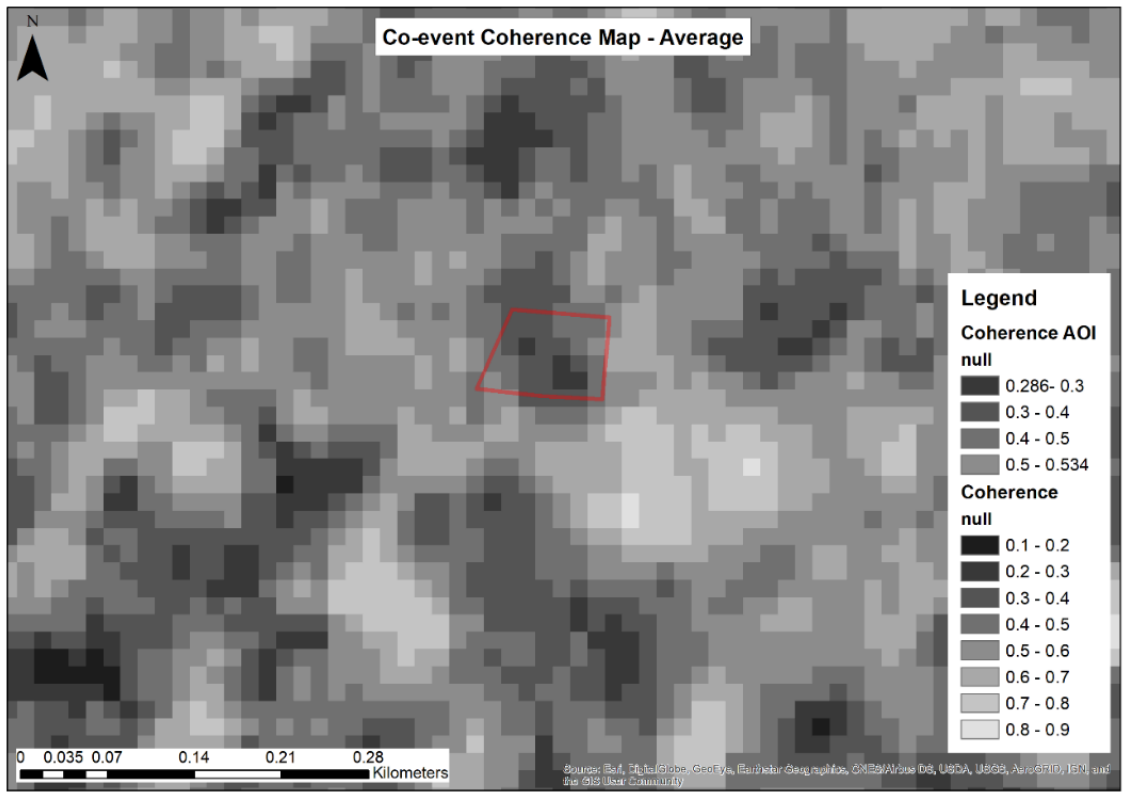


**Figure 93:** Average coherence map – Pissouri

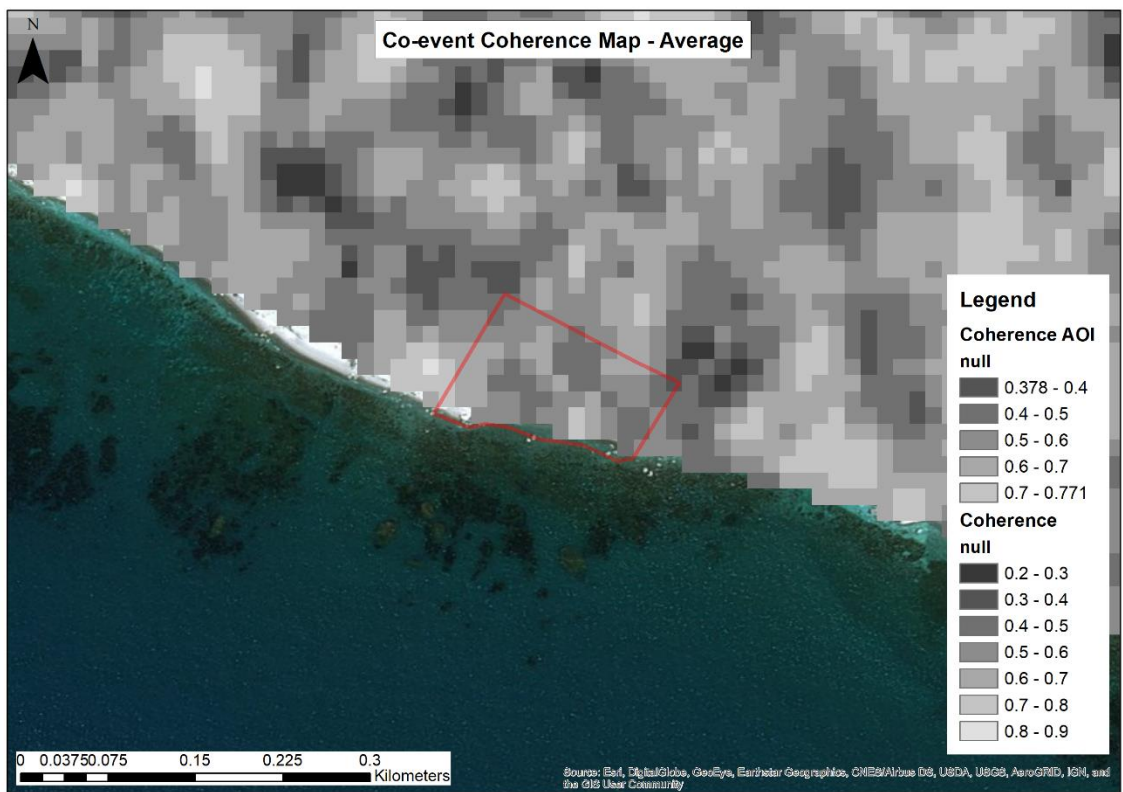


**Figure 94:** Average coherence map – Petra tou Romiou

In both cases, within the two AOIs, coherence values are lower compared to the entire scenes. However, there are other areas in both scenes individually that are characterised by similar values. The low coherence values could be due to the residing vegetation surrounding the case study site near Pissouri and the vegetation towards the north and west from the AOI near Petra tou Romiou (Zebker and Villasenor, 1992).

Additionally, as both events were induced by heavy rainfall, this is an important factor along with changes in soil moisture that can alter the radar signal significantly leading to loss of coherence, as analysed in literature (Zebker and Villasenor, 1992; Rocca *et al.*, 2000; Bouaraba *et al.*, 2014; Closson and Milisavljevic, 2017). However, from a first overview of the coherence maps, there seems to be valuable information regarding the extents of the two landslide events that took place on the 15<sup>th</sup> and 20<sup>th</sup> of February 2019.

To remove the effect of vegetation from the phase decorrelation (coherence loss), NDVI was calculated from *Equation 10* within SNAP, based on a Sentinel-2 satellite image downloaded from the Copernicus open access hub, dated February 3, 2019 (S2A\_MSIL2A\_20190203T083141\_N0211\_R021\_T36SVD\_20190203T111709). This was the closest to the landslides cloud-free and atmospherically corrected image (Level-2A).

$$\text{NDVI} = \frac{\text{NIR} - \text{Red}}{\text{NIR} + \text{Red}} \quad (\text{Eq. } 10)$$

A NDVI based mask was created, as seen in Figure 95, based on the fact that for NDVI values greater than 0.2, vegetation is present. From Literature, NDVI values range from -1 to +1, with the negative values of NDVI generally corresponding to water, whereas NDVI values between -0.1 and +0.2 usually represent barren areas of rock, sand, or snow (Sentinel Hub, no date).

Thus, all areas with  $\text{NDVI} > 0.2$ , were removed from the final coherence maps to exclude the vegetation's impact on phase decorrelation in the two areas of interest. The removal of the areas of vegetation from the coherence maps presented in Figure 93 and Figure 94 was performed in ArcGIS using the Raster Calculator tool, following a reclassification of the NDVI values in appropriate classes. The results are presented in Figure 96 and Figure 97.

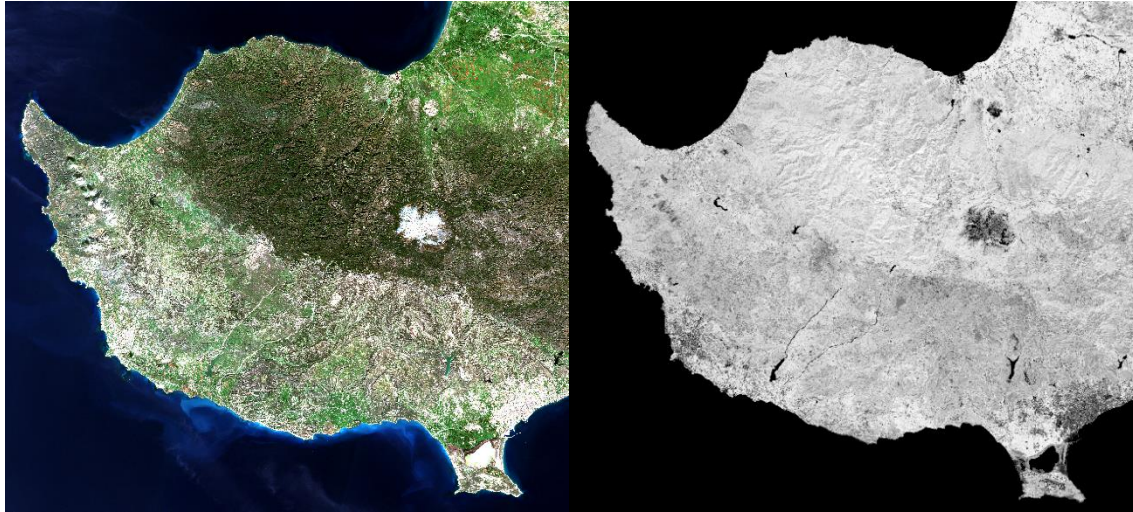


**Figure 95:** RGB (left) and NDVI (right) from Sentinel-2 image

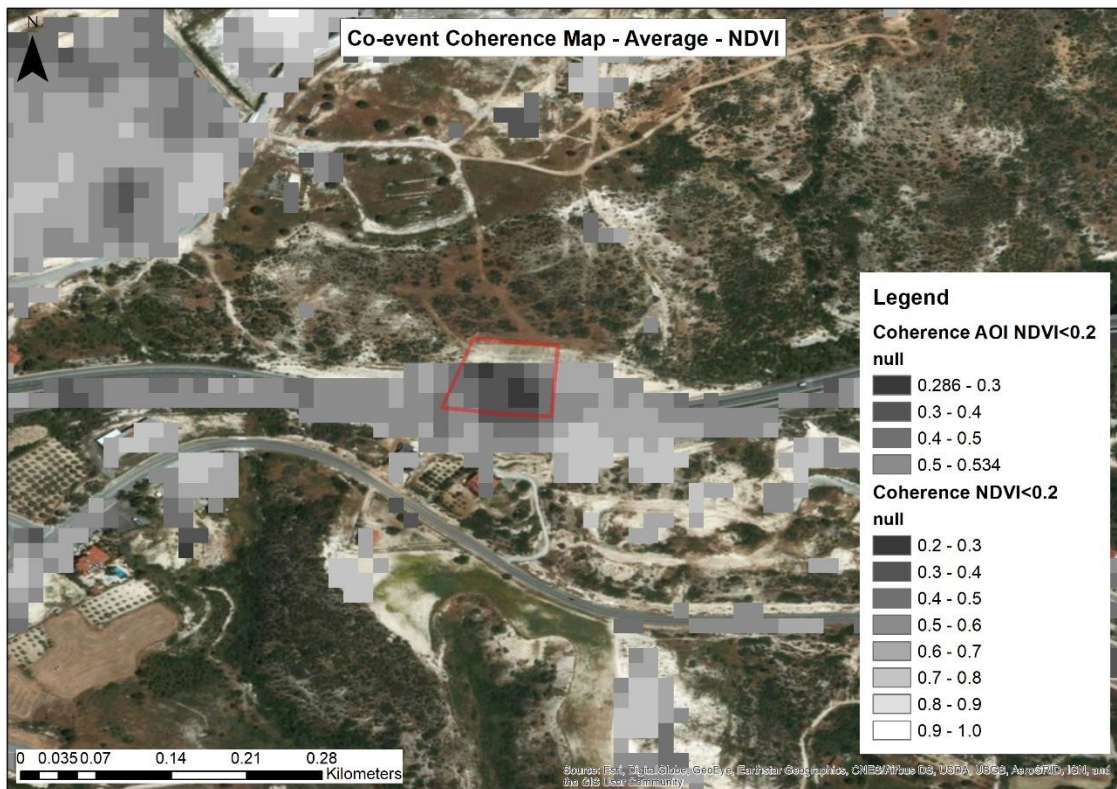



**Figure 96:** Average coherence map (NDVI mask) – Pissouri

Indeed, at the case study of the landslide by the A6 Paphos-Limassol motorway near Pissouri, there seems to be a substantial match, of a scale of 85%, between the area of landslide and the area of very low coherence ( $<0.4$ ). The areas to the north, northwest and east of the landslide area, are covered with vegetation, a matter that could explain the loss



of coherence between the SAR acquisitions, as supported by the Literature. These were removed through the application of the NDVI mask. However, due to the fact, that there is very limited vegetation at the specific slope, with the exception of the part at the top of AOI, within the determined area of landslide, other factors, such as the heavy rainfall or a sudden change in the topography could be the reasons for such a substantial phase decorrelation. All the coherence values for the AOI are presented in Table 17.

**Table 17:** Coherence results AOI – Pissouri



Point	Coherence (All)	Coherence (NDVI<0.2)
1	0.3441	
2	0.3071	
3	0.3169	
4	0.3605	
5	0.4915	
6	0.4440	
7	0.4758	
8	0.3758	0.3758
9	0.3000	0.3000
10	0.3171	0.3171
11	0.3999	0.3999
12	0.4390	0.4390
13	0.5345	0.5345
14	0.4841	0.4841
15	0.4178	0.4178
16	0.3522	0.3522
17	0.3146	0.3146
18	0.2938	0.2938
19	0.3491	0.3491
20	0.4921	0.4921
21	0.5150	0.5150
22	0.4578	0.4578
23	0.3608	0.3608
24	0.3169	0.3169
25	0.2869	0.2869
26	0.2856	0.2856
27	0.4383	0.4383
28	0.4400	0.4400
<b>Average</b>	<b>0.3897</b>	<b>0.3891</b>
<b>Min</b>	<b>0.2856</b>	<b>0.2856</b>
<b>Max</b>	<b>0.5345</b>	<b>0.5345</b>
<b>St. Deviation</b>	<b>0.0778</b>	<b>0.0799</b>

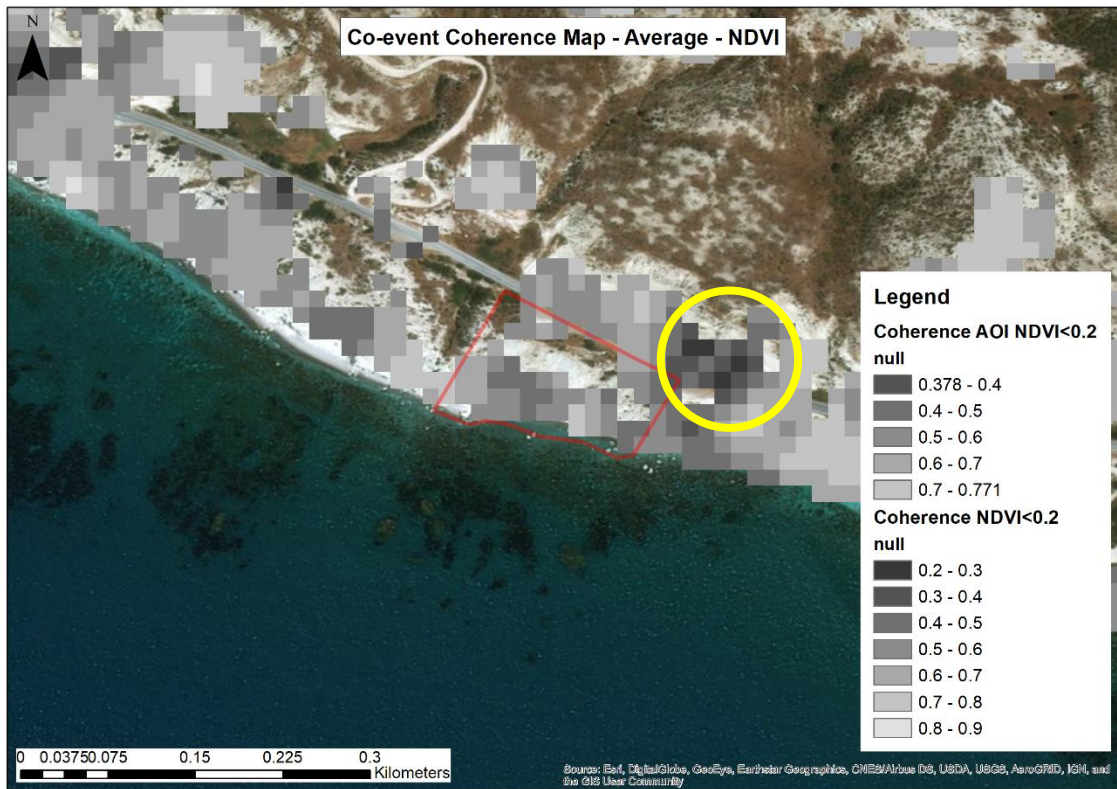
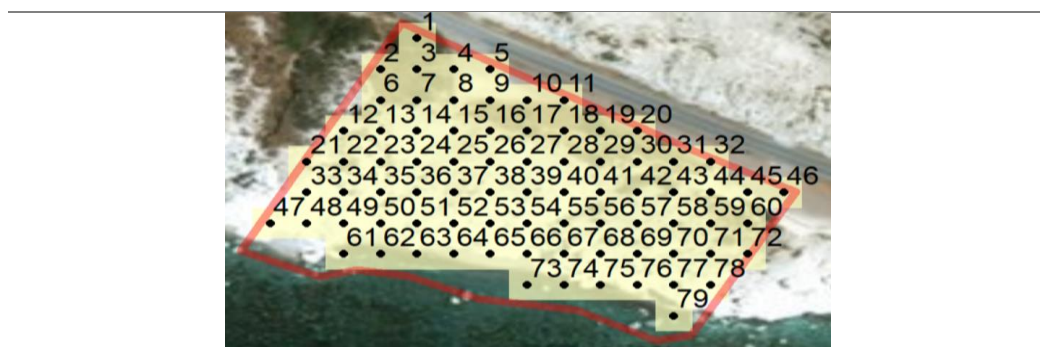


**Figure 97:** Average coherence map (NDVI mask) – Petra tou Romiou

At the second case study, near Petra tou Romiou, there are also indications that a sudden change in the topography has occurred within the predefined landslide area. However, there is some sparse vegetation that resides within the defined AOI and in close proximity to the area. The vast majority of the vegetation was successfully removed with the application of the NDVI mask, as seen from Figure 97, especially to the north and northwest part of the scene. Apart from the AOI, there seems to be an area (yellow circle) where there are low coherence values ( $<0.4$ ) that needs to be investigated further. All the coherence results for the AOI are presented in Table 18.

**Table 18:** Coherence results AOI – Petra tou Romiou



Point	Coherence (All)	Coherence (NDVI<0.2)	Point	Coherence (All)	Coherence (NDVI<0.2)
1	0.4324		43	0.5445	0.5445
2	0.4823		44	0.5436	0.5436
3	0.5146		45	0.4571	0.4571
4	0.5741	0.5741	46	0.3778	0.3778
5	0.5662		47	0.7216	0.7216
6	0.5705		48	0.6669	0.6669
7	0.5990	0.5990	49	0.6336	0.6336
8	0.5999	0.5999	50	0.5827	0.5827
9	0.6303	0.6303	51	0.5239	0.5239
10	0.5679	0.5679	52	0.4030	0.4030
11	0.4896		53	0.4808	0.4808
12	0.6002		54	0.5525	0.5525
13	0.6008	0.6008	55	0.5976	0.5976
14	0.5942		56	0.6195	0.6195
15	0.6543		57	0.4964	0.4964
16	0.6677		58	0.5091	
17	0.4994		59	0.5049	0.5049
18	0.4268		60	0.4224	0.4224
19	0.4896		61	0.5911	0.5911
20	0.5404		62	0.5994	0.5994
21	0.6757	0.6757	63	0.5681	0.5681
22	0.6106	0.6106	64	0.4204	0.4204
23	0.5409	0.5409	65	0.5102	0.5102
24	0.4919	0.4919	66	0.5765	0.5765
25	0.5545		67	0.7044	0.7044
26	0.6109		68	0.6359	0.6359
27	0.4970		69	0.5026	0.5026
28	0.4030		70	0.4156	
29	0.4269		71	0.4302	
30	0.6198		72	0.5089	0.5089
31	0.6230	0.6230	73	0.5922	
32	0.6091	0.6091	74	0.7713	0.7713
33	0.6732	0.6732	75	0.6561	0.6561
34	0.6384	0.6384	76	0.5763	0.5763
35	0.4970	0.4970	77	0.4256	0.4256
36	0.4326	0.4326	78	0.4423	0.4423
37	0.4719	0.4719	79	0.4410	0.4410
38	0.5174	0.5174	<b>Average</b>	<b>0.5457</b>	<b>0.5583</b>
39	0.6175	0.6175	<b>Min</b>	<b>0.3778</b>	<b>0.3778</b>
40	0.4702		<b>Max</b>	<b>0.7713</b>	<b>0.7713</b>
41	0.4824		<b>St. Deviation</b>	<b>0.0855</b>	<b>0.0883</b>
42	0.5373				

Following the findings from the coherence analysis, the Coherent Change Detection (CCD) methodology was applied, which is a part of the DInSAR process as the coherence maps are outputs of the Interferogram formation step. Due to the nature and complexity of the natural hazard phenomenon under investigation, another 22 SAR images were downloaded for the period starting from 11<sup>th</sup> of January 2019 until the 12<sup>th</sup> of April 2019. These were used to study the development of landslides further. The detailed processing that was carried out is presented in detail in *section 4.3 Implementation of CCD methodology*.

### 4.3 Implementation of CCD methodology

After the application of DInSAR methodology with the six selected co-event interferometric pairs, using a total of 10 SAR images (6 S1A and 4 S1B), another twenty-four SAR images were downloaded for the period starting from 11<sup>th</sup> of January 2019 until the 12<sup>th</sup> of April 2019.

This would assist in the direction to conduct a more comprehensive study of the landslides, starting one month before the landslides took place and one month following their occurrence. Due to the nature and complexity of the natural hazard phenomena under investigation, the study of the evolution of the landslides was considered the way forward towards the monitoring and rapid detection of the events that will in turn enable the establishment of an early warning system.

From the two areas of interest that landslides took place, within the case study Pissouri – Petra tou Romiou, the area by the A6 motorway was chosen to study the efficiency of the CCD methodology for monitoring the landslide impact, as all the details about the specific landslide, such as the exact landslide outline, the extents of construction works and their duration, as well as the exact date of the road re-opening back to the traffic were known.

Indeed, following the instructions by the Geological Survey Department, a smaller polygon (light blue) was used to define the exact landslide extents (Figure 98). Any further analysis, from this point forward was carried out based on this AOI.



**Figure 98:** The extents of the February 15, 2019 landslide near Pissouri

The 32 SAR images (16 S1A and 16 S1B) in total were combined into twenty-eight consecutive interferometric SAR pairs, fourteen ascending and fourteen descending, with all images in the respective pairs being acquired with a temporal baseline of 12 days to minimise the atmospheric and topography effects, as analysed in *chapter 2 Literature review*. The interferometric SAR pairs are presented in Table 19, in ascending order based on the master image acquisition date.

**Table 19:** SAR image interferometric pairs – Pissouri-Petra tou Romiou

No.	Platform	Date (master)	Date (slave)	Pass direction	Temp. baseline	Perp. baseline	Modelled coherence
1	Sentinel-1A	11/01/2019	23/01/2019	Ascending	12 days	16.36m	0.98
2	Sentinel-1A	12/01/2019	24/01/2019	Descending	12 days	108.39m	0.90
3	Sentinel-1B	17/01/2019	29/01/2019	Ascending	12 days	43.40m	0.95
4	Sentinel-1B	18/01/2019	30/01/2019	Descending	12 days	34.79m	0.96
5	Sentinel-1A	23/01/2019	04/02/2019	Ascending	12 days	155.91m	0.86
6	Sentinel-1A	24/01/2019	05/02/2019	Descending	12 days	79.26m	0.92
7	Sentinel-1B	29/01/2019	10/02/2019	Ascending	12 days	23.22m	0.97
8	Sentinel-1B	30/01/2019	11/02/2019	Descending	12 days	46.48m	0.95
9	Sentinel-1A	04/02/2019	16/02/2019	Ascending	12 days	102.44m	0.90
10	Sentinel-1A	05/02/2019	17/02/2019	Descending	12 days	12.46m	0.98
11	Sentinel-1B	10/02/2019	22/02/2019	Ascending	12 days	17.44m	0.97
12	Sentinel-1B	11/02/2019	23/02/2019	Descending	12 days	86.63m	0.92
13	Sentinel-1A	16/02/2019	28/02/2019	Ascending	12 days	84.72m	0.92
14	Sentinel-1A	17/02/2019	01/03/2019	Descending	12 days	14.88m	0.97
15	Sentinel-1B	22/02/2019	06/03/2019	Ascending	12 days	63.25m	0.94
16	Sentinel-1B	23/02/2019	07/03/2019	Descending	12 days	10.12m	0.98
17	Sentinel-1A	28/02/2019	12/03/2019	Ascending	12 days	3.15m	0.99
18	Sentinel-1A	01/03/2019	13/03/2019	Descending	12 days	87.86m	0.92
19	Sentinel-1B	06/03/2019	18/03/2019	Ascending	12 days	30.08m	0.96
20	Sentinel-1B	07/03/2019	19/03/2019	Descending	12 days	75.78m	0.93
21	Sentinel-1A	12/03/2019	24/03/2019	Ascending	12 days	17.67m	0.97
22	Sentinel-1A	13/03/2019	25/03/2019	Descending	12 days	63.94m	0.93
23	Sentinel-1B	18/03/2019	30/03/2019	Ascending	12 days	82.29m	0.92
24	Sentinel-1B	19/03/2019	31/03/2019	Descending	12 days	9.54m	0.98
25	Sentinel-1A	24/03/2019	05/04/2019	Ascending	12 days	51.98m	0.94
26	Sentinel-1A	25/03/2019	06/04/2019	Descending	12 days	57.14m	0.94
27	Sentinel-1B	30/03/2019	11/04/2019	Ascending	12 days	30.86m	0.96
28	Sentinel-1B	31/03/2019	12/04/2019	Descending	12 days	24.92m	0.97

The timeline of the SAR acquisitions and the landslide related events, such as rehabilitation works, road opened to traffic, etc., are presented in Figure 99.

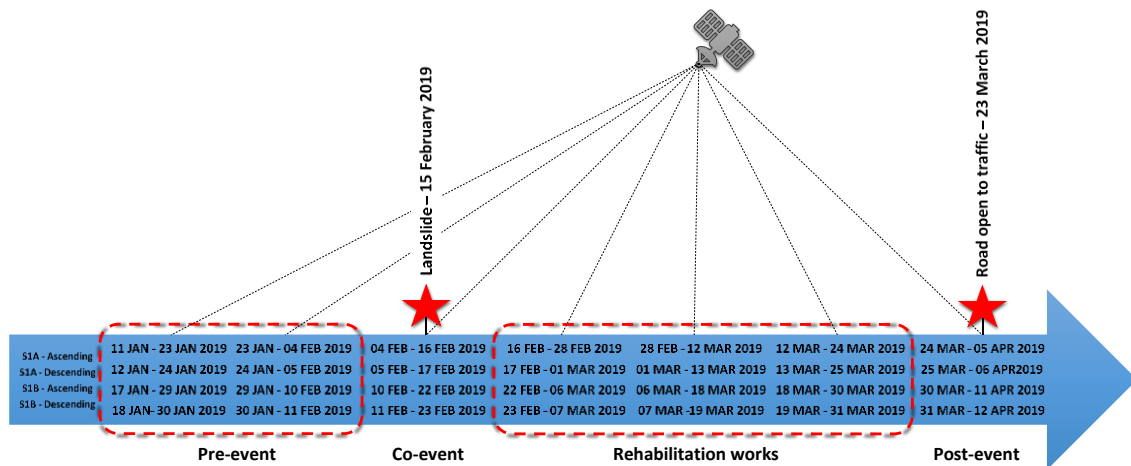


**Figure 99:** Timeline of SAR acquisitions and events

The perpendicular baselines for all 28 SAR pairs are shorter than the threshold of 200m that was set. Moreover, all pairs show high modelled coherence close to or greater than 0.90. Twenty-eight coherence maps were developed following the same methodology, as in DInSAR, through the Interferogram formation step, as shown below in Figure 100.

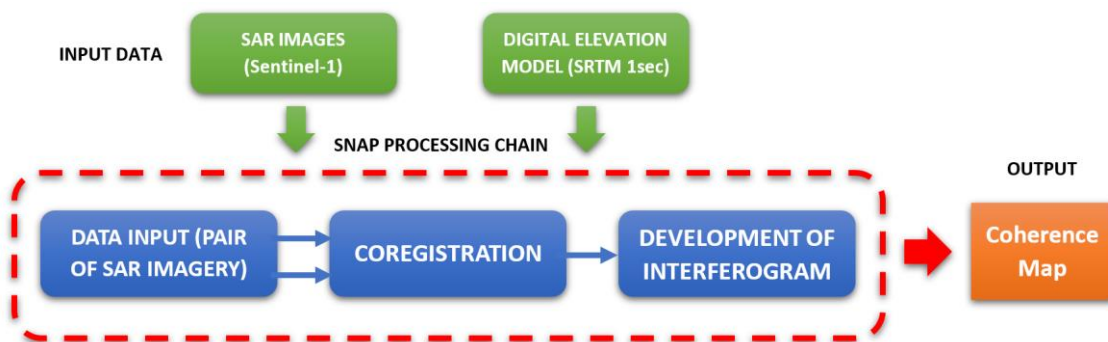


**Figure 100:** Coherence maps development methodology

These coherence maps were then geo-located using Range-Doppler Terrain correction and stacked separately using the coherence map of the first interferometric pair according to the satellite (Sentinel-1A / Sentinel-1B) and the satellite pass direction (ascending / descending). In total, four different stacks of coherence maps were developed, that were then stacked altogether using the coherence map dated 11 January 2019 – 23 January 2019 as the master image, to assist in the comparison of results on the same basis.

The coherence maps produced after stacking and geolocating, for Sentinel-1A ascending, Sentinel-1A descending, Sentinel-1B ascending and Sentinel-1B descending are presented in Figure 101, Figure 102, Figure 103 and Figure 104 respectively.

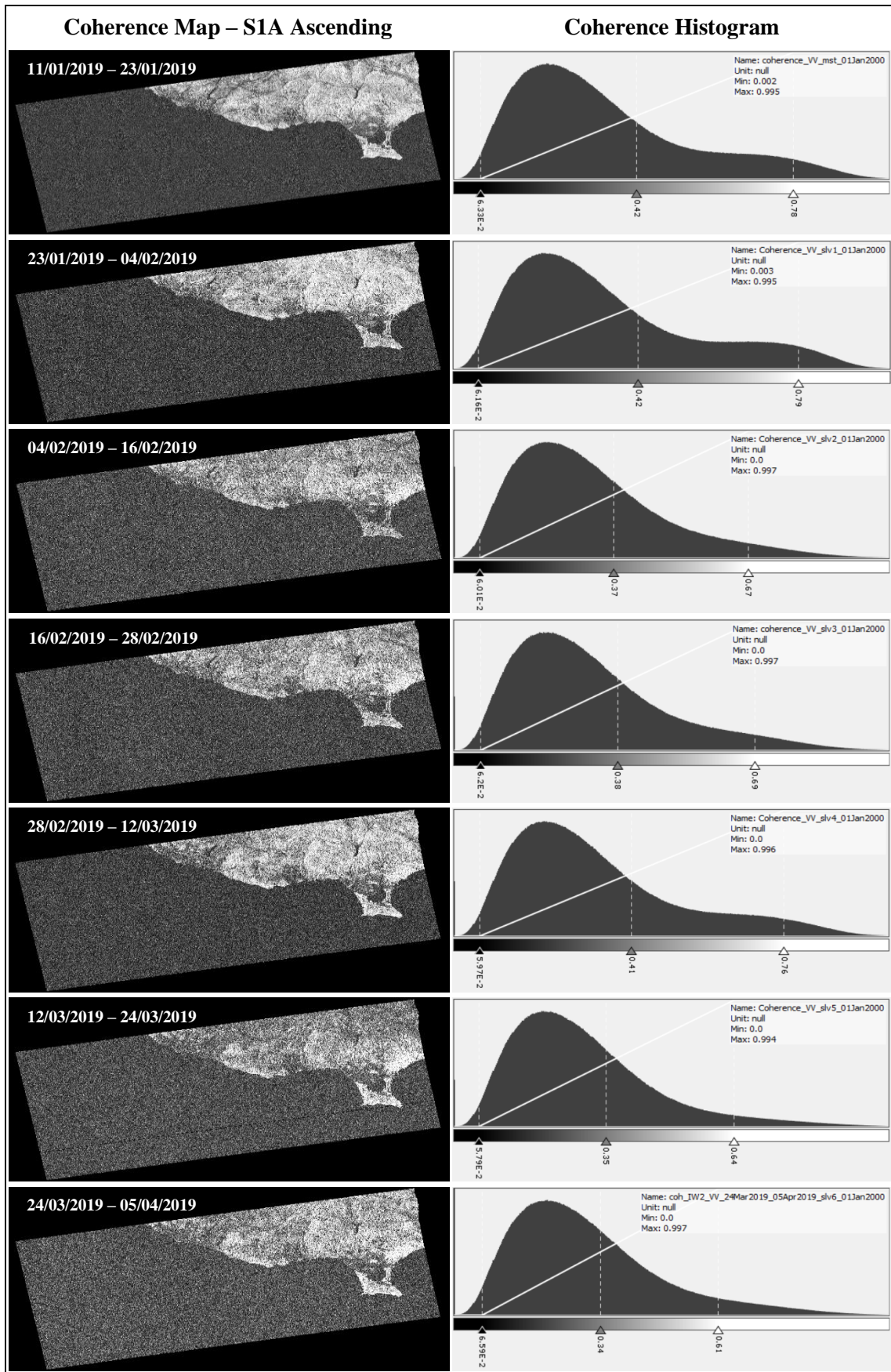


Figure 101: Coherence maps – Sentinel-1A ascending

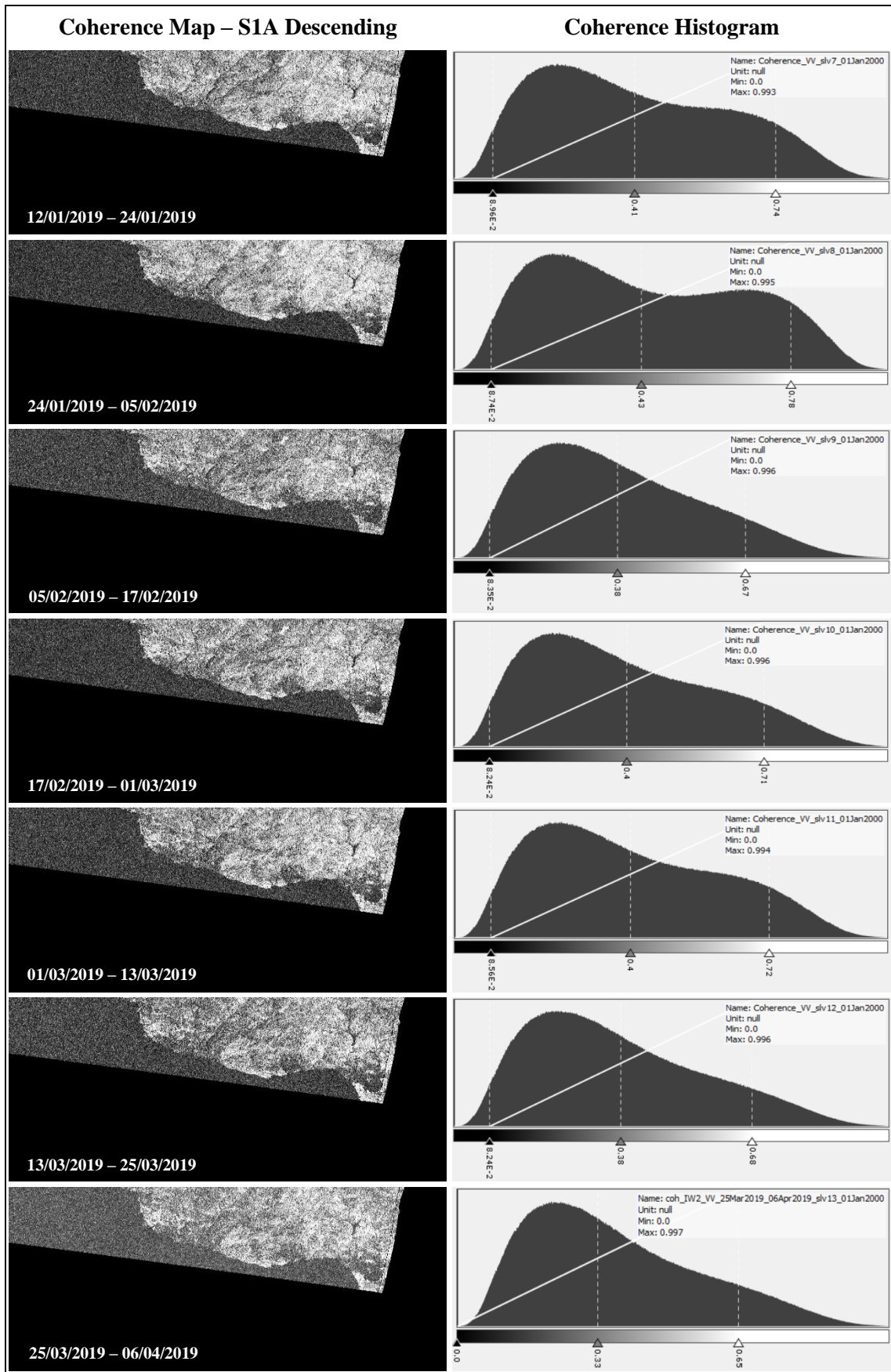


Figure 102: Coherence maps – Sentinel-1A descending



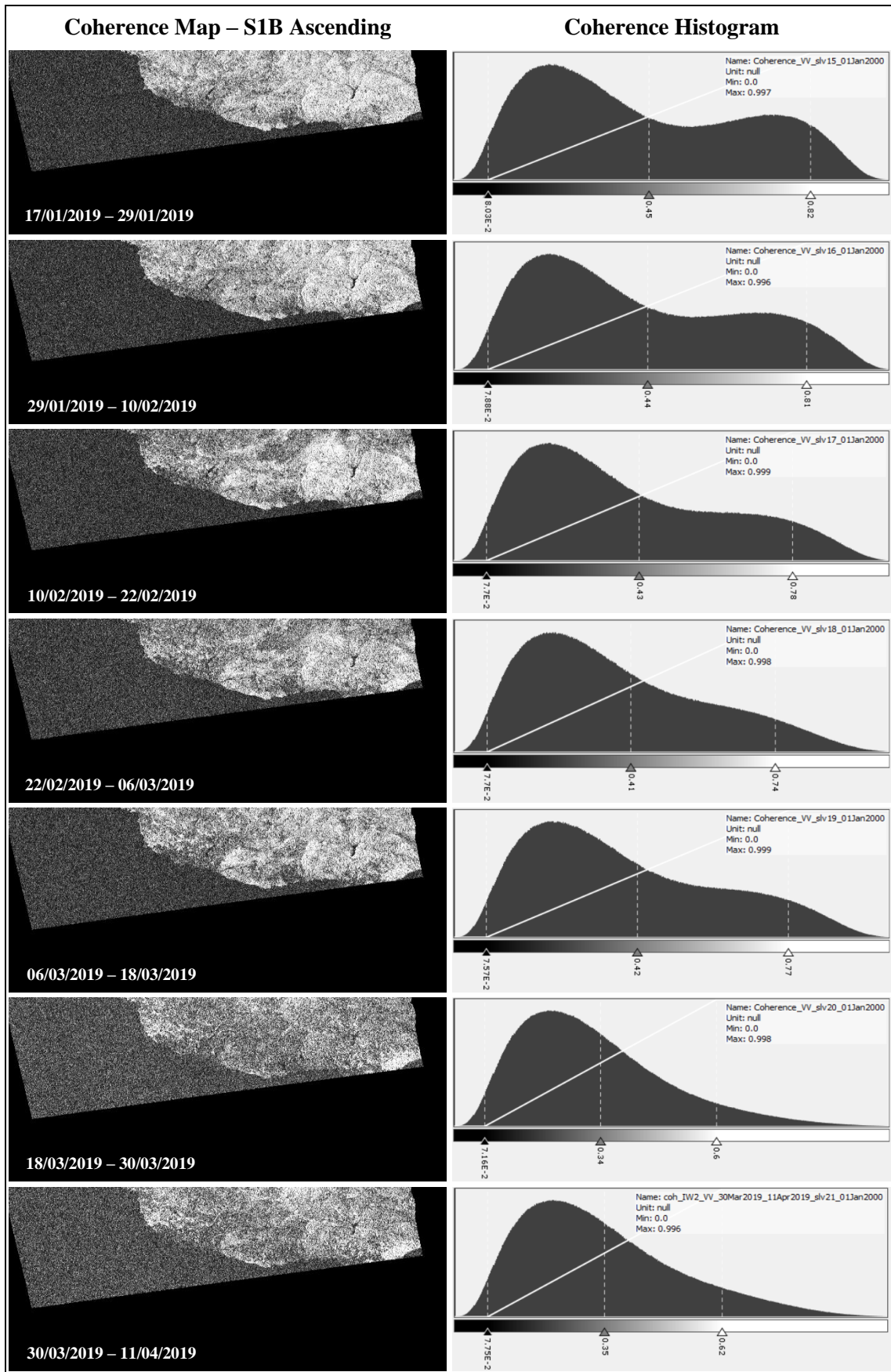


Figure 103: Coherence maps – Sentinel-1B ascending

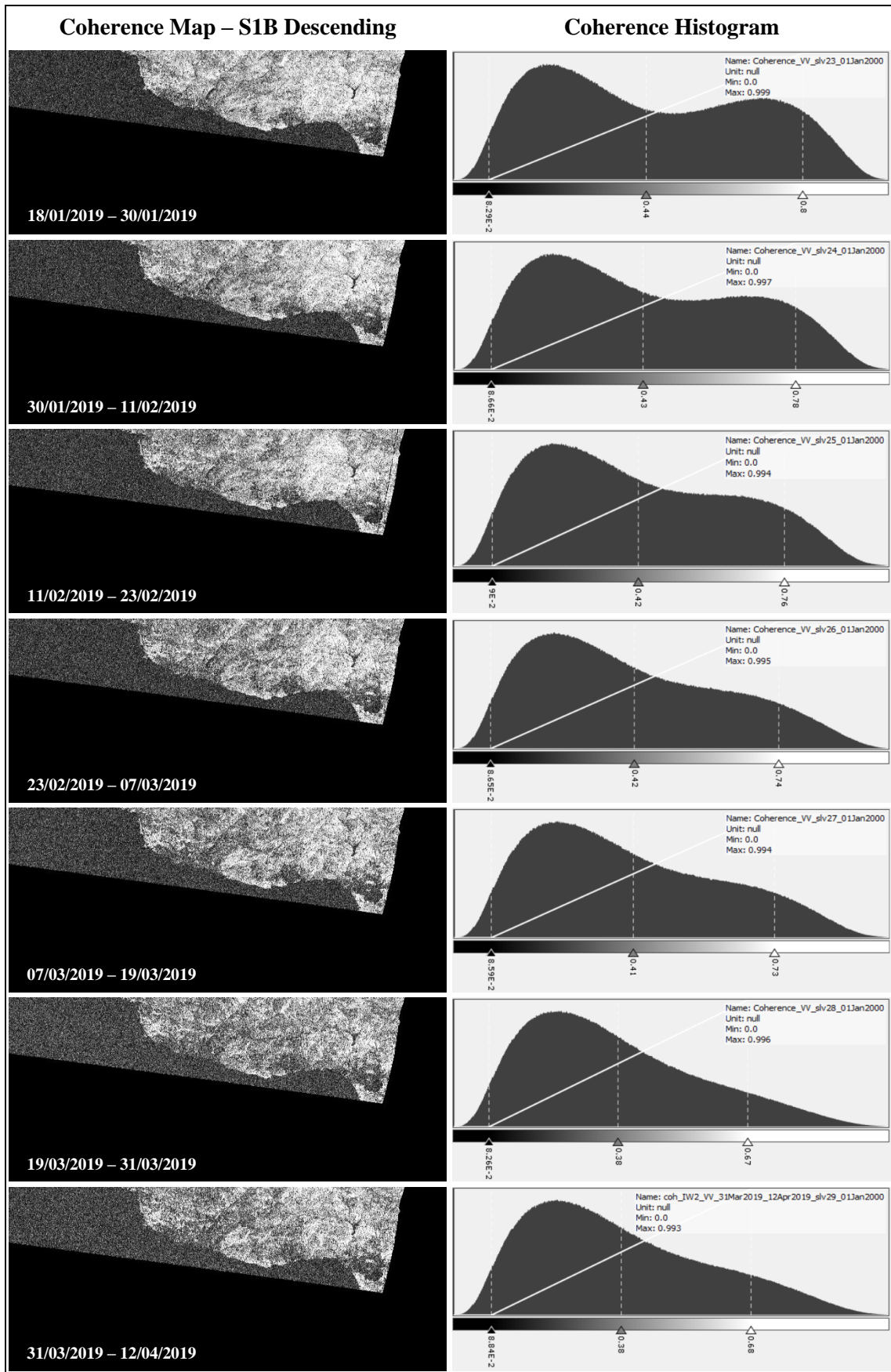
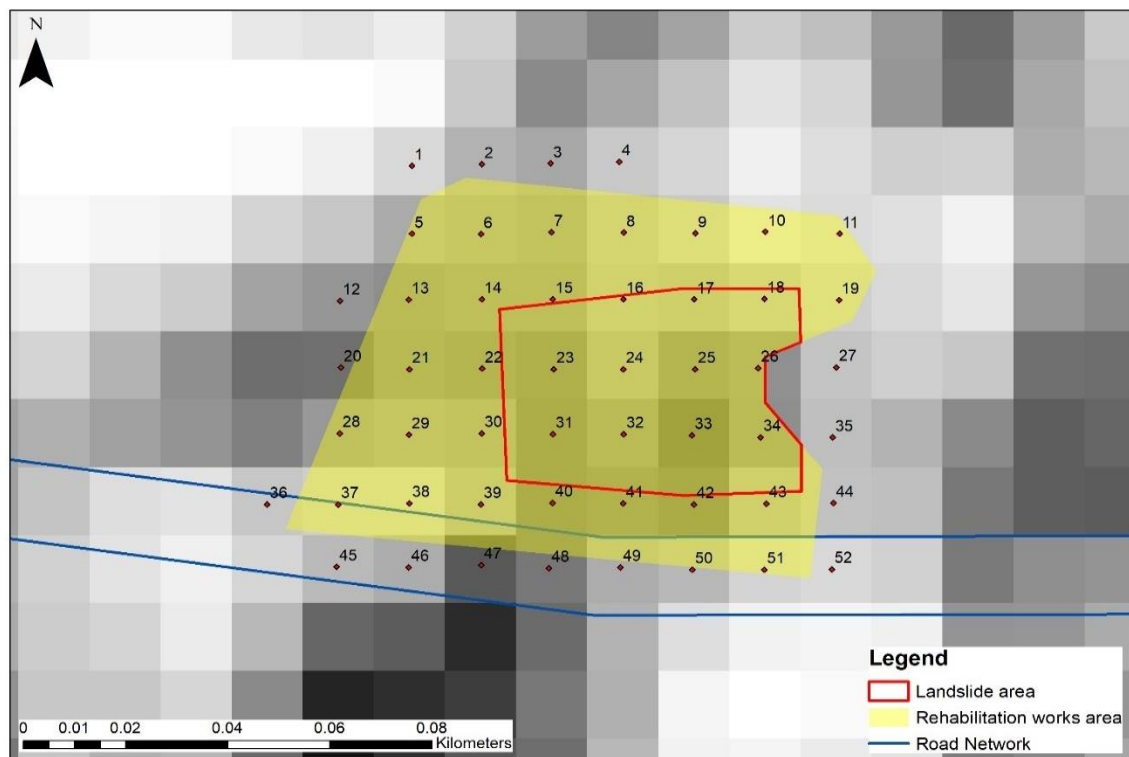


Figure 104: Coherence maps – Sentinel-1B descending

### 4.3.1 Statistical analysis

Both landslides affected critical infrastructures, thus it is of great importance to raise awareness of an upcoming danger in a timely manner. As noted in literature, it is the first time that the CCD methodology is applied for landslides induced by heavy rainfall, thus the evolution of the natural hazard needed to be investigated in detail.

A statistical analysis of all results is carried out in the present section. All coherence maps produced in SNAP were inserted in ArcGIS, where the sea was subtracted, and coherence values were classified appropriately for the development of the final coherence products. For the analysis of the data, a grid of 52 points (Figure 105) was created within ArcGIS, that covers the entire area where rehabilitation works took place, starting the day after the landslide occurred, i.e. 15 February 2019, until the road was opened again to the traffic (23 March 2019). From these 52 points, twenty points lie within the landslide area, which was defined after the directions of the Geological Survey Department.



**Figure 105:** Coherence maps – Point grid

A thorough analysis was carried out based on the coherence values obtained in the two aforementioned areas, with the first images dated one month before the landslide (11-18 January 2019), and the last ones nearly one month after the landslide (5-12 April 2019).

The coherence values obtained from Sentinel-1A and 1B images, for each pass direction, were studied separately for each of the two areas, and the results are presented below.

**Table 20:** Coherence values – Sentinel-1A ascending

Id	Coherence							Average
	11JAN-23JAN	23JAN-04FEB	04FEB-16FEB	16FEB-28FEB	28FEB-12MAR	12MAR-24MAR	24MAR-05APR	
Point 1	0.7642	0.7077	0.5645	0.1937	0.6852	0.4084	0.4544	0.5397
Point 2	0.6455	0.4138	0.5054	0.3291	0.6025	0.4922	0.3450	0.4762
Point 3	0.6110	0.3884	0.4400	0.4179	0.4360	0.6069	0.3703	0.4672
Point 4	0.7161	0.2587	0.4459	0.4244	0.3906	0.4635	0.3965	0.4423
Point 5	0.6210	0.6861	0.5884	0.2838	0.4518	0.4225	0.3402	0.4848
Point 6	0.5910	0.6046	0.4847	0.3900	0.5052	0.5059	0.4283	0.5014
Point 7	0.5703	0.6844	0.4420	0.3613	0.3995	0.5315	0.5497	0.5055
Point 8	0.6697	0.5525	0.4934	0.3486	0.4308	0.4937	0.5709	0.5085
Point 9	0.7157	0.4870	0.4261	0.3889	0.4290	0.4112	0.7429	0.5144
Point 10	0.8028	0.3067	0.5196	0.3002	0.4242	0.4114	0.5744	0.4770
Point 11	0.7774	0.3367	0.6330	0.5273	0.6174	0.4623	0.6704	0.5749
Point 12	0.5470	0.7654	0.5925	0.4853	0.3715	0.3430	0.4352	0.5057
Point 13	0.5288	0.6903	0.6005	0.3075	0.1779	0.2394	0.3867	0.4187
Point 14	0.5489	0.6322	0.4720	0.3631	0.3891	0.3474	0.5828	0.4765
Point 15	0.5558	0.6646	0.4513	0.1625	0.3735	0.4533	0.6149	0.4680
Point 16	0.6499	0.5750	0.4566	0.1802	0.4226	0.5148	0.6183	0.4882
Point 17	0.6301	0.5297	0.4394	0.1467	0.5219	0.4718	0.6591	0.4855
Point 18	0.6839	0.3804	0.5717	0.2440	0.4153	0.3785	0.4558	0.4471
Point 19	0.7350	0.3327	0.6074	0.4791	0.5267	0.4016	0.6951	0.5397
Point 20	0.4270	0.7520	0.6058	0.4561	0.1840	0.2543	0.3527	0.4331
Point 21	0.5191	0.7078	0.5800	0.2640	0.0617	0.3138	0.4284	0.4107
Point 22	0.4885	0.6737	0.4774	0.2559	0.2656	0.4071	0.6313	0.4571
Point 23	0.4647	0.5888	0.4797	0.2287	0.3986	0.5156	0.5946	0.4672
Point 24	0.5975	0.4480	0.4809	0.3022	0.4369	0.5124	0.5409	0.4741
Point 25	0.4884	0.5508	0.4394	0.2585	0.6127	0.4239	0.5431	0.4738
Point 26	0.5350	0.4770	0.5116	0.2309	0.3934	0.2697	0.3907	0.4012
Point 27	0.7015	0.5587	0.5050	0.4968	0.4409	0.1978	0.6661	0.5096
Point 28	0.5575	0.7854	0.5820	0.4002	0.2863	0.2792	0.3855	0.4680
Point 29	0.5842	0.7249	0.5602	0.3381	0.1579	0.3882	0.5301	0.4691
Point 30	0.5668	0.6805	0.4818	0.1194	0.2101	0.3484	0.5617	0.4241
Point 31	0.4473	0.5479	0.5001	0.4550	0.4956	0.5126	0.5268	0.4979
Point 32	0.5219	0.4902	0.5087	0.4451	0.4727	0.4423	0.4816	0.4804
Point 33	0.3898	0.6150	0.3686	0.2819	0.6196	0.3748	0.5657	0.4593
Point 34	0.5292	0.7564	0.4060	0.2604	0.2375	0.2926	0.4802	0.4232
Point 35	0.6862	0.8546	0.3718	0.4805	0.2409	0.3415	0.6150	0.5129
Point 36	0.7101	0.8390	0.6664	0.5995	0.3001	0.4726	0.4297	0.5739
Point 37	0.7374	0.7519	0.6842	0.5310	0.4486	0.4509	0.4341	0.5769
Point 38	0.7399	0.6380	0.5930	0.5883	0.3144	0.4914	0.5829	0.5640
Point 39	0.6260	0.5933	0.5376	0.3031	0.3354	0.4727	0.5130	0.4830
Point 40	0.4488	0.5084	0.5065	0.5293	0.5386	0.6264	0.5198	0.5254
Point 41	0.4757	0.4629	0.5534	0.5547	0.4462	0.4638	0.5886	0.5065
Point 42	0.4396	0.6966	0.4112	0.3839	0.4335	0.3442	0.6326	0.4774
Point 43	0.6455	0.9017	0.4054	0.4377	0.1026	0.2547	0.5534	0.4716
Point 44	0.6978	0.9269	0.4155	0.5257	0.1097	0.2689	0.5105	0.4936

Point 45	0.6703	0.6636	0.7399	0.6849	0.6526	0.4895	0.5699	0.6387
Point 46	0.6289	0.5370	0.6689	0.7467	0.5121	0.5789	0.7418	0.6306
Point 47	0.3507	0.4916	0.5742	0.6585	0.5184	0.6149	0.6018	0.5443
Point 48	0.4533	0.5165	0.5645	0.5884	0.5686	0.7170	0.5888	0.5710
Point 49	0.6254	0.4985	0.6447	0.6383	0.3564	0.5824	0.5976	0.5633
Point 50	0.6588	0.6924	0.4637	0.3482	0.1168	0.2286	0.4395	0.4212
Point 51	0.7531	0.8891	0.6243	0.5727	0.0920	0.4683	0.3497	0.5356
Point 52	0.7643	0.9105	0.6297	0.5755	0.2942	0.5830	0.3596	0.5881
<b>Average</b>	<b>0.6018</b>	<b>0.6101</b>	<b>0.5245</b>	<b>0.4014</b>	<b>0.3889</b>	<b>0.4296</b>	<b>0.5230</b>	<b>0.4971</b>
<b>Min</b>	<b>0.3507</b>	<b>0.2587</b>	<b>0.3686</b>	<b>0.1194</b>	<b>0.0617</b>	<b>0.1978</b>	<b>0.3402</b>	<b>0.4012</b>
<b>Max</b>	<b>0.8028</b>	<b>0.9269</b>	<b>0.7399</b>	<b>0.7467</b>	<b>0.6852</b>	<b>0.7170</b>	<b>0.7429</b>	<b>0.6387</b>
<b>St. Deviation</b>	<b>0.1112</b>	<b>0.1620</b>	<b>0.0867</b>	<b>0.1508</b>	<b>0.1559</b>	<b>0.1147</b>	<b>0.1075</b>	<b>0.0540</b>
<b>St. Error</b>	<b>0.0154</b>	<b>0.0225</b>	<b>0.0120</b>	<b>0.0209</b>	<b>0.0216</b>	<b>0.0159</b>	<b>0.0149</b>	<b>0.0075</b>
<b>Difference (%)</b>		<b>1.3811</b>	<b>-14.0266</b>	<b>-23.4727</b>	<b>-3.1067</b>	<b>10.4629</b>	<b>21.7397</b>	
<b>Normalised Difference (%)</b>		<b>0.6858</b>	<b>-7.5423</b>	<b>-13.2969</b>	<b>-1.5779</b>	<b>4.9714</b>	<b>9.8042</b>	

**Table 21:** Coherence values – Sentinel-1A ascending – AOI

Id	Coherence							Average
	11JAN-23JAN	23JAN-04FEB	04FEB-16FEB	16FEB-28FEB	28FEB-12MAR	12MAR-24MAR	24MAR-05APR	
Point 14	0.5489	0.6322	0.4720	0.3631	0.3891	0.3474	0.5828	0.4765
Point 15	0.5558	0.6646	0.4513	0.1625	0.3735	0.4533	0.6149	0.4680
Point 16	0.6499	0.5750	0.4566	0.1802	0.4226	0.5148	0.6183	0.4882
Point 17	0.6301	0.5297	0.4394	0.1467	0.5219	0.4718	0.6591	0.4855
Point 18	0.6839	0.3804	0.5717	0.2440	0.4153	0.3785	0.4558	0.4471
Point 22	0.4885	0.6737	0.4774	0.2559	0.2656	0.4071	0.6313	0.4571
Point 23	0.4647	0.5888	0.4797	0.2287	0.3986	0.5156	0.5946	0.4672
Point 24	0.5975	0.4480	0.4809	0.3022	0.4369	0.5124	0.5409	0.4741
Point 25	0.4884	0.5508	0.4394	0.2585	0.6127	0.4239	0.5431	0.4738
Point 26	0.5350	0.4770	0.5116	0.2309	0.3934	0.2697	0.3907	0.4012
Point 30	0.5668	0.6805	0.4818	0.1194	0.2101	0.3484	0.5617	0.4241
Point 31	0.4473	0.5479	0.5001	0.4550	0.4956	0.5126	0.5268	0.4979
Point 32	0.5219	0.4902	0.5087	0.4451	0.4727	0.4423	0.4816	0.4804
Point 33	0.3898	0.6150	0.3686	0.2819	0.6196	0.3748	0.5657	0.4593
Point 34	0.5292	0.7564	0.4060	0.2604	0.2375	0.2926	0.4802	0.4232
Point 39	0.6260	0.5933	0.5376	0.3031	0.3354	0.4727	0.5130	0.4830
Point 40	0.4488	0.5084	0.5065	0.5293	0.5386	0.6264	0.5198	0.5254
Point 41	0.4757	0.4629	0.5534	0.5547	0.4462	0.4638	0.5886	0.5065
Point 42	0.4396	0.6966	0.4112	0.3839	0.4335	0.3442	0.6326	0.4774
Point 43	0.6455	0.9017	0.4054	0.4377	0.1026	0.2547	0.5534	0.4716
<b>Average</b>	<b>0.5367</b>	<b>0.5887</b>	<b>0.4730</b>	<b>0.3072</b>	<b>0.4061</b>	<b>0.4214</b>	<b>0.5527</b>	<b>0.4694</b>
<b>Min</b>	<b>0.3898</b>	<b>0.3804</b>	<b>0.3686</b>	<b>0.1194</b>	<b>0.1026</b>	<b>0.2547</b>	<b>0.3907</b>	<b>0.4012</b>
<b>Max</b>	<b>0.6839</b>	<b>0.9017</b>	<b>0.5717</b>	<b>0.5547</b>	<b>0.6196</b>	<b>0.6264</b>	<b>0.6591</b>	<b>0.5254</b>
<b>St. Deviation</b>	<b>0.0823</b>	<b>0.1206</b>	<b>0.0523</b>	<b>0.1255</b>	<b>0.1299</b>	<b>0.0954</b>	<b>0.0672</b>	<b>0.0290</b>
<b>St. Error</b>	<b>0.0184</b>	<b>0.0270</b>	<b>0.0117</b>	<b>0.0281</b>	<b>0.0290</b>	<b>0.0213</b>	<b>0.0150</b>	<b>0.0065</b>
<b>Difference (%)</b>		<b>9.6898</b>	<b>-19.6548</b>	<b>-35.0560</b>	<b>32.2039</b>	<b>3.7626</b>	<b>31.1837</b>	
<b>Normalised Difference (%)</b>		<b>4.6210</b>	<b>-10.8985</b>	<b>-21.2532</b>	<b>13.8688</b>	<b>1.8466</b>	<b>13.4887</b>	

From the coherence outputs of the ascending Sentinel-1A images, the average coherence seems stable in the greater area during 11/01/2019 – 04/02/2019. The average coherence then dropped at the co-event pair i.e. 04/02/2019 – 16/02/2019, by 14%, and continued to decrease by 23.5% until the next pair. The coherence values during the period of rehabilitation works remained stable and then increased by 10.5% as the works completed and by 21.7% after the road re-opened. The average, minimum and maximum coherence results are presented in Figure 106.

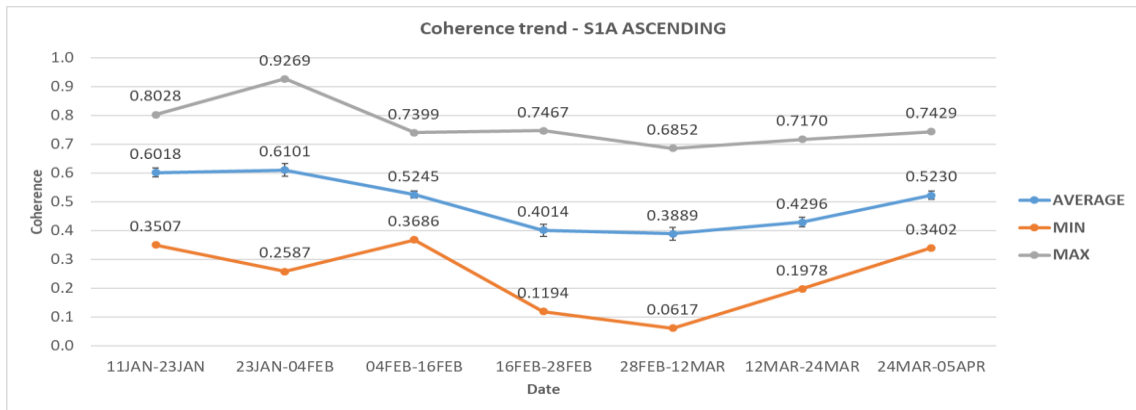


**Figure 106:** Coherence changes – Sentinel-1A ascending

In the case of the AOI, the coherence values decreased at a greater rate (19.7%) at the co-event SAR pair and at the start of the rehabilitation works (35%), reaching a minimum of 0.307. The coherence values were then increased by 36% as construction works reached completion and by 31.2% after the road opened to traffic. The average, minimum and maximum coherence values for each SAR image pair are presented in Figure 107.

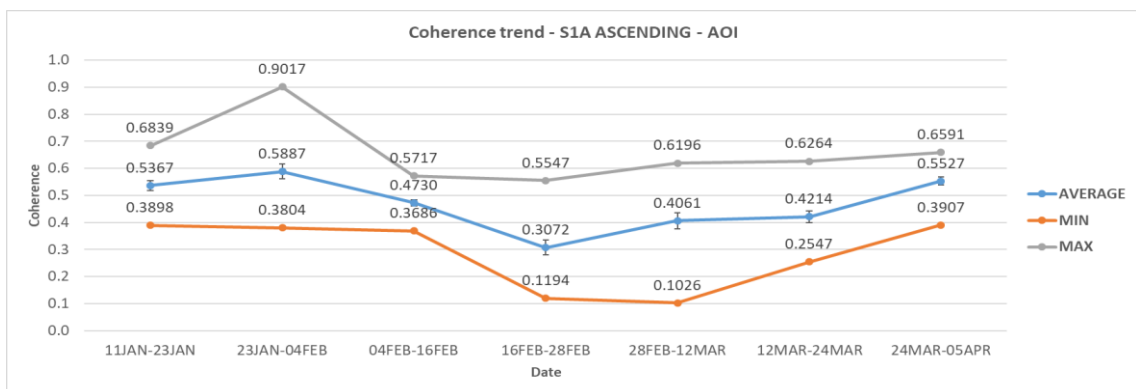


**Figure 107:** Coherence changes – Sentinel-1A ascending – AOI

The peak that is seen in the maximum values at both cases, in the image pair dated 23/01/2019 – 04/02/2019, is at point 43 which is located near the road.

**Table 22:** Coherence values – Sentinel-1A descending

Id	Coherence							Average
	12JAN-24JAN	24JAN-05FEB	05FEB-17FEB	17FEB-01MAR	01MAR-13MAR	13MAR-25MAR	25MAR-06APR	
Point 1	0.8004	0.6905	0.3134	0.3248	0.4550	0.3220	0.3481	0.4649
Point 2	0.8452	0.7730	0.2335	0.2778	0.4280	0.3871	0.2341	0.4541
Point 3	0.8241	0.7611	0.2302	0.3970	0.5512	0.4479	0.4445	0.5223
Point 4	0.8390	0.7869	0.3923	0.5658	0.5409	0.4835	0.5290	0.5911
Point 5	0.7618	0.6773	0.3498	0.3144	0.3393	0.3156	0.2816	0.4343
Point 6	0.8225	0.7715	0.3826	0.2660	0.2289	0.4255	0.2596	0.4510
Point 7	0.8443	0.8361	0.4140	0.4076	0.2994	0.5104	0.4084	0.5315
Point 8	0.8512	0.8385	0.5538	0.4785	0.3649	0.5310	0.5482	0.5952
Point 9	0.7632	0.7795	0.6370	0.5788	0.3806	0.5579	0.5515	0.6069
Point 10	0.6525	0.7596	0.5423	0.6048	0.5067	0.3668	0.5413	0.5677
Point 11	0.6192	0.5814	0.6422	0.6418	0.5697	0.5346	0.4335	0.5746
Point 12	0.5661	0.4165	0.5672	0.2443	0.2723	0.1242	0.2118	0.3432
Point 13	0.7508	0.6338	0.2768	0.2726	0.2181	0.1952	0.1201	0.3525
Point 14	0.8012	0.6863	0.2820	0.1868	0.1746	0.4395	0.3199	0.4129
Point 15	0.7630	0.7726	0.4110	0.3088	0.1270	0.5308	0.4726	0.4837
Point 16	0.7075	0.7695	0.6701	0.3590	0.2671	0.5542	0.6436	0.5673
Point 17	0.6684	0.6836	0.7562	0.4922	0.2038	0.5228	0.5396	0.5524
Point 18	0.5901	0.6456	0.5485	0.4801	0.3364	0.4758	0.6292	0.5294
Point 19	0.6539	0.5149	0.6155	0.5784	0.4917	0.6288	0.4785	0.5660
Point 20	0.5886	0.5579	0.5755	0.2921	0.2287	0.2174	0.1619	0.3746
Point 21	0.7222	0.5890	0.2480	0.2649	0.1031	0.1783	0.1898	0.3279
Point 22	0.7815	0.5931	0.2925	0.1731	0.1880	0.2569	0.2454	0.3615
Point 23	0.6457	0.6143	0.3311	0.2551	0.1218	0.5025	0.3270	0.3996
Point 24	0.4885	0.6438	0.5555	0.1366	0.1918	0.6153	0.6431	0.4678
Point 25	0.5006	0.6066	0.6676	0.2887	0.3084	0.5461	0.5652	0.4976
Point 26	0.5361	0.6407	0.6455	0.3703	0.3866	0.5480	0.6663	0.5419
Point 27	0.6992	0.5948	0.7114	0.4958	0.5486	0.6980	0.5470	0.6135
Point 28	0.5171	0.6729	0.4901	0.4048	0.1504	0.1690	0.4387	0.4061
Point 29	0.5897	0.5922	0.3062	0.2160	0.1447	0.2168	0.3104	0.3394
Point 30	0.6752	0.4998	0.3792	0.1071	0.2289	0.1114	0.3837	0.3408
Point 31	0.4752	0.3899	0.3475	0.2923	0.1241	0.4496	0.3767	0.3508
Point 32	0.3070	0.4192	0.3499	0.0947	0.1696	0.6177	0.5736	0.3617
Point 33	0.3494	0.4395	0.3902	0.1331	0.3414	0.5714	0.5519	0.3967
Point 34	0.4985	0.5967	0.4263	0.3538	0.4418	0.5491	0.6604	0.5038
Point 35	0.6887	0.6482	0.5780	0.3956	0.6098	0.6680	0.6243	0.6018
Point 36	0.6407	0.6614	0.2952	0.4825	0.2827	0.2068	0.4521	0.4316
Point 37	0.4348	0.7234	0.3789	0.4610	0.1306	0.2454	0.6573	0.4331
Point 38	0.3133	0.5892	0.2891	0.1854	0.1904	0.2702	0.5782	0.3451
Point 39	0.3581	0.4565	0.3645	0.0455	0.1944	0.0923	0.5268	0.2912
Point 40	0.1665	0.1940	0.3425	0.2566	0.2212	0.3768	0.3730	0.2758
Point 41	0.1974	0.1580	0.2040	0.0944	0.1462	0.6246	0.4688	0.2705
Point 42	0.3166	0.2537	0.2917	0.1243	0.3283	0.5855	0.4705	0.3387
Point 43	0.3332	0.4887	0.3878	0.4042	0.4950	0.4556	0.6174	0.4545
Point 44	0.5491	0.5825	0.5293	0.4740	0.5728	0.5846	0.6727	0.5664
Point 45	0.3235	0.6477	0.3077	0.5140	0.2565	0.2838	0.7166	0.4357
Point 46	0.2723	0.5615	0.3868	0.3770	0.2528	0.3461	0.7025	0.4141
Point 47	0.2405	0.5151	0.2877	0.2384	0.2813	0.2270	0.6463	0.3480
Point 48	0.2560	0.4146	0.2138	0.1562	0.1618	0.4440	0.4293	0.2965

Point 49	0.2418	0.4401	0.1082	0.2050	0.1325	0.6143	0.4682	0.3157
Point 50	0.3945	0.3789	0.2085	0.2758	0.2356	0.5753	0.4265	0.3564
Point 51	0.2353	0.3589	0.3032	0.4721	0.4616	0.4698	0.5542	0.4079
Point 52	0.3983	0.4563	0.4283	0.5907	0.5670	0.4987	0.6698	0.5156
<b>Average</b>	<b>0.5550</b>	<b>0.5838</b>	<b>0.4123</b>	<b>0.3348</b>	<b>0.3068</b>	<b>0.4263</b>	<b>0.4748</b>	<b>0.4420</b>
<b>Min</b>	<b>0.1665</b>	<b>0.1580</b>	<b>0.1082</b>	<b>0.0455</b>	<b>0.1031</b>	<b>0.0923</b>	<b>0.1201</b>	<b>0.2705</b>
<b>Max</b>	<b>0.8512</b>	<b>0.8385</b>	<b>0.7562</b>	<b>0.6418</b>	<b>0.6098</b>	<b>0.6980</b>	<b>0.7166</b>	<b>0.6135</b>
<b>St. Deviation</b>	<b>0.2063</b>	<b>0.1575</b>	<b>0.1537</b>	<b>0.1532</b>	<b>0.1488</b>	<b>0.1636</b>	<b>0.1544</b>	<b>0.0996</b>
<b>St. Error</b>	<b>0.0286</b>	<b>0.0218</b>	<b>0.0213</b>	<b>0.0212</b>	<b>0.0206</b>	<b>0.0227</b>	<b>0.0214</b>	<b>0.0138</b>
<b>Difference (%)</b>		<b>5.1891</b>	<b>-29.3732</b>	<b>-18.7952</b>	<b>-8.3661</b>	<b>38.9614</b>	<b>11.3691</b>	
<b>Normalised Difference (%)</b>		<b>2.5290</b>	<b>-17.2149</b>	<b>-10.3723</b>	<b>-4.3656</b>	<b>16.3045</b>	<b>5.3788</b>	

**Table 23:** Coherence values – Sentinel-1A descending – AOI

Id	Coherence							Average
	12JAN-24JAN	24JAN-05FEB	05FEB-17FEB	17FEB-01MAR	01MAR-13MAR	13MAR-25MAR	25MAR-06APR	
Point 14	0.8012	0.6863	0.2820	0.1868	0.1746	0.4395	0.3199	0.4129
Point 15	0.7630	0.7726	0.4110	0.3088	0.1270	0.5308	0.4726	0.4837
Point 16	0.7075	0.7695	0.6701	0.3590	0.2671	0.5542	0.6436	0.5673
Point 17	0.6684	0.6836	0.7562	0.4922	0.2038	0.5228	0.5396	0.5524
Point 18	0.5901	0.6456	0.5485	0.4801	0.3364	0.4758	0.6292	0.5294
Point 22	0.7815	0.5931	0.2925	0.1731	0.1880	0.2569	0.2454	0.3615
Point 23	0.6457	0.6143	0.3311	0.2551	0.1218	0.5025	0.3270	0.3996
Point 24	0.4885	0.6438	0.5555	0.1366	0.1918	0.6153	0.6431	0.4678
Point 25	0.5006	0.6066	0.6676	0.2887	0.3084	0.5461	0.5652	0.4976
Point 26	0.5361	0.6407	0.6455	0.3703	0.3866	0.5480	0.6663	0.5419
Point 30	0.6752	0.4998	0.3792	0.1071	0.2289	0.1114	0.3837	0.3408
Point 31	0.4752	0.3899	0.3475	0.2923	0.1241	0.4496	0.3767	0.3508
Point 32	0.3070	0.4192	0.3499	0.0947	0.1696	0.6177	0.5736	0.3617
Point 33	0.3494	0.4395	0.3902	0.1331	0.3414	0.5714	0.5519	0.3967
Point 34	0.4985	0.5967	0.4263	0.3538	0.4418	0.5491	0.6604	0.5038
Point 39	0.3581	0.4565	0.3645	0.0455	0.1944	0.0923	0.5268	0.2912
Point 40	0.1665	0.1940	0.3425	0.2566	0.2212	0.3768	0.3730	0.2758
Point 41	0.1974	0.1580	0.2040	0.0944	0.1462	0.6246	0.4688	0.2705
Point 42	0.3166	0.2537	0.2917	0.1243	0.3283	0.5855	0.4705	0.3387
Point 43	0.3332	0.4887	0.3878	0.4042	0.4950	0.4556	0.6174	0.4545
<b>Average</b>	<b>0.5080</b>	<b>0.5276</b>	<b>0.4322</b>	<b>0.2478</b>	<b>0.2498</b>	<b>0.4713</b>	<b>0.5027</b>	<b>0.4199</b>
<b>Min</b>	<b>0.1665</b>	<b>0.1580</b>	<b>0.2040</b>	<b>0.0455</b>	<b>0.1218</b>	<b>0.0923</b>	<b>0.2454</b>	<b>0.2705</b>
<b>Max</b>	<b>0.8012</b>	<b>0.7726</b>	<b>0.7562</b>	<b>0.4922</b>	<b>0.4950</b>	<b>0.6246</b>	<b>0.6663</b>	<b>0.5673</b>
<b>St. Deviation</b>	<b>0.1941</b>	<b>0.1777</b>	<b>0.1537</b>	<b>0.1342</b>	<b>0.1089</b>	<b>0.1539</b>	<b>0.1286</b>	<b>0.0951</b>
<b>St. Error</b>	<b>0.0434</b>	<b>0.0397</b>	<b>0.0344</b>	<b>0.0300</b>	<b>0.0243</b>	<b>0.0344</b>	<b>0.0287</b>	<b>0.0213</b>
<b>Difference (%)</b>		<b>3.8608</b>	<b>-18.0830</b>	<b>-42.6590</b>	<b>0.8021</b>	<b>88.6600</b>	<b>6.6706</b>	
<b>Normalised Difference (%)</b>		<b>1.8939</b>	<b>-9.9403</b>	<b>-27.1124</b>	<b>0.3995</b>	<b>30.7143</b>	<b>3.2276</b>	



From Table 22, it is clear that in the wider area, coherence values are nearly stable on average before the landslide, i.e. 12/01/2019 – 05/02/2019. There is a small increase of 0.028 (5.2%) on average that is though lower than the standard error estimated ( $\pm 0.0286$ ), and thus considered insignificant. Moreover, the coherence values dropped at the co-event pair (05/02/2019 – 17/02/2019), by 29.4%, and continued to decrease by 18.8% until the next one (17/2/2019 – 01/03/2019). During the period of rehabilitation works there was a small decrease of 8.4%, but the coherence values increased by 39% as the works ended and by 11.4% after the road re-opened to traffic. The average, minimum and maximum coherence values obtained from each pair of images are presented in Figure 108.

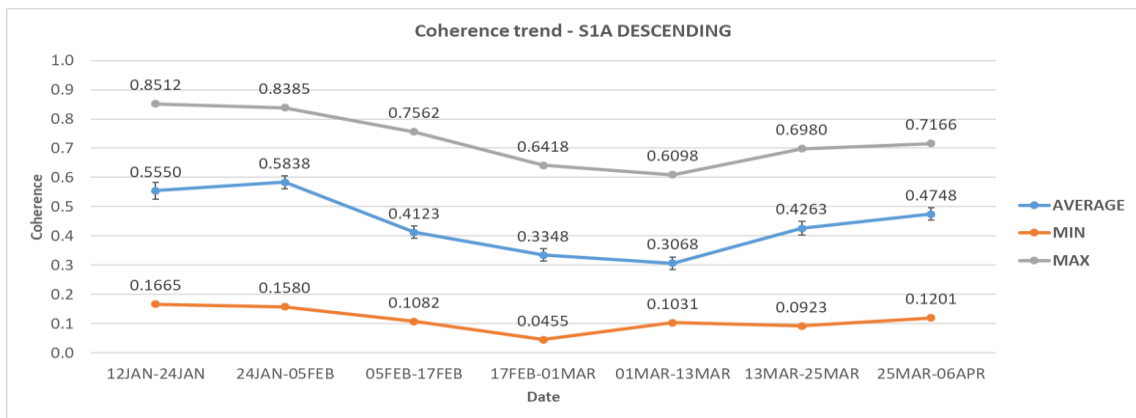


**Figure 108:** Coherence changes – Sentinel-1A descending

Within the AOI, the coherence values decreased by 18.1% at the co-event SAR pair and an additional 42.7% when the rehabilitation works commenced. The coherence values then increased by 88.7% as construction works reached completion and by 6.7% after the road re-opened to traffic. The average, minimum and maximum coherence values obtained from each pair of images are presented in Figure 109.

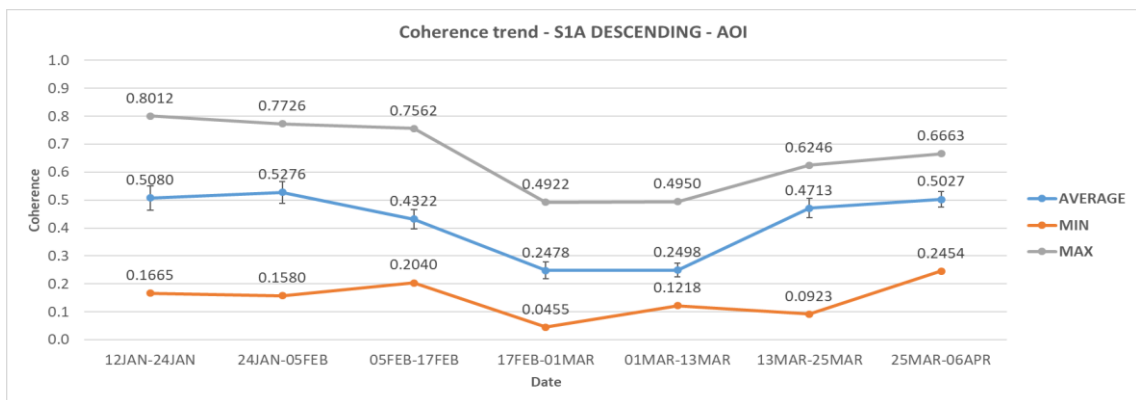


**Figure 109:** Coherence changes – Sentinel-1A descending – AOI

By averaging the coherence pixel values from ascending and descending Sentinel-1A pairs, a clearer representation of the coherence changes trends in all 3 categories, i.e. minimum, maximum and average values is provided, as shown in Figure 110 and Figure 111. At the same time, standard deviations are reduced leading to more reliable results. The x-axis values were changed from dates to periods, as shown earlier (Figure 99).

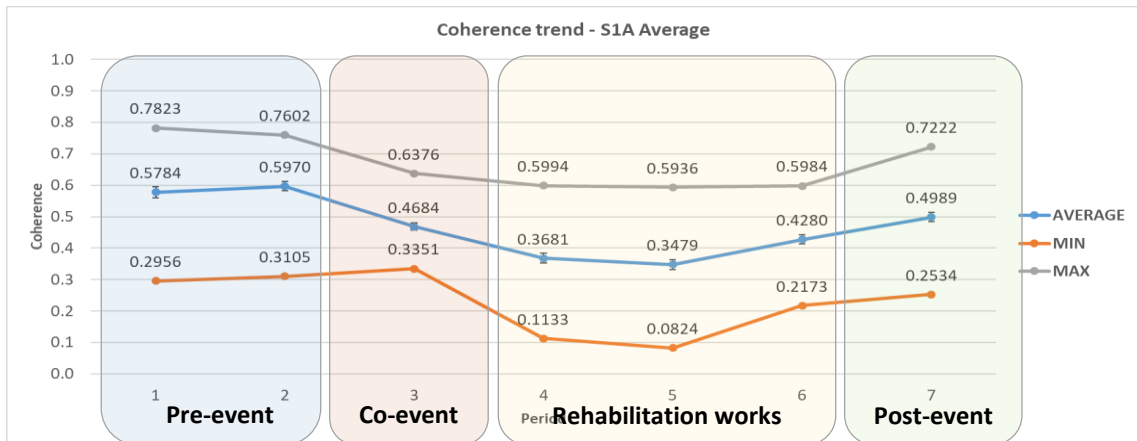


**Figure 110:** Coherence changes – Sentinel-1A average

The peaks that existed in the maximum values in the case of the Sentinel-1A ascending images, and other small fluctuations evened out, resulting in a common trend in coherence changes in maximum, minimum and average values. The average coherence is nearly stable within the error limits calculated in the pre-event period. It then decreased by 18.9% (co-event pair) and continued to decrease by 38.7% to reach the minimum value of 0.278 during the rehabilitation works. Then, the average coherence increased by 54.3% until the end of this period and by another 18.2% after the road opened. The maximum values of average coherence lie as expected within the pre-event and post-event periods.

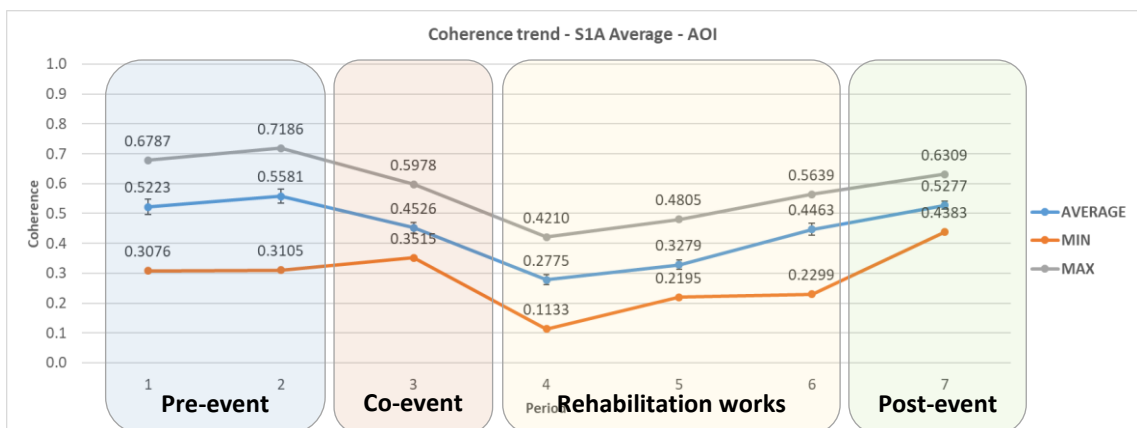


**Figure 111:** Coherence changes – Sentinel-1A average – AOI

**Table 24:** Coherence values – Sentinel-1B ascending

Id	Coherence							Average
	17JAN-29JAN	29JAN-10FEB	10FEB-22FEB	22FEB-06MAR	06MAR-18MAR	18MAR-30MAR	30MAR-11APR	
Point 1	0.6362	0.5373	0.2752	0.4432	0.5805	0.1891	0.6418	0.4719
Point 2	0.5857	0.5582	0.1685	0.4298	0.5414	0.5491	0.7234	0.5080
Point 3	0.5366	0.5632	0.2263	0.3329	0.5596	0.4606	0.6909	0.4815
Point 4	0.5450	0.5979	0.1942	0.4481	0.6447	0.3028	0.4096	0.4489
Point 5	0.6482	0.4814	0.1527	0.3798	0.5288	0.2630	0.7108	0.4521
Point 6	0.5121	0.5288	0.3839	0.3562	0.4662	0.7146	0.7916	0.5362
Point 7	0.4327	0.5143	0.3621	0.1709	0.5590	0.6138	0.8083	0.4945
Point 8	0.4693	0.5681	0.2886	0.1307	0.6744	0.3990	0.6056	0.4480
Point 9	0.4218	0.5280	0.0842	0.2814	0.6472	0.3690	0.4263	0.3940
Point 10	0.5025	0.5891	0.2734	0.3053	0.5024	0.4861	0.3188	0.4254
Point 11	0.7900	0.7728	0.5473	0.1318	0.6643	0.5683	0.3647	0.5485
Point 12	0.7754	0.6085	0.3533	0.4373	0.5370	0.3191	0.5502	0.5115
Point 13	0.6371	0.5697	0.4594	0.4021	0.3914	0.4324	0.7483	0.5201
Point 14	0.5173	0.5860	0.3738	0.1973	0.4202	0.7559	0.8150	0.5237
Point 15	0.4484	0.5184	0.3400	0.0750	0.5225	0.6168	0.8547	0.4823
Point 16	0.4668	0.5736	0.2663	0.1527	0.5688	0.3835	0.6950	0.4438
Point 17	0.3713	0.4891	0.1092	0.3134	0.4988	0.3553	0.6255	0.3947
Point 18	0.4576	0.5178	0.2669	0.2896	0.3523	0.3810	0.4643	0.3899
Point 19	0.7813	0.7438	0.5685	0.1136	0.6367	0.6395	0.5442	0.5754
Point 20	0.7585	0.6074	0.4276	0.4935	0.3596	0.3702	0.6466	0.5233
Point 21	0.6207	0.6024	0.6077	0.3995	0.2413	0.5473	0.7854	0.5435
Point 22	0.5747	0.6122	0.3904	0.0939	0.4114	0.7176	0.8435	0.5205
Point 23	0.5332	0.4861	0.2516	0.1811	0.4519	0.6072	0.8833	0.4849
Point 24	0.4508	0.5034	0.2270	0.2248	0.4504	0.4692	0.7396	0.4379
Point 25	0.3211	0.3377	0.1189	0.2566	0.4002	0.3691	0.7184	0.3603
Point 26	0.4661	0.4349	0.3389	0.2443	0.3430	0.2902	0.5929	0.3872
Point 27	0.7504	0.6856	0.5504	0.0584	0.6384	0.6148	0.6755	0.5676
Point 28	0.7058	0.5725	0.5625	0.5630	0.2997	0.3578	0.5743	0.5194
Point 29	0.6500	0.6353	0.6747	0.3869	0.1512	0.4547	0.7290	0.5260
Point 30	0.6422	0.6213	0.3781	0.1028	0.4259	0.6824	0.8273	0.5257
Point 31	0.6196	0.4796	0.1785	0.3733	0.4278	0.5752	0.8827	0.5052
Point 32	0.5409	0.4248	0.2241	0.1842	0.3638	0.5675	0.7422	0.4354
Point 33	0.4873	0.2261	0.1521	0.1777	0.3147	0.4150	0.7429	0.3594
Point 34	0.6101	0.4297	0.3537	0.0977	0.1993	0.3391	0.7211	0.3930
Point 35	0.6774	0.5318	0.3372	0.0887	0.4800	0.5023	0.7576	0.4821
Point 36	0.7089	0.6582	0.5373	0.2438	0.2436	0.3165	0.5586	0.4667
Point 37	0.7233	0.6705	0.6948	0.5808	0.3065	0.3015	0.5722	0.5499
Point 38	0.7562	0.6670	0.7399	0.4453	0.2334	0.3994	0.6198	0.5516
Point 39	0.7279	0.5610	0.3901	0.3898	0.5302	0.7534	0.7367	0.5842
Point 40	0.7509	0.5433	0.2200	0.5012	0.4800	0.6773	0.8428	0.5736
Point 41	0.7206	0.4724	0.3980	0.1315	0.4017	0.6743	0.7512	0.5071
Point 42	0.6886	0.3868	0.3644	0.1615	0.3721	0.4771	0.7626	0.4590
Point 43	0.6893	0.5502	0.5698	0.3031	0.2561	0.3459	0.7783	0.4989
Point 44	0.6225	0.5429	0.4047	0.2950	0.3628	0.3211	0.7536	0.4718
Point 45	0.7681	0.7963	0.7838	0.7816	0.6267	0.3996	0.6143	0.6815
Point 46	0.8166	0.7787	0.8120	0.7294	0.5340	0.5564	0.6476	0.6964
Point 47	0.7672	0.7344	0.6565	0.5982	0.6538	0.7209	0.7278	0.6941
Point 48	0.7590	0.6639	0.4033	0.3796	0.4302	0.6477	0.7293	0.5733

Point 49	0.7439	0.5547	0.6733	0.2853	0.2988	0.6367	0.7371	0.5614
Point 50	0.7432	0.5573	0.6339	0.1767	0.3351	0.4410	0.7463	0.5191
Point 51	0.7837	0.6969	0.7884	0.2531	0.4699	0.3339	0.6661	0.5703
Point 52	0.7079	0.7105	0.7182	0.2488	0.5208	0.3522	0.6262	0.5549
<b>Average</b>	<b>0.6235</b>	<b>0.5689</b>	<b>0.4088</b>	<b>0.3043</b>	<b>0.4483</b>	<b>0.4814</b>	<b>0.6831</b>	<b>0.5026</b>
<b>Min</b>	<b>0.3211</b>	<b>0.2261</b>	<b>0.0842</b>	<b>0.0584</b>	<b>0.1512</b>	<b>0.1891</b>	<b>0.3188</b>	<b>0.3594</b>
<b>Max</b>	<b>0.8166</b>	<b>0.7963</b>	<b>0.8120</b>	<b>0.7816</b>	<b>0.6744</b>	<b>0.7559</b>	<b>0.8833</b>	<b>0.6964</b>
<b>St. Deviation</b>	<b>0.1286</b>	<b>0.1101</b>	<b>0.1985</b>	<b>0.1674</b>	<b>0.1334</b>	<b>0.1486</b>	<b>0.1281</b>	<b>0.0756</b>
<b>St. Error</b>	<b>0.0178</b>	<b>0.0153</b>	<b>0.0275</b>	<b>0.0232</b>	<b>0.0185</b>	<b>0.0206</b>	<b>0.0178</b>	<b>0.0105</b>
<b>Difference (%)</b>		<b>-8.7607</b>	<b>-28.1458</b>	<b>-25.5610</b>	<b>47.3229</b>	<b>7.3925</b>	<b>41.8974</b>	
<b>Normalised Difference (%)</b>		<b>-4.5810</b>	<b>-16.3777</b>	<b>-14.6533</b>	<b>19.1340</b>	<b>3.5645</b>	<b>17.3203</b>	

**Table 25:** Coherence values – Sentinel-1B ascending – AOI

Id	Coherence							Average
	17JAN-29JAN	29JAN-10FEB	10FEB-22FEB	22FEB-06MAR	06MAR-18MAR	18MAR-30MAR	30MAR-11APR	
Point 14	0.5173	0.5860	0.3738	0.1973	0.4202	0.7559	0.8150	0.5237
Point 15	0.4484	0.5184	0.3400	0.0750	0.5225	0.6168	0.8547	0.4823
Point 16	0.4668	0.5736	0.2663	0.1527	0.5688	0.3835	0.6950	0.4438
Point 17	0.3713	0.4891	0.1092	0.3134	0.4988	0.3553	0.6255	0.3947
Point 18	0.4576	0.5178	0.2669	0.2896	0.3523	0.3810	0.4643	0.3899
Point 22	0.5747	0.6122	0.3904	0.0939	0.4114	0.7176	0.8435	0.5205
Point 23	0.5332	0.4861	0.2516	0.1811	0.4519	0.6072	0.8833	0.4849
Point 24	0.4508	0.5034	0.2270	0.2248	0.4504	0.4692	0.7396	0.4379
Point 25	0.3211	0.3377	0.1189	0.2566	0.4002	0.3691	0.7184	0.3603
Point 26	0.4661	0.4349	0.3389	0.2443	0.3430	0.2902	0.5929	0.3872
Point 30	0.6422	0.6213	0.3781	0.1028	0.4259	0.6824	0.8273	0.5257
Point 31	0.6196	0.4796	0.1785	0.3733	0.4278	0.5752	0.8827	0.5052
Point 32	0.5409	0.4248	0.2241	0.1842	0.3638	0.5675	0.7422	0.4354
Point 33	0.4873	0.2261	0.1521	0.1777	0.3147	0.4150	0.7429	0.3594
Point 34	0.6101	0.4297	0.3537	0.0977	0.1993	0.3391	0.7211	0.3930
Point 39	0.7279	0.5610	0.3901	0.3898	0.5302	0.7534	0.7367	0.5842
Point 40	0.7509	0.5433	0.2200	0.5012	0.4800	0.6773	0.8428	0.5736
Point 41	0.7206	0.4724	0.3980	0.1315	0.4017	0.6743	0.7512	0.5071
Point 42	0.6886	0.3868	0.3644	0.1615	0.3721	0.4771	0.7626	0.4590
Point 43	0.6893	0.5502	0.5698	0.3031	0.2561	0.3459	0.7783	0.4989
<b>Average</b>	<b>0.5542</b>	<b>0.4877</b>	<b>0.2956</b>	<b>0.2226</b>	<b>0.4095</b>	<b>0.5226</b>	<b>0.7510</b>	<b>0.4633</b>
<b>Min</b>	<b>0.3211</b>	<b>0.2261</b>	<b>0.1092</b>	<b>0.0750</b>	<b>0.1993</b>	<b>0.2902</b>	<b>0.4643</b>	<b>0.3594</b>
<b>Max</b>	<b>0.7509</b>	<b>0.6213</b>	<b>0.5698</b>	<b>0.5012</b>	<b>0.5688</b>	<b>0.7559</b>	<b>0.8833</b>	<b>0.5842</b>
<b>St. Deviation</b>	<b>0.1234</b>	<b>0.0964</b>	<b>0.1142</b>	<b>0.1124</b>	<b>0.0912</b>	<b>0.1565</b>	<b>0.1031</b>	<b>0.0678</b>
<b>St. Error</b>	<b>0.0276</b>	<b>0.0215</b>	<b>0.0255</b>	<b>0.0251</b>	<b>0.0204</b>	<b>0.0350</b>	<b>0.0231</b>	<b>0.0152</b>
<b>Difference (%)</b>		<b>-12.0017</b>	<b>-39.3952</b>	<b>-24.7036</b>	<b>84.0134</b>	<b>27.6152</b>	<b>43.6915</b>	
<b>Normalised Difference (%)</b>		<b>-6.3839</b>	<b>-24.5293</b>	<b>-14.0925</b>	<b>29.5808</b>	<b>12.1324</b>	<b>17.9290</b>	

In the case of Sentinel-1B ascending image pairs, in the wider area, coherence values started reducing on average by 8.8% before the landslide, i.e. 17/01/2019 – 10/02/2019. Moreover, the coherence values continued to drop during the period 10/02/2019 – 22/02/2019 (co-event pair) by 28.1%, and by 25.6% at the next pair dated 22/2/2019 – 06/03/2019, reaching their lowest value on average (0.304). During the period of rehabilitation works there was a significant increase of 54.7% until their completion, and an additional increase of 41.9% after the road re-opened to traffic. The average, minimum and maximum coherence values obtained at each period are presented in Figure 112.

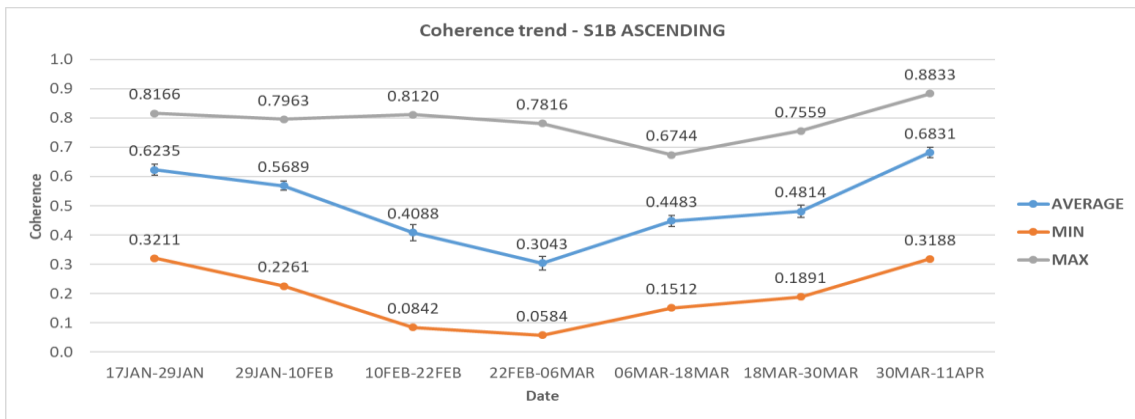


**Figure 112:** Coherence changes – Sentinel-1B ascending

Within the AOI, the coherence values decreased by 12% at the pre-event pair and further 39.4% at the co-event pair. The average coherence continued to drop by 24.7% during the start of rehabilitation works reaching its minimum value of 0.223. The coherence values then increased significantly by 111.6% as construction works reached completion and by 43.7% after the road re-opened to traffic. The average, minimum and maximum coherence values obtained from each pair of images are presented in Figure 113.

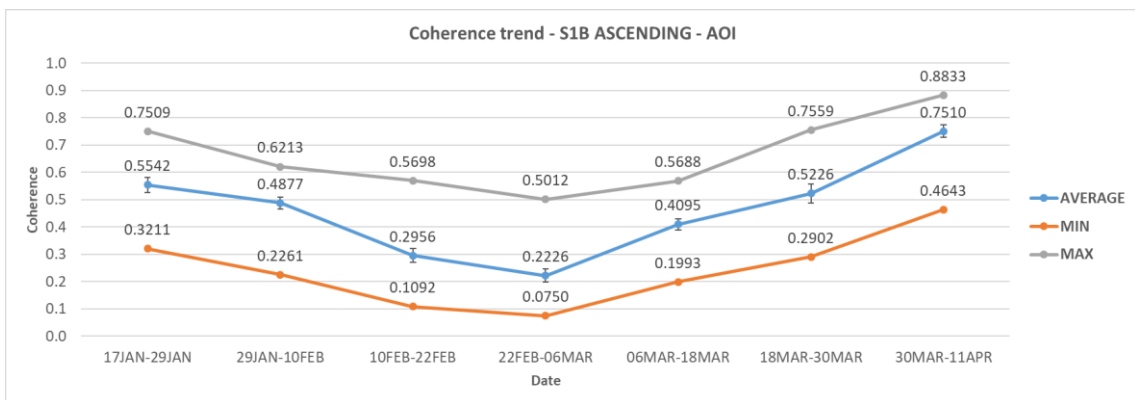


**Figure 113:** Coherence changes – Sentinel-1B ascending – AOI

**Table 26:** Coherence values – Sentinel-1B descending

Id	Coherence							Average
	18JAN-30JAN	30JAN-11FEB	11FEB-23FEB	23FEB-07MAR	07MAR-19MAR	19MAR-31MAR	31MAR-12APR	
Point 1	0.5669	0.4012	0.3748	0.2162	0.4405	0.2060	0.7889	0.4278
Point 2	0.6603	0.5317	0.2699	0.2373	0.3798	0.2473	0.6824	0.4298
Point 3	0.6097	0.5826	0.3199	0.2947	0.4517	0.3302	0.6487	0.4625
Point 4	0.7459	0.5899	0.3629	0.4867	0.5652	0.3053	0.6550	0.5301
Point 5	0.5101	0.3831	0.3984	0.1621	0.5688	0.3616	0.7946	0.4541
Point 6	0.6177	0.5022	0.2107	0.2222	0.4834	0.3348	0.7165	0.4411
Point 7	0.6475	0.5182	0.1168	0.2957	0.4256	0.4456	0.7318	0.4544
Point 8	0.7394	0.5948	0.2268	0.3266	0.5034	0.3522	0.6977	0.4915
Point 9	0.7552	0.4897	0.5140	0.1845	0.5493	0.4294	0.7029	0.5178
Point 10	0.6665	0.4219	0.5095	0.4647	0.5199	0.3044	0.7507	0.5196
Point 11	0.6472	0.5420	0.5617	0.5314	0.7282	0.4657	0.6490	0.5893
Point 12	0.4284	0.5588	0.5401	0.0815	0.6911	0.3041	0.7097	0.4734
Point 13	0.4661	0.4226	0.3742	0.1734	0.6016	0.3566	0.7877	0.4546
Point 14	0.5321	0.4473	0.1955	0.3613	0.4628	0.3745	0.7847	0.4512
Point 15	0.6396	0.4496	0.0615	0.3498	0.3566	0.5034	0.7535	0.4449
Point 16	0.6692	0.5733	0.1462	0.4699	0.3451	0.4041	0.7356	0.4776
Point 17	0.6552	0.4456	0.3214	0.2343	0.4541	0.4729	0.7313	0.4735
Point 18	0.5280	0.3562	0.5399	0.4674	0.5208	0.3499	0.8243	0.5124
Point 19	0.6207	0.4456	0.6538	0.5405	0.7139	0.5545	0.7703	0.6142
Point 20	0.6220	0.5960	0.6827	0.1078	0.6250	0.1479	0.7440	0.5036
Point 21	0.6067	0.5151	0.4131	0.2724	0.5291	0.1202	0.8088	0.4665
Point 22	0.5132	0.3974	0.1772	0.4756	0.3349	0.2236	0.8413	0.4233
Point 23	0.5368	0.4287	0.1617	0.4793	0.2213	0.4465	0.7817	0.4366
Point 24	0.5678	0.4570	0.1796	0.6120	0.1886	0.4334	0.7099	0.4498
Point 25	0.5517	0.4565	0.1174	0.4331	0.3574	0.5075	0.7095	0.4476
Point 26	0.4180	0.3860	0.4479	0.3849	0.5646	0.5532	0.8291	0.5120
Point 27	0.5308	0.5318	0.6914	0.5856	0.7770	0.6452	0.8512	0.6590
Point 28	0.7342	0.6250	0.6529	0.2197	0.4637	0.3107	0.7627	0.5384
Point 29	0.7007	0.5409	0.5364	0.2774	0.2816	0.1661	0.8146	0.4740
Point 30	0.6234	0.4356	0.3073	0.4329	0.1373	0.1570	0.8442	0.4197
Point 31	0.5453	0.4772	0.2188	0.4584	0.1419	0.3519	0.8032	0.4281
Point 32	0.5118	0.4330	0.2466	0.5659	0.1437	0.4312	0.6869	0.4313
Point 33	0.5082	0.4218	0.2109	0.4038	0.2516	0.6264	0.6431	0.4380
Point 34	0.4442	0.3789	0.3299	0.2387	0.5382	0.6853	0.7916	0.4867
Point 35	0.5231	0.5791	0.6057	0.6009	0.8486	0.6701	0.8644	0.6703
Point 36	0.7851	0.6047	0.6359	0.4578	0.3029	0.5422	0.6768	0.5722
Point 37	0.7873	0.6847	0.4404	0.3092	0.3293	0.5213	0.7799	0.5503
Point 38	0.7492	0.6200	0.4567	0.2497	0.0777	0.3472	0.8075	0.4726
Point 39	0.6645	0.5614	0.4259	0.2774	0.0875	0.3037	0.8434	0.4520
Point 40	0.5625	0.4633	0.3456	0.3894	0.1821	0.3188	0.8120	0.4391
Point 41	0.5318	0.4661	0.3394	0.5430	0.1567	0.4685	0.7308	0.4623
Point 42	0.5440	0.4376	0.2637	0.4405	0.1856	0.6804	0.5644	0.4452
Point 43	0.5473	0.4227	0.3363	0.2131	0.4424	0.7779	0.7694	0.5013
Point 44	0.5600	0.5749	0.4817	0.5818	0.8025	0.7813	0.8627	0.6635
Point 45	0.7858	0.6857	0.2021	0.3696	0.2433	0.6188	0.8034	0.5298
Point 46	0.7893	0.7126	0.3466	0.3287	0.1403	0.5371	0.7983	0.5219
Point 47	0.7511	0.7278	0.4843	0.1377	0.1565	0.4227	0.8342	0.5020
Point 48	0.6801	0.5749	0.4384	0.2866	0.1924	0.3599	0.7904	0.4747

Point 49	0.6603	0.5843	0.4223	0.4875	0.1484	0.4872	0.7572	0.5067
Point 50	0.6469	0.4533	0.3985	0.5262	0.1716	0.5743	0.5843	0.4793
Point 51	0.6749	0.4805	0.4881	0.4144	0.5003	0.7082	0.6635	0.5614
Point 52	0.6278	0.5793	0.4770	0.6250	0.6854	0.7964	0.7809	0.6531
<b>Average</b>	<b>0.6152</b>	<b>0.5106</b>	<b>0.3781</b>	<b>0.3709</b>	<b>0.4033</b>	<b>0.4389</b>	<b>0.7550</b>	<b>0.4960</b>
<b>Min</b>	<b>0.4180</b>	<b>0.3562</b>	<b>0.0615</b>	<b>0.0815</b>	<b>0.0777</b>	<b>0.1202</b>	<b>0.5644</b>	<b>0.4197</b>
<b>Max</b>	<b>0.7893</b>	<b>0.7278</b>	<b>0.6914</b>	<b>0.6250</b>	<b>0.8486</b>	<b>0.7964</b>	<b>0.8644</b>	<b>0.6703</b>
<b>St. Deviation</b>	<b>0.0985</b>	<b>0.0916</b>	<b>0.1611</b>	<b>0.1443</b>	<b>0.2071</b>	<b>0.1692</b>	<b>0.0703</b>	<b>0.0656</b>
<b>St. Error</b>	<b>0.0137</b>	<b>0.0127</b>	<b>0.0223</b>	<b>0.0200</b>	<b>0.0287</b>	<b>0.0235</b>	<b>0.0097</b>	<b>0.0091</b>
<b>Difference (%)</b>		<b>-17.0091</b>	<b>-25.9500</b>	<b>-1.9042</b>	<b>8.7381</b>	<b>8.8380</b>	<b>72.0104</b>	
<b>Normalised Difference (%)</b>		<b>-9.2951</b>	<b>-14.9095</b>	<b>-0.9612</b>	<b>4.1862</b>	<b>4.2320</b>	<b>26.4734</b>	

**Table 27:** Coherence values – Sentinel-1B descending – AOI

Id	Coherence							Average
	18JAN-30JAN	30JAN-11FEB	11FEB-23FEB	23FEB-07MAR	07MAR-19MAR	19MAR-31MAR	31MAR-12APR	
Point 14	0.5321	0.4473	0.1955	0.3613	0.4628	0.3745	0.7847	0.4512
Point 15	0.6396	0.4496	0.0615	0.3498	0.3566	0.5034	0.7535	0.4449
Point 16	0.6692	0.5733	0.1462	0.4699	0.3451	0.4041	0.7356	0.4776
Point 17	0.6552	0.4456	0.3214	0.2343	0.4541	0.4729	0.7313	0.4735
Point 18	0.5280	0.3562	0.5399	0.4674	0.5208	0.3499	0.8243	0.5124
Point 22	0.5132	0.3974	0.1772	0.4756	0.3349	0.2236	0.8413	0.4233
Point 23	0.5368	0.4287	0.1617	0.4793	0.2213	0.4465	0.7817	0.4366
Point 24	0.5678	0.4570	0.1796	0.6120	0.1886	0.4334	0.7099	0.4498
Point 25	0.5517	0.4565	0.1174	0.4331	0.3574	0.5075	0.7095	0.4476
Point 26	0.4180	0.3860	0.4479	0.3849	0.5646	0.5532	0.8291	0.5120
Point 30	0.6234	0.4356	0.3073	0.4329	0.1373	0.1570	0.8442	0.4197
Point 31	0.5453	0.4772	0.2188	0.4584	0.1419	0.3519	0.8032	0.4281
Point 32	0.5118	0.4330	0.2466	0.5659	0.1437	0.4312	0.6869	0.4313
Point 33	0.5082	0.4218	0.2109	0.4038	0.2516	0.6264	0.6431	0.4380
Point 34	0.4442	0.3789	0.3299	0.2387	0.5382	0.6853	0.7916	0.4867
Point 39	0.6645	0.5614	0.4259	0.2774	0.0875	0.3037	0.8434	0.4520
Point 40	0.5625	0.4633	0.3456	0.3894	0.1821	0.3188	0.8120	0.4391
Point 41	0.5318	0.4661	0.3394	0.5430	0.1567	0.4685	0.7308	0.4623
Point 42	0.5440	0.4376	0.2637	0.4405	0.1856	0.6804	0.5644	0.4452
Point 43	0.5473	0.4227	0.3363	0.2131	0.4424	0.7779	0.7694	0.5013
<b>Average</b>	<b>0.5547</b>	<b>0.4448</b>	<b>0.2686</b>	<b>0.4115</b>	<b>0.3037</b>	<b>0.4535</b>	<b>0.7595</b>	<b>0.4566</b>
<b>Min</b>	<b>0.4180</b>	<b>0.3562</b>	<b>0.0615</b>	<b>0.2131</b>	<b>0.0875</b>	<b>0.1570</b>	<b>0.5644</b>	<b>0.4197</b>
<b>Max</b>	<b>0.6692</b>	<b>0.5733</b>	<b>0.5399</b>	<b>0.6120</b>	<b>0.5646</b>	<b>0.7779</b>	<b>0.8442</b>	<b>0.5124</b>
<b>St. Deviation</b>	<b>0.0674</b>	<b>0.0522</b>	<b>0.1201</b>	<b>0.1092</b>	<b>0.1531</b>	<b>0.1570</b>	<b>0.0729</b>	<b>0.0283</b>
<b>St. Error</b>	<b>0.0151</b>	<b>0.0117</b>	<b>0.0269</b>	<b>0.0244</b>	<b>0.0342</b>	<b>0.0351</b>	<b>0.0163</b>	<b>0.0063</b>
<b>Difference (%)</b>		<b>-19.8200</b>	<b>-39.6029</b>	<b>53.1930</b>	<b>-26.2119</b>	<b>49.3473</b>	<b>67.4742</b>	
<b>Normalised Difference (%)</b>		<b>-11.0001</b>	<b>-24.6905</b>	<b>21.0089</b>	<b>-15.0827</b>	<b>19.7906</b>	<b>25.2264</b>	

Within the larger area, coherence values decreased by 17% on average before the landslide (18/01/2019 – 11/02/2019) took place. The coherence values continued to drop during the period 11/02/2019 – 23/02/2019 (co-event pair) by 26% reaching their minimum value of 0.371 on average. During the period of rehabilitation works there was an increase of 17.5% in coherence until their completion. Finally, the average coherence rose by 72% after the road re-opened to traffic. The average, minimum and maximum coherence values obtained at each period are presented in Figure 114.

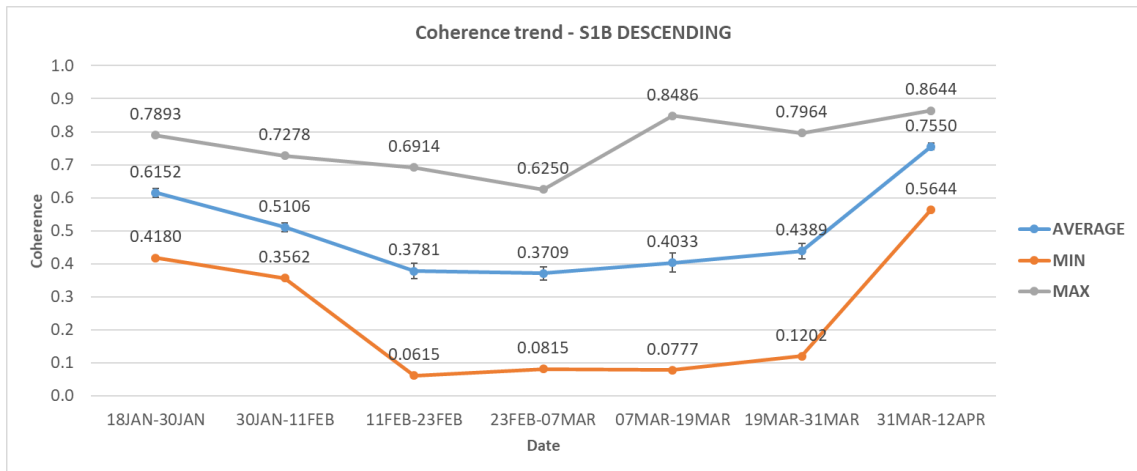


**Figure 114:** Coherence changes – Sentinel-1B descending

There is a peak at the maximum coherence (0.849) at the pair of SAR images dated 07/03/2019-19/03/2019, which corresponds to point 35. This is due to the fact the specific point is located at the eastern boundaries of the area, and only a small portion of the pixel is within its limits.

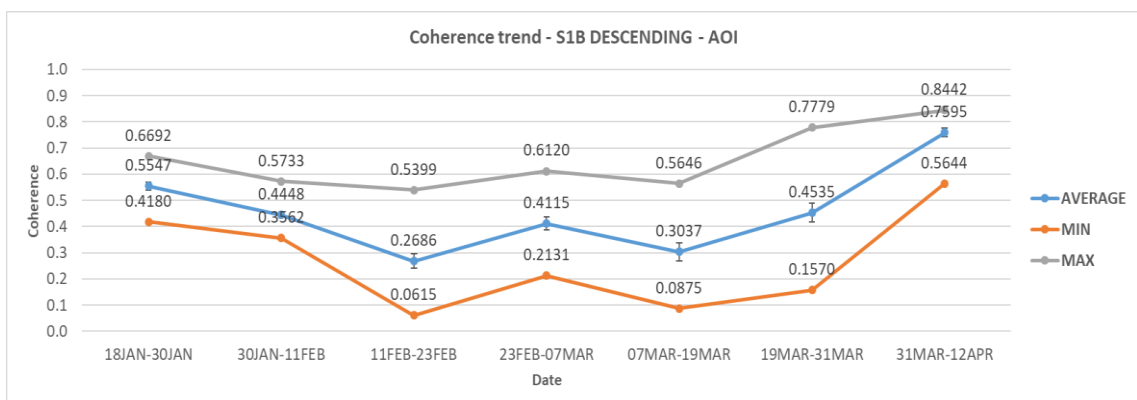


**Figure 115:** Coherence changes – Sentinel-1B descending – AOI

Within the AOI, the coherence values decreased by 20% at the pre-event pair and a further 39.6% at the co-event pair reaching its minimum average value of 0.269. During the



rehabilitation works average coherence fluctuated, increasing initially by 53.2% and then decreasing by 26.2%. Average coherence then increased by 49.3% close to the completion of the works and continued increasing by 67.5% after the road opened to traffic reaching its maximum value of 0.76. The average, minimum and maximum coherence values obtained from each pair of images are presented in Figure 115.

Coherence values from Sentinel-1B ascending images appeared to be the best fit of what was expected to see based on the landslide occurrence, rehabilitation works and road opening. Sentinel-1B descending also performed quite well with the exception of a high peak in the maximum coherence values in the larger area for the pair 07/03/2019 – 19/03/2019 and a high peak in maximum, minimum and average coherence values within the AOI for the image pair 23/02/2019 – 07/03/2019.

By averaging the coherence pixel values from ascending and descending Sentinel-1B pairs, a clearer representation of the coherence changes trends in all 3 categories, i.e. minimum, maximum and average values is provided, as shown in Figure 116 and Figure 117. The x-axis values were changed from dates to periods, as shown earlier (Figure 99).

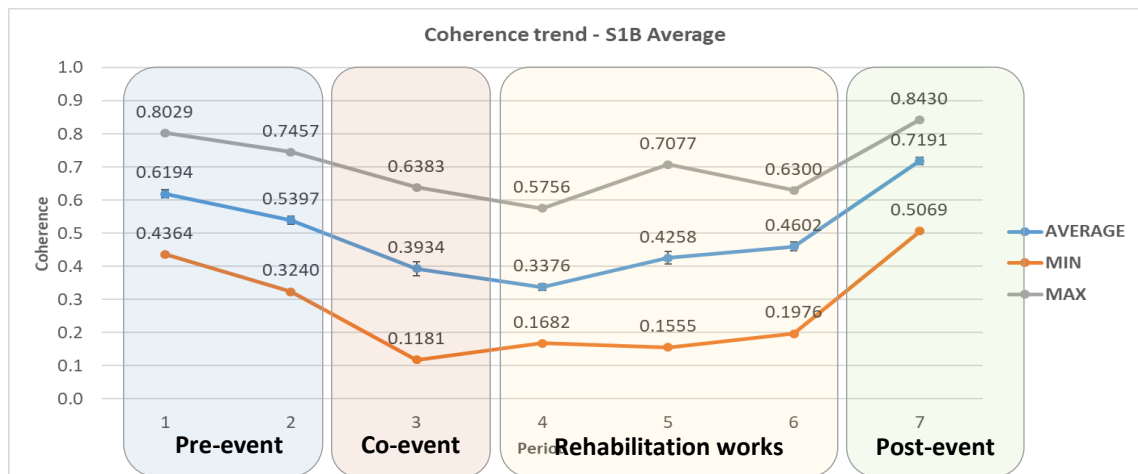


**Figure 116:** Coherence changes – Sentinel-1B average

The high peak that existed in the maximum values for the wider area, but also for the minimum, maximum and average values in the case of the Sentinel-1B descending images in the AOI, evened out completely, and there is a common trend in coherence changes in maximum, minimum and average values. The minimum values, as shown in Figure 116, lie within the rehabilitation works period and the maximum values in the post-event one. Through the averaging of coherence values, the standard deviations and standard of the

samples are minimised. However, there is still a peak at the maximum coherence (0.708) during the period of rehabilitation works, which corresponds to point 27. This is due to the fact the specific point is located at the eastern boundaries of the area, and only a small portion of the pixel lies within its limits.

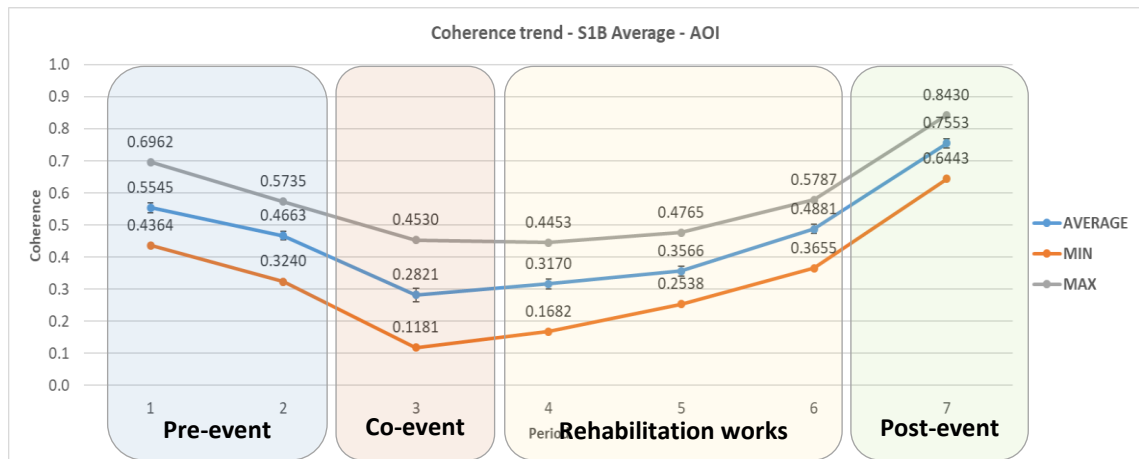


**Figure 117:** Coherence changes – Sentinel-1B average – AOI

In the landslide area, as presented in Figure 117, the three lines of minimum, average and maximum coherence follow the same trend, with their maximum values being in the post-event period. The range between minimum and maximum values is smaller compared with all other set of data seen before.

The average coherence decreased by 15.9% during the pre-event period, giving valuable information for the evolution of the landslide. It continued decreasing more rapidly by 39.5% at the co-event period, reaching its minimum value of 0.282. Then, the average coherence increased by cumulatively 60% until the end of the rehabilitation works and then increased by another 54.7% after the road opening back again reaching its maximum value of 0.755.

For the area of interest, within the boundaries of landslide alone, from the analysis of Sentinel-1A data, the minimum values of the average, maximum and minimum coherence lie within the rehabilitation works period. In the case of Sentinel-1B data, there seems to be a better match of the data with the timeline of incidents, as all minimum values of the average maximum and minimum coherence, that were obtained from the analysis of the co-event ascending and descending pairs for the area of interest, are within the co-event period, i.e. the period that the landslide took place. In both cases the maximum values are all within the pre-event and post-event periods.

The above results were combined further as per passing direction, to investigate if the information obtained by ascending and/or descending platforms provides more valuable input in the study conducted. The results are presented in the following figures.

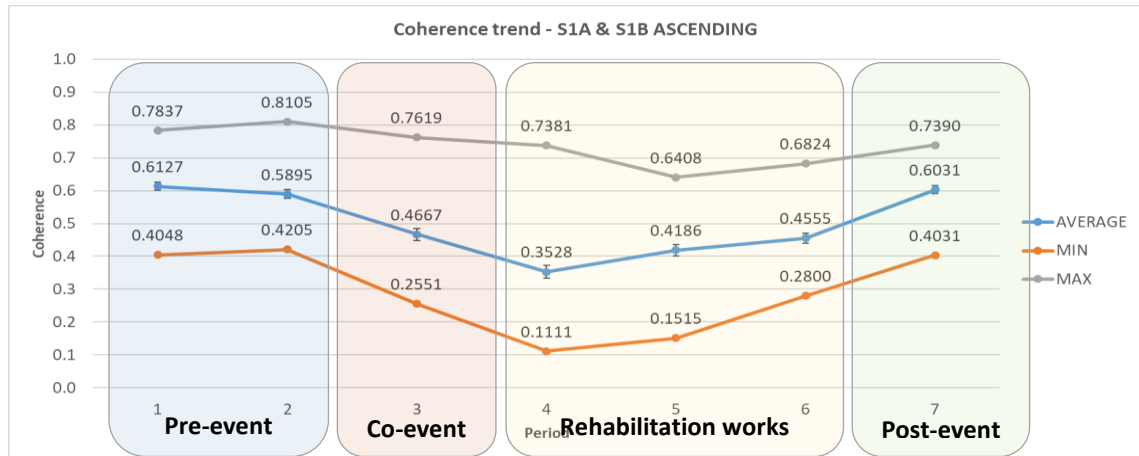


**Figure 118:** Coherence changes – S1A and S1B ascending

In the wider area, the averaging of coherence values from Sentinel-1A and Sentinel-1B ascending images, shows that maximum coherence values of the average, maximum and minimum coherence are found in the pre-event and post-event periods whereas their minimum values within the rehabilitation works period and more specifically at the next pairs of images following the co-event ones (Figure 118).

More specifically, the average coherence is stable in the pre-event period with a value over 0.50 (~0.60) and then decreases by 20.8% at the co-event period and continues to reduce by an additional 24.4% reaching its minimum value of 0.353 within the rehabilitation works period. Then the average coherence increases by 27.4% until the end of the rehabilitation works and by 32.4% after the road opening. Standard deviations and standard errors have decreased through the averaging based on the satellite pass direction.

As presented in Figure 119, within the AOI, the phenomenon looks intensified. The average coherence remains stable approximating 0.54 in the pro-event period and then reduces by 28.6% at the co-event one. It continues to decrease within the rehabilitation period at a rate of 31.1% reaching its minimum of 0.265 at the first at the first pairs of images following the co-event ones. The average coherence then increases at a cumulative rate of 69.7% until the end of the construction works and by a further 38.1% after the road was open to traffic. Overall, the coherence values are higher in the post-event than in the pre-event period.

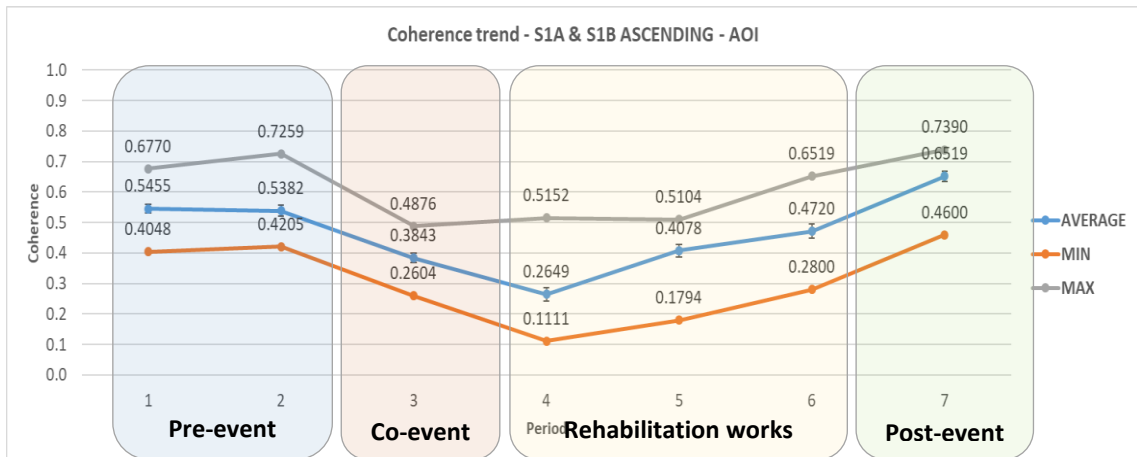


**Figure 119:** Coherence changes – S1A and S1B ascending – AOI

Coherence values were also calculated from the descending pass of Sentinel-1A and Sentinel-1B satellites. The results are presented in Figure 120 and Figure 121 for the wider area and the area of interest respectively.

More specifically, as presented in Figure 120, the average coherence is nearly stable in the pre-event period with a small decrease of 6.5% and a value over 0.50 in both sets of image pairs, 0.585 in the first pairs and 0.547 in the second ones. The average coherence then decreases by 27.8% at the co-event period and continues decreasing by 10.7% reaching its minimum value of 0.353 in the rehabilitation works period. It is noteworthy that the minimum average coherence value in both averages per pass direction is identical.

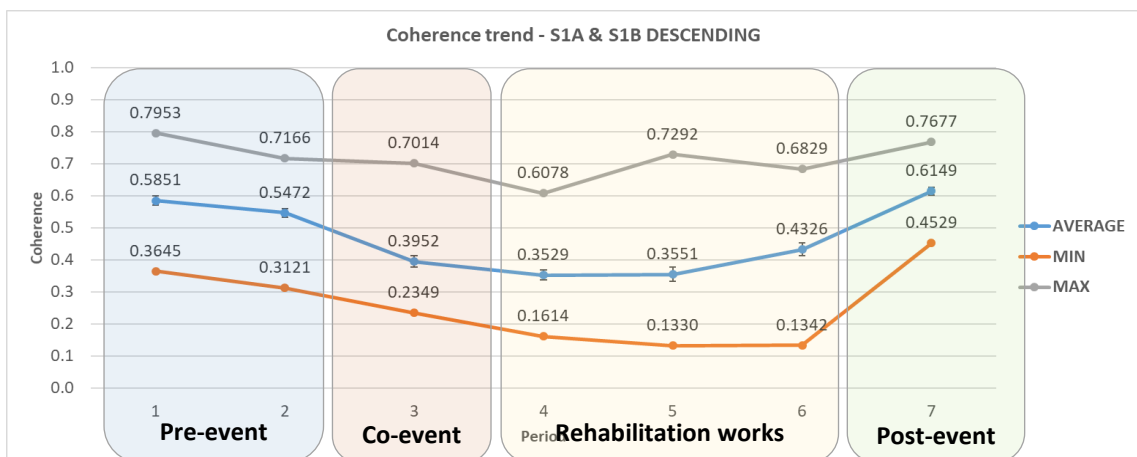


**Figure 120:** Coherence changes – S1A and S1B descending

Then the average coherence increases by 21.9% until the end of the rehabilitation works and by 42.1% after the road opening. Standard deviations and standard errors have also decreased, in this case, through the averaging of the satellites according to the descending

satellite pass direction. There is a peak at the maximum coherence (0.729) during the period of rehabilitation works, which corresponds to point 35. This is due to the fact the specific point is located at the eastern boundaries of the area, and only a small portion of the pixel lies within its limits.

Within the landslide area defined, there appears to be a more significant decrease within the pre-event period, compared with that in the previous case, of 8.5% with the average coherence value dropping below the threshold of 0.5 (0.486).

Following, the average coherence continues to reduce at the co-event pairs by 27.9% and at the rehabilitation works period by an additional rate of 22%, reaching its minimum value of 0.277. Then, the average coherence values increased by 67.1% as the road was opening and an additional 36.5% after the road opened, reaching its maximum value of 0.631. The results are presented in Figure 121.

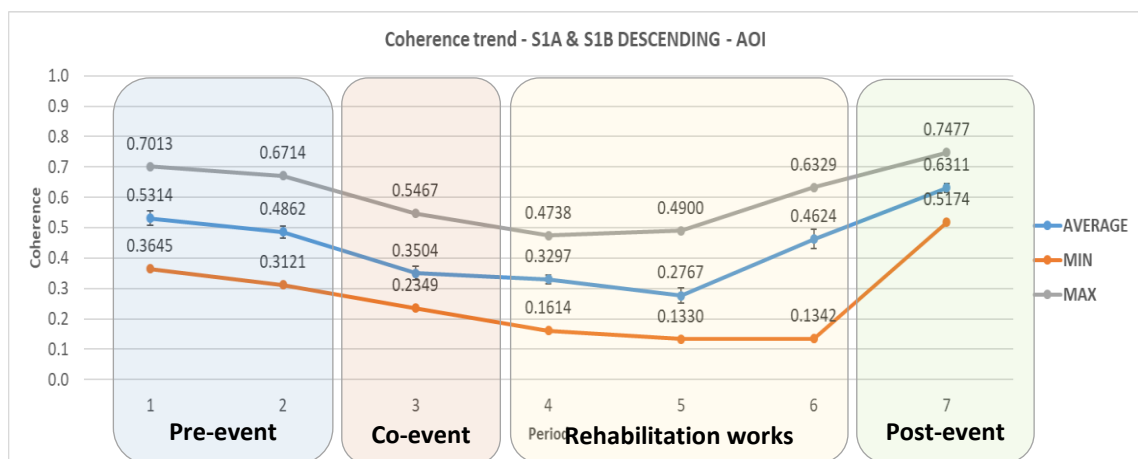


**Figure 121:** Coherence changes – S1A and S1B descending – AOI

The averaging of all coherence values, from both satellites and pass directions, was then carried out to see the effect that this will have on the overall coherence values. The results are presented in Figure 122 and Figure 123 for the larger area (52 points) and the more confined area (20 points) respectively.

In the larger area, average maximum and minimum coherence values follow the same trend, having their minimum values during the period of rehabilitation works and their maximum during the pre-event and post-event periods. The coherence is nearly stable within the pre-event period approximating at 0.58 and then drops by 24.2% during the co-event period and continues to decrease by 18.1% reaching its minimum value of 0.353

during the rehabilitation works period. Then average coherence increased by 26.4% in total by the end of the same period and by an additional 37.1% after the road opening, reaching its maximum value of 0.61.

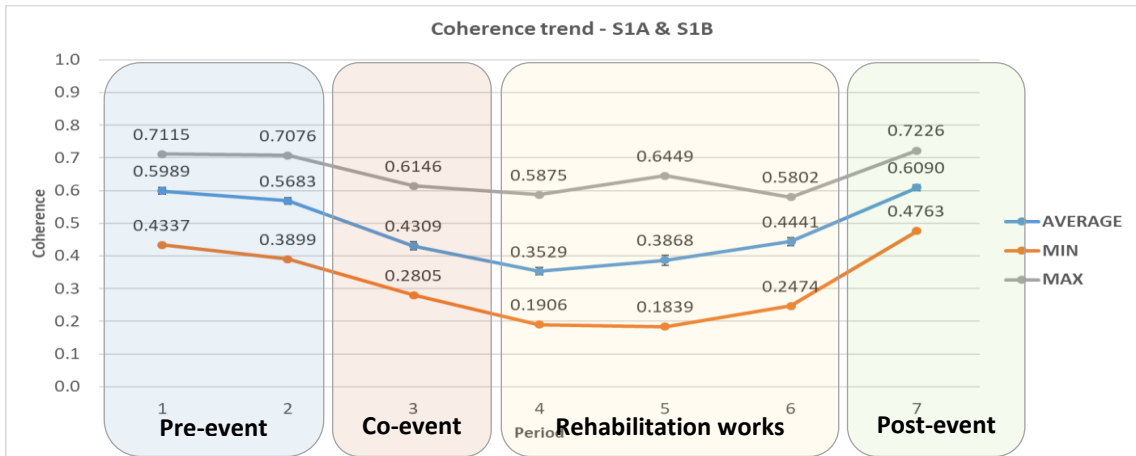


**Figure 122:** Coherence changes – S1A and S1B average

A high peak appears in the maximum coherence values in the middle of the period of rehabilitation works. By checking the point grid, this value is at point 11, located at the far north-eastern part of the wider area, near its boundaries. The fact that the entire pixel is not within the area of study, has introduced this unexpected rise in maximum values.

In the case of the landslide area (Figure 123), all three components, minimum, maximum and average coherence follow the same trend with a small range of values between min and max. However, a noteworthy point is that their maximum values, that are within the post-event period, range only from 0.593 to 0.68.

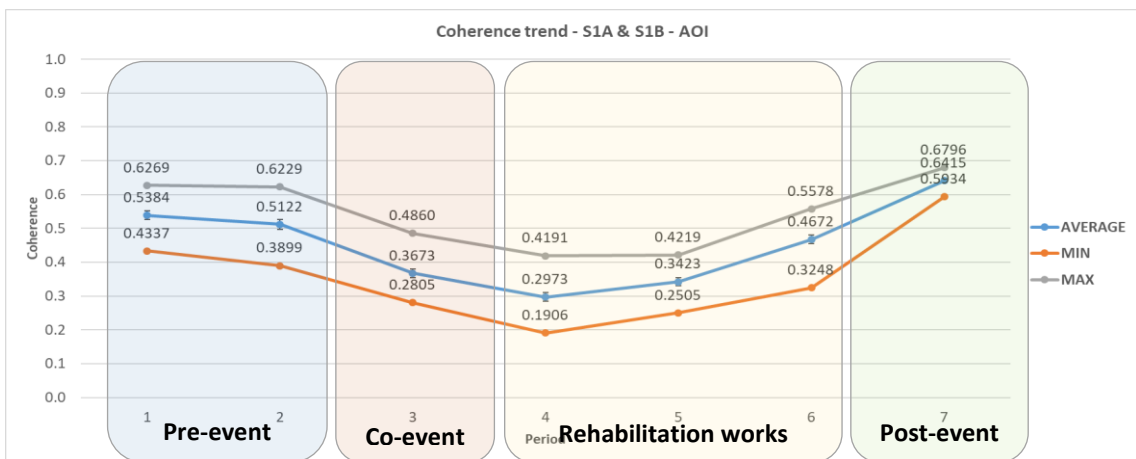


**Figure 123:** Coherence changes – S1A and S1B average – AOI

The coherence is nearly stable within the pre-event period averaging at 0.525 and then drops by 28.3% during the co-event period and continues to decrease by 19.1% reaching its minimum value of 0.297 during the rehabilitation works period. Then the average coherence increased by 51.6% in total by the end of the same period and by an additional 37.3% after the road opening, reaching its maximum value of 0.642.

Based on the findings, both Sentinel-1A and Sentinel-1B satellites performed quite well, with the sole difference being in the pre-event period where images from Sentinel-1A show a small increase in average coherence values, in comparison with a more significant reduction in average coherence values in the case of Sentinel-1B images during the same period. In all cases the maximum values were within the pre-event and post-event periods, and the lowest values during the rehabilitation works period. The latter is considered reasonable as there was a lot of soil disturbance during the period of rehabilitation works (Figure 124), that lasted from the 16<sup>th</sup> of February until the 23<sup>rd</sup> of March 2019, when the road was again open to traffic.



**Figure 124:** Rehabilitation works at the landslide area – Pissouri (Geological Survey Department)

It is clear that the coherence values change more significantly within the landslide area than in the wider area of rehabilitation works. Additionally, the average, minimum and maximum values are generally lower within the AOI. Averaging the coherence results as per satellite and satellite pass direction, has provided valuable input and reduced the

variations that existed when studying the values individually. Coherence values of pixels located at the boundaries of both areas and included partially within them, have affected the results of the analysis, but not greatly, as their impact was minimised by averaging observations from different satellites and pass directions.

The trend of the changes in coherence over time, in average, minimum and maximum values was similar after averaging of the coherence values from all SAR pairs. This finding was intensified in the case of the AOI where all three sets of values follow identical trends. At the same time, this led into a reduction of the range of values, i.e. the difference between maximum and minimum values, especially in the case of the confined area of the landslide as seen before in Figure 123.

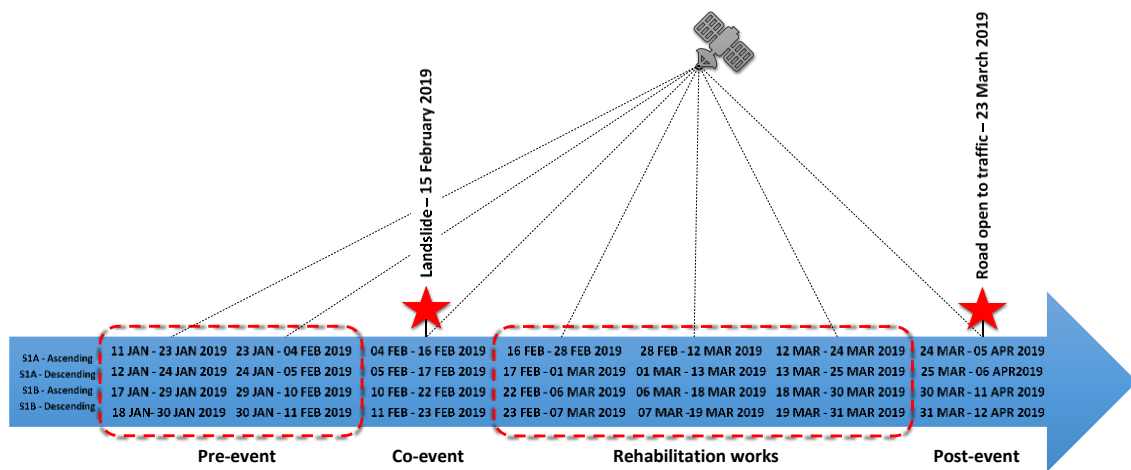


**Figure 125:** Timeline of SAR acquisitions and events

The results were then averaged for each period, using the coherence values from the interferometric SAR pairs with the images that were obtained during the specific periods of the event timeline, as seen in Figure 125. Therefore, for Sentinel-1A ascending image pairs, the average of coherence values obtained from pairs 11/01/2019 – 23/01/2019 and 23/01/2019 – 04/02/2019 was calculated, and this value will correspond to the coherence of the pre-event period based on Sentinel-1A ascending observations. The same was done for the observations in the other three satellites.

As the main purpose of the present study is the identification of coherence changes due to natural disasters, the period of rehabilitation works was excluded from further analysis. Therefore, only the pre-event, co-event and post-event periods are studied from this point



forward. An overview of the results for each satellite and satellite pass direction are presented in Figure 126.

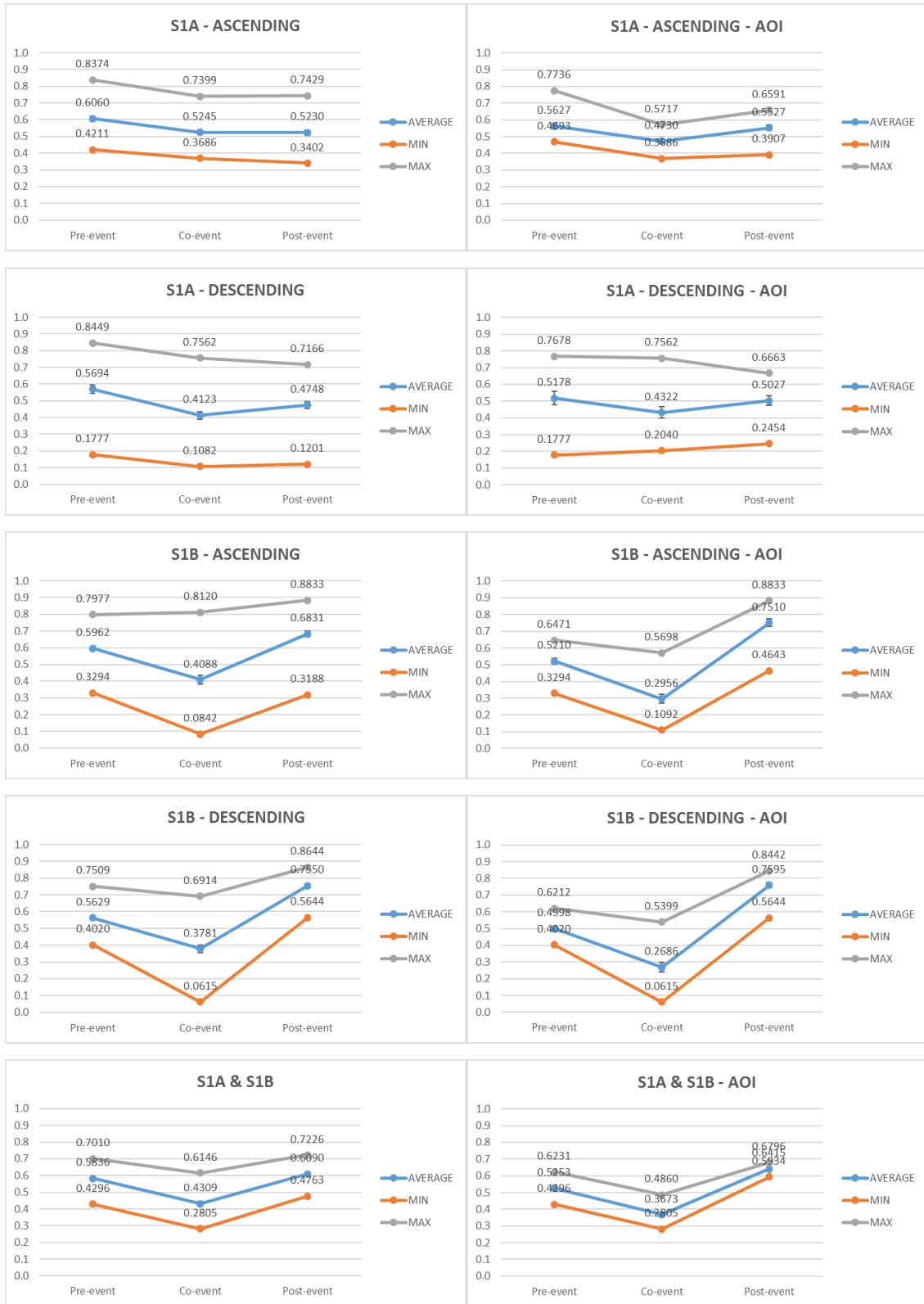
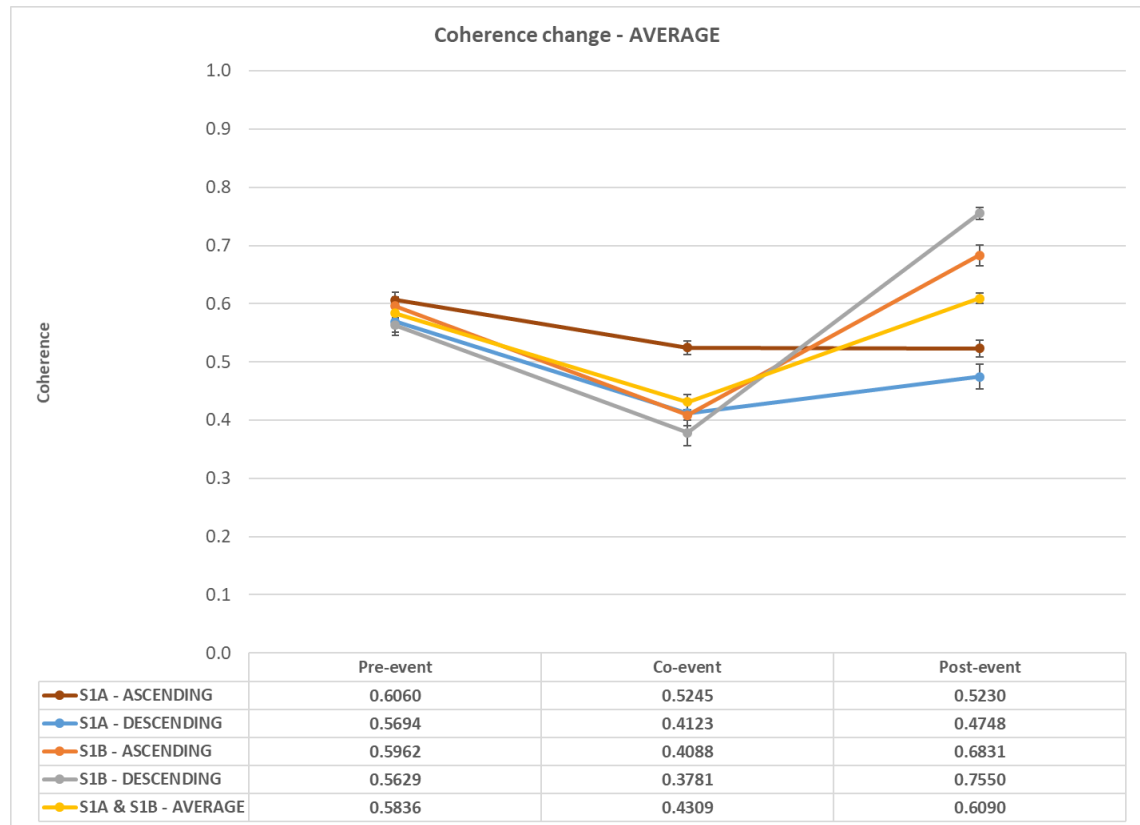


Figure 126: Coherence changes in the 3 periods for the entire area (left) and the AOI (right)

From the above, it is clear that both Sentinel-1A and Sentinel-1B satellites seem to be able to identify the sudden coherence loss, i.e. the phase decorrelation, from the pre-event to the co-event period, and the increase in coherence values between the co-event and post-event period.

The average coherence values for the three periods, based on observations from all satellites and satellite pass directions for the wider area (rehabilitation works) and the landslide area are shown in Figure 127 and Figure 128 respectively.



**Figure 127:** Coherence changes – Average

From the figure above, the decorrelation (coherence loss) between the pre-event and co-event periods and the coherence gain between the co-event and post-event periods become more obvious.

In fact, in Sentinel-1A ascending based interferometric pairs, coherence decreased by 13.4% from 0.606 to 0.525 between the pre-event and co-event periods and remained stable between the co-event and post-event periods. In the case of Sentinel-1A descending pairs, average coherence decreased significantly from 0.569 to 0.412 (-27.6%) and then increased by 15.2% from 0.412 to 0.475.

Moreover, in the case of Sentinel-1B ascending image pairs, average coherence was 0.596 during the pre-event period and dropped by 31.4% reaching its minimum value of 0.409 during the co-event period. Then it raised significantly by 67% during the post-event period reaching its maximum value of 0.683. For Sentinel-1B descending image pairs, average coherence decreased by 32.8% from 0.563 that was during the pre-event period to 0.378 (minimum value) within the co-event period. Average coherence then almost doubled (+99.7%) between the co-event and post-event periods reaching its maximum value of 0.755.

Therefore, interferometric pairs from Sentinel-1B imagery appear more efficient, compared to Sentinel-1A, in demonstrating the coherence loss between pre-event and co-event periods and the coherence gain from co-event to post-event periods. This is due to the fact that in the case of Sentinel-1B imagery minimum average coherence values are found in the co-event period, whereas in the Sentinel-1A based interferometric pairs, minimum average coherence values lie within the rehabilitation works period. Indeed, average coherence continues to decrease at a rate of 22.5% and 13.7% in period of rehabilitation works for ascending and descending pairs respectively. This, in turn, leads to their inability to present the maximum coherence loss and gain between the periods under study.

This problem seems to be minimised when averaging all results together. In this case, average coherence starts at 0.584 at the pre-event period and then decreases by 26% towards the co-event to a value of 0.431. This value is not the minimum, as it continues to decrease by another 8.4% reaching its minimum 0.395 during the rehabilitation works period. However, the earlier issue is mitigated by a significant increase of 41.3% between the co-event and post-event periods.

Within the determined landslide area, coherence loss and gain trends appear to be strengthened, as presented in Figure 128. For Sentinel-1A ascending pairs, average coherence starts at 0.563 at the pre-event period and reaches 0.473 during the co-event period (-15.9%). Then, it increases by 16.9% reaching 0.523 at the post-event period. In the case of Sentinel-1A descending, the situation is similar, as coherence decreased by 16.5% between the pre-event (0.518) and co-event periods (0.432) and then increased by 16.3% reaching 0.527. In both cases, the increase and decrease in coherence look

symmetrical. As before, the minimum average values are not within the co-event period as values appear to decrease even more during the rehabilitation works.

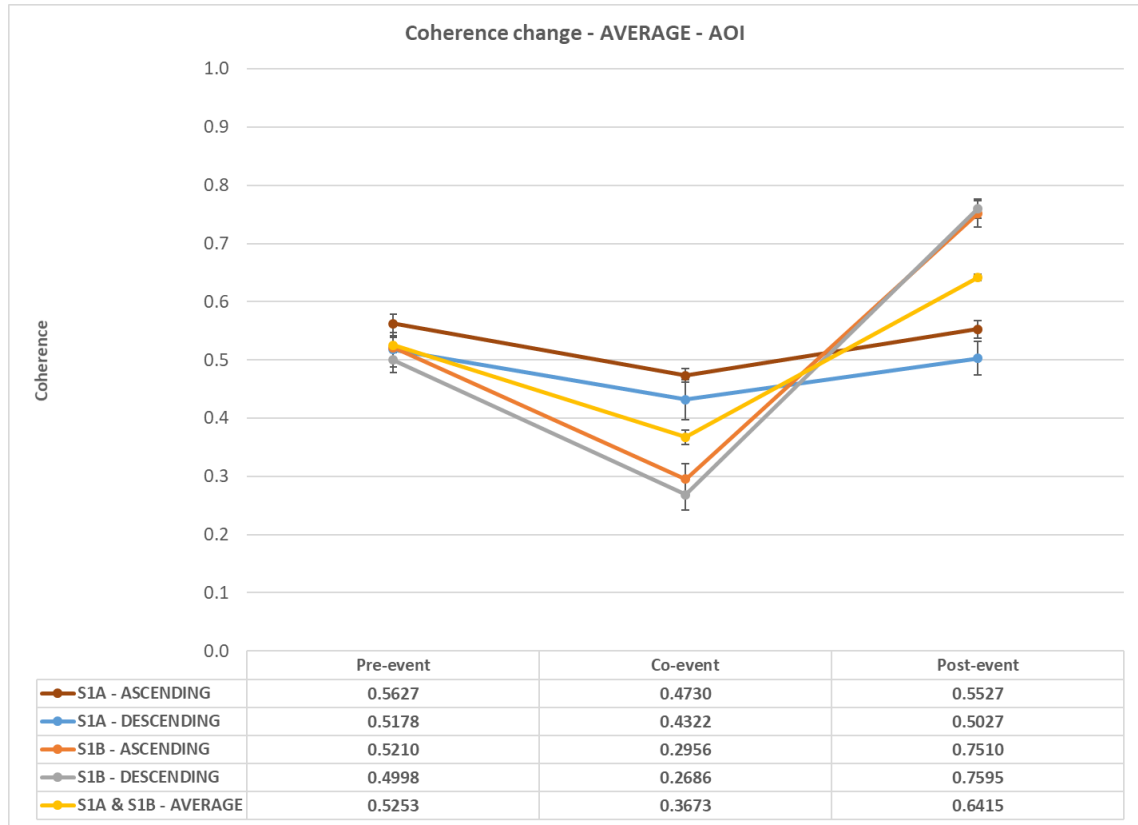


**Figure 128:** Coherence changes – Average – AOI

In the case of Sentinel-1B ascending pairs, there is a significant coherence loss of 43.3% between the pre-event (0.521) and co-event (0.296) periods. Then, from its minimum value, it increases by a substantial 154.1% to reach its maximum value of 0.751 during the post-event period. The average coherence values for the Sentinel-1B descending pairs, follow similar coherence changes as in the previous case. In fact, average coherence starting at 0.500 before the landslide, decreases by 46.2% reaching its minimum value of 0.269 during the co-event period. Then it increases by a vast 182.7% reaching its maximum value of 0.760 after the road opened to traffic.

The averaging of the results within the AOI, show a decrease of 30.1% in coherence between the pre-event (0.525) and co-event pairs (0.367) and an increase of 74.6% between the co-event and post-event pairs, reaching its maximum value of 0.642. The main difference is that the minimum value of average coherence is during the co-event period and not during the rehabilitation works, as in the case of the average for the wider

area. This finding is quite promising, as it provides a clear distinction between the landslide and rehabilitation works area.

Analysis of variance (ANOVA) statistical tests and two-tail t-tests were carried out, in EXCEL, to prove the statistical significance of the results using a 95% level of confidence. T-tests were used to determine if there is a significant difference between the means of two samples, i.e. time periods, based on a null hypothesis that the means of two populations are equal. The vast majority of the results rejected this null hypothesis, with t values calculated being outside the predefined limits set by the level of confidence.

However, there was one exception in the rehabilitation works area, regarding the Sentinel-1A ascending pairs between the co-event and post-event period datasets. Within the AOI, there were two cases between the pre-event and post-event datasets for Sentinel-1A ascending and descending pairs that failed to reject the null hypothesis, and thus the datasets for these two periods do not differ significantly.

Moreover, ANOVA tests were performed to test the null hypothesis that the means of several populations are all equal for the data corresponding to the wider area and the landslide area. The only case that marginally failed the ANOVA tests were the coherence value datasets obtained from Sentinel-1A descending pairs within the landslide area failed in this test. This fact is also supported by the results of the t-tests presented above.

These results are well supported from the findings of the analysis that was carried out in the present section of the thesis concluding in Figure 127 and Figure 128. The observed variations between the average coherence values between the specific periods were not great enough to assume that the results differ significantly. In the case of Sentinel-1A ascending interferometric pairs, average coherence values in the wider area between the co-event and post-period were almost identical, i.e. 0.525 and 0.523 respectively. Concerning the landslide area, average coherence values, in the case of Sentinel-1A ascending pairs were similar in the cases of pre-event (0.563) and post-event periods (0.553). The same case is with Sentinel-1A descending pairs as pre-event and post-event average coherence values were very close, 0.518 and 0.503. In all cases, these findings do not limit the use of Sentinel-1A pairs, as results are compared between consecutive time periods and more importantly between the pre-event and co-event periods in the landslide timeline.

Covariance and correlation tables were also calculated to study the direction and strength of the relationship between the individual samples of coherence values. The following equations were used for the determination of covariance  $COV$  and correlation  $\rho$ :

$$COV(X, Y) = \frac{\sum (X_i - \bar{X})(Y_j - \bar{Y})}{n} \quad (Eq. 11)$$

$$\rho(x, y) = \frac{COV(X, Y)}{\sigma_X \cdot \sigma_Y} \quad (Eq. 12)$$

The results of all the statistical tests can be seen in *Appendix I*.

### 4.3.2 Coherent Change Detection analysis

The distinction between coherence changes due to geological hazards and coherence changes due to natural variations was attempted through the calculation of the coherence differences, and normalised coherence differences between the pre-event coherence and co-event coherence.

The coherence maps were developed by averaging the consecutive pre-event pairs for each satellite and satellite pass direction, within ArcGIS, using the Raster Calculator tool (Spatial Analyst) as seen in Figure 129.

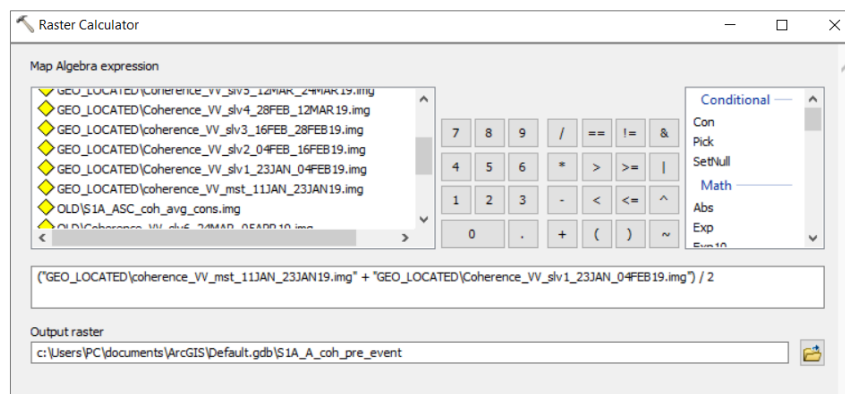


**Figure 129:** Raster calculator – Coherence averaging

Coherence maps were produced for the three time periods for each satellite and satellite pass direction. The maps from Sentinel-1A ascending pairs are presented in Figure 130, Figure 131 and Figure 132 for the pre-event, co-event and post-event periods respectively.

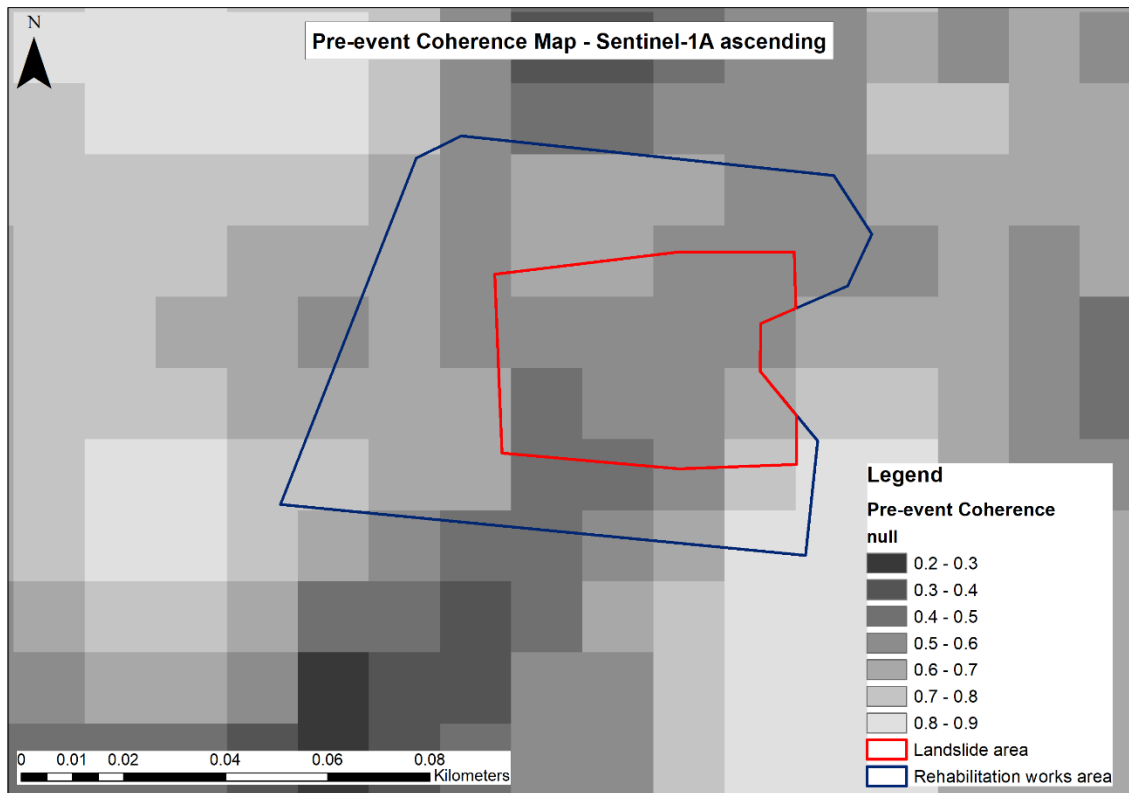


**Figure 130:** Pre-event coherence map – Sentinel-1A ascending

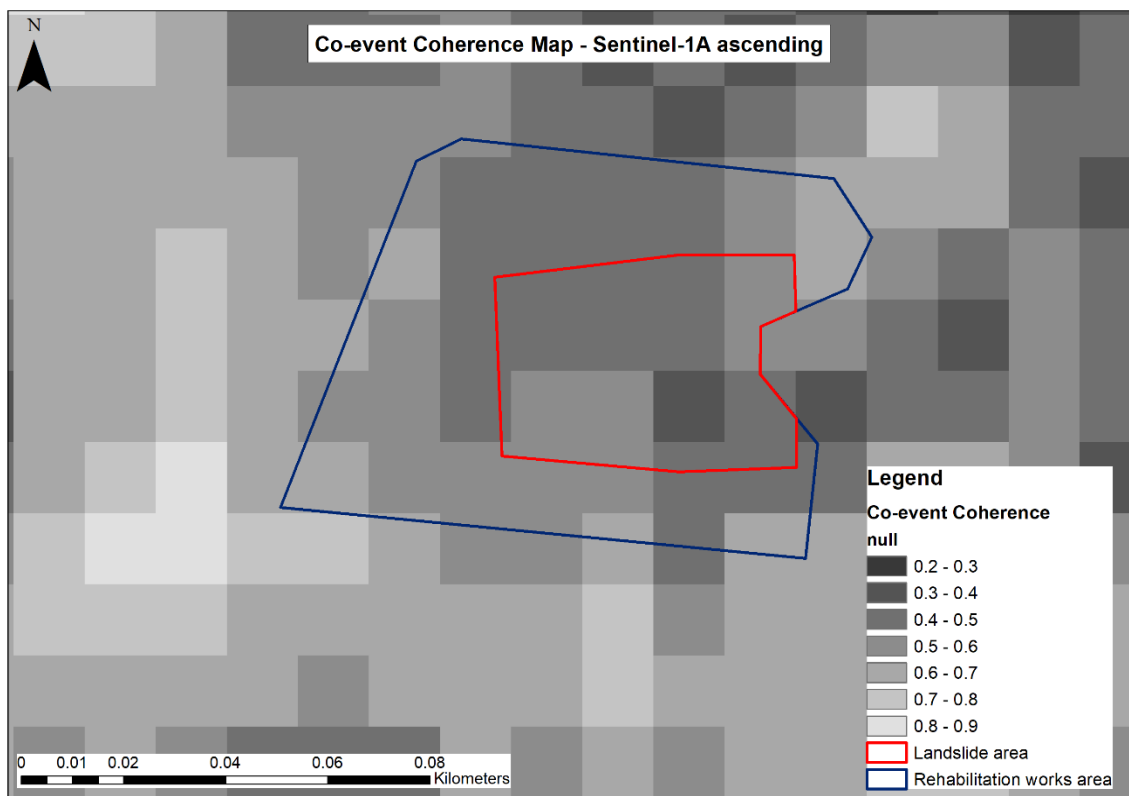


**Figure 131:** Co-event coherence map – Sentinel-1A ascending

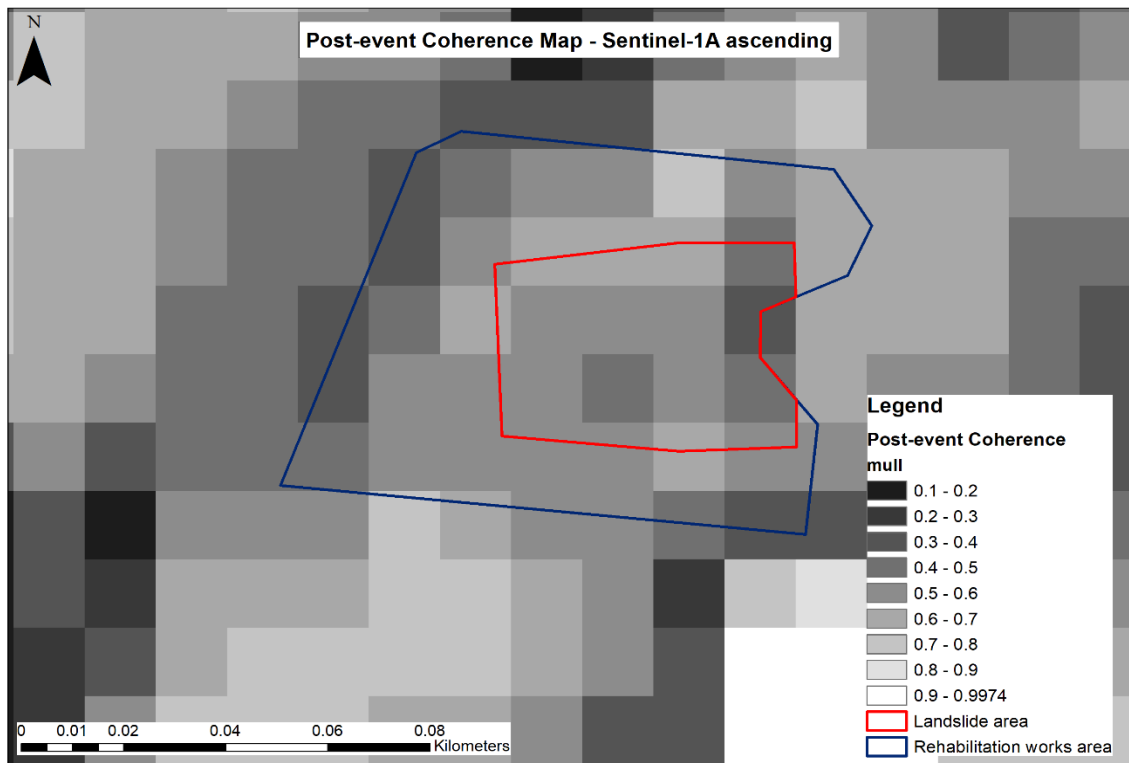


**Figure 132:** Post-event coherence map – Sentinel-1A ascending

The coherence maps from Sentinel-1A descending pairs are presented in Figure 133, Figure 134 and Figure 135 for the pre-event, co-event and post-event periods respectively.

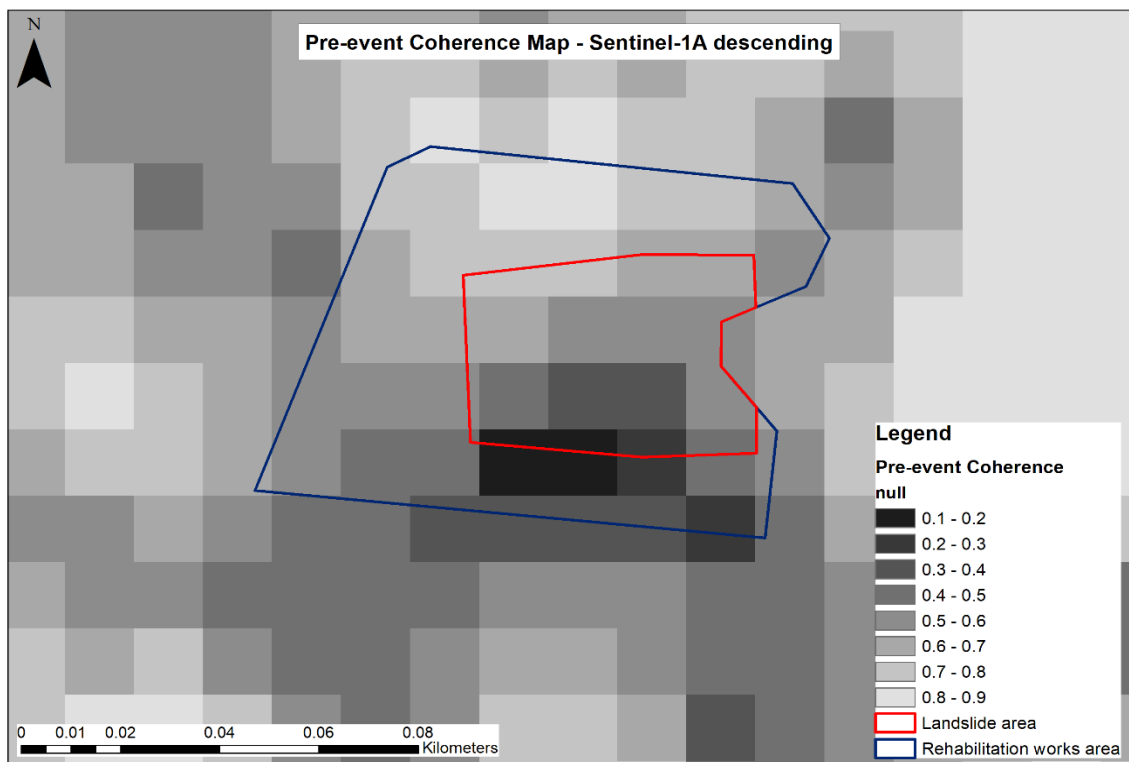


**Figure 133:** Pre-event coherence map – Sentinel-1A descending



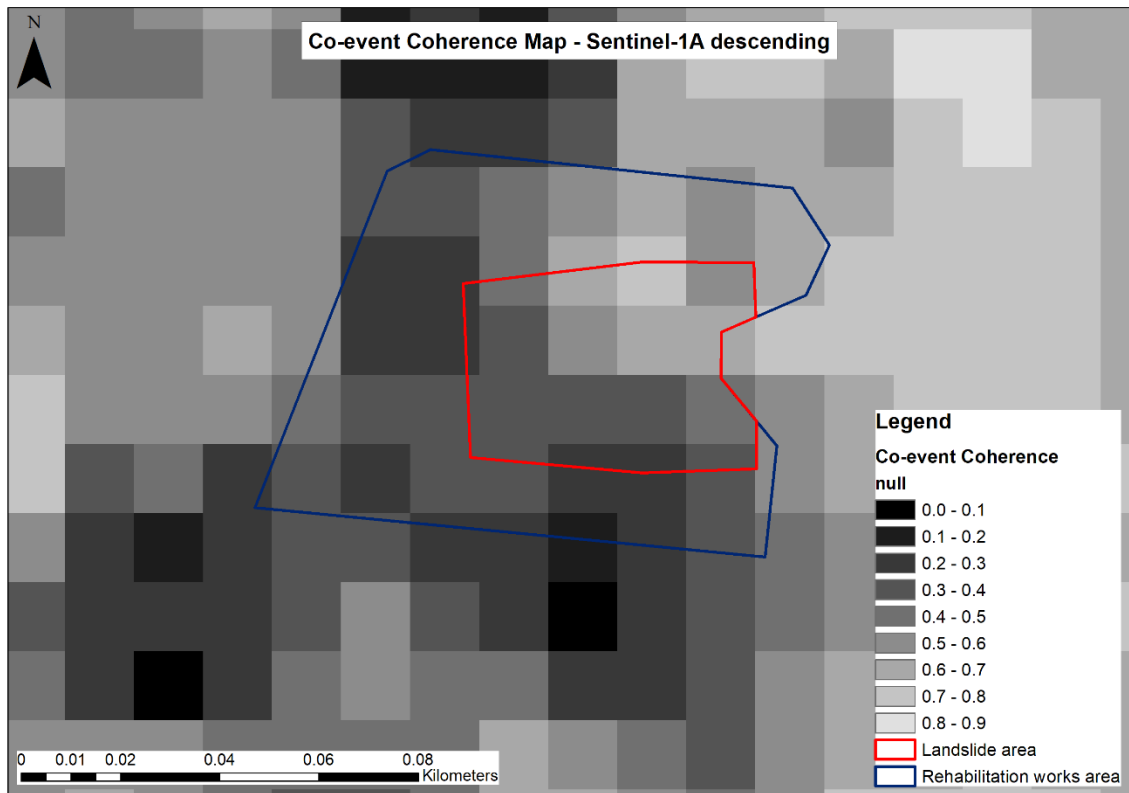


**Figure 134:** Co-event coherence map – Sentinel-1A descending

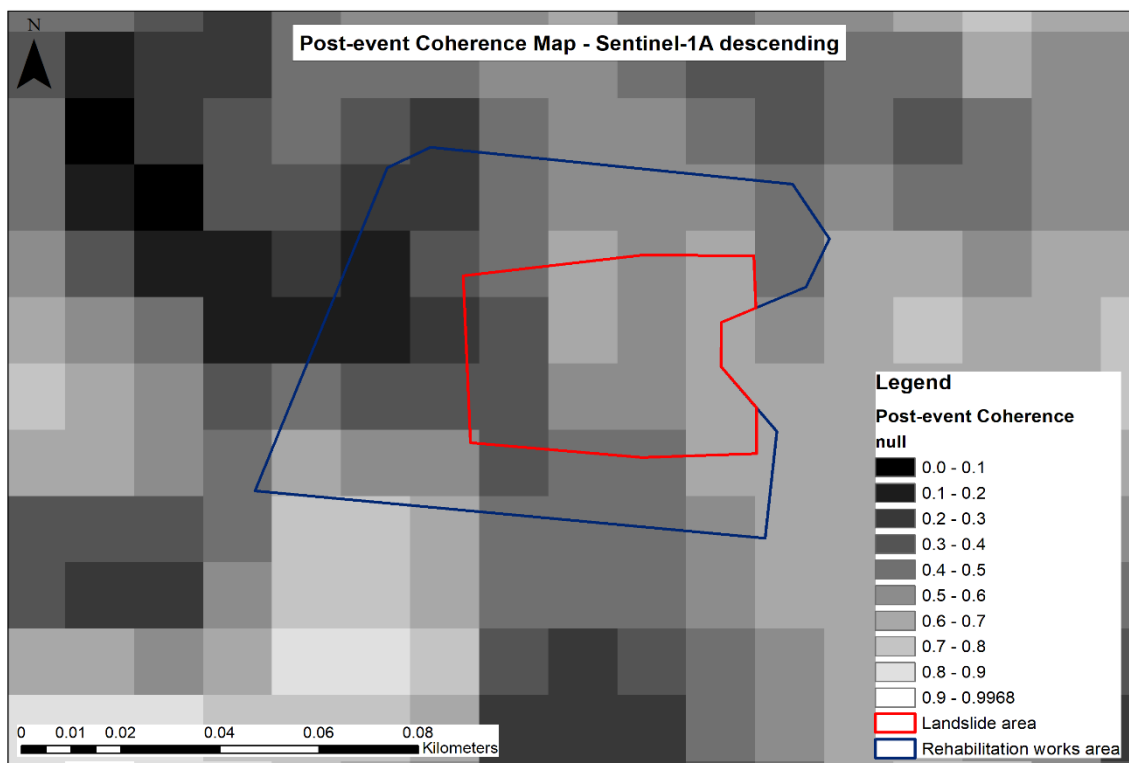


**Figure 135:** Post-event coherence map – Sentinel-1A descending

The coherence maps from Sentinel-1B ascending pairs are presented in Figure 136, Figure 137 and Figure 138 for the pre-event, co-event and post-event periods respectively.

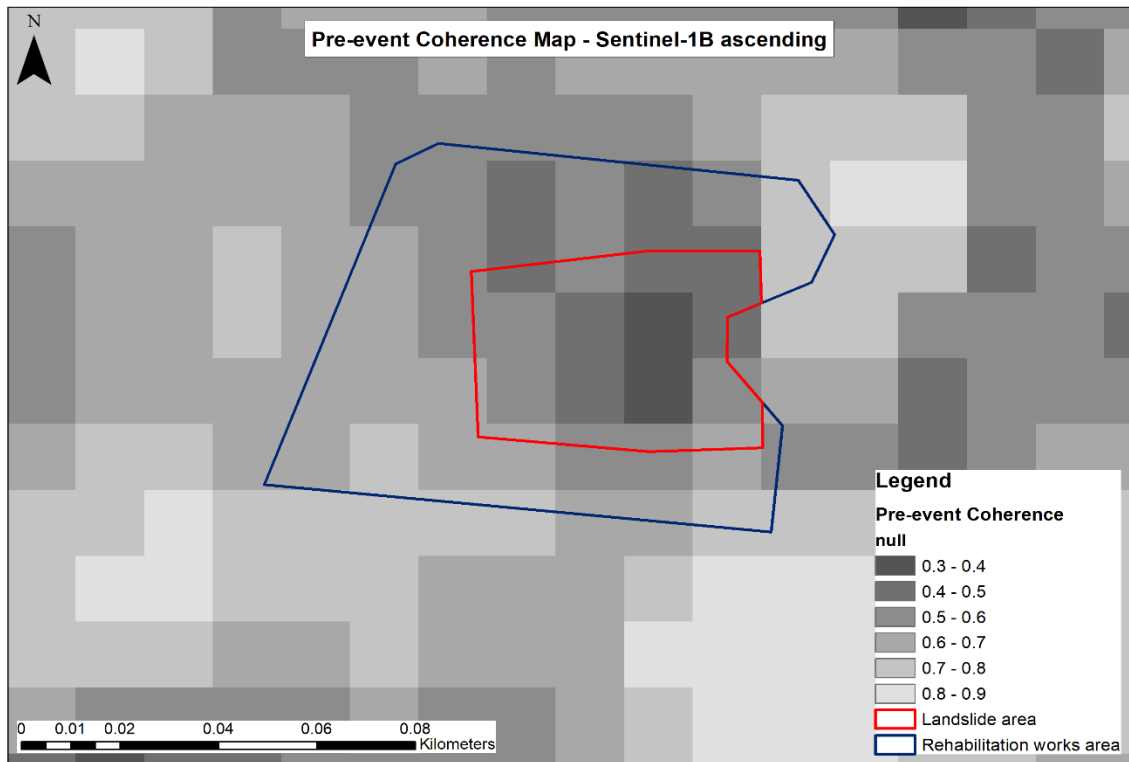


**Figure 136:** Pre-event coherence map – Sentinel-1B ascending

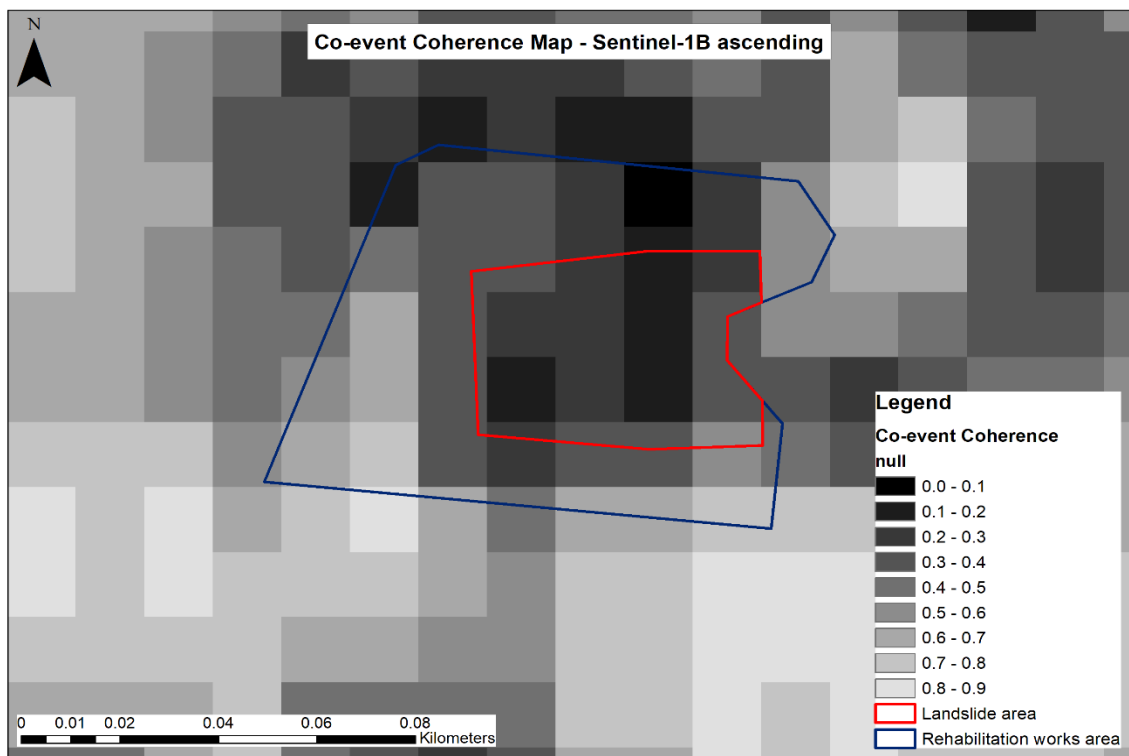


**Figure 137:** Co-event coherence map – Sentinel-1B ascending

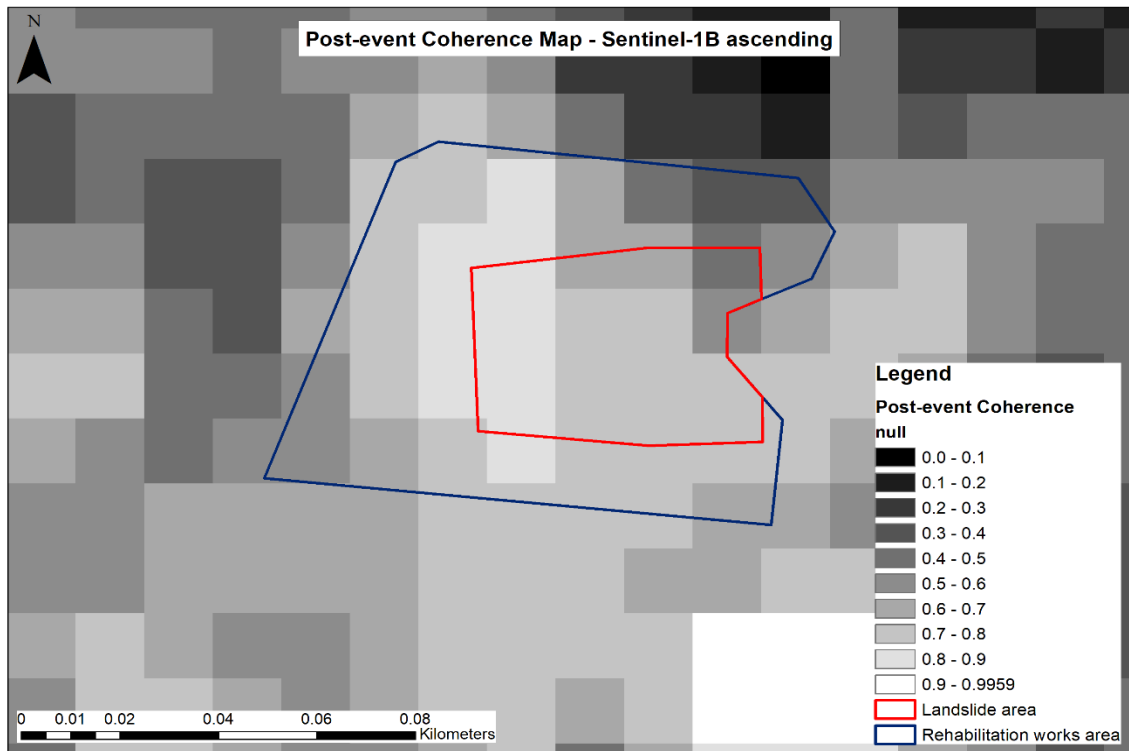


**Figure 138:** Post-event coherence map – Sentinel-1B ascending

The coherence maps from Sentinel-1B descending pairs are presented in Figure 139, Figure 140 and Figure 141 for the pre-event, co-event and post-event periods respectively.

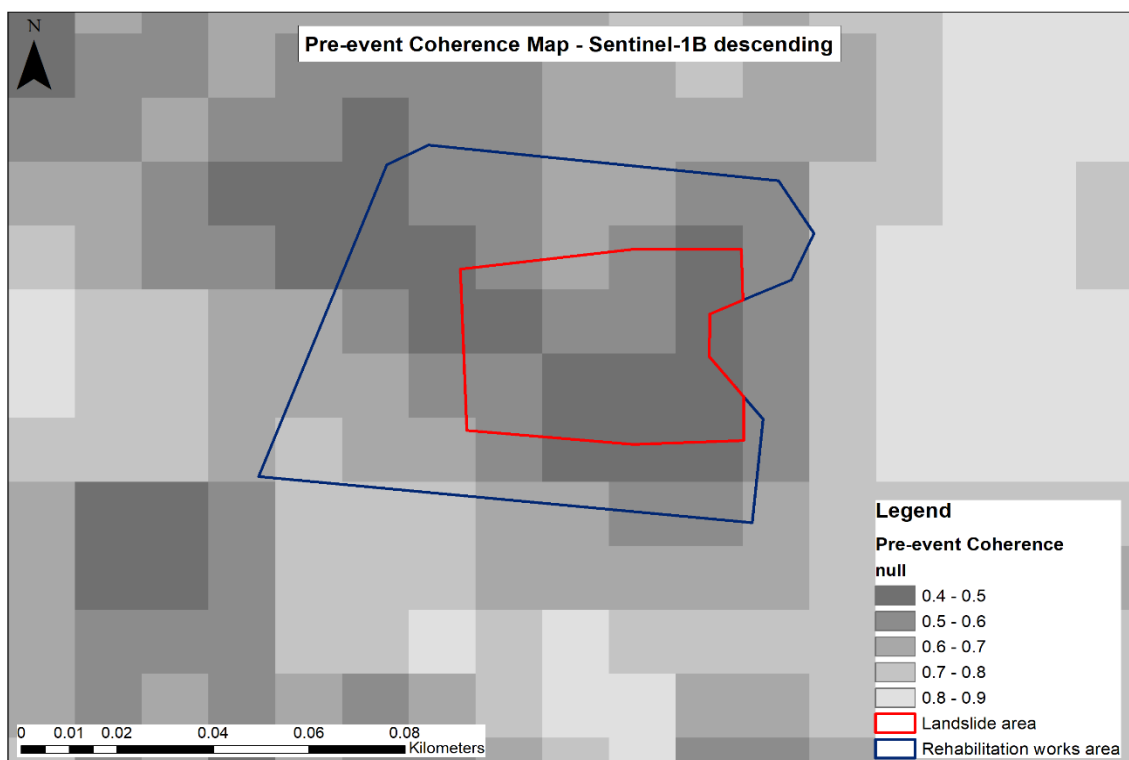


**Figure 139:** Pre-event coherence map – Sentinel-1B descending

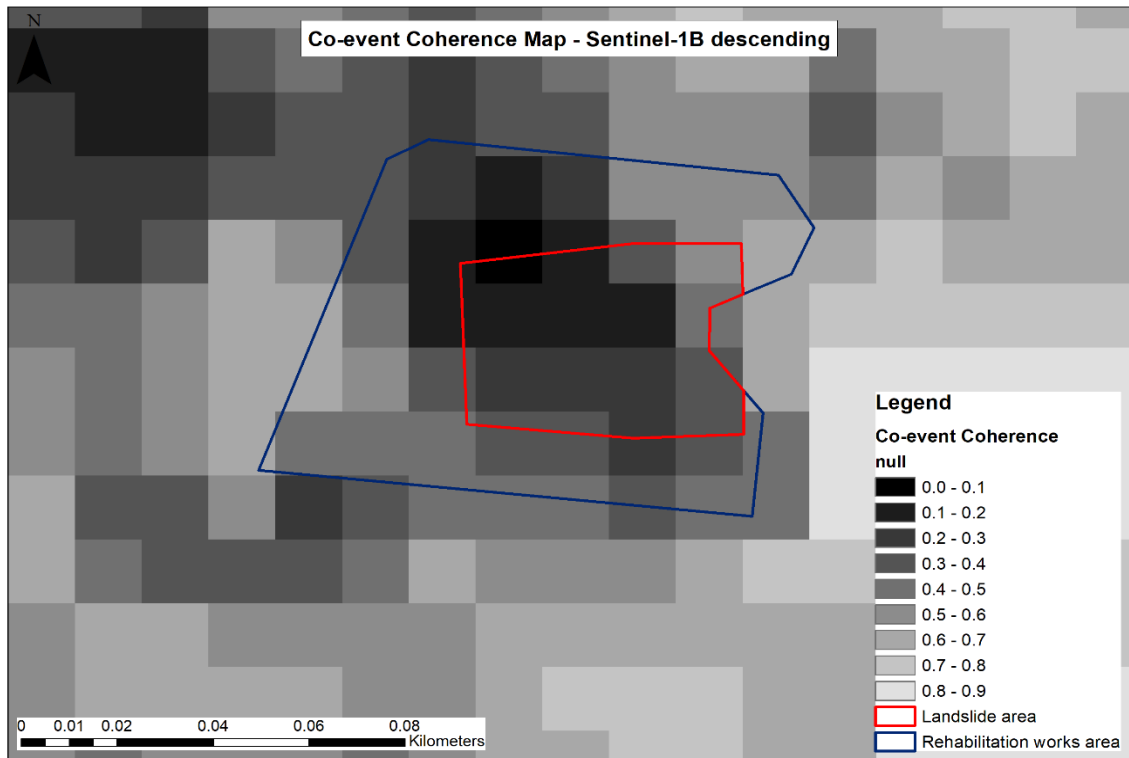


**Figure 140:** Co-event coherence map – Sentinel-1B descending

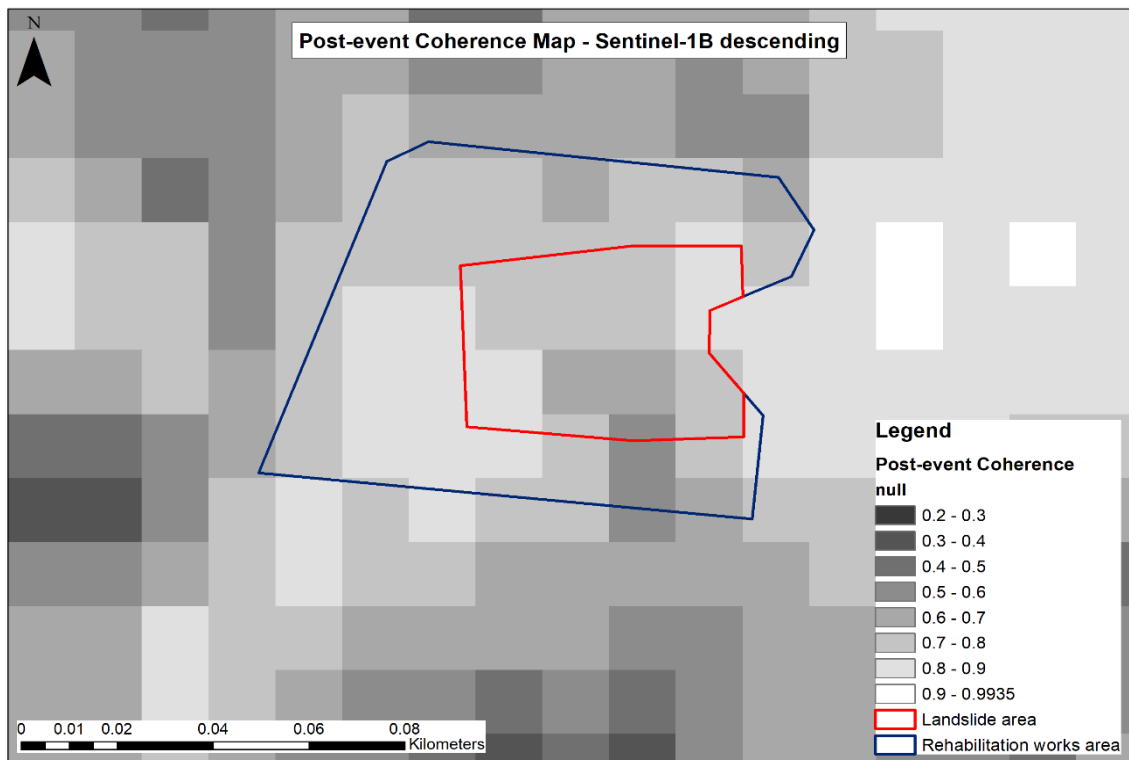


**Figure 141:** Post-event coherence map – Sentinel-1B descending

The average coherence maps were then developed by averaging the above results for the pre-event (Figure 142), co-event (Figure 143) and post-event (Figure 144) periods.

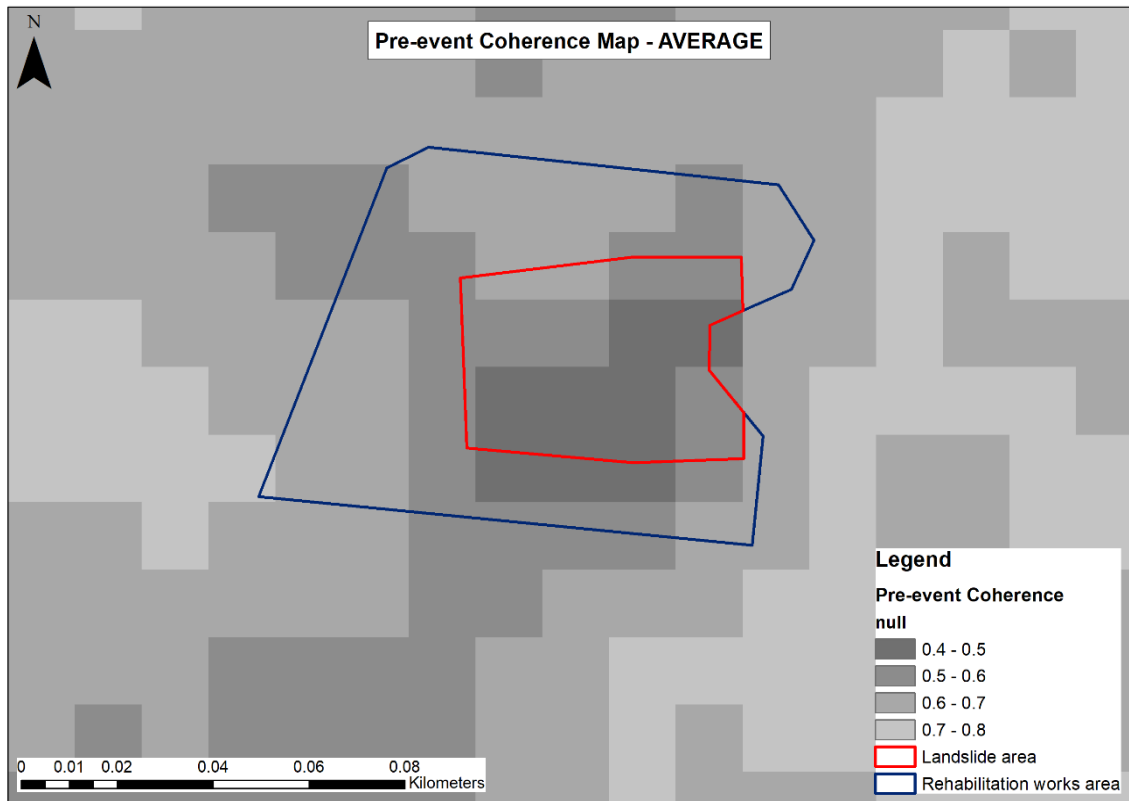


**Figure 142:** Pre-event coherence map – Average

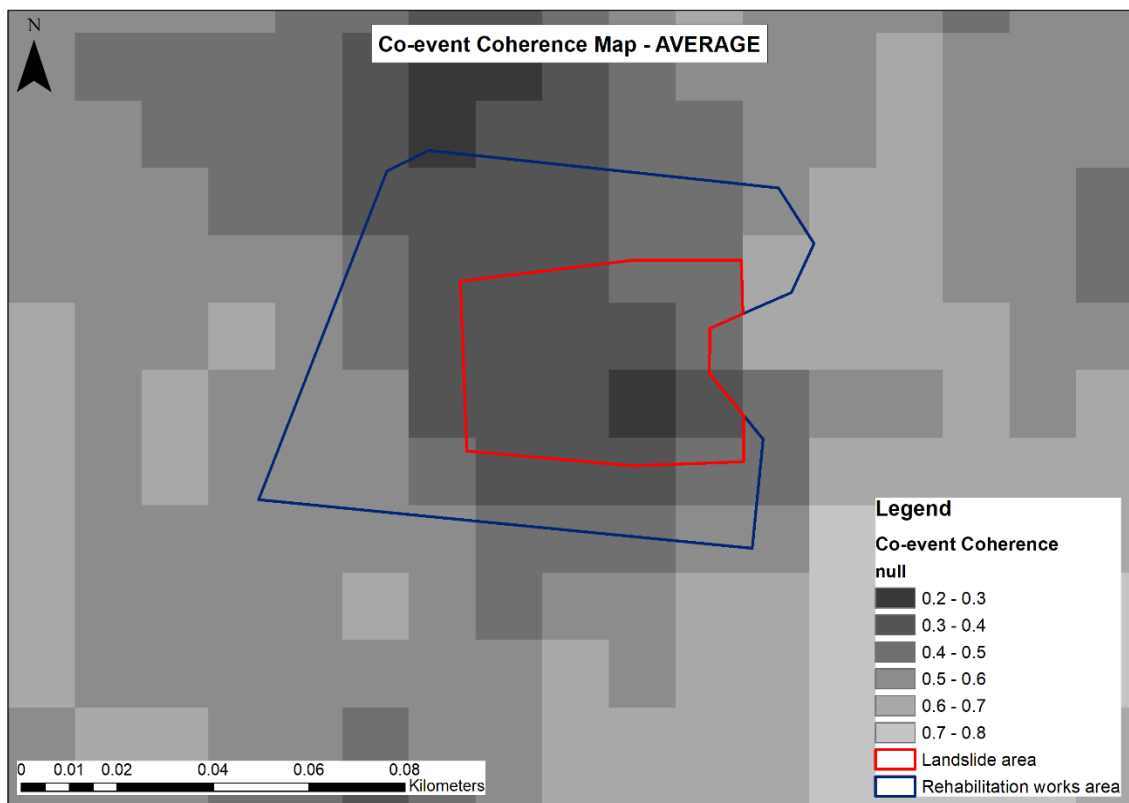


**Figure 143:** Co-event coherence map – Average

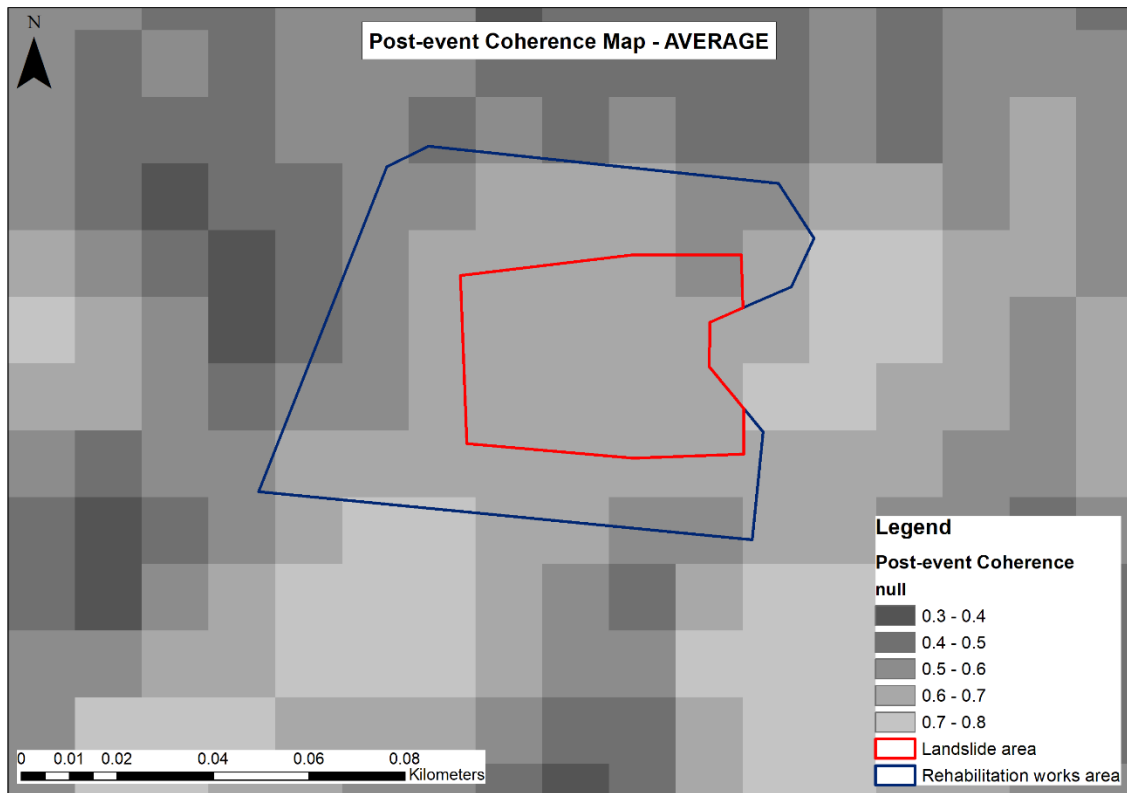


**Figure 144:** Post-event coherence map – Average

A perfect relationship/correlation between two consecutive SAR images is represented by a coherence value of 1, corresponding to no phase decorrelation, i.e. no changes between two or more SAR images. Coherence values of 0.5 and 0.75 usually show moderate and strong correlation between SAR images respectively. When coherence values drop below the value of 0.5, correlation of two or more images is lower than the moderate relationship, and the change in coherence is assumed higher than expected due to the temporal separation of the SAR images used in the interferometric image pair.

From a first view of the produced maps, Sentinel-1A based coherence maps appear to have misinterpreted the impact of the landslide under investigation. For Sentinel-1A ascending SAR pairs, there was minimal coherence loss between the pre-event and co-event periods, whereas in the case of descending images, the area with coherence loss appear towards the south and west from the defined landslide area.

There appears to be a better representation of the landslide impact in the Sentinel-1B based products with the coherence dropping in the co-event period and then increasing back again during the post-event one. The average maps provided also similar results. However, to distinguish between coherence loss due to the landslide under investigation

and natural coherence loss due to the temporal baseline of SAR images, all the above maps were further compared.

#### 4.3.2.1 Identification of natural hazards

Following the development of the coherence maps for the three periods under study, the analysis, during this section of the thesis, is concentrated on the identification of natural hazards. Therefore, the coherence differences and normalised coherence differences were calculated using only the pre-event and co-event maps, produced earlier, by *Equations 13 and 14*, through the Raster Calculator tool (Figure 145) in ArcGIS.

$$\Delta C = C_2 - C_1 \quad (\text{Eq. 13})$$

$$\text{Normalised } \Delta C = \frac{C_2 - C_1}{C_2 + C_1} \quad (\text{Eq. 14})$$

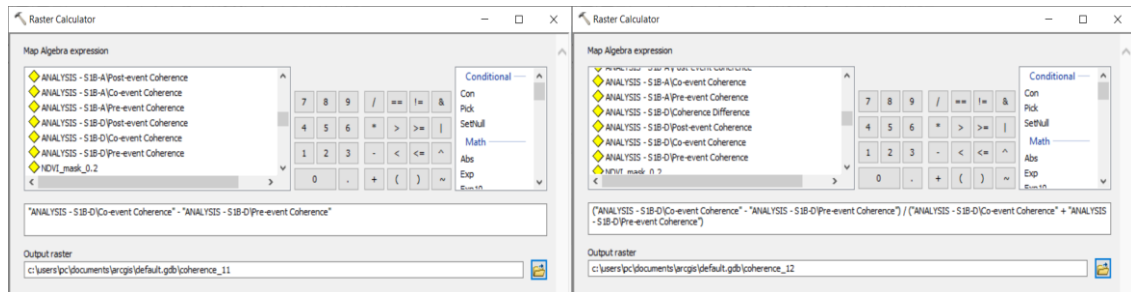


**Figure 145:** Raster calculator – Coherence difference (left) and normalised difference (right)

Both approaches are based on the assumption that the phase decorrelation caused by geo-hazard phenomena is stronger than the phase decorrelation induced by natural temporal changes. This assumption is nonetheless intensified via the use of multi-pass SAR imagery with identical and short temporal baselines for all interferometric SAR image pairs. The selection of SAR pairs of 12 days apart assists in ruling out significant nature-derived phase decorrelations. In fact, Sentinel-1 SAR takes full advantage of the long-term coherence, the frequent revisit, the small baselines, and the dual polarisations (Monti-Guarnieri *et al.*, 2018).

Significant changes of coherence need to be identified in order to be able to distinguish between natural coherence decrease and coherence decrease due to the occurrence of a natural disaster. As mentioned earlier, a perfect relationship between two consecutive SAR images is represented by a coherence value of 1. Ideally, in areas that no significant

change occurred, coherence difference and normalised difference should have zero values. However, this is never the case as natural decay takes place with coherence values decreasing over time. Maintaining the temporal baseline of the acquired images, combined into interferometric pairs, at a minimum of twelve days, minimised the impact of temporal baseline on coherence values.

The distinction between the coherence loss due to the landslide under investigation and the natural coherence loss due to the temporal baseline of SAR images was further enhanced via the calculation of the expected natural reduction in coherence. This was calculated by developing coherence maps via DInSAR processing, using a single SAR image as a master and the rest of the images as slaves for each satellite and pass direction separately. The coherence maps produced were then stacked together and geolocated, so that results can be correctly combined on a common basis. Then, the coherence maps that were developed by SAR images, which were both acquired during the pre-event and post-event periods, were used for the calculation of the average coherence values at the wider area. During these two periods, no known landslides, earthquakes or other land movement inducing phenomena occurred. The results are shown in Figure 146.

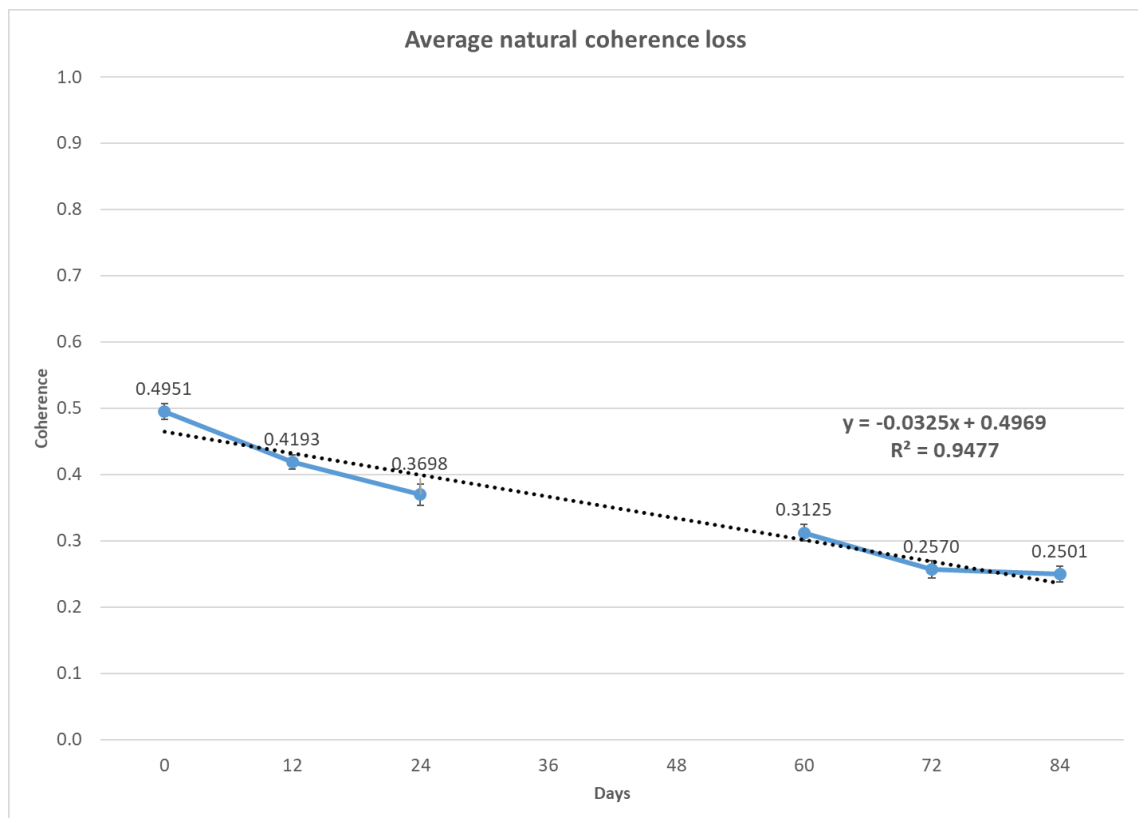


**Figure 146:** Average natural coherence loss



There seems to be a natural decay in coherence values in the order of 3.25% every 12 days. Thus, any coherence reduction lower or equal to this threshold was considered normal and all other coherence changes over 3.25% were considered significant.

Moreover, as the area of interest is surrounded by vegetation, this can lead to phase decorrelation, as seen in literature. In the present study, the impact of vegetation is minimised through the use satellite images with short temporal baselines (12 days). However, to test the efficiency of the methodology in non-vegetated areas, a coherence mask ( $NDVI < 0.2$ ) was applied to all products. Additionally, sea was also removed from all layers, in order to calculate mean values and standard deviations more accurately.

All results obtained from the application of the two indicators were classified, in ArcGIS, to highlight the possibility for the occurrence of a landslide in the case study site. The classification was based on the mean value and the standard deviation of each dataset.

The standard deviations in all datasets varied from 0.15 to 0.20 for the individual products and improved to approximately 0.09 in the case of average coherence difference and normalised coherence difference products. Therefore, areas/pixels with values outside of the confidence lower limits (negative values) for 99.73% level of confidence, i.e. three standard deviations from the mean value, were defined as areas with very high probability of landslide occurrence, or else, areas that is very highly probable that were affected by landslide. Coherence difference and normalised difference values between two and three standard deviations from the mean value, i.e. 95.45% - 99.73% level of confidence, were included in the class "High", i.e. areas with high probability of landslide occurrence.

In the class "Low – Medium", the values between one and two standard deviations were entered. All values that were within one standard deviation, positive or negative, from each dataset mean value were included in the class named "None – Very Low", along with all other positive values, that indicate coherence increase, and thus they are areas that there is no possibility that a landslide or any other natural hazard phenomenon took place. The conditions used to classify all values were the following:

$$"Very\ High" \leq \mu - 3\sigma \leq "High" \leq \mu - 2\sigma \leq "Low - Medium" \leq \mu - 1\sigma \leq "None - Very Low"$$

where:  $\mu$  the mean value and  $\sigma$  the standard deviation of each dataset.

The final products with the differences and normalised differences of coherence are presented below for each satellite and satellite pass direction separately.

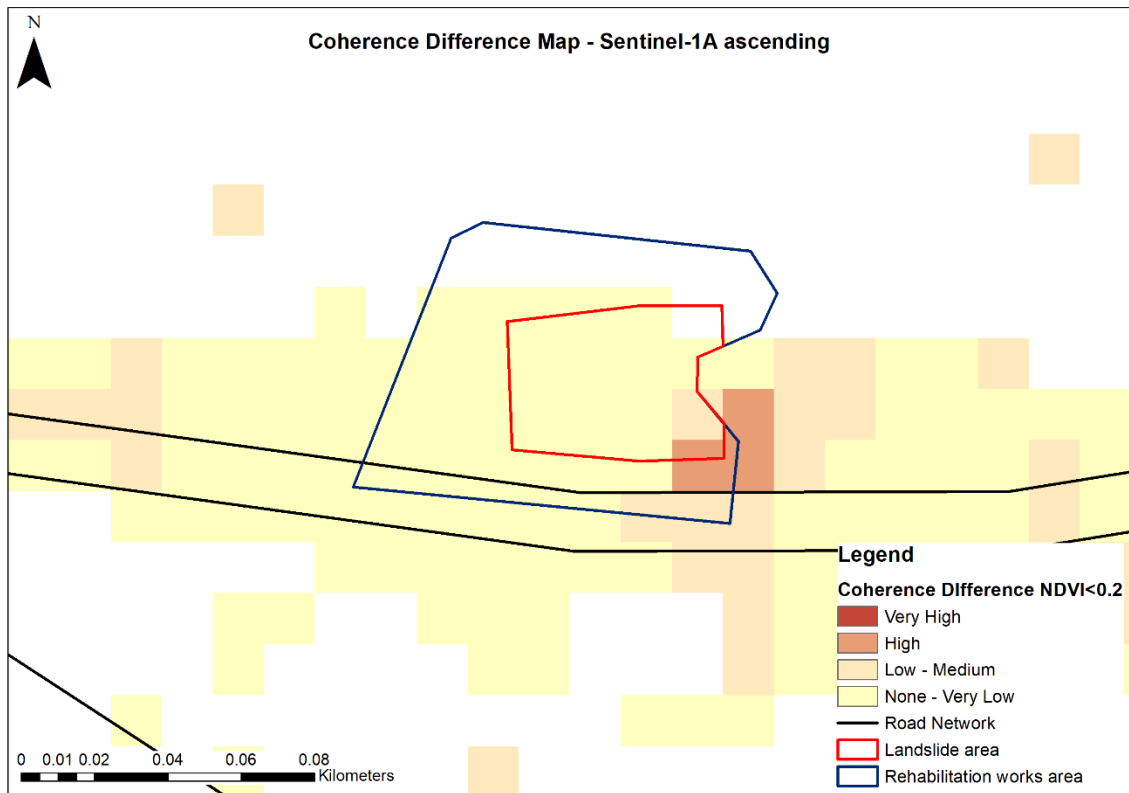


**Figure 147:** Coherence difference map – Sentinel-1A ascending

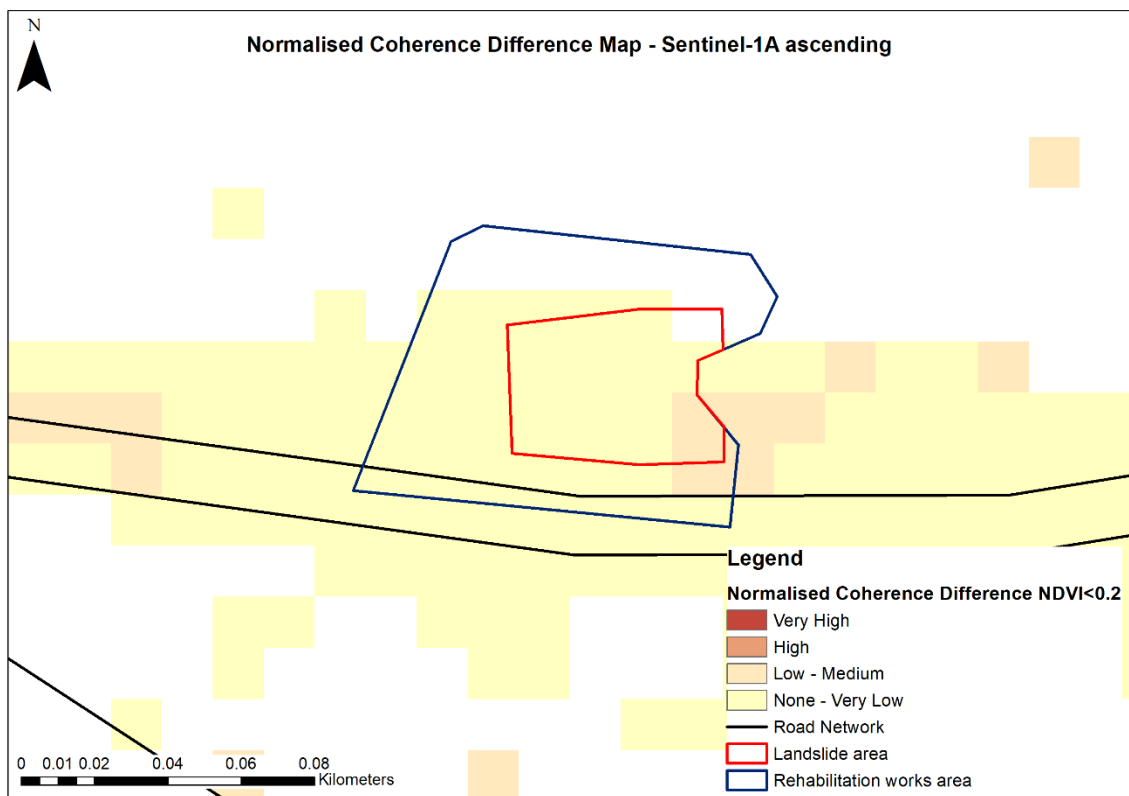


**Figure 148:** Normalised coherence difference map – Sentinel-1A ascending

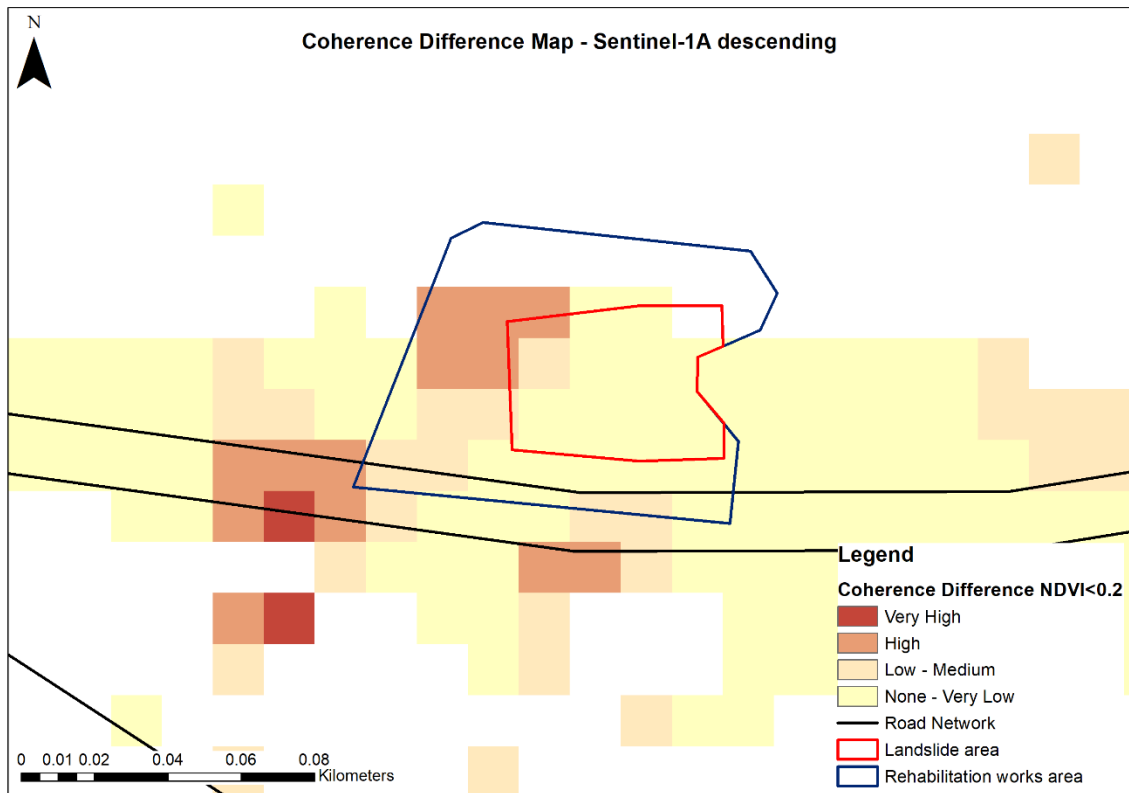


**Figure 149:** Coherence difference map – Sentinel-1A descending

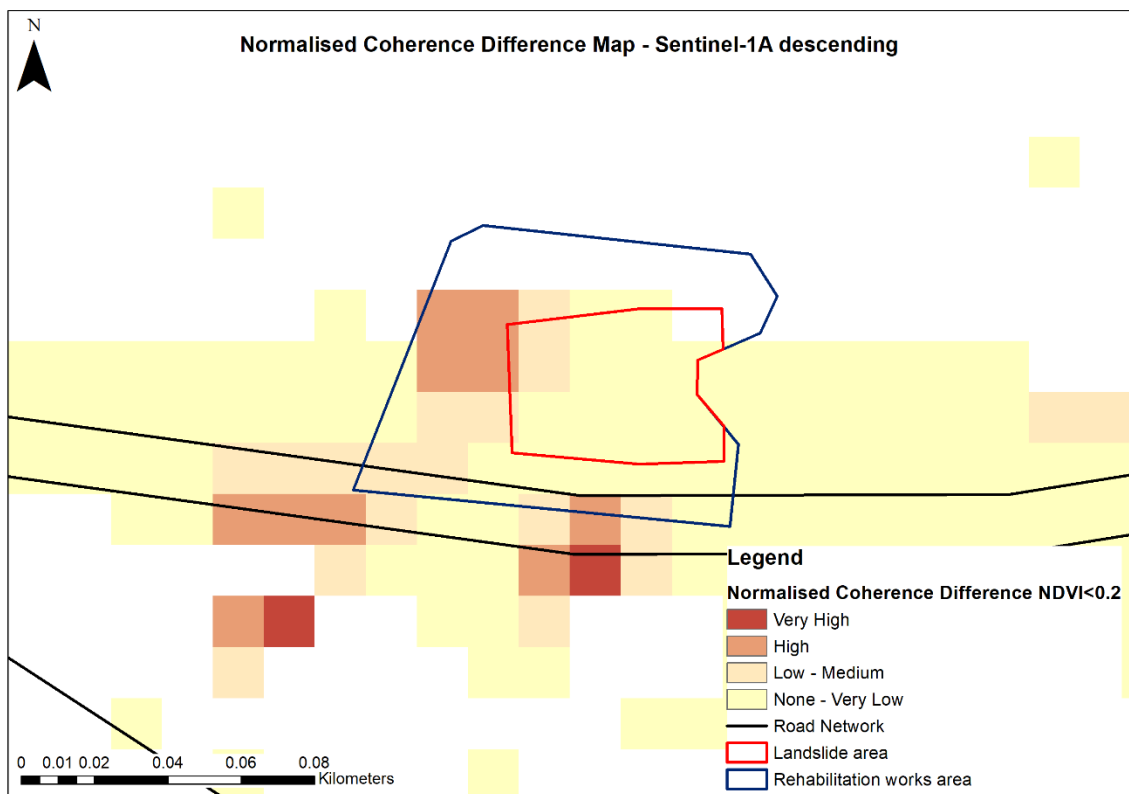


**Figure 150:** Normalised coherence difference map – Sentinel-1A descending

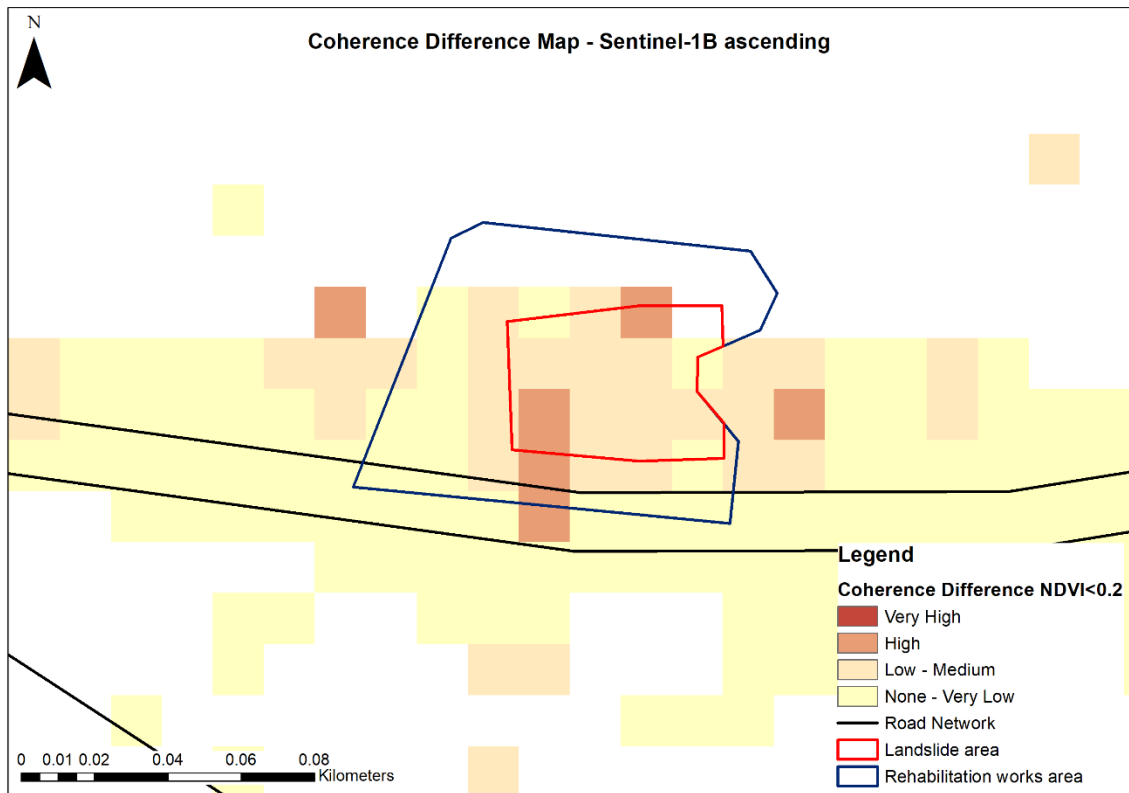


**Figure 151:** Coherence difference map – Sentinel-1B ascending

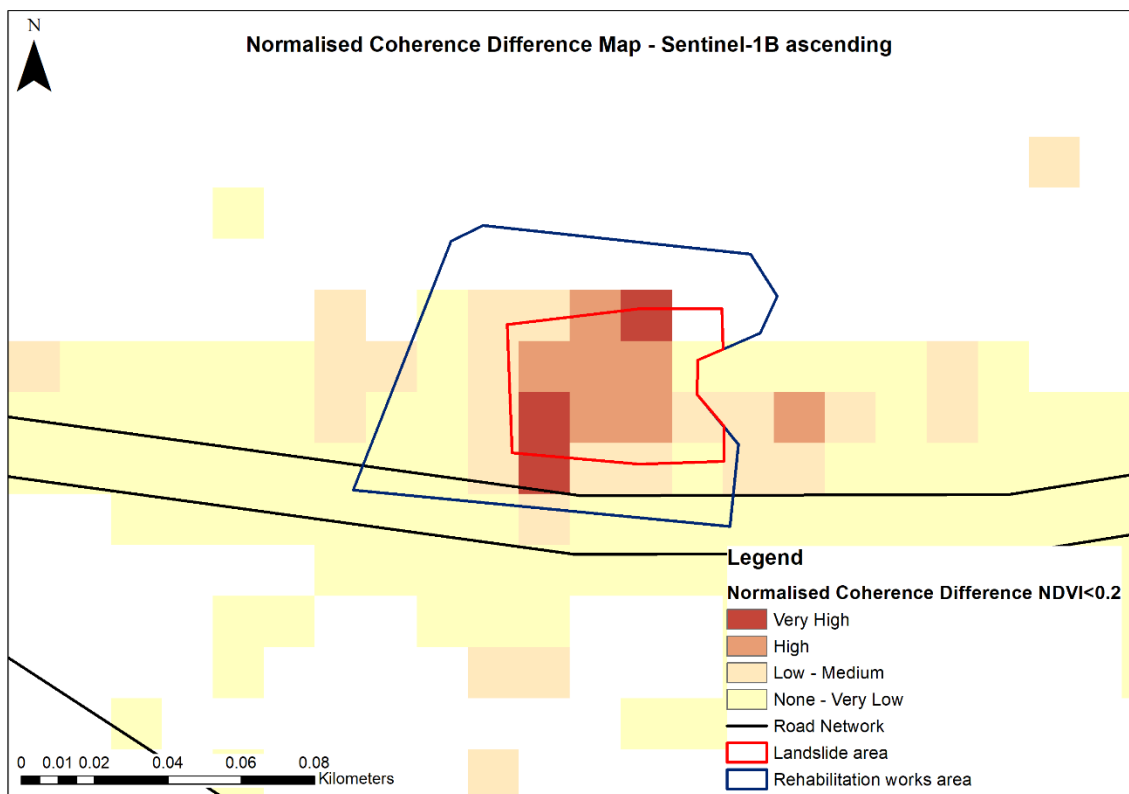


**Figure 152:** Normalised coherence difference map – Sentinel-1B ascending

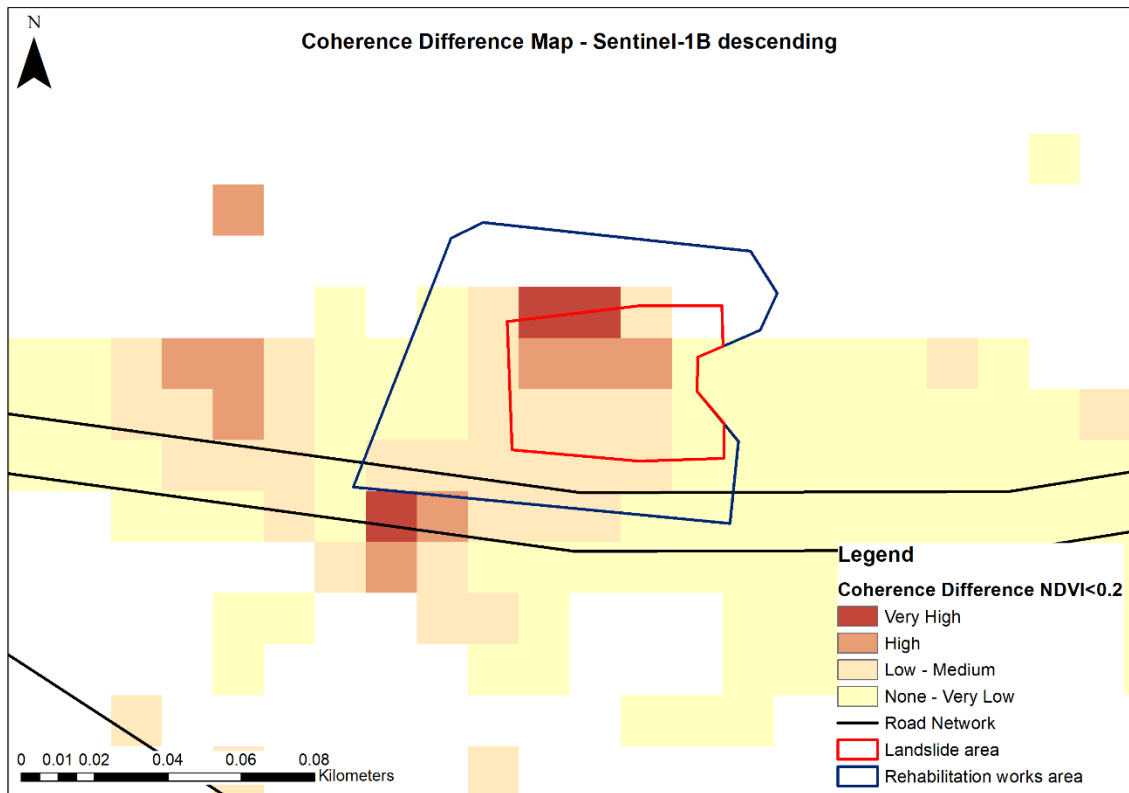


**Figure 153:** Coherence difference map – Sentinel-1B descending

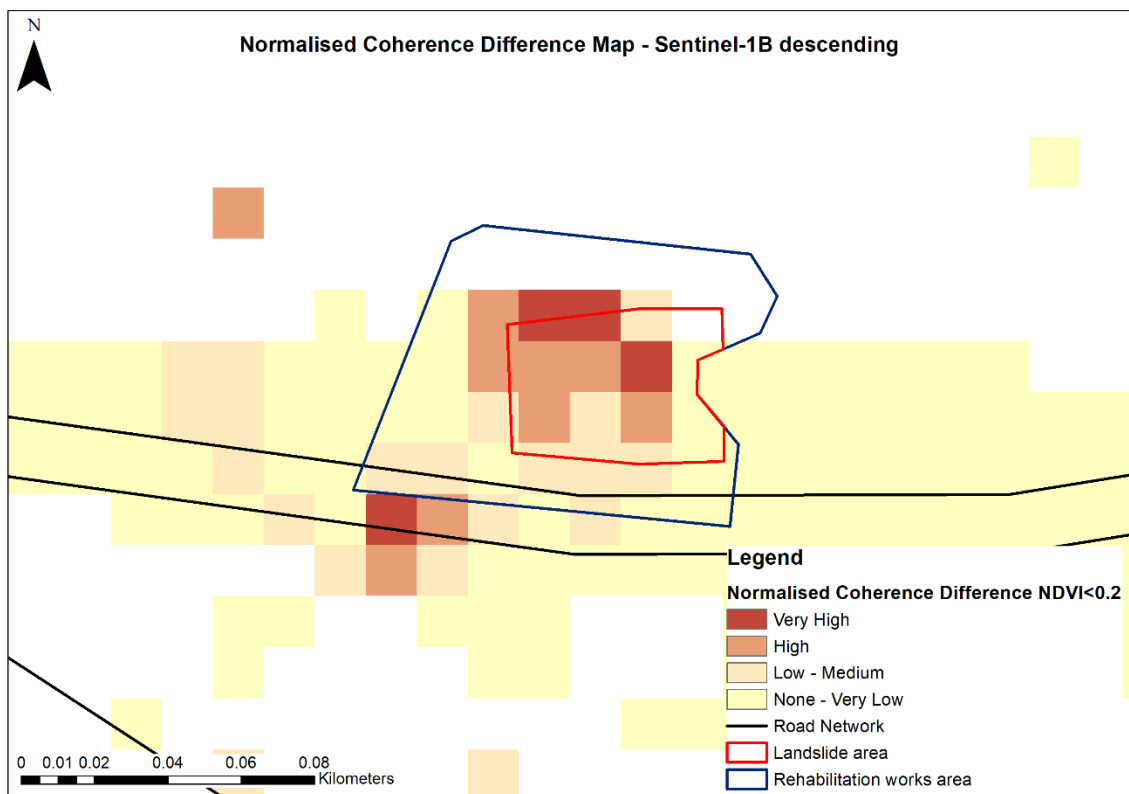


**Figure 154:** Normalised coherence difference map – Sentinel-1B descending

The above maps fully support the results of the statistical analysis that was conducted earlier in *section 4.3.1*. The coherence difference and the normalised coherence difference show similar spatial patterns in all four cases individually.

Interferometric pairs from Sentinel-1A ascending and descending images failed to identify the area affected by the landslide. This was pointed out during the statistical analysis, based on the findings from the t-tests and ANOVA tests that were carried out, but also as the minimum coherence values, obtained from Sentinel-1A imagery, were found within the period of rehabilitations works, which follows the co-event one.

More specifically, Sentinel-1A ascending based maps show a small area of high probability of landslide occurrence at the eastern boundaries of the defined area adjacent to the A6 motorway, via the calculation of coherence differences (Figure 147), which turns to Low-Medium when the normalised differences were calculated (Figure 148). As presented in Figure 149, the Sentinel-1A descending based coherence difference products, detected a small area of high landslide occurrence probability at the northwest boundaries of the AOI and some smaller areas to the west and southwest of the AOI with high and very high probability for landslides. However, in the case of the false alarm at the area towards the west, this is due to the fact that is situated within the boundaries of the A6 motorway. These indications were minimised after the calculation of the normalised coherence differences, as seen in Figure 150.

Sentinel-1B satellite appears to perform significantly better in the identification of areas that is highly and very highly possible for a landslide to have occurred. Indeed, the normalised coherence difference maps based on ascending and descending interferometric SAR pairs, as presented in Figure 152 and Figure 154 respectively, have succeeded to identify the extents of the landslide, confirming in a spatial manner the results of the statistical analysis. In fact, they enhanced the results obtained through the calculation of simple coherence differences (Figure 151 and Figure 153) by turning areas of low and medium probability to high probability ones and areas of high probability to very high probability of landslide occurrence. At the same time, they minimised false alarms that were indicated by the simple coherence differences products.

As all the acquisition and sensor characteristics of the Sentinel-1A and Sentinel-1B satellites are nearly identical, an explanation to this could be the different dates between the co-event SAR acquisitions of the Sentinel-1A and Sentinel-1B as shown in Table 28.

Sentinel-1A images were acquired 10-11 days prior and 1-2 days after the landslide, whereas the Sentinel-1B images dated 4-5 days before and 7-8 days after the landslide. The difference in dates could have introduced additional phase decorrelations due to the residing meteorological conditions on the specific dates.

**Table 28:** Co-event SAR pairs

<b>Platform</b>	<b>Date</b>	<b>Time</b>	<b>Pass direction</b>	<b>Polarisation</b>	<b>Mode / type</b>	<b>Relative orbit</b>
Sentinel-1A	04/02/2019	15:49:52	Ascending	VV VH	IW/SLC	160
Sentinel-1A	05/02/2019	03:51:42	Descending	VV VH	IW/SLC	167
Sentinel-1B	10/02/2019	15:49:26	Ascending	VV VH	IW/SLC	160
Sentinel-1B	11/02/2019	03:51:06	Descending	VV VH	IW/SLC	167
Sentinel-1A	16/02/2019	15:49:52	Ascending	VV VH	IW/SLC	160
Sentinel-1A	17/02/2019	03:51:42	Descending	VV VH	IW/SLC	167
Sentinel-1B	22/02/2019	15:49:26	Ascending	VV VH	IW/SLC	160
Sentinel-1B	23/02/2019	03:51:06	Descending	VV VH	IW/SLC	167

Comparing the two coherence differences, i.e. the simple and the normalised one, the main distinction between the two detection indicators is that the coherence difference provided many incorrect detections, while the normalised coherence difference has less cases of such false alarms. In fact, the normalised coherence difference performed better than the coherence difference in all cases.

In general, the coherence difference indicator shows greater changes in areas with originally (pre-event) high coherence values, whereas the normalised coherence difference method adjusts the difference based on the sum of the pre-event and co-event values, i.e. denominator in Equation 13.

As found in literature, coherence values can vary significantly as the temporal baseline between two SAR acquisitions increases. Thus, to ensure the efficiency of the proposed CCD methodology, it is very important to keep temporal baselines at an absolute minimum. This condition is satisfied by the Sentinel-1 mission with the very short revisit times it offers. This fact can also assist in the further improvement of the proposed method into a multi-pass CCD methodology for the detection and monitoring of natural hazards.

In that aspect, average maps of coherence difference (Figure 155) and normalised difference (Figure 156) were developed from all the maps produced earlier to benefit from the multi-pass capabilities of the Sentinel-1 mission.

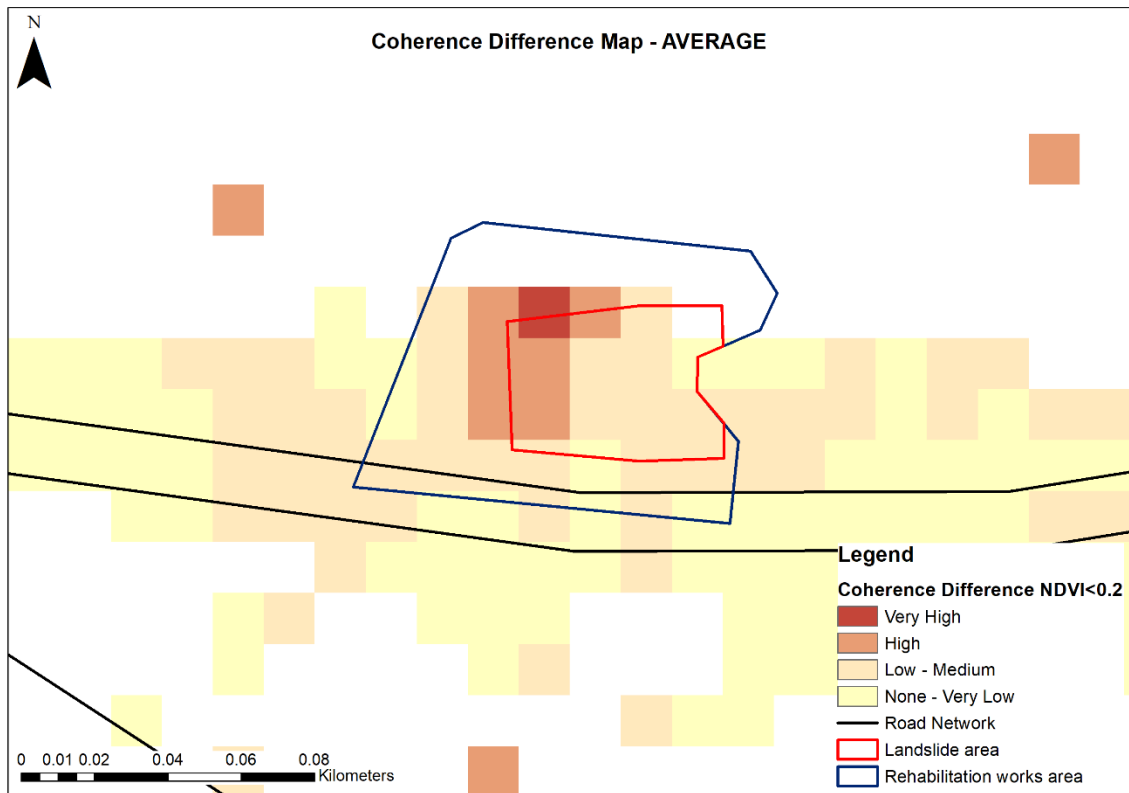


**Figure 155:** Coherence difference map – Average

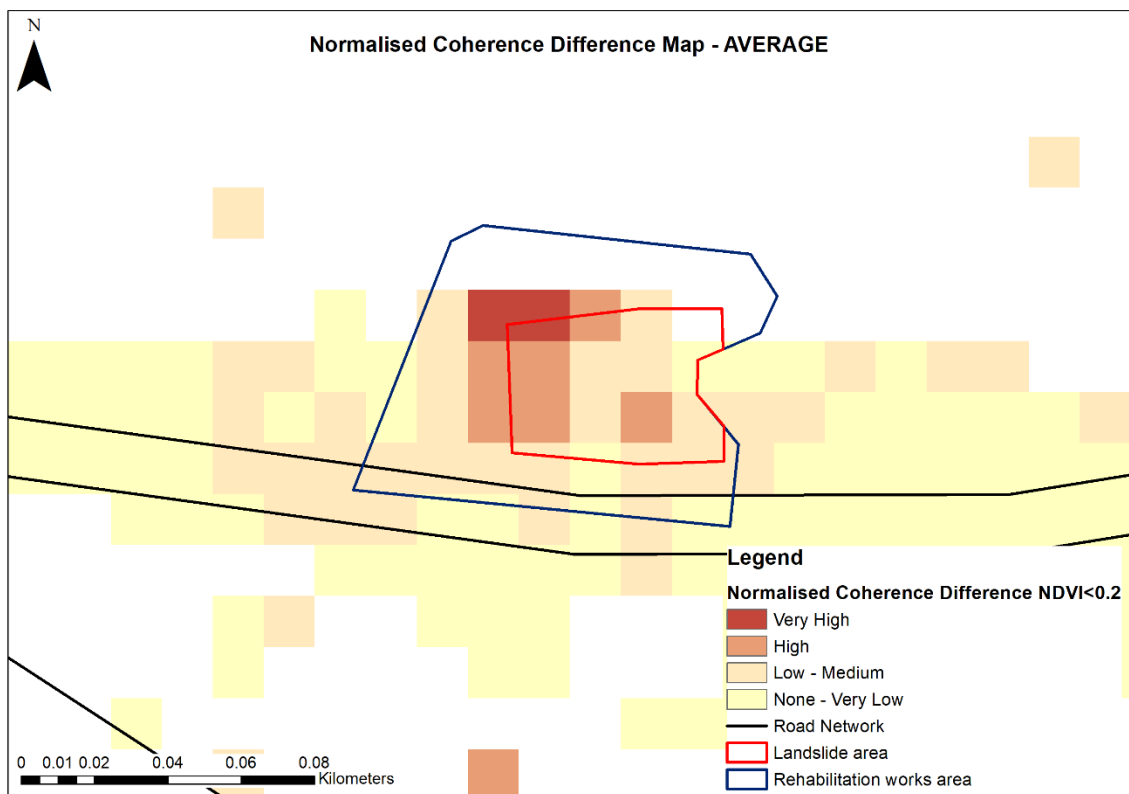


**Figure 156:** Normalised coherence difference map – Average



The averaging of all maps has provided some valuable input in the benchmarking of the methodology; however, the results were influenced significantly by the poor results obtained by the Sentinel-1A interferometric SAR pairs. There is a better distinction between areas affected and not affected by the landslide, compared with the Sentinel-1A satellite-based products but their overall performance is inferior to that of the Sentinel-1B based coherence difference and normalised difference maps.

In that aspect, based on the superior performance of the Sentinel-1B satellite, the results from the coherence difference and normalised coherence difference maps, which were developed by Sentinel-1B ascending (Figure 151 and Figure 152) and descending (Figure 153 and Figure 154) SAR image pairs, were utilised to produce Sentinel-1B average coherence difference and normalised coherence difference products, as presented in Figure 157 and Figure 158 respectively.

The averaging of these two products has further improved the previous individual results of the Sentinel-1B ascending and descending SAR pairs, matching the landslide defined area, especially in the case of the normalised coherence difference indicator. The pixels of very high landslide probability almost cover fully the extents of the landslide area.

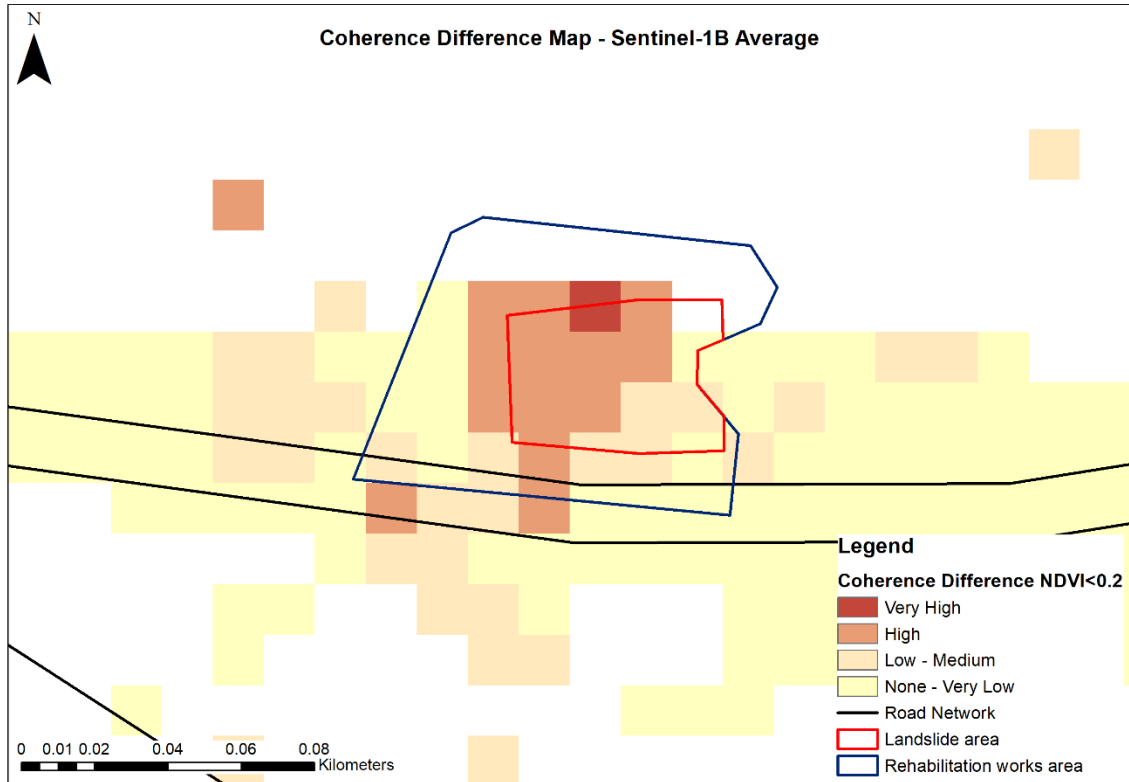


**Figure 157:** Coherence difference map – Sentinel-1B average

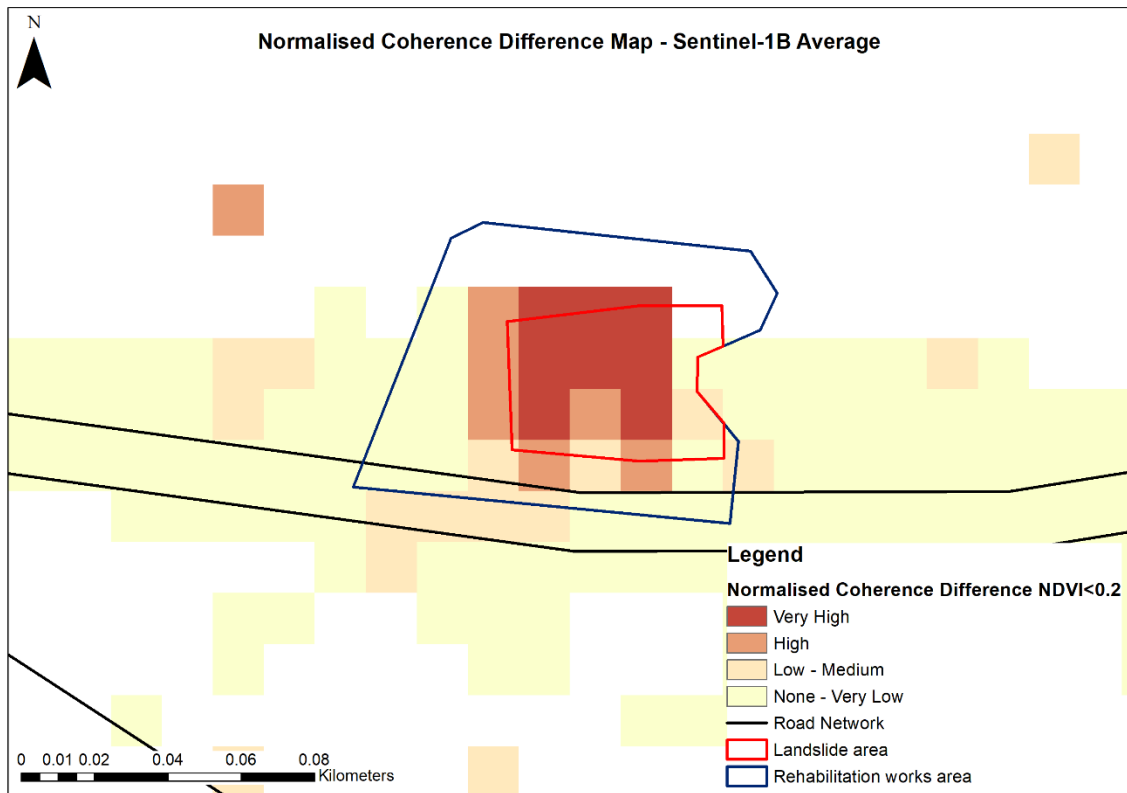


**Figure 158:** Normalised coherence difference map – Sentinel-1B average

At the same time, the number of false alarms was reduced, compared to the individual Sentinel-1B ascending and descending based results, with some sparse incidents (single pixels) located to the west and east of the area under study, being in the majority of cases in the class of “Low – Medium” probability. The few pixels within the motorway boundaries can be removed from the analysis, as most probably the coherence changes are due to the traffic using the A6 motorway on its other direction.

The performance of the coherence difference and normalised coherence difference indicators was further tested by the Receiver Operating Characteristic (ROC) analysis. ROC analysis has been widely used for the benchmarking of natural hazard detection methods (Beguería, 2006; Burrows *et al.*, 2019; Jung and Yun, 2020). A map of landslide and non-landslide pixels is created and the trade-off between the true positive fraction and the false positive fraction with some thresholds are calculated. In this case, four different thresholds were defined that correspond to the probability classes set for the development of the coherence difference and normalised coherence difference maps. So, the very high probability corresponded to the “definitely positive” threshold, the high

landslide probability to “probably positive”, the low-medium probability to the “probably negative” and the none – very low probability to the “definitely negative” threshold.

Then, the true positive fraction (y-axis), i.e. the number of pixels within the landslide area that were detected as a landslide and the non-landslide pixels that were correctly classified as non-landslide pixels, is then plotted against the false positive fraction (x-axis), i.e. non-landslide pixels that were detected as landslide ones and landslide pixels that were detected as non-landslide ones. A good landslide detection indicator is expected to detect true positive pixels faster than false positive ones. Hence, the more accurate the detection indicator is, the closer the ROC curve should lie to the upper left corner of the plot.

The ROC curves were developed for the coherence and coherence difference products based on the better performing Sentinel-1B images average, as presented earlier in Figure 157 and Figure 158 respectively.

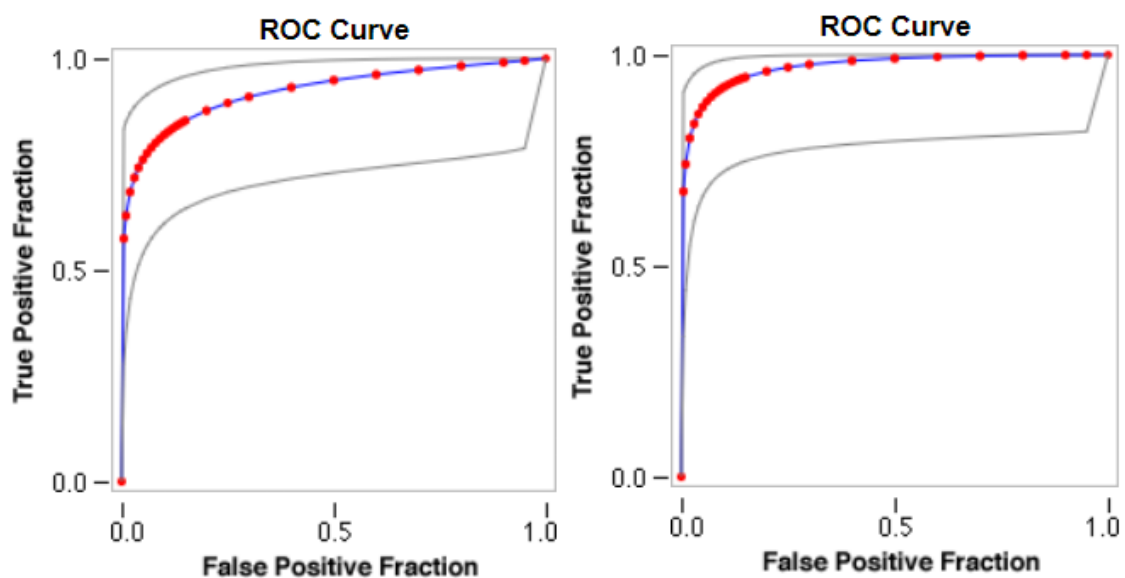


**Figure 159:** ROC curves for coherence difference (left) and normalised coherence difference (right) – Sentinel-1B average

In Figure 159, the blue line and red marks represent the fitted ROC curve and the grey lines are the 95% confidence intervals of the fitted ROC curves. The coherence difference performed with an overall accuracy of 93% and the normalised coherence difference with an overall accuracy of 94.8% for the detection of the landslide and non-landslide areas. The true-positive rate, also known as sensitivity or probability of landslide detection was 63.2% in the case of the coherence difference and increased to 73.7% for the normalised

coherence difference. Finally, the false-positive rate, or else the probability of false alarm, was calculated as  $1 - \text{specificity}$  and for both indicators was approximately 1%. The summary statistics calculated are presented in Table 29.

**Table 29:** ROC analysis – Summary statistics

	<b>Coherence Difference</b>	<b>Normalised Coherence Difference</b>
Number of cases	115	115
Number correct	107	109
Accuracy	93%	94.8%
Sensitivity	63.2%	73.7%
Specificity	99%	99%
Positive cases missed	7	5
Negative cases missed	1	1
Fitted ROC area	0.922	0.972
Empirical ROC area	0.897	0.952

The ROC analysis also proved that the normalised coherence difference performed better than the coherence difference indicator as it can detect the areas affected by landslide more efficiently. The five cases/pixels that were missed by the normalised coherence difference indicators were all at the edges of the area of interest and the majority of those lie only partially within it, causing their wrong characterisation as pixels of none-very low and low-medium landslide occurrence probability, as described earlier.

The ROC curves and the complete statistics from the ROC analysis were calculated using the web-based calculator for ROC curves (Eng, no date) and are included in *Appendix II*.

In conclusion, the multi-pass CCD methodology through the application of the normalised coherence difference indicator, based on averaging Sentinel-1B products, proved to be the most beneficial for the detection of landslide phenomena and their impact on critical infrastructure. It is the first time that this methodology is applied in the case of landslides induced by heavy rainfall.

The validation of the proposed methodology follows in the next section of the thesis, using the other landslide event that occurred on the 20<sup>th</sup> of February 2019, by the old Paphos – Limassol road near Petra tou Romiou as the validation site.

#### 4.3.2.2 Validation of methodology

The performance of the CCD methodology applied in *section 4.3.2.1*, was tested at another case study site, which was described in *section 3.1.3 Pissouri – Petra tou Romiou*, affected by a landslide, following heavy rainfall.

The landslide event took place on the 20<sup>th</sup> of February 2019 causing structural issues, that led to the closure of a 3km long part of the old road from Paphos to Limassol, approximately 200m away from “Petra to Romiou”, which remains closed until today for security reasons. The extensive precipitation and residing soil erosion issues were found to be the main reasons for this phenomenon. To date, the access from Paphos to Limassol, is carried out only via the Paphos – Limassol motorway A6.

As this case study was used for validation purposes, no intermediate steps are analysed within the present section. Therefore, the final coherence difference and normalised coherence difference results produced from the various Sentinel-1 datasets using the CCD methodology are presented below. The present landslide was not well documented by the local authorities, so the landslide extents were approximately defined after a site visit.

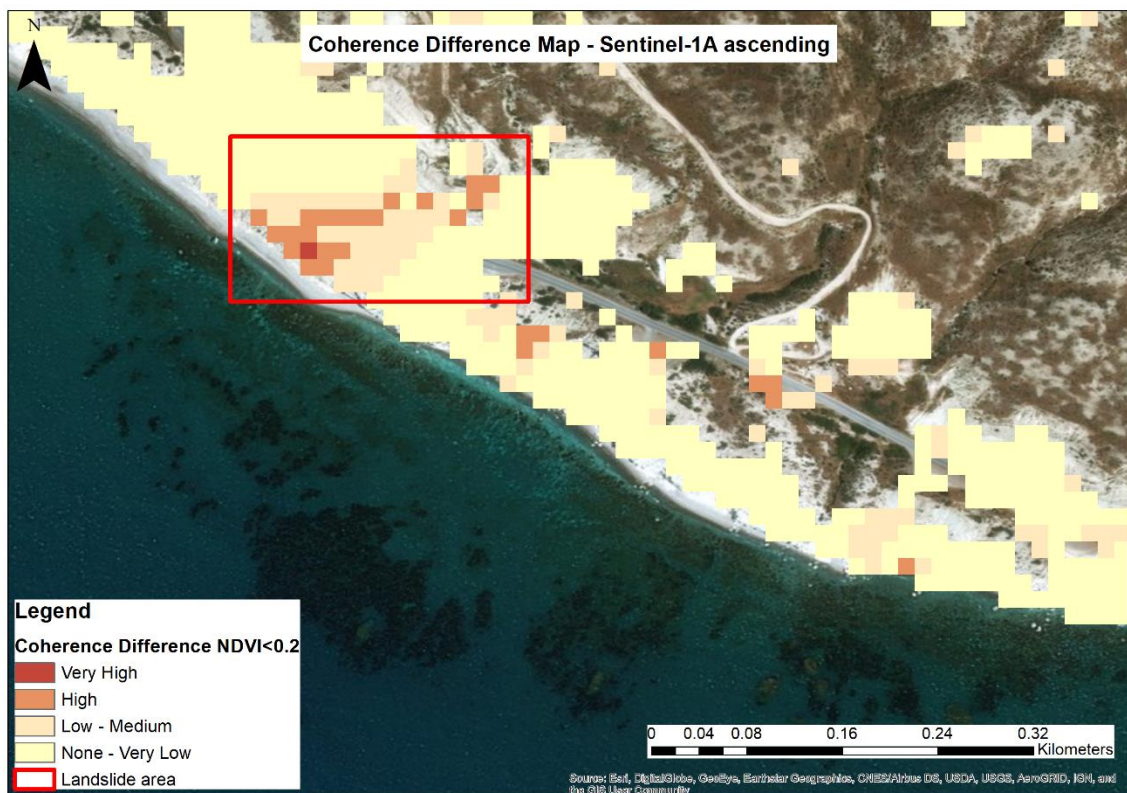


**Figure 160:** Coherence difference map – Sentinel-1A ascending

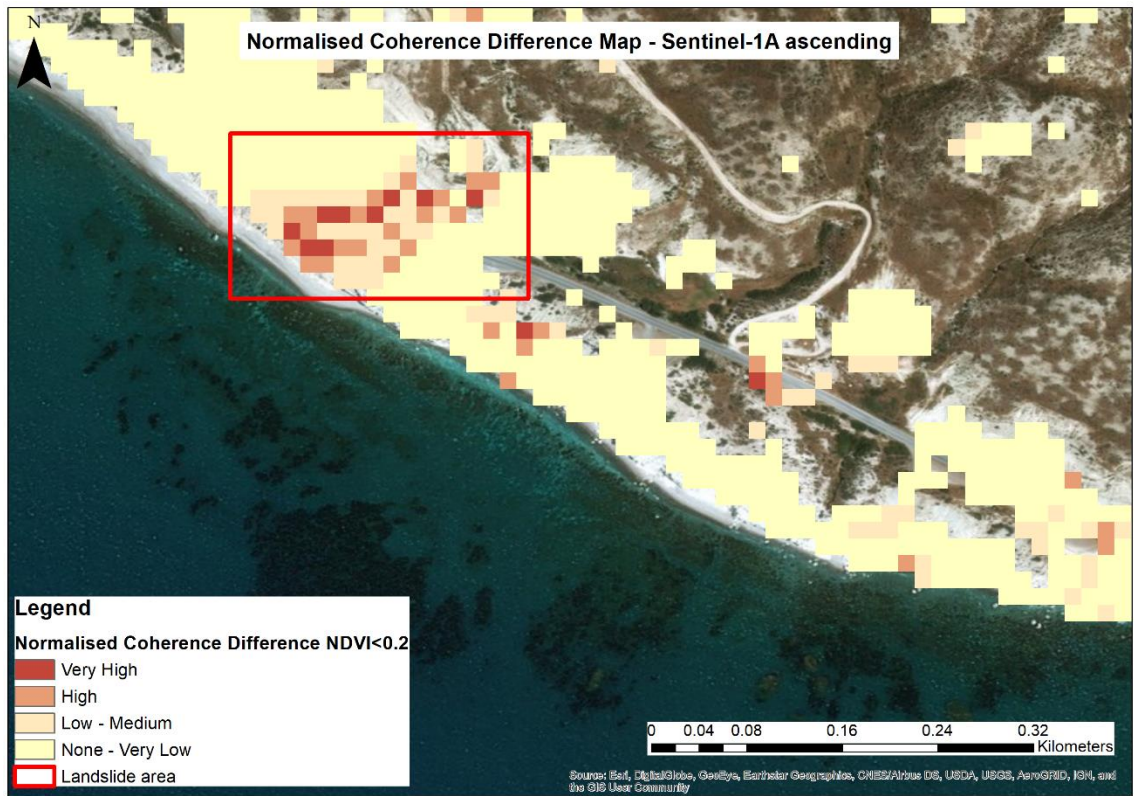


**Figure 161:** Normalised coherence difference map – Sentinel-1A ascending

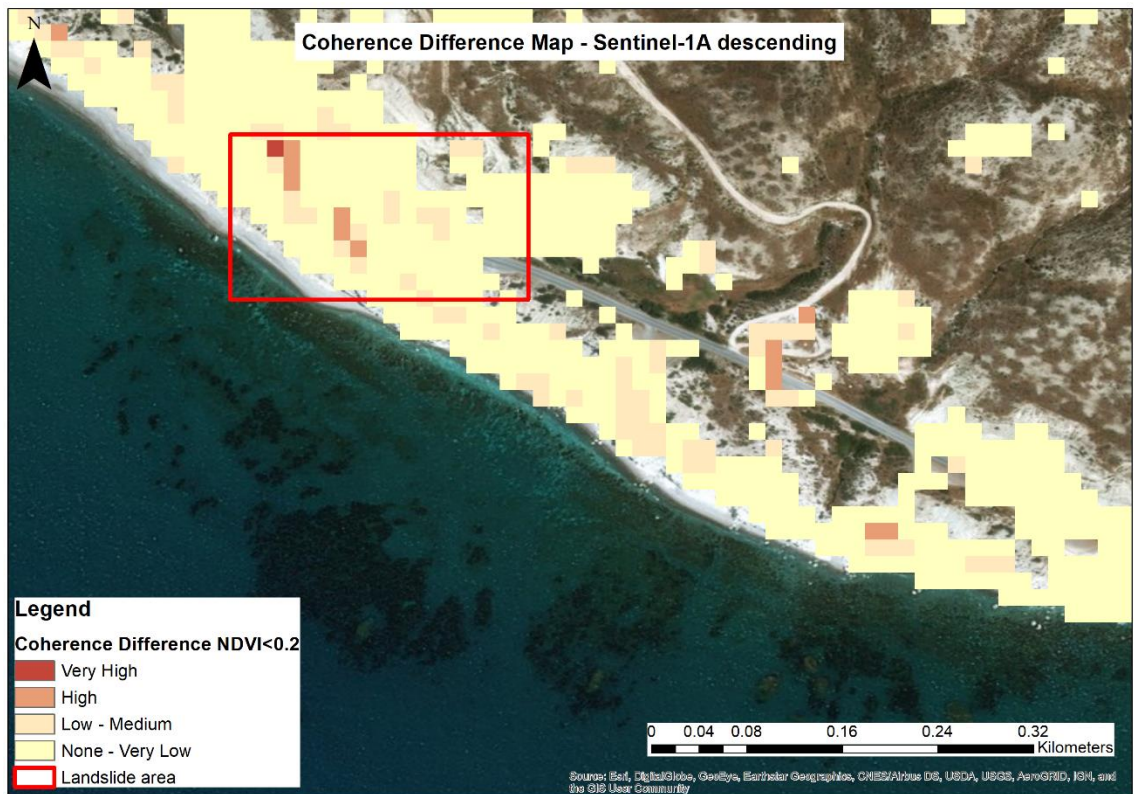


**Figure 162:** Coherence difference map – Sentinel-1A descending

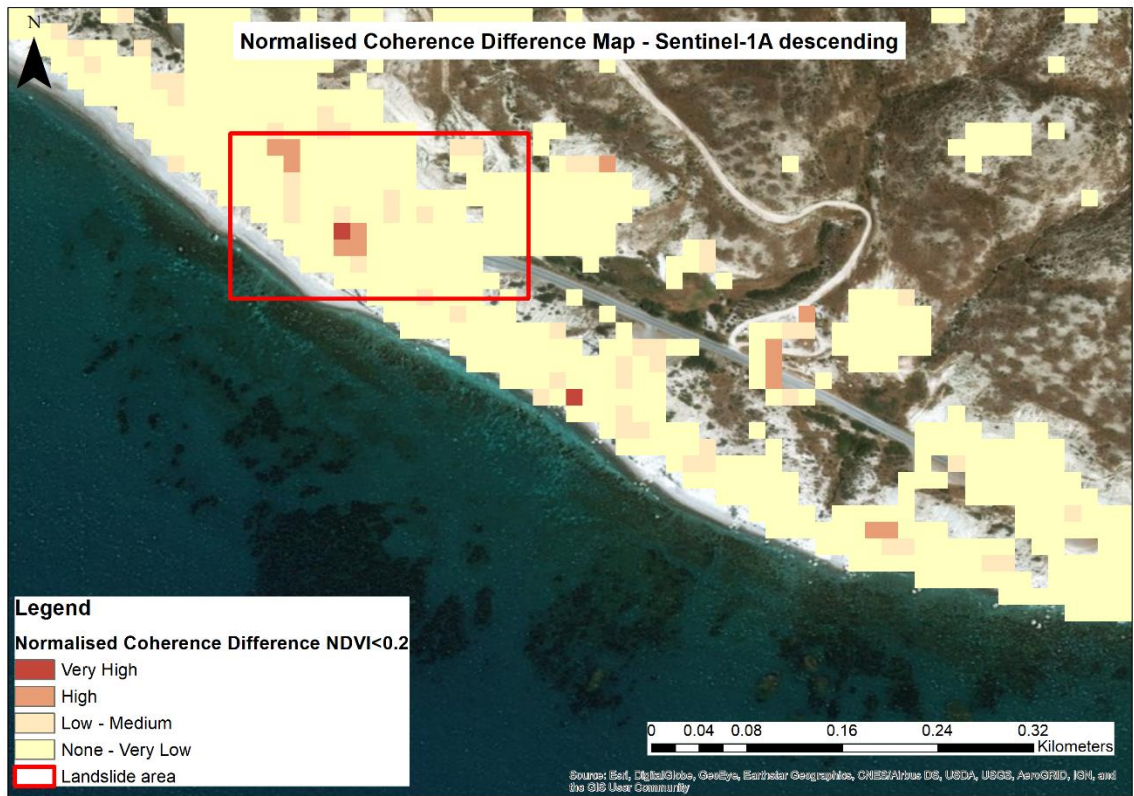


**Figure 163:** Normalised coherence difference map – Sentinel-1A descending

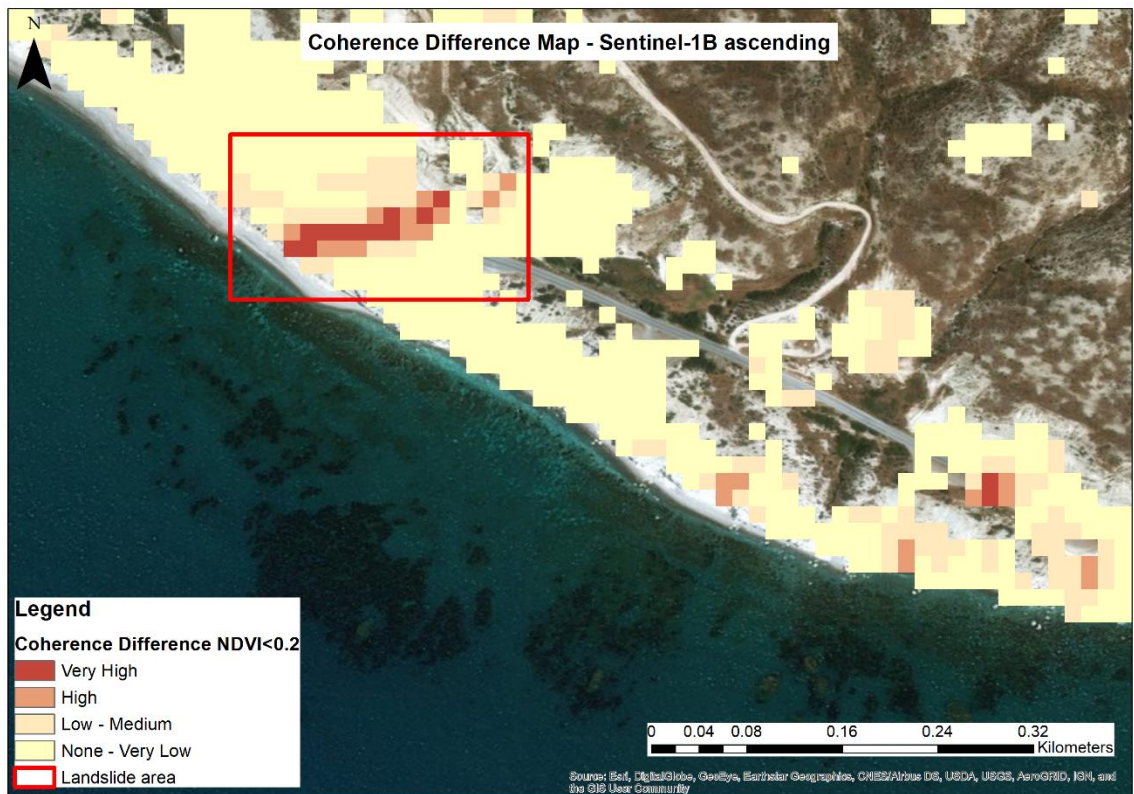


**Figure 164:** Coherence difference map – Sentinel-1B ascending

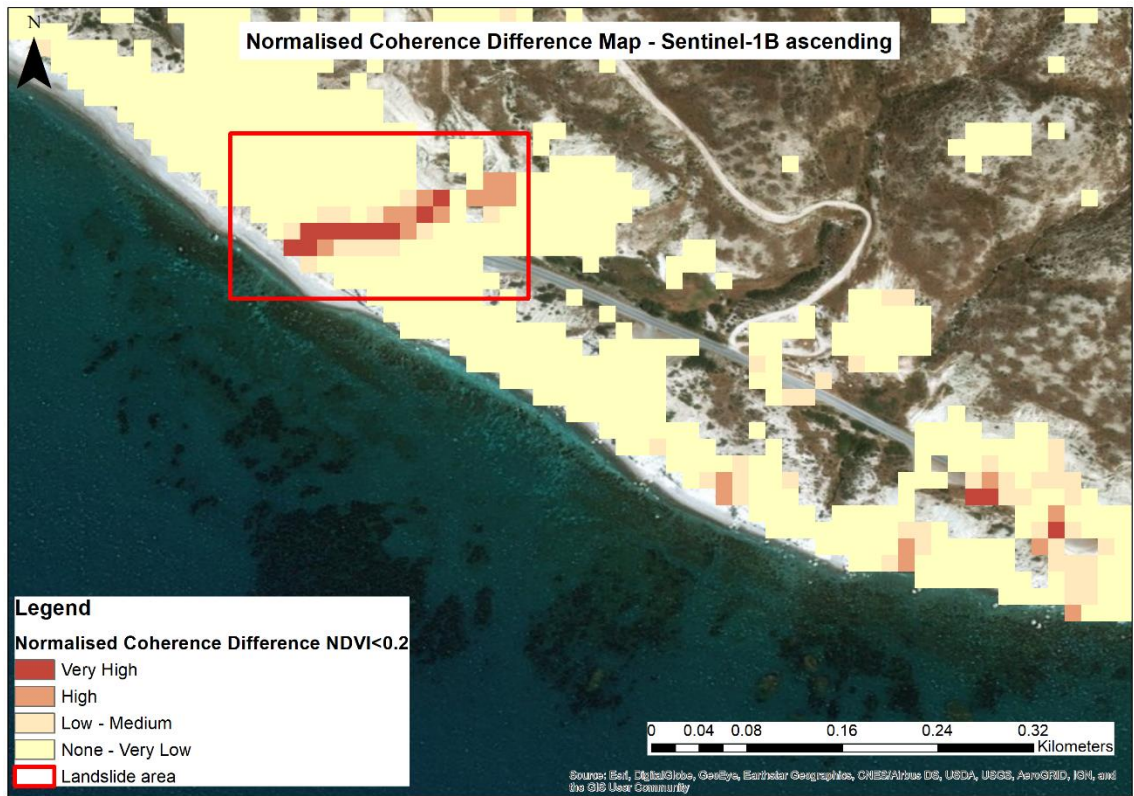


**Figure 165:** Normalised coherence difference map – Sentinel-1B ascending

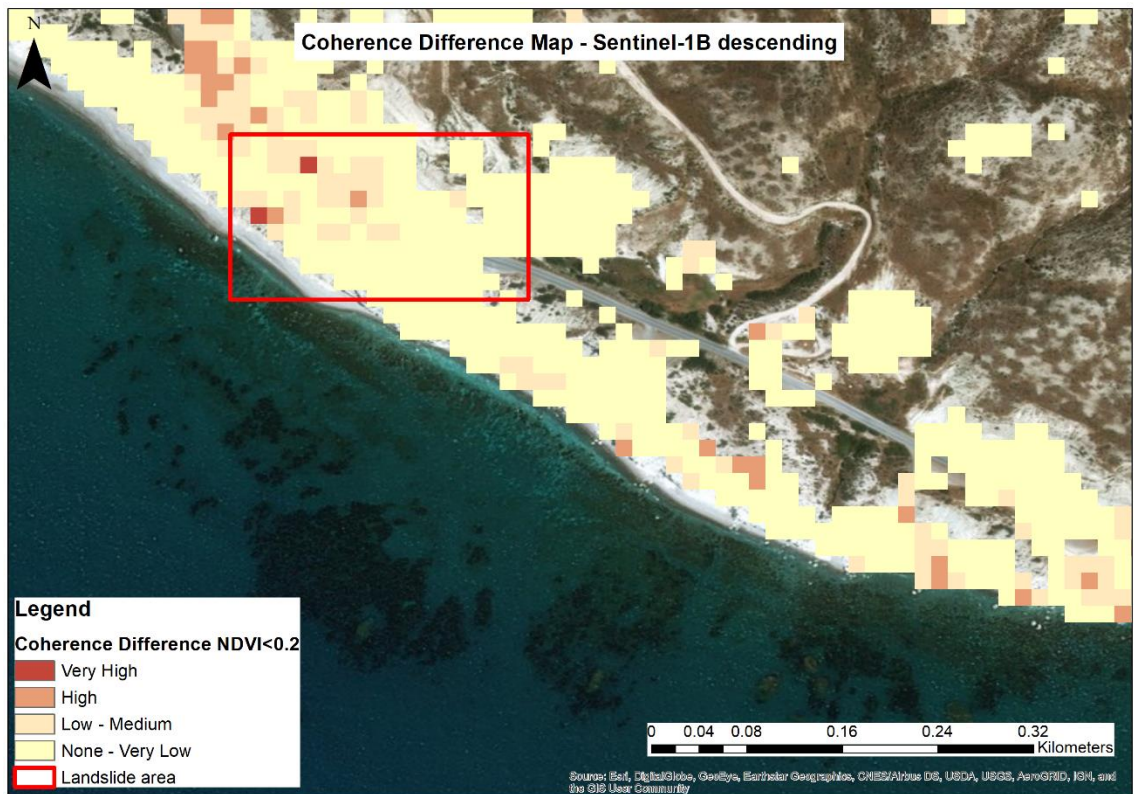


**Figure 166:** Coherence difference map – Sentinel-1B descending



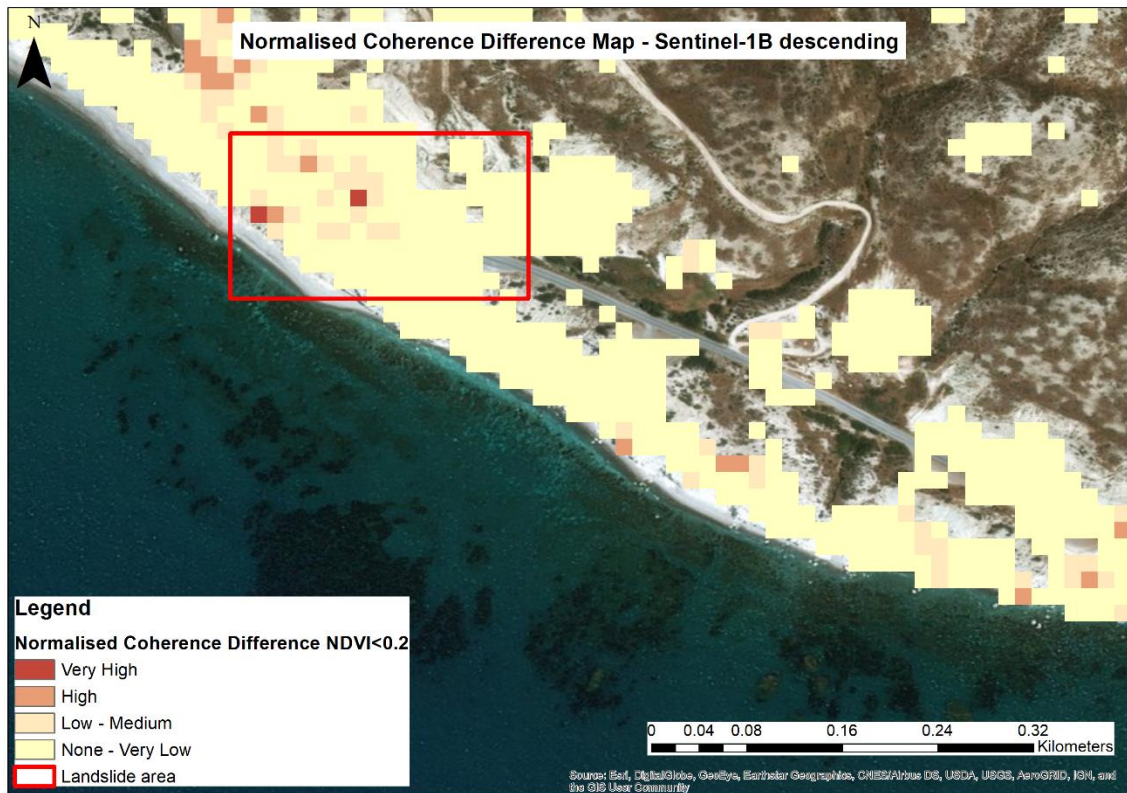


**Figure 167:** Normalised coherence difference map – Sentinel-1B descending

From a first overview of the above maps, it is noticeable that both Sentinel-1A (Figure 160 and Figure 161) and Sentinel-1B (Figure 164 and Figure 165) satellites in their ascending pass successfully detected the landslide under study, whereas descending pass satellites failed to identify the areas affected by the landslide.

This was due to the fact that the landslide occurred at a slope facing in the southwest direction, enabling thus satellites of the ascending pass direction to acquire geometrically correct images and avoid shadow and/or overlay effects that can be introduced in the processing due to the topography of the area with the residing steep slopes. This problem was also encountered during the application of the DInSAR methodology that was applied for the case study of Nea Paphos – Tombs of the Kings. In that case, the ascending SAR images were also selected for further processing.

Moreover, the ascending pass satellites detected some areas of high and very high probability of landslide occurrence to the southeast of the study area. Although some of these areas are within the boundaries of the old Paphos – Limassol road, some others, especially from the level of the road downslope towards the sea are noteworthy. As one

of the main reasons for this landslide was the residing soil erosion issues, there might be additional areas that were eroded and collapsed or subsided following the heavy rainfall. In all cases, the normalised coherence difference indicator, managed to detect more successfully the areas affected by landslide providing at the same time less false alarms. In fact, the majority of the false indications fall within the road boundaries, a matter that could have led to a loss of coherence as traffic was present during the acquisition dates of the images used as master during the interferometric processing.

The average coherence difference and normalised coherence difference maps were also developed to study the impact of the landslide further, taking at the same time advantage of the short revisit times of the Sentinel-1 satellites. The multi-pass capabilities were explained in detail in the previous section and also in *sections 2.3 Monitoring natural hazards through Earth Observation* and *3.2.1 Data*.

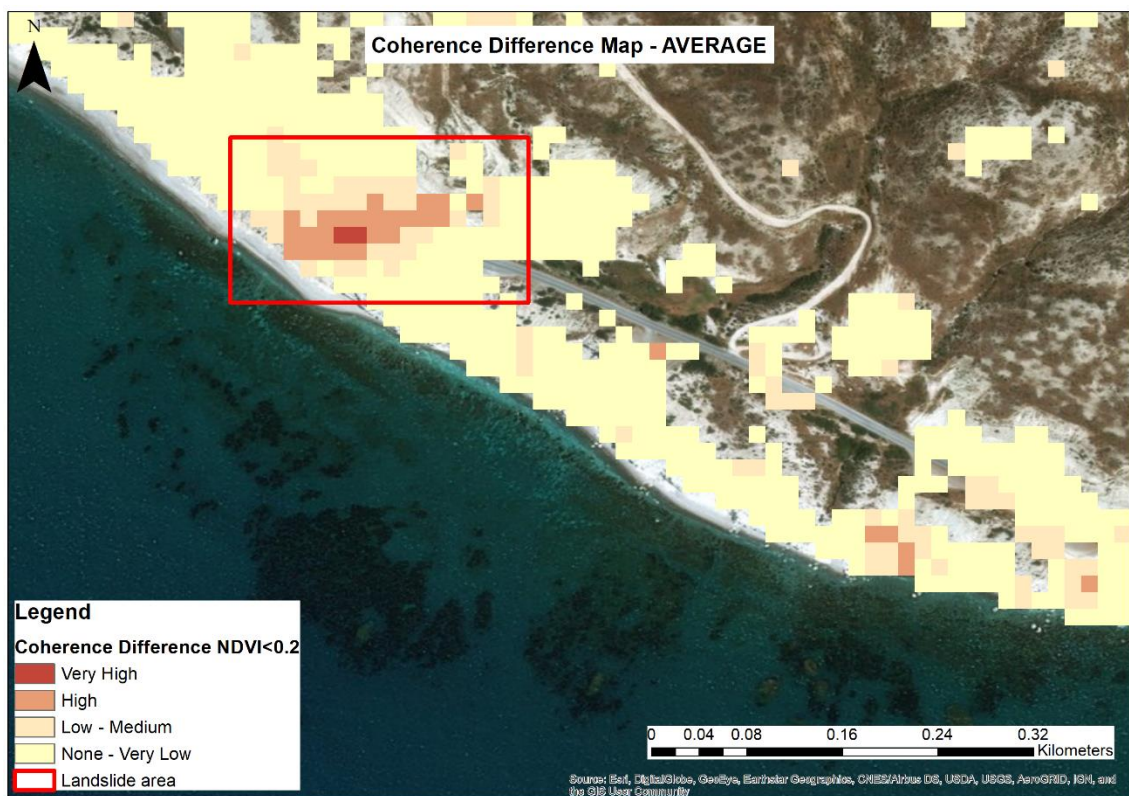


**Figure 168:** Coherence difference map – Average

The averaging of all results resulted in improved and more accurate end-products, compared to the individual Sentinel-1A and Sentinel-1B based ones. The average coherence difference and normalised coherence difference products show the extents of

the area affected by the landslide whereas at the same time managed to nearly eliminate all false indications that were located on the old Paphos – Limassol road. Moreover, the area to the southeast of the AOI is now highlighted partially as an area of high landslide probability in both maps, as presented in Figure 168 and Figure 169.

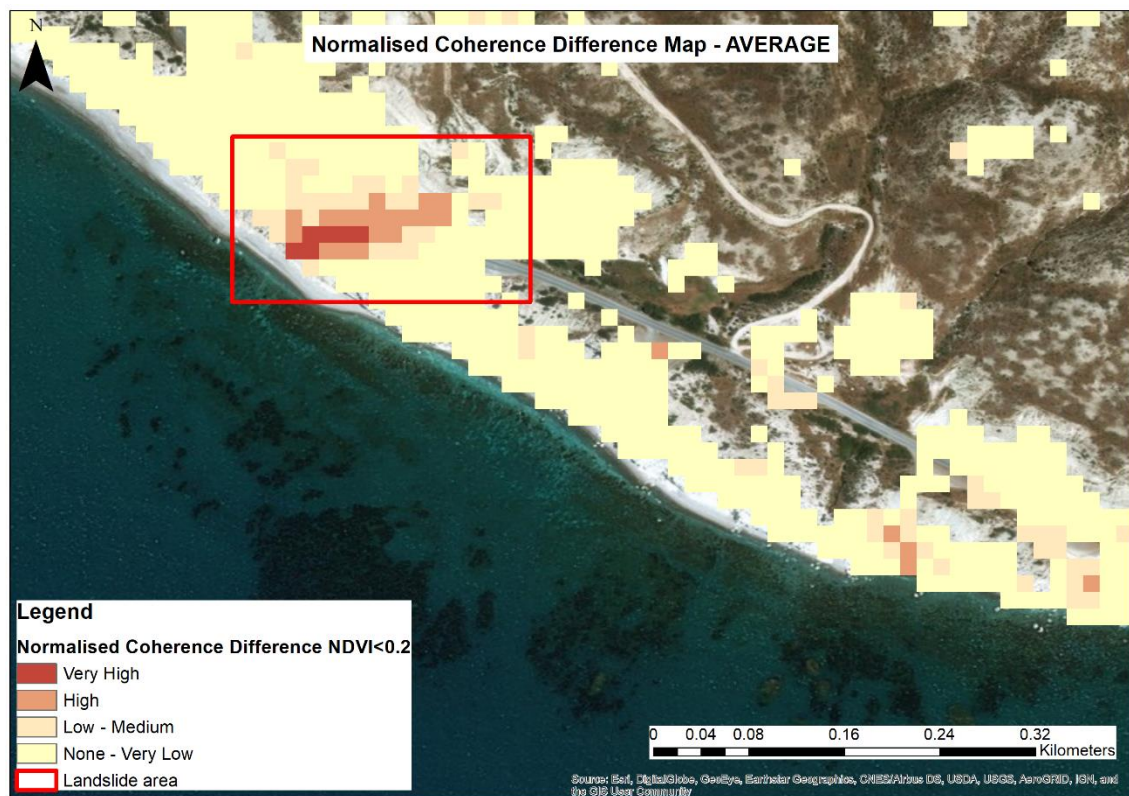


**Figure 169:** Normalised coherence difference map – Average

The further optimisation of the detection results was attempted by combining the results of the two successful products based on ascending Sentinel-1A and Sentinel-1B imagery, as it was performed earlier for the case study near Pissouri. Based on the superior performance of both satellites (ascending), the results from the coherence difference and normalised coherence difference maps, which were developed earlier, were averaged to produce Sentinel-1A and B average coherence difference and normalised coherence difference products, as presented in Figure 170 and Figure 171 respectively.

Once more, this combination resulted in the further improvement in landslide detection providing a clear representation of the area affected by the landslide and at the same time minimised the false indications, limiting to those located along the old Paphos – Limassol road, in the case of the normalised coherence difference map.

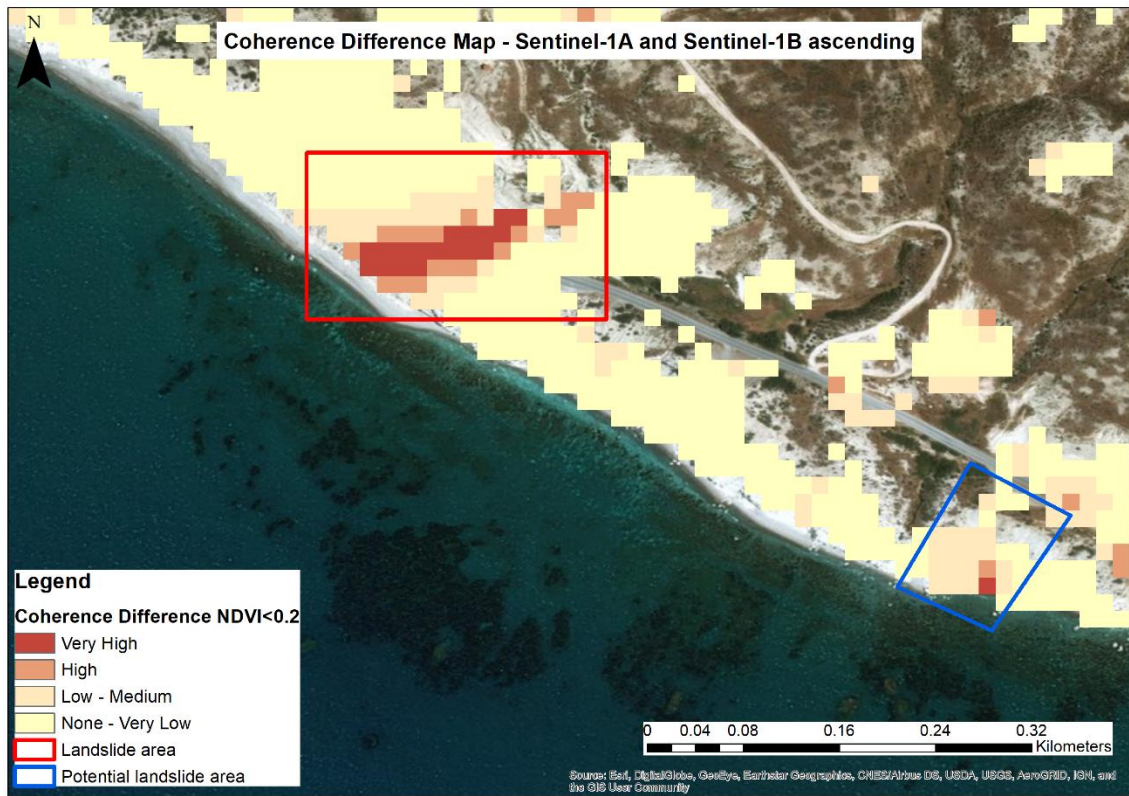


**Figure 170:** Coherence difference map – Sentinel-1A and Sentinel-1B ascending

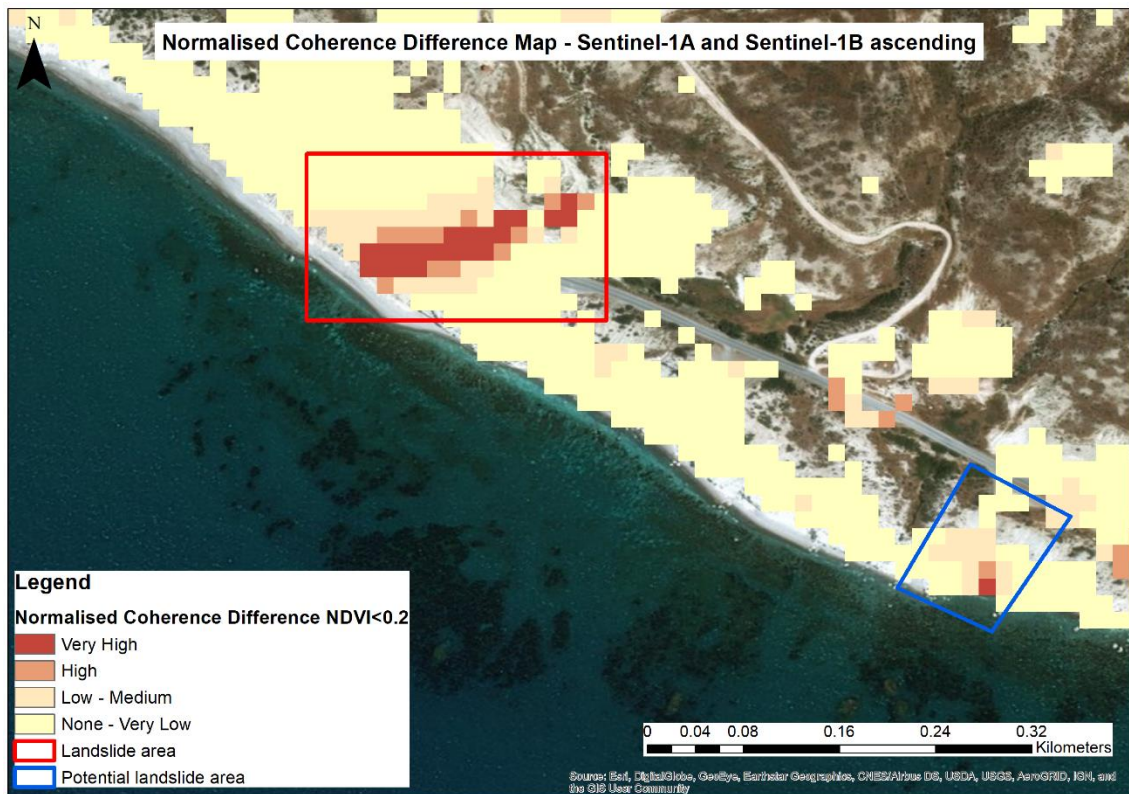


**Figure 171:** Normalised coherence difference map – Sentinel-1A and Sentinel-1B ascending

The averaging of the two products based on ascending Sentinel-1 imagery, i.e. S1A and S1B, has further improved the previous results that were based on individual satellite observations, optimising the detection of the area that was affected by the landslide (very high probability), especially in the case of the normalised coherence difference indicator.

Other areas marked with high probability are all along the road and are not taken into consideration, with the exception of the area to the southeast of the AOI, that the values mostly fall into the “Low – Medium” class, with some areas of high and very high probability of landslide occurrence, downhill towards the sea. As seen in Figure 170 and Figure 171, this area was marked as a site that was potentially affected by a landslide.

The normalised coherence difference has once more performed better than the coherence difference indicator, as happened in the case of the landslide by A6 motorway near Pissouri, providing more accurate results for the detection of the area affected by a landslide and less number of false indications regarding the occurrence of a landslide.

Based on the thorough analysis that was carried out in the present *section 4.3 Implementation of CCD methodology*, the proposed methodology has proven to be efficient in the detection and monitoring of natural hazards as well as for the assessment of their impact on infrastructure. Despite the fact, that the results are not quantifiable, as in the case of DInSAR methodology, CCD methodology provides valuable input for the extents of the affected area and can even detect landslides that occurred in remote areas and were not recorded before. It was the first time that such a technique has been successfully applied for landslides induced by heavy rainfall.

It is worth noting that the Coherent Change Detection technique can be used at two different stages producing different types of outputs. At a first stage, CCD can provide very quickly an initial assessment of the impact due to the occurrence of a natural hazard, using a minimum number of three SAR images, creating two interferometric SAR pairs, one pre-event and one co-event pair. Finally, CCD can develop more accurate end-products, showing the exact extents of the natural hazard affected area through the exploitation of the multi-pass advantages of the Copernicus Sentinel-1 mission, combining numerous pre-event and co-event SAR imagery.

## 5 Discussion

Earthquakes and landslides are considered to be two of the most devastating natural hazards worldwide. They are triggered by many factors that can be monitored via ground-based or satellite-based techniques, as described in detail in the *Introduction* and *Literature review* sections of the present thesis.

Conventional ground-based geodetic, photogrammetric, geophysical and geotechnical techniques are being used for many decades for monitoring the geological stability and other parameters that can induce land displacement events. These techniques involve time-consuming and costly field surveys and the use and installation of expensive equipment. They are usually conducted at specific areas with proven history in hazardous events, as monitoring networks are difficult and costly to be established everywhere.

Space-based passive and active remote sensing techniques, utilising optical and radar images respectively, are widely used in many applications and research fields, as they are very efficient in monitoring changes on the Earth's surface. The continuously improving spatial and temporal characteristics of the satellites, and the capabilities to acquire images day and night and under all weather conditions as in the case of SAR images, have laid the ground for continuous monitoring of land and sea. This, in fact, is enhanced through the complementarity of datasets that the various satellite missions provide. During the last years, the Earth Observation (EO) sector has provided remarkable opportunities for monitoring infrastructure resilience in urban and cultural heritage sites.

There seems to be a complementarity of the different monitoring techniques, as they were presented in *sections 2.2* and *2.3*. Geophysical techniques provide data on sub-surface characteristics; geodetic techniques measure absolute displacements at specific points; geotechnical methods provide information on soil mechanical properties; photogrammetric methods can give valuable information through archive aerial photos; and EO methods, provide the advantages of spatial and temporal coverage characteristics in land displacement studies. Therefore, the integration of EO based derived data with all available information on ground deformation collected through other in-situ techniques, is the way forward to achieve accurate and continuous monitoring and mapping of land displacement, and reliable assessment of the impact of natural hazards to infrastructure.

In the present thesis, the main aim was the integration of optical and SAR images, with GNSS coordinates at three different case studies in order to identify areas vulnerable to land movements and evaluate the impact of specific events, such as earthquakes and landslides to infrastructure resilience and cultural heritage landscape.

More specifically, the use of optical remote sensing techniques and GIS for land displacement susceptibility zonation was attempted. The goal was to develop a methodology that can provide critical information based on parameters extracted solely from satellite imagery data, as with the freely distributed archive Landsat 5 TM images. Additionally, other data originating from satellite images, such as the CORINE Land Use / Land Cover map, which is based on Sentinel-2 images, and data provided by local authorities through the INSPIRE directive, can be used to collect the required parameters and update the current hazard maps.

All these parameters were rated for their contribution to possible land displacement events and a certain weight factor was assigned to each parameter through AHP methodology, based on experts' opinion, to identify the areas susceptible to land displacement triggering phenomena. The land displacement susceptibility maps were then compared to recorded known landslide events for evaluation purposes. This information can be used in the decision-making process by stakeholders and responsible authorities.

Furthermore, the impact of these natural hazards on infrastructure resilience and Cultural Heritage landscapes was assessed through the use of freely distributed Sentinel-1 SAR datasets and open-source software. The Sentinel-1 sensors, due to their high temporal resolution, enabled us to acquire radar images before and after the specific events, which were then processed using the DInSAR and CCD methodologies.

The DInSAR technique can assist in monitoring the displacement pattern over large areas, as those in all case studies, thus providing fast and reliable information to local stakeholders and policy makers about a specific hazard. DInSAR processing can, therefore, be part of a continuous updated risk management plan for the built environment and critical infrastructure, along with state-of-the-art geoinformation technologies such as those provided under the Copernicus umbrella.

Moreover, the CCD methodology can operate complementarily with DInSAR or as a stand-alone technique for the monitoring of ground deformations over large areas

providing useful information, of qualitative nature, regarding the impact of a natural hazard. Its advantage compared with DInSAR methodology is the fact that the processing time required is limited, thus providing valuable information very quickly to responsible local authorities. Additionally, CCD techniques, using the advantages of Sentinel-1 satellites and other contributing missions, can be used for the continuous update of natural hazard risk maps and geological suitability maps (Figure 172) as they can detect areas affected by natural hazards, such as landslides, with great accuracy, as in the case of the normalised coherence difference indicator.

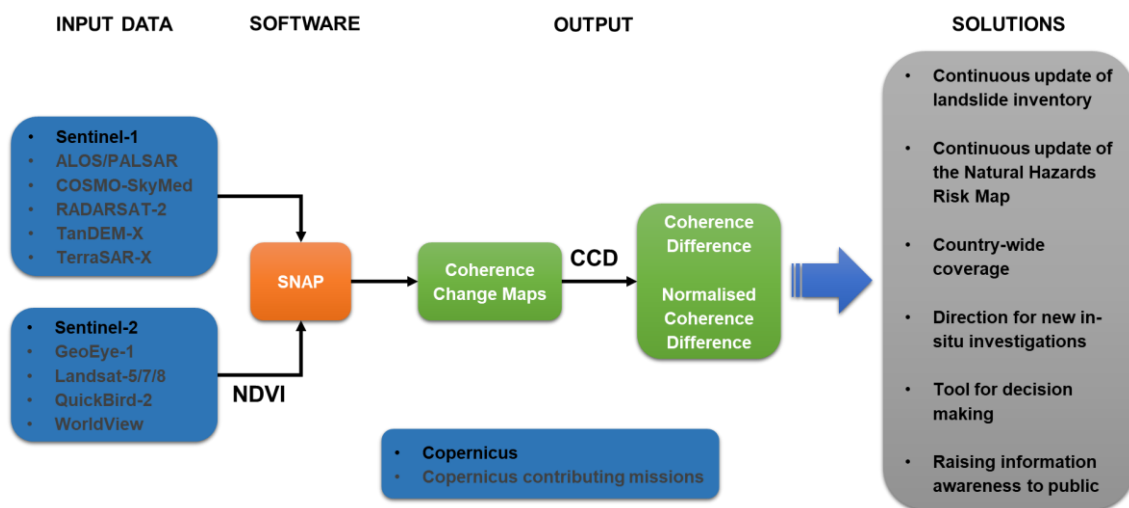


**Figure 172:** The proposed CCD methodology

Indeed, the contributions of the Copernicus program through the freely available Sentinel-1 and Sentinel-2 satellite data along with the open-source software SNAP provided freely by ESA, as well as SNAPHU plugin/software developed at Stanford university, which can be used to process the Copernicus data, can lead to the collection of valuable information in a timely manner due to the high temporal resolution and multi-pass nature of the Sentinel satellites (Figure 173).

Apart from datasets provided by the Copernicus Sentinel missions, the Copernicus contributing missions (Landsat, WorldView, COSMO-SkyMed, ALOS/PALSAR, etc.) play also a crucial role to meet the observational needs, as they deliver complementary data to those of Copernicus (ESA, no date a). Geographic information systems (GIS) were employed in order to provide a valuable mapping representation of all the different parameters and collected data, enabling the spatial representation of the various findings.



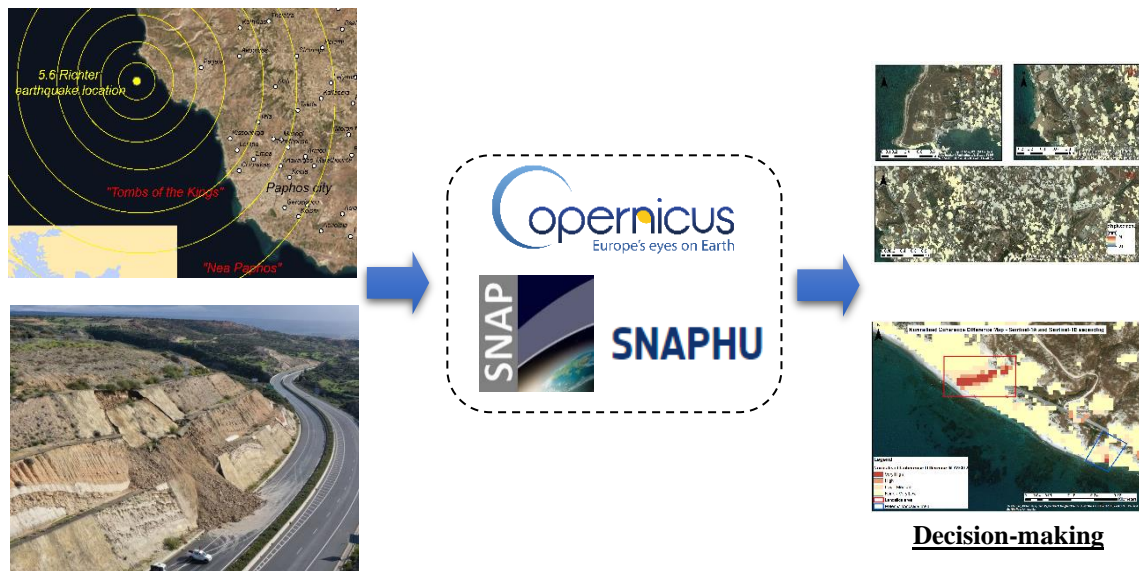


**Figure 173:** The contribution of Copernicus, ESA, and Stanford University on natural hazards monitoring via DInSAR and CCD methodologies

As presented in Figure 174, the results of this study can be used as a roadmap for stakeholders to take specific actions regarding the identification of land movement vulnerable areas in Cyprus. The local authorities will be capable to identify areas prone to land movements on a systematic basis, by updating the area’s land displacement susceptibility map through the automated use of AHP methodology using satellite or other GIS based data (INSPIRE), prior to the issue of a new building permit or the construction of new infrastructure.

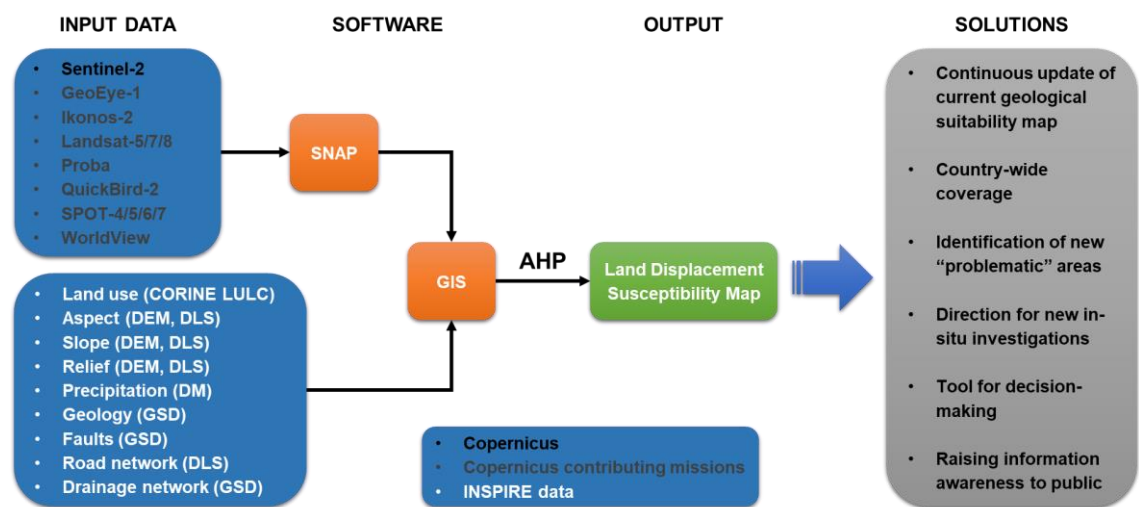


**Figure 174:** The AHP methodology for the continuous monitoring of land displacement susceptibility

AHP, as a knowledge driven qualitative method methodology, has certain limitations, as the result depend on the experts' opinion. Despite the subjective nature of the AHP methodology, it can be applied easily in GIS, combining a number of factors in the form of layers/maps. Additionally, the weights assigned to the natural hazard triggering factors are clear and can be discussed among experts and decision makers; and reviewed if necessary.

Moreover, the land displacement information provided in the form of displacement maps and normalised coherence difference maps can be utilised in the decision-making process of local stakeholders and responsible authorities. This information can be used for the on-time activation of disaster/emergency management services for the protection of the environment and citizens. Such a solution will allow stakeholders to observe, monitor, and even model natural hazards such as earthquakes and landslides in minimum time (Figure 175). This hazard-related information combined with vulnerability maps that will present the condition of cultural heritage monuments and infrastructure of interest can enable authorities to apply specialised protective measures for the respective monuments and road networks based on their characteristics and residing risks on each specific site.

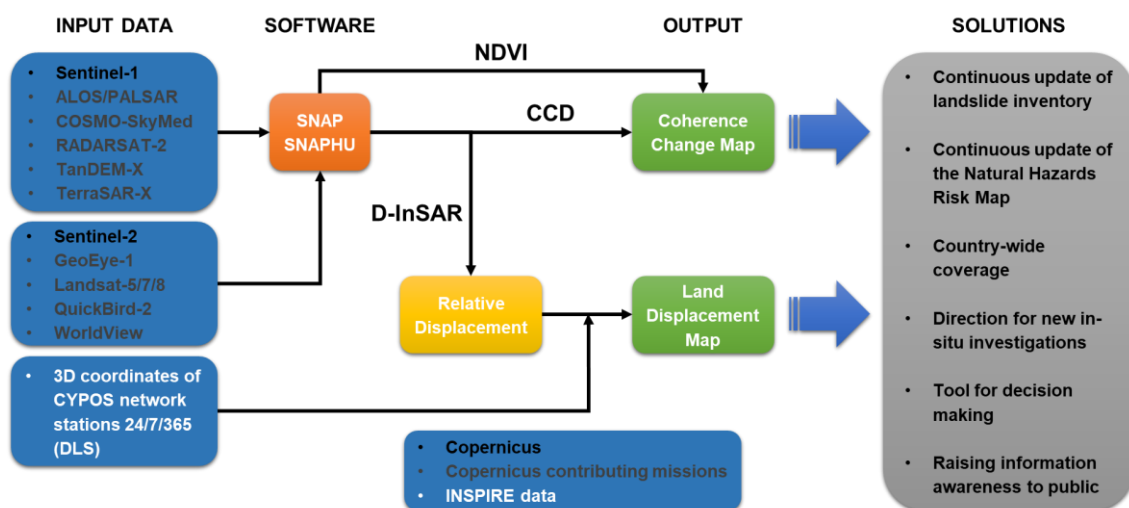


**Figure 175:** The integrated CCD – DInSAR methodology for the continuous monitoring of land movements

The complementarity of the Coherent Change Detection and DInSAR methodologies is necessary due to the limitations that exist in the application of DInSAR. As seen in section 4.2.1, DInSAR methodology performed exceptionally well for the detection and measurement in the form of displacement values of the impact of an earthquake in the

case study of Nea Paphos – Tombs of the Kings, but failed to do so for the assessment of the landslide impact in Pissouri – Petra tou Romiou case study. As seen in *Literature review*, fast moving land displacements cannot be detected via DInSAR due to a phenomenon called temporal phase aliasing. In fact, when land movement values exceed the threshold of  $\lambda/4$ , i.e.  $\sim 1.39\text{cm}$  in the case of Sentinel-1 C band, between two subsequent satellite acquisitions, these are detected ambiguously by DInSAR methodology.

On the other hand, in the same case study, the application of the proposed CCD methodology provided valuable information for the location of the area that was affected by the landslide through the study of the normalised coherence difference between two sets of interferometric SAR pairs, a pre-event and a co-event one. Its application proved, that the phase decorrelation caused by a natural disaster is far more significant than the one caused by the natural coherence loss due to the temporal baseline of two or more consecutive SAR images.

The results from the application of the CCD methodology in the case study near Pissouri and its validation through the successful detection of two other landslides in the area near Petra tou Romiou, have proved that this methodology can provide significant information for the coordination of emergency response services and other responsible authorities in limited time. Additionally, it can provide directions for carrying out new site-specific investigations. It was the first time that this methodology was applied successfully for the detection of natural hazards induced by intense precipitation. Thus, the integration of the two methodologies, CCD and DInSAR, can successfully monitor natural hazards and assess their impact on infrastructure resilience irrespectively of the magnitude of the hazardous event under study.

Another disadvantage of the DInSAR methodology has always been the difficulty in the measurement of absolute displacement values, in order to monitor the land displacement events and their impact to infrastructure resilience in their full extent and in a global scale. This is achieved by converting the relative displacement values to absolute ones, by introducing, in the process, a point of known displacement, as described in detail in *sections 3.3.2 and 4.2*. This information is not always available, and thus in most studies the results are in relative displacement values.

In the present dissertation, a novel calibration / validation methodology is proposed for country-wide applications, for monitoring the impact of natural hazards on infrastructure, through the use of coordinates of the permanent GNSS network stations of CYPOS that is operated by the Department of Lands and Surveys (Figure 176). These positions are received on a 24/7/365 basis, providing useful information in monitoring natural hazard phenomena causing land movements. The fact, that the island of Cyprus, and consequently all seven CYPOS network stations can be seen in a single Sentinel-1 image, can assist in the effective calibration and validation of the DInSAR processing results. The methodology and the final results are analysed thoroughly in *sections 3.3.3 and 4.2.1.1* respectively.

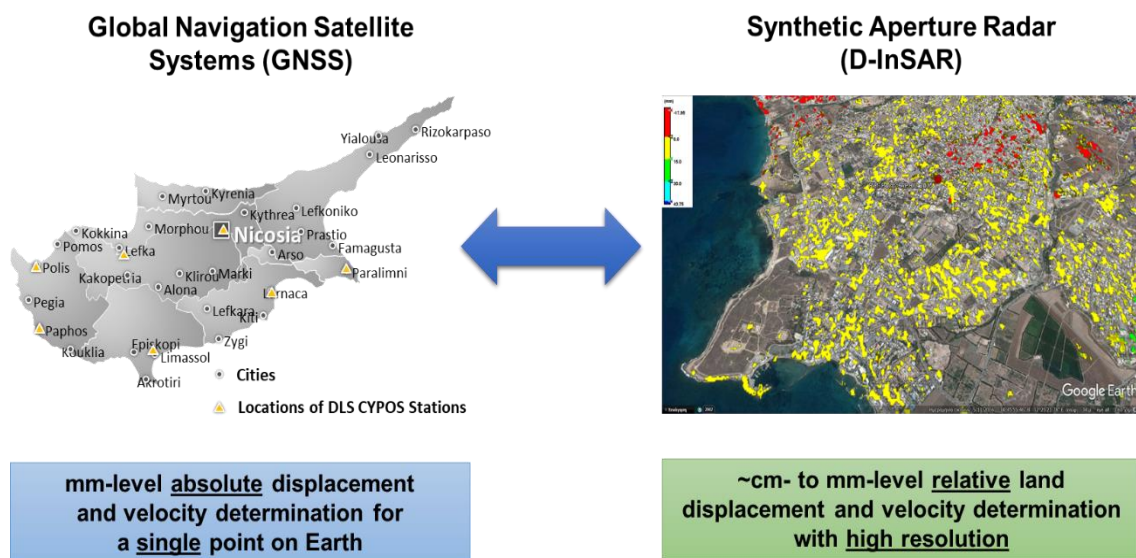


**Figure 176:** The integration of DInSAR processing results and GNSS measurements

Despite all the advantages that EO techniques have, as they were discussed thoroughly in the present section, certain limitations exist mostly because of the spatial resolution of Sentinel-1 images and the C-band wavelength. As presented in the literature review, areas covered with vegetation cannot be monitored very efficiently with Sentinel-1 images; thus, P-band SAR images, which have enhanced capabilities for penetration, are preferred instead. Finally, higher resolution SAR data, such as COSMO-SkyMed and TerraSAR-X are required in the case of more detailed monitoring. In the case study of Pissouri – Petra tou Romiou, the effect of vegetation was removed for the application of the CCD methodology, using an NDVI mask created based on Sentinel-2 imagery.

Last but not least, the provision of information about an upcoming hazard in a timely manner is of vital importance, when lives are in danger. There is an emerging need for real-time and/or near real-time monitoring systems, the so-called Early Warning Systems (EWS). To achieve real-time and/or near real-time monitoring, the entire process from data acquisition to the release of the warning must be fully automated for a real-time hazard assessment.

Indeed, with the proposed integrated CCD – DInSAR methodology, products can be developed at two stages. A first stage with quick products that can be developed based on the normalised coherence difference calculation by three SAR images, two before and one after the natural hazard occurrence. These can provide an initial assessment of the impact of the natural disaster, which is valuable information for the coordination of emergency response services and for raising information awareness to public.

Finally, at a second stage, CCD can develop more accurate multi-pass end-products, showing the exact extents of the natural hazard affected area through the exploitation of the multi-pass advantages of the Copernicus Sentinel-1 mission, combining numerous pre-event and co-event SAR imagery. At the same time displacement maps will be developed through the proposed DInSAR techniques to provide information regarding the quantitative aspects of the disaster. These second stage products can be used for the continuous update of the landslide inventory and natural hazard risk map, as well as to provide directions for carrying out new site-specific investigations.

In the present thesis, a first attempt is made to consider all the relevant information required to identify areas vulnerable to potential hazards and assess the impact of natural hazards to infrastructure, the monitoring and processing techniques to be applied, and how all these can potentially be included in an automated procedure that can lead towards the implementation of a country-wide Early Warning System in Cyprus.

## CONCLUSIONS

In this thesis, the integrated use of Earth Observation (EO) techniques and GIS for the monitoring and assessment of the impact of natural hazards on infrastructure resilience was accomplished. The main aim of the study was to develop a novel EO based methodology that can be used for the continuous and systematic monitoring of natural hazards and the assessment of their impact on critical infrastructure, such as road networks and on areas of cultural heritage significance, minimising, at the same time, the in-situ field campaigns and related costs. The concluding remarks of this thesis are the following:

1. The results of the AHP methodology were successfully compared with already known landslide events in the case study area. The Landslide Hazard Zonation Map that was developed can be continuously updated with more recent data, that are currently available in Cyprus through the INSPIRE framework and by exploiting Copernicus products, either directly by processing Sentinel-2 imagery or indirectly by using the Sentinel-2 based CORINE LULC.
2. A novel integrated CCD – DInSAR methodology was proposed to overcome the qualitative knowledge-driven nature of the AHP and provide displacement outputs in the other two cases study sites, Nea Paphos – Tombs of the Kings and Pissouri – Petra tou Romiou. The geological and geomorphological characteristics of the two areas differ significantly and thus, the proposed methodology needed to be operational irrespectively of the residing geological and geomorphological aspects of the case study sites.
3. In the case study of Nea Paphos – Tombs of the Kings, the findings from the DInSAR processing of SAR images dated 14 April 2015 and 26 April 2015, recorded absolute vertical displacement values, ranging between a maximum uplift of 74mm and a maximum subsidence of 31mm. As shown, both archaeological sites in the eastern part of the area showed nearly zero displacement, whereas some vertical displacement was observed in the northern part of the city of Paphos.
4. A novel calibration/validation methodology of DInSAR results was proposed using the 3D coordinates of the CYPOS network permanent GNSS stations, converting relative displacement values to absolute ones. The results were also

validated through a GNSS study, used as a ground truth of this analysis, confirming the above results.

5. There are certain limitations in the application of the proposed DInSAR methodology, especially in the case that it is applied for operational monitoring of areas of interest. Atmospheric phase delay can seriously affect the accuracy of DInSAR measurements if not properly corrected. Additionally, areas of rough topography cannot be monitored at all as they can be affected by geometric distortions due to satellite acquisition geometries and local topography. Monitoring of fast-moving landslides cannot be achieved using Sentinel-1 images due to the limitations of the C-band wavelength and the images' medium spatial resolution. Vegetation and the residing meteorological conditions can also influence the DInSAR results significantly.
6. DInSAR failed to detect the ground deformation due to the landslides that occurred in the case study of Pissouri – Petra tou Romiou on the 15<sup>th</sup> and 20<sup>th</sup> of February 2019.
7. Interferometric SAR coherence, a different product of the DInSAR methodology, was used to overcome the limitations of DInSAR, and investigate the landslides under study.
8. The Coherent Change Detection (CCD) methodology was applied for the case study of Pissouri – Petra tou Romiou producing results at two stages, a quick product by combining the results of one pre-event and one co-event interferometric SAR image pair, and a more refined product based on multiple passes of the Sentinel-1 satellites exploiting its capabilities at its full extents.
9. The results of the CCD methodology were very promising as the normalised coherence difference indicator managed to detect accurately the extents of both landslides. The normalised coherence difference detected landslide and non-landslide areas with an overall accuracy of 94.8%, whereas the probability of landslide detection was 73.7% and the probability of false alarm was approximately 1%.
10. It was the first time that CCD methodology was successfully applied for the identification of areas affected by landslides that were induced by heavy precipitation. This is due to the fact that rainfall is one of the factors, as analysed in *section 2.3*, that can cause severe phase decorrelation leading to false alarms in

detection of areas affected by natural hazards. The impact of vegetation in phase decorrelation was also addressed through the application of a NDVI mask that was developed solely using cloud-free Sentinel-2 optical imagery of the area.

11. The use of open-source software and freely distributed images was also highlighted in the present thesis. Freely distributed Earth Observation datasets supported by national and international space agencies, such as those of the Copernicus space program and Landsat series, will continue to provide optical and radar images with a high temporal resolution around the world. The need to provide tangible end-products and services to non-experts in remote sensing, thus addressing societal challenges both on a local and a regional level, is essential to the scientific community.
12. The Sentinel-1 constellation benefits its users with its very short revisit times and continuity of a wide area coverage; however, it has a low spatial resolution compared with other SAR satellites such as COSMO-SkyMed or TerraSAR-X. For Cyprus, Interferometric Wide swath Sentinel-1 products are only available with a resolution of  $2.7 \times 22\text{m}$  to  $3.5 \times 22\text{m}$ . This can be a constraint for smaller scale studies where more detailed monitoring is required, as described in the case of Pissouri – Petra tou Romiou.
13. The application of interferometric stacking methods through the proposed integrated CCD – DInSAR methodology helped to study the vulnerability of cultural heritage monuments and critical infrastructure, such as the A6 motorway and the old Paphos – Limassol road, to the residing site-specific risks, and can indeed aid in the development of appropriate vulnerability maps that will assist local authorities in adopting protective measures to protect the general public and conserve cultural and archaeological heritage. Moreover, the more detailed second stage multi-pass products can be used for the continuous update of the landslide inventory and natural hazard risk maps, as well as to provide directions to the authorities responsible for conducting new site-specific investigations.
14. The proposed CCD – DInSAR methodology has proved to be an invaluable source of information both of qualitative nature, as in the case of CCD, and quantitative nature, as in the case of DInSAR, on ground displacements. In all cases, natural hazard impact assessment results from EO based techniques, that are used for the systematic and continuous monitoring of large areas should always be statistically



assessed for false alarms, or else they could provide misleading information. An extensive statistical analysis and validation was carried out in the case of CCD and DInSAR methodologies.

15. It should also be stressed, at this point, that EO based techniques can only act as an aid to in-situ engineering investigations, providing complimentary information to that obtained from field campaigns and other observation techniques.
16. In this thesis, a first attempt is made to consider all the relevant information required to identify areas vulnerable to potential hazards and assess the impact of natural hazards to infrastructure, the monitoring and processing techniques to be applied, and how all these can potentially be included in an automated procedure that can lead towards the implementation of a country-wide Early Warning System in Cyprus. The time of data availability and the data processing time are the main two limiting factors for the realisation of such a goal.

### **Future Work**

1. In the future, new ways of how Copernicus sensors can be exploited further for non-invasive monitoring of critical infrastructure resilience will be investigated. The exploitation of the Copernicus program in its full capacity, including all other sensors, is expected to enhance research in new directions and methodologies. The integration of different SAR interferometry techniques can overcome any obstacles by combining their respective advantages.
2. As the selection of the type of SAR imagery is case-specific, different combinations of SAR sensors are planned to be tested for applications at different areas to achieve optimum results. The proposed CCD – DInSAR methodology is planned to be tested exploiting longer wavelength SAR acquisitions, such as L-band and P-band, for applications at areas covered with vegetation and higher resolution SAR products, such as those produced by the TerraSAR-X and COSMO-SkyMed missions for the establishment of an Early Warning System in Cyprus.

3. In fact, as a next step, a research project, the Cyprus Continuously Operating Natural Hazards Monitoring and Prevention System, abbreviated *CyCLOPS*<sup>17</sup> (RPF/INFRASTRUCTURES/1216/0050), which is co-financed by the European Union Regional Fund and the Republic of Cyprus through the Research Promotion Foundation was successfully obtained by the Cyprus University of Technology and the Eratosthenes Research Centre. The main objective of the project is the establishment of a novel Strategic Research Infrastructure Unit for monitoring Geohazards in Cyprus and the broader EMMENA region. *CyCLOPS* will deploy permanent co-located multi-sensor configurations (Tier-1 GPS/GNSS reference stations, SAR Corner Reflectors, weather stations, tiltmeters, etc.) throughout Cyprus to promote geohazard monitoring, critical infrastructure resilience and enhance National Geodetic and Spatial Data Infrastructure.
4. Moreover, the *EXCELSIOR*<sup>18</sup> H2020 Teaming Phase 2 project (Grant agreement ID: 857510), was successfully submitted by the Eratosthenes Research Centre with the final objective to be upgraded into the Eratosthenes Centre of Excellence (ECoE) for Earth Surveillance and Space-Based Monitoring of the Environment. An EO Satellite Data Acquisition Station (DAS) will be established by the ECoE in cooperation with DLR, to directly receive data from EO satellite missions, which will allow Near Real Time (NRT) monitoring over the wider EMMENA region.
5. The proposed novel integrated CCD – DInSAR methodology combined with the flagship infrastructure that will soon be established in Cyprus, through the upgraded Eratosthenes Centre of Excellence, are expected to overcome all obstacles from the nature of SAR sensors, such as the temporal and spatial resolution, the data availability time and the processing speed, and will lead to the development of an Early Warning System in Cyprus and the wider EMMENA region for the systematic geohazard monitoring and critical infrastructure resilience.

---

<sup>17</sup> *CyCLOPS*: <https://cyclops-rpf.eu/>

<sup>18</sup> *EXCELSIOR*: <https://excelsior2020.eu/>

## REFERENCES

- Abdelfattah, R. and Nicolas, J. M. (2006) “Interferometric Synthetic Aperture Radar Coherence Histogram Analysis for Land Cover Classification,” in *2006 2nd International Conference on Information & Communication Technologies*. IEEE, pp. 343–348. doi: 10.1109/ICTTA.2006.1684393.
- Agapiou, A., Alexakis, D. D., Sarris, A. and Hadjimitsis, D. G. (2014) “Evaluating the Potentials of Sentinel-2 for Archaeological Perspective,” *Remote Sensing*, 6(3), pp. 2176–2194. doi: 10.3390/rs6032176.
- Agapiou, A., Hadjimitsis, D. G., Papoutsas, C., Alexakis, D. D. and Papadavid, G. (2011) “The Importance of accounting for atmospheric effects in the application of NDVI and interpretation of satellite imagery supporting archaeological research: The case studies of Palaepaphos and Nea Paphos sites in Cyprus,” *Remote Sensing*, 3(12), pp. 2605–2629. doi: 10.3390/rs3122605.
- Agapiou, A. and Lysandrou, V. (2015) “Remote sensing archaeology: Tracking and mapping evolution in European scientific literature from 1999 to 2015,” *Journal of Archaeological Science: Reports*. Elsevier Ltd, 4, pp. 192–200. doi: 10.1016/j.jasrep.2015.09.010.
- Akinlabi, I. . A., Akinrimisi, O. E. and Fabunmi, M. A. (2018) “Subsurface Investigation of Landslide Using Electrical Resistivity,” *IOSR Journal of Applied Geology and Geophysics*, 6(5), pp. 67–74. doi: 10.9790/0990-0605016774.
- Alexakis, D. D., Agapiou, A., Tzouvaras, M., Themistocleous, K., Neocleous, K., Michaelides, S. and Hadjimitsis, D. G. (2014) “Integrated use of GIS and remote sensing for monitoring landslides in transportation pavements: the case study of Paphos area in Cyprus,” *Natural Hazards*, 72(1), pp. 119–141. doi: 10.1007/s11069-013-0770-3.
- Alexandris, A., Griva, I. K. and Abarioti, M. (2016) “Remediation of The Pissouri Landslide in Cyprus,” *International Journal of Geoengineering Case histories*, 4(1), pp. 14–28. doi: 10.4417/IJGCH-04-01-02.
- Allasia, P., Manconi, A., Giordan, D., Baldo, M. and Lollino, G. (2013) “ADVICE: A New Approach for Near-Real-Time Monitoring of Surface Displacements in Landslide Hazard Scenarios,” *Sensors*, 13(7), pp. 8285–8302. doi: 10.3390/s130708285.

- Althuwaynee, O. F., Pradhan, B., Park, H.-J. and Lee, J. H. (2014) “A novel ensemble bivariate statistical evidential belief function with knowledge-based analytical hierarchy process and multivariate statistical logistic regression for landslide susceptibility mapping,” *CATENA*. Elsevier B.V., 114, pp. 21–36. doi: 10.1016/j.catena.2013.10.011.
- Andriani, Ibrahim, E., Putranto, D. D. A. and Affandi, A. K. (2018) “Evaluation of Land Subsidence Impact at Lowland Areas Using Analytical Hierarchy Process (AHP) Method,” *E3S Web of Conferences*. Edited by M. Amin, 68, p. 04017. doi: 10.1051/e3sconf/20186804017.
- Ardizzone, F., Cardinali, M., Galli, M., Guzzetti, F. and Reichenbach, P. (2007) “Identification and mapping of recent rainfall-induced landslides using elevation data collected by airborne Lidar,” *Natural Hazards and Earth System Sciences*, 7(6), pp. 637–650. doi: 10.5194/nhess-7-637-2007.
- Aschmann, H. (1973) “Distribution and Peculiarity of Mediterranean Ecosystems,” in di Castri, F.; Mooney, H. A. (ed.) *Mediterranean Type Ecosystems*. Springer, Berlin, Heidelberg, pp. 11–19. doi: 10.1007/978-3-642-65520-3\_2.
- Ban, Y., Zhang, P., Nascetti, A., Bevington, A. R. and Wulder, M. A. (2020) “Near Real-Time Wildfire Progression Monitoring with Sentinel-1 SAR Time Series and Deep Learning,” *Scientific Reports*, 10(1), pp. 1–15. doi: 10.1038/s41598-019-56967-x.
- Baroň, I. and Supper, R. (2013) “Application and reliability of techniques for landslide site investigation, monitoring and early warning - outcomes from a questionnaire study,” *Natural Hazards and Earth System Sciences*, 13(12), pp. 3157–3168. doi: 10.5194/nhess-13-3157-2013.
- Barzaghi, R., Cazzaniga, N. E., De Gaetani, C. I., Pinto, L. and Tornatore, V. (2018) “Estimating and Comparing Dam Deformation Using Classical and GNSS Techniques,” *Sensors*, 18(3), p. 756. doi: 10.3390/s18030756.
- Beck, H. E., Zimmermann, N. E., McVicar, T. R., Vergopolan, N., Berg, A. and Wood, E. F. (2018) “Present and future Köppen-Geiger climate classification maps at 1-km resolution,” *Scientific Data*. The Author(s), 5(1). doi: 10.1038/sdata.2018.214.
- Beguería, S. (2006) “Validation and Evaluation of Predictive Models in Hazard Assessment and Risk Management,” *Natural Hazards*, 37(3), pp. 315–329. doi:

10.1007/s11069-005-5182-6.

Béjar-Pizarro, M., Guardiola-Albert, C., García-Cárdenas, R., Herrera, G., Barra, A., López Molina, A., *et al.* (2016) “Interpolation of GPS and Geological Data Using InSAR Deformation Maps: Method and Application to Land Subsidence in the Alto Guadalentín Aquifer (SE Spain),” *Remote Sensing*, 8(11), p. 965. doi: 10.3390/rs8110965.

Bell, R., Kruse, J.-E., Garcia, A., Glade, T. and Hördt, A. (2006) “Subsurface investigations of landslides using geophysical methods : geoelectrical applications in the Swabian Alb (Germany),” *Geographica Helvetica*, 61(3), pp. 201–208. doi: 10.5194/gh-61-201-2006.

Bhattacharya, A., Arora, M. K., Sharma, M. L., Vöge, M. and Bhasin, R. (2014) “Surface displacement estimation using space-borne SAR interferometry in a small portion along Himalayan Frontal Fault,” *Optics and Lasers in Engineering*. Elsevier, 53, pp. 164–178. doi: 10.1016/j.optlaseng.2013.09.001.

Bhattarai, R. and Kondoh, A. (2017) “Risk Assessment of Land Subsidence in Kathmandu Valley, Nepal, Using Remote Sensing and GIS,” *Advances in Remote Sensing*, 06(02), pp. 132–146. doi: 10.4236/ars.2017.62010.

Bichler, A., Bobrowsky, P., Best, M., Douma, M., Hunter, J., Calvert, T. and Burns, R. (2004) “Three-dimensional mapping of a landslide using a multi-geophysical approach: the Quesnel Forks landslide,” *Landslides*, 1(1), pp. 29–40. doi: 10.1007/s10346-003-0008-7.

Biggs, J., Wright, T., Lu, Z. and Parsons, B. (2007) “Multi-interferogram method for measuring interseismic deformation: Denali Fault, Alaska,” *Geophysical Journal International*, 170(3), pp. 1165–1179. doi: 10.1111/j.1365-246X.2007.03415.x.

Biswajeet, P. and Saro, L. (2007) “Utilization of Optical Remote Sensing Data and GIS Tools for Regional Landslide Hazard Analysis Using an Artificial Neural Network Model,” *Earth Science Frontiers*, 14(6), pp. 143–152. doi: 10.1016/s1872-5791(08)60008-1.

Bitelli, G., Bonsignore, F., Carbognin, L., Ferretti, A., Strozzi, T., Teatini, P., Tosi, L. and Vittuari, L. (2010) “Radar interferometry-based mapping of the present land subsidence along the low-lying northern Adriatic coast of Italy,” in *Land Subsidence*,

*Associated Hazards and the Role of Natural Resources Development*. IAHS Publ, pp. 279–286.

Bouaraba, A., Acheroy, M. and Closson, D. (2013) “Coherent Change Detection Performance Using High-resolution SAR Images,” *International Journal of Engineering Research & Technology (IJERT)*, 2(11), pp. 3160–3166.

Bouaraba, A., Milisavljević, N., Acheroy, M. and Closson, D. (2014) “Change Detection and Classification Using High Resolution SAR Interferometry,” in *Land Applications of Radar Remote Sensing*. InTech. doi: 10.5772/57246.

Bovenga, F., Belmonte, A., Refice, A., Pasquariello, G., Nutricato, R., Nitti, D. O. and Chiaradia, M. T. (2018) “Performance analysis of satellite missions for multi-temporal SAR interferometry,” *Sensors (Switzerland)*, 18(5), pp. 1–16. doi: 10.3390/s18051359.

Bovenga, F., Pasquariello, G., Pellicani, R., Refice, A. and Spilotro, G. (2017) “Landslide monitoring for risk mitigation by using corner reflector and satellite SAR interferometry: The large landslide of Carlantino (Italy),” *CATENA*, 151, pp. 49–62. doi: 10.1016/j.catena.2016.12.006.

Bozdağ, A., Yavuz, F. and Günay, A. S. (2016) “AHP and GIS based land suitability analysis for Cihanbeyli (Turkey) County,” *Environmental Earth Sciences*, 75(9), p. 813. doi: 10.1007/s12665-016-5558-9.

Braun, A. and Veci, L. (2020) *Sentinel-1 Toolbox - TOPS Interferometry Tutorial*. Available at: [http://step.esa.int/docs/tutorials/S1TBX TOPSAR Interferometry with Sentinel-1 Tutorial\\_v2.pdf](http://step.esa.int/docs/tutorials/S1TBX_TOPSAR_Interferometry_with_Sentinel-1_Tutorial_v2.pdf).

Burrows, K., Walters, R. J., Milledge, D., Spaans, K. and Densmore, A. L. (2019) “A New Method for Large-Scale Landslide Classification from Satellite Radar,” *Remote Sensing*, 11(3), p. 237. doi: 10.3390/rs11030237.

Calamia, M., Franceschetti, G., Lanari, R., Casu, F. and Manzo, M. (2008) “Comparison and Integration of GPS and SAR Data,” in Del Re, E. and Ruggieri, M. (eds.) *Satellite Communications and Navigation Systems*. Boston, MA: Springer, pp. 19–24. doi: 10.1007/978-0-387-47524-0\_2.

Canisius, F., Brisco, B., Murnaghan, K., Van Der Kooij, M. and Keizer, E. (2019) “SAR backscatter and InSAR coherence for monitoring wetland extent, flood pulse and

vegetation: A study of the Amazon lowland,” *Remote Sensing*, 11(6), pp. 1–18. doi: 10.3390/RS11060720.

Cereceda, P., Larrain, H., Osses, P., Farías, M. and Egaña, I. (2008) “The climate of the coast and fog zone in the Tarapacá Region, Atacama Desert, Chile,” *Atmospheric Research*, 87(3–4), pp. 301–311. doi: 10.1016/j.atmosres.2007.11.011.

Charalambous, M. and Petrides, G. (1997) “Contribution of Engineering Geology in the planning and development of landslide prone rural areas in Cyprus,” in *Engineering Geology and the Environment*. London: Balkema, pp. 1205–1210.

Chen, C. W. and Zebker, H. A. (2001a) “Network approaches to two-dimensional phase unwrapping: intractability and two new algorithms: erratum,” *Journal of the Optical Society of America A*, 18(5), p. 1192. doi: 10.1364/JOSAA.18.001192.

Chen, C. W. and Zebker, H. A. (2001b) “Two-dimensional phase unwrapping with use of statistical models for cost functions in nonlinear optimization,” *Journal of the Optical Society of America A*, 18(2), pp. 338–351. doi: 10.1364/JOSAA.18.000338.

Chen, C. W. and Zebker, H. A. (2002) “Phase unwrapping for large SAR interferograms: statistical segmentation and generalized network models,” *IEEE Transactions on Geoscience and Remote Sensing*. IEEE, 40(8), pp. 1709–1719. doi: 10.1109/TGRS.2002.802453.

Chen, F., Lasaponara, R. and Masini, N. (2017) “An overview of satellite synthetic aperture radar remote sensing in archaeology: From site detection to monitoring,” *Journal of Cultural Heritage*. Elsevier Masson SAS, 23, pp. 5–11. doi: 10.1016/j.culher.2015.05.003.

Chen, W., Li, W., Chai, H., Hou, E., Li, X. and Ding, X. (2016) “GIS-based landslide susceptibility mapping using analytical hierarchy process (AHP) and certainty factor (CF) models for the Baozhong region of Baoji City, China,” *Environmental Earth Sciences*. Springer Berlin Heidelberg, 75(1), p. 63. doi: 10.1007/s12665-015-4795-7.

Closson, D. and Milisavljevic, N. (2017) “InSAR Coherence and Intensity Changes Detection,” in *Mine Action - The Research Experience of the Royal Military Academy of Belgium*. InTech, p. 23. doi: 10.5772/65779.

Colomina, I. and Molina, P. (2014) “Unmanned aerial systems for photogrammetry and

remote sensing: A review,” *ISPRS Journal of Photogrammetry and Remote Sensing*. International Society for Photogrammetry and Remote Sensing, Inc. (ISPRS), 92, pp. 79–97. doi: 10.1016/j.isprsjprs.2014.02.013.

Community Council of Statos-Agios Photios (no date) *General – Statos – Agios Photios*. Available at: <https://www.statos-aggiosphotios.org/en/tour/general/#toggle-id-1> (Accessed: December 10, 2019).

Corsetti, M., Fossati, F., Manunta, M. and Marsella, M. (2018) “Advanced SBAS-DInSAR Technique for Controlling Large Civil Infrastructures: An Application to the Genzano di Lucania Dam,” *Sensors*, 18(7), p. 2371. doi: 10.3390/s18072371.

Crozier, M. J. and Glade, T. (2012) “Landslide Hazard and Risk: Issues, Concepts and Approach,” in *Landslide Hazard and Risk*. Chichester, West Sussex, England: John Wiley & Sons, Ltd, pp. 1–40. doi: 10.1002/9780470012659.ch1.

Cruden, D. M. and Varnes, D. J. (1996) “Landslide Types and Processes,” *Transportation Research Board: Special Report*, 247, pp. 36–75. Available at: [https://www.researchgate.net/publication/269710355\\_CrudenDM\\_Varnes\\_DJ\\_1996\\_Landslide\\_Types\\_and\\_Processes\\_Special\\_Report\\_Transportation\\_Research\\_Board\\_National\\_Academy\\_of\\_Sciences\\_24736-75](https://www.researchgate.net/publication/269710355_CrudenDM_Varnes_DJ_1996_Landslide_Types_and_Processes_Special_Report_Transportation_Research_Board_National_Academy_of_Sciences_24736-75).

Cuca, B., Tzouvaras, M., Agapiou, A., Lysandrou, V., Themistocleous, K., Nisantzi, A. and Hadjimitsis, D. G. (2016) “Earth observation technologies in service to the cultural landscape of Cyprus: risk identification and assessment,” in *Fourth International Conference on Remote Sensing and Geoinformation of the Environment (RSCy2016)*, p. 96880Y. doi: 10.1117/12.2241669.

Cyprus Organisation for Standardisation (2004) *NATIONAL ANNEX TO CYS EN 1998-1:2004 (Including AI:2013 and AC:2009)*. Nicosia, Cyprus.

Cyprus Tourism Organisation (no date) “Petra tou Romiou ( The Rock of the Greek ),” pp. 1–7. Available at: [https://www.visitcyprus.com/files/audio\\_guides/written\\_form/Petra\\_tou\\_Romiou\\_afigisi\\_en.pdf](https://www.visitcyprus.com/files/audio_guides/written_form/Petra_tou_Romiou_afigisi_en.pdf).

D’Aranno, P., Di Benedetto, A., Fiani, M. and Marsella, M. (2019) “REMOTE SENSING TECHNOLOGIES FOR LINEAR INFRASTRUCTURE MONITORING,” *ISPRS* -



*International Archives of the Photogrammetry, Remote Sensing and Spatial Information Sciences*, XLII-2/W11(2/W11), pp. 461–468. doi: 10.5194/isprs-archives-XLII-2-W11-461-2019.

Dalla Via, G., Crosetto, M. and Crippa, B. (2012) “Resolving vertical and east-west horizontal motion from differential interferometric synthetic aperture radar: The L’Aquila earthquake,” *Journal of Geophysical Research: Solid Earth*, 117(B2), p. n/a-n/a. doi: 10.1029/2011JB008689.

Danezis, C., Chatzinikos, M. and Kotsakis, C. (2019) “Linear and NonLinear Deformation Effects in the Permanent GNSS Network of Cyprus,” in *4th Joint International Symposium on Deformation Monitoring (JISDM)*. Athens, p. 137. Available at: <https://jisdm2019.org/wp-content/uploads/2019/05/100.pdf>.

Das, I., Sahoo, S., van Westen, C., Stein, A. and Hack, R. (2010) “Landslide susceptibility assessment using logistic regression and its comparison with a rock mass classification system, along a road section in the northern Himalayas (India),” *Geomorphology*. Elsevier B.V., 114(4), pp. 627–637. doi: 10.1016/j.geomorph.2009.09.023.

Dedeoğlu, M. and Dengiz, O. (2019) “Generating of land suitability index for wheat with hybrid system approach using AHP and GIS,” *Computers and Electronics in Agriculture*. Elsevier, 167, p. 105062. doi: 10.1016/j.compag.2019.105062.

Department of Antiquities (no date a) *Department of Antiquities - Archaeological Sites - Nea Pafos*. Available at: <http://www.mcw.gov.cy/mcw/DA/DA.nsf/All/59FFC9310818070EC225719B003A2EB8?OpenDocument> (Accessed: July 17, 2019).

Department of Antiquities (no date b) *Department of Antiquities - Archaeological Sites - Tombs of the Kings*. Available at: <http://www.mcw.gov.cy/mcw/DA/DA.nsf/All/238DE8D409BF6077C225719B0039F785?OpenDocument> (Accessed: July 17, 2019).

Department of Antiquities (no date c) *Department of Antiquities - Home Page*. Available at: [http://www.mcw.gov.cy/mcw/da/da.nsf/DMLindex\\_en/DMLindex\\_en](http://www.mcw.gov.cy/mcw/da/da.nsf/DMLindex_en/DMLindex_en) (Accessed: June 26, 2019).

Department of Lands and Surveys (2016) *CYPOS Network*. Available at:

[https://portal.dls.moi.gov.cy/en-us/FrontEndHelp/Pages/CYPOS\\_Network.aspx](https://portal.dls.moi.gov.cy/en-us/FrontEndHelp/Pages/CYPOS_Network.aspx)  
(Accessed: December 26, 2019).

Dong, Y., Li, Q., Dou, A. and Wang, X. (2011) “Extracting damages caused by the 2008 Ms 8.0 Wenchuan earthquake from SAR remote sensing data,” *Journal of Asian Earth Sciences*, 40(4), pp. 907–914. doi: 10.1016/j.jseaes.2010.07.009.

Duncan, J. M. (1996) *Landslides: Investigation and Mitigation - Soil Slope Stability Analysis, Transportation Research Board Special Report 247*. Washington, D.C. Available at: <http://onlinepubs.trb.org/Onlinepubs/sr/sr247/sr247-013.pdf>.

Dunnicliff, J. (1994) *Geotechnical Instrumentation for Monitoring Field Performance*. Washington, D.C.: Wiley. Available at: <https://www.wiley.com/ency/Geotechnical+Instrumentation+for+Monitoring+Field+Performance-p-9780471005469>.

Durieux, A. M., Calef, M. T., Arko, S., Chartrand, R., Kontgis, C., Keisler, R. and Warren, M. S. (2019) “Monitoring forest disturbance using change detection on synthetic aperture radar imagery,” in Zelinski, M. E., Taha, T. M., Howe, J., Awwal, A. A., and Iftkharuddin, K. M. (eds.) *Applications of Machine Learning*. SPIE, p. 39. doi: 10.1117/12.2528945.

Dzurisin, D. (2007a) “Classical surveying techniques,” in *Volcano Deformation*. Berlin, Heidelberg: Springer Berlin Heidelberg, pp. 33–80. doi: 10.1007/978-3-540-49302-0\_2.

Dzurisin, D. (2007b) “The Global Positioning System: A multipurpose tool,” in *Volcano Deformation*. Berlin, Heidelberg: Springer Berlin Heidelberg, pp. 111–152. doi: 10.1007/978-3-540-49302-0\_4.

Earth Observing System (no date) *Landsat 5 (TM)*. Available at: <https://eos.com/landsat-5-tm/> (Accessed: December 26, 2019).

Eng, J. (no date) *ROC Analysis: Web-based Calculator for ROC Curves*. Available at: <http://www.rad.jhmi.edu/jeng/javarad/roc/JROCFITi.html> (Accessed: March 18, 2020).

Engram, M., Arp, C. D., Jones, B. M., Ajadi, O. A. and Meyer, F. J. (2018) “Analyzing floating and bedfast lake ice regimes across Arctic Alaska using 25 years of space-borne SAR imagery,” *Remote Sensing of Environment*. Elsevier, 209(February), pp. 660–676. doi: 10.1016/j.rse.2018.02.022.

- Erten, E., Lopez-Sanchez, J. M., Yuzugullu, O. and Hajnsek, I. (2016) “Retrieval of agricultural crop height from space: A comparison of SAR techniques,” *Remote Sensing of Environment*, 187, pp. 130–144. doi: 10.1016/j.rse.2016.10.007.
- ESA (2014) *Geometry Glossary*, *ESA Handbooks*. Available at: <https://earth.esa.int/handbooks/asar/CNTR5-5.html> (Accessed: March 6, 2020).
- ESA (no date a) *Contributing missions overview*. Available at: [https://www.esa.int/Applications/Observing\\_the\\_Earth/Copernicus/Contributing\\_missions\\_overview](https://www.esa.int/Applications/Observing_the_Earth/Copernicus/Contributing_missions_overview) (Accessed: January 20, 2020).
- ESA (no date b) *Sentinel-1 - Missions - Sentinel Online*. Available at: <https://sentinels.copernicus.eu/web/sentinel/missions/sentinel-1> (Accessed: December 26, 2019).
- ESA (no date c) *Sentinel-2 - Missions - Sentinel Online*. Available at: <https://sentinels.copernicus.eu/web/sentinel/missions/sentinel-2> (Accessed: December 26, 2019).
- ESA (no date d) *Sentinel 1 Toolbox | STEP*. Available at: <https://step.esa.int/main/toolboxes/sentinel-1-toolbox/> (Accessed: December 26, 2019).
- ESA (no date e) *Sentinel Data Access Overview - Sentinel Online*. Available at: <https://sentinel.esa.int/web/sentinel/sentinel-data-access> (Accessed: June 26, 2019).
- ESA (no date f) *SNAP | STEP*. Available at: <https://step.esa.int/main/toolboxes/snap/> (Accessed: July 17, 2019).
- Fall, M., Azzam, R. and Noubactep, C. (2006) “A multi-method approach to study the stability of natural slopes and landslide susceptibility mapping,” *Engineering Geology*, 82(4), pp. 241–263. doi: 10.1016/j.enggeo.2005.11.007.
- Fan, H., Wen, B., Liu, Jie, Liu, Jiuli and Yin, J. (2019) “An improved method of three-dimensional displacement field generation in mining areas with a single InSAR pair,” *European Journal of Remote Sensing*. Taylor & Francis, 52(1), pp. 493–503. doi: 10.1080/22797254.2019.1654927.
- Ferretti, A., Monti-guarnieri, A., Prati, C. and Rocca, F. (2007) “InSAR Principles: Guidelines for SAR Interferometry Processing and Interpretation,” *European Space Agency*. ESA Publications, p. 71. doi: 10.1787/9789264101630-5-en.

Ferro-Famil, L. and Pottier, E. (2014) “Radar Polarimetry Basics and Selected Earth Remote Sensing Applications,” in Sidiropoulos, N. D., Gini, F., Chellappa, R., and Theodoridis, S. (eds.) *Academic Press Library in Signal Processing: Volume 2: Communications and Radar Signal Processing*. Elsevier Ltd., pp. 1119–1244. doi: 10.1016/B978-0-12-396500-4.00021-1.

Foti, S. (2005) “Surface Wave Testing for Geotechnical Characterization,” in Lai, C. G. and Wilmański, K. (eds.) *Surface Waves in Geomechanics: Direct and Inverse Modelling for Soils and Rocks*. Vienna: Springer Vienna (CISM International Centre for Mechanical Sciences), pp. 47–71. doi: 10.1007/3-211-38065-5\_2.

Fourniadis, I. G., Liu, J. G. and Mason, P. J. (2007) “Landslide hazard assessment in the Three Gorges area, China, using ASTER imagery: Wushan–Badong,” *Geomorphology*, 84(1–2), pp. 126–144. doi: 10.1016/j.geomorph.2006.07.020.

Fruneau, B., Achache, J. and Delacourt, C. (1996) “Observation and modelling of the Saint-Étienne-de-Tinée landslide using SAR interferometry,” *Tectonophysics*, 265(3–4), pp. 181–190. doi: 10.1016/S0040-1951(96)00047-9.

Galli, M., Ardizzone, F., Cardinali, M., Guzzetti, F. and Reichenbach, P. (2008) “Comparing landslide inventory maps,” *Geomorphology*, 94(3–4), pp. 268–289. doi: 10.1016/j.geomorph.2006.09.023.

Garthwaite, M. C., Thankappan, M., Williams, M. L., Nancarrow, S., Hislop, A. and Dawson, J. (2013) “Corner reflectors for the Australian Geophysical Observing System and support for calibration of satellite-borne synthetic aperture radars,” in *2013 IEEE International Geoscience and Remote Sensing Symposium - IGARSS*. IEEE, pp. 266–269. doi: 10.1109/IGARSS.2013.6721143.

Geological Survey Department (2012) “The seismicity of Cyprus.” Nicosia, Cyprus. Available at: [http://www.moa.gov.cy/moa/gsd/gsd.nsf/All/BEF32774C6AB6F77C22583940034B8A9/\\$file/seismology\\_EN.pdf?OpenElement](http://www.moa.gov.cy/moa/gsd/gsd.nsf/All/BEF32774C6AB6F77C22583940034B8A9/$file/seismology_EN.pdf?OpenElement).

Geological Survey Department (2013) “Landslides in Cyprus and their consequences to built environment.” Nicosia: Republic of Cyprus. Available at: [http://www.moa.gov.cy/moa/gsd/gsd.nsf/All/34D8AE683B6986D5C225839400348AC6/\\$file/landslidesCyprus\\_EN.pdf?OpenElement](http://www.moa.gov.cy/moa/gsd/gsd.nsf/All/34D8AE683B6986D5C225839400348AC6/$file/landslidesCyprus_EN.pdf?OpenElement).

Geological Survey Department (2014) “Earthquake FAQ.”

Geological Survey Department (2016) “Geology of Cyprus.” Available at: [http://www.moa.gov.cy/moa/gsd/gsd.nsf/All/2F7369F2DBCEF1DEC225819C0034B070/\\$file/GEOLOGY OF CYPRUS WEB.pdf?OpenElement](http://www.moa.gov.cy/moa/gsd/gsd.nsf/All/2F7369F2DBCEF1DEC225819C0034B070/$file/GEOLOGY%20OF%20CYPRUS%20WEB.pdf?OpenElement).

Geological Survey Department (2018) *The technology and the new capabilities of the seismic network of the Geological Survey Department (in greek)*. Nicosia, Cyprus. Available at: [http://www.moa.gov.cy/moa/gsd/gsd.nsf/All/72ED633A78B37D4BC22583CA0041242F/\\$file/the-new-seismological-network-of-cyprus\\_sylvana\\_pilidou-2018.pdf](http://www.moa.gov.cy/moa/gsd/gsd.nsf/All/72ED633A78B37D4BC22583CA0041242F/$file/the-new-seismological-network-of-cyprus_sylvana_pilidou-2018.pdf).

Geological Survey Department (2019) *Seismic maps*. Available at: <http://www.moa.gov.cy/moa/gsd/gsd.nsf/All/22DFDADB34114C14C22583C4003B526C?OpenDocument> (Accessed: December 24, 2019).

Geological Survey Department (no date a) *Geological Survey Department | Ground Suitability*. Available at: [http://www.moa.gov.cy/moa/gsd/gsd.nsf/page37\\_en/page37\\_en?OpenDocument](http://www.moa.gov.cy/moa/gsd/gsd.nsf/page37_en/page37_en?OpenDocument) (Accessed: January 12, 2020).

Geological Survey Department (no date b) *Geological Survey Department | Home, Geological Survey Department*. Available at: [http://www.cyprus.gov.cy/moa/gsd/gsd.nsf/page01\\_en/page01\\_en?OpenDocument](http://www.cyprus.gov.cy/moa/gsd/gsd.nsf/page01_en/page01_en?OpenDocument) (Accessed: June 25, 2019).

Geological Survey Department (no date c) *Seismic Network*. Available at: <http://www.moa.gov.cy/moa/gsd/gsd.nsf/All/E1C083DA8E90EFFDC22583C50044A2EE?OpenDocument> (Accessed: December 6, 2019).

Geoscience Australia (2014) *Interferometric Synthetic Aperture Radar*. Available at: <http://www.ga.gov.au/scientific-topics/positioning-navigation/geodesy/geodetic-techniques/interferometric-synthetic-aperture-radar> (Accessed: December 19, 2019).

Ghorbanzadeh, O., Feizizadeh, B. and Blaschke, T. (2018) “An interval matrix method used to optimize the decision matrix in AHP technique for land subsidence susceptibility mapping,” *Environmental Earth Sciences*. Springer Berlin Heidelberg, 77(16), p. 584. doi: 10.1007/s12665-018-7758-y.

- Godio, A. and Bottino, G. (2001) “Electrical and electromagnetic investigation for landslide characterisation,” *Physics and Chemistry of the Earth, Part C: Solar, Terrestrial & Planetary Science*, 26(9), pp. 705–710. doi: 10.1016/S1464-1917(01)00070-8.
- Grit, M. and Kanli, A. I. (2016) “Integrated Seismic Survey for Detecting Landslide Effects on High Speed Rail Line at Istanbul–Turkey,” *Open Geosciences*, 8(1), pp. 161–173. doi: 10.1515/geo-2016-0017.
- Gu, G. and Wang, W. (2013) “Advantages of GNSS in Monitoring Crustal Deformation for Detection of Precursors to Strong Earthquakes,” *Positioning*, 04(01), pp. 11–19. doi: 10.4236/pos.2013.41003.
- Gualandi, A., Perfettini, H., Radiguet, M., Cotte, N. and Kostoglodov, V. (2017) “GPS deformation related to the M<sub>w</sub> 7.3, 2014, Papanao earthquake (Mexico) reveals the aseismic behavior of the Guerrero seismic gap,” *Geophysical Research Letters*, 44(12), pp. 6039–6047. doi: 10.1002/2017GL072913.
- Guzzetti, F., Carrara, A., Cardinali, M. and Reichenbach, P. (1999) “Landslide hazard evaluation: a review of current techniques and their application in a multi-scale study, Central Italy,” *Geomorphology*, 31(1–4), pp. 181–216. doi: 10.1016/S0169-555X(99)00078-1.
- Guzzetti, F., Gariano, S. L., Peruccacci, S., Brunetti, M. T., Marchesini, I., Rossi, M. and Melillo, M. (2020) “Geographical landslide early warning systems,” *Earth-Science Reviews*. Elsevier, 200(October 2019), p. 102973. doi: 10.1016/j.earscirev.2019.102973.
- Hadjimitsis, D. G. (2010) “Brief communication ‘Determination of urban growth in catchment areas in Cyprus using multi-temporal remotely sensed data: risk assessment study,’” *Natural Hazards and Earth System Sciences*, 10(11), pp. 2235–2240. doi: 10.5194/nhess-10-2235-2010.
- Hadjimitsis, D. G., Agapiou, A., Themistocleous, K., Alexakis, D. D. and Sarris, A. (2013) “Remote Sensing for Archaeological Applications: Management, Documentation and Monitoring,” in *Remote Sensing of Environment - Integrated Approaches*. InTech, pp. 57–96. doi: 10.5772/39306.
- Hadjimitsis, D. G., Clayton, C. R. I. and Hope, V. S. (2004) “An assessment of the effectiveness of atmospheric correction algorithms through the remote sensing of some

reservoirs,” *International Journal of Remote Sensing*, 25(18), pp. 3651–3674. doi: 10.1080/01431160310001647993.

Haidara, I., Tahri, M., Maanan, M. and Hakdaoui, M. (2019) “Efficiency of Fuzzy Analytic Hierarchy Process to detect soil erosion vulnerability,” *Geoderma*. Elsevier, 354(September 2018), p. 113853. doi: 10.1016/j.geoderma.2019.07.011.

Hart, A. B. and Hearn, G. J. (2010) *Paphos Landslide Study*. Nicosia, Cyprus.

Hart, A. B. and Hearn, G. J. (2013) “Landslide assessment for land use planning and infrastructure management in the Paphos District of Cyprus,” *Bulletin of Engineering Geology and the Environment*, 72(2), pp. 173–188. doi: 10.1007/s10064-013-0463-x.

Hart, A. B., Ruse, M. E., Hobbs, P. R. N., Efthymiou, M. and Hadjicharalambous, K. (2010) “Assessment of Landslide Susceptibility in Paphos District, Cyprus,” in *GRSG-AGM Geoenvironmental Remote Sensing Conference*. London: The Geological Society of London.

Hearn, G. J. and Hart, A. B. (2019) “Landslide susceptibility mapping: a practitioner’s view,” *Bulletin of Engineering Geology and the Environment*. *Bulletin of Engineering Geology and the Environment*, 78(8), pp. 5811–5826. doi: 10.1007/s10064-019-01506-1.

Hearn, G. J., Larkin, H., Hadjicharalambous, K., Papageorgiou, A. and Zoi, G. E. (2018) “Proving a landslide: ground behaviour problems at Pissouri, Cyprus,” *Quarterly Journal of Engineering Geology and Hydrogeology*, 51(4), pp. 461–482. doi: 10.1144/qjegh2017-134.

Hill, C. D. and Sippel, K. D. (2002) “Modern Deformation Monitoring: A Multi Sensor Approach,” in *FIG XXII International Congress*. Washington, D.C., pp. 1–12.

Hirschmugl, M., Deutscher, J., Sobe, C., Bouvet, A., Mermoz, S. and Schardt, M. (2020) “Use of SAR and Optical Time Series for Tropical Forest Disturbance Mapping,” *Remote Sensing*, 12(4), p. 727. doi: 10.3390/RS12040727.

Höser, T. (2018) *Analysing the Capabilities and Limitations of InSAR using Sentinel-1 data for Landslide Detection and Monitoring*. University of Bonn. doi: 10.13140/RG.2.2.35085.59362.

Hsieh, C. S., Shih, T. Y., Hu, J. C., Tung, H., Huang, M. H. and Angelier, J. (2011) “Using

differential SAR interferometry to map land subsidence: A case study in the Pingtung Plain of SW Taiwan,” *Natural Hazards*, 58(3), pp. 1311–1332. doi: 10.1007/s11069-011-9734-7.

Intrieri, E., Gigli, G., Casagli, N. and Nadim, F. (2013) “Brief communication &quot;Landslide Early Warning System: toolbox and general concepts&quot;,” *Natural Hazards and Earth System Sciences*, 13(1), pp. 85–90. doi: 10.5194/nhess-13-85-2013.

Jenelius, E. and Mattsson, L. G. (2012) “Road network vulnerability analysis of area-covering disruptions: A grid-based approach with case study,” *Transportation Research Part A: Policy and Practice*. Elsevier Ltd, 46(5), pp. 746–760. doi: 10.1016/j.tra.2012.02.003.

Jenelius, E., Petersen, T. and Mattsson, L. G. (2006) “Importance and exposure in road network vulnerability analysis,” *Transportation Research Part A: Policy and Practice*, 40(7), pp. 537–560. doi: 10.1016/j.tra.2005.11.003.

Jenks, G. F. (1967) “The Data Model Concept in Statistical Mapping,” *International Yearbook of Cartography*, 7, pp. 186–190.

Jo, M. J., Jung, H. S. and Yun, S. H. (2017) “Retrieving Precise Three-Dimensional Deformation on the 2014 M6.0 South Napa Earthquake by Joint Inversion of Multi-Sensor SAR,” *Scientific Reports*. Springer US, 7(1), pp. 1–10. doi: 10.1038/s41598-017-06018-0.

Jongmans, D. and Garambois, S. (2007) “Geophysical investigation of landslides: a review,” *Bulletin de la Societe Geologique de France*, 178(2), pp. 101–112. doi: 10.2113/gssgfbull.178.2.101.

Jung, J. and Yun, S.-H. (2020) “Evaluation of Coherent and Incoherent Landslide Detection Methods Based on Synthetic Aperture Radar for Rapid Response: A Case Study for the 2018 Hokkaido Landslides,” *Remote Sensing*, 12(2), p. 265. doi: 10.3390/rs12020265.

Kalogeras, I., Stavrakakis, G. and Solomi, K. (1999) “The October 9, 1996 earthquake in Cyprus: seismological, macroseismic and strong motion data,” *Annals of Geophysics*, 42(1). doi: 10.4401/ag-3702.



- Kaur, L., Rishi, M. S., Singh, G. and Nath Thakur, S. (2020) “Groundwater potential assessment of an alluvial aquifer in Yamuna sub-basin (Panipat region) using remote sensing and GIS techniques in conjunction with analytical hierarchy process (AHP) and catastrophe theory (CT),” *Ecological Indicators*. Elsevier, 110, p. 105850. doi: 10.1016/j.ecolind.2019.105850.
- Kayastha, P., Dhital, M. R. and De Smedt, F. (2013) “Application of the analytical hierarchy process (AHP) for landslide susceptibility mapping: A case study from the Tinau watershed, west Nepal,” *Computers & Geosciences*. Elsevier, 52, pp. 398–408. doi: 10.1016/j.cageo.2012.11.003.
- Kearey, P., Brooks, M. and Hill, I. (2002) *An Introduction to Geophysical Exploration*. 3rd ed. Oxford: Wiley-Blackwell. Available at: <https://www.wiley.com/ency/An+Introduction+to+Geophysical+Exploration%2C+3rd+Edition-p-9781118698938>.
- Khatri, U., Kumar, V., Bandyopadhyay, D., Musthafa, M. and Singh, G. (2018) “Identification of forest cutting in managed forest of Haldwani, India using ALOS-2/PALSAR-2 SAR data,” *Journal of Environmental Management*. Elsevier Ltd, 213, pp. 503–512. doi: 10.1016/j.jenvman.2018.02.025.
- Klees, R. and Massonnet, D. (1998) “Deformation measurements using SAR interferometry: potential and limitations,” *Geologie en Mijnbouw*, 77, pp. 161–176. doi: 10.1023/A:1003594502801.
- Kouli, M., Loupasakis, C., Soupios, P., Rozos, D. and Vallianatos, F. (2013) “Comparing multi-criteria methods for landslide susceptibility mapping in Chania Prefecture, Crete Island, Greece,” *Natural Hazards and Earth System Sciences Discussions*, 1(1), pp. 73–109. doi: 10.5194/nhessd-1-73-2013.
- Kouli, M., Loupasakis, C., Soupios, P. and Vallianatos, F. (2010) “Landslide hazard zonation in high risk areas of Rethymno Prefecture, Crete Island, Greece,” *Natural Hazards*, 52(3), pp. 599–621. doi: 10.1007/s11069-009-9403-2.
- Kovács, I. P., Bugya, T., Czigány, S., Defilippi, M., Lóczy, D., Riccardi, P., Ronczyk, L. and Pasquali, P. (2019) “How to avoid false interpretations of Sentinel-1A TOPSAR interferometric data in landslide mapping? A case study: recent landslides in Transdanubia, Hungary,” *Natural Hazards*. Springer Netherlands, 96(2), pp. 693–712.

doi: 10.1007/s11069-018-3564-9.

Kyriou, A. and Nikolakopoulos, K. (2018) “Assessing the suitability of Sentinel-1 data for landslide mapping,” *European Journal of Remote Sensing*. Taylor & Francis, 51(1), pp. 402–411. doi: 10.1080/22797254.2018.1444944.

Lasaponara, R. and Masini, N. (2011) “Satellite remote sensing in archaeology: past, present and future perspectives,” *Journal of Archaeological Science*, 38(9), pp. 1995–2002. doi: 10.1016/j.jas.2011.02.002.

Lasaponara, R. and Masini, N. (eds.) (2012) *Satellite Remote Sensing: A New Tool for Archaeology*. 1st ed. Springer Netherlands (Remote Sensing and Digital Image Processing). doi: 10.1007/978-90-481-8801-7.

Lee, S. (2005) “Application of logistic regression model and its validation for landslide susceptibility mapping using GIS and remote sensing data,” *International Journal of Remote Sensing*, 26(7), pp. 1477–1491. doi: 10.1080/01431160412331331012.

Lee, S. and Lee, M.-J. (2006) “Detecting landslide location using KOMPSAT 1 and its application to landslide-susceptibility mapping at the Gangneung area, Korea,” *Advances in Space Research*, 38(10), pp. 2261–2271. doi: 10.1016/j.asr.2006.03.036.

Li, Z. and Bethel, J. (2008) “Image coregistration in SAR interferometry,” *The International Archives of the Photogrammetry, Remote Sensing and Spatial Information Sciences*, 37, pp. 433–438. Available at: [http://www.isprs.org/proceedings/XXXVII/congress/1\\_pdf/72.pdf](http://www.isprs.org/proceedings/XXXVII/congress/1_pdf/72.pdf).

Lin-lin, G., Cheng, E., Polonska, D., Rizos, C., Collins, C. and Smith, C. (2003) “Earthquake monitoring in australia using satellite radar interferometry,” *Wuhan University Journal of Natural Sciences*, 8(2), pp. 649–658. doi: 10.1007/BF02899830.

Da Lio, C. and Tosi, L. (2018) “Land subsidence in the Friuli Venezia Giulia coastal plain, Italy: 1992–2010 results from SAR-based interferometry,” *Science of The Total Environment*. Elsevier B.V., 633, pp. 752–764. doi: 10.1016/j.scitotenv.2018.03.244.

Liosis, N., Marpu, P. R., Pavlopoulos, K. and Ouarda, T. B. M. J. (2018) “Ground subsidence monitoring with SAR interferometry techniques in the rural area of Al Wagan, UAE,” *Remote Sensing of Environment*. Elsevier, 216(July), pp. 276–288. doi: 10.1016/j.rse.2018.07.001.

- Liu, C., Chen, Z., Shao, Y., Chen, J., Hasi, T. and Pan, H. (2019) “Research advances of SAR remote sensing for agriculture applications: A review,” *Journal of Integrative Agriculture*. CAAS. Publishing services by Elsevier B.V, 18(3), pp. 506–525. doi: 10.1016/S2095-3119(18)62016-7.
- Liu, S. and Wang, Z. (2008) “Choice of surveying methods for landslides monitoring,” in *Landslides and Engineered Slopes. From the Past to the Future*. CRC Press, pp. 1211–1216. doi: 10.1201/9780203885284-c160.
- Lu, C.-H., Ni, C.-F., Chang, C.-P., Yen, J.-Y. and Chuang, R. (2018) “Coherence Difference Analysis of Sentinel-1 SAR Interferogram to Identify Earthquake-Induced Disasters in Urban Areas,” *Remote Sensing*, 10(8), p. 1318. doi: 10.3390/rs10081318.
- Lu, D., Mausel, P., Brondizio, E. and Moran, E. (2002) “Assessment of atmospheric correction methods for Landsat TM data applicable to Amazon basin LBA research,” *International Journal of Remote Sensing*, 23(13), pp. 2651–2671. doi: 10.1080/01431160110109642.
- Lu, Z. (2005) “Comparison of GPS and InSAR deformation measurements at Okmok volcano, Alaska,” *Alaska Satellite Facility News & Notes*. Alaska Satellite Facility, pp. 1–4. Available at: [https://www.asf.alaska.edu/wp-content/uploads/2019/03/asfnn\\_2-3.pdf](https://www.asf.alaska.edu/wp-content/uploads/2019/03/asfnn_2-3.pdf).
- Lyu, H.-M., Shen, S.-L., Zhou, A. and Yang, J. (2019) “Risk assessment of mega-city infrastructures related to land subsidence using improved trapezoidal FAHP,” *Science of The Total Environment*. Elsevier B.V., p. 135310. doi: 10.1016/j.scitotenv.2019.135310.
- Manconi, A. (2019) “Technical Note: Limitations on the use of space borne differential SAR interferometry for systematic monitoring and failure forecast of alpine landslides,” *EarthArXiv*, pp. 1–20. doi: <https://doi.org/10.31223/osf.io/3nmqj>.
- Manconi, A. and Giordan, D. (2016) “Landslide failure forecast in near-real-time,” *Geomatics, Natural Hazards and Risk*. Taylor & Francis, 7(2), pp. 639–648. doi: 10.1080/19475705.2014.942388.
- Manconi, A., Kourkouli, P., Caduff, R., Strozzi, T. and Loew, S. (2018) “Monitoring surface deformation over a failing rock slope with the ESA sentinels: Insights from Moosfluh instability, Swiss Alps,” *Remote Sensing*, 10(5). doi: 10.3390/rs10050672.

Mandal, B. and Mandal, S. (2018) “Analytical hierarchy process (AHP) based landslide susceptibility mapping of Lish river basin of eastern Darjeeling Himalaya, India,” *Advances in Space Research*. COSPAR, 62(11), pp. 3114–3132. doi: 10.1016/j.asr.2018.08.008.

Di Martire, D., Tessitore, S., Brancato, D., Ciminelli, M. G., Costabile, S., Costantini, M., *et al.* (2016) “Landslide detection integrated system (LaDIS) based on in-situ and satellite SAR interferometry measurements,” *CATENA*. Elsevier B.V., 137, pp. 406–421. doi: 10.1016/j.catena.2015.10.002.

Mathew, J., Majumdar, R. and Kumar, K. V. (2015) “SAR interferometry and optical remote sensing for analysis of co-seismic deformation, source characteristics and mass wasting pattern of Lushan (China, April 2013) earthquake,” *International Journal of Applied Earth Observation and Geoinformation*. Elsevier B.V., 35(PB), pp. 338–349. doi: 10.1016/j.jag.2014.10.005.

Mercier, J., Vergely, P. and Delibassis, N. (1973) “Comparison between deformation deduced from the analysis of recent faults and from focal mechanisms of earthquakes (an example: the Paphos region, Cyprus).,” *Tectonophysics*, 19, pp. 315–332. doi: 10.1016/0040-1951(73)90026-7.

Meric, O., Garambois, S., Jongmans, D., Wathelet, M., Chatelain, J. L. and Vengeon, J. M. (2005) “Application of geophysical methods for the investigation of the large gravitational mass movement of Séchilienne, France,” *Canadian Geotechnical Journal*, 42(4), pp. 1105–1115. doi: 10.1139/t05-034.

Méric, O., Garambois, S., Malet, J., Cadet, H., Guéguen, P. and Jongmans, D. (2007) “Seismic noise-based methods for soft-rock landslide characterization,” *Bulletin de la Societe Geologique de France*, 178(2), pp. 137–148. doi: 10.2113/gssgfbull.178.2.137.

Meyer, F. J., McAlpin, D. B., Gong, W., Ajadi, O. A., Arko, S., Webley, P. W. and Dehn, J. (2015) “Integrating SAR and derived products into operational volcano monitoring and decision support systems,” *ISPRS Journal of Photogrammetry and Remote Sensing*. International Society for Photogrammetry and Remote Sensing, Inc. (ISPRS), 100, pp. 106–117. doi: 10.1016/j.isprsjprs.2014.05.009.

Ministry of Foreign Affairs (no date) *Destruction of Cultural Heritage*. Available at: [http://www.mfa.gov.cy/mfa/mfa2016.nsf/mfa16\\_en/mfa16\\_en?OpenDocument](http://www.mfa.gov.cy/mfa/mfa2016.nsf/mfa16_en/mfa16_en?OpenDocument)

(Accessed: December 5, 2019).

Montgomery, D. R., Schmidt, K. M., Greenberg, H. M. and Dietrich, W. E. (2000) “Forest clearing and regional landsliding,” *Geology*, 28(4), p. 311. doi: 10.1130/0091-7613(2000)28<311:FCARL>2.0.CO;2.

Monti-Guarnieri, A. V., Brovelli, M. A., Manzoni, M., Mariotti d’Alessandro, M., Molinari, M. E. and Oxoli, D. (2018) “Coherent Change Detection for Multipass SAR,” *IEEE Transactions on Geoscience and Remote Sensing*. IEEE, 56(11), pp. 6811–6822. doi: 10.1109/TGRS.2018.2843560.

Moretto, S., Bozzano, F., Esposito, C., Mazzanti, P. and Rocca, A. (2017) “Assessment of Landslide Pre-Failure Monitoring and Forecasting Using Satellite SAR Interferometry,” *Geosciences*, 7(2), p. 36. doi: 10.3390/geosciences7020036.

Morishita, Y., Lazecky, M., Wright, T. J., Weiss, J. R., Elliott, J. R. and Hooper, A. (2020) “LiCSBAS: An Open-Source InSAR Time Series Analysis Package Integrated with the LiCSAR Automated Sentinel-1 InSAR Processor,” *Remote Sensing*, 12(3), p. 424. doi: 10.3390/rs12030424.

Le Mouélic, S., Raucoules, D., Carnec, C. and King, C. (2005) “A Least Squares Adjustment of Multi-temporal InSAR Data: Application to the ground deformation of Paris,” *Photogrammetric Engineering & Remote Sensing*, 71(2), pp. 197–204. doi: 10.14358/PERS.71.2.197.

Mullissa, A. G., Tolpekin, V., Stein, A. and Perissin, D. (2017) “Polarimetric differential SAR interferometry in an arid natural environment,” *International Journal of Applied Earth Observation and Geoinformation*. Elsevier B.V., 59, pp. 9–18. doi: 10.1016/j.jag.2017.02.019.

Murray-Moraleda, J. (2011) “GPS: Applications in Crustal Deformation Monitoring,” in *Extreme Environmental Events*. New York: Springer New York, pp. 589–622. doi: 10.1007/978-1-4419-7695-6\_33.

Nanometrics (2015) *Mission Critical Seismic Network CQ Net : Republic of Cyprus*.

NASA (no date) *Advanced Rapid Imaging and Analysis (ARIA) Project for Natural Hazards*. Available at: <https://aria.jpl.nasa.gov/> (Accessed: March 6, 2020).

Ni, J.-R., Li, X.-X. and Borthwick, A. G. L. (2008) “Soil erosion assessment based on

minimum polygons in the Yellow River basin, China,” *Geomorphology*, 93(3–4), pp. 233–252. doi: 10.1016/j.geomorph.2007.02.015.

Nicu, I. C. (2016) “Cultural heritage assessment and vulnerability using Analytic Hierarchy Process and Geographic Information Systems (Valea Oii catchment, North-eastern Romania). An approach to historical maps,” *International Journal of Disaster Risk Reduction*, 20(October), pp. 103–111. doi: 10.1016/j.ijdr.2016.10.015.

Northmore, K. J., Charalambous, M., Hobbs, P. R. N. and Petrides, G. (1986) *Engineering geology of the Kannaviou, 'Melange' and Mamonia Complex formations - Phiti / Statos area, S W Cyprus: engineering geology of cohesive soils associated with ophiolites, with particular reference to Cyprus*. Nottinghamshire, Nicosia. Available at: <http://nora.nerc.ac.uk/id/eprint/19494/>.

Northmore, K. J., Charalambous, M., Hobbs, P. R. N. and Petrides, G. (1988) “Complex landslides in the Kannaviou, Melange, and Mamonia formations of south-west Cyprus,” in Bonnard, C. (ed.) *5th International Symposium on Landslides*. Lausanne, pp. 263–268.

Oikonomidis, D., Dimogianni, S., Kazakis, N. and Voudouris, K. (2015) “A GIS/Remote Sensing-based methodology for groundwater potentiality assessment in Tirnavos area, Greece,” *Journal of Hydrology*. Elsevier B.V., 525, pp. 197–208. doi: 10.1016/j.jhydrol.2015.03.056.

Ouchi, K. (2013) “Recent Trend and Advance of Synthetic Aperture Radar with Selected Topics,” *Remote Sensing*, 5(2), pp. 716–807. doi: 10.3390/rs5020716.

Pan, Z., Hu, Y. and Wang, G. (2019) “Detection of short-term urban land use changes by combining SAR time series images and spectral angle mapping,” *Frontiers of Earth Science*, 13(3), pp. 495–509. doi: 10.1007/s11707-018-0744-6.

Pantazis, T. M. (1969) “Landslides in Cyprus,” pp. 1–20.

Paphos Life (no date) *The deadly earthquake of Paphos in 1953 - Rare pictures and video - Paphos Life*. Available at: <https://www.paphoslife.com/forum/viewtopic.php?t=6936> (Accessed: December 10, 2019).

Parcak, S. H. (2009) *Satellite Remote Sensing for Archaeology*. 1st ed. London and New York: Routledge, Taylor and Francis Group. doi: 10.4324/9780203881460.

Parihar, N., Das, A., Rathore, V. S., Nathawat, M. S. and Mohan, S. (2014) “Analysis of

- L-band SAR backscatter and coherence for delineation of land-use/land-cover,” *International Journal of Remote Sensing*, 35(18), pp. 6781–6798. doi: 10.1080/01431161.2014.965282.
- Park, N. -W. and Chi, K. -H. (2008) “Quantitative assessment of landslide susceptibility using high-resolution remote sensing data and a generalized additive model,” *International Journal of Remote Sensing*, 29(1), pp. 247–264. doi: 10.1080/01431160701227661.
- Parker, A. L., Featherstone, W. E., Penna, N. T., Filmer, M. S. and Garthwaite, M. C. (2017) “Practical Considerations before Installing Ground-Based Geodetic Infrastructure for Integrated InSAR and cGNSS Monitoring of Vertical Land Motion,” *Sensors*, 17(8), p. 1753. doi: 10.3390/s17081753.
- Pasierb, B., Grodecki, M. and Gwóźdź, R. (2019) “Geophysical and geotechnical approach to a landslide stability assessment: a case study,” *Acta Geophysica*. Springer International Publishing, 67(6), pp. 1823–1834. doi: 10.1007/s11600-019-00338-7.
- Patuelli, R., Reggiani, A., Gorman, S. P., Nijkamp, P. and Bade, F.-J. (2007) “Network Analysis of Commuting Flows: A Comparative Static Approach to German Data,” *Networks and Spatial Economics*, 7(4), pp. 315–331. doi: 10.1007/s11067-007-9027-6.
- Pavez, A., Remy, D., Bonvalot, S., Diament, M., Gabalda, G., Froger, J.-L., Julien, P., Legrand, D. and Moisset, D. (2006) “Insight into ground deformations at Lascar volcano (Chile) from SAR interferometry, photogrammetry and GPS data: Implications on volcano dynamics and future space monitoring,” *Remote Sensing of Environment*, 100(3), pp. 307–320. doi: 10.1016/j.rse.2005.10.013.
- Pazzi, V., Morelli, S. and Fanti, R. (2019) “A Review of the Advantages and Limitations of Geophysical Investigations in Landslide Studies,” *International Journal of Geophysics*, pp. 1–27. doi: 10.1155/2019/2983087.
- Peel, M. C., Finlayson, B. L. and McMahon, T. A. (2007) “Updated world map of the Köppen-Geiger climate classification,” *Hydrology and Earth System Sciences*, 11(5), pp. 1633–1644. doi: 10.5194/hess-11-1633-2007.
- Pieraccini, M., Mecatti, D., Noferini, L., Luzi, G., Franchioni, G. and Atzeni, C. (2002) “SAR interferometry for detecting the effects of earthquakes on buildings,” *NDT & E*

*International*, 35(8), pp. 615–625. doi: 10.1016/S0963-8695(02)00047-6.

Pilz, M., Parolai, S., Bindi, D., Saponaro, A. and Abdybachaev, U. (2014) “Combining Seismic Noise Techniques for Landslide Characterization,” *Pure and Applied Geophysics*, 171(8), pp. 1729–1745. doi: 10.1007/s00024-013-0733-3.

Plank, S., Twele, A. and Martinis, S. (2016) “Landslide Mapping in Vegetated Areas Using Change Detection Based on Optical and Polarimetric SAR Data,” *Remote Sensing*, 8(4), p. 307. doi: 10.3390/rs8040307.

Polcari, M., Albano, M., Saroli, M., Tolomei, C., Lancia, M., Moro, M. and Stramondo, S. (2014) “Subsidence Detected by Multi-Pass Differential SAR Interferometry in the Cassino Plain (Central Italy): Joint Effect of Geological and Anthropogenic Factors?,” *Remote Sensing*, 6(10), pp. 9676–9690. doi: 10.3390/rs6109676.

Pourghasemi, H. R., Pradhan, B. and Gokceoglu, C. (2012) “Application of fuzzy logic and analytical hierarchy process (AHP) to landslide susceptibility mapping at Haraz watershed, Iran,” *Natural Hazards*, 63(2), pp. 965–996. doi: 10.1007/s11069-012-0217-2.

Pradhan, B. (2010) “Remote sensing and GIS-based landslide hazard analysis and cross-validation using multivariate logistic regression model on three test areas in Malaysia,” *Advances in Space Research*. COSPAR, 45(10), pp. 1244–1256. doi: 10.1016/j.asr.2010.01.006.

Pritchard, M. E. and Simons, M. (2002) “A satellite geodetic survey of large-scale deformation of volcanic centres in the central Andes,” *Nature*, 418(6894), pp. 167–171. doi: 10.1038/nature00872.

Quinn, B., Schiel, K. and Caruso, G. (2015) “Mapping uncertainty from multi-criteria analysis of land development suitability, the case of Howth, Dublin,” *Journal of Maps*. Taylor & Francis, 11(3), pp. 487–495. doi: 10.1080/17445647.2014.978907.

Rabus, B. and Pichierri, M. (2018) “A new InSAR phase demodulation technique developed for a typical example of a complex, multi-lobed landslide displacement field, Fels Glacier Slide, Alaska,” *Remote Sensing*, 10(7). doi: 10.3390/rs10070995.

Raucoules, D., Bourguin, B., de Michele, M., Le Cozannet, G., Closset, L., Bremmer, C., *et al.* (2009) “Validation and intercomparison of Persistent Scatterers Interferometry:



PSIC4 project results,” *Journal of Applied Geophysics*. Elsevier B.V., 68(3), pp. 335–347. doi: 10.1016/j.jappgeo.2009.02.003.

Reid, M. E., LaHusen, R. G., Baum, R. L., Kean, J. W., Schulz, W. H. and Highland, L. M. (2012) “Real-Time Monitoring of Landslides,” *U.S. Geological Survey*. Denver, USA: U.S. Geological Survey. Available at: <https://pubs.usgs.gov/fs/2012/3008/contents/FS12-3008.pdf>.

Research & Development Center-Intercollege, U. of E. S. (2004a) *Cyprus Geological Heritage educational tool-Geotechnical hazards*. Available at: [http://www.cyprusgeology.org/english/7\\_2\\_hazards.htm](http://www.cyprusgeology.org/english/7_2_hazards.htm) (Accessed: December 6, 2019).

Research & Development Center-Intercollege, U. of E. S. (2004b) *Cyprus Geological Heritage educational tool-The Geological Structure of Cyprus*. Available at: [http://www.cyprusgeology.org/english/2\\_2\\_geology.htm](http://www.cyprusgeology.org/english/2_2_geology.htm) (Accessed: December 6, 2019).

Reynolds, J. M. (2011) *An Introduction to Applied and Environmental Geophysics*. 2nd ed. Oxford: Wiley-Blackwell. Available at: <https://www.wiley.com/ency/An+Introduction+to+Applied+and+Environmental+Geophysics%2C+2nd+Edition-p-9780470975442>.

Richards, J. A. (2009) *Remote Sensing with Imaging Radar*. 1st ed. Berlin, Heidelberg: Springer Berlin Heidelberg (Signals and Communication Technology). doi: 10.1007/978-3-642-02020-9.

Rocca, F., Prati, C., Guarnieri, A. M. and Ferretti, A. (2000) “Sar interferometry and its applications,” *Surveys in Geophysics*, 21(2–3), pp. 159–176. doi: 10.1023/A:1006710731155.

Rodrigue, J. P., Comtois, C. and Slack, B. (2006) *The geography of transport systems*. 2nd ed, *The Geography of Transport Systems*. 2nd ed. London and New York: Routledge Taylor & Francis. doi: 10.4324/9781315618159.

Rosen, P. A., Hensley, S., Joughin, I. R., Li, F. K., Madsen, S. N., Rodriguez, E. and Goldstein, R. M. (2000) “Synthetic aperture radar interferometry,” *Proceedings of the IEEE*, 88(3), pp. 333–382. doi: 10.1109/5.838084.

Rossi, M. and Reichenbach, P. (2016) “LAND-SE: A software for statistically based landslide susceptibility zonation, version 1.0,” *Geoscientific Model Development*, 9(10),

pp. 3533–3543. doi: 10.5194/gmd-9-3533-2016.

Saaty, R. W. (1987) “The analytic hierarchy process—what it is and how it is used,” *Mathematical Modelling*, 9(3–5), pp. 161–176. doi: 10.1016/0270-0255(87)90473-8.

Saaty, T. L. (1980) *The Analytic Hierarchy Process*. New York: McGraw-Hill International.

Saaty, T. L. (2008) “Decision making with the analytic hierarchy process,” *International Journal of Services Sciences*, 1(1), p. 83. doi: 10.1504/IJSSCI.2008.017590.

Saha, A. K., Gupta, R. P. and Arora, M. K. (2002) “GIS-based Landslide Hazard Zonation in the Bhagirathi (Ganga) Valley, Himalayas,” *International Journal of Remote Sensing*, 23(2), pp. 357–369. doi: 10.1080/01431160010014260.

Saha, A. K., Gupta, R. P., Sarkar, I., Arora, M. K. and Csaplovics, E. (2005) “An approach for GIS-based statistical landslide susceptibility zonation—with a case study in the Himalayas,” *Landslides*, 2(1), pp. 61–69. doi: 10.1007/s10346-004-0039-8.

Saha, S., Gayen, A., Pourghasemi, H. R. and Tiefenbacher, J. P. (2019) “Identification of soil erosion-susceptible areas using fuzzy logic and analytical hierarchy process modeling in an agricultural watershed of Burdwan district, India,” *Environmental Earth Sciences*. Springer Berlin Heidelberg, 78(23), p. 649. doi: 10.1007/s12665-019-8658-5.

Savvaidis, P. D. (2003) “Existing landslide monitoring systems and techniques,” in *From Stars to Earth and Culture*, pp. 242–258. Available at: [http://der.topo.auth.gr/tsioumis/Tsioumis CD/StarsToEarth/26\\_Savvaidis.pdf](http://der.topo.auth.gr/tsioumis/Tsioumis CD/StarsToEarth/26_Savvaidis.pdf).

Schaefer, L. N., Di Traglia, F., Chaussard, E., Lu, Z., Nolesini, T. and Casagli, N. (2019) “Monitoring volcano slope instability with Synthetic Aperture Radar: A review and new data from Pacaya (Guatemala) and Stromboli (Italy) volcanoes,” *Earth-Science Reviews*. Elsevier, 192, pp. 236–257. doi: 10.1016/j.earscirev.2019.03.009.

Sentinel Hub (no date) *NDVI (Normalized Difference Vegetation Index) | Sentinel Hub, Sentinel 2 EO products*. Available at: <https://www.sentinel-hub.com/eoproducts/ndvi-normalized-difference-vegetation-index> (Accessed: March 9, 2020).

Sorensen, J. H. (2000) “Hazard Warning Systems: Review of 20 Years of Progress,” *Natural Hazards Review*, 1(2), pp. 119–125. doi: 10.1061/(ASCE)1527-6988(2000)1:2(119).

Stanford Radar Interferometry Research Group (1995) *SNAPHU: statistical-cost, network-flow algorithm for phase unwrapping*. Available at: <https://web.stanford.edu/group/radar/softwareandlinks/sw/snaphu/> (Accessed: July 17, 2019).

Stewart, C., Lasaponara, R. and Schiavon, G. (2014) “Multi-frequency, polarimetric SAR analysis for archaeological prospection,” *International Journal of Applied Earth Observation and Geoinformation*. Elsevier B.V., 28(1), pp. 211–219. doi: 10.1016/j.jag.2013.11.007.

Stow, D. A. V., Braakenburg, N. E. and Xenophontos, C. (1995) “The Pissouri Basin fan-delta complex, southwestern Cyprus,” *Sedimentary Geology*, 98(1–4), pp. 245–262. doi: 10.1016/0037-0738(95)00035-7.

Strozzi, T., Klimeš, J., Frey, H., Caduff, R., Huggel, C., Wegmüller, U. and Rapre, A. C. (2018) “Satellite SAR interferometry for the improved assessment of the state of activity of landslides: A case study from the Cordilleras of Peru,” *Remote Sensing of Environment*, 217, pp. 111–125. doi: 10.1016/j.rse.2018.08.014.

Suga, Y. and Takeuchi, S. (2000) “Application of JERS-1 InSAR for monitoring deforestation of tropical rain forest,” *International Geoscience and Remote Sensing Symposium (IGARSS)*, 1, pp. 432–434. doi: 10.1109/igarss.2000.860555.

Tamm, T., Zalite, K., Voormansik, K. and Talgre, L. (2016) “Relating Sentinel-1 interferometric coherence to mowing events on grasslands,” *Remote Sensing*, 8(10), pp. 1–19. doi: 10.3390/rs8100802.

Tapete, D., Casagli, N., Luzi, G., Fanti, R., Gigli, G. and Leva, D. (2013) “Integrating radar and laser-based remote sensing techniques for monitoring structural deformation of archaeological monuments,” *Journal of Archaeological Science*. Elsevier Ltd, 40(1), pp. 176–189. doi: 10.1016/j.jas.2012.07.024.

Tapete, D. and Cigna, F. (2017a) “InSAR data for geohazard assessment in UNESCO World Heritage sites: state-of-the-art and perspectives in the Copernicus era,” *International Journal of Applied Earth Observation and Geoinformation*. Elsevier, 63, pp. 24–32. doi: 10.1016/j.jag.2017.07.007.

Tapete, D. and Cigna, F. (2017b) “Trends and perspectives of space-borne SAR remote

sensing for archaeological landscape and cultural heritage applications,” *Journal of Archaeological Science: Reports*. The Authors, 14, pp. 716–726. doi: 10.1016/j.jasrep.2016.07.017.

Tapete, D., Fanti, R., Cecchi, R., Petrangeli, P. and Casagli, N. (2012) “Satellite radar interferometry for monitoring and early-stage warning of structural instability in archaeological sites,” *Journal of Geophysics and Engineering*, 9(4), pp. S10–S25. doi: 10.1088/1742-2132/9/4/S10.

Tarchi, D., Casagli, N., Fanti, R., Leva, D. D., Luzi, G., Pasuto, A., Pieraccini, M. and Silvano, S. (2003) “Landslide monitoring by using ground-based SAR interferometry: An example of application to the Tessina landslide in Italy,” *Engineering Geology*, 68(1–2), pp. 15–30. doi: 10.1016/S0013-7952(02)00196-5.

Teshebaeva, K., Roessner, S., Echtler, H., Motagh, M., Wetzel, H.-U. and Molodbekov, B. (2015) “ALOS/PALSAR InSAR Time-Series Analysis for Detecting Very Slow-Moving Landslides in Southern Kyrgyzstan,” *Remote Sensing*, 7(7), pp. 8973–8994. doi: 10.3390/rs70708973.

Themistocleous, K., Cuca, B., Agapiou, A., Lysandrou, V., Tzouvaras, M., Hadjimitsis, D. G., *et al.* (2016) “The protection of cultural heritage sites from geo-hazards: The PROTHEGO project,” in *EUROMED 2016*, pp. 91–98. doi: 10.1007/978-3-319-48974-2\_11.

Thompson, R. A. and Schilling, S. P. (2007) “Photogrammetry,” in *Volcano Deformation*. Berlin, Heidelberg: Springer Berlin Heidelberg, pp. 195–221. doi: 10.1007/978-3-540-49302-0\_6.

Tofani, V., Segoni, S., Agostini, A., Catani, F. and Casagli, N. (2013) “Technical Note: Use of remote sensing for landslide studies in Europe,” *Natural Hazards and Earth System Sciences*, 13(2), pp. 299–309. doi: 10.5194/nhess-13-299-2013.

Transportation Research Board (2009) *Critical Issues in Transportation 2009 update, TRB Miscellaneous Publications*. Washington, D.C.: Transportation Research Board. Available at: <http://www.trb.org/Transportationgeneral/Blurbs/161896.aspx>.

Tsai, F., Hwang, J.-H., Chen, L.-C. and Lin, T.-H. (2010) “Post-disaster assessment of landslides in southern Taiwan after 2009 Typhoon Morakot using remote sensing and

spatial analysis,” *Natural Hazards and Earth System Sciences*, 10(10), pp. 2179–2190. doi: 10.5194/nhess-10-2179-2010.

Tzouvaras, M., Kouhartsiouk, D., Agapiou, A., Danezis, C. and Hadjimitsis, D. G. (2019) “The Use of Sentinel-1 Synthetic Aperture Radar (SAR) Images and Open-Source Software for Cultural Heritage: An Example from Paphos Area in Cyprus for Mapping Landscape Changes after a 5.6 Magnitude Earthquake,” *Remote Sensing*, 11(15), p. 1766. doi: 10.3390/rs11151766.

Uemoto, J., Moriyama, T., Nadai, A., Kojima, S. and Umehara, T. (2019) “Landslide detection based on height and amplitude differences using pre- and post-event airborne X-band SAR data,” *Natural Hazards*. Springer Netherlands, 95(3), pp. 485–503. doi: 10.1007/s11069-018-3492-8.

United Nations (2009) *2009 UNISDR Terminology on Disaster Risk Reduction, International Strategy for Disaster Reduction*. Geneva, Switzerland. Available at: <http://www.unisdr.org/we/inform/publications/7817>.

USGS (no date a) *Landsat 5*. Available at: [https://www.usgs.gov/land-resources/nli/landsat/landsat-5?qt-science\\_support\\_page\\_related\\_con=0#qt-science\\_support\\_page\\_related\\_con](https://www.usgs.gov/land-resources/nli/landsat/landsat-5?qt-science_support_page_related_con=0#qt-science_support_page_related_con) (Accessed: December 26, 2019).

USGS (no date b) *USGS EROS Archive - Digital Elevation - Shuttle Radar Topography Mission (SRTM) 1 Arc-Second Global*. Available at: [https://www.usgs.gov/centers/eros/science/usgs-eros-archive-digital-elevation-shuttle-radar-topography-mission-srtm-1-arc?qt-science\\_center\\_objects=0#qt-science\\_center\\_objects](https://www.usgs.gov/centers/eros/science/usgs-eros-archive-digital-elevation-shuttle-radar-topography-mission-srtm-1-arc?qt-science_center_objects=0#qt-science_center_objects) (Accessed: March 6, 2020).

Veci, L. (2016) *Sentinel-1 Toolbox - TOPS Interferometry Tutorial*. Available at: [http://step.esa.int/docs/tutorials/S1TBX TOPSAR Interferometry with Sentinel-1 Tutorial.pdf](http://step.esa.int/docs/tutorials/S1TBX_TOPSAR_Interferometry_with_Sentinel-1_Tutorial.pdf).

Washaya, P., Balz, T. and Mohamadi, B. (2018) “Coherence Change-Detection with Sentinel-1 for Natural and Anthropogenic Disaster Monitoring in Urban Areas,” *Remote Sensing*, 10(7), p. 1026. doi: 10.3390/rs10071026.

Wasowski, J. and Bovenga, F. (2014) “Investigating landslides and unstable slopes with satellite Multi Temporal Interferometry: Current issues and future perspectives,”

*Engineering Geology*. Elsevier B.V., 174, pp. 103–138. doi: 10.1016/j.enggeo.2014.03.003.

Watanabe, M., Thapa, R. B., Ohsumi, T., Fujiwara, H., Yonezawa, C., Tomii, N. and Suzuki, S. (2016) “Detection of damaged urban areas using interferometric SAR coherence change with PALSAR-2,” *Earth, Planets and Space*. Springer Berlin Heidelberg, 68(1), p. 131. doi: 10.1186/s40623-016-0513-2.

Wei, M., Sandwell, D. and Smith-Konter, B. (2010) “Optimal combination of InSAR and GPS for measuring interseismic crustal deformation,” *Advances in Space Research*. COSPAR, 46(2), pp. 236–249. doi: 10.1016/j.asr.2010.03.013.

Whiteley, J. S., Chambers, J. E., Uhlemann, S., Wilkinson, P. B. and Kendall, J. M. (2019) “Geophysical Monitoring of Moisture-Induced Landslides: A Review,” *Reviews of Geophysics*, 57(1), pp. 106–145. doi: 10.1029/2018RG000603.

Wiseman, J. and El-Baz, F. (eds.) (2007) *Remote Sensing in Archaeology, Interdisciplinary Contributions to Archaeology*. New York, NY: Springer New York (Interdisciplinary Contributions To Archaeology). doi: 10.1007/0-387-44455-6.

World Health Organization (2010) *Cyprus: Seismic hazard distribution map*. Available at: <http://data.euro.who.int/e-atlas/europe/countries/cyprus/cyprus-seismic-map.html> (Accessed: December 24, 2019).

World Heritage Centre UNESCO (2007) *Climate Change and World Heritage, World Heritage Reports 22*. Paris. Available at: <https://whc.unesco.org/document/8977>.

Yague-Martinez, N., Prats-Iraola, P., Gonzalez, F. R., Brcic, R., Shau, R., Geudtner, D., Eineder, M. and Bamler, R. (2016) “Interferometric Processing of Sentinel-1 TOPS Data,” *IEEE Transactions on Geoscience and Remote Sensing*. IEEE, 54(4), pp. 2220–2234. doi: 10.1109/TGRS.2015.2497902.

Yalcin, A. (2008) “GIS-based landslide susceptibility mapping using analytical hierarchy process and bivariate statistics in Ardesen (Turkey): Comparisons of results and confirmations,” *CATENA*, 72(1), pp. 1–12. doi: 10.1016/j.catena.2007.01.003.

Yalcin, A., Reis, S., Aydinoglu, A. C. and Yomralioglu, T. (2011) “A GIS-based comparative study of frequency ratio, analytical hierarchy process, bivariate statistics and logistics regression methods for landslide susceptibility mapping in Trabzon, NE

Turkey,” *CATENA*. Elsevier B.V., 85(3), pp. 274–287. doi: 10.1016/j.catena.2011.01.014.

Yan, F., Zhang, Q., Ye, S. and Ren, B. (2019) “A novel hybrid approach for landslide susceptibility mapping integrating analytical hierarchy process and normalized frequency ratio methods with the cloud model,” *Geomorphology*. Elsevier B.V., 327, pp. 170–187. doi: 10.1016/j.geomorph.2018.10.024.

Yang, L. and Qian, D. (2012) “Vulnerability Analysis of Road Networks,” *Journal of Transportation Systems Engineering and Information Technology*. China Association for Science and Technology, 12(1), pp. 105–110. doi: 10.1016/S1570-6672(11)60188-8.

Yao, H., Qin, R. and Chen, X. (2019) “Unmanned Aerial Vehicle for Remote Sensing Applications—A Review,” *Remote Sensing*, 11(12), p. 1443. doi: 10.3390/rs11121443.

Yau, Y. (2009) “Multi-criteria decision making for urban built heritage conservation: application of the analytic hierarchy process,” *Journal of Building Appraisal*, 4(3), pp. 191–205. doi: 10.1057/jba.2008.34.

Yin, Y., Wang, H., Gao, Y. and Li, X. (2010) “Real-time monitoring and early warning of landslides at relocated Wushan Town, the Three Gorges Reservoir, China,” *Landslides*, 7(3), pp. 339–349. doi: 10.1007/s10346-010-0220-1.

Yoshimatsu, H. and Abe, S. (2006) “A review of landslide hazards in Japan and assessment of their susceptibility using an analytical hierarchic process (AHP) method,” *Landslides*, 3(2), pp. 149–158. doi: 10.1007/s10346-005-0031-y.

Yu, C., Li, Z. and Penna, N. T. (2018) “Interferometric synthetic aperture radar atmospheric correction using a GPS-based iterative tropospheric decomposition model,” *Remote Sensing of Environment*. Elsevier, 204(October 2017), pp. 109–121. doi: 10.1016/j.rse.2017.10.038.

Yun, H. W., Kim, J. R., Choi, Y. S. and Lin, S. Y. (2019) “Analyses of time series InSAR signatures for land cover classification: Case studies over dense forestry areas with L-band SAR images,” *Sensors (Switzerland)*, 19(12). doi: 10.3390/s19122830.

Zahid Khalil, R. and Saad-ul-Haque (2018) “InSAR Coherence-based land cover classification of Okara, Pakistan,” *Egyptian Journal of Remote Sensing and Space Science*. National Authority for Remote Sensing and Space Sciences, 21, pp. S23–S28.

doi: 10.1016/j.ejrs.2017.08.005.

Zebker, H. A., Rosen, P. A. and Hensley, S. (1997) “Atmospheric effects in interferometric synthetic aperture radar surface deformation and topographic maps,” *Journal of Geophysical Research: Solid Earth*, 102(B4), pp. 7547–7563. doi: 10.1029/96JB03804.

Zebker, H. A. and Villasenor, J. (1992) “Decorrelation in interferometric radar echoes,” *IEEE Transactions on Geoscience and Remote Sensing*, 30(5), pp. 950–959. doi: 10.1109/36.175330.

Zhou, W., Chen, F. and Guo, H. (2015) “Differential Radar Interferometry for Structural and Ground Deformation Monitoring: A New Tool for the Conservation and Sustainability of Cultural Heritage Sites,” *Sustainability*, 7(2), pp. 1712–1729. doi: 10.3390/su7021712.

Zhu, L., Chen, Y., Gong, H. L., Liu, C. and Wang, R. (2013) “Spatial risk assessment on land subsidence in Beijing, China,” in *20th International Congress on Modelling and Simulation*. Adelaide, Australia. Available at: [www.mssanz.org.au/modsim2013](http://www.mssanz.org.au/modsim2013).



## APPENDIX I – Statistical tests

### 1. ANOVA tests: single factor

#### Sentinel-1A ascending

##### SUMMARY

<i>Groups</i>	<i>Count</i>	<i>Sum</i>	<i>Average</i>	<i>Variance</i>
Pre-event	52	31.5103375	0.605968029	0.00963497
Co-event	52	27.276288	0.524544	0.007515291
Post-event	52	27.198441	0.523046942	0.011553534

##### ANOVA

<i>Source of Variation</i>	<i>SS</i>	<i>df</i>	<i>MS</i>	<i>F</i>	<i>P-value</i>	<i>F crit</i>
Between Groups	0.234139018	2	0.117069509	12.23561315	1.17654E-05	3.055161773
Within Groups	1.463893523	153	0.009567932			
Total	1.698032541	155				

#### Sentinel-1A descending – AOI

##### SUMMARY

<i>Groups</i>	<i>Count</i>	<i>Sum</i>	<i>Average</i>	<i>Variance</i>
Pre-event	52	29.608446	0.569393192	0.029604203
Co-event	52	21.440338	0.412314192	0.023630925
Post-event	52	24.69043	0.474815962	0.023826759

##### ANOVA

<i>Source of Variation</i>	<i>SS</i>	<i>df</i>	<i>MS</i>	<i>F</i>	<i>P-value</i>	<i>F crit</i>
Between Groups	0.65043569	2	0.325217845	12.66064945	8.16297E-06	3.055161773
Within Groups	3.93015623	153	0.025687296			
Total	4.58059192	155				

#### Sentinel-1A – Average

##### SUMMARY

<i>Groups</i>	<i>Count</i>	<i>Sum</i>	<i>Average</i>	<i>Variance</i>
Pre-event	52	30.5593918	0.587680611	0.010488439
Co-event	52	24.358313	0.468429096	0.006286503
Post-event	52	25.9444355	0.498931452	0.011395409

##### ANOVA

<i>Source of Variation</i>	<i>SS</i>	<i>df</i>	<i>MS</i>	<i>F</i>	<i>P-value</i>	<i>F crit</i>
Between Groups	0.39914733	2	0.199573665	21.25358706	7.16058E-09	3.055161773
Within Groups	1.43668787	153	0.009390117			
Total	1.8358352	155				

## Sentinel-1B ascending

### SUMMARY

<i>Groups</i>	<i>Count</i>	<i>Sum</i>	<i>Average</i>	<i>Variance</i>
Pre-event	52	31.0019885	0.596192087	0.011597808
Co-event	52	21.2557515	0.408764452	0.039383789
Post-event	52	35.52187	0.683112885	0.016400019

### ANOVA

<i>Source of Variation</i>	<i>SS</i>	<i>df</i>	<i>MS</i>	<i>F</i>	<i>P-value</i>	<i>F crit</i>
Between Groups	2.044491035	2	1.022245518	45.51295604	3.09061E-16	3.055161773
Within Groups	3.436462445	153	0.022460539			
Total	5.48095348	155				

## Sentinel-1B descending

### SUMMARY

<i>Groups</i>	<i>Count</i>	<i>Sum</i>	<i>Average</i>	<i>Variance</i>
Pre-event	52	29.270858	0.562901115	0.007764885
Co-event	52	19.6603463	0.378083583	0.02595015
Post-event	52	39.260762	0.755014654	0.004943149

### ANOVA

<i>Source of Variation</i>	<i>SS</i>	<i>df</i>	<i>MS</i>	<i>F</i>	<i>P-value</i>	<i>F crit</i>
Between Groups	3.694464184	2	1.847232092	143.3511789	8.45759E-36	3.055161773
Within Groups	1.971567393	153	0.012886061			
Total	5.666031577	155				

## Sentinel-1B – Average

### SUMMARY

<i>Groups</i>	<i>Count</i>	<i>Sum</i>	<i>Average</i>	<i>Variance</i>
Pre-event	52	30.1364233	0.579546601	0.00737082
Co-event	52	20.4580489	0.393424017	0.022393032
Post-event	52	37.391316	0.719063769	0.006327045

### ANOVA

<i>Source of Variation</i>	<i>SS</i>	<i>df</i>	<i>MS</i>	<i>F</i>	<i>P-value</i>	<i>F crit</i>
Between Groups	2.77589701	2	1.387948505	115.3710726	2.81756E-31	3.055161773
Within Groups	1.840635754	153	0.012030299			
Total	4.616532764	155				

## Sentinel-1A and Sentinel-1B ascending

### SUMMARY

<i>Groups</i>	<i>Count</i>	<i>Sum</i>	<i>Average</i>	<i>Variance</i>
Pre-event	52	31.256163	0.601080058	0.006907241
Co-event	52	24.26601975	0.466654226	0.017335408
Post-event	52	31.3601555	0.603079913	0.007066489

### ANOVA

<i>Source of Variation</i>	<i>SS</i>	<i>df</i>	<i>MS</i>	<i>F</i>	<i>P-value</i>	<i>F crit</i>
Between Groups	0.635895379	2	0.31794769	30.46532535	7.29473E-12	3.055161773
Within Groups	1.596766027	153	0.010436379			
Total	2.232661406	155				

## Sentinel-1A and Sentinel-1B descending

### SUMMARY

<i>Groups</i>	<i>Count</i>	<i>Sum</i>	<i>Average</i>	<i>Variance</i>
Pre-event	52	29.439652	0.566147154	0.00944975
Co-event	52	20.55034215	0.395198888	0.015107842
Post-event	52	31.975596	0.614915308	0.007622017

### ANOVA

<i>Source of Variation</i>	<i>SS</i>	<i>df</i>	<i>MS</i>	<i>F</i>	<i>P-value</i>	<i>F crit</i>
Between Groups	1.384533764	2	0.692266882	64.53778435	4.74172E-21	3.055161773
Within Groups	1.641160043	153	0.010726536			
Total	3.025693806	155				

## Sentinel-1A and Sentinel-1B - Average

### SUMMARY

<i>Groups</i>	<i>Count</i>	<i>Sum</i>	<i>Average</i>	<i>Variance</i>
Pre-event	52	30.3479075	0.583613606	0.004301833
Co-event	52	22.40818095	0.430926557	0.008789493
Post-event	52	31.66787575	0.608997611	0.003990601

### ANOVA

<i>Source of Variation</i>	<i>SS</i>	<i>df</i>	<i>MS</i>	<i>F</i>	<i>P-value</i>	<i>F crit</i>
Between Groups	0.96489437	2	0.482447185	84.72940727	1.70065E-25	3.055161773
Within Groups	0.87117828	153	0.005693976			
Total	1.836072649	155				

### Sentinel-1A ascending – AOI

#### SUMMARY

<i>Groups</i>	<i>Count</i>	<i>Sum</i>	<i>Average</i>	<i>Variance</i>
Pre-event	20	11.253141	0.56265705	0.005197518
Co-event	20	9.459158	0.4729579	0.002735179
Post-event	20	11.054951	0.55274755	0.004512817

#### ANOVA

<i>Source of Variation</i>	<i>SS</i>	<i>df</i>	<i>MS</i>	<i>F</i>	<i>P-value</i>	<i>F crit</i>
Between Groups	0.096736826	2	0.048368413	11.65923922	5.69105E-05	3.158842719
Within Groups	0.23646479	57	0.004148505			
Total	0.333201616	59				

### Sentinel-1A descending – AOI

#### SUMMARY

<i>Groups</i>	<i>Count</i>	<i>Sum</i>	<i>Average</i>	<i>Variance</i>
Pre-event	20	10.355876	0.5177938	0.031931101
Co-event	20	8.64388	0.432194	0.023627422
Post-event	20	10.054683	0.50273415	0.016530394

#### ANOVA

<i>Source of Variation</i>	<i>SS</i>	<i>df</i>	<i>MS</i>	<i>F</i>	<i>P-value</i>	<i>F crit</i>
Between Groups	0.083533544	2	0.041766772	1.738135637	0.185037905	3.158842719
Within Groups	1.369689425	57	0.024029639			
Total	1.453222968	59				

### Sentinel-1A – Average – AOI

#### SUMMARY

<i>Groups</i>	<i>Count</i>	<i>Sum</i>	<i>Average</i>	<i>Variance</i>
Pre-event	20	10.804509	0.540225425	0.01138683
Co-event	20	9.051519	0.45257595	0.006125907
Post-event	20	10.554817	0.52774085	0.003239013

#### ANOVA

<i>Source of Variation</i>	<i>SS</i>	<i>df</i>	<i>MS</i>	<i>F</i>	<i>P-value</i>	<i>F crit</i>
Between Groups	0.089920382	2	0.044960191	6.499720334	0.002865749	3.158842719
Within Groups	0.394283254	57	0.00691725			
Total	0.484203636	59				

### Sentinel-1B ascending – AOI

#### SUMMARY

<i>Groups</i>	<i>Count</i>	<i>Sum</i>	<i>Average</i>	<i>Variance</i>
Pre-event	20	10.4197155	0.520985775	0.00784828
Co-event	20	5.911712	0.2955856	0.013045793
Post-event	20	15.020007	0.75100035	0.01062782

#### ANOVA

<i>Source of Variation</i>	<i>SS</i>	<i>df</i>	<i>MS</i>	<i>F</i>	<i>P-value</i>	<i>F crit</i>
Between Groups	2.074096921	2	1.03704846	98.69792378	3.05772E-19	3.158842719
Within Groups	0.598915965	57	0.010507298			
Total	2.673012886	59				

### Sentinel-1B descending – AOI

#### SUMMARY

<i>Groups</i>	<i>Count</i>	<i>Sum</i>	<i>Average</i>	<i>Variance</i>
Pre-event	20	9.9950305	0.499751525	0.003093643
Co-event	20	5.3726643	0.268633215	0.014429365
Post-event	20	15.190088	0.7595044	0.005312033

#### ANOVA

<i>Source of Variation</i>	<i>SS</i>	<i>df</i>	<i>MS</i>	<i>F</i>	<i>P-value</i>	<i>F crit</i>
Between Groups	2.41227833	2	1.206139165	158.4589855	5.22766E-24	3.158842719
Within Groups	0.433865787	57	0.00761168			
Total	2.846144117	59				

### Sentinel-1B – Average – AOI

#### SUMMARY

<i>Groups</i>	<i>Count</i>	<i>Sum</i>	<i>Average</i>	<i>Variance</i>
Pre-event	20	10.207373	0.51036865	0.003318118
Co-event	20	5.64218815	0.282109408	0.008569091
Post-event	20	15.1050475	0.755252375	0.004075334

#### ANOVA

<i>Source of Variation</i>	<i>SS</i>	<i>df</i>	<i>MS</i>	<i>F</i>	<i>P-value</i>	<i>F crit</i>
Between Groups	2.239563922	2	1.119781961	210.4517916	4.79993E-27	3.158842719
Within Groups	0.303288327	57	0.005320848			
Total	2.542852249	59				

### Sentinel-1A and Sentinel-1B ascending – AOI

#### SUMMARY

<i>Groups</i>	<i>Count</i>	<i>Sum</i>	<i>Average</i>	<i>Variance</i>
Pre-event	20	10.83642825	0.541821413	0.004317919
Co-event	20	7.685435	0.38427175	0.004080434
Post-event	20	13.037479	0.65187395	0.005271227

#### ANOVA

<i>Source of Variation</i>	<i>SS</i>	<i>df</i>	<i>MS</i>	<i>F</i>	<i>P-value</i>	<i>F crit</i>
Between Groups	0.723629297	2	0.361814649	79.40580281	3.32125E-17	3.158842719
Within Groups	0.259722013	57	0.004556527			
Total	0.983351311	59				

### Sentinel-1A and Sentinel-1B descending – AOI

#### SUMMARY

<i>Groups</i>	<i>Count</i>	<i>Sum</i>	<i>Average</i>	<i>Variance</i>
Pre-event	20	10.17545325	0.508772663	0.009187403
Co-event	20	7.00827215	0.350413608	0.010045616
Post-event	20	12.6223855	0.631119275	0.004354177

#### ANOVA

<i>Source of Variation</i>	<i>SS</i>	<i>df</i>	<i>MS</i>	<i>F</i>	<i>P-value</i>	<i>F crit</i>
Between Groups	0.792279704	2	0.396139852	50.38409701	2.50541E-13	3.158842719
Within Groups	0.448156718	57	0.007862399			
Total	1.240436423	59				

### Sentinel-1A and Sentinel-1B - Average– AOI

#### SUMMARY

<i>Groups</i>	<i>Count</i>	<i>Sum</i>	<i>Average</i>	<i>Variance</i>
Pre-event	20	10.50594075	0.525297038	0.003559414
Co-event	20	7.346853575	0.367342679	0.003151663
Post-event	20	12.82993225	0.641496613	0.000508376

#### ANOVA

<i>Source of Variation</i>	<i>SS</i>	<i>df</i>	<i>MS</i>	<i>F</i>	<i>P-value</i>	<i>F crit</i>
Between Groups	0.757415334	2	0.378707667	157.3696799	6.17497E-24	3.158842719
Within Groups	0.137169606	57	0.002406484			
Total	0.89458494	59				

## 2. t-tests: two-tailed

### S1A-ASCENDING

	Pre-event	Co-event	Post-event
Pre-event		9.57261E-06	0.000539818
Co-event			0.943077639
Post-event			

### S1A-DESCENDING

	Pre-event	Co-event	Post-event
Pre-event		2.45531E-07	0.010569338
Co-event			0.015453758
Post-event			

### S1A-ASCENDING & DESCENDING

	Pre-event	Co-event	Post-event
Pre-event		9.41403E-10	0.000233505
Co-event			0.059862792
Post-event			

### S1B-ASCENDING

	Pre-event	Co-event	Post-event
Pre-event		4.36485E-14	0.001191176
Co-event			8.34419E-11
Post-event			

### S1B-DESCENDING

	Pre-event	Co-event	Post-event
Pre-event		1.27005E-10	1.33418E-16
Co-event			2.73028E-22
Post-event			

### S1B-ASCENDING & DESCENDING

	Pre-event	Co-event	Post-event
Pre-event		5.28205E-18	1.69375E-10
Co-event			8.5456E-18
Post-event			

### S1A & S1B-ASCENDING

	Pre-event	Co-event	Post-event
Pre-event		1.61673E-15	0.911695689
Co-event			2.9423E-07
Post-event			

### S1A & S1B-DESCENDING

	Pre-event	Co-event	Post-event
Pre-event		2.77832E-11	0.012479896
Co-event			1.61829E-16
Post-event			

### S1A & S1B

	Pre-event	Co-event	Post-event
Pre-event		6.09313E-18	0.071081328
Co-event			3.92623E-15
Post-event			

### S1A-ASCENDING - AOI

	Pre-event	Co-event	Post-event
Pre-event		0.00122976	0.617983269
Co-event			0.002076731
Post-event			

### S1A-DESCENDING - AOI

	Pre-event	Co-event	Post-event
Pre-event		0.038996251	0.763966871
Co-event			0.020244528
Post-event			

### S1A-ASCENDING & DESCENDING - AOI

	Pre-event	Co-event	Post-event
Pre-event		0.002198526	0.620935556
Co-event			0.000142155
Post-event			



### S1B-ASCENDING - AOI

	Pre-event	Co-event	Post-event
Pre-event		3.13013E-10	8.52148E-09
Co-event			1.04638E-11
Post-event			

### S1B-DESCENDING - AOI

	Pre-event	Co-event	Post-event
Pre-event		9.20315E-07	1.30066E-10
Co-event			7.78797E-14
Post-event			

### S1B-ASCENDING & DESCENDING - AOI

	Pre-event	Co-event	Post-event
Pre-event		6.48861E-10	1.31486E-13
Co-event			1.06476E-13
Post-event			

### S1A & S1B-ASCENDING - AOI

	Pre-event	Co-event	Post-event
Pre-event		7.32742E-12	9.62576E-06
Co-event			2.17045E-10
Post-event			

### S1A & S1B-DESCENDING - AOI

	Pre-event	Co-event	Post-event
Pre-event		2.76945E-05	8.15739E-05
Co-event			5.55534E-14
Post-event			

### S1A & S1B - AOI

	Pre-event	Co-event	Post-event
Pre-event		1.09459E-08	3.08208E-09
Co-event			4.60317E-14
Post-event			

### 3. Covariance

#### S1A - Ascending

	Pre-event	Co-event	Post-event
Pre-event	0.0094		
Co-event	0.0014	0.0074	
Post-event	-0.0025	-0.0017	0.0113

#### S1B - Ascending

	Pre-event	Co-event	Post-event
Pre-event	0.0114		
Co-event	0.0166	0.0386	
Post-event	-0.0026	-0.0015	0.0161

#### S1A & S1B - Ascending

	Pre-event	Co-event	Post-event
Pre-event	0.0068		
Co-event	0.0083	0.0170	
Post-event	-0.0014	-0.0017	0.0069

#### S1A - Descending

	Pre-event	Co-event	Post-event
Pre-event	0.0290		
Co-event	0.0083	0.0232	
Post-event	-0.0062	0.0074	0.0234

#### S1B - Descending

	Pre-event	Co-event	Post-event
Pre-event	0.0076		
Co-event	0.0030	0.0255	
Post-event	-0.0002	0.0021	0.0048

#### S1A & S1B - Descending

	Pre-event	Co-event	Post-event
Pre-event	0.0093		
Co-event	0.0016	0.0148	
Post-event	-0.0007	0.0026	0.0075

**S1A - Average**

	Pre-event	Co-event	Post-event
Pre-event	0.0103		
Co-event	0.0017	0.0062	
Post-event	-0.0021	0.0023	0.0112

**S1B - Average**

	Pre-event	Co-event	Post-event
Pre-event	0.0072		
Co-event	0.0095	0.0220	
Post-event	-0.0011	-0.0020	0.0062

**S1A & S1B - Average**

	Pre-event	Co-event	Post-event
Pre-event	0.0042		
Co-event	0.0030	0.0086	
Post-event	-0.0008	-0.0004	0.0039

**S1A - Ascending - AOI**

	Pre-event	Co-event	Post-event
Pre-event	0.0049		
Co-event	-0.0015	0.0026	
Post-event	0.0010	-0.0013	0.0043

**S1B - Ascending - AOI**

	Pre-event	Co-event	Post-event
Pre-event	0.0075		
Co-event	0.0065	0.0124	
Post-event	0.0034	0.0018	0.0101

**S1A & S1B - Ascending - AOI**

	Pre-event	Co-event	Post-event
Pre-event	0.0041		
Co-event	0.0029	0.0039	
Post-event	0.0013	-0.0002	0.0050

**S1A - Descending - AOI**

	Pre-event	Co-event	Post-event
Pre-event	0.0303		
Co-event	0.0122	0.0224	
Post-event	-0.0002	0.0117	0.0157

**S1B - Descending - AOI**

	Pre-event	Co-event	Post-event
Pre-event	0.0029		
Co-event	-0.0017	0.0137	
Post-event	-0.0001	0.0031	0.0050

**S1A & S1B - Descending - AOI**

	Pre-event	Co-event	Post-event
Pre-event	0.0087		
Co-event	0.0012	0.0095	
Post-event	0.0007	0.0049	0.0041

**S1A - Average - AOI**

	Pre-event	Co-event	Post-event
Pre-event	0.0108		
Co-event	0.0025	0.0058	
Post-event	0.0011	0.0021	0.0031

**S1B - Average - AOI**

	Pre-event	Co-event	Post-event
Pre-event	0.0032		
Co-event	0.0018	0.0081	
Post-event	0.0018	-0.0001	0.0039

**S1A & S1B - Average - AOI**

	Pre-event	Co-event	Post-event
Pre-event	0.0034		
Co-event	0.0006	0.0030	
Post-event	0.0007	-0.0001	0.0005

#### 4. Correlation

##### **S1A - Ascending**

	Pre-event	Co-event	Post-event
Pre-event	1.0000		
Co-event	0.1695	1.0000	
Post-event	-0.2380	-0.1913	1.0000

##### **S1B - Ascending**

	Pre-event	Co-event	Post-event
Pre-event	1.0000		
Co-event	0.7914	1.0000	
Post-event	-0.1931	-0.0606	1.0000

##### **S1A & S1B - Ascending**

	Pre-event	Co-event	Post-event
Pre-event	1.0000		
Co-event	0.7724	1.0000	
Post-event	-0.1982	-0.1537	1.0000

##### **S1A - Descending**

	Pre-event	Co-event	Post-event
Pre-event	1.0000		
Co-event	0.3213	1.0000	
Post-event	-0.2369	0.3183	1.0000

##### **S1B - Descending**

	Pre-event	Co-event	Post-event
Pre-event	1.0000		
Co-event	0.2191	1.0000	
Post-event	-0.0331	0.1905	1.0000

##### **S1A & S1B - Descending**

	Pre-event	Co-event	Post-event
Pre-event	1.0000		
Co-event	0.1395	1.0000	
Post-event	-0.0804	0.2514	1.0000

**S1A - Average**

	Pre-event	Co-event	Post-event
Pre-event	1.0000		
Co-event	0.2197	1.0000	
Post-event	-0.1939	0.2730	1.0000

**S1B - Average**

	Pre-event	Co-event	Post-event
Pre-event	1.0000		
Co-event	0.7526	1.0000	
Post-event	-0.1675	-0.1673	1.0000

**S1A & S1B - Average**

	Pre-event	Co-event	Post-event
Pre-event	1.0000		
Co-event	0.4898	1.0000	
Post-event	-0.1892	-0.0625	1.0000

**S1A - Ascending - AOI**

	Pre-event	Co-event	Post-event
Pre-event	1.0000		
Co-event	-0.4314	1.0000	
Post-event	0.2137	-0.3960	1.0000

**S1B - Ascending - AOI**

	Pre-event	Co-event	Post-event
Pre-event	1.0000		
Co-event	0.6759	1.0000	
Post-event	0.3963	0.1629	1.0000

**S1A & S1B - Ascending - AOI**

	Pre-event	Co-event	Post-event
Pre-event	1.0000		
Co-event	0.7289	1.0000	
Post-event	0.2920	-0.0418	1.0000

**S1A - Descending - AOI**

	Pre-event	Co-event	Post-event
Pre-event	1.0000		
Co-event	0.4687	1.0000	
Post-event	-0.0091	0.6238	1.0000

**S1B - Descending - AOI**

	Pre-event	Co-event	Post-event
Pre-event	1.0000		
Co-event	-0.2697	1.0000	
Post-event	-0.0289	0.3681	1.0000

**S1A & S1B - Descending - AOI**

	Pre-event	Co-event	Post-event
Pre-event	1.0000		
Co-event	0.1309	1.0000	
Post-event	0.1195	0.7720	1.0000

**S1A - Average - AOI**

	Pre-event	Co-event	Post-event
Pre-event	1.0000		
Co-event	0.3135	1.0000	
Post-event	0.1887	0.4869	1.0000

**S1B - Average - AOI**

	Pre-event	Co-event	Post-event
Pre-event	1.0000		
Co-event	0.3577	1.0000	
Post-event	0.5285	-0.0121	1.0000

**S1A & S1B - Average - AOI**

	Pre-event	Co-event	Post-event
Pre-event	1.0000		
Co-event	0.1855	1.0000	
Post-event	0.5724	-0.1002	1.0000

## APPENDIX II – ROC analysis

### Coherence Difference – Sentinel-1B average

JROCFIT:

Maximum likelihood estimation of a binormal ROC curve from categorical rating data.

Java translation by John Eng, M.D.

The Russell H. Morgan Department of Radiology and Radiological Science

Johns Hopkins University, Baltimore, Maryland, USA

Version 2.0.1, June 2017

Original Fortran program ROCFIT by Charles Metz and colleagues

Department of Radiology, University of Chicago

January 1994

-----

#### DATA CHARACTERISTICS:

Data collected in 4 categories with category 4 representing strongest evidence of positivity (e.g., that abnormality is present).

Number of actually negative cases = 96

Number of actually positive cases = 19

#### RESPONSE DATA:

Category	1	2	3	4
Actually negative cases	72	23	1	0
Actually positive cases	2	5	11	1



OBSERVED OPERATING POINTS:

FPF: 0.0000 0.0000 0.0104 0.2500 1.0000

TPF: 0.0000 0.0526 0.6316 0.8947 1.0000

INITIAL VALUES OF PARAMETERS:

A = 2.1629

B = 1.1754

Z(K): 0.6742 2.3114 2.5621

LOGL = -94.0040

FINAL VALUES OF PARAMETERS:

Procedure converges after 7 iterations.

A = 1.6297

B = 0.5598

Z(K): 0.6745 2.3110 5.8050

LOGL = -78.2751

VARIANCE-COVARIANCE MATRIX:

A 0.2694 0.1069 0.0131 -0.0251 -0.6464

B 0.1069 0.0665 0.0034 -0.0450 -0.4870

Z(1) 0.0131 0.0034 0.0193 0.0093 -0.0122

Z(2) -0.0251 -0.0450 0.0093 0.1408 0.4215

Z(3) -0.6464 -0.4870 -0.0122 0.4215 4.4709

CORRELATION MATRIX:

A	1.0000	0.7989	0.1822	-0.1291	-0.5890
B	0.7989	1.0000	0.0961	-0.4650	-0.8934
Z(1)	0.1822	0.0961	1.0000	0.1777	-0.0416
Z(2)	-0.1291	-0.4650	0.1777	1.0000	0.5313
Z(3)	-0.5890	-0.8934	-0.0416	0.5313	1.0000

SUMMARY OF ROC CURVE:

Area = 0.9225

Std. Dev. (Area) = 0.0495

ESTIMATED BINORMAL ROC CURVE WITH ASYMMETRIC 95% CONFIDENCE

INTERVAL:

FPF	TPF	95% Conf. Interv.
0.005	0.5744	(0.2757, 0.8342)
0.010	0.6282	(0.3504, 0.8505)
0.020	0.6843	(0.4316, 0.8711)
0.030	0.7179	(0.4798, 0.8857)
0.040	0.7420	(0.5133, 0.8972)
0.050	0.7608	(0.5385, 0.9067)
0.060	0.7761	(0.5583, 0.9149)
0.070	0.7891	(0.5745, 0.9220)
0.080	0.8004	(0.5881, 0.9283)
0.090	0.8103	(0.5996, 0.9339)
0.100	0.8192	(0.6097, 0.9389)
0.110	0.8272	(0.6185, 0.9435)

0.120 0.8344 (0.6263, 0.9476)  
 0.130 0.8411 (0.6333, 0.9513)  
 0.140 0.8473 (0.6396, 0.9547)  
 0.150 0.8530 (0.6453, 0.9578)  
 0.200 0.8767 (0.6680, 0.9701)  
 0.250 0.8948 (0.6842, 0.9786)  
 0.300 0.9093 (0.6967, 0.9845)  
 0.400 0.9316 (0.7155, 0.9919)  
 0.500 0.9484 (0.7298, 0.9959)  
 0.600 0.9617 (0.7419, 0.9981)  
 0.700 0.9728 (0.7530, 0.9992)  
 0.800 0.9822 (0.7642, 0.9998)  
 0.900 0.9905 (0.7775, 1.0000)  
 0.950 0.9946 (0.7871, 1.0000)

ESTIMATES OF EXPECTED OPERATING POINTS ON FITTED ROC CURVE:

Expected Operating Point ( FPF , TPF )	95% C.I. of Lower Bound ( FPF , TPF )	95% C.I. of Upper Bound ( FPF , TPF )
(0.0000, 0.0526)	(0.0000, 0.0000)	(0.0484, 0.7581)
(0.0104, 0.6316)	(0.0012, 0.4699)	(0.0576, 0.7727)
(0.2500, 0.8947)	(0.1718, 0.8642)	(0.3439, 0.9199)

WARNINGS AND ERROR MESSAGES:

Chi-square goodness of fit not calculated because some expected cell frequencies are less than 5.

Summary statistics:

Number of Cases: 115

Number Correct: 107

Accuracy: 93%

Sensitivity: 63.2%

Specificity: 99%

Positive Cases Missed: 7

Negative Cases Missed: 1

(A rating of 3 or greater is considered positive.)

Fitted ROC Area: 0.922

Empirical ROC Area: 0.897

**Normalised Coherence Difference – Sentinel-1B average**

JROCFIT:

Maximum likelihood estimation of a binormal ROC curve from categorical rating data.

Java translation by John Eng, M.D.

The Russell H. Morgan Department of Radiology and Radiological Science

Johns Hopkins University, Baltimore, Maryland, USA

Version 2.0.1, June 2017

Original Fortran program ROCFIT by Charles Metz and colleagues

Department of Radiology, University of Chicago

January 1994

-----

DATA CHARACTERISTICS:

Data collected in 4 categories with category 4 representing strongest evidence of positivity (e.g., that abnormality is present).

Number of actually negative cases = 96

Number of actually positive cases = 19

RESPONSE DATA:

Category	1	2	3	4
Actually negative cases	82	13	1	0
Actually positive cases	1	4	6	8

OBSERVED OPERATING POINTS:

FPF: 0.0000 0.0000 0.0104 0.1458 1.0000

TPF: 0.0000 0.4211 0.7368 0.9474 1.0000

INITIAL VALUES OF PARAMETERS:

A = 2.8001

B = 1.0704

Z(K): 1.0545 2.3114 2.5621

LOGL = -70.4433

FINAL VALUES OF PARAMETERS:

Procedure converges after 7 iterations.

A = 2.3971

B = 0.7527

Z(K): 1.0540 2.3272 3.4536

LOGL = -66.5271

VARIANCE-COVARIANCE MATRIX:

A	0.6424	0.2726	0.0243	-0.0485	-0.4097
B	0.2726	0.1458	0.0056	-0.0633	-0.2849
Z(1)	0.0243	0.0056	0.0248	0.0148	0.0067
Z(2)	-0.0485	-0.0633	0.0148	0.1381	0.2240
Z(3)	-0.4097	-0.2849	0.0067	0.2240	0.7945

CORRELATION MATRIX:

A	1.0000	0.8909	0.1927	-0.1629	-0.5735
B	0.8909	1.0000	0.0930	-0.4460	-0.8372
Z(1)	0.1927	0.0930	1.0000	0.2532	0.0479
Z(2)	-0.1629	-0.4460	0.2532	1.0000	0.6762
Z(3)	-0.5735	-0.8372	0.0479	0.6762	1.0000

SUMMARY OF ROC CURVE:

Area = 0.9723

Std. Dev. (Area) = 0.0232

ESTIMATED BINORMAL ROC CURVE WITH ASYMMETRIC 95% CONFIDENCE

INTERVAL:

FPF	TPF	95% Conf. Interv.
0.005	0.6765	(0.3336, 0.9108)
0.010	0.7408	(0.4421, 0.9246)

0.020 0.8026 (0.5494, 0.9427)  
0.030 0.8367 (0.6054, 0.9549)  
0.040 0.8597 (0.6406, 0.9639)  
0.050 0.8767 (0.6648, 0.9707)  
0.060 0.8900 (0.6826, 0.9760)  
0.070 0.9008 (0.6964, 0.9802)  
0.080 0.9098 (0.7073, 0.9835)  
0.090 0.9174 (0.7162, 0.9862)  
0.100 0.9240 (0.7237, 0.9884)  
0.110 0.9297 (0.7301, 0.9902)  
0.120 0.9348 (0.7355, 0.9917)  
0.130 0.9393 (0.7403, 0.9929)  
0.140 0.9434 (0.7445, 0.9940)  
0.150 0.9471 (0.7483, 0.9948)  
0.200 0.9611 (0.7624, 0.9975)  
0.250 0.9706 (0.7719, 0.9988)  
0.300 0.9774 (0.7788, 0.9994)  
0.400 0.9863 (0.7887, 0.9998)  
0.500 0.9917 (0.7957, 1.0000)  
0.600 0.9952 (0.8012, 1.0000)  
0.700 0.9974 (0.8059, 1.0000)  
0.800 0.9988 (0.8104, 1.0000)  
0.900 0.9996 (0.8153, 1.0000)  
0.950 0.9999 (0.8185, 1.0000)

ESTIMATES OF EXPECTED OPERATING POINTS ON FITTED ROC CURVE:

Expected Operating Point	95% C.I. of Lower Bound	95% C.I. of Upper Bound
( FPF , TPF )	( FPF , TPF )	( FPF , TPF )
(0.0003, 0.4198)	(0.0000, 0.0646)	(0.0439, 0.8670)
(0.0100, 0.7407)	(0.0011, 0.5387)	(0.0549, 0.8837)
(0.1460, 0.9456)	(0.0865, 0.9149)	(0.2280, 0.9668)

WARNINGS AND ERROR MESSAGES:

Chi-square goodness of fit not calculated because some expected cell frequencies are less than 5.

Summary statistics:

Number of Cases: 115

Number Correct: 109

Accuracy: 94.8%

Sensitivity: 73.7%

Specificity: 99%

Positive Cases Missed: 5

Negative Cases Missed: 1

(A rating of 3 or greater is considered positive.)

Fitted ROC Area: 0.972

Empirical ROC Area: 0.952